

FLUID AND HEAT FLOW IN TUBES
OF ARBITRARY CROSS-SECTION

by

Charles W. Rapley
B.Sc.(Dunelm), M.Sc.(Dunelm),
C.Eng., M.I.Mech.E.

Thesis submitted for the degree of
Doctor of Philosophy
in the Faculty of Engineering
University of London
and
for the Diploma of Membership
of Imperial College

Department of Mechanical Engineering,
Imperial College of Science and
Technology,
London. SW 7

June, 1980

ABSTRACT

A numerical finite-difference calculation method has been developed from an existing recirculating flow procedure for application to fully developed flow and heat transfer in straight passages of arbitrary cross-section. The method is formulated with reference to an orthogonal curvilinear co-ordinate mesh which is fitted exactly into each passage shape. For turbulent flows, the Reynolds stresses are calculated from simplified algebraic forms of their general transport equations, previously derived for square duct flow calculations and coupled, in this study, with a turbulence model in which transport equations are solved for turbulence kinetic energy and its dissipation rate. This turbulent stress model enabled secondary flows to be included in the non-circular passage calculations.

Predictions are presented for 28 passage geometries and compared with available analytical or numerical solutions and experimental data. The laminar flow and heat transfer calculations are in good agreement with previous solutions. The turbulent flow predictions of local secondary and axial velocity, wall shear stress and Nusselt number are in reasonable agreement with experiment for the fully-developed flow cases. The predicted turbulence structure is however in less satisfactory agreement with the measurements, particularly near the passage walls where turbulence kinetic energy and the anisotropy of the cross-plane normal stresses are generally under-predicted. The calculated friction factors and mean Nusselt numbers are also about 10% less than the measurements. These shortcomings are believed to be mainly due to

(ii)

the values of the empirical constants used in the algebraic stress model which were selected to give reasonable secondary flows but made the model relatively insensitive to the damping effect of the walls. The calculations also show that although the secondary velocities are usually only about 1% of the mean axial velocity, they exert a considerable influence on local mean flow distributions.

ACKNOWLEDGEMENTS

It is with pleasure and sincere thanks that I acknowledge the guidance and encouragement received from my Supervisor, Dr A. D. Gosman. His kindly and constructive criticisms of my work and patience at all times have been of much value, particularly with the intermittent nature of the present work which has been carried out on a part-time basis.

I would like to acknowledge the helpful and informative discussions enjoyed with many of the research and academic staff in the Mechanical Engineering Department at Imperial College, in particular Dr M. M. Gibson, Gordon Reece, Richard Johns, Andrew Pollard and Vinoth Ramachandra.

I am grateful for the support received from Sunderland Polytechnic which has played a significant part in enabling me to carry out this course of research. I am particularly indebted to the Manager of the Computer Unit, Mr Len Walker, and his staff for providing the facilities for carrying out much of the computing work, and to Miss E. Moss for typing this thesis.

Lastly, but by no means least, I am especially grateful to my wife Moira and daughter Lyn for their unfailing support throughout this research effort.

CONTENTS

	page
ABSTRACT	i
ACKNOWLEDGEMENTS	iii
CONTENTS	iv
CHAPTER 1 INTRODUCTION	
1.1 Background to the present work	1
1.2 Secondary flows in non-circular passages	2
1.3 The present contribution	3
1.4 Contents of the thesis	5
CHAPTER 2 THE BASIC THEORETICAL PROBLEM	
2.1 Introduction	7
2.2 Equations of motion	7
2.3 Scalar transport	8
2.4 The equations in general orthogonal co-ordinates	9
2.5 Closure	14
CHAPTER 3 REVIEW OF PREVIOUS WORK	
3.1 Introduction	15
3.2 Experimental studies of the flow field	15
3.3 Experimental heat transfer	30
3.4 Theoretical studies	39
3.5 Closure	66

	page
CHAPTER 4 CLOSURE OF THE GOVERNING EQUATIONS FOR TURBULENT FLOW AND HEAT TRANSFER	
4.1 Introduction	68
4.2 The algebraic stress transport model	68
4.3 Transport equations for k and ϵ	74
4.4 The turbulent heat flux model	76
4.5 Summary of the equations solved	78
4.6 Boundary conditions	79
4.7 Empirical constants	82
4.8 Closure	84
CHAPTER 5 SOLUTION PROCEDURE	
5.1 Introduction	85
5.2 The finite-difference grid	86
5.3 The finite-difference equations	87
5.4 The SIMPLE solution method	96
5.5 The near-boundary control volumes	99
5.6 The Thomas algorithm	104
5.7 Summary of overall solution procedure	105
5.8 Grid generation	106
5.9 Convergence and accuracy	107
5.10 Closure	115

	page
CHAPTER 6 LAMINAR FLOW PREDICTIONS	
6.1 Introduction	116
6.2 Elliptical ducts	117
6.3 Isosceles triangular ducts	120
6.4 Axial flow in rod bundles	121
6.5 Closure	123
CHAPTER 7 TURBULENT FLOW PREDICTIONS	
7.1 Introduction	124
7.2 Circular pipe	125
7.3 Square duct	129
7.4 Square duct with one rough wall	134
7.5 Rectangular ducts	138
7.6 Equilateral triangular duct	142
7.7 Acute-angles isosceles triangular ducts	147
7.8 Elliptical ducts	152
7.9 Axial flow passages in triangular array rod bundles	156
7.10 Closure	174
CHAPTER 8 HEAT TRANSFER PREDICTIONS	
8.1 Introduction	177
8.2 Laminar heat transfer	180
8.3 Turbulent heat transfer	188
8.4 Closure	204

	page
CHAPTER 9 SUMMARY AND CONCLUSIONS	
9.1 Introduction	206
9.2 Achievements and limitations of the present work	206
9.3 Overall comparison of predictions	210
9.4 Recommendations for further work	216
REFERENCES	220
NOMENCLATURE	233
APPENDICES	
1 Publications arising from the present work	238
2 The modelled Reynolds stress transport equations	246
3 General orthogonal co-ordinate transformations	250
4 Modelling the turbulent heat flux transport equations	252
5 Orthogonal curvilinear grid calculation method	254
6 Source terms in the finite-difference equations	257
7 Tri-diagonal matrix algorithm (TDMA)	262
8 Block adjustment	263
THE FIGURES	264

1.1 Background to the present work

In recent years, the rising demand for energy and the consequent concern for its conservation has increased the need for compact, highly rated and efficient heat exchangers for a wide range of applications. This has led to an urgent need for the detailed knowledge of flow and heat transfer in non-circular passages, required as part of the input for the optimum design of such heat exchangers.

An involvement in the gas turbine regenerator aspect of this work (e.g. Bayley and Rapley, 1965; Rapley et al, 1974; Rapley, 1978) has led the present author into a wider interest in the problem of flow and heat transfer in arbitrary-shaped passages. It was readily apparent that the bulk of knowledge available was based on experiment, most of which provided only (and sometimes conflicting) overall characteristics. The development of non-circular passage design for compact heat exchangers was mainly by 'trial and error' make-and-test methods.

The demand for more detailed knowledge and for more systematic methods of development was also apparent, particularly in such important applications as the cooling and heating processes in nuclear reactors, gas turbines, all kinds of waste-heat recovery, chemical and other process and power plant. An S.R.C. Round Table meeting on convective heat and mass transfer in September 1975 (Science Research Council, 1975) echoed this demand as successive

speakers representing the Nuclear Power, Gas Turbine, Chemical Engineering and related industries made pleas for 'further research on ducts of non-circular cross-section'.

The work reported in this thesis is the present author's response to this need for more research in non-circular ducts and for more systematic methods in the design and optimisation of passage flows and heat transfer. With the almost overwhelming variety of passage shapes, flow and heat transfer conditions that could be of interest, a theoretical approach, using the recently developed computer-based numerical methods of analysis, appeared to offer the most effective path. The immediate objective of the present work is to provide a base for such an approach by the development of a calculation procedure for fully developed flow and heat transfer in straight, arbitrary-shaped passages, capable of predicting the main local and overall features of these flows with the minimum of complexity in the procedure. This latter restriction was included as part of the aim to produce a realistic design tool for this class of flows.

1.2 Secondary flows in non-circular passages

Turbulent flows in straight non-circular passages are considerably more complex than those in circular ducts, due to the presence of turbulence-driven secondary flow which causes the main flow to spiral in the axial direction. Here the term 'secondary flow' refers to a cross-flow field in a plane that is normal to the axial direction. These flows are relatively weak compared with the main flow, but can

have significant influence on the local mean flow characteristics. Indeed, the distortions caused to the axial velocity distribution were the main early evidence of the existence of these flows in non-circular channels (see the rectangular and triangular duct isovel contours measured by Nikuradse (1926) and reproduced in figure 3.2.1). The general character of these secondary motions, as deduced from experiment for various passage shapes are indicated in figures 3.2.2 to 3.2.5. In this thesis, secondary flow and cross-flow refer to the same motions.

Prandtl suggested that turbulence-driven secondary flows be identified as of the 'second kind', to distinguish them from those of the 'first kind' which, unlike the former, can occur in laminar flow as well, being due to external influences such as convergence, divergence or lateral curvature of the axial flow, or to the lateral motion of a passage wall. Secondary flows of the first kind, if present, will normally dominate the usually much weaker second kind flows. Studies of secondary flow of the first kind have been reported elsewhere (e.g. Patankar et al, 1975) and are outside the scope of the present work.

1.3 The present contribution

In the present study a numerical finite-difference calculation procedure has been developed for application to fully developed steady laminar and turbulent flow and heat transfer in straight passages of arbitrary cross-section. The turbulent stresses are calculated from simplified algebraic forms of the general transport equations for these stresses, first proposed for the calculation of

square duct flows by Launder and Ying (1973) and further analysed by Gessner and Emery (1976).

The equations solved for the flow, stress, turbulence and enthalpy fields have been formulated with reference to a curvilinear orthogonal co-ordinate system which is generated in such a way that the boundaries of the co-ordinate system coincide with the passage boundaries.

The calculation method so developed has been applied to a wide range of laminar and turbulent passage flows, with and without heat transfer. The results of these calculations have been compared with analytical or previous numerical solutions and with experimental data. Such comparisons have been used to validate the calculation method and demonstrate its accuracy and flexibility of application. These comparisons have also enabled a detailed examination to be made of the turbulent stress model used and thus to identify its strengths and weaknesses. In addition the predictions obtained have enabled an extensive study to be made of the local and overall characteristics of this class of flows and, in particular, have allowed some useful general observations to be made on the origin and maintenance of turbulence-driven secondary flow. Finally, the method has been used to clarify the consistency of various experimental measurements and to investigate effects in the flow that may influence measurements, such as that of the containing end walls in an experimental rod-bundle test rig.

1.4 Contents of the thesis

The thesis is divided into nine chapters of which Chapters 6 to 8 present the predictions obtained from the present calculation method. The initial mathematical problem is stated and formulated in orthogonal curvilinear co-ordinates in Chapter 2. This is followed by a review of relevant experimental and previous theoretical work in Chapter 3. This Chapter contains tables chronologically listing the main experimental investigations which have been performed with some details of the measurements made and instrumentation used.

The methods used to calculate the turbulent stresses and heat fluxes required for solution of the governing equations are the subject of Chapter 4. This chapter also contains a summary of the boundary conditions for each main variable solved. The re-casting of the equations into a general form and the discretization into finite-difference form is described in Chapter 5. The solution method for these equations is also presented in this chapter, together with an appraisal of its accuracy.

Chapter 6 contains comparisons of the laminar flow predictions with existing theoretical solutions for three different passage shapes. The turbulent flow predictions are presented and analysed in extensive detail in Chapter 7. Flows in eight different passage shapes with a wide range of geometry and flow conditions are compared with experiment, and where possible with previous calculations to assess the performance of the calculation method developed. The heat transfer solutions, obtained for both laminar and turbulent flow in a variety of passage shapes are described and compared with previous analysis and experiment in Chapter 8.

In Chapter 9, a summary is made of the present achievements and limitations and some overall observations are drawn from the detailed predictions of the previous three chapters. This final chapter then concludes with suggestions for further work.

Lists of references and nomenclature follow the final chapter, together with the appendices which provide supplementary details of the formulation and solution of the mathematical problem. The thesis terminates with the figures.

2.1 Introduction

In this chapter the theoretical problem is stated in the form of time-averaged partial differential conservation equations representing the flow and the transport of a scalar quantity. The equations are first presented in Cartesian tensor notation to take advantage of the compactness and physical clarity which these equations offer. The further relationships required for closure of the equations is discussed and then they are finally presented in general orthogonal co-ordinate form appropriate to fully-developed flow in arbitrary shaped ducts.

2.2 Equations of motion

The Reynolds equations for a steady, incompressible, time-averaged turbulent flow can be written in Cartesian tensor notation as (Tennekes and Lumley, 1972):

$$\partial(\rho U_i U_j) / \partial x_i = - \partial p / \partial x_j - \partial(\tau_{ij}) / \partial x_i \quad (2.2.1)$$

and the continuity equation as

$$\partial(\rho U_i) / \partial x_i = 0 \quad (2.2.2)$$

The stress tensor T_{ij} is the sum of the viscous stress tensor τ_{ij} and the turbulent (Reynolds) stress tensor t_{ij} . The viscous stress tensor is related to the mean strain rate in a Newtonian fluid (Hinze, 1975) by:

$$\tau_{ij} = -\mu(\partial U_i/\partial x_j + \partial U_j/\partial x_i) \quad (2.2.3)$$

and the Reynolds stress tensor is, by definition, linked to the fluctuating velocities u by

$$t_{ij} = \rho \overline{u_i u_j} \quad (2.2.4)$$

Equations (2.2.1) can be applied to laminar flow by setting $T_{ij} = \tau_{ij}$, which, together with the appropriate boundary conditions, yields a closed set of equations. Closure for time-averaged turbulent flows is obtained by representing the Reynolds stresses in terms of calculable properties of the flow - a process known as 'turbulence modelling', which has been the source of much effort and publication in recent years.

2.3 Scalar transport

The steady, low speed turbulent transport of a scalar quantity C (e.g. enthalpy) can be represented in time averaged terms by partial differential equations of the form (Hinze, 1975):

$$\partial(\rho U_i C)/\partial x_i = \partial(D_c \partial C/\partial x_i - \overline{u_i C})/\partial x_i + S_c \quad (2.3.1)$$

The left-hand-side of equations (2.3.1) represents the convective transport, the first term on the right-hand-side the diffusive

transport and the term S_c the source or sink of C. D_c stands for the molecular diffusivity of C while $\overline{u_i c}$ is the turbulent scalar flux in direction x_i .

For laminar flow, the turbulent scalar flux is zero and the solution of equation (2.3.1) is then in principle possible for a given velocity field and boundary conditions. For turbulent flow however, the turbulent scalar flux is required to be represented (modelled) in terms of calculable quantities before closure can be obtained.

2.4 The equations in general - orthogonal co-ordinates

A co-ordinate frame is required for the foregoing partial differential equations that can be fitted exactly into any passage cross-sectional shape. This requirement disqualifies conventional systems such as rectangular and polar-cylindrical and leaves a choice mainly between orthogonal curvilinear and non-orthogonal co-ordinates. The orthogonal curvilinear system was adopted in the present study on the grounds that it is less complex, particularly near boundary surfaces where boundary conditions need to be applied, and thus is more easily incorporated into the numerical procedure originally devised for the conventional systems.

The Reynolds equations (2.2.1), continuity equation (2.2.2) and scalar transport equation (2.3.1) can be expressed in general-orthogonal co-ordinate form by the novel transformation procedure recently proposed by Pope (1978). In this procedure, vectors and tensors are represented in terms of their components in the direction

of their orthogonal co-ordinate lines relative to the Cartesian system. In this way a relatively compact orthogonal co-ordinate form of the equations can be obtained directly from the Cartesian tensor version. The transformation relations required are given in Appendix 3 with any further derivations and details available in Pope (1978). The equations resulting from transformation of (2.2.1) and (2.2.2) are given as equations A3.5 and A3.6 which can now be expressed in terms of the orthogonal co-ordinates y_1 , y_2 and y_3 where directions y_1 and y_2 are in the cross-plane and y_3 in the axial direction as shown in figure 2.4.1. The corresponding metric coefficients are h_1 , h_2 and h_3 . The local radii of curvature r_1 and r_2 , along co-ordinate lines y_1 and y_2 respectively, are given by

$$1/r_1 = (1/h_1 h_2)(\partial h_1 / \partial y_2) \quad (2.4.1)$$

$$1/r_2 = (1/h_1 h_2)(\partial h_2 / \partial y_1) \quad (2.4.2)$$

When the appropriate simplifications are invoked for fully developed flow ($\partial/\partial y_3 = 0$, except $\partial p/\partial y_3$) in straight ducts ($h_3 = 1$ and $r_3 \rightarrow \infty$), the momentum equations can be written for each co-ordinate direction as:-

Direction 1

$$\begin{aligned} \partial(h_2 \rho U_1 U_1) / \partial y_1 + \partial(h_1 \rho U_1 U_2) / \partial y_2 &= - h_2 \partial p / \partial y_1 \\ - \partial(h_2 T_{11}) / \partial y_1 - \partial(h_1 T_{12}) / \partial y_2 + \left[- h_1 h_2 (\rho U_1 U_2 \right. \\ \left. + T_{12}) / r_1 + h_1 h_2 (\rho U_2 U_2 + T_{22}) / r_2 \right] & \end{aligned} \quad (2.4.3)$$

Direction 2

$$\begin{aligned} \partial(h_2\rho U_1 U_2)/\partial y_1 + \partial(h_1\rho U_2 U_2)/\partial y_2 &= - h_1 \partial p / \partial y_2 \\ - \partial(h_2 T_{12})/\partial y_1 - \partial(h_1 T_{22})/\partial y_2 + \left[h_1 h_2 (\rho U_1 U_1 + T_{11})/r_1 \right. \\ \left. - h_1 h_2 (\rho U_1 U_2 + T_{12})/r_2 \right] & \end{aligned} \quad (2.4.4)$$

Direction 3

$$\begin{aligned} \partial(h_2\rho U_1 U_3)/\partial y_1 + \partial(h_1\rho U_2 U_3)/\partial y_2 &= - h_1 h_2 \partial p / \partial y_3 \\ - \partial(h_2 T_{13})/\partial y_1 - \partial(h_1 T_{23})/\partial y_2 & \end{aligned} \quad (2.4.5)$$

These show clearly the extra terms (in square brackets), in the cross-plane momentum equations (2.4.3) and (2.4.4) which are due to the curvature of the co-ordinate lines.

The velocity components U_1 and U_2 in equations (2.4.3) to (2.4.5) are the cross-plane secondary velocities that occur in turbulent non-circular passage flows as already mentioned in Chapter 1.

The above set (2.4.3) to (2.4.5) can now be expressed in a form suitable for the solution procedure by substituting the orthogonal co-ordinate versions of the stress tensor relations (2.2.3) and (2.2.4). This leads to the following final forms:-

Direction 1

$$\begin{aligned}
 & \partial(h_2\rho U_1 U_1)/\partial y_1 + \partial(h_1\rho U_2 U_1)/\partial y_2 = - h_2 \partial p/\partial y_1 \\
 & + \partial(2\mu \frac{h_2}{h_1} (\frac{\partial U_1}{\partial y_1}))/\partial y_1 + \partial(2\mu h_2 \frac{U_2}{r_1})/\partial y_1 + \partial(\mu \frac{h_1}{h_2} (\frac{\partial U_1}{\partial y_2}))/\partial y_2 \\
 & - \partial(\mu h_1 \frac{U_1}{r_1})/\partial y_2 + \partial(\mu \frac{h_1}{h_1} (\frac{\partial U_2}{\partial y_1}))\partial y_2 - \partial(\mu h_1 \frac{U_2}{r_2})/\partial y_2 \\
 & - h_1 h_2 [2\mu \partial U_2/h_2 \partial y_2 + 2\mu U_1/r_2 - \rho U_2 U_2 - \rho \overline{u_2 u_2}]/r_2 \\
 & + h_1 h_2 [\mu \partial U_1/h_2 \partial y_2 + \mu \partial U_2/h_1 \partial y_1 - \mu U_1/r_1 - \mu U_2/r_2 \\
 & - \rho U_1 U_2 - \rho \overline{u_1 u_2}]/r_1 - \partial(h_2 \rho \overline{u_1 u_1})/\partial y_1 \\
 & - \partial(h_1 \rho \overline{u_1 u_2})/\partial y_2 \tag{2.4.6}
 \end{aligned}$$

Direction 2

$$\begin{aligned}
 & \partial(h_2\rho U_1 U_2)/\partial y_1 + \partial(h_1\rho U_2 U_2)/\partial y_2 = - h_1 \partial p/\partial y_2 \\
 & + \partial(\mu \frac{h_2}{h_1} (\frac{\partial U_2}{\partial y_1}))\partial y_1 - \partial(\mu h_2 \frac{U_2}{r_2})/\partial y_1 + \partial(\mu \frac{h_2}{h_2} (\frac{\partial U_1}{\partial y_2}))/\partial y_1 \\
 & - \partial(\mu h_2 \frac{U_1}{r_1})/\partial y_1 + \partial(2\mu \frac{h_1}{h_2} (\frac{\partial U_2}{\partial y_2}))/\partial y_2 + \partial(2\mu h_1 \frac{U_1}{r_2})/\partial y_2 \\
 & - h_1 h_2 [2\mu \partial U_1/h_1 \partial y_1 + 2\mu U_2/r_1 - \rho U_1 U_1 - \rho \overline{u_1 u_1}]/r_1 \\
 & + h_1 h_2 [\mu \partial U_2/h_1 \partial y_1 + \mu \partial U_1/h_2 \partial y_2 - \mu U_2/r_2 - \mu U_1/r_1 \\
 & - \rho U_1 U_2 - \rho \overline{u_1 u_2}]/r_2 - \partial(h_2 \rho \overline{u_1 u_2})/\partial y_1 \\
 & - \partial(h_1 \rho \overline{u_2 u_2})/\partial y_2 \tag{2.4.7}
 \end{aligned}$$

Direction 3

$$\begin{aligned} \partial(h_2\rho U_1 U_3)/\partial y_1 + \partial(h_1\rho U_2 U_3)/\partial y_2 &= - h_1 h_2 \partial\rho/\partial y_3 \\ + \partial\left(h_2\left(\frac{\partial U_3}{\partial y_1}\right)\right)/\partial y_1 + \partial\left(h_1\left(\frac{\partial U_3}{\partial y_2}\right)\right)/\partial y_2 \\ - \partial(h_2\rho\overline{u_1 u_3})/\partial y_1 - \partial(h_1\rho\overline{u_2 u_3})/\partial y_2 \end{aligned} \quad (2.4.8)$$

The orthogonal co-ordinate form of the continuity equation becomes (from A3.6)

$$\partial(h_2\rho U_1)/\partial y_1 + \partial(h_1\rho U_2)/\partial y_2 = 0 \quad (2.4.9)$$

For laminar flow, the turbulent stresses disappear and since there is then no source of cross-plane momentum, the velocities U_1 and U_2 become zero. Thus, for laminar flow equations (2.4.6) and (2.4.7) disappear and there remains equation (2.4.8) with the last two (turbulent stress) terms absent.

The scalar transport equation (2.3.1) can also be transformed (Appendix 3, equation A3.7) and written in terms of orthogonal co-ordinates for steady fully-developed flow in straight passages as:

$$\begin{aligned} \partial(h_2\rho U_1 C)/\partial y_1 + \partial(h_1\rho U_2 C)/\partial y_2 + \partial(h_1 h_2 \rho U_3 C)/\partial y_3 \\ = \partial\left(D_c \frac{h_2}{h_1} \left(\frac{\partial C}{\partial y_1}\right)\right)/\partial y_1 + \partial\left(D_c \frac{h_1}{h_2} \left(\frac{\partial C}{\partial y_2}\right)\right)/\partial y_2 \\ - \partial(h_2\overline{u_1 c})/\partial y_1 - \partial(h_1\overline{u_2 c})/\partial y_2 \end{aligned} \quad (2.4.10)$$

For laminar flow U_1 and U_2 are zero and the turbulent fluxes $\overline{u_1 c}$ and $\overline{u_2 c}$ disappear to leave a balance between axial convection and cross-plane diffusion.

2.5 Closure

The mathematical problem of steady fully-developed turbulent flow and scalar transport in straight passages of arbitrary cross-section is represented by equations (2.4.6) - (2.4.10). The velocity components U_1 and U_2 are identified as the cross-plane secondary velocities which, as mentioned in Chapter 1, are an important feature of turbulent flow in non-circular passages. The laminar flow problem reduces to the solution of equation (2.4.8) with U_1 , U_2 and the turbulent stresses set to zero. To obtain a solution of the turbulent flow problem, the Reynolds stresses and the turbulent scalar fluxes have to be modelled in terms of calculable properties. This problem is discussed in the context of previous theoretical work in the next chapter, and the modelling used in the present work is presented in Chapter 4.

3.1 Introduction

In the first part of this chapter, a review is made of the published experimental work which has established the current picture of the characteristics of turbulent flow and heat transfer in non-circular passages. Particular attention is paid to the origin and role of turbulence-driven secondary flows. In the second part of the chapter, the theoretical work reported in the literature is reviewed, concentrating mainly on the more recent computer-based calculation methods for solving the fundamental conservation equations of the flow with the aid of mathematical models of the turbulence and the stresses which it produces.

3.2 Experimental studies of the flow field

The early experimental work reported on turbulent flow in non-circular passages consists mainly of measurements of friction factor-Reynolds number characteristics and, occasionally, axial velocity profiles. Amongst the earliest investigations are those of Schiller (1923) and Nikuradse (1926, 1930), both of whom measured the friction factor characteristics of square, rectangular and triangular ducts. Additionally, Nikuradse reported pitot-tube measurements of axial velocity profiles. In the years following this work, friction factors were reported for flow in a wide range of passage shapes by various workers.

A critical survey of the friction factor data available in 1952 was made by Claiborne (1952), who attempted to correlate the measurements via the equivalent diameter concept and found deviations of more than 20% when compared with the Blasius (Schlichting, 1968) circular duct equation. There were no consistent geometric trends in the correlations and Claiborne concluded that the deviations from equivalent circular duct pressure drop were mainly due to the effects of turbulence driven secondary flow in the cross-plane, the presence of which was evident from the distortion of the axial velocity profiles and from flow visualisation. The axial velocity contours plotted in figure 3.2.1 taken from the measurements of Nikuradse (1926) in a 3.5:1 aspect ratio rectangular duct show these distortions clearly. The contours bulge well into the duct corners indicating a significant secondary flow carrying high-velocity fluid from the core region towards the corners. A similar effect (although not as marked) can be observed with the measured velocity profiles in an equilateral triangular duct (figure 3.2.1) indicating again secondary flow from the core into the corners.

In the decade or so following Claiborne's survey, there was a continuing effort on the measurement of friction factors and, to a lesser extent, pitot tube measurements of axial velocity profiles. Measurements of wall shear stress profiles began to appear following the publication of the method by Preston (1954) which employed surface pitot tubes. During this decade and through to the present time, the development and refinement of hot wire anemometers, and more recently laser-doppler anemometers, has enabled detailed investigations to be made into the structure of turbulent flow. The main effort in non-circular passages seems to have been made on flows

in square and rectangular ducts and in the axial flow passages found in nuclear rod bundles. A representative chronological summary of the experiments reported since the survey of Claiborne is shown in table 3.2.1 which gives an indication of the quantities measured and the type of instrument used. The data from these investigations forms the bulk of the currently available information on turbulent flow in straight non-circular passages and as such will be used as a basis for comparison and validation of predictions from the current method. Because of this, the results from many of these investigations will be plotted and described in more detail in later chapters. Where appropriate in the following overall descriptions of this work, reference will be made to these later plots.

All the measured axial velocity and wall shear stress profiles reported for the wide range of passage shapes listed in table 3.2.1 show distortions attributable to secondary flow. In some cases the secondary velocities were also measured and the flow pattern determined. Many workers presented axial velocity distributions plotted on inner 'law-of-the-wall' co-ordinates along normals to boundary surfaces and found that the universal law

$$U_3^+ = A \ln(y^+) + B \quad (3.2.1)$$

was satisfied with constants A and B varying between geometries and sometimes with position around the perimeter in a particular geometry. Table 3.2.2 summarises the typical average values proposed for a range of passage shapes. With few exceptions the variation of A and B in table 3.2.2 is in fact not much more than the variation found in the literature for different flat plate and circular pipe investigations.

No.	Year	Author(s)	Shape(s)	Geometry	Quant.	Instr.	Fluid	Comments
1	1954	Lowdermilk et al	□ ▽	$a = 1,5; \theta = 60^{\circ}$	f		air	
2	1955	Le Tourneau et al	○○	$a = 1.12$	f		water	19 rod cluster
3	1956	Eckert & Irvine	▽	$\theta = 11.7^{\circ}, 24.8^{\circ}$	f w	PT	air	
4	1956	Dingee & Chastain	○○	$a = 1.12, 1.2, 1.27$	f		water	9 rod cluster
5	1956	Miller et al	○○	$a = 1.46$	f		water	37 rod cluster
6	1956	Wantland	○○ ○○	$a = 1.106, 1.19$	f		water	100 rod clusters
7	1957	Eckert & Irvine	▽ □	$\theta = 24.8^{\circ}, a = 3$	f		air	entrance length and transition
8	1960	Hoagland	□	$a = 1$	w \bar{u}_i $\frac{\bar{u}_i \bar{u}_j}{\text{sec}}$	HWA	air	
9	1961	Carlson & Irvine	▽	$\theta = 4^{\circ}, 8^{\circ}, 12^{\circ}, 22.3^{\circ}, 38.8^{\circ}$	f		air	

Note: A key to the notation appears at the end of the Table

Table 3.2.1

A selection of turbulent non-circular passage experiments reported since 1952. Cont'd

No.	Year	Author(s)	Shape(s)	Geometry	Quant.	Instr.	Fluid	Comments
10	1961	Gessner & Jones	□	$a = 1$	w \tilde{u}_i	PT HWA	air	
11	1961	Palmer & Swanson	○○	$a = 1.015$	f w	PT	air	7 rod cluster
12	1962	Cremers & Eckert	▷	$\theta = 11.7^\circ$	\tilde{u}_i $\overline{u_i u_j}$	HWA	air	same duct as 3
13	1962	Hartnett et al	□ □	$a = 1, 5, 10$	f		air	
14	1962	Ushakov et al	○○	$a = 1$	f		h_g & N_{ak}	9 rod cluster
15	1963	Leutheusser	□ □	$a = 1, 3$	w τ_0 f	PT	air	
16	1964	Brundrett & Baines	□	$a = 1$	w \tilde{u}_i $\overline{u_i u_j}$ sec f	HWA	air	same duct as 15
17	1964	Brighton & Jones	⊙	$Dd = 16, 8, 2.67,$ 1.78	w \tilde{u}_i $\overline{u_i u_j}$ f	PT HWA	water air	

Table 3.2.1 continued

Cont'd









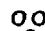
No.	Year	Author(s)	Shape(s)	Geometry	Quant.	Instr.	Fluid	Comments
18	1965	Tracy		$a = 6.4$	w \bar{u}_i $\bar{u}_i \bar{u}_j$	PT HWA	air	
19	1965	Gessner & Jones	 	$a = 1,2$	sec $\bar{u}_i \bar{u}_j$	PT	air	$u_i u_j$ along selected isotachs
20	1965	Liggett et al		$\theta = 90^\circ$	w sec τ_0	PT & HFA PR	water	open channel
21	1965 1967	Eifler & Nijsing		$a = 1.05, 1.1, 1.15$	w f	PT	water	4 rod cluster
22	1968	Levchenko et al		$a = 1.0$	w τ_0	PT PR	air & water	
23	1970	Perkins		$\theta = 90^\circ$	w $\bar{u}_i \bar{u}_j$	HWA	air	open corner
24	1971	Cain & Duffy		$a = 2.67, 2.93$	w f τ_0	PT PR	air	
25	1971	Hall & Svenningsson		$a = 1.217$	sec	HWA	air	6 rod cluster

Table 3.2.1 continued

Cont'd

No.	Year	Author(s)	Shape(s)	Geometry	Quant.	Instr.	Fluid	Comments
26	1971	Kjellstrom	○○	$a = 1.217$	w τ_0 \hat{u}_i $\overline{u_i u_j}$ sec f	PT PR		same rig as 25
27	1971b	Kokorev et al	□ ▷	$a = 1; \theta = 20^\circ$	sec	PT	air	3 rod channel
28	1971	Subbotin et al	○○	$a = 1.05, 1.1, 1.2$	w τ_0 f	PT PR	air	
29	1972	Launder & Ying	□	$a = 1$	w sec	HWA	air	
30	1972	Rehme	○○	$a = 1.025 \rightarrow 2.315$	f		water	25 different 'a' and No. of rods
31	1972	Thomas & Easter	□	$a = 1$	w τ_0 f	PT BLF & HFA	air	
32	1973	Kacker	⊙		w τ_0 sec	PT BLF HWA	air	

Table 3.2.1 continued

Cont'd

No.	Year	Author(s)	Shape(s)	Geometry	Quant.	Instr.	Fluid	Comments
33	1973	Gessner	□	a = 1	w $\frac{\overline{u_i u_j}}{\text{sec}}$	PT HWA	air	along corner bisector
34	1973	Marek et al	○○	a = 1.283	f		helium	
35	1974	Rehme	⊙	Dd = 10, 25, 50	w f	PT	air	
36	1974	Rowe et al	○○	a = 1.125, 1.25	w \tilde{u}_i	LDA		6 rod cluster
37	1975	Rehme	⊙	Dd = 10, 25, 50	\tilde{u}_i $\frac{\overline{u_i u_j}}$	HWA		
38	1975	Trupp & Azad	○○	a = 1.2, 1.35, 1.5	w τ_0 \tilde{u}_i $\frac{\overline{u_i u_j}}$	PT HFA HWA	air	7 rod cluster
39	1976	Carajilescov & Todreas	○○	a = 1.123	w \tilde{u}_i $\frac{\overline{u_i u_j}}$	LDA	water	4 rod channel
40	1976	Melling & Whitelaw	□	a = 1	w \tilde{u}_i $\frac{\overline{u_i u_j}}{\text{sec}}$	LDA	water	not fully developed

Table 3.2.1 continued

Cont'd

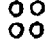

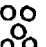
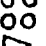





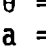
No.	Year	Author(s)	Shape(s)	Geometry	Quant.	Instr.	Fluid	Comments
41	1977	Gerard & Baines		$a = 1$	w τ_o f	PT PR	air	
42	1978	Aly et al		$\theta = 60^\circ$	w τ_o \bar{u}_i $\overline{u_i u_j}$ sec f	PT PR	air	
<p>Key: Shape:  rod bundle, triangular array.  rod bundle, square array.  isosceles triangular duct.  square duct.  rectangular duct.  elliptical duct.  eccentric pins in a circular tube.  annulus.</p> <p>Geometry: θ = apex angle a = aspect ratio or P/D ratio Dd = outer dia./inner dia.</p> <p>Quantity measured: f friction factor w axial velocity τ_o wall shear stress \bar{u}_i turbulence intensity $\overline{u_i u_j}$ Reynolds stresses sec secondary velocity</p> <p>Instrument used: PT pitot tube PR Preston tube HWA hot wire anemometer HFA hot film anemometer BLF boundary layer fence LDA laser doppler anemometer</p>								

Table 3.2.1

A selection of turbulent non-circular passage experiments reported since 1952.

Year	Author	Duct shape	A	B
1968	Schlichting*	Circular	2.5	5.5
1965	Patel	Circular (& Flat Plate)	2.39	5.45
1963	Leutheusser	Square and Rectangular (AR = 3)	2.46	5.5
1965	Tracy	Rectangular (AR = 6.4)	1.43	6.5
1977	Gerard & Baines	Rod Bundle P/D = 1.0	2.39	5.45
1978	Aly et al	Equilateral Triangle	2.47	5.08
1975	Trupp & Azad	Rod Bundle (AR = 1.2, 1.35, 1.5($\theta = 0^\circ$ & 30°))	2.12	5.93
		$\theta = 0^\circ$ only	1.8	7.28
1973	Cain et al	Elliptical (AR = 1.5 & 2.0)	2.39	5.45

*using data of Nikuradse and Reichardt.

Table 3.2.2 Experimental inner-axial-velocity law constants

The measured friction factors were found in many cases to be correlated to within $\pm 15\%$ of the circular duct values when the 'equivalent' or 'hydraulic' diameter concept was used in the evaluation of the Reynolds number. In closed ducts, the largest deviations from the circular duct data were found in duct shapes radically different from circular, such as narrow isosceles triangular ducts (Carlson and Irvine, 1961). In these ducts use of the hydraulic diameter increasingly over-estimated friction as the apex angle 2θ was reduced, giving for example, an over-estimation of 25% at $2\theta = 4^\circ$. An indication of the likely spread of measured friction factor in all of these measurements, due to differences in test rigs, measurement techniques and experimental errors for

apparently similar passage configurations can be seen in the plot of friction factor measurements for a range of P/D ratio in rod bundles shown in figure 7.9.33. For example, for a P/D of 1.2 and $Re = 10^4$ the scatter is about $\pm 25\%$ from the circular duct values.

Various attempts have been made to develop universal friction factor equations that take passage shape into account, often on the basis of fully developed laminar flow behaviour where $fRe = F_L =$ constant, depending only on geometry. An example of one of the more recent and least complex of these formulae is that developed by Malak et al (1975) which is written as:

$$f = 0.046 K_T^{1.12} Re^{-0.2} \quad (3.2.2)$$

where $K_T = (1 + 3K_L)/4$ and $K_L = (F_L/16)^{\frac{1}{2}}$. As with most of these formulae, this equation still uses the equivalent diameter concept and is an improvement on the Blasius equations for some geometries but does not appear to be universal. For example, it fails to correlate the square and rectangular duct data (see figures 7.3.11 and 7.5.11).

In the investigations where turbulent stresses were measured, the distributions along perpendicular bisectors of the walls were usually found to be broadly similar to those for a circular pipe. The experimental normal stress distributions for the latter are shown in figure 7.2.3a and can be compared with the corresponding distribution for a square duct (figure 7.3.10), triangular duct (figure 7.6.8) and a rod bundle channel (figure 7.9.9). As the wall is approached, the normal turbulent fluctuations are damped by the wall to produce anisotropic normal stresses in non-circular ducts generally similar to those in circular ducts.

Direct measurement of secondary velocities by such workers as Hoagland (1960), Brundrett and Baines (1964), Gessner and Jones (1965), Tracy (1965) and Launder and Ying (1972) has established the cross-flow pattern prevailing in square and rectangular ducts. These patterns are shown diagrammatically in figure 3.2.2 and are seen to be consistent with earlier deductions from the distortion of the axial velocity profiles (e.g. figure 3.2.1). The direction of secondary motion is from the core region into the corner along the corner bisecting planes, returning to the core along the wall and then the wall bisecting planes. The largest secondary velocities were found to be about $1\frac{1}{2}\%$ of the bulk velocity and occur near the walls and along the corner bisecting planes.

These flow patterns can be used to explain the distortions found in measured wall shear stress profiles, an example of which (Leutheusser, 1963) can be found in figure 7.3.3. Instead of decreasing monotonically from a maximum at mid-wall to zero at the corner, as in a laminar flow, the shear stress is uniform along the central half of the wall with the maximum values appearing, not at mid-wall, but at a point about half-way towards the corner. The increased wall shear stress in the corner region and the decreased stress in the middle are attributable to the secondary flow being directed towards the wall in the former region and away from the wall in the latter region. A more detailed discussion of these and other effects are given in Chapter 7 when comparisons are made between these experiments and the present work.

Measurement of secondary velocities in rod-bundles has been somewhat less successful than in square and rectangular ducts. The measurements in triangular array bundles of Kjellström (1971) and Hall and Svenningsson (1971) were too scattered to reveal any flow pattern and the anemometers used by Trupp and Azad (1975) and Carajilescov and Todreas (1976) lacked sufficient resolution to detect the small velocities involved. Secondary flow was, however, manifested as distortions of the measured axial velocity contours and wall shear stress profiles, as seen for example in figures 7.9.3 and 7.9.6. Trupp and Azad postulated a secondary flow pattern from such distortions, although there is some uncertainty about its validity, as will be discussed in Chapter 7. This pattern, shown diagrammatically in figure 3.2.4 consists of a single cell of secondary flow in each symmetry element of the effectively infinite array, with circulation from the core region towards the gap, returning via the wall and the $\theta = 30^\circ$ plane. Eckert and his co-workers at Minnesota reported a series of investigations in narrow isosceles triangular ducts (Eckert et al, 1954; Eckert and Irvine, 1956, 1960; Cremers and Eckert, 1962). Axial velocity profile distortions (rapid changes in gradient) were found in the narrow apex corner and axial velocity contours showed slight bulges into the corners near the base. The former effect was attributed to possible laminarisation of the flow due to the damping effects of the closely spaced walls and the latter to secondary flow, although no direct measurements of secondary flow were made. The more recent investigations of Aly et al (1978) in an equilateral-triangular duct did include measurement of secondary velocity which, as shown diagrammatically in figure 3.2.3, confirmed the earlier deductions of

Nikuradse (1926) and others from the axial velocity data. Six symmetrical counter-rotating cells of flow were detected giving circulations from the core into the corners that are basically similar to those found in square ducts. The magnitude and locations of the maximum secondary velocities were also found to be similar to those in square ducts. Consistent with these secondary motions, the measured axial velocity contours were found to bulge into the corners and the wall shear stress profile to be flat along much of the wall. These and other experimental measurements, including some from the narrow isosceles triangular ducts, are shown in figures 7.6.3 to 7.7.6.

The axial velocity contours and wall shear profiles measured by Cain and Duffy (1971) in an elliptical duct of aspect ratio 2.0 also showed distortions that were attributed to secondary flow although no attempt was made to measure the secondary velocities.

An experimental study by Kacker (1973) of the flow in a tube containing one or more off-set pins revealed the presence of secondary flow by direct measurement. The measured cross - flow pattern for the single pin case is shown diagrammatically in figure 3.2.5. The flow is from the higher axial velocity core region towards the lower axial velocity gap region, returning to the core via the pin surface. This was considered by the investigator to be broadly analogous to square duct secondary flows since the direction of flow was from the higher axial velocity core region towards a lower axial velocity (corner type) region. The measured axial velocity contours showed extensive bulging into the gap region and the wall shear stress peripheral variation was found to be less than

10% on both the pin and the tube surfaces. These effects were both attributed to the secondary motions.

It is clear from these experimental investigations that the distinguishing feature of fully developed turbulent flow in straight non-circular passages is the significant influence of the small turbulence driven secondary motions on the mean flow characteristics. This feature was apparent even from the early investigations and led to much speculation on how and why these flows were sustained. With the refinement of anemometry systems for turbulence measurement came the possibility of detailed investigations aimed specifically at determining the origins of these secondary flows.

In what appears to be the first attack on the problem, Brundrett and Baines (1964) measured and mapped the various terms in the mean flow vorticity transport equation for the case of a square duct. They concluded that secondary flow represented a convective transport of vorticity generated by the need to balance production and diffusion. It was further concluded that gradients in, and anisotropy of, the cross-plane normal stresses were the main source of vorticity production and thus of secondary flows.

This view of the dominance of normal stresses in secondary flow production gained further support from the experiments of Perkins (1970) and Eichelbrenner and Preston (1971) on turbulent boundary layers in corners. An alternative view was, however, proposed by Gessner (1973) in another direct attack on the problem. Momentum balances along secondary flow streamlines were determined experimentally in an earlier investigation (Gessner and Jones, 1965) of

flow in a square duct and led to the conclusion that rather more than the normal stresses seemed to be involved in secondary flow production. Following a suggestion made by Hinze (1967), Gessner focussed attention on the balance of mechanical energy in the cross-plane as well as the balance of mean flow vorticity. Meticulous experimental evaluations of the terms in these balances led this author to conclude that, contrary to Brundrett and Baines's suggestions, the anisotropy of normal stresses was of only minor consequence in the generation of secondary flows. Instead, evidence from the mechanical energy balance suggested that it was the gradients of turbulent shear stress in planes normal to the plane of the corner bisector that played the major role. The measurements showed that, along a corner bisector, the two dominant mechanical energy transfer mechanisms were an energy loss due to the working of the mean flow against the transverse turbulent shear stress gradients which is balanced by a gain due to convection of mean flow energy by secondary flow. It was further concluded that, since this balance was the mechanism that maintained secondary motions in fully developed flow, it must also be the mechanism that generates these motions in developing flow. However, it remains indisputable that the only source of axial vorticity in its governing equation is the normal stress anisotropy, which Gessner has acknowledged in recent unpublished work as the true source of these motions.

3.3. Experimental heat transfer

There appears to be paucity of detailed experimental data available in the literature for turbulent heat transfer in non-circular passages. As with flow measurements, most of the published

heat-transfer experiments have been in square and rectangular ducts and in rod bundles. A representative chronological summary of the investigations reported is given in table 3.3.1. Although liquid metal flows lie beyond the scope of the present work, references to some rod-bundle investigations have been included as they have an important application in nuclear reactors.

It is readily apparent from this table that most of the measurements have been of overall heat transfer in order to establish a Nusselt number/Reynolds number characteristic or its equivalent. The majority of investigations for a particular passage shape were with one fluid and one, or perhaps a small range of geometry and thus were not able to investigate the full dependence of the Nusselt number which would be also a function of Prandtl number, boundary conditions and asymmetry of heating and the mean temperature difference between boundary surface and fluid. It is probably for this reason that most authors chose to use the equivalent diameter concept and compare their measured heat transfer with the Dittus-Boelter (1930) relationship for circular tubes:

$$(N_u)_{DB} = 0.023 R_e^{.8} Pr^{.4} \quad (3.3.1)$$

Although this formula has been superseded by more recent correlations (e.g. see Kays (1966), p. 173) its previous extensive use makes it a convenient basis for comparison.

When the passage corners are not cusped or very acute angled, the dependence of Nusselt number on Reynolds number appears to be similar to that in equation (3.3.1) i.e. $Nu \propto R_e^{.8}$. This was so for the square and rectangular duct heat transfer measurements of

No.	Year	Author(s)	Shape(s)	Geometry	Quant.	Heat	Fluid	Comments
1	1954	Lowdermilk et al	□ ▷	$a = 1.5; \theta = 60^\circ$	Nu	E(d)	air	
2	1955	Dingee et al	⊙ ⊙	$a = 1.12, 1.2, 1.27$	Nu h	E(d)	water	
3	1956	Parrette & Grimble	⊙ ⊙	$a = 1.14, 1.2$	Nu h	E(i)	air	Naphthalene sublimation for h
4	1956	Miller et al	⊙ ⊙	$a = 1.46$	Nu	E(d)	water	No variation found in local h
5	1956	Wantland	⊙ ⊙	$a = 1.106, 1.19$	Nu	E(d) & WW	water	
6	1960	Eckert & Irvine	▷	$\theta = 11.7^\circ$	Nu h T	E(d)	air	
7	1960	Subbotin et al	⊙ ⊙	$a = 1$	Nu q h T	E(i)	water hg	
8	1961	Draycott & Lawther	⊙ ⊙	$a = 1.35 \rightarrow 1.6$	Nu	E(i)	air	Some roughened rods, geometry not clear

Table 3.3.1 A selection of turbulent non-circular passage heat transfer experiments reported since 1954

Cont'd

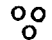
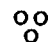
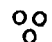
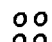
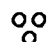

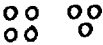

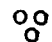

No.	Year	Author(s)	Shape(s)	Geometry	Quant.	Heat	Fluid	Comments
9	1961	Friedland et al		$a = 1.38, 1.75$	Nu	E(d)	hg	
10	1961	Palmer & Swanson		$a = 1.015$	Nu q	E(i)	air	
11	1961	Hoffman et al		$A = 1.179, 1.447, 1.715$	h	E(d)	air	Naphthalene coating
12	1962	Ushakov et al		$a = 1$	Nu T	E(i)	hg Nak	
13	1964	Maresca & Dwyer		$a = 1.75$	Nu	E(d)	hg	
14	1964	Novotny et al		$a = 1, 5, 10$	Nu T h	E(d)	air	Asymmetric heating
15	1964	Subbotin et al		$a = \text{various}$	Nu T q	E(i)	water air hg Nak	Appears to be summary of other work with origins not clear
16	1966	James et al		$a = 1, 1.5, 2, 2.5, 3, 4$	Nu	CG	water & glyc.	Asymmetric heating
17	1966	Redman et al		$a = 1, 1.1, 1.25, 1.5$	T h	E(d)	air	Part 6 tube chan. Heat influence functions
18	1966	Sparrow et al		$a = 5$	Nu	E(d)	air	Same rig as 14

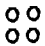

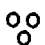

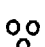
Table 3.3.1 continued

Cont'd

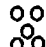






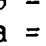
No.	Year	Author(s)	Shape(s)	Geometry	Quant.	Heat	Fluid	Comments
19	1966	Sutherland & Kays	⊙	$a = 1.15, 1.25$	Nu	E(d)	air	Superposition method
20	1966	Wilkie	⊙	$Dd = 1.97$	Nu	E(i)	air	Rib roughened inner surfaces
21	1967	Brundrett & Burroughs	□	$a = 1$	Nu q T_f	E(i)	air	Air temp. inner law
22	1968	Kidd & Stelzman	⊙	$a = 1\frac{1}{4}$ (approx)	Nu T	E(d)	air	Geometry not clear
23	1970	Barrow & Roberts	○	$a = 3.52$	Nu T	E(d)	water	
24	1971	Borishanskiy et al	⊙	$a = 1.1, 1.3, 1.4, 1.5$	Nu	E(i)	water	7 rod cluster
25	1971	Chiranjivi & Rao	▱	$a = 1$	Nu		water & glyc.	
26	1972	Markoczy	⊙ ⊙	$a = 1.167$ to 1.86	Nu	E(d)	air	In German
27	1972	Walker et al	⊙ ⊙	Mixed $a = 1.5 \rightarrow 2.0$	Nu T	E(d)	Nit.	Roughened rods
28	1973	Cain et al	○	$a = 1.5, 2.0, 2.67, 2.93$	Nu h	E(d)	air water	

Table 3.3.1 continued

Cont'd

No.	Year	Author(s)	Shape(s)	Geometry	Quant.	Heat	Fluid	Comments
29	1973	Marek et al		$a = 1.283$	Nu	E(d)	Helium	9 & 16 rod clusters
30	1974	Bobkov et al		$a = 1$	Nu T T _f q	E(i)	water	
31	1974	Pankin et al		$a = 1.05 - 1.16$	h	E(i)	air	$Re = 500 - 5,000$
32	1975	Sukomei		not given	Nu		air	Entry length
33	1977	LeI'Chuk et al		$a = 1.17$	Nu T	E(d)	air	7 rod cluster

Key: Shape:

-  rod bundle, triangular array.
-  rod bundle, square array.
-  isosceles triangular duct.
-  square duct.
-  rectangular duct.
-  elliptical duct.
-  Trapezoidal duct.
-  Annulus

Geometry:

- θ = apex angle
- a = aspect ratio or P/d
- Dd = Outer dia./inner dia.

Quantity:
measured

Quant: Nu = Nusselt number (overall)
T = wall temperature
h = local heat transfer coeff.
q = local heat flux
T_f = fluid temperature

Heating used:

E(d) = Electrical, into wall
E(i) = Electrical, indirect heating coils
CG = Combustion gases
WW = water/water recuperator

Table 3.3.1 A selection of turbulent non-circular passage heat transfer experiments reported since 1954

Lowdermilk (1954), Brundrett and Burroughs (1967) and Sukomei (1975), the equilateral triangular duct measurements of Lowdermilk (1954), the elliptical duct measurements of Barrow and Roberts (1970) and Cain et al (1973) and much of the rod bundle heat transfer measurements for $P/D > 1.05$. Further, most of the data for these investigations were within $\pm 15\%$ or so of the Dittus-Boelter correlation, the differences being probably of the same order as the experimental error in most heat transfer measurements. The latter point is reinforced to some extent by the reported experimental heat transfer data for rod-bundles, most of which for triangular arrays is shown plotted in figure 3.3.1 as a ratio of the measured Nusselt number to the Dittus-Boelter value. The lines, which represent the mean values obtained by each author, are mainly horizontal and clustered around unity with considerable disagreement between authors except perhaps a common trend of increasing heat transfer with P/D ratio. This latter trend is shown also in figure 8.3.21 for a fixed Reynolds number of 5×10^4 and appears to give an increase of something like 25% for a P/D increase from 1.1 to 1.5. However, the large scatter of results precludes the extraction of any quantitative relationship between Nusselt number and P/D ratio. The case of $P/D = 1.0$ (rods touching) is strongly dependent on the thermal conduction between and within the rods which partly explains the wide differences in overall heat transfer in the three investigations of that case. Although there is less data available for square arrays, a plot of the measured Nusselt numbers with P/D ratio is no less scattered, as shown in figure 3.3.2.

When the heating was markedly asymmetric or the duct aspect ratio (nominally the height/base ratio with the height defined as the maximum dimension) is greater than about 4 or 5, the Nusselt number behaviour usually became rather different than implied by equation (3.3.1). This was also the case for rod-bundle measurements for $P/D < 1.05$. Thus, for example, the Nusselt numbers measured by Eckert and Irvine in an isosceles triangular duct of aspect ratio 5 were found to be proportional to $Re^{.66}$ and would have been over-estimated by up to 100% by the Dittus-Boelter formula. Similarly the overall heat transfer measurements of Bobkov et al (1974) in rod bundles for $P/D = 1.0$ would have been over-estimated by 300% or more by equation (3.3.1). In the latter case, the rods were touching and thermal conduction was found to influence the results.

The heat transfer data from the asymmetric heating experiments of Novotny et al (1964), Sparrow et al (1966) and James et al (1966) in square and rectangular ducts and of Chiranjivi and Rao (1971) in a trapezoidal duct were also not correlated by equation (3.3.1). The Nusselt numbers measured by the latter, were found to be proportional to $Re^{0.4}$ and to depend significantly on Prandtl number. The dependence of Nusselt number on Prandtl number was also investigated by James et al (1966) who developed an elaborate empirical formula in an endeavour to correlate also the effects of Reynolds number, duct aspect ratio and the variation of fluid viscosity. When this formula is simplified for a square duct and constant property fluids it reads

$$N_u = 0.0283 Re^{(0.0016 Pr + .75)} Pr^{.4} e^{-0.013 Pr} \quad (3.3.2)$$

which suggests a more complex variation of Nusselt number with Prandtl number than is implied by equation (3.3.1). For Prandtl number of 0.7 or 5.0, the Dittus-Boelter formula would over-predict the values given by the above equation by about 30%.

The measured local variations of heat transfer coefficient around the passage periphery obtained by the various authors indicated in table 3.3.1 were usually less than 15% unless the duct aspect ratio was above about 2 to 3 or the rod bundle $P/D < 1.15$. A variation of about 30% was detected by Cain et al (1973) for an elliptical duct of aspect ratio 8/3, with the peak value at the minor axis. In rod bundles, Dingee et al (1955) and Redman et al (1966) found peripheral variations of about 20% for P/D ratios of 1.12 and 1.1 respectively, with the lowest values at the gap (closest approach of the rods). The measured temperature along the long wall of the narrow heated isosceles triangular duct of Eckert and Irvine (1960) was found to vary by a factor of more than 2 with the lowest temperature near the base. It seems likely that this large wall temperature variation would make the overall heat transfer behaviour more sensitive to the boundary conditions than for most of the other cases of turbulent heat transfer where, due to geometry and secondary flow, variations are usually only a few percent. The latter part of this premise is partly confirmed by the results reported by Redman et al (1966) whose rod-bundle test channel was constructed to allow various boundary conditions such as constant peripheral wall temperature or constant peripheral heat flux to be set up. The difference between the two boundary conditions appeared to make only a few percent difference in measured local and overall heat transfer coefficients for assemblies with P/D of 1.2 and above where, as

previously mentioned, the peripheral variations of heat transfer coefficient etc., are relatively small.

The direct electrical method of heating the passage wall used by Eckert and Irvine (1960) and by the many others shown in table 3.3.1, is usually assumed to produce a constant peripheral heat flux boundary condition. However, when prompted by written discussion of their paper, Eckert and Irvine checked the actual peripheral wall heat flux variation and found it to be far from constant (see figure 8.3.12), implying that their heat transfer data is not for the assumed constant heat flux boundary condition but for some condition between that and a constant peripheral wall temperature. It follows that, in this configuration, heat transfer at constant peripheral heat flux could behave significantly differently from that measured by Eckert and Irvine.

3.4 Theoretical studies

3.4.1 Laminar flow and heat transfer

The bulk of flow and heat transfer information available on laminar flow in non-circular passages is from theoretical analysis. A useful summary of much of this work can be found in Shah and London (1978), which shows that solutions of the governing differential equations have been obtained by both analytical and numerical methods for a wide range of passage shapes and for various heat transfer boundary conditions.

Prominent in this work is a series of papers by Sparrow and co-workers which includes studies of laminar flow and heat transfer in square ducts (Sparrow and Siegel, 1959), isosceles triangular ducts (Sparrow and Hadji-Sheikh, 1965), and axial flow in rod bundles (Sparrow and Loeffler, 1959; Sparrow et al, 1961). The latter work was extended by Axford (1967) in a multi-region analysis of a finite rod bundle. In all these, and most other geometries such as elliptical ducts studied by Tao (1961), the duct shape and heat transfer boundary conditions were found to have a significant influence on heat transfer and pressure drop. For example, for fully developed laminar heat transfer in an isosceles triangular duct with an apex angle of 30° , the Nusselt number for the 'H1' boundary condition (constant peripheral temperature and constant axial heat flux) is 2.91, whereas for the 'H3' boundary condition (constant peripheral and axial heat flux) it becomes 0.85. This latter boundary condition yields a Nusselt number of 0.08 when the apex angle is 10° , thus demonstrating the significant effect of geometry in this case.

3.4.2 Turbulent flow

The sparsity of experimental data for turbulent flow (and also heat transfer) in non-circular passages revealed in sections 3.2 and 3.3, is evidence of the severe difficulties of arranging such experiments. This has led to much previous and contemporary effort in the development of prediction procedures as an alternative method of filling the gap and providing methods of analysis and design. Indeed the present work, some of which has already been reported in

the literature (Gosman and Rapley, 1978,1980), can be seen as part of that effort (see Appendix 1).

During the evolution of turbulent duct flow prediction methods, succeeding generations have tended to rely less on empirical input and more on solutions of the governing partial differential conservation equations. The key features in this development are the mathematical representation of the Reynolds stresses and of turbulence driven secondary flow, together with numerical procedures for solving the derived equations.

It must have seemed to early workers that secondary velocities could be neglected as a second order effect in the early non-circular passage analyses for this was done by, for example, Diessler and Taylor (1956,1958), Buleev (1964), Rapier and Redman (1964), Dwyer (1966), Nijssing et al (1966), Bender et al (1967) and Cook (1969). In these 'first generation' methods, the axial velocity was assumed to be the only non-zero component and the Reynolds stresses were usually modelled with a simple quasi-linear stress-strain relationship containing an isotropic turbulent or eddy viscosity ν_t . The eddy viscosity concept was originally proposed to deal with simple shear flows containing a single predominant velocity gradient, e.g.

$$-\overline{u_2 u_3} = \nu_t dU_3/dx_2 \quad (3.4.1)$$

However, for two and three dimensional flows possessing a more complex strain field a co-ordinate-invariant extension of equation (3.4.1) can be made (e.g. Hinze, 1975) to give

$$-\overline{u_i u_j} = \nu_t (\partial U_i / \partial x_j + \partial U_j / \partial x_i) - \delta_{ij} \overline{u_m u_m} / 3 \quad (3.4.2)$$

The term $\delta_{ij}u_m u_m/3$ ensures that the normal stresses sum to $2k$. The eddy viscosity was, and indeed, in the case of boundary layers, often still is obtained from algebraic expressions based on characteristics of the mean flow and passage geometry. Typically, Prandtl's mixing length theory was employed, i.e.

$$v_t = \lambda_m^2 \left| \partial U_3 / \partial x_2 \right| \quad (3.4.3)$$

where λ_m is the mixing length. It soon became apparent however from these calculations that, although very small, the secondary flows could not be ignored, for the predictions of say, axial velocity or wall shear stress could be up to 100% in error for reasons which could not be entirely attributed to the relatively simple way in which the Reynolds stresses were calculated. The experimental data available at that time indicated that, in most cases, universal velocity distributions could be assumed along normals to the passage walls; indeed this assumption had been used to infer velocity profiles from local mean velocities in some of the early graphical methods, such as that of Diessler and Taylor, (1956). However, the local wall shear stress values required for calculation of the absolute velocities from these distributions were wrongly calculated when secondary velocities were neglected (recall that, as noted in section 3.2, secondary flows tend to flatten wall shear stress profiles, whereas predictions in which these flows are ignored indicate monotonic decay from mid-wall to the corner). Further, the fairly flat profiles of axial velocity observed in the regions away from walls were also not predicted when secondary motions were omitted.

The above deficiency gave rise to a number of what can be termed 'second generation' calculation procedures which attempted to allow for the overall effects of secondary flow. These procedures were usually based on measured features such as the wall shear stress profiles, from which the velocity field was calculated. This was the method used by Ibragimov et al (1966), who correlated the measured wall shear stress profiles in a rod bundle, a triangular duct and a square duct in terms of an equation which linked the local normalised wall shear stress around the passage wall periphery with the geometry of the passage shape only and was claimed to apply to any passage shape. The axial velocity distribution was obtained in the conventional way by assuming universal velocity distributions along normals to the passage walls, and the absolute values were evaluated from the local wall shear stresses derived from the empirical formula. The predicted axial velocity profiles, reported for rectangular, triangular and grooved-circular ducts and for eccentric annular and rod-bundle passages appear to be within 10% of the experimental data with which they were compared. A later publication (Ibragimov et al, 1967) proposed an expression based on the foregoing type of analysis for the ratio between the friction factor for passages of any specified geometry and that for a circular tube. The method of Ibragimov et al (1966) was further used by Bender and Magee (1969), Dwyer and Berry (1971) and Pfann (1973, 1975) to establish axial flow fields for heat transfer calculations in rod-bundles mostly with liquid metal coolants. However, since little comparison of the results was made with experiment, the success or otherwise of the method has yet to be proved.

The numerical finite difference method developed by Meyder (1975) for rod-bundle flow and heat transfer calculation was of the second generation type in that secondary flow was neglected but, in this instance, partly compensated for by introduction of an anisotropic eddy viscosity field. The radial eddy viscosity was calculated from the Prandtl/Van Driest formula and the tangential eddy viscosity from a modified mixing length formula which contained an anisotropy multiplying factor. This factor was adjusted until predicted wall shear stress profiles matched experiment. The difference between experimental axial velocity profiles and those predicted with isotropic eddy viscosities was reduced by about one-half with this anisotropic viscosity method. Ramm and Johannsen (1975a) also employed anisotropic eddy viscosity in a second generation calculation method for rod bundle flows, in which the length scales used to calculate the eddy viscosity components in the tangential and radial directions were obtained from the Buleev (1963) formula which has the form

$$1/\ell = 0.5 \int_0^{2\pi} \frac{d\phi}{s} \quad (3.4.4)$$

where s is the distance to the boundary surface in direction ϕ . In this application, different artificial boundaries were assumed for the calculation of ℓ in each direction. These boundaries appeared to be postulated intuitively and mainly to match the resulting eddy viscosities and diffusivities of heat with turbulent pipe flow measurements. The results obtained (Ramm and Johannsen 1975a, 1975b) were not compared with experiment.

Kokorev et al (1971b) used their experimental measurements of secondary flow in a square duct to propose a 'universal' secondary velocity profile. This profile was inserted in the axial momentum equation which was then solved to yield wall shear stress distributions and friction factors in non-circular ducts in the first of what might be termed 'third generation' methods (in which prescribed secondary flows are included). The method of solution involved further simplifications which included the assumption of universal axial velocity profiles (Kokorev, 1971a). Predictions of shear stress profiles were obtained for square and equilateral-triangular ducts, and in rod-bundle channels for the limiting case of rods touching. It was only possible to compare the first case with experiment, for which a considerable improvement on predictions neglecting secondary flows was obtained. Although this method represents a simple approach to a fairly complex problem, the full capabilities of it have yet to be properly assessed since the only validated results are for a square duct which is the geometry used to obtain the measurements on which the secondary velocity profile was based. The method is unlikely to be universal, however, in that it implies relatively simple secondary flow circulations in all non-circular passages, an assumption not always supported by experiment, as demonstrated earlier in this chapter.

Nijsing and co-workers have tried various methods of calculating axial velocity and wall shear stress in rod bundles, starting (Nijsing et al, 1966) with a modification of the graphical method of Diessler and Taylor (1956). Their calculation procedures progressed through several modifications to a third-generation-type proposal in which

secondary flows were included and also anisotropic eddy viscosities, which were linked to the passage P/D ratio (Nijsing, 1972). A phenomenological explanation of the origin of secondary flow was given, based on the experimental observations of Kline et al (1967) that the rate of fluid ejection away from a boundary wall was directly related to the local shear stress. It was concluded that this will give rise to a circular secondary motion tending to transport high momentum fluid through the main flow in the direction of the decreasing wall shear stress. This reasoning led to expressions for the peripheral variations of tangential secondary velocity component in terms of geometry and local wall shear stress gradient with the radial variation to be prescribed from experiment. The radial velocity component was obtained from mass continuity. Lack of experimental data on secondary flow compelled the author to prescribe, arbitrarily, the secondary velocity profiles in the calculations. The limited axial velocity predictions obtained, however, compared favourably with experiment. The deficiencies of this method are obvious in that detailed knowledge of secondary velocity distributions are required before predictions can be generated. This means that the data required for prediction is considerably more difficult to obtain than the data which is supposed to be provided by the calculation method. Further, in the light of the work of Gessner (1973) on the origin of secondary flow, the peripheral variation of wall shear stress is more likely to be a consequence of, rather than the cause of, secondary flow.

A numerical finite element procedure developed to solve a form of momentum equation was reported by Gerard (1974) for the calculation of axial velocity distribution and wall shear stress in square, triangular and other shaped ducts using an isotropic eddy viscosity formulation based on the Van Driest mixing length equation. The square duct application was developed into a third-generation method by including secondary velocities prescribed from the experimental measurements of Gessner and Jones (1965). The predicted axial velocity and wall shear stress obtained were a significant improvement on the predictions without secondary flow, yielding wall shear stresses that matched experiment and reduced the error in predicted axial velocity. For example, at the point three-quarters of the way into the corner along the corner bisector, the error in predicted axial velocity was reduced from 15% to under 5%. The main objections to this method are the same as for the previous method in that the experimental input required is likely to be more difficult to obtain than the predictions given by the procedure.

All the methods mentioned so far rely heavily on special empirical input for successful calculation of turbulent flow and should, therefore, be regarded as empirical calculation methods rather than as true prediction procedures. A prediction procedure should calculate velocity and stresses from direct solution of the governing partial differential conservation equations and associated boundary conditions. Any empirical input should ideally be universal for all geometries and flows: more ideally still, there should be no such input required. The recently developed 'fourth generation' methods to be described now represent a further step towards such prediction procedures.

Currently the most effective and widely-used class of prediction methods for turbulent flow are the numerical procedures that solve the Reynolds equations by finite differences. These methods have now been well established for more than a decade (e.g. Gosman et al, 1969; Patankar and Spalding, 1970; Amsden and Harlow, 1970) and usually employ turbulence models that enable the Reynolds stresses to be calculated either directly or indirectly from the time-averaged properties of the flow. Much of the earlier work in the assembly of such models was centred around determining an eddy viscosity ν_t from the Prandtl-Kolmogorov formula:

$$\nu_t = C_v k^{\frac{1}{2}} \ell \quad (3.4.5)$$

where C_v is a constant, k is the turbulence kinetic energy ($\frac{1}{2} \overline{u_i u_j}$) and thus $k^{\frac{1}{2}}$ is a turbulence velocity scale, and ℓ a turbulence length scale. The latter is not, in general, the same as mixing length ℓ_m , although they can become equivalent when the mean flow and turbulence structure have the same length scale, such as in a local-equilibrium wall layer (Townsend, 1961) (see also section 4.6 in this thesis). Some of the transport effects on the structure of turbulence, such as convection and diffusion, can be included in the prediction method if k and ℓ are evaluated from partial-differential transport equations, which can be derived from the Navier-Stokes equations.

It has now become customary to classify the level of turbulence model by the number of partial differential transport equations solved. If k and ℓ are both obtained from algebraic formula, the model is classified as 'zero' equation. In 'one' equation models, k is usually obtained from its own partial differential transport

equation and ℓ from an algebraic formula. In 'two' equation models, ℓ or a related variable is also obtained from its own partial differential transport equation. Several alternative related variables have been used for the calculation of ℓ , and a useful summary of these and their associated transport equations can be found in Launder and Spalding (1972) with a more recent review given by Reynolds and Cebeci in Chapter 5 of Bradshaw (1978).

The most successful and widely used variable for the determination of ℓ appears to be the isotropic dissipation rate ϵ of turbulence kinetic energy. This, in conjunction with k , gives rise to what has become known as the $k - \epsilon$ turbulence model. Since the dissipation of turbulence kinetic energy occurs mainly in the smallest eddies in the flow, it can be assumed locally isotropic and should depend only on ρ , k and ℓ . Thus, for dimensional consistency, ϵ can be represented by (Launder and Spalding, 1972):

$$\epsilon = C_D k^{3/2}/\ell \quad (3.4.6)$$

where C_D is an empirical constant. When this relation is substituted into equation 3.4.5, the Prandtl Kolmogorov formula becomes

$$\nu_t = C_\mu k^2/\epsilon \quad (3.4.7)$$

which is the form of turbulent viscosity used in the $k - \epsilon$ turbulence model with C_μ a constant. This model has been used to successfully predict a wide range of turbulent flows (Launder and Spalding, 1974).

The eddy viscosity concept was, as previously noted, introduced primarily for application to simple flows in conjunction with the stress relation equation (3.4.1). In more complex flows such as

those in non-circular passages, the isotropic eddy viscosity stress relation of equation (3.4.2) fails, mainly because the stresses are not simply related to the local co-planer mean strain. Indeed it is easy to see that with such an eddy viscosity model, the cross-plane stresses in fully developed flows are uniquely linked to gradients in the cross-plane velocity field, which in turn rely on the cross-planar stresses for their existence; thus no secondary flows are predicted by isotropic eddy viscosity models. This implies that something more elaborate than even the two-equation turbulence model is required for the calculation of turbulent non-circular duct flows.

The next step upwards from the eddy viscosity model is apparently to calculate the required Reynolds stresses directly from their own transport equations. The prediction procedure of Hanjalic and Launder (1972), which was applied to an asymmetric channel, an annulus and other two dimensional turbulent flows, operated in this way. The stress equations are based on the exact form which can be derived from the Navier-Stokes equations by manipulation and time averaging (e.g. see Hinze, 1975) and are shown in Appendix 2 as equations A2.1.

The exact equations cannot however be solved as they stand since they contain unknowns such as the triple correlations $\overline{u_i u_j u_k}$. The arguments used by Hanjalic and Launder in the modelling process leading to the elimination of these unknowns are outlined in Appendix 2 and the final modelled forms are given as equations A2.7. In their application of this model to thin shear flows, the required Reynolds shear stress was calculated from equations A2.7 with the normal stresses prescribed from algebraic equations obtained by reducing A2.7

to the forms appropriate to plane homogenous shear flow. The fields of k and ϵ required for solution of these equations were obtained by solving their modelled transport equations, thus giving a 'three-equation' model. The numerical finite-difference procedure used to simultaneously solve the momentum and turbulence partial differential equations was based on the parabolic method of Patankar and Spalding (1970) for turbulent boundary layers. The predictions obtained were in good agreement with experiment in most respects including the non-coincidence of the planes of maximum velocity and zero shear stress in the asymmetric channel and annulus, a feature that could not have been predicted by an eddy viscosity model.

In the case of three-dimensional flows, such as in non-circular ducts, all six Reynolds stresses are usually required. In the methods of Naot et al (1974) and Reece (1977), developed for the prediction of flow in square ducts, all six stresses were obtained from their own modelled partial differential transport equations. In addition, Reece (1977) solved a differential transport equation for ϵ thus giving a 'seven-equation' model for the solution of developing square duct flow. The modelled Reynolds stress equations were similar in most respects to those used by Hanjalic and Launder (1972) (equation A2.7) with the notable exception of the redistribution (pressure-strain) terms. These terms were modified and a wall damping correction introduced in an effort to obtain the redistribution between the normal stresses leading to the anisotropy of these stresses found from experiment in near wall regions. Details of these modifications and the relatively successful application of the stress model to various two-dimensional flows can be found in Launder, Reece and Rodi (1975).

The wall damping correction developed for two dimensional flows with parallel walls could not be used without further modification for the case of perpendicular walls found in a square duct. On the basis of physical argument Reece (1977) treated the two walls as the superposition of two orthogonal two-dimensional walls. This assumption appeared to be adequate as the predictions obtained for square duct flows were generally in good agreement with experiment, although no predicted Reynolds stresses were presented for comparison with measurements in fully-developed flow. It was therefore not possible to assess the success of the wall-damping correction in predicting the near-wall anisotropy of the cross-plane normal stresses in this case. The distortion of axial velocity and turbulence kinetic energy profiles by secondary flow were much in evidence and generally well predicted (see figures 7.3.5 and 7.3.6). The predictions of developing flow were also in good agreement with experiment.

The numerical finite-difference procedure used by Launder, Reece and Rodi (1975) to simultaneously solve the partial differential equations representing the mean flow, stresses and turbulence was based on the method of Patankar and Spalding (1970) for two dimensional parabolic equations. In the square duct flow calculations of Reece (1977), the parabolic finite difference procedure of Patankar and Spalding (1972) for three-dimensional flows was used. In this method the stability and convergence of the recirculating flow calculations in the cross-plane was obtained by means of a hybrid differencing scheme which switches to upwind differencing when the local Peclet number Pe becomes large.

Naot et al (1974) evaluated turbulence length scale from a simple geometric formula in their 'six equation' turbulent stress model used to predict fully developed square duct flow. The modelled Reynolds stress equations used were derived independently from the equations used by Reece (1977) and thus differed in some details. The main differences, however, appear to lie in the re-distribution terms, and in particular, the wall damping correction that appears in the equations of Reece but not in those of Naot et al. The elliptic numerical finite difference procedure developed by Naot et al for simultaneous solution of the differential equations evolved through several modifications before converged solutions could be obtained. The main problem appeared to be the elimination of instabilities caused by the closely-coupled, source-dominated non-linearity of the equations. Convergence was eventually obtained for Reynolds numbers less than 2×10^5 by linearising the source terms and introducing different differencing schemes for selected terms; details are given in Naot et al (1974). Most of the predictions presented compared reasonably with experiment, although no calculated normal stress profiles were shown for comparison. The predicted turbulence kinetic energy contours were relatively poor however, in that the characteristic bulging of the contours into the corner due to secondary flow was much underpredicted (see figure 7.3.6). For example, at the point three-quarters of the way along the corner bisector into the corner, turbulence kinetic energy was overpredicted by some 30%; this can be compared with the prediction of Reece (1977) which was within a few percent of experiment.

In contrast to the multi-differential turbulence equation methods described above, Launder and Ying (1973)[†] developed an approach for the prediction of square duct flows based on the reduction of the differential Reynolds stress transport equations to algebraic form and the use of an algebraic length scale prescription. The resulting method required the solution of only one differential transport equation for turbulence kinetic energy k . In their analysis, the Hanjalic and Launder (1972) formulation of the Reynolds stress transport equations was used, as quoted in Appendix 2, and the equations were further simplified by neglecting convective and diffusive transport on the basis that these effects are small in the region near the wall where vorticity generation has been shown to be large (Brundrett and Baines, 1964). This resulted in degenerate forms of the transport equations from which the cross-plane (kinematic) stresses could be extracted in the following form:

$$\overline{u_1^2} - \overline{u_2^2} = 2C_6(k/\epsilon)(\overline{u_1 u_3} \partial U_3 / \partial x_1 - \overline{u_2 u_3} \partial U_3 / \partial x_2) \quad (3.4.8)$$

$$\overline{u_1 u_2} = C_6(k/\epsilon)(\overline{u_2 u_3} \partial U_3 / \partial x_1 + \overline{u_1 u_3} \partial U_3 / \partial x_2) \quad (3.4.9)$$

The above equations exhibit an interesting effect in the flow with stresses in the cross-plane being a consequence of mean strain rates in planes orthogonal to them. The axial plane kinematic shear stresses $\overline{u_1 u_3}$ and $\overline{u_2 u_3}$ were calculated in the Launder and Ying (1973) study from the Prandtl-Kolmogorov eddy viscosity formula (equation 3.4.5) with ℓ prescribed by the Buleev (1963) geometric formula (equation 3.4.4), ϵ calculated from equation (3.4.6) and k calculated from its own differential transport equation (similar to 4.3.1).

[†] The earlier square duct calculations of Ying (1971) were of the third generation type.

The differential equations were solved simultaneously by the elliptic finite difference procedure of Gosman et al (1969). In this procedure, the cross-plane momentum and continuity equations are transformed to equations for vorticity and stream function and the whole set solved by a point iteration method. The resulting predictions were encouraging in that the secondary flows generated in the cross-plane were of the pattern expected from experimental measurement and gave predictions of mean flow nearer to experiment than previous methods which ignored or only approximately accounted for secondary flow. The bulging effect of secondary flow into the corners was evident in the axial velocity and turbulence kinetic energy contours. The levels of the latter, however, were lower than experiment giving, for example, an underprediction of some 15% at a point three quarters of the distance along the corner bisector into the corner. The predicted Reynolds stress profiles were unfortunately not reported so that no comparisons can be made. The detailed predictions of the secondary velocity profiles were qualitatively correct although there were some local discrepancies of up to 200% in places. Nevertheless, taking into account the likely large errors in experimental data, particularly the detailed turbulence and secondary velocity measurements, the overall level of agreement was satisfactory.

The 'algebraic stress transport' model of Launder and Ying was also used by Carajilescov and Todreas (1976) to predict turbulent flow in rod bundle passages. In this case turbulence length scale was prescribed from a formula based on experimental measurement of axial velocity gradients, turbulent shear stress and turbulence kinetic energy i.e. via equations (3.4.1) and (3.4.5). The cross-plane shear

stresses were omitted from the calculations on the basis of the square-duct measurements and arguments of Brundrett and Baines (1964) that normal stresses are dominant. Differential conservation equations for vorticity, stream function, axial velocity and turbulence kinetic energy were solved simultaneously by finite differences on a cylindrical co-ordinate mesh with a solution method similar to the elliptic procedure of Gosman et al (1969). Since a standard co-ordinate mesh is used for an irregular passage shape, special control volumes are required where mesh boundaries do not coincide with passage boundaries and the method thus suffers from the consequent disadvantages of reduced flexibility, accuracy and efficiency. The former usually occurs when, to avoid complications that could frustrate convergence of the numerical solution, location of the special cells are limited to simple boundaries, such as symmetry planes. Losses in accuracy and efficiency occur when, as in the Carajilescov and Todreas case, grid node spacings are partly dictated by the location of the special boundary cells rather than chosen for the optimisation of the numerical solution method.

The empirical constants in the model were adjusted to match the prediction to experiment. The predictions presented for $P/D = 1.123$ were mainly within the error band quoted for their experimental results. The poorest axial velocity prediction was in the gap (closest approach of the rods) where it was low by about 5%. Also in the gap, the level of turbulence kinetic energy in the near wall region was overpredicted by as much as 35% (see figures 7.9.5 and 7.9.8).

No predictions of Reynolds stresses were reported or even given in the thesis of Carajilescov (1975) for comparison with the experimental measurements obtained. As previously discussed, no measurements were made of the secondary flows, so that the predicted pair of counter-rotating circulations of secondary flow obtained by Carajilescov and Todreas (1976) for the $P/D = 1.123$ channel and shown in figure 3.4.1a could not be confirmed. Distortions consistent with the predicted secondary flow could be seen in the calculated contours of axial velocity and turbulence kinetic energy (see figures 7.9.3 and 7.9.7).

A further application of the Launder and Ying algebraic stress transport model was made by Aly et al (1978) to predict turbulent flow in an equilateral-triangular duct, employing in this instance, the length scale obtained from the Buleev (1963) formula (equation 3.4.4). The differential equations were solved for a one-sixth duct symmetry element, by finite differences on a Cartesian mesh, with an elliptic procedure based on the vorticity/stream function method of Gosman et al (1969). This is another example of a standard coordinate finite-difference mesh being applied to an irregular passage shape with the consequent limitations in flexibility and efficiency. Much difficulty was apparently found in obtaining a satisfactorily converged solution (Trupp and Aly, 1978), due mainly to the instabilities induced by the vorticity source terms arising from the turbulent stresses. This was eventually overcome by imposing a condition of immutable sign on the vorticity source, a condition which also, therefore, imposed a unique sense of rotation on the secondary flow (i.e. a single swirl) in the calculation domain.

The empirical constant in the vorticity source was adjusted to match predictions to their experimental data, and good overall agreement was obtained. The pattern of a single swirl of secondary flow obtained from the method was, as expected, in accordance with the measurements. The latter circulation was, as shown in figure 3.2.3, from the core along the corner bisector into the corner, thence along the wall and back to the core via the wall bisector. The predicted secondary velocity profiles were mainly in accord with experiment except in the near-wall region where they were under-predicted by as much as 60% towards the corner (see figure 7.6.7). The effect of secondary flow could be seen in distortions of the predicted axial velocity and turbulence kinetic energy contours, which bulged into the corner. The calculated wall shear stress profile appeared to be quite sensitive to the secondary flows in that the peak stress occurred at a point some 40% from mid-wall to the corner (see figure 7.6.6), where it lay about 8% above the more uniform experimental profile. No Reynolds stress predictions were presented for comparison with their measurements.

Trupp and Aly (1978) repeated the rod bundle calculations of Carajilescov and Todreas (1976) for $P/D = 1.123$ and, with an apparently identical procedure, and obtained a single swirl of secondary flow in a symmetry element, as shown diagrammatically in figure 3.4.1b. They suggested that the Carajilescov and Todreas solution with two swirls (figure 3.4.1a) was probably a consequence of incomplete convergence of the iterative procedure. When, however, Trupp and Aly later included in their calculations the cross-plane shear stresses (omitted by Carajilescov and Todreas), they were

unable to obtain a converged solution without imposing the same immutable sign restriction on the cross-plane vorticity source as used by them (Aly et al, 1978) in their triangular duct predictions. This means that the solution method of Trupp and Aly (1978) was forced to predict a single swirl of secondary velocity in the symmetry element for all P/D ratios. The question of the validity of both predictions of the secondary flow pattern will therefore have to await the acquisition of secondary velocity measurements for this rod bundle configuration before it can be resolved, although as will be demonstrated elsewhere in this thesis, the present predictions suggest they are both wrong.

The results obtained by Trupp and Aly (1978) for the rod bundle were similar to those of Carajilescov and Todreas (1976), with a slightly larger underprediction of gap velocity (11%) and a much increased overprediction of turbulence kinetic energy in the gap near wall region (60%).

The Launder and Ying algebraic stress transport model was further analysed by Gessner and Emery (1976), who showed that the axial plane shear stresses could also be extracted from the simplified Reynolds stress transport equation to give a convenient form of the algebraic model in which all six stresses are explicitly related to k , ϵ and gradients of axial velocity by the equations:

$$\overline{u_3^2} = C_1 k \quad (3.4.10)$$

$$\overline{u_2^2} = C_3 k - C_2 C_4 (k^3 / \epsilon^2) (\partial U_3 / \partial x_2)^2 \quad (3.4.11)$$

$$\overline{u_1^2} = C_3 k - C_2 C_4 (k^3 / \epsilon^2) (\partial U_3 / \partial x_1)^2 \quad (3.4.12)$$

$$\overline{u_1 u_2} = -C_2 C_4 (k^3 / \epsilon^2) (\partial U_3 / \partial x_1) (\partial U_3 / \partial x_2) \quad (3.4.13)$$

$$\overline{u_1 u_3} = - C_4 (k^2/\epsilon) (\partial U_3/\partial x_1) \quad (3.4.14)$$

$$\overline{u_2 u_3} = - C_4 (k^2/\epsilon) (\partial U_3/\partial x_2) \quad (3.4.15)$$

where C_1 , C_2 , C_3 and C_4 are related empirical constants such that only two have to be assigned (further details of the development of the above set will be given in Chapter 4).

The authors then simplified the above equations using a prescribed length scale ℓ and an algebraic equation for k obtained by summing equations (3.4.10) - (3.4.12) to give

$$1/c_4 = (k^2/\epsilon^2) ((\partial U_3/\partial x_1)^2 + (\partial U_3/\partial x_2)^2) \quad (3.4.16)$$

Using this equation and equation (3.4.6) k and ϵ can be eliminated from equations (3.4.10) - (3.4.15) to give the final stress relations:

$$\overline{u_3^2} = \alpha_1 \ell^2 G \quad (3.4.17)$$

$$\overline{u_2^2} = - \alpha_2 \ell^2 (\partial U_3/\partial x_2)^2 + \alpha_3 \ell^2 G \quad (3.4.18)$$

$$\overline{u_1^2} = - \alpha_2 \ell^2 (\partial U_3/\partial x_1)^2 + \alpha_3 \ell^2 G \quad (3.4.19)$$

$$\overline{u_1 u_2} = - \alpha_2 \ell^2 (\partial U_3/\partial x_1) (\partial U_3/\partial x_2) \quad (3.4.20)$$

$$\overline{u_1 u_3} = - \ell^2 (\partial U_3/\partial x_1) G^{1/2} \quad (3.4.21)$$

$$\overline{u_2 u_3} = - \ell^2 (\partial U_3/\partial x_2) G^{1/2} \quad (3.4.22)$$

where

$$G = (\partial U_3/\partial x_1)^2 + (\partial U_3/\partial x_2)^2 \quad (3.4.23)$$

and α_1 , α_2 , α_3 are empirical constants. This simplification gives a zero-equation turbulent stress model when ℓ is prescribed, but suffers from the disadvantage of most zero-equation models in that the stresses

become zero when the gradients of axial velocity are zero. Thus in contradiction with experiment, normal stresses would be zero at the maximum axial velocity planes in a duct.

In an accompanying paper, Gessner and Po (1976) applied this algebraic model to the calculation of Reynolds stresses from experimental axial velocities in a square and a rectangular duct. The prescribed length scale used was based on the Buleev geometric formula (equation 3.4.4) modified to match length scale profiles calculated from experimental data and then further modified with a near-wall damping factor (Launder and Priddin, 1973). The empirical constants in the model were adjusted to give the best match between calculated and experimental stresses. As may be expected, with so much adjustment to match experiment, the resulting predictions of Reynolds stress were in reasonable agreement with experiment. The anisotropy of the normal stresses near the wall was also satisfactorily predicted. Most of the predicted profiles, however, contained undulations not present in experimental data; these were attributed to errors in the calculated axial velocity gradients which were obtained graphically from the experimental data. The calculated normal stresses were, of course, in error at the duct centre line where the model forced all the stresses to zero. The empirical constants used by Gessner and Po in order to procure this general agreement with experiment were found to be quite different from the equivalent of those used by Launder and Ying in their mean and secondary flow predictions.

The Launder and Ying (1973) algebraic stress transport model was also used by Tatchell (1975) to predict developing flow in a square duct, with turbulence length scale calculated from the isotropic dissipation rate ϵ of turbulence kinetic energy, which was obtained from its modelled transport equation (Hanjalic and Launder, 1972). The predictions of fully developed flow did not appear to be any improvement on those of Launder and Ying. No predicted wall shear stress or Reynolds stress profiles were reported.

Finally, Benodeker and Date (1978) used the Launder and Ying (1973) algebraic stress transport model, with length scales obtained via a differential transport equation for ϵ , to predict fully developed turbulent flow in finite rod bundle clusters. A finite-difference method was used with an elliptical procedure based on the vorticity-stream function method of Gosman et al (1969) in cylindrical co-ordinates. In using a standard co-ordinate mesh for an irregular solution domain, the method suffers from the usual disadvantages of reduced flexibility and efficiency. In this case the grid lines did not intersect the rod surfaces orthogonally and necessitated the development of various special treatments and limitations to the near-surface nodes to cope with the cases of laminar and turbulent flow studied.

Predictions of local axial velocity and wall shear stress were reported for a symmetry sector of a seven rod bundle in a cylindrical casing, although no comparisons were made with experiment. The predicted friction factor was compared with experiment however, and found to be more than 30% low when the Launder and Ying (1973) constants were used in the stress model.

3.4.3 Turbulent heat transfer theoretical work

The development of calculation methods for turbulent heat transfer lags behind that for turbulent flow. This is perhaps understandable as the turbulent flow and stress fields are a necessary input to the heat flux equations and thus development of their calculation procedures must precede that for the heat fluxes. A further and important factor will be obvious from section 3.3, in that there is a great shortage of reliable heat transfer data and thus, little detailed knowledge of thermal turbulence structures exists on which to base and validate heat flux models.

In a direct analogy with laminar heat transfer, the turbulent heat flux $\overline{u_2 c}$ in direction 2 can be modelled with an isotropic eddy (turbulent) diffusivity of heat γ_c such that

$$-\overline{u_2 c} = \gamma_c dC/dx_2 \quad (3.4.24)$$

where C is enthalpy. The eddy diffusivity γ_c is seen to be a scalar counterpart of the isotropic eddy viscosity (equation 3.4.1). The ratio of eddy viscosity to eddy diffusivity is called the 'turbulent Prandtl number' σ_c thus

$$\sigma_c = \nu_t / \gamma_c \quad (3.4.25)$$

which is found experimentally to have an approximately constant value near unity. The latter fact is commonly exploited to calculate the turbulent heat flux via the above equations with ν_t obtained from an appropriate model. Equation (3.4.24) implies that the heat flux depends mainly on the enthalpy gradient dC/dx_2 . This is in fact often the case in near-wall regions and indeed experimental measure-

ments have confirmed this (see review by Kader and Yaglom, 1972), and have also indicated that the turbulent Prandtl number is constant in this region with a value near 0.9. Further confirmation has come from successful turbulent boundary layer heat transfer calculation procedures using isotropic eddy viscosities and diffusivities where σ_c has been assumed to be at or near this value (e.g. Patankar and Spalding, 1970; Gosman et al, 1969; Jones and Launder, 1969; Cebeci et al, 1970). Although this latter evidence is not as strong as reliable experimental measurements it is nonetheless indicative.

In non-circular passage flows the early graphical turbulent heat transfer calculations of Deissler and Taylor (1956, 1958) in triangular and square ducts and in square and triangular array rod bundles, and of Nijssing et al (1966) in rod bundles evaluated the heat flux from relations similar to equation (3.4.24) with σ_c taken as unity. For liquid metal heat transfer calculations, special empirical formulae for σ_c have been developed (e.g. Dwyer, 1963; Bobkov et al 1968, 1970) and used in the calculations of Ibragimov et al (1971), Nijssing and Eifler (1972), Nijssing (1972), Dwyer and Berry (1972), Pfan (1975) and Meyder (1975) with moderate success considering secondary flow was neglected. It is probable, however, that due to the high thermal conductivity of liquid metals, secondary flow effects would be less important in these circumstances. These empirical formulae for σ_c involved the laminar Prandtl number and other variables such as Reynolds number, local axial velocity and normal distance to the wall, i.e. the constancy of σ_c no longer prevails. A review of the values and variations of σ_c previously measured or proposed in various flows is given by Launder in Chapter 6 of Bradshaw (1978). From this review, it is evident that

calculations made with $\sigma_c = \text{constant}$ and near unity were as successful as any in near wall flows.

Some 'third generation' type heat transfer calculations, using mixing-length derived anisotropic eddy viscosities and diffusivities, have been made (e.g. Pankin et al, 1974; Meyder, 1975), but there do not appear to be any 'fourth generation' type calculations available in the literature other than some square-duct predictions by Launder and Ying (1973). The latter assumed $\sigma_c = \text{constant} = 0.9$ and obtained satisfactory agreement with the measurements of Brundrett and Burroughs (1967).

When the heat transfer along the perimeter of the duct is strongly asymmetric or otherwise non-uniform such that the enthalpy gradient dC/dx_2 normal to the wall is no longer the only significant gradient, then the isotropic eddy diffusivity concept must become less appropriate. In this case, differential transport models may be required for the heat fluxes to enable all the important transport effects to be included. A review of recent developments in heat flux modelling is given by Launder in Chapter 6 of Bradshaw (1978) and reveal them to be in an early stage of development and, as yet, relatively untried. One of the most recent contributions in this area is the theoretical study of Samaraweera (1978) in circular pipes with asymmetric heating. His numerical study employed differential Reynolds stress and heat flux models and required the simultaneous solution of up to 12 partial differential equations which was achieved with an elliptical finite-difference procedure based on that of Caretto et al (1972). The predictions obtained were encouragingly much closer to experiment than previous predictions

using isotropic turbulent diffusivities of heat; indeed, the study revealed an unexpectedly complex anisotropic behaviour of the diffusivities confirming the inapplicability of an isotropic assumption.

3.5 Closure

A survey of past experimental work has revealed a significant influence of turbulence-driven secondary flow in straight, non-circular passages. The secondary velocities have a magnitude of order 1% of the mean axial velocity and a characteristic pattern of flow from the core towards corners or regions of lower axial velocity, returning to the core via the walls and wall bisectors. In non-circular ducts, the presence of these flows causes the core fluid to penetrate into the corners (or towards regions of lower axial velocity) giving rise to characteristic bulges of measured axial velocity and turbulence kinetic energy contours in those directions.

The origin of these secondary flows has been identified by detailed experimental studies as a convection of mean flow energy necessary to balance work done by the mean flow on axial plane shear stress gradients in the flow. Normal stresses are now believed to have only a minor role in the generation and maintenance of these flows.

The development of turbulent stress models for this class of flows has been characterised by increasingly less dependence on empirical input at the expense of increased complexity. The present

stage of development gives a choice of models that require solution of from zero to seven or more partial differential transport equations. These equations, together with the equations of motion, are usually solved by finite-differences.

The algebraic stress transport model is a simplification of the seven equation model and, in its most general form, requires the solution of two differential equations and the specification of six empirical constants in order to calculate all six Reynolds stresses via algebraic equations. The success of a simplified version of this model in the prediction of square and equilateral triangular duct flows, and the flow through rod bundle channels gives it much potential as a basis for a general prediction procedure for flow in arbitrary shaped passages. If empirical constants can be found that are reasonably independent of geometry, then no special empirical input will be required in the prediction method other than the specification of the passage shape. The remainder of this thesis describes the development of such a prediction procedure and presents the resulting predictions, which are then compared with the available experimental data.

CHAPTER 4 CLOSURE OF THE GOVERNING
EQUATIONS OF TURBULENT FLOW AND HEAT TRANSFER

4.1 Introduction

It is clear from the survey of Chapter 3 that the prediction of turbulent flow and heat transfer in non-circular passages must include calculation of the turbulence driven secondary flows. It is also clear that, as a consequence, the turbulent (Reynolds) stresses required for this purpose cannot be calculated by a simple isotropic eddy viscosity model. Indeed, it is possible to show that this model yields equations similar in form to those for non-uniform viscosity laminar flow which, as already demonstrated, contains no stress-generated secondary motions. This chapter describes the method used to calculate these Reynolds stresses, and also the approach selected for calculation of the turbulent heat fluxes for heat transfer predictions. The mathematical formulation is then completed by specification of the boundary conditions and the empirical constants appearing in the equations.

4.2 The Algebraic stress transport model

The Reynolds stresses are calculated from a generalised curvilinear co-ordinate form of the algebraic stress transport model first derived and used by Launder and Ying (1972) and further analysed by Gessner and Emery (1976). The starting point is the full Reynolds-stress transport model of Hanjalic and Launder (1972) given in

Appendix 2 as equations A2.7 (auxiliary relations in equations A2.5). The main simplification made by Launder and Ying was to neglect transport by convection and diffusion on the basis of experimental evidence of Brundrett and Baines (1964) that the near-wall region in square duct flow is dominated by vorticity generation. With this simplification equations A2.7 became:

$$\begin{aligned}
 & - (\overline{u_j u_k} \partial U_i / \partial x_k + \overline{u_i u_k} \partial U_j / \partial x_k) - 2\delta_{ij} \epsilon / 3 \\
 & - C_{\phi 1} \epsilon (\overline{u_i u_j} - 2\delta_{ij} k / 3) / k + a_{lj}^m \partial U_l / \partial x_m \\
 & + a_{li}^m \partial U_l / \partial x_m = 0 \quad (4.2.1)
 \end{aligned}$$

where $\overline{u_i u_j}$ are the Reynolds stresses and the other quantities and nomenclature are defined in Appendix 2.

The above equations can now be resolved into their appropriate Cartesian directions neglecting all generation terms due to cross-plane velocity gradients, since in the present class of flows these are some two orders of magnitude less than axial velocity gradients. This process yields the following six equations connecting the six stress components (i.e. 3 shear and 3 normal stresses):

$$\begin{aligned}
 & - C_{\phi 1} \epsilon \overline{u_1^2} / k + 2\epsilon (C_{\phi 1} - 1) / 3 + 2(\beta \overline{u_1 u_3} - C_{\phi 2} \overline{u_1 u_3} \cdot \overline{u_1^2} / k) \\
 & (\partial U_3 / \partial x_1) + 2(\beta \overline{u_2 u_3} - C_{\phi 2} \overline{u_2 u_3} \cdot \overline{u_1^2} / k) (\partial U_3 / \partial x_2) = 0 \quad (4.2.2)
 \end{aligned}$$

$$\begin{aligned}
 & - C_{\phi 1} \epsilon \overline{u_2^2} / k + 2\epsilon (C_{\phi 1} - 1) / 3 + 2(\beta \overline{u_1 u_3} - C_{\phi 2} \overline{u_1 u_3} \cdot \overline{u_2^2} / k) \\
 & (\partial U_3 / \partial x_1) + 2(2\beta \overline{u_2 u_3} - C_{\phi 2} \overline{u_2 u_3} \cdot \overline{u_2^2} / k) (\partial U_3 / \partial x_2) = 0 \quad (4.2.3)
 \end{aligned}$$

$$\begin{aligned}
 & - C_{\phi 1} \epsilon \overline{u_3^2} / k + 2\epsilon(C_{\phi 1} - 1) / 3 + 2((\lambda + \beta) \overline{u_1 u_3} - C_{\phi 2} \overline{u_1 u_3} \cdot \overline{u_3^2} / k) \\
 & (\partial U_3 / \partial x_1) + 2((\lambda + \beta) \overline{u_2 u_3} - C_{\phi 2} \overline{u_2 u_3} \cdot \overline{u_3^2} / k) (\partial U_3 / \partial x_2) = 0
 \end{aligned} \tag{4.2.4}$$

$$\begin{aligned}
 & - C_{\phi 1} \epsilon \overline{u_1 u_2} / k + (\beta \overline{u_2 u_3} - 2C_{\phi 2} \overline{u_1 u_3} \cdot \overline{u_1 u_2} / k) (\partial U_3 / \partial x_1) \\
 & + (\beta \overline{u_1 u_3} - 2C_{\phi 2} \overline{u_2 u_3} \cdot \overline{u_1 u_2} / k) (\partial U_3 / \partial x_2) = 0
 \end{aligned} \tag{4.2.5}$$

$$\begin{aligned}
 & - C_{\phi 1} \epsilon \overline{u_1 u_3} / k + (\lambda \overline{u_1^2} + \beta \overline{u_3^2} + (\gamma + \eta)k - 2C_{\phi 2} \overline{u_1 u_3} \cdot \overline{u_1 u_3} / k) \\
 & (\partial U_3 / \partial x_1) + (\lambda \overline{u_1 u_2} - 2C_{\phi 2} \overline{u_2 u_3} \cdot \overline{u_1 u_3} / k) (\partial U_3 / \partial x_2) = 0
 \end{aligned} \tag{4.2.6}$$

$$\begin{aligned}
 & - C_{\phi 1} \epsilon \overline{u_2 u_3} / k + (\lambda \overline{u_1 u_2} - 2C_{\phi 2} \overline{u_1 u_3} \cdot \overline{u_2 u_3} / k) (\partial U_3 / \partial x_1) \\
 & + (\lambda \overline{u_2^2} + \beta \overline{u_3^2} + (\gamma + \eta)k - 2C_{\phi 2} \overline{u_2 u_3} \cdot \overline{u_2 u_3} / k) (\partial U_3 / \partial x_2) = 0
 \end{aligned} \tag{4.2.7}$$

where λ is a constant given by

$$\lambda = \alpha + \beta - 1. \tag{4.2.8}$$

When equations (4.2.2) - (4.2.4) are summed there results the useful relation

$$\epsilon = - \overline{u_1 u_3} (\partial U_3 / \partial x_1) - \overline{u_2 u_3} (\partial U_3 / \partial x_2) \tag{4.2.9}$$

Equations (4.2.2) to (4.2.7) and (4.2.9) form a set of seven simultaneous algebraic equations for the six Reynolds stresses $\overline{u_1^2}$, $\overline{u_2^2}$, $\overline{u_3^2}$, $\overline{u_1 u_2}$, $\overline{u_1 u_3}$, $\overline{u_2 u_3}$ and the turbulent kinetic energy dissipation rate ϵ : solution is therefore possible and is facilitated by the further manipulations described below, in which the equations are transformed from implicit to quasi-explicit form.

Firstly, equations (4.2.2) to (4.2.5) and (4.2.9) are rearranged to give:

$$\overline{u_1^2} = C_3 k + C_2(k/\epsilon)\overline{u_1 u_3} \partial U_3/\partial x_1 \quad (4.2.10)$$

$$\overline{u_2^2} = C_3 k + C_2(k/\epsilon)\overline{u_2 u_3} \partial U_3/\partial x_2 \quad (4.2.11)$$

$$\overline{u_3^2} = C_1 k \quad (4.2.12)$$

$$\overline{u_1 u_2} = C_2(k/2\epsilon) (\overline{u_2 u_3} \partial U_3/\partial x_1 + \overline{u_1 u_3} \partial U_3/\partial x_2) \quad (4.2.13)$$

where C_1 , C_2 and C_3 are constants defined by

$$C_1 = \frac{2[(C_{\phi 1} - 1)/3 - (\alpha + 2\beta - 1)]}{(C_{\phi 1} - 2C_{\phi 2})} \quad (4.2.14)$$

$$C_2 = 2\beta/(C_{\phi} - 2C_{\phi 2}) \quad (4.2.15)$$

$$C_3 = (2(C_{\phi 1} - 1)/3 - 2\beta)/(C_{\phi 1} - 2C_{\phi 2}) \quad (4.2.16)$$

When equations (4.2.9) to (4.2.13) are used to substitute for $\overline{u_1^2}$, $\overline{u_2^2}$, $\overline{u_3^2}$ and $\overline{u_1 u_2}$ in equations (4.2.6) and (4.2.7), the latter can be arranged in terms of $\overline{u_1 u_3}$ and $\overline{u_2 u_3}$ so that when one is divided by the other, there results

$$\overline{u_1 u_3}/\overline{u_2 u_3} = (\partial U_3/\partial x_1)/(\partial U_3/\partial x_2)$$

i.e. $\overline{u_1 u_3} \partial U_3/\partial x_2 = \overline{u_2 u_3} \partial U_3/\partial x_1$

This identity then allows the equations for $\overline{u_1 u_3}$ and $\overline{u_2 u_3}$ to be reduced to

$$\overline{u_1 u_3} = - C_4(k^2/\epsilon) \partial U_3/\partial x_1 \quad (4.2.17)$$

$$\overline{u_2 u_3} = - C_4(k^2/\epsilon) \partial U_3/\partial x_2 \quad (4.2.18)$$

where the constant C_4 is given by

$$C_4 = -(\beta C_1 + \gamma + \eta + \lambda(C_3 - C_2))/(C_{\phi 1} - 2C_{\phi 2}) \quad (4.2.19)$$

Substitution of the axial-planes kinematic stresses $\overline{u_1 u_3}$ and $\overline{u_2 u_3}$ from equations (4.2.17) and (4.2.18) into the cross-plane stress equations (4.2.10), (4.2.11) and (4.2.13) gives

$$\overline{u_1^2} = C_3 k - C_2 C_4 (k^3/\epsilon^2) (\partial U_3/\partial x_1)^2 \quad (4.2.20)$$

$$\overline{u_2^2} = C_3 k - C_2 C_4 (k^3/\epsilon^2) (\partial U_3/\partial x_2)^2 \quad (4.2.21)$$

$$\overline{u_1 u_2} = - C_2 C_4 (k^3/\epsilon^2) (\partial U_3/\partial x_1) (\partial U_3/\partial x_2) \quad (4.2.22)$$

Equations (4.2.12), (4.2.17), (4.2.18) and (4.2.20) to (4.2.22) are now transformed into curvilinear co-ordinate form to yield the final set

$$\overline{u_3^2} = C_1 k \quad (4.2.23)$$

$$\overline{u_2^2} = C_3 k - C_2 C_4 (k^3/\epsilon^2) (\partial U_3/h_2 \partial y_2)^2 \quad (4.2.24)$$

$$\overline{u_1^2} = C_3 k - C_2 C_4 (k^3/\epsilon^2) (\partial U_3/h_1 \partial y_1)^2 \quad (4.2.25)$$

$$\overline{u_1 u_2} = - C_2 C_4 (k^3/\epsilon^2) (\partial U_3/h_1 \partial y_1) (\partial U_3/h_2 \partial y_2) \quad (4.2.26)$$

$$\overline{u_1 u_3} = - C_4 (k^2/\epsilon) \partial U_3/h_1 \partial y_1 \quad (4.2.27)$$

$$\overline{u_2 u_3} = - C_4 (k^2/\epsilon) \partial U_3/h_2 \partial y_2 \quad (4.2.28)$$

in which the individual stress components are now expressed as explicit functions of k , ϵ and mean velocity gradients. This set will hereafter be referred to as the 'Algebraic Stress Transport Model' (ASTM), in which the constants C_1 , C_2 , C_3 and C_4 can be expressed in terms of the constants $C_{\phi 1}$ and $C_{\phi 2}$ using equations (A2.6) in Appendix 2 thus:

$$C_1 = (22C_{\phi 1} - 24C_{\phi 2} + 8)/33(C_{\phi 1} - 2C_{\phi 2}) \quad (4.2.29)$$

$$C_2 = (12C_{\phi_2} - 4)/11(C_{\phi_1} - 2C_{\phi_2}) \quad (4.2.30)$$

$$C_3 = (22C_{\phi_1} - 36C_{\phi_2} - 10)/33(C_{\phi_1} - 2C_{\phi_2}) \quad (4.2.31)$$

$$C_4 = (44C_{\phi_1} - 22C_{\phi_1}C_{\phi_2} - 128C_{\phi_2} - 36C_{\phi_2}^2 + 10)/165(C_{\phi_1} - 2C_{\phi_2})^2 \quad (4.2.32)$$

Two interesting features are readily apparent in the ASTM. Firstly the axial plane shear stress equations (4.2.27) and (4.2.28) are identical to those of a turbulent-viscosity model (equation (3.4.1)) with the kinematic turbulent viscosity ν_t given by

$$\nu_t = C_4 k^2 / \epsilon \quad (4.2.33)$$

Comparison of this equation with the Prandtl-Kolmogorov formula of equation (3.4.7) shows that $C_4 \equiv C_\mu$. Secondly equations (4.2.24) to (4.2.26) for the cross-plane stresses show that these are linked solely to mean strain rates $\partial U_3/h_1 \partial y_1$ and $\partial U_3/h_2 \partial y_2$ in planes orthogonal to the cross-plane. This is in direct contrast to the axial-plane shear stresses where the planes of stress and strain are co-aligned. It is this cross-planar effect in the former case that is responsible for the generation of secondary flows of the second kind as now revealed in the application of the ASTM to turbulent non-circular passage flow. The ASTM further reveals a link between the cross-plane and the axial plane Reynolds stresses, both of which are connected to axial plane strain rates.

Compared with a multi-equation Reynolds stress model (e.g. Reece, 1977), the main simplifications made in derivation of the ASTM is the neglect of transport of stress by diffusion and convection. These simplifications should be acceptable in the calculation of

fully developed flow in straight passages since (i) diffusion should be small, even in the regions of high stress gradients near walls, as generation reaches a maximum there and should dominate, and (ii) convection will be due to secondary flows of the second kind and, as such, should be small (1% - 2% of the mean axial velocity from experimental evidence). It follows also from (ii) that the ASTM would not be valid in passage flows with strong secondary motions, such as those of the first kind that can be produced by axial curvature or by lateral motion of a passage wall. In these cases, however, the weaker stress-induced motions of the second kind would probably have little influence on the overall flow.

4.3 Transport equations for k and ϵ

The values of k and ϵ required in the ASTM are calculated in this study from their modelled transport equations. This is considered necessary since the present calculation procedure is intended for application to passages of arbitrary geometry, which precludes the more simple alternatives of using an algebraic length scale formula for the calculation of either ϵ or both k and ϵ as proposed by Gessner and Emery, (1976); since there is no such formula available that is known to calculate length scale accurately for arbitrary-shaped ducts. In particular the length scale formulae used in previous applications of the Launder and Ying (1973) ASTM were either obtained from experiments for the particular passage shape (e.g. Carajilescov and Todreas, 1976) or based on simple geometric formula known from measurements to be adequate for the particular duct shape considered (e.g. Launder and Ying, 1973; Gessner and Po, 1976; Aly et al, 1978).

The modelled transport equations here used for k and ϵ are the now-accepted forms appropriate to high Reynolds number flows in which viscous effects are deemed negligible. The equation for k was first proposed by Kolmogorov (1942) and is now widely used in one and two equation turbulence models (Launder and Spalding, 1972) and that for ϵ was first formulated by Daly and Harlow (1970) and is also now commonly used in two and higher-order turbulence and stress models (Reynolds and Cebeci in Chapter 5 of Bradshaw, 1978). The equations are, in Cartesian tensor notation:

$$\partial(U_i k) / \partial x_i = \partial \left(\frac{C_k k^2}{\epsilon \sigma_k} \frac{\partial k}{\partial x_i} \right) / \partial x_i + P / \rho - \epsilon \quad (4.3.1)$$

$$\partial(U_i \epsilon) / \partial x_i = \partial \left(\frac{C_\epsilon k^2}{\epsilon \sigma_\epsilon} \frac{\partial \epsilon}{\partial x_i} \right) / \partial x_i + \epsilon (C_{\epsilon 1} P - \rho C_{\epsilon 2} \epsilon) / \rho k \quad (4.3.2)$$

where σ_k and σ_ϵ are the turbulent Prandtl (Schmidt) numbers for k and ϵ respectively, $C_{\epsilon 1}$ and $C_{\epsilon 2}$ constants and P is the production rate of k given by

$$P = - \rho \overline{u_i u_j} (\partial U_i / \partial x_j) \quad (4.3.3)$$

Transformation of the above into curvilinear co-ordinate form via the relations of Appendix 3 and specialisation to the case of fully developed flow yields:

$$\begin{aligned} \partial(h_2 \rho U_1 k) / \partial y_1 + \partial(h_1 \rho U_2 k) / \partial y_2 &= h_1 h_2 P - h_1 h_2 \rho \epsilon \\ + \partial \left(\frac{h_2}{h_1} \left(\frac{C_k \rho k^2}{\sigma_k \epsilon} \right) \left(\frac{\partial k}{\partial y_1} \right) \right) / \partial y_1 &+ \partial \left(\frac{h_1}{h_2} \left(\frac{C_k \rho k^2}{\sigma_k \epsilon} \right) \left(\frac{\partial k}{\partial y_2} \right) \right) / \partial y_2 \end{aligned} \quad (4.3.4)$$

$$\begin{aligned} \partial(h_2\rho U_1\varepsilon)/\partial y_1 + \partial(h_1\rho U_2\varepsilon)/\partial y_2 &= h_1h_2C_{\varepsilon 1}\varepsilon P/k \\ - h_1h_2C_{\varepsilon 2}\rho\varepsilon^2/k + \partial\left(\frac{h_2}{h_1}\left(\frac{C_4\rho k^2}{\sigma_\varepsilon\varepsilon}\right)\left(\frac{\partial\varepsilon}{\partial y_1}\right)\right)/\partial y_1 \\ + \partial\left(\frac{h_1}{h_2}\left(\frac{C_4\rho k^2}{\sigma_\varepsilon\varepsilon}\right)\left(\frac{\partial\varepsilon}{\partial y_2}\right)\right)/\partial y_2 &\quad (4.3.5) \end{aligned}$$

$$P = - \rho\overline{u_1u_3}\partial U_3/h_1\partial y_1 - \rho\overline{u_2u_3}\partial U_3/h_2\partial y_2 \quad (4.3.6)$$

where, in the expression for the production rate of turbulent kinetic energy P (equation 4.3.3), only gradients in axial velocity are retained in conformity with the overall model.

4.4 The turbulent heat flux model

When the scalar transport equation (2.4.10) is applied to heat transport, the turbulent heat fluxes $\overline{u_1c}$ and $\overline{u_2c}$ are required to be calculated. The method most commonly-used in previous calculations (see section 3.4.3) is also employed here; namely a gradient diffusion model incorporating an isotropic turbulent diffusivity of heat γ_c i.e.

$$- \overline{u_1c} = \gamma_c \partial C/h_1\partial y_1 \quad (4.4.1)$$

$$- \overline{u_2c} = \gamma_c \partial C/h_2\partial y_2 \quad (4.4.2)$$

where

$$\gamma_c = \nu_t/\sigma_c \quad (4.4.3)$$

with σ_c the turbulent Prandtl number for heat transport. From previous measurements, σ_c can be assumed constant at a value near 0.9 (see section 3.4.3).

It is of interest to assemble an alternative model for the turbulent heat fluxes $\overline{u_j c}$ in a similar way to that used to derive the ASTM for turbulent stresses (Launder, Chapter 6, Bradshaw, 1978). This involves simplifying and modelling the transport equation for $\overline{u_j c}$ as detailed in Appendix 4 and leads to equation A4.3 quoted below in Cartesian tensor notation:

$$\begin{aligned}
 & - \overline{u_j u_k} \partial C / \partial x_k - \overline{u_k c} \partial U_j / \partial x_k + C_{1c} (\epsilon/k) \overline{u_j c} \\
 & + C_{2c} \overline{u_k c} \partial U_j / \partial x_k = 0
 \end{aligned} \tag{A4.3}$$

For the case of fully-developed turbulent flow through non-circular passages considered here gradients of the cross-plane velocities can be neglected and since, additionally, the axial gradients ($\partial/h_3 \partial y_3$) are zero, the turbulent heat fluxes can be expressed from equation A4.3, after transformation to curvilinear coordinate form (Appendix 3) as:

$$\overline{u_1 c} = - k(\overline{u_1^2} \partial C / h_1 \partial y_1 + \overline{u_1 u_2} \partial C / h_2 \partial y_2) / C_{1c} \epsilon \tag{4.4.4}$$

$$\overline{u_2 c} = - k(\overline{u_2^2} \partial C / h_2 \partial y_2 + \overline{u_1 u_2} C / h_1 \partial y_1) / C_{1c} \epsilon \tag{4.4.5}$$

Experimental measurements in a square duct (Brundrett and Baines, 1964) and attempts made at measurements in other ducts (e.g. Aly et al, 1978) have shown the cross-plane shear stresses $\overline{u_1 u_2}$ to be at least two orders of magnitude less than the normal stresses and they can, therefore, be omitted giving:

$$\overline{u_1 c} = - (k \overline{u_1^2} / C_{1c} \epsilon) \partial C / h_1 \partial y_1 \tag{4.4.6}$$

$$\overline{u_2 c} = - (k \overline{u_2^2} / C_{1c} \epsilon) \partial C / h_2 \partial y_2 \tag{4.4.7}$$

The above relations will hereafter be referred to as the Algebraic Heat Flux Transport Model (AHFTM). Comparing equations (4.4.6) and (4.4.7) with equations (4.4.1) and (4.4.2), the AHFTM can be interpreted as a gradient diffusion model with anisotropic turbulent diffusivities linked to the turbulence structure via the relations

$$\gamma_{c1} = \overline{u_1^2} k / C_{1c} \epsilon \quad (4.4.8)$$

$$\gamma_{c2} = \overline{u_2^2} k / C_{1c} \epsilon \quad (4.4.9)$$

in which γ_{c_j} is seen to be proportional to the corresponding normal stress $\overline{u_j^2}$.

Some comparisons will be made between predictions based on the above AHFTM and on the isotropic turbulent diffusivity model.

4.5 Summary of the equations solved

A summary can now be made of all the equations requiring solution for the prediction of steady, fully developed flow and heat transfer in straight passages of arbitrary cross-section. These are:

- (i) Direction 1 momentum (2.4.6)
- (ii) Direction 2 momentum (2.4.7)
- (iii) Direction 3 momentum (2.4.8)
- (iv) Mass continuity (2.4.9)
- (v) Heat transport (2.4.10)
- (vi) k transport (4.3.4)
- (vii) ϵ transport (4.3.5)

- (viii) ASTM (4.2.24) to (4.2.28)
- (ix) Turbulent heat fluxes (4.4.1) and (4.4.2)

Equations (i) to (vii) can be seen to be closely coupled non-linear elliptic partial differential equations, which require specification of the conditions prevailing at all lateral boundaries of the passages.

4.6 Boundary conditions

Typically, a passage flow calculation will involve one or both of the following two types of boundary; symmetry planes and stationary channel walls. At the former, the normal gradients of all the dependent variables are zero, apart from the velocity normal to the plane, which is itself zero. At the latter, although all variables assume known values (e.g. the U_i are all zero) the approach adopted here is to use 'wall functions' to match the inner solution to the wall conditions. This eliminates the necessity for a detailed calculation of the complex near wall region with its steep gradients of the main variables which would otherwise entail fine grids, and with viscous effects which would invalidate the use of the high Reynolds number turbulence model.

The algebraic nature of the stress equations precludes the necessity to specify boundary conditions for them, and the treatment of the remaining variables follows the practices of earlier workers, as outlined by Launder and Spalding (1972) and summarised below.

The wall function employed for velocity is based on the well known logarithmic 'law of the wall' which has been experimentally established as applying to the near wall region in a variety of turbulent flows including the present class (section 3.2 and table 3.2.2.). In this region, the shear stress can be taken as constant along a wall normal to a good approximation and is therefore equal to the local wall shear stress. The resultant shear stress τ_0 at the wall is given by

$$\tau_0 = \rho U^* C_4^{1/2} k^{1/2} \quad (4.6.1)$$

where the friction velocity U^* is given by the log-law (e.g. Schlichting, 1968) as

$$U^* = U \kappa / \ln(Es^+) \quad (4.6.2)$$

in which U is the resultant velocity parallel to the wall, κ and E are the log-law constants and

$$s^+ = C_4^{1/2} k^{1/2} s / \nu \quad (4.6.3)$$

where s is the distance normal to the wall surface.

The value of ϵ near the wall is obtained by neglecting transport of k by convection and diffusion and assuming a length scale that, like mixing length in this region, varies linearly with s (Launder and Spalding, 1972) so that

$$\epsilon = C_4^{3/4} k^{3/2} / \kappa s \quad (4.6.4)$$

This near-wall behaviour of ϵ implies a particular value of σ_ϵ as follows. Applying the ϵ transport equation (4.3.2) to a control volume in the wall region, assuming gradients normal to the wall only, with convection transport negligible and retaining turbulent effects only yields:

$$d((\mu_t/\sigma_\epsilon)\partial\epsilon/\partial s)/ds = \epsilon(C_{\epsilon 1}P - C_{\epsilon 2}\rho\epsilon)/k$$

Assuming local equilibrium with $P = \rho\epsilon$, integrating twice with constant average values of all the variables, and substituting from equation (4.6.4) yields

$$\sigma_\epsilon = \kappa^2/(C_4^{\frac{1}{2}}(C_{\epsilon 2} - C_{\epsilon 1})) \quad (4.6.5)$$

The turbulent kinetic energy k near the wall is obtained by neglecting convection and diffusion to the wall and calculating generation and dissipation from the local wall shear stress (equation (4.6.1)).

A semi-logarithmic law is used for the near wall region in the thermal energy equation. The form used is that proposed by Jayatilleke (1969) from a review of a wide range of experimental data:

$$q'' = \rho U^* C_p (T - T_w) / \sigma_c (U/U^* + P^*) \quad (4.6.6)$$

where U and T are the near wall velocities and temperature, T_w is the wall temperature U^* is the local friction velocity (equation (4.6.2)) and P^* is a function devised to take account of the thermal resistance due to the viscous sublayer, given by Jayatilleke (1969)

as:

$$P^* = 9.24(R^{3/4} - 1)(1 + 0.28e^{-.007R}) \quad (4.6.7)$$

where $R = P_r/\sigma_c$ with P_r the laminar Prandtl number.

4.7 Empirical constants

The various independent 'constants' appearing in the model equations are collected together in table 4.7.1, which shows the values ascribed to them in the present work. These values have been taken from those recommended by earlier users of the Launder and Ying ASTM and the $k-\epsilon$ turbulence model. A square bracket in the 'basis of selection' column cites a further source for the value used if it has evolved from that given in the original reference (curved brackets) by subsequent tests on other turbulent flows.

It is of interest to note that test calculations in the present work showed the predictions to be relatively insensitive to changes in all of these constants except $C_{\phi 2}$ which controls the strength of the stress-generated sources in the cross-plane momentum equations. The values selected here for $C_{\phi 1}$ and $C_{\phi 2}$ were taken as a mean of those used by Launder and Ying (1972) in square duct calculations ($C_{\phi 1} = 2.6$, $C_{\phi 2} = 0.365$) and Aly et al (1978) in equilateral triangular duct calculations (constants used implied values of $C_{\phi 1} = 3.0$, $C_{\phi 2} = 0.35$). These two sets of values were chosen in preference to other previous users of the Launder and Ying ASTM since they either neglected cross-plane shear, calculated stresses only from experimental measurement or did not validate their predictions against experiment.

Table 4.7.1 The values of the universal empirical turbulence model constants employed in the present calculations.

Constant	Value	Basis of selection
$C_{\phi 1}$	2.78	Return to isotropy in absence of mean strain (Launder and Ying, 1973); [Aly et al, 1978]
$C_{\phi 2}$	0.358	Plane homogenous shear flow (Launder and Ying, 1973); [Aly et al, 1978]
$C_{\epsilon 1}$	1.55	Measurement of turbulence near to walls (Launder and Spalding, 1972); [Tatchell, 1975]
$C_{\epsilon 2}$	2.0	Decay of turbulence behind a grid (Launder and Spalding, 1972); [Tatchell, 1975]
σ_k	1.0	Near unity from physical argument (Launder and Spalding, 1972).
σ_c	0.9	Near wall measurements (Launder, Chap. 6, Bradshaw, 1978).
E	9.025] Average of experimental data for smooth walls (Schlichting, 1968).
κ	0.4	

There are a number of constants appearing in the various equations solved that are dependent on those listed in Table (4.7.1). To assist the reader, these are summarised here, together with their defining equation numbers:

$$C_2 = 0.013 \quad (4.2.30)$$

$$C_3 = 0.562 \quad (4.2.31)$$

$$C_4 = 0.085 \quad (4.2.32)$$

$$\sigma_\epsilon = 1.22 \quad (4.6.5)$$

All the constants in Table (4.7.1) were used, as listed, for the whole range of turbulent flows and passage geometries calculated in

the present study: i.e. no attempt was made to 'tune' them to give optimum agreement with experiment for particular cases, since one of the objectives of the present work is to determine the extent to which they are universal.

4.8 Closure

The mathematical model presented in Chapter 2 has been completed in this chapter by the formulation of equations for calculation of the Reynolds stress tensor, the turbulent scalar fluxes and the conditions prevailing at the passage boundaries. Algebraic equations were obtained for the turbulent stresses (the ASTM) by simplification of the Reynolds Stress Transport Equations, the main simplification being the neglect of transport by convection and diffusion. The ASTM revealed a direct link between the cross-plane stresses and the axial plane strain rates which, in turn, are linked to the axial plane shear stresses.

The boundary conditions to be used for each partial differential equation and the values of the universal empirical constants in these and the other equations are entirely conventional and based on those used in previously published work. The next chapter presents the finite difference form of the partial differential equations and the method developed to obtain their simultaneous solution.

5.1 Introduction

The partial differential equations which govern fully developed flow and heat transfer in arbitrary shaped passages are set out in Chapters 2 and 4. In this chapter, the numerical approximations and procedures used for the simultaneous solution of these equations are presented. A finite-difference approach has been used, in which the partial differential equations are approximately integrated over imaginary, finite control volumes which are contiguous over the solution domain. These control volumes surround grid nodes which are located at the intersection of grid lines, which in this study, are curvilinear and orthogonal. Detailed descriptions of the grid and formulation of the finite-difference equations are given in sections 5.2 and 5.3.

The finite difference equations obtained are algebraic in form. strongly coupled and non-linear. An existing solution scheme, usually referred to as 'SIMPLE' (Semi-Implicit Method for Pressure Linked Equations) has been used to simultaneously solve these equations. Details of this scheme are given in section 5.4, a description of how the boundary conditions are incorporated is provided in section 5.5 and an outline of the solution algorithm in section 5.6. The grid generation methods used are outlined in section 5.8. Finally, in section 5.9 details are presented of the practices that have been introduced to aid convergence of the solution and of the methods used to check the accuracy of the procedure.

5.2 The finite-difference grid

The finite-difference grid consists of a set of orthogonally intersecting grid lines in three dimensions. In the cross-plane of the passage, the grid lines are curvilinear and intersect orthogonally with each other and with the boundaries of the passage. The main grid nodes, designated ' ϕ ' nodes, are at the points of intersection, through which pass the straight axial lines which complete the three dimensional grid. A portion of such a grid is shown in figure 5.2.1a, with the cross-plane mesh in heavier lines and the ϕ nodes indicated with small filled circles.

The ' ϕ ' grid nodes are surrounded by ' ϕ ' control volumes or 'cells', the boundaries of which are formed, in the cross-plane, by a mesh of lines representing axial planes, mid-way between the main grid lines and, in the axial direction by a pair of cross-sectional planes. Figure 5.2.1b shows a typical ϕ cell (hatched) with the cell boundaries as broken lines. The methods used to calculate the location of the main grid nodes are presented in a later section.

Grid nodes can be identified by grid line numbers 'i' or 'j' in each orthogonal direction as shown in figure 5.2.2a. The ϕ cell surrounding the node $\phi_p (\equiv \phi_{i,j})$ is the orthogonal curvilinear rectangle n-e-s-w in figure 5.2.2a. The grid line spacing is in general non-uniform so the cell size and shape can vary across the passage cross-section.

The main variables p , U_3 , k , ϵ and T are calculated and stored in the computation scheme at the ϕ node, whereas the cross-plane velocities U_1 and U_2 are computed at intervening locations, displaced

mid-way between the ϕ nodes in the direction of the velocity component in question. For example, in figure 5.2.2a, U_1 is calculated at w, e etc. whereas U_2 is calculated at n, s etc. The control volume cell for the U_1 location in the cross-plane is bounded by planes represented by the nearest grid lines and the ϕ control volume planes each side of the location. A similar arrangement applies for the U_2 control volume as illustrated for each case in figures 5.2.2b and c. This staggered grid arrangement is now conventional practice in finite-difference procedures for fluid flow since it enhances stability and convergence (Harlow and Welch, 1965; Caretto et al, 1972) due mainly to the cross-plane velocities being located mid-way between the pressures which drive them. These pressures are, in fact, needed at the U_1 and U_2 control volume faces which is exactly where they are computed and stored in this staggered grid scheme. In addition to this, the velocities are available at the ϕ control volume faces which is also exactly where they are needed for calculation of the convective fluxes of the main variables.

5.3 The finite-difference equations

5.3.1 The ϕ equation

The governing partial differential equations can all be cast into the following common form:

$$\begin{aligned} \frac{\partial(h_2 G_\phi \phi)}{\partial y_1} + \frac{\partial(h_1 G_\phi \phi)}{\partial y_2} &= \frac{\partial(h_2 D_\phi \phi / h_1 \partial y_1)}{\partial y_1} \\ + \frac{\partial(h_1 D_\phi \phi / h_2 \partial y_2)}{\partial y_2} + C_\phi & \end{aligned} \quad (5.3.1)$$

where ϕ stands for any of the main dependent variables U_1 , U_2 , U_3 , k and ϵ , D_ϕ is the exchange coefficient and C_ϕ represents the source. The latter is also a receptacle for the terms not already contained in the other components. Table 5.3.1 summarises the terms appearing in C_ϕ and D_ϕ for each main variable. The two terms on the l.h.s. of equation (5.3.1) are usually referred to as the 'convection' terms, and the first two on the r.h.s. as the 'diffusion' terms.

5.3.2 The finite-difference scheme

The finite-difference equivalent of equation (5.3.1) is obtained for each location by integrating each term over the control volume (appropriate to the variable considered when ϕ represents U_1 or U_2). This micro-integration technique helps to ensure that the resulting finite-difference equations satisfy the relevant conservation principles embodied in each partial differential equation. (The control volumes are here all assumed to be interior; the modifications necessary near the boundaries will be discussed later). The integrated terms will contain values of ϕ at each control volume face which are a weighted average of values at adjacent nodes. The weighting used depends on the differencing scheme adopted. In the present method a hybrid differencing scheme (HDS) is used for convection of ϕ and a central differencing scheme (CDS) for diffusion of ϕ (see Caretto et al, 1972). The HDS is essentially a CDS with provision to switch to upwind differencing with diffusion neglected when the absolute cross-plane flow is such that the local absolute Peclet number $|Pe|$ is equal to, or greater than 2.0. This preserves the accuracy of central differencing at the

ϕ	D_ϕ	C_ϕ
U_1	μ	$- h_2 \partial p / \partial y_1 + \partial(\mu h_2 \partial U_1 / h_1 \partial y_1) / \partial y_1 + \partial(2\mu h_2 U_2 / r_1) / \partial y_1$ $- \partial(\mu h_1 U_1 / r_1) / \partial y_2 + \partial(\mu \partial U_2 / \partial y_1) / \partial y_2$ $- \partial(\mu h_1 U_2 / r_2) / \partial y_2 - \partial(h_2 \rho \overline{u_1 u_1}) / \partial y_1 - \partial(h_1 \rho \overline{u_1 u_2}) / \partial y_2$ $- h_1 h_2 (2\mu \partial U_2 / h_2 \partial y_2 + 2\mu U_1 / r_2 - \rho U_2 U_2 - \rho \overline{u_2 u_2}) / r_2$ $+ h_1 h_2 (\mu \partial U_1 / h_2 \partial y_2 + \mu \partial U_2 / h_1 \partial y_1 - \mu U_1 / r_1 - \mu U_2 / r_2$ $- \rho U_1 U_2 - \rho \overline{u_1 u_2}) / r_1$
U_2	μ	$- h_1 \partial p / \partial y_2 + \partial(\mu h_1 \partial U_2 / h_2 \partial y_2) / \partial y_2 + \partial(2\mu h_1 U_1 / r_2) / \partial y_2$ $- \partial(\mu h_2 U_2 / r_2) / \partial y_1 + \partial(\mu \partial U_1 / \partial y_2) / \partial y_1$ $- \partial(\mu h_2 U_1 / r_1) / \partial y_1 - \partial(h_1 \rho \overline{u_2 u_2}) / \partial y_2 - \partial(h_2 \rho \overline{u_1 u_2}) / \partial y_1$ $- h_1 h_2 (2\mu \partial U_1 / h_1 \partial y_1 + 2\mu U_2 / r_1 - \rho U_1 U_1 - \rho \overline{u_1 u_1}) / r_1$ $+ h_1 h_2 (\mu \partial U_2 / h_1 \partial y_1 + \mu \partial U_1 / h_2 \partial y_2 - \mu U_2 / r_2 - \mu U_1 / r_1$ $- \rho U_1 U_2 - \rho \overline{u_1 u_2}) / r_2$
U_3	μ_{eff}	$- h_1 h_2 \partial p / \partial y_3$
k	μ_t / ν_k	$h_1 h_2 P - h_1 h_2 \rho \epsilon$
ϵ	μ_t / ν_ϵ	$h_1 h_2 C_{\epsilon 1} \epsilon P / k - h_1 h_2 C_{\epsilon 2} \rho \epsilon^2 / k$
C	μ_t / ν_C	$- \partial(h_1 h_2 \rho U_3 C) / \partial y_3$

Table 5.3.1 Coefficients of the ϕ equation

lower cross-flows and affords the stability and good convergence of upwind differencing at higher cross-flows.

In the following approximate integration of equation (5.3.1) CDS will be used initially for the convection, diffusion and source terms: then the HDS modifications to the resulting coefficients will be indicated. It is convenient to consider first of all, a variable ϕ_p calculated at node $\phi_{i,j}$. With reference to figure 5.2.2(a), the nodes adjacent to $\phi_{i,j}$ are designated as 'N' at $\phi_{i,j+1}$, 'S' at $\phi_{i,j-1}$, 'E' at $\phi_{i+1,j}$ and 'W' at $\phi_{i-1,j}$. These letters, together with n, s, e, w which represent the (intermediate) locations of the control volume faces, will be used as suffices to indicate a value at that location. The axial distance between the upstream and downstream planes defining the control volume faces normal to the axial direction is constant and represented by ΔZ . The integrals are as follows:

(i) Convection terms

$$\text{let } I_{C1} = \int_S^n \int_W^e (\partial(h_2 G_1 \phi) / \partial y_1) \Delta Z dy_2 dy_1$$

$$\text{then } I_{C1} = \int_S^n ((h_2 G_1 \phi)_e - (h_2 G_1 \phi)_w) \Delta Z dy_2$$

which is approximated as

$$I_{C1} \approx (G_1 \phi)_e \Delta Z S_{2e} - (G_1 \phi)_w \Delta Z S_{2w}$$

where S_i is the curvilinear arc distance $\int h_i dy_i$ e.g. S_{2e} is the arc length of the control volume boundary passing through the point e in the direction y_2 ('deb' in figure 5.2.2a). Assuming a CDS, ϕ_e and ϕ_w can be written in terms of the value at adjacent nodes to give

$$I_{C1} \approx G_{1e}(\phi_E + \phi_p) \Delta Z S_{2e} / 2 - G_{1w}(\phi_p + \phi_w) \Delta Z S_{2w} / 2 \quad (5.3.2)$$

Using a similar method, the second convection term can be written as

$$I_{C2} \approx G_{2n}(\phi_N + \phi_P)\Delta Z S_{1n}/2 - G_{2s}(\phi_P + \phi_S)\Delta Z S_{1s}/2 \quad (5.3.3)$$

It should be noted that in the above G_{1e} , G_{1w} , G_{2n} and G_{2s} denote the lateral mass fluxes at the ϕ control volume faces.

(ii) Diffusion terms

$$\text{let } I_{D1} = \int_S^n \int_W^e (\partial(h_2 D_\phi / \partial \phi / h_1 \partial y_1) / \partial y_1) \Delta Z dy_2 dy_1$$

$$\text{then } I_{D1} = \int_S^n ((h_2 D_\phi \partial \phi / h_1 \partial y_1)_e - (h_2 D_\phi \partial \phi / h_1 \partial y_1)_w) \Delta Z dy_2$$

which is approximated as

$$I_{D1} \approx D_{\phi e}(\phi_E - \phi_P)S_{2e}/S_{1Pe} - D_{\phi w}(\phi_P - \phi_W)S_{2w}/S_{1Pw} \quad (5.3.4)$$

where S_{1Pe} represents the arc length across the control volume between e and P and S_{1Pw} that between w and P. Similarly the second diffusion term can be integrated to give

$$I_{D2} \approx D_{\phi n}(\phi_N - \phi_P)S_{1n}/S_{2PN} - D_{\phi s}(\phi_P - \phi_S)S_{1s}/S_{2PS} \quad (5.3.5)$$

(iii) Source

$$\text{let } I_S = \int_S^n \int_e^w C_\phi \Delta Z dy_2 dy_1$$

Assuming the source to be uniform over the control volume yields

$$I_S \approx C_\phi V_P \quad (5.3.6)$$

where V_p is the volume of the control volume, calculated as:

$$V_p = (S_{2e} + S_{2w})(S_{1n} + S_{1s})/4 \quad (5.3.7)$$

Some examples of the evaluation of C_ϕ are provided in Appendix 6.

The complete finite difference equation for ϕ is now given by

$$I_{C1} + I_{C2} - I_{D1} - I_{D2} - I_s = 0$$

which can be written, from equations (5.3.2) to (5.3.6), as

$$\begin{aligned} & C_e(\phi_E + \phi_P) - C_w(\phi_P + \phi_W) + C_n(\phi_N + \phi_P) \\ & - C_s(\phi_P + \phi_S) - B_e(\phi_E - \phi_P) + B_w(\phi_P - \phi_W) \\ & - B_n(\phi_N - \phi_P) + B_s(\phi_P - \phi_S) - g\phi - e' = 0 \end{aligned} \quad (5.3.8)$$

where

$$\left. \begin{aligned} C_e &= G_{1e}\Delta Z S_{2e}/2 \\ C_w &= G_{1w}\Delta Z S_{2w}/2 \\ C_n &= G_{2n}\Delta Z S_{1n}/2 \\ C_s &= G_{2s}\Delta Z S_{1s}/2 \\ B_e &= D_{\phi e} S_{2e}/S_{1PE} \\ B_w &= D_{\phi w} S_{2w}/S_{1PW} \\ B_n &= D_{\phi n} S_{1n}/S_{2PN} \\ B_s &= D_{\phi s} S_{1s}/S_{2PS} \end{aligned} \right\} \quad (5.3.9)$$

and the source has been linearised such that

$$C_\phi V_p = g\phi_P + e' \quad (5.3.10)$$

5.3.3 The continuity equation

Equation (5.3.8) is now manipulated into its final form by using the finite-difference equivalent of the continuity equation (2.4.9) obtained for the ϕ control volume, with faces at n, e, s, w in figure 5.2.2a. This equation is obtained from

$$\int_s^n \int_w^e (\partial(h_2 G_1)/\partial y_1) \Delta Z dy_2 dy_1 + \int_s^n \int_w^e (\partial(h_1 G_2)/\partial y_2) \Delta Z dy_1 dy_2 = 0$$

i.e.

$$G_{1e} \Delta Z S_{2e} - G_{1w} \Delta Z S_{2w} + G_{2n} \Delta Z S_{1n} - G_{2s} \Delta Z S_{1s} = 0 \quad (5.3.11)$$

$$\text{or } 2C_e - 2C_w + 2C_n - 2C_s = 0 \quad (5.3.12)$$

It is of interest to note that the differential continuity equation can alternatively be obtained from the ϕ equation (5.3.1) by setting $\phi = 1$, $D_\phi = 0$ and $C_\phi = 0$. Similarly (5.3.12) can be obtained from (5.3.8) by setting all ϕ 's to unity, all D_ϕ 's to zero and C_ϕ to zero: this is an important consequence of ensuring that the difference equations correctly express the relevant conservation laws.

5.3.4 The final form of the finite-difference equations

Rearranging equation (5.3.8) in terms of ϕ_p yields

$$\begin{aligned} & \phi_p ((B_e + C_e) + (B_w - C_w) + (B_n + C_n) + (B_s - C_s) - g) \\ & = \phi_E (B_e - C_e) + \phi_W (B_w + C_w) + \phi_N (B_n - C_n) \\ & + \phi_S (B_s + C_s) + e' \end{aligned}$$

Using equation (5.3.11) this can be written as

$$\begin{aligned} \phi_P((B_e - C_e) + (B_W + C_W) + (B_n - C_n) + (B_S + C_S) - g) \\ = \phi_E(B_e - C_e) + \phi_W(B_W + C_W) + \phi_N(B_n - C_n) \\ + \phi_S(B_S + C_S) + e' \end{aligned}$$

or more compactly as

$$(A_P - g)\phi_P = A'_E\phi_E + A'_W\phi_W + A'_N\phi_N + A'_S\phi_S + e' \quad (5.3.13)$$

where $A_P = A'_E + A'_W + A'_N + A'_S$ and the coefficients A'_E , A'_W , A'_N and A'_S represent the combined affects of convection and diffusion. The central differencing form of these coefficients as derived above is shown in the first column of table 5.3.2 for $|P_e| < 2.0$. The other two columns show the HDS modifications for higher positive and negative P_e .

	$ P_e < 2.0$	$P_e \geq 2.0$	$P_e \leq -2.0$
A'_E	$B_e - C_e$	0	$2C_e$
A'_W	$B_W + C_W$	$2C_W$	0
A'_N	$B_n - C_n$	0	$2C_n$
A'_S	$B_S + C_S$	$2C_S$	0

Table 5.3.2 Coefficients in the finite difference equation

The final form of the finite-difference equation for ϕ_P can now be written as

$$\phi_P = A_E\phi_E + A_W\phi_W + A_N\phi_N + A_S\phi_S + e \quad (5.3.14)$$

where

$$\left. \begin{aligned} A_E &= A'_E / (A_P - g) \\ A_W &= A'_W / (A_P - g) \\ A_N &= A'_N / (A_P - g) \\ A_S &= A'_S / (A_P - g) \\ e &= e' / (A_P - g) \end{aligned} \right\} \quad (5.3.15)$$

Equation (5.3.14) is the finite-difference equivalent of equation (5.3.1) and relates ϕ_p to the ϕ values of the neighbouring nodes in the curvilinear orthogonal grid.

The finite-difference form of the momentum equations are similar to (5.3.14). It is, however, convenient to separate the pressure terms from the remaining source terms in order to later explain the solution method more easily. The finite-difference equations for U_1 and U_2 are written, therefore, as

$$\begin{aligned} U_{1p} &= A_E U_E + A_W U_{1W} + A_N U_{1N} + A_S U_{1S} + e'' \\ &+ F_{1p}(p_W - p_p) \end{aligned} \quad (5.3.16)$$

$$\begin{aligned} U_{2p} &= A_E U_E + A_W U_{2W} + A_N U_{2N} + A_S U_{2S} + e'' \\ &+ F_{2p}(p_S - p_p) \end{aligned} \quad (5.3.17)$$

where $(e'' + gU_{1p})$ and $(e'' + gU_{2p})$ are the linearised and integrated sources excluding the pressure terms and

$$F_{1p} = S_{2W} \Delta Z / (A_P - g) \quad (5.3.18)$$

$$F_{2p} = S_{1S} \Delta Z / (A_P - g) \quad (5.3.19)$$

It should also be noted that the control volumes for U_1 and for U_2 are different from those for all the other variables and thus the appropriate arc lengths and neighbouring values of all variables must be used in (5.3.16) and (5.3.17); details are given in Figure 5.2.2. and Appendix 6.

The main variables U_3 , k and ϵ can be obtained from the solution of equation (5.3.14) and the cross-plane pressure and velocities from solution of equations (5.3.12), (5.3.16) and (5.3.17) with the appropriate source terms (table 5.3.1). Each set of equations for a particular variable is solved with a line-by-line iterative procedure based on the tri-diagonal matrix algorithm (TDMA) which is outlined later. The equation sets are solved in sequence with the sequence repeated in an outer iteration loop. The sequence starts with solution of the cross-plane continuity and momentum equations which are strongly linked together through the cross-plane pressure field. Details are provided below.

5.4 The SIMPLE solution method

The cross-plane continuity and momentum equations are solved with a 'guess and correct' procedure first proposed by Patankar and Spalding (1972) and commonly known as SIMPLE. In this method a first estimate of the cross-plane velocities is obtained by solution of the momentum equations for a guessed pressure field (which may be initial guesses or values from the previous iterations) and then corrections are obtained to the latter so as to drive the velocities in the direction of satisfying continuity. This cycle is then

repeated in an iteration sequence which also includes solution of the equation for U_3 , k and ϵ and updating of the stresses until convergence is obtained, by which time the corrections should, of course, be negligible. The development of the method will be given here with more details obtainable in Patankar and Spalding (1972) and in Caretto et al (1972).

The preliminary values of the cross-plane velocities are calculated from equations (5.3.16) and (5.3.17) as

$$U_{1p}^* = A_E U_{1E}^* + A_W U_{1W}^* + A_N U_{1N}^* + A_S U_{1S}^* + g^1 + F_{1p}(p_W^* - p_p^*) \quad (5.4.1)$$

$$U_{2p}^* = A_E U_{2E}^* + A_W U_{2W}^* + A_N U_{2N}^* + A_S U_{2S}^* + g^1 + F_{2p}(p_S^* - p_p^*) \quad (5.4.2)$$

where the superscript * denotes values obtained by using the guessed pressure field p^* (usually the values from the previous iteration). These velocities will, in general, not satisfy the continuity equation so that, locally, there will be a finite mass imbalance M_p represented by (equation 5.3.11)

$$M_p = \rho U_{1p}^* \Delta Z S_{2e} - \rho U_{1E}^* \Delta Z S_{2w} + \rho U_{2N}^* \Delta Z S_{1n} - \rho U_{2p}^* \Delta Z S_{1s} \quad (5.4.3)$$

A set of pressure corrections (p^1) are now obtained such that the resulting velocity corrections (U_1^1 and U_2^1) will reduce this mass source to zero i.e.

$$\rho U_{1p}^1 \Delta Z S_{2e} - \rho U_{1E}^1 \Delta Z S_{2w} + U_{2N}^1 \Delta Z S_{1n} - \rho U_{2p}^1 \Delta Z S_{1s} = - M_p \quad (5.4.4)$$

These corrections are obtained from the assumption that the velocity component is a linearised function of the pressure gradient in that direction so that

$$U'_{1p} = \left| \frac{\partial U_1}{\partial (p'_W - p'_p)} \right| (p'_W - p'_p) = F_{1p}(p'_W - p'_p) \quad (5.4.5)$$

similarly

$$U'_{2p} = F_{2p}(p'_S - p'_p) \quad (5.4.6)$$

The substitution of equations (5.4.5), (5.4.6) and the corresponding equations for U'_{1E} and U'_{2N} into equation (5.4.4) leads to

$$p'_p = F_E p'_E + F_W p'_W + F_N p'_N + F_S p'_S + g_p \quad (5.4.7)$$

where

$$F_E = \Delta Z S_{2e} F_{1p} / F_p$$

etc.

$$g_p = - M_p / F_p$$

$$\text{and } F_p = \rho \Delta Z S_{2e} F_{1p} + \rho \Delta Z S_{2w} F_{1E} + \rho \Delta Z S_{1n} F_{2N} + \rho \Delta Z S_{1s} F_{2p} \quad (5.4.8)$$

Equation (5.4.7) can be solved by the TDMA solution method (section 5.6) to yield a field of p' ; the pressures and velocities are then corrected as follows

$$p_p = p_p^* + p'_p \quad (5.4.9)$$

$$U_{1p} = U_{1p}^* + U'_{1p} \quad (5.4.10)$$

$$U_{2p} = U_{2p}^* + U'_{2p} \quad (5.4.11)$$

The above corrected values of U_{1p} and U_{2p} are then used in solution of the ϕ equation for U_3 , k and ϵ which is followed by the updating of μ_t , $\overline{u_1^2}$, $\overline{u_2^2}$ and $\overline{u_1 u_2}$ to complete an iteration sequence. If the solution is not converged, the corrected pressure field will be used as the 'guessed' pressures in the next iteration.

5.5 The near-boundary control volumes

This section outlines the methods used to incorporate the boundary conditions, particularly the wall functions, into the finite-difference procedure.

At a symmetry plane, convection and diffusion across the plane is eliminated by setting the appropriate 'A' coefficient (equation 5.3.14) in the finite-difference equation to zero (e.g. A_E for the ϕ cell 'C' in figure 5.5.1). For the ϕ 's the gradient is then made zero by equating the values at the nodes each side of the plane (e.g. $\phi_E = \phi_P$ for the ϕ cell 'C' in figure 5.5.1). A velocity component normal to the symmetry plane is simply set to zero and this constitutes the appropriate boundary condition for the relevant momentum equation.

Near a wall the staggered grid is modified so that the ϕ nodes and lateral velocity locations coincide with the wall surface as shown in figure 5.5.1 with ϕ cells A and B. The wall functions for each main variable are entered into the finite-difference equation as follows:

(a) Axial velocity (U_3)

The resultant wall shear stress τ_0 is calculated from equations (4.6.1), (4.6.2) and (4.6.3) using the latest values available at the near wall node (P): thus for example for the ϕ cell 'A' near the y_2 boundary surface in figure 5.5.1 (suffix 'P' indicates the value at the ϕ node as usual), the resultant velocity U is obtained from

$$U^2 = U_{3P}^2 + U_{2P}^2 \quad (5.5.1)$$

Since velocity and shear stress are assumed colinear, the components of τ_0 will be given by

$$\tau_{03} = (\tau_0/U)U_{3P} \quad (5.5.2)$$

$$\tau_{02} = (\tau_0/U)U_{2P} \quad (5.5.3)$$

$$\tau_{01} = (\tau_0/U)U_{1P} \quad (5.5.4)$$

Equation (5.5.2) is used to calculate the axial component of wall shear stress which is then used to obtain the shearing force at the wall control volume face. This force is a function of U_{3P} and is therefore entered into the finite equation through the 'g' component of the integrated source, with the wall-side coefficient (e.g. A_W for the ϕ cell A in figure 5.5.1) set to zero.

(b) Cross-plane velocities (U_1 and U_2)

The velocity component normal to the wall is, of course, set to zero.

For the velocity component parallel to the wall, the method used is identical to that described in (a) for the U_3 component, except that the appropriate component of wall shear stress (either equation (5.5.3) or (5.5.4)) must be evaluated at the corresponding wall control volume face.

(c) Turbulence kinetic energy (k)

Convection and diffusion to the wall is set to zero by making the wall-side finite difference 'A' coefficient zero (e.g. A_W for the ϕ cell 'A' in figure 5.5.1). It should be noted that this does not impose local equilibrium since there can be transport by diffusion and/or convection through the other three faces of the control volume. The production and dissipation of k are both calculated using the wall shear stress τ_0 in this near-wall (constant shear layer region) control volume, as will now be illustrated with reference to the ϕ cell 'A' in figure 5.5.1.

Since the strain field in the wall region is dominated by the axial velocity gradient normal to the wall, equation (4.3.6) can be simplified to

$$P \approx - \rho \overline{u_1 u_3} dU_3 / h_1 dy_1$$

which can be approximated to by replacing the turbulent shear stress $\rho \overline{u_1 u_3}$ by the wall stress τ_0 , and then integrated to give the volume average \bar{P} where

$$\begin{aligned} \bar{P} &= \frac{1}{(\text{vol.})} \int_{\text{vol.}} \tau_0 dU_3 / dS d(\text{vol.}) \\ \bar{P} &\approx \tau_0 U_{3p} / S \end{aligned} \quad (5.5.5)$$

where U_{3p} is the nodal value at P and S is the distance to the wall.

From equation (4.2.33):

$$\epsilon = C_4 k^2 / \nu_t$$

Since $-\rho \overline{u_1 u_3} = \nu_t \partial U_3 / \partial y_1 \approx \tau_0$ and making the same approximation with the axial velocity gradient as in (5.5.5), the above can be integrated to give the volume average $\bar{\epsilon}$ as

$$\begin{aligned} \bar{\epsilon} &= 1/(\text{vol.}) \int_{\text{vol.}} \rho C_4 k^2 (dU_3/dS) / \tau_0 d(\text{vol.}) \\ \bar{\epsilon} &\approx \rho C_4 k_p^2 U_{3p} / \tau_0 S \end{aligned} \quad (5.5.6)$$

Equations (5.5.5) and (5.5.6) are the expressions used for the production and dissipation rates in the near-wall k control volume.

(d) Dissipation rate of turbulence kinetic energy (ϵ)

The near-wall value of ϵ is obtained directly from equation (4.6.4) i.e. the differential equation is not employed here, in conformity with Launder, Reece and Rodi (1975) and others.

(e) Enthalpy (C)

Of the many boundary conditions that can be specified for fully developed heat transfer in passages, the following three, designated H1, H2 and H3, have received the most attention in the literature:

H1 Constant peripheral temperature and axial heat flux.

H2 Constant peripheral and axial temperature (isothermal wall).

H3 Constant peripheral and axial heat flux.

The reason for such attention appears to be their amenability to analysis (particularly H1) rather than their practical occurrence which is somewhat limited (see section 8.1). Due to their common usage, these three conditions will be studied in the present work. Since, however, there are no restrictions on the heat transfer boundary conditions that can be imposed in numerical analysis, other conditions, such as might arise in experimental work will be imposed where appropriate. The methods used to incorporate the above standard boundary conditions are outlined below:

(i) H1 boundary conditions

The heat flux is calculated for the near wall control volume from equation (4.6.6) in terms of the temperature $T = T_p$ at the near-wall node (T_w is fixed at the prescribed value), i.e. for the ϕ cell 'B' in figure 5.5.1

$$\dot{q}_s = - C_p(T_p - T_w)S_{1s}\Delta Z\tau_0 / (C_4^{\frac{1}{2}} k_p^{\frac{1}{2}} \nu_c (U_{3p}/U_{3p}^* + P^*)) \quad (5.5.7)$$

This is the heat flux through the wall-side control volume face (Launder and Ying, 1973), and is entered into the finite-difference equation through the 'g' and 'e' components of the integrated source, with the wall-side 'A' coefficient set to zero.

(ii) H2 boundary conditions

The near-wall modification is identical to that for the H1 case above since the peripheral wall temperature is again constant.

(iii) H3 boundary conditions

The constant prescribed value of heat flux (say \dot{q}_w'' is used, via equation (4.6.6), to calculate the temperature difference

between the near-wall node and the wall, and thus the temperature at the wall node, i.e. for the ϕ cell 'A' in figure 5.5.1

$$T_w = T_p + \dot{q}_w'' C_4^{1/2} k_p^{1/2} \nu_c (U_{3p}/U_{3p}^* - P^*)/\tau_0 \quad (5.5.8)$$

5.6 The Thomas algorithm

As mentioned in section 5.4, solution of the finite-difference equations is obtained by line-by-line iteration. This is accomplished with the well known Thomas or tri-diagonal matrix algorithm (TDMA) outlined in Appendix 7. The finite-difference equation for ϕ (equation 5.3.14) can be written for solution by the TDMA along a y_2 line (figure 5.2.2a) as

$$\phi_p = A_N \phi_N + A_S \phi_S + (A_E \phi_E + A_W \phi_W + e) \quad (5.6.1)$$

Comparing this with equation (A7.1) shows that the terms in the bracket (corresponding to C_i) are assumed constant i.e. the ϕ values on adjacent y_2 lines are assumed known. The equations (5.6.1) for each location on a y_2 line constitute a linear simultaneous equation set that is solved by application of the TDMA, yielding new values of ϕ at each location on the line. A complete pass through the solution domain visiting and solving for new ϕ values on each y_2 line successively is called a 'sweep' in the y_1 direction. However solving each line changes the values of ϕ considered known in the solution of the previous line, so that one sweep will not yield the correct solution. A number of sweeps can be made, but even with this efficient solution method, convergence can be slow. The various practices developed and introduced in the present work to effect more rapid convergence are discussed in section 5.9.

5.7 Summary of the overall solution procedure

Using the current values of all main variables, stress components etc., the following main sequence of operations is performed during an iteration of the solution procedure:-

1. The complete fields of U_1^* and U_2^* are calculated from equations (5.4.1) and (5.4.2).
2. The pressure correction at each node is then calculated from equation (5.4.7) and the pressure, U_1 and U_2 fields are corrected using equations (5.4.9) to (5.4.11).
3. The axial velocity (U_3) field is calculated from equation (5.3.14) using the corrected values of U_1 and U_2 from step 2 to evaluate the coefficients.
4. All scalar variables (k , ϵ and C in turbulent flow with heat transfer) are then calculated from equations (5.3.14) using the prevailing velocity field.
5. The turbulent stresses, effective viscosity and eddy diffusivity are updated at each node from the new values of all variables.
6. The residual source in each variable field solved is compared with that deemed acceptable for a converged solution. If the procedure has not converged, it proceeds to the next iteration, and the whole cycle 1 - 6 is repeated.

5.8 Grid generation

An orthogonal curvilinear grid was required to fit the passage cross-sectional shape for each case (other than those where Cartesian meshes were used e.g. rectangular and most square duct calculations) studied. In some instances the grid could be specified directly as for the circular pipe where polar-cylindrical co-ordinates were used for the sector-shaped domain solved (see figure 5.8.1). This was also the case for the quadrant of an elliptical duct where elliptical-cylindrical co-ordinate grids were used: in this system the Cartesian co-ordinates x_1 and x_2 are related to the curvilinear co-ordinates y_1 and y_2 by the equations

$$\begin{aligned}x_1 &= C_e \cosh y_1 \cos y_2 \\x_2 &= C_e \sinh y_1 \sin y_2\end{aligned}\tag{5.8.1}$$

where C_e is a constant dependent on the duct aspect ratio. Figure 5.8.2 shows a typical mesh generated from these equations for a duct with an aspect ratio of 2.

To enable the present method to be applied to arbitrary-shaped passages, a general method for orthogonal curvilinear grid calculation was adopted, similar to that described by Antonopoulos et al (1978). In this method, the transformation equations relating the Cartesian and orthogonal-curvilinear co-ordinates are solved by finite differences. The curvilinear mesh boundaries are made to coincide with the passage boundaries.

An outline of the method is given in Appendix 5 and examples of grids generated, for an equilateral-triangular half-duct and for the symmetry element of an infinite-array rod-bundle of triangular pitch are shown in figures 5.8.3. and 5.8.4 respectively. If required, variable spacing can be obtained by appropriate specification of the transformed rectangular mesh.

To test orthogonality and convergence, the physical co-ordinates of the intersecting curvilinear grid lines are assumed to obey local quadratic functions and the angle of intersections calculated at each node. Orthogonality was found to improve with iteration of the grid generation procedure and was accepted when within 1° everywhere. With this criterion a 20 x 12 mesh could be generated with, typically, 7 seconds of CPU time on a CDC 6600 computer.

The arc lengths S_{1n} , S_{2e} etc. required for the finite-difference equations, and also the local radii of curvature r_1 and r_2 required in the cross-plane momentum sources were calculated by fitting a parabola through three known points (e.g. a, n, b for S_{1n} in figure 5.2.2a).

5.9 Convergence and accuracy

Convergence of the method was found to be uncertain due to the close coupling and non-linearity of the equations being solved. This was further compounded by the strong source terms in the cross-plane momentum equations associated with the Reynolds stresses and grid curvature. Indeed, this problem was found to be insoluble by Trupp and Aly (1978) with a less complex method (turbulence length scale

prescribed) based on an earlier version of the ASTM. As discussed in Chapter 3, Trupp and Aly were eventually forced to prescribe the direction of secondary motions in order to obtain converged solution. Remedies were developed in the present study to overcome these difficulties without imposing any restrictions on the flow; these and efforts made to maximise the accuracy of the method are now described.

5.9.1 Convergence criteria

The convergence criteria used in the present method were based on the sum of the absolute residual sources in each field of variables calculated. From equation (5.3.13), the residual source (error) R_S at each node is defined by

$$R_S = A'_E \phi_E + A'_W \phi_W + A'_N \phi_N + A'_S \phi_S + e' - (A_p - g) \quad (5.9.1)$$

This was calculated at all cells and the absolute values summed for each variable using the prevailing values of these. The solution was assumed to be converged when the value of this sum, normalised by an appropriate overall reference quantity N_R , was below a pre-set value e_r for each variable monitored i.e.

$$E_r = \epsilon |R_S| / N_R < e_r \quad (5.9.2)$$

The values of E_r (hereafter called the 'residuals') for each main variable were printed out after every outer iteration and tests showed that the value of e_r could normally be set at 10^{-3} since reduction of E_r below this level usually resulted in insignificant further changes in the solution. In addition to the above criteria,

the values of each variable were monitored at a 'sensitive' location in the field and printed out after each iteration. This, together with an inspection of the full field values of each main variable every 50 or 100 iterations, provided means of checking that the solution was proceeding smoothly to convergence.

In the present work, the axial and cross-plane momentum and cross-plane mass continuity residuals were found to be the most sensitive tests for convergence and thus were monitored using the following values of N_R :

Axial momentum	N_{RA}	$= - (dp/dS_3) \Sigma V_p$
Cross-plane momentum	N_{RC}	$= 0.1 N_{RA}$
Cross-plane mass continuity	N_{RM}	$= H(\rho N_{RC})^{\frac{1}{2}}$

where H is a dimension across the passage.

The above 'residual source' convergence criterion was considered more satisfactory than the commonly used 'fractional change' criterion based on the maximum change in value of each variable between iterations. The problems of very slow convergence, mentioned in the previous section, often resulted in little change in the values of the variables for a few iterations during the course of the solution. This situation could be falsely taken as a converged solution by the latter, but not by the former, criterion.

5.9.2 Methods used to achieve convergence

The problem of obtaining convergence was largely overcome by the development of a combination of under-relaxation, careful starting procedures and block adjustment. The TDMA solution method (see

section 5.6 and Appendix 7) was also improved by the addition of a second sweep to give two consecutive sweeps of the entire field in alternate directions. This ADI version of the TDMA is widely used and is current practice in the solution of elliptical equations.

The non-linearity and close-coupling effects in the finite-difference equations were attenuated by under-relaxation of most of the variables solved. Typically U_3 , k , ϵ and μ_{eff} were under-relaxed by 0.7 with U_1 and U_2 usually under-relaxed by 0.3 or less. This attenuation was found, however, not to be enough to procure convergence. Further under-relaxation applied to these and other variables and also other quantities, such as the cross-plane momentum sources, invariably just slowed down any changes in the solution without necessarily procuring convergence.

The following additional measures were however found to be effective. The six equations to be solved were divided into two groups and after establishing U_3 , k and ϵ fields, initial calculations were made with not more than one group of equations being solved simultaneously. A typical such starting procedure involved the following steps:-

1. Calculate an initial U_3 field, based on the 'one-seventh power' law.
2. Solve for k and ϵ only with U_3 fixed and U_1 , U_2 and p all zero, for about 6 iterations.
3. Calculate U_3 , k and ϵ together, with the cross-flow solution still suppressed, until a converged solution is obtained (this prediction was also later used to illustrate the effects of cross-flow).

4. Keep U_3 , k and ϵ fixed and calculate U_1 , U_2 and p' for 15 iterations.
6. Solve all equations simultaneously (as sequence in section 5.7) until the solution is converged.

The stresses are updated after each iteration in which U_3 , k and ϵ were involved. This approach was found to be successful, even with the most difficult cases (e.g. the square duct with one rough wall) where, if necessary, steps 4, 5 and 6 (for about 20 iterations) were repeated a few times before step 6 was applied to convergence.

Consideration of the elliptical nature of the equations being solved led to the introduction of a 'block adjustment' procedure (Gosman et al, 1977). With iterative solution of elliptical equations, residuals can often be just moved around the field with little reduction rather than filtered through the boundaries. Block adjustment, as described below, is a means of reducing these residuals by simultaneous reduction of the residual source sums for strips of cells, spanning the cross-section of the passage.

Following an alternating direction sweep of the TDMA for a variable ϕ , an adjustment $\delta\phi_i$ is calculated along each strip 'i' of cells such that when $\delta\phi_i$ is added to the value of ϕ at each node in the strip the residuals along that strip sum to zero. The equation for $\delta\phi_i$ is derived in Appendix 8 and is seen to be of a form suitable for solution by the TDMA (c.f. equation A7.1). It should be noted that although the strip-wise residual source sums have been reduced to zero overall by this procedure the resulting field of ϕ 's is not, in general, a converged solution since the local residuals will not necessarily be zero at each node.

5.9.3 Accuracy of the solutions

The errors in a solution are due either to errors in modelling or in the subsequent numerical solution of modelled differential equations. Modelling errors are discussed in Chapters 7 and 8 when the present predictions are compared with experimental data for turbulent flows; clearly they are quite distinct from numerical errors.

Numerical errors may arise from discretization assumptions, incomplete convergence and computer round-off. The latter depends on the number of significant figures used in the numerical calculations and will be negligible in the present work since the digital computers used worked to sixteen figures.

(i) Discretization errors

These result from approximation of the continuous distribution of a variable by values at a discrete number of locations (nodes) with interpolation approximations between them. The magnitude of these errors should depend mainly on the number and distribution of the nodes across the solution domain. However, since in the present work flexible curvilinear grids were used a study was also made of the effect of grid control volume shape, size and orientation in relation to the duct cross-section. This involved comparing solutions for a given duct obtained with different meshes and also examining for the expected flow symmetries. An example of such a test is described in section 7.3 where turbulent flow in a square duct was calculated using a Cartesian grid in a quadrant of the duct and a curvilinear grid in an octant of the duct. Satisfactory agreement was obtained between the two arrangements.

A typical symmetry comparison test is described in section 7.6 for the triple symmetry case of an equilateral triangular half-duct. Again the results were satisfactory.

Discretization errors were further minimised in the present work by concentrating nodes as far as possible in the regions of high gradients (the near-wall regions) and by performing grid refinement tests to ensure that sufficient nodes were used. Here the approach was to systematically increase the number of nodes until the solution ceases to show any significant changes. Figures 5.9.1 to 5.9.5 show results typical of such tests, performed for the case of turbulent flow in a rod-bundle channel symmetry element with $P/D = 1.123$. A typical mesh of 16×10 grid lines (112 internal nodes) is shown in figure 5.8.4. This is one of the smallest P/D ratios calculated and thus will contain the largest gradients of the main variables. Evidently there is little difference between the profiles for the 20×12 mesh (180 internal nodes) and the 16×10 mesh (112 internal nodes) cases. Similar results were obtained with most of the other geometries studied and consequently, to keep computing time and storage to a minimum, most predictions presented in the succeeding chapters of this thesis were obtained with 16×10 mesh (or similar number of internal nodes). The exceptions to this were the rectangular ducts and the triangular half-duct calculations, where grid-refinement tests showed meshes of 180 internal nodes to be required for grid-independent solutions.

(ii) Convergence errors

The convergence criteria described in section 5.9.1, should have ensured that errors due to lack of overall convergence would not be significant in the present work. However, the symmetry tests mentioned above revealed that convergence may not be uniform throughout the field in some cases, as described below.

When the curvilinear grid arrangement was such as to cause large spatial variations in the finite-difference coefficients it was found that part of the field where the cells are small may converge more slowly than the remainder. This could result in an apparently complete solution containing significant residuals in a small part of the field. A case in point is the equilateral triangular half-duct mesh shown in figure 5.8.3, where the small size of the mesh near the corner E, gave rise to small finite-difference coefficients.

This problem was overcome with the use of block adjustment and a novel self-adjusting multi-sweep version of the TDMA. The full ADI solution method was used until a converged solution was obtained according to standard criteria. The TDMA was then switched to a single direction sweep only (in the sense of E to D in figure 5.8.3) and the residuals on each line were required to be below an appropriate fraction of ϵ_r . As each line from D to E satisfied the criterion it was dropped from the sweep, which therefore covered fewer and fewer lines as the solution further proceeded. Eventually, there was only a single line remaining (that adjacent to E) which was duly solved by the final application of the TDMA. Although the final residuals on each line could be above that when it was dropped from the sweep (due to subsequent solution of the neighbouring line) an improvement in local residuals was obtained.

5.10 Closure

A method of formulating the finite difference equations and their associated boundary conditions has been presented, together with practices developed to obtain satisfactory simultaneous solutions of these equations. The considerable care taken to ensure good accuracy and efficiency of the numerical procedure has been stressed in the latter part of the chapter. Particular attention has been paid in this respect to the special problems associated with the use of an orthogonal-curvilinear finite-difference grid.

The next few chapters describe the results obtained from applying this calculation procedure to a range of flow and heat transfer problems and comparing them with known solutions or experimental data.

6.1 Introduction

The laminar flow calculations reported in this chapter serve a number of purposes. The primary purpose is to test the accuracy of the orthogonal-curvilinear finite difference procedure presented in the previous chapter, in the calculation of axial velocity and wall shear stress in passage geometries for which analytical solutions are available. The flexibility of the calculation method in application to different passage shapes can also be demonstrated. Additionally, since many of the passage geometries selected for these tests are also those for which turbulent flow predictions have been made in the present work (see next chapter), features of the latter can be compared and contrasted with the corresponding laminar case. This has also some practical use in that laminar flow represents a limiting case and, indeed, may even be the type of flow prevailing in the small passages of some compact heat exchangers.

Some of the work presented in this chapter can also be compared with previously published calculations, such as those for the axial passage in rod bundles, obtained by different numerical methods. Finally, the laminar flow velocity fields obtained here are used as input into laminar heat transfer calculations, the results of which are reported in a later chapter.

The bulk of the applications are to non-circular passages, however, preliminary calculations were made for laminar flow in a circular tube using a sector shaped field and a polar-cylindrical grid (see figure 5.8.1). With fully developed laminar flow, the friction factor x Reynolds number (fR_e) parameter depends only on geometry. For the circular tube the expected value of 16.0 was obtained (within 0.02%) and the parabolic axial velocity profile obtained within 0.5% with a 3 x 18 grid.

6.2 Elliptical ducts

The elliptical-polar curvilinear grid used in the flow predictions for a one-quarter duct symmetry element was generated analytically using elliptical cylindrical co-ordinates as described in Chapter 5 and illustrated in figure 5.8.2. The ratio of major to minor axes (a/b) is defined as the aspect ratio (AR) of the duct.

This duct shape provides a useful check on the calculation procedure since the boundary wall has a continuously changing curvature and the axial velocity profiles along the major and minor axis planes are identical when plotted on the same dimensionless basis. This can be readily seen from the following analytical expression for the axial velocity profile, taken from Knudsen and Katz (1958):

$$U_3/\bar{U}_3 = 2[1 - (x_1/a)^2 - (x_2/b)^2] \quad (6.2.1)$$

where U_3 and \bar{U}_3 are the local and mean axial velocities respectively and the other symbols are defined in figure 5.8.2.

The predicted axial velocity profiles are shown in figure 6.2.1 to be in good agreement with the above analytical solution and a considerable improvement on the numerical finite-difference solution (AR = 2 case) of Cain et al (1972). This latter solution is seriously in error around the focus point of the elliptical-polar grid, a shortcoming attributed by the authors to the rapid decrease in metric coefficient as the focal point is approached. This problem is avoided in the present method due to the fact that the finite difference equations are (a) derived by integration over finite volumes and (b) expressed in terms of curvilinear arc length. Much care was taken to identify the correct arc lengths in this region and thus maintain good accuracy even though the grid geometry changed rapidly. It is worth noting that this test represents a good example of how the simple laminar flow case can provide a useful check on the calculation method, in order to identify and eliminate inaccuracies, which otherwise may be difficult to trace in the more complex turbulent flow calculations.

The predicted wall shear stress profiles are shown in figure 6.2.2 to be in good agreement with the analytical profiles, and further show the significant effect of duct aspect ratio on these profiles. The profile in the higher aspect ratio duct is fairly uniform around the slowly curving part of the wall with a rapid decay as the wall curvature changes sharply near the major axis plane. There is a more monotonic decrease in wall shear in the lower aspect ratio duct with, as expected in both cases, the lower wall shear stresses associated with the regions of lower axial velocity gradient.

The fR_e parameter for fully developed laminar flow depends only on duct aspect ratio and the present predictions are shown in table 6.2.1 to be almost identical (within 0.3%) to the analytical values for the range of aspect ratios covered.

Aspect ratio	fR_e	
	Predicted, this work	Analytical, Tao (1961)
1.5	16.32	16.31
2.0	16.88	16.82
5.0	18.55	18.60
10.0	19.26	19.32

Table 6.2.1 Comparison of the fR_e parameters for elliptical ducts

The close agreement between the finite difference calculations and the analytical solutions over a wide range of duct aspect ratio is particularly encouraging since this is a case where grid control volumes vary significantly in size, shape and orientation across the duct cross-section. The most severe variations occur, as previously noted, in the region around the focus of the ellipse where the control volumes contract rapidly, and rotate through 90° on passing through the focus along the major axis (see figure 5.8.2). Even in this region there is no detectable grid effect on the predictions.

6.3 Isosceles triangular ducts

This flow was first solved over a domain encompassing one-half of an equilateral triangular duct in order to check that the asymmetry of the curvilinear grid did not prevent the expected triple flow symmetries from being obtained. The grid used was similar to that in figure 5.8.3 with the duct walls along EC and CD; the lines CF and GF have been superimposed to show the expected three flow symmetry elements CFD, CFG and EFG. The size, shape and orientation of the grid control volumes clearly will be different in each of the symmetry elements.

The computed fully-developed laminar flow wall shear stress distribution along EC is shown in figure 6.3.1 where the expected symmetry about the mid-wall point has been obtained. The distribution of shear stress along the other wall (CD) also matches this and both the wall shear stress and axial velocity profiles are seen to be in excellent agreement with the analytical profiles.

Laminar predictions have also been made with the present method for fully developed flow in isosceles triangular ducts with apex angles of 22.12° and 11.7° . Comparisons have been made in figures 6.3.2 to 6.3.4 with the experimental measurements of Eckert et al (1954) as well as with the analytical solutions of Sparrow (1962). The steep gradients of axial velocity predicted by the present method for these ducts are in good agreement with the analytical predictions and in fair agreement with the experimental measurements except in the core region where, as suggested by the experimenters, turbulent flow may exist (the possibility of simultaneous laminar and

turbulent flow in small apex angled triangular ducts is well known and has been reported elsewhere in the literature, e.g. Eckert and Irvine, 1956; Cope and Hanks, 1972; Bandopadhyay and Hinwood, 1973).

The wall shear stress profiles along the main wall calculated by the present method are shown to be in excellent agreement with the analytical profiles in figure 6.3.4.

A comparison between the analytical values of the fR_e parameter and those computed from the present method are shown in Table 6.3.1. The values of fR_e from the present work are

Apex angle	fR_e	
	Predicted	Analytical Sparrow (1962)
60°	13.31	13.33
22.12°	12.7	12.85
11.7°	12.3	12.54

Table 6.3.1 Comparison of fR_e parameters for isosceles triangular ducts

slightly below the analytical values but the difference is less than 2%.

6.4 Axial flow in rod bundles

Solutions have been obtained for the symmetry elements of flows parallel to infinite triangular arrays of rods using orthogonal grids similar to that shown in figure 5.8.4. The relevant symmetry elements are depicted in figure 3.2.4.

Axial velocity profiles along the limiting radial planes of $\theta = 0^\circ$ and $\theta = 30^\circ$ calculated from the present method are shown in figure 6.4.1. Results for two different rod bundle P/D ratios have been plotted to allow comparison of flow characteristics of closely-spaced rods (represented by P/D = 1.1) with those for wider spacing (represented by P/D = 1.5) both arrangements being illustrated in figure 6.4.2. It is evident from figure 6.4.1 that axial velocity is a strong function of both radial and angular position between the rods as well as of the P/D ratio. The effect of the narrow gap between rods at $\theta = 0^\circ$ in the P/D = 1.1 geometry is quite dramatic in that the maximum axial velocity is reduced to less than one-quarter of that in the core along the $\theta = 30^\circ$ plane. As to be expected with these markedly different axial velocities, the wall shear stress varies rapidly around the perimeter for the P/D = 1.1 case, as shown in figure 6.4.2. Also as expected, the lower wall stress is associated with the lower axial velocities in the gap ($\theta = 0^\circ$), where it is less than one-half of the stress at $\theta = 30^\circ$. It is encouraging to note that the profiles of axial velocity and wall shear stress evaluated from the present method, even though varying rapidly across the calculation domain, are in good agreement with those calculated and plotted from the analytical/numerical results of Sparrow and Loeffler (1959).

A comparison between the fR_e parameters obtained from the present calculations and those from the Sparrow and Loeffler (1959) method is shown in table 6.4.1 for a range of P/D ratio. Although the present values are slightly lower at the larger rod spacings, the difference is everywhere less than $2\frac{1}{2}\%$.

P/D ratio	fR_e	
	This work	Sparrow and Loeffler (1959)
1.1	20.14	20.377
1.2	24.64	24.95
1.3	27.03	27.417
1.5	30.51	30.035
2.0	38.51	39.38

Table 6.4.1 Comparison of the parameters for rod-bundles

6.5 Closure

The fully developed laminar flow predictions from the present method are in good agreement with the analytical solutions for all passage geometries calculated. The good accuracy and flexibility of the present curvilinear finite-difference method in the calculation of axial velocity and wall shear stress in this class of flows is thereby established.

These calculations, although of interest and value in the study of flow in arbitrary shaped passages are here essentially preliminary to the turbulent flow calculations which form the major part of the current work and which are presented in the following chapter.

7.1 Introduction

The present prediction procedure has been applied to the calculation of fully developed turbulent flow in a range of basically different passage shapes. The results of these calculations are presented in this Chapter, arranged in separate sections for each passage shape studied. Where appropriate, and where experimental measurements are available for comparison, parametric studies of the effects of, for example, different aspect ratios or P/D ratios have been made for a given passage shape. Some tests have also been made of the accuracy and consistency of the procedure and the results of these are described in the section appropriate to the particular passage shape.

The main objective of these calculations is to test the effectiveness and flexibility of the finite-difference method, and in particular the Launder and Ying based algebraic stress transport model (ASTM) used to represent the Reynolds stresses, in predicting the axial velocity, local wall shear stress and mean friction characteristics of flows through arbitrary-shaped passages, for these are considered to be of primary importance to a designer concerned with such flows. However, it is clear from Chapter 3, that these features are much influenced by the turbulence driven secondary flows occurring in planes normal to the axial direction; thus the correct prediction of these motions and their influence on the mean flow are also part of the main objective of the present work. To highlight the effect of these cross-flows on the characteristics, calculations are also made with them suppressed.

7.2 Circular pipe

Calculations were initially made for this geometry as it is the basic duct shape with which, as discussed in Chapter 3, much of the data for other geometries has been previously compared. The geometric simplicity of the passage shape, the absence of secondary flows and the availability of well-established and widely-accepted experimental measurements also make it a useful initial test of the turbulent flow method.

Predictions have been obtained using a polar cylindrical grid in a symmetry sector of the duct (see figure 5.8.1) and compared with the widely-accepted experimental data of Laufer (1954) and also the more recent data of Lawn (1971) and Acrivlellis (1977).

The present predictions of axial velocity are compared with experiment for two Reynolds numbers (R_e) in figure 7.2.1. Agreement is good, with the prediction mostly within 1% of experiment and, thus, generally within the likely experimental error band.

The prediction of turbulence kinetic energy (k) is shown in figure 7.2.2 to be in accord with the measurements in the core region but much lower than the measurements in the near-wall region. The predicted near-wall level is, as expected, near that for local equilibrium, which can be deduced as follows from the transport equation (4.3.1) for k .

The measured turbulence kinetic energy balance in a circular pipe (e.g. Laufer, 1954; Lawn, 1971) shows that the near wall region is dominated by generation and dissipation of k , with diffusion only of

minor consequence. Under these conditions of approximate local equilibrium, equation (4.3.1) simplifies to

$$\overline{u_1 u_3} \, dU_3/dx_1 = \epsilon$$

Near the wall, turbulent shear stress is approximately constant and can be made equal to the wall value τ_0 . Substituting for this stress, and also for ϵ from equation (3.4.7), the above becomes

$$(\tau_0/\rho)(dU_3/x_1) = C_4 k^2/\nu_t$$

which, using equation (3.4.1), can now be written as

$$k/(\tau_0/\rho) = 1/C_4^{1/2} \quad (7.2.1)$$

The empirical constants used in the current ASTM (see section 4.7) yield a value of 0.085 for C_4 (which is near the value of 0.09 used to compute a wide range of turbulent flows - see Launder and Spalding, 1974) which, from equation (7.2.1) results in a near-wall equilibrium value of 3.4 for k/U_3^2 . The measured level of k/U_3^2 is, however, some 35% or more above this in the measurements shown in figure 7.2.2. This could be due to some influence beyond that of local equilibrium or, perhaps, to the effect of the wall on the probes not being fully corrected for in the measurements, particularly since this effect is much exaggerated when measured turbulence intensities are squared and summed to obtain k ; or maybe an incorrect value of C_4 .

The individual turbulence intensities calculated from the present Launder and Ying based ASTM are presented in figure 7.2.3. The calculated axial intensity (\tilde{u}_3) and lateral intensity (\tilde{u}_2) profiles

compare reasonably well with the measured profiles at $R_e = 5 \times 10^4$ as shown in figure 7.2.3a. The damping effect of the wall on the radial intensity \bar{u}_1 is, however, not predicted. This is a consequence of tuning the constants in the ASTM to match equilibrium stress levels in plane homogeneous shear rather than near-wall shear (see table 4.7.1). The relevant stress levels in the former are (Champagne et al, 1970)

$$\bar{u}_1^2/k = .56, \quad \bar{u}_2^2/k = .49, \quad \bar{u}_2 u_3/k = .3 \quad (7.2.2)$$

whereas, near the wall in a circular pipe (Laufer, 1954), these levels are

$$\bar{u}_1^2/k = .46, \quad \bar{u}_2^2/k = .29, \quad \bar{u}_2 u_3/k = .29 \quad (7.2.3)$$

The main difference between these measurements is, as expected, in \bar{u}_2^2/k , the reduced level of which implies a value of $C_2 = 0.272$ in the ASTM. The effect of using the latter value in the calculation of the turbulence intensities is shown in figure 7.2.4. The asymmetry of the cross-plane intensities is now quite well predicted, perhaps suggesting that 0.272 is a better value for C_2 than 0.013, which is the value adopted in the present study (section 4.7). However, if the value of $C_2 = 0.272$ is used in the ASTM for calculation of flow in non-circular passages, the level of secondary flows predicted turns out to be unrealistically high. This apparent conflict in the ASTM is further discussed in the light of predicted secondary flows in square ducts in section 7.3 and also in regard to the prediction of heat transfer in Chapter 8.

The predicted eddy viscosity profile shown in figure 7.2.5 is in fair agreement with the measured profile considering the measurements contain the uncertainties of calculated velocity gradients. As may be

expected, eddy viscosity is sensibly constant across the core where the influence of the wall on the formation of turbulent eddies is minimal. This latter influence is seen however in the approximately linear increase of eddy viscosity with distance from the wall in the near-wall region.

More detail of the turbulent structure is shown in figure 7.2.6 where the predicted dissipation rate ϵ of turbulence kinetic energy is seen to be in accord with the experimental measurements of Laufer (1954). The high dissipation rate of k near the wall, referred to earlier in discussion of the local equilibrium level of k , is clearly evident here.

Figure 7.2.7 shows a comparison between turbulence length scale predicted from the present method and that calculated from the measurements of Laufer (1954). The satisfactory agreement obtained is to be expected from the agreement between the k and ϵ profiles. The length scale profile calculated from the Buleev (1963) formula (equation 3.4.4) is also seen to be in reasonable agreement for this simple geometry, as it was undoubtedly formulated to be.

Finally, the calculated friction factor-Reynolds number characteristic is compared in figure 7.2.8 with the empirical equations of Blasius and Prandtl, as well as with the experimental measurement band given by Schlichting (1968).

The former equations are:

$$\text{Blasius equation} \quad f = 0.079/R_e^{\frac{1}{4}} \quad (7.2.4)$$

$$\text{Prandtl equation} \quad 1/f^{\frac{1}{2}} = 2.0 \log (R_e f^{\frac{1}{2}}) - 0.8 \quad (7.2.5)$$

The present result is seen to be about 5% below the Prandtl formula, which appears to represent the mean of the experimental results. This may be partly due to the calculations being for a theoretically 'perfect' and smooth duct whereas, in experiments with real ducts, any imperfections would tend to increase rather than decrease the measured f . This is consistent with the present prediction matching only the lowest experimental value of f . This slight apparent underprediction of f is not serious and is accepted here without any fine-tuning of the empirical constants in the model, since these are to be kept unchanged for all passage geometries.

7.3 Square duct

Some preliminary test calculations were made in this passage geometry as further accuracy checks on the present calculation method. In these tests, the same flow was calculated using a Cartesian grid in a quadrant of the duct and a curvilinear grid in a symmetry octant of the duct (similar to figure 5.8.3, with $\theta = 45^\circ$). Results from these tests are shown in figures 7.3.1 to 7.3.3. the first of which also indicates the shape of the calculation domain in each case. Agreement between predictions is within 2% for axial velocity and wall shear stress and within 5% for turbulence kinetic energy. Since this latter calculation depends on gradients of axial velocity, and will, therefore, be quite sensitive to grid shape and node spacing, agreement is considered satisfactory.

Since the square duct flow has been used as a test case by most previous authors presenting numerical fourth-generation turbulent duct

flow calculation procedures (e.g. Launder and Ying (1973), Naot et al (1974), Tatchell (1975), Reece (1977) - see section 3.4), the opportunity is taken here to compare the present results with these previous predictions and with experiment. This comparison is presented in figures 7.3.3 to 7.3.7.

In accord with experiment and previous predictions, two identical counter rotating cells of secondary flow were predicted in a one-quarter duct symmetry element as shown in figure 7.3.4. The largest secondary velocities were about 1% of the mean axial velocity and were located near the wall and along the corner bisector. There appears to be little difference between the present and earlier predictions of axial velocity (figure 7.3.5), secondary velocity (figure 7.3.7) and wall shear stress (figure 7.3.3), all of which are in reasonable agreement with experiment. In figure 7.3.6 however, the turbulence kinetic energy predictions of Reece (1977) appear to be significantly nearer to experiment than the others, whereas the present method is similar to that of Launder and Ying (1973) in under-predicting the near-wall levels. The superior results of Reece may be due to the transport effects on turbulence kinetic energy being better represented by his multi-equation stress model with wall damping corrections. Alternatively it may be due to the near-wall boundary treatment he employed which allowed the near-wall turbulence kinetic energy level to rise above $4 U_3^*{}^2$; whereas in the present method, as noted earlier, the level will be near that for local equilibrium i.e. $k = 3.4 U_3^*{}^2$ with the present ASTM.

The distortion of mean flow profiles and contours by secondary flow is much in evidence in the results obtained. As observed by Brundrett and Baines (1964), the turbulence kinetic energy contours are considerably more distorted by secondary flow than those of axial velocity. Secondary flow along the corner bisector towards the wall flattens the axial velocity profile in the core and increases the axial velocity gradient near the wall as evidenced by the contours bulging into the corner in figure 7.3.5. The consequently smaller axial velocity gradients in the core results in lower turbulence kinetic energy levels there. Nearer the corner the increased axial velocity gradients augment turbulence generation and make the turbulence kinetic energy contours bulge markedly into the corner (figure 7.3.6) a feature which together with the like effect on axial velocity contours, have become widely recognised characteristics of corner flows in non-circular passages, as noted in section 3.2. Opposite effects occur along a wall bisector, where secondary flow is directed away from the wall. The overall pattern of wall shear stress can be seen in figure 7.3.3, where the increased velocity gradient near the wall in the corner region increases wall shear, and the decreased gradient near mid-wall decreases wall shear, causing the wall shear stress to be more uniform along the central two thirds of the wall than it would otherwise be.

Detailed secondary velocity profiles from the available predictions are compared in figure 7.3.7 with the experimental measurements of Launder and Ying (1972) obtained with a pitot tube and a single hot wire probe using a method developed by Brundrett and Baines (1964). The main differences between calculation and

experiment are along the $x/B = 0.2$ plane where, from the centre-plane towards the wall, the predicted velocity changes fairly monotonically (all predictions agree) in comparison with the measured velocity which is reasonably constant for the first one-third of the distance from the centre-plane. This disagreement is almost certainly due to measurement error since continuity normal to the x/B plane is clearly not satisfied (more flow away from the wall than towards it) in the experiments whereas, it is necessarily satisfied in the calculations. The experimenters mentioned that probe interference from the wall caused some discrepancies in secondary flow continuity in this region. In view of this, and of the relatively small magnitude of the measured velocities, agreement between prediction and experiment is good. The present method was also used to calculate the square duct flow of Gessner and Jones (1965), who reported secondary velocity profiles in an octant of the duct, obtained with a single hot wire probe using the method of Hoagland (1960). The comparison between prediction and experiment is shown in figure 7.3.8 to be satisfactory, again taking into account the possibility of probe interference near the wall, and is further evidence of the capability of the Launder and Ying based ASTM used in the present method to predict secondary flow accurately.

The turbulence length scale profile calculated along a duct centre-plane is shown in figure 7.3.9 compared with values calculated from the experimental data of Brundrett and Baines (1964) and the Buleev (1963) length scale formula (equation 3.4.4)). The length scale appears to be under-predicted by the present method although it may well be within the experimental error band which will include uncertainties in the measurement and calculation of shear stress and

local axial velocity gradient. The Buleev formula length scale profile is similar to the present one, which is consistent with the similarity between the present predictions and those of Launder and Ying (1973) who, it will be recalled, used the Buleev length scale in an otherwise basically similar ASTM.

The calculated turbulent stress profiles are compared with experiment in figure 7.3.10. Comparison with previous predictions cannot be made here since none of the earlier authors presented these features. The present results are in agreement with experiment in the core but, except for $\overline{u_2^2}$, are too low near the wall where the anisotropy of the cross-plane normal stresses is also not well reproduced. Both failures are, it is believed, a consequence of the constants (in particular C_2) used in the ASTM as discussed below.

As demonstrated in the previous section, for the case of a circular pipe, better prediction of the normal stresses in the near wall region can be obtained by setting $C_2 = 0.272$ as implied by measured near-wall stress levels. However, this value cannot be used for the calculation of mean flow and secondary flow in non-circular ducts as unrealistically high secondary flows are predicted. This follows from equations (2.4.6), (2.4.7) and (4.2.24) to (4.2.26) which show C_2 to appear in the cross-plane momentum sources. The effect of a relatively small increase in C_2 on secondary velocity is shown in figure 7.3.8 and it is clear that changing C_2 by an order of magnitude and more will obviously result in very high secondary flows. In fact they are so high that in a test calculation with C_2 set at 0.272, satisfactory convergence of the solution, which looked unrecognisably distorted, could not be obtained.

As noted by Launder (1976), it does not appear to be possible to predict both flow and near-wall stress satisfactorily with the same constants in the ASTM. In the present study, a discrepancy in near wall normal stress levels is therefore accepted in order to fix the values of the constants in the ASTM for flow prediction. This latter aim appears to have been satisfactorily achieved for the case of a square duct from the evidence of figures 7.3.3 to 7.3.7.

The measured friction factors are shown in figure 7.3.11 to be reasonably well represented by the Blasius equation based on the equivalent diameter concept. The present predictions however, lie below the experiments by about 10% at the lower Reynolds numbers, as do those of the independent but basically similar method of Launder and Ying (1973). This slight underprediction of friction factor is similar to that obtained in the circular pipe calculations reported in the previous section.

7.4 Square duct with one rough wall

An attempt was made to calculate the asymmetric flow measured by Ali (1978) in a square duct with one rib-roughened wall. Details of the duct and the transverse ribs are given in figures 7.4.1(a) and (b). Measurements of axial velocity, turbulence intensity, secondary velocity and turbulent shear stress were made in the plane DC, mid-way between ribs and 36 duct widths from the entrance. From the axial velocity measurements, logarithmic laws were calculated (Ali, 1978) of the following form:

$$\text{For rough walls } U/U^* = (1/.385)\ln(2.88S/e) \quad (7.4.1)$$

$$\text{For smooth walls } U/U^* = (1/.385)\ln(13.92S^+) \quad (7.4.2)$$

The predictions presented in this section have been made with equations (7.4.1) and (7.4.2) replacing equation (4.6.2) in the wall functions for axial and secondary velocity applied near rough and smooth walls respectively. These were the only modifications made to the calculation procedure, which was otherwise identical to that used for the smooth square duct cases reported in the previous section, with calculations made in this case for a symmetry half-duct.

The effect of the rough wall on the measured secondary flow is shown in figure 7.4.2. The four symmetric counter-rotating cells of a fully smooth half-duct are replaced by a strong circulation in the smooth walled part with a much weaker circulation (just detectable) near the rough wall. The present secondary flow prediction is shown in figure 7.4.3 to have also a large circulation in the smooth walled part of the half-duct, and in addition, a similar, counter-rotating, circulation in the rough-walled part of the half-duct. The predicted maximum secondary velocity is, however, less than half that measured. The main differences in secondary flow pattern between the present prediction and experiment are in the rough-wall part of the half-duct. However, it is clear from figure 7.4.2 that the measurements in this region clearly fail to satisfy continuity - in fact all the flow is towards the wall up to a distance of about 0.15 of the duct width from the wall. This implies a measurement error which is considerably more than that reported for fully smooth square ducts. If such a large and obvious flow continuity violation is not due to experimental error, it may well be due to a slight axial flow deflection effect

from the upstream rib as sketched in figure 7.4.1(c). A deflection of only 1° will give a cross-flow of nearly 2% of the local axial velocity, implying an effect that could easily account for the near-rough-wall measurements. There is some evidence of this happening in the flow visualisation experiments of Mantle (1966) on similar discrete roughnesses which show separation of the flow at the rib with re-attachment at least 4 rib heights downstream (the Ali measurement plane is at 5 rib heights downstream). Launder and Ying (1972) measured secondary velocities in a rib roughened square duct (all four walls rough) and satisfied continuity within about 10%. In this case however, the ribs were less than one-third of the height (relative to the duct width) of the Ali ribs and any disturbed flow would be much nearer the wall and thus much less detectable.

The comparison of centre-plane axial velocity profiles in figure 7.4.4 shows the prediction to have a much greater asymmetry than the measurements. Indeed away from the rough wall, the latter profile is not greatly different from the symmetric smooth duct measurement of Brundrett and Baines. The large error in calculated axial velocity, particularly near the rough wall, must be due at least in part, to deficiencies in the wall functions used (particularly since these functions were the only changes made to the fully smooth duct calculations). However some of the differences between the present prediction and the measurements of Ali can perhaps also be attributed to the different secondary flows if the measurements are in fact correct. In the secondary flow along plane DC (figure 7.4.3) in the rough wall part of the duct is away from the wall, reducing axial velocity gradient significantly below that likely to be obtained with, as in the measurements, secondary flow towards the wall.

The general trend of much increased turbulence kinetic energy levels near the rough wall as compared with the smooth wall measurements of Brundrett and Baines, is quite well predicted, as shown in figure 7.4.5. A reduced k level near the smooth wall is also predicted with, as may be expected from the axial velocity comparisons, greater asymmetry in the predicted profile than in the measurements. The same picture is apparent in the turbulence intensity profiles shown in figure 7.4.6. A surprising feature of the measurements of Ali, however, is the decay in the cross-plane turbulence intensities (\tilde{u}_1 and \tilde{u}_2) near the rough wall from a maximum at about $0.3B$ from the wall to about the same as the smooth wall measurements of Brundrett and Baines. It is difficult to account for this reduction in both turbulence intensities in this region assuming uniform surface roughness which would be expected to make the near-wall region highly turbulent giving, as in the predictions, a fairly constant and elevated turbulence level. Only the normal intensity \tilde{u}_1 would be expected to decay near the wall, although as anticipated from previous discussion, this decay is not predicted by the present ASTM. The measured decay in \tilde{u}_2 near the rough wall may be another indication of the previously suggested disturbed flow in that region due to the upstream rib, or some other effect of the rough wall that the present method has been unable to predict.

On the latter point, the ASTM used here, with its eddy-viscosity form of equation for the calculation of turbulent shear stress, cannot be expected to simulate the full shear stress behaviour in this asymmetric flow. As in the case of a channel with one rough wall studied by Hanjalic and Launder (1972), zero shear stress and axial velocity gradient are not co-incident. This is shown in the present

case in figure 7.4.7 which compares the measured and predicted loci of zero shear stress ($\overline{u_2 u_3}$) and axial velocity gradient ($\partial U_3 / \partial x_2$) across the measurement plane. As expected from equation (4.2.28), and contrary to the measurements, the predicted shear stress is coincidentally zero with the axial velocity gradient and must be a significant contributing factor in the discrepancy between measured and calculated loci of $\partial U_3 / \partial x_2$ evident in figure 7.4.7. A further point to note is that the much increased levels of secondary flow and gradients of turbulent stress caused by the rough wall may make the assumptions of negligible transport of stress by convection and diffusion made in the Launder and Ying ASTM, less appropriate in this case.

7.5 Rectangular ducts

Predictions have been made for rectangular ducts of aspect ratio 2.0, 3.0 and 6.4 and compared with the measurements of Gessner and Jones (1965), Leutheusser (1963) and Tracy (1965) respectively. None of the previously developed fourth-generation calculation procedures appear to have been applied to such cases.

The published measurements of Gessner and Jones (1965) in a rectangular duct of aspect ratio 2.0 were confined mainly to secondary velocity profiles, obtained with a single hot wire probe using the method developed by Hoagland (1960). Measurements were however made at two different Reynolds numbers, thus affording an opportunity to check the predicted secondary velocity profiles and their Reynolds number dependence. The comparison is shown in figure 7.5.2 with the calculated overall secondary flow pattern displayed in figure 7.5.1.

Although there is no measured overall pattern with which to compare the latter, the two eddies obtained are consistent with the square duct case in that flow is from the now larger core region towards the corner along the line of the corner bisecting plane, returning via the walls and wall bisecting planes.

There appears to be some underprediction of secondary velocity near the wall, although, as noted earlier this may well be due to probe interference from the wall in the measurements. Indeed, the authors mention this possibility in discussion of the failure of the measured velocity profiles to satisfy continuity by some 20% (more flow away from the wall). In view of this uncertainty, and the small magnitude of the velocities concerned, the comparison is considered reasonable. The effect of increased Reynolds number on the secondary velocity measurements is a reduced velocity when normalised as shown with the maximum axial velocity U_{3CL} . Although there is some evidence of this in the predictions, the effect is not as obvious as in the measurements.

The predicted secondary velocity vectors in the duct of aspect ratio 3.0 are shown in figure 7.5.3. Compared with the square-duct and aspect ratio 2.0 duct patterns, the flow from the core region is now deflected more by the other, minor, counter-rotating secondary flow cell, before it reaches the corner. As with the other patterns, the return flows are along the walls and wall bisectors. It appears that the elongation of the duct cross-section has, not unexpectedly, allowed growth of the inner cell.

Calculated axial velocity contours are compared with the pitot-tube measurements of Leutheusser in figure 7.5.4. The bulging of the contours into the corner due to secondary flow is much in evidence and fairly well predicted. The effect of secondary flow in making the wall shear stress more uniform can be seen in figure 7.5.5 which also shows quite good agreement between the present predictions and the Preston-tube measurements of Leutheusser.

The secondary velocity measurements of Tracy (1965) in the corner region of a rectangular duct of aspect ratio 6.4 are shown in figure 7.5.6 and the corresponding predictions in figure 7.5.7. The predicted flow pattern continues the trend noted in the other rectangular ducts where, as aspect ratio increases, the flow from the core to the corner is increasingly deflected by the circulation cells before reaching the corner. The measured secondary velocity vectors also show the flow from the core to be deflected by the minor circulation cell before reaching the corner, but the effect is not quite as marked as the prediction since the deflection effect of the major cell is not present. The differences in detail between prediction and experiment extends to the magnitude of the velocities which tend to be underpredicted near the short wall and overpredicted near the centre-plane away from the wall.

The calculated axial velocity profiles are plotted in figures 7.5.8 and 7.5.9 with the measured profiles of Tracy. The predicted transverse profile in the central duct region $x_1/B = 4.0$ in figure 7.5.8) matches experiment almost exactly, whereas nearer the short wall of the duct, the comparison is much less satisfactory. The main discrepancy is that, for $x_1/B < 1.0$, the measured maximum axial

velocity becomes further displaced from the centre-plane the nearer the profile is to the short wall, whereas in the prediction it is always at the centre plane. This is almost certainly due to the difference in secondary flows in this region and emphasises the over-prediction of the growth of the minor circulation cell and deflection of the flow from the core away from the corner. As a consequence, the calculated secondary flow is mainly transverse from the centre-plane towards the long wall instead of obliquely towards the corner as in the measurements. The predicted secondary flow away from the short wall along the centre-plane is much weaker than that measured and explains at least part of the discrepancy between the centre-plane axial velocity profiles shown in figure 7.5.9.

The measurements of turbulence intensity along the centre-plane made by Tracy with a constant-current hot-wire anemometer are shown in figure 7.5.10a. These measurements have been summed to give turbulence kinetic energy centre-plane profile in figure 7.5.10b. There is good agreement in the latter between prediction and experiment except near the wall where, as also noted in the square-duct case, the measured turbulence kinetic energy level is higher than predicted. Figure 7.5.10a shows the higher measured turbulence level to be mainly in the axial component (\bar{u}_3). The picture seen in previous cases, of reasonable prediction except near the wall, is repeated again here.

The friction factor characteristics of rectangular ducts are shown in figure 7.5.11, plotted in the conventional way using the equivalent diameter concept. The predictions are generally some 5 - 10% below experiment with a slight dependence on aspect ratio (an

increase in f with aspect ratio). There is a similar but much less well defined trend in the measurements of Hartnett et al (1962), although the differences are in any case probably within the experimental error band. This underprediction of friction factor is consistent with all the flows discussed thus far.

7.6 Equilateral triangular duct

The triple symmetry expected in one-half of an equilateral triangular duct affords a useful test of the accuracy and consistency of the present turbulent flow prediction method in reproducing these symmetries (a similar test was used for laminar flow). The curvilinear grid used for this test was similar to that shown in figure 5.8.3. with the boundary walls along CE and CD, and the symmetry centre-plane along ED. The expected three symmetry elements (one-sixth duct elements) are shown as CFD, CFG and EFG. The shape and orientation of the grid control volumes will clearly vary significantly in each element. The predicted secondary velocity vectors obtained with this grid show, in figure 7.6.1, that the required symmetries have been successfully obtained. The predictions of wall shear stress along GE, GC and DC in figure 5.8.3 are shown, in figure 7.6.2, and also exhibit the required symmetry as well as comparing well with experiment. Similar agreement was obtained with the axial velocity profiles.

It is noteworthy that this type of symmetry check was found to be a searching test of the working of the procedure and proved very useful in the development of the procedure and associated computer-code.

Some of the improvements made to both would almost certainly not have been performed without these tests. A typical example of such an improvement, is the method developed to calculate the production term P in the turbulence kinetic energy transport equation. The equation for P is (4.3.6), in which the turbulent shear stresses are usually expressed in terms of the turbulent viscosity (in this case, equations (4.2.27) and (4.2.28)) to give

$$P = \rho C_4 (k^2/\epsilon) [(\partial U_3/h_1 \partial y_1)^2 + (\partial U_3/h_2 \partial y_2)^2] \quad (7.6.1)$$

which was then calculated for each control volume using central difference representations of the gradients. The distribution of turbulence kinetic energy calculated using this method was found, however, to be dependent on the shape and orientation of the control volume, producing 10% - 20% discrepancies from the required symmetries. Although not critical, these were considered unsatisfactory and were eventually removed by obtaining P directly from equation (4.3.6) which entailed calculating the relevant average turbulent shear stress at each required control volume face as shown in Appendix 6. This approach was adopted in the calculation of all stresses in the computer code and helped towards attaining the level of accuracy demonstrated by the results shown in figures 7.6.1 and 7.6.2 (and also figures 7.3.1 to 7.3.3 in the square duct tests).

After the above tests were completed, full advantage was taken of the available symmetries and all subsequent predictions for this geometry were made for a one-sixth duct element using a grid similar to that in figure 5.8.3. in which the boundary wall is along ED and symmetry planes along EC and CD. As expected, a single circulation

of secondary flow was obtained, consistent with the flows in figure 7.6.1. The resulting predictions are compared in detail with the experiments and predictions of Aly et al (1978) in figures 7.6.3 to 7.6.9.

The axial velocity and turbulence kinetic energy contours and profiles are shown in figures 7.6.3 to 7.6.5. The distortion of the contours into the corner due to secondary flow is much in evidence with, as noted in the square duct flows, a more marked effect on the turbulence kinetic energy contours. A detailed inspection of these contours reveals a slight but consistent underprediction of the effect by the present method and some overprediction by Aly et al. This latter overprediction does not however appear to penetrate right into the corner, but is confined to the lower levels of k (e.g. the $k/U_3^2 = 1.5$ contour) and U_3/\bar{U}_3 . This effect can also be seen in the wall shear stress profiles in figure 7.6.6. The secondary flow has made the profile more uniform for the reasons described earlier. The overprediction of this secondary flow effect by Aly et al is evident in the 'hump' in their profile at $0.2 < x/B < .5$ where τ_0 is high by some 7% (the present calculation is low by 2½%). The opposite effect occurs, however, in the corner where, at $x/B = .9$, the calculated τ_0 of Aly et al is low by more than 20%, implying underprediction of the secondary flow effect. The present calculation is low by about 7%. Although it is possible to draw implications from such detailed differences in predictions, it should be noted that these differences are relatively small and likely to be of the same order as the error band of the measurement. This also applies to the centre-plane axial velocity and turbulence kinetic energy profiles in figure 7.6.5. The

flattening effect of secondary flow on the axial velocity profile is evident, particularly from the core towards the corner. The reduced axial velocity gradients in this region ($.5 < y/H < .9$) have reduced turbulence kinetic energy generation and hence the levels, which are almost half of the 'zero cross-flow' prediction.

Secondary velocity profiles are compared in figure 7.6.7 which shows the present results to be in good agreement with experiment and an improvement on those of Aly et al. This is particularly so near the corner (i.e. $x/B = .48$ and 0.82) where the Aly et al velocities are only about one-half or less of the experimental values. This also confirms the implied underprediction of corner region secondary flow in the Aly et al wall shear stress profile.

Figure 7.6.8 shows the Reynolds stress profiles along the centre-plane between the core and the base. There is good agreement between the predicted and the experimental shear stress profiles with the prediction following the slight undulation of the experimental profile. As anticipated, there is less agreement in the normal stresses, with the prediction showing little anisotropy of the cross-plane near-wall normal stresses. It is of interest to note that the measured level of the latter anisotropy is only about one-half of that in the square duct, a feature that is difficult to account for in the difference in Reynolds numbers and geometry and is, perhaps, an indication of the experimental differences likely in such near-wall measurements. The comparison is, nevertheless, broadly similar to that in the square duct. Unfortunately, no comparison can be made with the predictions of Aly et al as no calculated stresses were published, even though much detail was given of the measured ones.

The calculated turbulence (dissipation) length scale from the present method is compared with experiment and the Buleev (1963) length scale formula (equation 3.4.4) in figure 7.6.9. As with the square duct case, there appears to be some underprediction between the core and the wall although the discrepancy is unlikely to be significant and is perhaps within experimental error which includes calculation of axial velocity gradients. The profile from the Buleev formula is noted as being fairly similar to the present prediction.

The overall performance of the present method for this case is quite good, even right down to secondary velocity detail. Although there are some improvements in prediction of wall shear stress and secondary velocity over those of Aly et al (1978), the two predictions are comparable in performance as should be expected with basically similar fourth-generation methods. The present method does, however, represent an improvement on that of Aly et al in one important respect. As discussed in section 3.4.2, the numerical procedure they employ forces a single swirl of secondary flow (by fixing the sign of the vorticity source) in the solution domain and thus suffers from a severe disadvantage in that it cannot be used to calculate flows where more than one secondary flow swirl could be present as in the example of figure 7.6.1. As evident from this latter figure, the present method does not suffer from this disadvantage.

The dependence of the overall flow characteristics on Reynolds number was investigated and found to be relatively weak when the characteristics are normalised as presented in this section. An example of this is shown in figure 7.6.10 where nearly quadrupling the Reynolds number causes only a few percent change in the normalised

wall shear stress profile. A small decrease was also noted in secondary velocity (normalised with mean axial velocity) with increase in Reynolds number, similar to that previously discussed for rectangular ducts.

The friction factor characteristics are shown in figure 7.6.11 which compares predictions with two experiments and two empirical equations, all based on the equivalent diameter. The experimental values of f obtained by Lowdermilk et al (1954) are a little higher than those of Aly et al (1978). This is probably due to more care being taken by the latter in construction of the test duct which was also used for detailed measurements and, therefore, had to produce the required flow symmetries in the cross-plane. The present prediction is about 5% below the Aly et al measurements which is consistent with earlier results. The empirical constants in the calculation procedure of Aly et al were adjusted to match the predictions to experimental measurement for this particular duct shape, with the desired result over the limited measurement range.

The Blasius equation tends to overpredict the friction factor (Aly et al measurements) by about 5 - 10%, whereas the Malak et al equation, which uses a correction based on the laminar flow fully-developed fR_e parameter for the passage shape (see section 3.2), appears to be an improvement on Blasius in this case.

7.7 Acute-angled isosceles triangular ducts

Calculations have been made for flow in isosceles triangular ducts with apex angle of 22.12° and 11.7° , and the results compared

with the measurements of Eckert and Irvine (1956) and Cremers and Eckert (1962). These flows must represent one of the more severe tests of the present calculation method, particularly in the duct with the smaller apex angle, where the axial velocity, turbulence properties and stresses change rapidly across the narrow duct with asymmetries caused by the small- 11.7° and large- 84.15° angled internal corners. A further physical feature of this flow should be the significant damping effect of the walls on turbulence in the acute-angled corner. The predictions have been made for a symmetry half-duct on a grid similar to figure (5.8.3) with $\theta = 11.7/2^\circ$ and $22.12/2^\circ$, with walls along EC and CD and a symmetry plane along ED. This appears to be the first reported fourth-generation calculation of these flows.

The predicted secondary velocity vectors in a symmetry half of the 11.7° apex angled duct are shown in figure 7.7.1 together with an outline of the whole duct geometry. Three swirls of secondary flow are predicted with two counter-rotating cells near the base and the other occupying the remaining 80% of the domain. Although there are no experimental data available for comparison, the overall pattern seems a logical extrapolation of the equilateral triangular duct flow pattern, and contains the usual features of flow from the core region along corner bisectors into the corners, thence returning to the core via the walls and their perpendiculars. The largest secondary velocities are about 1% of the mean axial velocity and occur along the corner bisectors and base wall.

Axial velocity profiles along the duct centre plane for two turbulent Reynolds numbers are plotted in figure 7.7.2. The difference

between prediction and experiment can be attributed at least in part to lack of full flow development in the experiment. This was unexpected by the authors, who had constructed a test duct of nearly 80 equivalent diameters in length. However, the reported plots of axial pressure gradient show clearly that, at these higher Reynolds numbers, the pressure gradient was still decreasing and thus the flow was still developing at the measuring section of the test duct.

An alternative phenomenon which could affect axial velocity profiles is laminarisation of the flow in the test duct apex corner region, a feature already referred to in discussion of laminar flow in these ducts (section 6.3). This can be examined in two different ways. Firstly, laminarisation of the flow in the acute corner ($x/B > 0.5$) would increase the axial velocity above that expected for turbulent flow, since the effective viscosity acting on the fluid would be nearer the laminar value; this appears to be the case. However, the flow visualisation experiments in this duct (Eckert and Irvine (1956)),^{suggest that} laminarisation in the corner would be expected not to extend below $x/B = 0.9$ for Reynolds numbers above 5000.

Because of the lack of full flow development, an extension was added to the test rig of Eckert and Irvine giving 167 equivalent diameters of flow development, before turbulence measurements were made by Cremers and Eckert (1962). Axial pressure gradient measurements apparently indicated that the flow was fully developed after 130 equivalent diameters. Unfortunately, no further axial velocity measurements appear to have been published.

The present predictions are compared with these turbulence measurements in the form of centre-plane turbulence kinetic energy and normal stress profiles in figure 7.7.3. Agreement is good with the predicted turbulence kinetic energy profile showing little apparent effect of the secondary flow. Since, as noted previously, this profile is likely to be quite sensitive to secondary flow distortions, it implies a generally small secondary flow effect in this duct. This is confirmed with the axial velocity and other predicted profiles, none of which show any significant secondary flow effect. This is probably due to the relatively high mean flow gradients between the core and the wall, making convection a minor transport mechanism in the cross-plane.

It is surprising to note that the measured cross-plane normal stresses ($\overline{u_1^2}$ and $\overline{u_2^2}$) are almost isotropic near the base wall. This is in contrast to the measurements of Tracy (1965) in a large aspect ratio duct (figure 7.5.10), a geometry not too dissimilar to that under consideration in the short wall region, in which the anisotropy of these stresses was found to be significant and fairly similar to that in a square duct (figure 7.3.10). The reduced anisotropy of the near wall normal stresses in the present case however, continues a trend noted in the previous section from measurements in an equilateral triangular duct and if not a measurement error, may imply an unexpected effect of the angled side walls on the transverse damping of turbulence near the base.

The steep gradients of turbulence kinetic energy and normal stress near the base wall are well predicted as is the more gradual decay of turbulence, due to the dampening effect of the walls, into the acute corner.

Some values of local wall shear stress along the long wall were calculated by Cremers and Eckert from measured near-wall axial velocity gradients and these are shown in figure 7.7.4 compared with the present predictions. The latter are in reasonable agreement with the measurements and also show that, for much of the wall, the profile is not too dissimilar to that for laminar flow. This is, perhaps an indication that viscous effects have more influence in this duct than in less narrow ducts.

Calculations were also made in a duct of apex angle 22.12° for comparison with the pitot-tube axial velocity measurements of Eckert and Irvine (1956). The predicted secondary velocity vectors are plotted in figure 7.7.5 and show, as may be expected, a secondary flow pattern similar to that in the duct of apex angle 11.7° (figure 7.7.1). The measured axial pressure gradient indicated that the flow was still developing at the plane of measurement (as in the 11.7° apex angled duct) which could particularly account for the slight difference between measured and predicted axial velocity profiles in figure 7.7.6. The arguments marshalled above in the discussion of flow in the 11.7° apex angled duct will apply again here.

The calculated turbulence (dissipation) length scale profiles along the duct centre-plane are shown in figure 7.7.7 where the profiles from the Buleev formula (equation 3.4.4) appear to be a reasonable, simplified, approximation of those from the present calculations. There were insufficient measurements available for calculation of experimental length scale profiles for comparison.

Finally, the friction factor characteristics for these ducts are presented in figure 7.7.8 where the present predictions are compared with the measurements and with empirical formulae. The predictions are 10% - 15% below experiment which is consistent with the lack of flow development and, thus, higher apparent friction expected in the measurements. However, from the comparisons between predictions and experiment for previous duct shapes, it is likely that not all this difference is due to under-developed flow. The friction factor is overpredicted by the Blasius formula by 10% - 15%, which is further evidence of the inadequacy of the equivalent diameter to correlate pressure drop when the duct shape is markedly different from circular. The correlation proposed by Malak et al (see section 3.2) appears, in this case, to give a result that is likely to be nearer to experiment.

7.8 Elliptical ducts

Calculations have been made for elliptical ducts with aspect ratios of 1.5 and 2.0 using curvilinear orthogonal grids similar to those described in section 5.8 and illustrated in figure 5.8.2. These calculations are compared with the experiments of Cain and Duffy (1971) and also, for the aspect ratio 2.0 case, with the finite-difference predictions of Cain et al (1972). Their method neglected secondary flow and modelled the Reynolds stresses with an eddy viscosity based on a Van-Driest type mixing length. The present work appears to be the first application of a fourth-generation prediction procedure to this case.

The grid nodes and predicted secondary velocity vectors for a symmetry quadrant of a duct of aspect ratio 1.5 are shown in figure 7.8.1. The prediction for the aspect ratio 2.0 duct is similar, as shown in figure 7.8.2, and indicates a single swirl of secondary flow in the quadrant, directed from the core towards the wall along the region of the major axis plane, returning via the wall and the minor axis plane. Although there are no measurements available for comparison, this circulation pattern is consistent with that found in ducts of other geometry in that flow is from the core towards a region bounded by a wall convergence (or alternatively, from the region of highest axial velocity towards the region of lowest axial velocity). The largest secondary velocities calculated along the major axis plane are about 1.2% of the mean axial velocity.

The measured axial velocities were presented by Cain et al in the form of velocity-defect profiles along the major and minor axis planes. As there was insufficient data provided to convert these profiles into more useful plots of axial velocity normalised with either the mean or maximum axial velocity, the present predictions are compared with the measured defect law profiles in figures 7.8.3 and 7.8.4. The effect of the secondary motions is clearly to increase the velocities along the major axis and to decrease them along the minor one. This is consistent with the secondary flow circulation patterns in figures 7.8.1 and 7.8.2, where the higher velocity core fluid is convected along the major axis and the lower velocity wall fluid convected along the minor axis. Agreement is satisfactory although there is a slight overprediction along the major axis in both ducts. It is difficult, however, to identify any

effects positively since three measurements are involved (U_3 , U_{3CL} and U_{3L}^*) and their effects cannot be separated.

The above difficulty can be resolved for the case of the $AR = 2.0$ duct since, in the paper by Cain et al (1972), U_3/U_{3CL} profiles were presented from the measurements of Cain and Duffy (1971) for comparison with their calculations. This comparison, together with the present predictions, are shown in figure 7.8.5. Agreement between the present predictions and experiment appears to be much better now that only the axial velocities are involved. The effect of secondary flow, described in the previous paragraph, is evident again here, and the discrepancies between the calculations of Cain et al and the present prediction, mainly reflect their neglect of these flows and is further evidence of the necessity of including them in calculation procedures.

A small feature of the measured axial velocities not predicted is the curious dip in the major axis profile at x_1/B between .3 and .6. This distortion could be due to a stronger and/or more complex secondary flow circulation pattern than predicted. The effect of secondary flow on wall shear stress is shown in figure 7.8.6 which compares the present predictions with the Preston-tube measurements of Duffy and Cain (1972). The effect is quite dramatic with the calculations showing secondary flow to reduce the variation from nearly 30% to about 5%. The experimental variation is 8% and implies a little less strong and perhaps slightly different secondary flow pattern than predicted. The overall differences are, however, quite small and are probably the same order of magnitude as the experimental errors.

Calculated turbulence (dissipation) length scale profiles for a duct of aspect ratio 2.0 are shown in figure 7.8.7 compared with the turbulence length scale profiles from the Buleev formula (equation 3.4.4).. The latter appear to be reasonable approximations to those from the present method with the largest differences along the major axis plane.

The friction factors for elliptical ducts are plotted in figure 7.8.8, which shows the present method to underpredict, by up to 20%, the measurements of Cain et al which are significantly above the Blasius equation. This latter feature is surprising and inconsistent with the results for other non-circular ducts, especially since elliptical duct cross-sections are not too different from circular, particularly for $AR = 1.5$. The measurements of Barrow and Roberts (1970) for higher aspect ratio elliptical ducts, although of limited Reynolds number range, are clearly below those of Cain et al and also near the Blasius equation. It seems possible therefore, that the friction factors of Cain et al are uncharacteristically high, due probably to such effects as incomplete flow development, tube surface roughness and inaccuracies in duct alignment etc. Few details of the latter are given by the authors although it must be difficult to accurately manufacture and assemble a long elliptical duct with its continuously curving walls (certainly in comparison with the flat walls of square, rectangular and triangular ducts), and any imperfection existing would tend to increase, rather than decrease, the measured pressure drop. It would take very little axial twist or change in duct cross-section to alter the cross-flow completely from that generated by the turbulence field, and this could also account for some of the differences between experimental and predicted axial

velocity and wall shear stress profiles. Both experimental and predicted friction characteristics are consistent in showing a tendency to increase slightly with increasing aspect ratio. This is also so for the Malak et al empirical characteristics.

Any final conclusions on the differences between the measurements and the present predictions will probably have to be postponed until further experiments have been made and reported with details on the accuracy of the ducts and required flow symmetries, and hopefully, measurements of secondary flow and turbulence structure as well as axial velocity and wall shear stress.

7.9 Axial flow passages in triangular array rod bundles

This passage shape appears to have received as much, if not more attention than most others in experimental turbulent flow investigations. This is evident from table 3.2.1, which also shows that most of the work has been in the more compact triangular array arrangement. The most comprehensive experiments appear to be those reported by Subbotin ($P/D = 1.1$ and 1.2), Kjellström ($P/D = 1.217$), Carajilescov and Todreas ($P/D = 1.123$) and Trupp and Azad ($P/D = 1.2$ and larger) and these have therefore been chosen for comparison with the present predictions. The quantities measured and instruments used are summarised in table 3.2.1 and the cross-sections of the test channels are shown in figure 7.9.1, with the measurement region shaded. In addition comparisons have been made with previously published predictions from the fourth-generation finite difference methods of Carajilescov and Todreas (1976) and Trupp and Aly (1978),

both of which used a cylindrical polar co-ordinate grid with special cells at the maximum axial velocity plane. These two methods and their results have already been discussed in section 3.4.2.

The present predictions have been made with an orthogonal grid in a symmetry subchannel of an infinite triangular array rod bundle, similar to that shown for the $P/D = 1.123$ case in figure 5.8.4. Although the measurements have been made in similarly shaped symmetry subchannels (figure 7.9.1), there will be a difference in that the experimental rod bundle or simulated rod-bundle channel will be finite. This aspect has also been studied in the present work by calculating the effect of the end wall on the flow in the measurement subchannel of Subbotin's test section (figure 7.9.1a) for two different P/D ratios.

7.9.1 Infinite triangular array with $P/D = 1.123$ and 1.1

The calculated secondary velocity vectors for the $P/D = 1.123$ geometry are displayed in figure 7.9.2, which also shows the grid nodes of the orthogonal mesh (tails of the vectors). The predicted pattern is seen to be a single swirl from the core towards the gap ($\theta = 0^\circ$ plane), returning to the core parallel to the wall and then the $\theta = 30^\circ$ plane. The maximum secondary velocities are about 1% of the mean axial velocity and occur near the wall and along the maximum axial velocity plane (BC). There are no measurements available with which to compare these calculations, although an attempt to measure them was made by Carajilescov and Todreas (1976) who found their laser-doppler anemometer lacked the resolution required for detection of these small velocities.

Previous predictions of secondary flow pattern in this geometry are inconclusive. As discussed in section 3.4.2, the calculations of Carajilescov and Todreas (1976) neglected cross-plane shear and obtained two counter-rotating cells of flow in the symmetry sub-channel (figure 3.4.1a), whereas Trupp and Aly (1978) with an apparently identical calculation procedure, obtained a single swirl (similar to 3.4.1b). However, when the latter included cross-plane shear in their calculations, it was necessary to employ practices which effectively imposed a single swirl of secondary flow (see section 3.4.2). The present calculation is, therefore, the first to obtain, without prescription, a single swirl of secondary flow in this geometry, with all the stresses in the calculation. Although not as yet confirmed by experiment, this flow pattern is consistent with that found in other passage cross-sections in that flow is from the core (or higher axial velocity region) towards a wall convergence (lower axial velocity) region, returning to the core via the wall and wall normals.

The axial velocity contours calculated from the present method are compared with experiment in figure 7.9.3. Since both profiles will obviously contain interpolation errors, agreement is reasonable with the contours showing the expected distortions due to secondary flow. These distortions are shown more clearly in figure 7.9.4 which compares contours calculated with and without secondary flow. The secondary flow from the core towards the gap and then, along the $\theta = 0^\circ$ plane towards the wall has caused the contours to bulge in this direction, whereas the secondary flow away from the wall at the $\theta = 30^\circ$ plane has caused the contours to move away from the wall. These effects

are also readily apparent in the axial velocity profiles along the $\theta = 0^\circ$ and 30° planes which are presented in figure 7.9.5. Again, comparing the predictions with and without secondary flow, it is clear that core fluid (at $\theta = 30^\circ$, $x/\hat{R} > 0.4$) is convected to the gap ($\theta = 0^\circ$), decreasing the core axial velocity and increasing the gap velocity.

Comparison between the present predictions and experiments in figure 7.9.5 is good, except apparently in the gap, where all the predictions are lower than experiment. The experimenters suggested that the gap flow may have been too high due to incomplete flow development in this region. This is, perhaps, probable in view of the surprisingly long duct (130 equivalent diameter) needed to achieve fully developed flow in the narrow isosceles triangular duct experiments of Eckert and Irvine (1956) discussed in section 7.7. The gap region here, can be regarded as a similar narrow flow region with only about 77 equivalent diameters available for flow development. The various predictions are in reasonable agreement, with those of Trupp and Aly appearing to show less secondary flow effect, particularly in the gap.

As there are no measured wall shear stress profiles for the $P/D = 1.123$ geometry, calculations have been made for the quite similar geometry of $P/D = 1.1$ for comparison with the Preston tube measurements of Subbotin (1971). The secondary flow pattern and axial velocity profiles obtained (not shown) were similar to those in the $P/D = 1.123$ geometry. The predicted wall shear stress profile is seen in figure 7.9.6 to be in accord with the measurements which are reported for a small range of Reynolds number. The predicted profile

did not change significantly over this Reynolds number range so the spread of experimental points in figure 7.9.6 may be an indication of experimental error. Secondary flow is seen to have a large effect on the profile, reducing the peripheral variation of local τ_0 from over 70% to about 25%. As would be expected from the secondary flow pattern, the motion towards the wall in the gap region has increased the axial velocity gradients and hence local wall shear, whereas the flow away from the wall at θ approaching 30° has had the opposite effect. All the predictions are in reasonable agreement with, and are within the spread of, the experimental data.

The turbulence kinetic energy contours are compared with experiment in figure 7.9.7, which shows reasonable agreement, considering the inevitable interpolation errors. The expected distortion of these contours due to secondary flow is evident; thus like the axial velocity contours, but with a more noticeable effect, the k contours are moved closer to the wall at the gap ($\theta = 0^\circ$) and further away from the wall at the $\theta = 30^\circ$ plane. The level of agreement between the present results and experiment is seen again in the k profiles shown in figure 7.9.8, which also usefully shows the typical experimental error bands indicated by the authors. There is more disagreement here between the various predictions than with the axial velocity profiles (figure 7.9.5), with the present results generally an improvement on the previous ones except in the gap, where the flow is probably not fully developed. The underprediction of near-wall k levels by the present method in previous cases is noticeably absent here. The poorest prediction is that of Trupp and Aly, which is consistently high, particularly at the $\theta = 30^\circ$ plane.

In contrast to measurements in most other duct or channel geometries covered here, the cross-plane normal stress ($\overline{u_1^2}$ and $\overline{u_2^2}$) profiles measured by Carajilescov (1975) display, in figure 7.9.9, almost as much anisotropy in the core as near the wall. It is difficult to see what effect could either dampen normal fluctuations or increase tangential fluctuations in the core region to give this effect. This central core stress anisotropy does not appear for other P/D ratios (see figures 7.9.16 and 7.9.23). Except for the usual underprediction of near-wall anisotropy in the cross-plane normal stresses, the present predictions of Reynolds stresses are roughly in agreement with the experiments, taking into account the error bands of the latter. The calculated turbulent shear stresses lie below the measurements by 35% or so, although the large error band associated with the latter will inevitably make the comparison inconclusive. There are no previous turbulent stress predictions with which to compare the present work, as none were presented by either Carajilescov and Todreas or Trupp and Aly. This is perhaps surprising in that such information, particularly for the $\theta = 0^\circ$ section, is of particular value in the study of finite rod-bundle flows where turbulent interchannel mixing is important.

The above noted shear stress error band must form part of that for the measured length scale profile since it will be calculated from the same stresses with additional errors from measured axial velocity gradient and turbulence kinetic energy. These cumulative errors in the measured length scale profile are most apparent in the core, as shown in figure 7.9.10, where length scale apparently reduces rapidly, a behaviour for which there is no physical basis.

However, the core region is not sensitive to length scale errors, as evidenced by the predictions of Carajilescov and Todreas (1976) and Trupp and Aly (1978), both of which used an average of these measured profiles as a length scale prescription. The Buleev length scale profiles are seen to be a little higher than the present predictions, but otherwise a reasonable representation of them.

Overall, the present predictions for P/D ratios of 1.123 and 1.1 are seen to be in reasonable agreement with experiment and an improvement on previous predictions, particularly since the latter required prescription of length scale and also, in one case, the sense of the secondary flow eddies.

7.9.2 Infinite triangular array with P/D = 1.2

The predicted secondary velocity vectors for this geometry are shown in figure 7.9.11, where the flow pattern is seen to be similar to that in the lower P/D ratio passage (figure 7.9.2) with an additional minor swirl near the gap. The effect of this minor circulation on the mean flux should not be significant, as the secondary flow is clearly dominated by the main swirl with (as in the P/D = 1.123 case) circulation from the core towards the wall near the gap ($\theta = 0^\circ$), along the wall, then away from it back into the core region near the $\theta = 30^\circ$ plane. The maximum secondary velocities are 0.6% of the mean axial velocity and occur near the wall and along the maximum axial velocity plane (note the contrast with the P/D = 1.123 results).

The calculated axial velocity is compared with experiment in figures 7.9.12 and 7.9.13, and shows quite good agreement for both contours and profiles. The slight underprediction in the gap is not more than 3½% and, thus, likely to be within the experimental error.

Figure 7.9.14 shows the considerable effect of secondary flow on the calculated wall shear stress profile, reducing the peripheral variation by a factor of 3 and moving the point of maximum stress from $\theta = 30^\circ$ to $\theta = 18^\circ$. As with the $P/D = 1.1$ case, the secondary flow has increased the wall shear at the gap and decreased it at $\theta = 30^\circ$. Both experiments show maximum wall shear at θ less than 30° , with the present and previous predictions in reasonable agreement, the former being within 1½% of the hot film measurements of Trupp and Azad.

The dimensionless radial distance scales used appear to have made the measured turbulence kinetic energy profiles independent of θ , as shown in figure 7.9.15. The present calculations do not show this independence since the gap profile is in accord with experiment, whilst the $\theta = 30^\circ$ level is some 10% to 15% higher in the region away from the wall. This latter effect can perhaps be expected with the different calculated axial velocity profiles and thus k generation rates. The predictions of Trupp and Aly are some 10% - 15% higher than experiment, a trend noted in their prediction of the $P/D = 1.123$ geometry, with little dependence on θ .

Figure 9.7.16 shows the measured cross-plane turbulence intensities to be unexpectedly isotropic, a feature in disagreement with all other rod bundle measurements, including the same authors' in larger P/D ratio ducts. There is no obvious reason for the radial component \tilde{u}_2 to be

apparently unaffected by the wall. This inconsistency must cast some doubt on the measurements. The present predictions do not, as expected, show much anisotropy of the cross-plane intensities and are about 25% higher than the measurements, except for the core region, where there is some accord with experiment in the cross-plane.

The turbulent shear stress profiles calculated from the present method are in reasonable accord with the measurements at $\theta = 0^\circ$, but show more dependence on θ as shown in figure 9.7.17. The measured gap stress appears to change sign before reaching the maximum axial velocity plane ($x/\hat{R} = 1$) a feature that cannot be predicted by the present model (in effect an eddy viscosity type for axial plane shear stresses) without a change in sign of the axial velocity gradient. There appears again to be much less dependence on θ in the measurements than in the predictions, although the experimental error in the measurements will probably be more than these differences.

7.9.3 Infinite triangular array with $P/D = 1.217$

It is of interest to compare the present predictions with a different set of experimental data (Kjellstrom, 1971) in a passage geometry not too different from that of the above case. The experimental test sections are different, however, (figure 9.7.1(c) and (d)) as are the Reynolds numbers of the flow, being, in this case, three times higher.

The predicted secondary velocity vectors are seen in figure 7.9.18 to be similar to those in the $P/D = 1.2$ channel (figure 7.9.11) with a slightly larger minor swirl near the gap. The maximum

secondary velocities are some 0.55% of mean axial velocity, occurring, as in the previous case, near the wall and along the maximum axial velocity plane. Although there are no measured vectors, with which to compare this prediction, Kjellstrom did attempt to measure the circumferential component of secondary velocity. The results are rather scattered (additional measurements by Hall and Svenningsson (1971) in the same test rig were no improvement) but, since there are no other measurements available for rod-bundles, they have been plotted and compared with the present results along $\theta = 12^\circ$, 18° and 24° radial planes, in figure 7.9.19. Although no definite conclusions can be drawn, the calculated profiles do follow the general trend of the data.

The agreement in respect of axial velocity profiles is shown in figure 7.9.20 to be reasonable with, as in the previous case, some underprediction (about 7% near the wall) in the gap. The effect of the secondary flow in convecting core fluid into the gap can again be clearly seen. The calculations of Carajilescov and Todreas are also in reasonable agreement with experiment with slight underprediction, this time, in the core. The differences are however, likely to be within the measurement error band. It is of interest to note that these measured profiles are within a few percent of the Trupp and Azad measurements in the $P/D = 1.2$ duct.

The Preston tube wall shear stress measurements of Kjellstrom shown in figure 7.9.21 were made around 60° of the tube periphery in four test runs. The spread of data thus gives an indication of the reproducibility of the measurements. The general shape of the

measured wall shear stress profile is similar to the Trupp and Azad measurements with a slight difference in the point of maximum stress. There is, therefore, good agreement between the experiments, considering different measurement techniques were used, with tests at different Reynolds numbers. The present prediction is also in fair agreement with the measurements and is an improvement on previous predictions. Once again the considerable effect of secondary flow on the predicted profile is evident.

The measured turbulence kinetic energy levels of Kjellstrom, plotted in figure 7.9.22 are significantly higher than the measurements of Trupp and Azad, an effect unlikely to be due entirely to the difference in Reynolds numbers since the average friction velocity is used for normalisation. The measurements are similar, however, in showing little dependence on θ , a feature not found in the present predictions which are in accord with experiment at $\theta = 30^\circ$, but low by some 35% at $\theta = 0^\circ$. The previous predictions do not show much dependence on θ either but disagree on the level of turbulence kinetic energy. A test was made with the present method to determine the sensitivity of the predicted normalised turbulence kinetic energy level to changes in Reynolds number. A three fold change in Reynolds number (from 5×10^4 to 1.5×10^5) caused less than 2% change in the normalised levels everywhere except in the core where the level was about 10% lower at the lower Reynolds number. The comparison of turbulence kinetic energy levels is, therefore, inconclusive, except perhaps to indicate an overdependence on θ in the present results.

As may be expected from the above there are significant differences in the measured turbulence intensities from the two sources. The Kjellstrom measurements at $\theta = 30^\circ$ are shown in figure 7.9.23 (the $\theta = 0^\circ$ measurements are similar with about 5% higher levels at $x/\hat{R} = 1.0$), with the Trupp and Azad measurements appearing in figure 7.9.16. The main differences are (a) an anisotropy of the near wall cross-plane intensities that is evident in the Kjellstrom measurements but, as previously noted, is absent from the Trupp and Azad data and (b) the axial intensities are much higher in the Kjellstrom measurements. The present predictions are in fair agreement with the latter although, as expected, the anisotropy of the cross-plane intensities is not predicted.

The overall comparison between the present results and the two sets of measurements in fairly similar rod bundle channels shows good agreement on axial velocity and wall shear stress with much less agreement on the turbulent structure. The turbulence measurements of Kjellstrom, however, are perhaps more convincing than those of Trupp and Azad. The present predictions are also in good agreement with the data on axial velocity and wall shear stress, and in better agreement with the turbulence measurements of Kjellstrom than with the less consistent looking measurements of Trupp and Azad.

7.9.4 Symmetry sub-channel in the test section of Subbotin (1971)

This section describes the results of a study made of the difference between finite and infinite array behaviour. A symmetry quadrant of the experimental test section of Subbotin is seen in figure 7.9.1a to comprise two subchannels, the 'inner' subchannel in

which the experimental measurements were made and the 'outer' sub-channel which contains the end wall. The authors claimed that the flow in the inner subchannel simulates that in an infinite array, having checked using an electrical analogue of laminar flow (the resistance paper technique). It was assumed that laminar flow would be more influenced than turbulent flow which would also, therefore, be unaffected. It is not clear which P/D ratios were checked in this way.

The proximity of the end wall to the measurement subchannel (shaded in figure 7.9.1a) makes the Subbotin test channel the most likely of those shown in figure 7.9.1 to show finite array effects. Calculations were made with the present method for a symmetry quadrant (i.e. the combined inner and outer subchannels) of the Subbotin test section for two different P/D ratios and the results are compared with the measurements of Subbotin (who reported some axial velocity measurements in both the inner and outer subchannels) and with the present predictions for an infinite array.

The predicted secondary velocity vectors for $P/D = 1.1$ are shown in figure 7.9.24. The circulation in the outer subchannel is seen to penetrate slightly into the inner subchannel and is significantly stronger than the circulation in that channel. However, the infinite-array pattern of a single circulation of secondary flow (similar to that of figure 7.9.2) is largely preserved in the inner subchannel with the maximum secondary velocities reduced by about 10% compared with the former prediction.

Figure 7.9.25 shows the axial velocity contours to be quite well predicted for the symmetry quadrant, with the influence of the end wall

evident but mainly in the outer-subchannel. This influence is seen again in the axial velocity profiles along the channel centre-plane (bcd in figure 7.9.25) plotted in figure 7.9.26. There is fair agreement between the present prediction and experiment in both sub-channels. There is also a similar agreement between the prediction for an infinite array and the inner channel profile thus confirming the simulation of an infinite array by the inner channel for axial velocity.

The wall shear stress profile for the inner channel is shown in figure 7.9.27 compared with the measurements of Subbotin, where the prediction is seen to be reasonably similar to that for an infinite array (within 3%) and within the band of experimental measurements. There are no measurements available for a comparison to be made in the outer channel.

The predicted secondary velocity vectors in a symmetry quadrant with $P/D = 1.2$ are shown in figure 7.9.28. In this instance there is a strong circulation of secondary flow in the outer subchannel which clearly penetrates into and influences the much weaker circulation in the inner channel. The small circulation near the gap in the infinite array calculation (figure 7.9.11) does not appear, although the secondary velocities there are almost zero in any case.

Centre-plane axial velocity profiles are plotted in figure 7.9.29 and show quite good agreement between prediction and experiment in both channels. The predicted infinite array profile is about 5% below the inner channel measurement, showing that the end wall in the outer channel does have some influence in this case. The inner channel with

$P/D = 1.2$ is therefore not as convincing a simulation of the infinite array as for $P/D = 1.1$, as might be expected since the larger gap in the former case allows more interaction.

Figure 7.9.30 shows the predicted wall shear stress profile in the inner subchannel to be influenced by the end wall such that the shear stress is nearly constant along most of the wall. This profile matches the measurements of Subbotin and, when compared with the infinite array prediction and the measurements of Trupp and Azad, apparently reveals the reason for the difference between the two measurements. Clearly the profile measured by Subbotin is affected by the end wall in the test section, whereas, that measured by Trupp and Azad is much nearer the infinite array condition. This conclusion is consistent with the test sections used (figure 7.9.1) since the measurement subchannel of Subbotin is, as previously noted, only one subchannel away from an end wall whereas that of Trupp and Azad is at least seven subchannels away. Although the differences between the two sets of measurements are small, the trend of each set is clear and it is most encouraging that the present method has successfully simulated both.

7.9.5 Local and overall friction characteristics

The predicted local friction velocity, or wall shear stress, was found to be only a weak function of Reynolds number as shown in figure 7.9.31. For example, a four-fold increase in Reynolds number (5×10^4 to 2×10^5) results in a reduction of peripheral variation in τ_0 from $22\frac{1}{2}\%$ to 19% for the $P/D = 1.1$ case and from 7.6% to 7.4% for the $P/D = 1.2$ case.

The predicted dependence of local τ_0 on the P/D ratio is however, quite strong as shown in figure 7.9.32. A change in P/D ratio from 1.1 to 1.2 reduces the peripheral variation of τ_0 from 22½% to about 7½%. The reason for this is seen in the significant reduction in the variation of transverse radial distance across the subchannel (wall to centre-plane). For example, from figures 7.9.2 and 7.9.11, this variation from $\theta = 0^\circ$ to $\theta = 30^\circ$ is 140% for P/D = 1.1 and 90% for P/D = 1.2. When the P/D ratio is about 1.3 or higher the peripheral variation of τ_0 is less than 3% and, as such, is probably within the error band of experimental measurement and unlikely to be significant.

Table 3.2.1 shows that there have been many experimental measurements of overall pressure drop in a wide range of rod-bundle test rigs. Probably the most systematic and comprehensive of these was reported by Rehme (1972), who measured the variation of friction factor with Reynolds number for eleven different triangular array P/D ratios from 1.025 to 2.32 and with rod numbers varying from 7 to 61, making 25 different test sections in all. In these tests the gap between the outer rods and the hexagonal casing was made the same as the gap between the interior rods. This latter detail was a consequence of an observation made from the results of a survey of some 60 previous publications of pressure drop measurements in triangular array rod bundles, given by Rehme in the first part of his paper. The survey showed that these previous measurements were very scattered, as demonstrated by the plots in figure 7.9.33 which shows many of these pre-1972 measurements for two Reynolds numbers. Although no conclusions could be drawn, Rehme made the observation that the

method of calculation of equivalent diameter in the wide range of test sections could influence the final result significantly. A trend could apparently be detected in the survey in that some of the highest and lowest values of friction factor for rod bundles, with similar interior equivalent diameter, correlated with the gap between the outer rods and the shell wall. This and other observations appeared to be incorporated into the design of the Rehme test sections.

The experimental results of Rehme (1972) are plotted in figure 7.9.34 for P/D ratios up to 1.23 and are compared with the present predictions, which are seen to be in good agreement with these measurements and also with those of Carajilescov and Todreas (1976) and Subbotin (1971). The previous predictions, the empirical formula of Malak et al (1975) and the data of Trupp and Azad (1975) and Kjellstrom (1971) lie mainly above the Rehme results. There is a slight increase of friction factor with P/D ratio in both the latter and the present predictions. This trend is shown again in figure 7.9.33. The agreement between the Rehme measurements and the present prediction is good, with virtually identical behaviour at $Re = 10^5$.

The predictions of Carajilescov and Todreas (1976) and Trupp and Aly (1978) with similar fourth generation methods, are 15% - 20% higher than the present predictions, due, most probably, to the different length scales and empirical constants used, and appear to match the experiments of Trupp and Azad (1975) and of Kjellstrom (1971). However, some of the findings and conclusions of Rehme are perhaps relevant here in that he found his measurements to approach an upper limit as P/D was increased. This upper limit was that given

by the 'equivalent annulus' solution, which can be obtained by neglecting the variation of τ_0 around the perimeter and replacing the hexagonal elementary fluid cell around the rod by a circular cell of the same area and assuming a universal profile for axial velocity. This model was not reviewed in Chapter 3 as it applies to large P/D ratios only, a necessary restriction since there must be no significant peripheral τ_0 variation. The model has been frequently used, however, in flow and heat transfer analysis in large P/D ratio rod bundles (e.g. Dwyer and Tu, 1959; Friedland and Bonilla, 1961; Maresca and Dwyer, 1964) and in this case yields the limiting curves shown in figure 7.9.33, which can be assumed valid for P/D greater than about 1.3 where, as noted previously, the peripheral variation of τ_0 becomes negligible (see figure 7.9.32). The present predictions are in accord with this which appears to be a reasonably logical limiting case for the infinite array rod bundle and further, since f tends to decrease as P/D decreases below P/D = 1.3, must represent an upper limit of f for all P/D. The measurements of such as Trupp and Azad, Kjellstrom and the others represented by the measurements in figure 7.9.33 which are significantly above this limit, must be due to inconsistencies and effects such as (a) an equivalent diameter effect for the test section, (b) influence of surface roughness, spacers, misalignment of rods etc., (c) inaccurate knowledge of geometric parameters for calculation of equivalent diameter, (d) flow not fully developed or (e) measurement inaccuracies when, for example, pressure drop was measured as part of heat transfer measurements.

The equivalent diameter concept fails to correlate the friction factors for P/D < 1.1 as seen by the significantly higher values implied by the Blasius equation in figure 7.9.33. The Malak et al

equation improves this for $R_e = 10^4$ and $P/D < 1.08$ but otherwise tends to over-predict.

As a result of this examination of overall friction factor in rod bundles and the general agreement of the present results with the comprehensive measurements of Rehme (1972) some useful conclusions can be drawn from, what seemed at first sight, an inconclusive situation with a wide scatter of experimental results and different predictions. These conclusions can be briefly summarised as:-

Friction factor is a strong function of P/D ratio for $P/D < 1.1$ and reaches a limiting value given by the equivalent annulus model for $P/D > 1.3$. The dependence of f on R_e similar to that in the Blasius equation i.e. $f \propto R_e^{-\frac{1}{4}}$.

7.10 Closure

An extensive and systematic programme of calculation and comparison with experiment has been carried out with the ASTM-based curvilinear finite difference method developed in the earlier part of this thesis. Predictions for fully developed flow have been compared with measurements in 18 different passage cross-sections, with a range of turbulent flow Reynolds number that has given a total of 28 flows for which detailed comparisons have been presented. These flow predictions are believed to be the first to be made with a fully consistent ASTM describing the complete Reynolds stress tensor.

The present predictions of local wall shear stress and velocity are in fair agreement with experiment, right down to secondary velocity

level. The main exceptions to this were the cases where the experimental flows were clearly not fully developed. The present calculations of the detailed turbulence structure were found to be in less agreement with experiment particularly near the wall. In this region the two main differences were (a) the calculated turbulence kinetic levels were mostly found to be low compared with the measurements, which were often much above the level predicted by the model for local equilibrium, and (b) the anisotropy of the cross-plane normal stresses was not predicted. The former deficiency may be due to near-wall effects in the measurement of k , or alternatively to inadequate wall functions for the calculation of k ; the latter deficiency is due to the empirical constants used in the ASTM and was accepted in order to adequately simulate the remainder of the flow. A further characteristic shortcoming of the predictions, which may also be due to the above-mentioned constants, is the general under-prediction of friction factor by between 5% and 10% in most cases.

An unsuccessful attempt was made to calculate the asymmetric flow in a square duct with one rib-roughened wall measured by Ali (1978). The calculated secondary flow was much weaker than indicated in the measurements whereas the asymmetries caused by the rough wall were generally much stronger than the measurements. It is suggested that the failure of the predictions may be due, at least in part, to the flow at the measurement plane being influenced by the upstream rib (from evidence in the measured secondary flow) to give effects not possible to reproduce with the present calculation method for fully developed flow. In addition, the method used here of simply inserting special wall functions does not appear to adequately account for the

effect of the rough wall on the calculated flow; on particular, the shear stress behaviour cannot be properly predicted with the ASTM used.

In addition to the validating comparisons discussed above, the predictions presented in this chapter have also been informative, particularly on the effects of cross-plane secondary flows, and also in revealing second order effects in the flow, such as that of the channel end-wall in the experiments of Subbotin (1971). These and other overall implications of this work are discussed more fully in Chapter 9.

The general accord with experiment of the calculated flow fields from the present method has encouraged further calculations using these flow fields as a basis for a study of heat transfer in arbitrary shaped ducts. The results of these calculations are presented in the next chapter.

CHAPTER 8 HEAT TRANSFER PREDICTIONS

8.1 Introduction

In this chapter predictions are presented of laminar and turbulent heat transfer in arbitrary shaped passages obtained from the present procedure.

The laminar heat transfer predictions are shown in the first part of this chapter, for three different passage shapes and various boundary conditions. These calculations have been made in part as an accuracy check on the present method by comparison with available analytical solutions, and in part to compare with some of the previously published work, obtained by different numerical approximations. In the second part of the chapter turbulent heat transfer predictions are presented for five different passage geometries and compared with experiment for different specified boundary conditions.

Heat transfer boundary conditions are known to effect laminar heat transfer significantly (Shah and London, 1978) although, as discussed in section 3.3, the effect on turbulent heat transfer in passages is less well known. The opportunity is taken to study the latter aspect in the present work. The three most commonly identified boundary conditions were designated H1, H2 and H3 in Chapter 5 and are re-stated here:

- H1 Constant peripheral temperature and constant axial heat flux.
- H2 Constant peripheral and axial temperature (isothermal wall).
- H3 Constant peripheral and axial heat flux.

Examples of situations where these boundary conditions may approximately obtain are:

H1 Uniform, thin, high thermal conductivity passage walls with electrical resistance or external radiation heating.

H2 Condenser and evaporator tubes, high coolant flow automotive type radiators.

H3 As H1 with low thermal conductivity passage walls.

The local heat flux \dot{q}'' between the passage wall and fluid is usually expressed in terms of the local heat transfer coefficient h_L as

$$\dot{q}'' = h_L (T_w - T_b) \quad (8.1.1)$$

where T_w is the local wall temperature and T_b is the 'bulk' fluid temperature defined as

$$T_b = (1/\bar{U}_3 A) \int_0^A U_3 T dA \quad (8.1.2)$$

Here U_3 is the local fluid axial velocity through an elementary flow area dA , T is the local fluid temperature, A the total flow area and \bar{U}_3 the mean axial velocity.

The mean heat transfer coefficient h for a surface is defined in terms of the peripherally averaged wall heat flux $\bar{\dot{q}}''$ as

$$\bar{\dot{q}}'' = h(\bar{T}_w - T_b) \quad (8.1.3)$$

where \bar{T}_w is the average wall temperature given by

$$\bar{T}_w = (1/m) \int_0^m T_w dS \quad (8.1.4)$$

and \bar{q}'' is given by

$$\bar{q}'' = (1/m) \int_0^m \dot{q}'' dS \quad (8.1.5)$$

in which T_w and \dot{q}'' are the local wall temperature and heat flux respectively for an elementary peripheral length dS , and m is the passage perimeter. It is important to note that if T_w varies around the perimeter, as in the H3 case, then h is not equal to \bar{h} the peripherally averaged value of heat transfer coefficient which is expressed as

$$\bar{h} = (1/m) \int_0^m h_L dS \quad (8.1.6)$$

The peripheral variations in local heat transfer coefficient and temperature are of considerable interest in non-circular passage heat transfer, designs for which are usually required to satisfy local as well as overall heat transfer criteria. For example, knowledge of the variation in wall temperature will enable the possible 'hot' (or 'cold') spots to be identified and checked for compatibility with the design.

The mean and local heat transfer coefficients are usually represented in dimensionless form as mean and local Nusselt numbers N_u and N_{uL} respectively, defined as

$$N_u = hD_e/k_f \quad (8.1.7)$$

$$N_{uL} = h_L D_e / k_f \quad (8.1.8)$$

where D_e is the equivalent diameter of the passage and k_f the fluid thermal conductivity.

8.2 Laminar heat transfer

It is noticeable that the majority of published theoretical laminar heat transfer analyses in non-circular passages have been concerned more with overall heat transfer (mean or 'asymptotic' Nusselt numbers) than with local variations. The present study has therefore concentrated on comparisons with cases where some detailed analytical or numerical distributions are available in addition to mean Nusselt numbers. Where appropriate, any gaps have been filled with distributions from the present work.

8.2.1 Elliptical ducts

Analytical solutions for fully developed laminar heat transfer in elliptical ducts with HI boundary conditions were apparently first presented by Tao (1961) using a complex variable method. The fluid temperature profiles along the major and minor axes calculated from the present method are seen to be in excellent agreement with these analytical solutions in figure 8.2.1. Since only average wall temperatures and Nusselt numbers were presented by Tao, the peripheral variations of local Nusselt number are presented from the present method in figures 8.2.2 and 8.2.3 to complete the local heat transfer characteristics for this boundary condition. As can be expected from the similarity between the axial momentum and energy equations for the

H1 case the peripheral variations are qualitatively similar to the wall shear stress profiles in the corresponding ducts (figure 6.2.2).

The H2 and H3 boundary conditions have been investigated for fully developed heat transfer in elliptical ducts by Dunwoody (1962) and Iqbal et al (1972) respectively with complex variable and variational methods. The average N_U values for all three boundary conditions are compared with the analytical values for a range of duct aspect ratios in table 8.2.1. Agreement is excellent, attesting to the good accuracy of the present method.

The main effect of increased aspect ratio is seen in Table 8.2.1 to be the significant reduction of N_U for the H3 boundary condition. This is due to a much increased variation in temperature around the periphery, an effect not present in the H1 and H2 cases where the peripheral wall temperature is constant. The temperature variation in the H3 case is caused by the increasing thermal resistance between the fluid core and the remoter parts of the wall which from equation (8.1.1) implies that h_L must decrease since \dot{q}'' is constant. This effect is evident in figure 8.2.3 where the H3 variation in N_{UL} is more than double the others. The authors listed in table 8.2.1 presented only mean wall temperatures and Nusselt numbers so no analytical profiles can be shown for comparison.

The variation of wall temperature in the H3 case is responsible also for N_U always being less than that for the H1 case with a given geometry. In the H1 case, the mean heat transfer coefficient is obtained from equation (8.1.3) with $\bar{T}_w = T_w = \text{constant}$ so that

$$h_{H1} = \bar{q}'' / (T_w - T_b)$$

Bound. Cond.	Reference	Aspect ratio		
		1.5	2.0	5.0
H1	this work	4.438	4.558	4.967
H1	Tao (1961)	4.438	4.558	4.962
H2	this work	3.69	3.80	3.78
H2	Dunwoody (1962)	3.71	3.80	3.795
H3	this work	4.17	3.735	1.85
H3	Iqbal et al (1972)	-	3.742	1.82

Table 8.2.1 Mean Nusselt numbers for elliptical ducts

In the H3 case, equation (8.1.3) gives

$$h_{H3} = \bar{q}'' / (\bar{T}_w - T_b)$$

Since, in the H3 case the local temperature difference $|\bar{T}_w - T_b|$ must increase for the remoter parts of the wall, then clearly \bar{T}_w (equation 8.1.4) is greater than T_w . Hence, for a given \bar{q}'' and T_b , N_u for the H3 case must be less than that for the H1 case with a given geometry and for any passage shape.

8.2.2 Equilateral triangular duct

The fluid temperature profiles calculated from the present method for fully developed laminar heat transfer with H1 boundary conditions in an equilateral triangular duct are seen in figure (8.2.4) to be in excellent agreement with the analytical solutions from the complex variable method of Tao (1961). The mean Nusselt number was

calculated by Tao as 28/9. The peripheral variation in local Nusselt number is not given by Tao, so the present prediction for the H1 case is compared in figure (8.2.5) with the analytical solution derived by Marco and Han (1955) from thin plate theory. Agreement is excellent and, as expected from previous discussions, the N_{uL} profile for this case is qualitatively similar to the τ_0 profile for laminar flow (figure 6.3.1).

A mean Nusselt number of 2.47 has been obtained for the H2 boundary condition by Wibulswas (1966), Schmidt and Newell (1967) and Nakamura et al (1972) with finite-difference methods. The mean N_u for the H3 boundary condition was calculated to be 1.89 by Cheng (1969) with a boundary point matching method and also by Shah (1975) with a discrete least squares method. These results are compared with the present calculations in table 8.2.2 which also shows the N_u comparison with Tao for the H1 case. Agreement is good for the H1 and H3 cases and acceptable (within 5%) for the H2 case which compares values from different finite difference methods.

Reference	Boundary conditions		
	H1	H2	H3
Present method	3.14	2.52	1.98
Previous work	3.11	2.47	1.89

Table 8.2.2 Mean Nusselt numbers for an equilateral triangular duct

The variations in N_{uL} are given for these cases from the present method in figure 8.2.5. The profile for the H3 case shows the greatest variation, and has a mean N_u in table 8.2.2 lower than for the H1 case, as expected from discussion of the corresponding elliptical duct case.

8.2.3 Rod bundles

Fully developed laminar heat transfer for axial flow in rod bundles with the H1 boundary condition was first analysed by Sparrow et al (1961) with a boundary point-matching method. This work was later confirmed and extended by Dwyer and Berry (1970) using finite differences. The present calculations are in excellent agreement with these solutions as shown in the plots of local Nusselt number for various P/D ratios in figure 8.2.6.

A strong dependence of N_{uL} on the P/D ratio is evident from figure 8.2.6, which shows a variation of over 150% about the mean Nusselt number N_u for the P/D = 1.1 case, reducing to about 10% for the P/D = 1.3 case. The expected qualitative similarity between the N_{uL} profiles for this case and the τ_0 profiles (figure 6.4.2) is apparent once again.

The constant peripheral and axial heat flux (H3) boundary condition problem was solved by Dwyer and Berry (1970) with a finite difference method. The local Nusselt number profiles calculated from the present method are seen in figure 8.2.7 to be in good agreement with the Dwyer and Berry solutions. Comparing figures 8.2.6 and 8.2.7 and noting the difference in scales, the variation in N_{uL} for the H3 case is many times that in the H1 case, particularly at the

lower P/D ratios. The minimum N_{uL} occurs at the gap ($\theta = 0^\circ$) which is at the greatest distance from the core and is thus subject to the highest fluid thermal resistance. As discussed in previous cases, since h_L is low and \dot{q}' constant then, from equation (8.1.1), T_w must be high i.e. the 'hot' spot is at the gap.

Another feature of this (H3) boundary condition can also be seen in figure 8.2.7 where the peripherally averaged Nusselt number N_u (with h based on equation (8.1.5)) will clearly not be equal to the mean Nusselt number N_u (with h based on equation (8.1.3)) particularly in the P/D = 1.1 case. This situation was mentioned in the introduction and is a consequence of the varying wall temperature which makes $1/(\bar{T}_w - T_b)$ different from $(1/m) \int_0^m ds / (T_w - T_b)$. This temperature variation is shown as a semi-logarithmic dimensionless plot in figure 8.2.8, which is particularly useful since the ordinate is actually the reciprocal of N_{uL} . As anticipated from the previous comparisons, agreement between the present predictions and those of Dwyer and Berry is good, attesting to the accuracy of both methods.

There is an order of magnitude difference in temperature variation, in figure 8.2.8 between the almost isothermal P/D = 1.5 case and the large variation P/D = 1.1 case. As anticipated from previous discussion, the largest temperature difference is at the gap and the plot reveals the magnitude of this 'hot' spot problem for the low P/D case. The difference between \bar{N}_u and N_u can be quite significant with, from the present calculations, $\bar{N}_u = 6.3$ when $N_u = 2.9$ for the P/D = 1.1 case. Although less exaggerated, a difference between \bar{N}_u and N_u for the H3 case is to be expected and is evident in the elliptical duct results (figure 8.2.3) and the equilateral triangular duct results (figure 8.2.5). This difference has

an important implication in experimental heat transfer where measured values of \bar{N}_U have sometimes been assumed equal to N_U without due regard to peripheral wall temperature variation.

There do not appear to be any previously published calculations for the H2 (isothermal wall) boundary condition for fully developed laminar heat transfer in rod bundles. Although of no interest in nuclear reactor design, this boundary condition is relevant in certain condensers, evaporators and high convection recuperators. The peripheral variation in local Nusselt number, calculated from the present method with $P/D = 1.1$ is shown in figure 8.2.9 compared with profiles for the other boundary conditions. The constant wall temperature constraint precludes the large variation in N_{UL} found in the H3 case.

The present and previous predictions of mean Nusselt numbers for each boundary condition are given in table 8.2.3 for a range of P/D ratio, and show good agreement. It is apparent that there is

Bound. cond.	Reference	P/D ratio				
		1.1	1.2	1.3	1.5	2.0
H1	This work	4.5	7.4	9.16	11.27	15.29
H1	Dwyer & Berry (1970)	4.62	7.48	9.19	11.26	15.27
H2	This work	3.27	5.76	7.75	10.23	14.33
H3	This work	2.9	6.86	9.036	11.26	15.29
H3	Dwyer & Berry (1970)	2.94	6.9	9.03	11.22	15.26

Table 8.2.3 Mean Nusselt numbers for rod-bundles

little difference between the H1 and H3 cases for $P/D > 1.3$. This is to be expected since the peripheral variation in temperature for the H3 case (figure 8.2.8) and heat flux (proportional to h_L) in the H1 case (figure 8.2.6) and thus the differences between the two cases are both less than 10% for $P/D > 1.3$.

The Nusselt number appears to increase rapidly with P/D ratio in table 8.2.3 giving perhaps the impression that h increases also. This is however, not necessarily the case since N_U also involves the equivalent diameter D_e , which increases rapidly with P/D . A clearer insight into the physical processes involved in this rod-bundle case can be obtained by re-calculating N_U with D_e replaced by the rod diameter D i.e. with $N_{ud} = hD/k_f$. The variation of N_{ud} with P/D is shown in figure 8.2.10, revealing a peak in the value of N_{ud} , occurring at $P/D = 1.21$ for the H3 case. This peak occurs as the effect of decreasing fluid thermal resistance is counter-acted by increasing circumferential heat transfer as P/D decreases.

At the higher P/D ratios, circumferential variations will be negligible and heat flux is practically all in the radial direction. As P/D decreases from large values, the fluid thermal resistance (represented by the distance between the wall and the core) decreases, thus N_{ud} increases. However, for $P/D < 1.3$, circumferential variations become significant until eventually, for $P/D < 1.2$, circumferential heat transfer becomes dominant and N_{ud} decreases. The circumferential variations in the H1 are less significant than in the H3 case, giving a maximum N_{ud} at the lower P/D ratio of 1.1.

8.2.4 Summary of the laminar heat transfer predictions

The accuracy, flexibility and universality of the present method in the prediction of fully developed laminar heat transfer has been demonstrated with calculations in elliptical, triangular and rod-bundle passages for three different boundary conditions and for ranges of geometry within each passage shape. Agreement with previous work is good for both overall Nusselt numbers and for local fluid and wall temperatures and Nusselt number profiles. Some of the profiles presented from the present work do not appear to be available in the current literature. This detail has, in many cases, enabled a good understanding of the main heat transfer characteristics in each passage shape.

8.3 Turbulent heat transfer

8.3.1 Circular tube

Calculations were made for this simple geometry since the results could be compared with the well established experimental data, which is often used as a basis of comparison for heat transfer in non-circular passages. As mentioned in Chapter 3, the Dittus-Boelter equation (3.3.1), has been most frequently used, in conjunction with the equivalent diameter concept, to represent the circular tube data. This equation is a global correlation of the data from pre-1930 experiments with liquid and gases and as such does not represent either very accurately, nor does it take advantage of the more recent experimental data. In addition to this, as also discussed in Chapter 3, the dependence of N_u on P_r is likely to be more complex

than given by the Dittus-Boelter equation. However, if the advantage of the relative simplicity of the Dittus-Boelter equation is to be retained, then different constants should at least be employed for various liquids and gases. This is the philosophy followed by Kays (1966), who also allowed for the effects of boundary conditions in proposing the following equations for fully developed circular tube heat transfer for fluids including water and air:-

(i) $0.5 < P_r < 1.0$ (Gases)

$$(a) \text{ H1 (and H3) boundary conditions } N_u = 0.022 R_e^{.8} P_r^{.6} \quad (8.3.1)$$

$$(b) \text{ H2 boundary condition } N_u = 0.021 R_e^{.8} P_r^{.6} \quad (8.3.2)$$

(ii) $1.0 < P_r < 20$ (Water and light liquids)

$$\text{All boundary conditions } N_u = 0.0155 R_e^{.83} P_r^{.5} \quad (8.3.3)$$

As will be seen from the above and in contrast to the laminar heat transfer case, the boundary conditions do not appear to have much influence in turbulent flow.

The present predictions of mean Nusselt number for P_r typical of air and water and with $\sigma_c = 0.9$ are compared with the Dittus-Boelter equation and the Kays equations in figure 8.3.1. The difference between the Dittus-Boelter and Kays equations is about 10%, with the present predictions generally nearer Kays, particularly for the $P_r = 0.7$ case. The present calculations also confirm that the heat transfer boundary conditions have only a negligible effect (too small to be shown in figure 8.3.1).

Figure 8.3.2 shows the calculated fluid temperature profiles from the present method to be in good agreement with experiment for two different Prandtl numbers. The predictions for a turbulent Prandtl number σ_c of 0.8 are also shown for comparison and appear to be a marginal improvement. The expected result of a 'flatter' temperature profile with increased P_r is well predicted.

The eddy diffusivity profile from the present method (equation (4.4.3)) is compared with experiment in figure 8.3.3. There is some underprediction although the differences are not large taking into account the likely measurement error involved in calculating the axial and radial temperature gradients required. Agreement appears to be improved with $\sigma_c = 0.8$, in accord with the temperature profiles.

The air heat transfer values of turbulent Prandtl number implied by the combined eddy diffusivity measurements of Johnk and Hanratty (1962) and eddy viscosity measurements of Laufer (1954) have been calculated and plotted in figure 8.3.4, together with the water measurements of Smith et al (1967). The scatter and disagreement is not untypical of such measurements which show the value of σ_c to be mainly between 0.8 and 1.0. The value of $\sigma_c = 0.9$ recommended by Laufer (Chapter 6, Bradshaw, 1978) and used in the present study appears, therefore, to be an acceptable average. It should also be noted that a slightly lower value, as found to give an apparent improvement in the present predictions discussed thus far, would also be acceptable. However, a further and important point to note is that, in view of the general underprediction of friction factor with the present method, some underprediction of heat transfer should perhaps be expected here.

The availability in the literature of measured fluid temperature profiles in this simple duct shape (apparently none are available for non-circular passages) has enabled a comparison to be made with predictions using the algebraic heat flux transport model (AHFTM), derived in Appendix 4 and described in section 4.4. This model yields anisotropic eddy diffusivities given by equations (4.4.8) and (4.4.9) with C_{1c} as an empirical constant.

The values of C_{1c} appropriate to various heat flux models and heat transfer situations are extensively discussed by Launder, in Chapter 6 of Bradshaw (1978), who recommends a value of 3.4 for near-wall heat transfer. Using this value in the AHFTM, the predicted temperature profile and eddy diffusivity are seen in figure 8.3.5 to be in disagreement with experiment. Comparing these results with figure 8.3.2 and 8.3.3 show them also to be in disagreement with the present predictions based on the constant turbulent Prandtl number heat flux model with $\sigma_c = 0.9$. The reason for this disagreement can be made apparent by calculating the value of σ_c implied by using $C_{1c} = 3.4$ with the present ASTM. From equations (3.4.25), (4.2.33) and (4.4.8) we can write:

$$\sigma_c = \nu_t / \gamma_{c1} = (C_4 k^2 / \epsilon) / (\overline{u_1^2} k / C_{1c})$$

$$\text{or} \quad \sigma_c = C_4 C_{1c} k / \overline{u_1^2} \quad (8.3.4)$$

With $C_4 = 0.085$ (see section 4.7), $C_{1c} = 3.4$ and $\overline{u_1^2} / k = 0.49$ for homogenous shear flow (see section 7.2) then from equation (8.3.4)

$$\sigma_c = 0.59 \quad (8.3.5)$$

This value of σ_c is much lower than that of 0.9 adopted for the

present predictions, and considerably lower than the main body of measurements in figure 8.3.4. The value in equation (8.3.5) is, in fact, more appropriate to heat transfer in flows remote from walls (see Laufer, Chapter 6 in Bradshaw, 1978). The reason for this is, of course, the homogenous shear value of $\overline{u_1^2}/k$ that was used above and in assigning the constants in the ASTM. If a wall-flow level of $\overline{u_1^2}/k$ is used, such as the value of 0.29 for a circular pipe (Laufer, 1954) then with $C_4 = 0.085$ and $C_{1C} = 3.4$, equation (8.3.4) gives:

$$\sigma_C = 1.0 \quad (8.3.6)$$

Indeed, this must be expected since the value of C_{1C} was deduced from measurements of σ_C and $\overline{u_1^2}/k$.

The AHFTM cannot, therefore, be used with the present ASTM since the empirical constants in the latter have been fixed from stress levels in homogenous shear flows and not the near-wall region for which the AHFTM has been derived. This could have been compensated for by calculating a value of C_{1C} compatible with the ASTM (it would be $C_{1C} = 5.2$). However, the resulting heat flux model would not be consistent and would anyway have little advantage over the constant turbulent Prandtl number heat flux model adopted in the present study, since the anisotropy of cross-plane normal stresses is much under-predicted.

8.3.2 Elliptical ducts

Heat transfer measurements with both water and air in elliptical ducts have been reported by Cain et al (1973). The air flow experiments were conducted in ducts of aspect ratio 1.5 and 2.0 and, since the peripheral variations in local Nusselt number were less

than $\pm 2\%$ and thus likely to be within the experimental error band in the former duct, only the latter will be used for comparison of local characteristics. This comparison is shown in figure 8.3.6 where the present prediction is seen to be in reasonable overall agreement with experiment. The experimental duct had electrically heated walls which were assumed to produce a constant heat flux (H3) boundary condition. The present calculations show, however, that there is little difference between the H1 and H3 profiles. This will be due to the small peripheral variations in either temperature or heat flux which are less than 10% for the latter in the H1 case (where heat flux is proportional to heat transfer coefficient or Nusselt number in figure 8.3.6).

The relatively small peripheral variations in N_{UL} are a consequence of the secondary flow, as seen from the calculations in figure 8.3.6. A variation of more than 50% for the hypothetical case is reduced to only 10% by these flows. The undulation in the present prediction will be due to this secondary flow, which convects core fluid along the major axis ($\theta = 90^\circ$) towards the wall (see figure 7.8.2). A similar undulation may be suggested by the experimental measurements, although the results are too scattered for any certainty.

The water flow heat transfer experiments were conducted by Cain et al in ducts with aspect ratios of 8/3 and 2.93 using electrically heated walls. The reported measurements of local Nusselt number are reproduced in figure 8.3.7, in comparison with the present predictions. The calculated profiles show, as expected, slightly larger variations than in the AR = 2 case but, however, much less

variation than in the measurements. Some inconsistencies can, in any case, be detected in the latter which may account in part for these differences. The measurements are clearly different on the upper and lower surfaces for both cases, due most likely to effects such as natural convection, flow asymmetries and heating asymmetries. Also, contrary to expectations, the data for the lower aspect ratio duct appears to have larger variations in N_{uL} than the higher aspect ratio duct. This again, is likely to be due to one or more of the previously mentioned effects.

The effect of secondary flow is evident again in the calculated profiles, with undulations similar to that shown in figure 8.3.6. The measurements appear to be too scattered to show this kind of detail.

The mean Nusselt number-Reynolds number characteristics are shown in figures 8.3.8 and 8.3.9. The present predictions for air flow are some 5% - 10% low with some improvement once again implied with $\sigma_c = .8$. The water flow prediction appears to be in good agreement with experiment passing right through the centre of the measurements. It is not clear whether, in this case, the prediction is improved with $\sigma_c = .8$. It is interesting to note that, using the Dittus-Boelter equation, the equivalent diameter concept appears to be valid for elliptical ducts, whereas with the Kays correlations, there is an apparent underprediction by 10% or more.

The effect of secondary flow on mean Nusselt number was found to be small (a reduction of less than 5%) and so has been omitted from figures 8.3.8 and 8.3.9 to retain clarity. Secondary flow appears,

therefore, to have much more effect on local Nusselt number than on the mean Nusselt number.

8.3.3 Equilateral-triangular duct

The overall turbulent heat transfer measurements of Lowdermilk (1954) in an equilateral triangular duct with electrically heated walls appear to be the only ones available for this passage geometry. These are compared in figure 8.3.10 with the present prediction which is some 15% lower. This is improved, as with the previous air heat transfer predictions, by taking $\sigma_c = .8$.

The predicted peripheral variations in local Nusselt number are shown in figure 8.3.11 where, as expected from previous discussion, the H3 profile shows more variation than the H1 profile. The significant effect of secondary flow in making the peripheral variation more uniform is evident from these results. In contrast with the previous case this effect seems to increase the mean Nusselt number significantly as shown in figure 8.3.10 where the predicted characteristic with secondary flow omitted is some 25% below experiment.

The close agreement between the Kays circular tube correlation and experiment implies that the equivalent diameter concept is valid for this geometry. It is interesting to note that this result would not have been obtained if comparison had been made with the Dittus-Boelter equation.

8.3.4 Acute isosceles triangular duct

Calculations have been made with the present method for comparison with the air flow measurements of Eckert and Irvine (1960) in an isosceles triangular duct with electrically heated walls and an apex angle of 11.7° . The intended experimental boundary conditions were constant axial and peripheral heat flux (H3), but the measurements showed a significant peripheral variation in both temperature and heat flux. In reply to written discussion of their paper, the authors stated the true boundary condition to be somewhere between H3 and H1. This is confirmed by the present calculations which show, in figures 8.3.12 and 8.3.13, the measured heat flux variation on the long side of the duct to be less than that calculated for the H1 case and the measured temperature variation to be also less than that calculated for the H3 case. Further calculations were therefore made with these measurements as prescribed distributions. Figure 8.3.12 shows the calculated heat flux profile obtained by using the experimental temperature profile in figure 8.3.13. This latter figure also shows the temperature profile calculated using the prescribed measured heat flux variation in figure 8.3.12. This shows that, according to the present calculations, the measured temperature profile does not correspond to the measured heat flux profile. This is most likely due to experimental error, probably in measurement of the heat flux variation, which was not obtained directly but calculated from local temperature measurements.

This latter conclusion is confirmed by the comparison of overall heat transfer given in figure 8.3.14. The measured mean Nusselt numbers are seen to lie, as expected from the above

discussion, between the present predictions for the H1 and H3 boundary conditions. The mean N_u calculated from the present method with the prescribed measured heat flux lies well below these measurements, whereas that calculated with the prescribed measured temperature profile is in reasonable accord with the measurements.

It is noticeable that, unlike the earlier turbulent heat transfer cases (and the rod bundle case of the next section), the predictions in this duct are quite sensitive to the imposed boundary conditions. This is because there are large variations in wall temperature and/or heat flux in this geometry, caused by the rapidly changing velocity and temperature in the narrow corner region. The contrast between this and the other cases of turbulent heat transfer extends also to the effect of secondary flow as discussed in the previous chapter. In the other ducts studied, secondary flow has the effect of making wall shear stress (and thus heat and/or temperature) more uniform and hence the heat transfer more insensitive to boundary conditions. In this acute isosceles triangular duct, however, the effect of secondary flow along the wall is almost negligible (see also the shear stress profile section 7.7 and figure 7.7.4) and, hence, the temperature and heat flux profiles are also relatively unaffected.

The measured (and present prediction using the measured temperature profile) mean Nusselt numbers are only some 50% of the values calculated from the correlation of Kays for gases, showing that the equivalent diameter concept is not valid for this duct. This is due to the acuteness of the corner and is in agreement with the observation made on the flow characteristics in this duct (see section 7.7).

8.3.5 Rod bundles

Results will now be presented for heat transfer with axial flow in triangular and square array rod bundles of different P/D ratio and for a range of Reynolds numbers. Experimental investigations (see table 3.3.1 and section 3.3) have reported negligible variation in local heat transfer coefficient for triangular arrays with $P/D > 1.2$, thus detailed comparisons have been made here with the measurements of Dingee et al (1955) and Redman et al (1966) in rod bundles of $P/D = 1.12$ and 1.1 respectively. The former authors employed a test rig of conducting rods, with electrically heated walls, cooled by water, whereas the latter authors used air as the coolant with insulated rods covered by metal foil strips, that were each independently electrically heated. Calculations have also been made corresponding to the experimental situation investigated by Parrette and Grimble (1956) in a square array rod bundle with $P/D = 1.2$. These authors used a transient technique to determine mean Nusselt numbers (the 'single-blow' technique, see Kays and London, 1958 and Rapley, 1978) and a naphthalene sublimation method to determine local heat transfer coefficients by analogy.

Figure 8.3.15 compares the present calculations of local Nusselt number with the measurements of Dingee et al, whose heating method was assumed to give the constant peripheral and axial heat flux (H_3) boundary conditions. The predictions are seen to be in reasonable agreement with experiment with the scatter of the latter a likely indication of the experimental uncertainty. As expected, the minimum Nusselt numbers are at the gap where the coolant velocities are lowest and which is also, therefore, where the temperature hot-spot will

occur. Secondary flow is seen to reduce the variation of N_{uL} (and thus the hot spot effect) by more than half.

The foil strip heating method of Redman et al enabled them to control the boundary conditions of heat transfer and to measure the local Nusselt number profiles reproduced here in figure 8.3.16 and which are claimed to be for the H1 and H3 boundary conditions. These measurements were obtained from the super-position of influence functions obtained by systematically varying the strips heated and measuring the influence of each one on the others. In the event, as discussed in section 3.3, there is little difference between the two boundary conditions for turbulent flow in this geometry (since the variation in temperature and/or heat flux is small compared with, say, the laminar flow case where the boundary conditions have a significant effect - see Chapter 6).

The profiles calculated from the present method show more variation of N_{uL} than experiment, with the H1 case much nearer the measurements than the H3 case. The flatter experimental profiles could be due to inter-channel cross-flow effects, likely to be present since adjacent subchannels are unlikely to be entirely homogenous in an experimental test rig where small misalignments, non-uniform flow and heating etc. can occur. The considerable effect of secondary flow in flattening the N_{uL} profile, as shown in figure 8.3.16, is an indication of the likely effect if these turbulence driven flows are augmented by interchannel cross-flow. Since, as seen in section 7.7, the secondary velocities are only some 1% of the mean axial velocity, very little augmentation would be required to match the calculated profiles to experiment.

The N_{uL} profile calculated by Deissler and Taylor (1958), who used a graphical method which neglected secondary flows, is seen in figure 8.3.16 to be similar to that calculated from the present method with secondary flow suppressed. This similarity should be expected as the Deissler and Taylor method effectively assumed a turbulent Prandtl number of unity and is another reminder of the necessity of including secondary flows in the calculation of local variations in heat transfer and temperature etc.

Calculations have also been made for a triangular array with $P/D = 1.25$ for comparison with the measurements of Redman et al (1966). Although, as mentioned previously, the measured peripheral variation in heat transfer coefficient is small (less than 3%), it is still of interest to compare the present predictions as shown in figure 8.3.17. The latter are in good agreement with experiment and show that the local Nusselt number may be lower in the gap (and hence the 'hot-spot' higher) than the measurements imply. There is little difference between the calculated profiles for the H1 and H3 boundary conditions, as expected when peripheral variations are small. The effect of secondary flow is significant once again, causing a considerable reduction in the peripheral variation from the hypothetical no-cross-flow case (from 20% to 7%) and moving the point of maximum heat transfer towards the gap.

The present predictions for heat transfer in a square array rod bundle with $P/D = 1.2$ are compared with the measurements of Parrette and Grimble (1956) in figure 8.3.18 where agreement is seen to be poor. However, since the variation in flow cross-section is greater

in this arrangement than in the equivalent P/D ratio triangular array, the effect on coolant velocity, wall shear stress and hence N_{UL} should be correspondingly larger. Thus, more variation in N_{UL} should be expected for this geometry, than in a triangular array with a similar or larger P/D ratio. Although this expectation is confirmed in the predictions it is not apparent in the measurements. This could be due to the turbulence driven secondary flow being augmented by inter-channel cross-flow etc. in the test rig. Obviously, more detailed experiments will be necessary before any firm conclusions can be drawn.

The predicted mean Nusselt numbers from the present method are compared in figure 8.3.19 with the measurements of Dingee et al (1955) at two Prandtl numbers of the water coolant. An indication of the reproducibility of the experimental measurements is given by the re-test results for the P/D = 1.2 case, which are between 20% and 50% higher than the original test results for that P/D ratio. The predictions are in general agreement with the measurements and show a weak dependence on the P/D ratio that is not apparent in the experiments - probably because the variation is within the measurement error band. The scatter of experimental results precludes any deductions on whether an improvement in predictions would be obtained with a decreased value of σ_c . The equivalent diameter concept used with the Kays circular pipe correlation appears to represent the average of the measurements reasonably well in each case.

The work of Redman et al was mainly concerned with establishing local N_u variation and influence functions and, as such, no mean Nusselt number characteristics were presented. From their plots of

local N_u , the mean Nusselt numbers could be expected to be some 25% or more above the Kays correlation for circular pipes. This is in agreement with the experiments of Sutherland and Kays (1966) who measured mean Nusselt numbers in electrically heated triangular array rod bundles with $P/D = 1.15$ and with air as the coolant. The results are shown in figure 8.3.20 to be some 20% - 30% above the Kays correlation, with the present predictions lying between these two characteristics. As in the previous cases with heat transfer to air, the present predictions under-estimate N_u (by 10% - 15% in this case) and are apparently improved by assuming a slightly lower value of σ_c .

The experimental mean Nusselt number characteristic of Parrette and Grimble (1956), for a square array rod bundle with $P/D = 1.2$ and air coolant, is shown in figure 8.3.21. The comparison with the present predictions and with the Kays correlation is similar to that described for the Sutherland and Kays experiments in the previous paragraph.

Table 3.3.1 shows there to be many investigations of overall heat transfer in rod bundles, in addition to those already discussed above. It is of interest to correlate these measurements on some convenient basis for an overall comparison with the present work. Since, as mentioned in the review in section 3.3, most of the measured mean Nusselt numbers have approximately the same dependence on Reynolds number as the Dittus-Boelter equation (3.3.1), a popular method of representing the results is to calculate a constant C for a correlation of the form:

$$N_u = CR_e^{.8}P_r^{.4} \quad (8.3.7)$$

Indeed, from only a few previous measurements, Weisman (1959) produced a simple formula relating N_U to P/D . Figure 8.3.22 shows a plot of the values of C obtained from the present predictions and those obtained or estimated from, the various triangular array rod-bundle experiments in which either water or air were used as the coolant. The present calculations are seen to show a dependence of N_U on both the P/D ratio and the coolant. Although scattered, the measurements show a similar variation with P/D , that of increasing N_U with increasing P/D . This effect does not necessarily imply an increase in heat transfer coefficient, however, since D_e also increases with P/D ratio. Although the majority of the water measurements are higher than the air measurements, the dependence of N_U on the coolant is not as clearly marked as in the predictions and remains inconclusive. The Weisman empirical formula shows a greater variation of N_U with P/D than perhaps suggested by the measurements (for $P/D > 1.1$). However, the scatter in the measurements precludes any final statement except perhaps that the commonly used correlation method in figure 8.3.22 is not very successful, even taking into account probable experimental error. The most likely reason for the scatter (which is least $\pm 25\%$) is the unrealistically simple dependence of N_U on P_r implied in equation (8.3.7). As discussed in section 3.3, this is likely to be more complex, and its correlation will have to await more carefully controlled and systematic experimental investigations than are available at the present.

8.4 Closure

The present method has been used to predict laminar and turbulent heat transfer in a range of passage flows and for various heat transfer boundary conditions. The laminar calculations demonstrated the flexibility and accuracy of the method and confirmed the significant effect of both passage shape and boundary conditions on the mean and local heat transfer.

The initial turbulent heat transfer calculations, made for circular tubes, showed that the algebraic heat flux transport model (AHFTM) would not have any advantage over the constant turbulent Prandtl number for enthalpy (σ_c) model in the symmetric heating problems calculated with the present method. The latter heat flux model was therefore adopted with σ_c set at the recently recommended value for wall heat transfer of 0.9.

Predictions for turbulent heat transfer have been made and compared with measurements in elliptical and triangular ducts and in rod-bundle passages (10 different geometries in all). These calculations showed the significant effect of secondary flow in reducing peripheral variations in local Nusselt number, thus making the mean Nusselt numbers relatively insensitive to the boundary conditions in most cases. The calculated local and mean N_u were seen to be in fair agreement with the measurements, with some underprediction (around 10%) of the latter indicated, mainly in comparison with the air flow heat transfer measurements. Some underprediction can, however, be expected since the flow calculations from the present method tended to underpredict friction factor (by a similar amount). Some improvement in the calculated air

flow heat transfer was implied with the assumption of a lower value of σ_c (e.g. 0.8) although it is believed that this effect may be compensating for the flow field or even for the wall function for enthalpy rather than suggesting a better value of σ_c .

9.1 Introduction

In this the final chapter a summary is made of the achievements and limitations of the present work and then some overall conclusions are drawn from a comparison between the predictions made in the various passages studied. The chapter concludes with recommendations for further research.

9.2 Achievements and limitations of the present work

A computer based, numerical, orthogonal curvilinear finite-difference solution method capable, in principle, of simultaneously solving the governing equations of flow in arbitrary shaped passages has been developed from an existing procedure employing a Cartesian mesh and an eddy-viscosity-based two equation ($k - \epsilon$) turbulence model. The main advantage of the orthogonal curvilinear co-ordinate system was that it enabled the finite-difference mesh to be fitted exactly into the solution domain with the minimum of complexity in the calculations, both in the interior and at the boundaries.

The two-equation turbulence model was combined with an algebraic stress transport model (ASTM) originally developed by Launder and Ying (1973) for square duct calculations and used in the present method for the calculation of all the required Reynolds stresses. The resulting method was applied to the calculation of fully developed flow and heat transfer in a wide range of passage shapes and the results compared in

detail with the available measurements and previous predictions. These validating applications enabled an examination to be made of the performance of the Launder and Ying ASTM and also showed the method to be flexible in accommodating the various passage cross-sectional shapes, and universal in that the same empirical constants were used throughout so that no special information was required for a particular passage other than the geometry and type of boundary planes.

Laminar flow and heat transfer calculations were made in some 12 non-circular passage geometries with various heat transfer boundary conditions, demonstrating the accuracy of the present method to be acceptable since close agreement was obtained with available analytical and numerical solutions.

Turbulent flow calculations were made in some 17 different passage geometries which included the following passages that do not appear to have been studied theoretically this way before: elliptical ducts, rectangular ducts, square duct with one rough wall, isosceles-triangular ducts and two cases of finite rod bundle passage. In the smooth walled passages the local mean and secondary flow characteristics were found to be in reasonable agreement with the measurements when the latter were confirmed to be for fully developed flow, and showed the considerable effect of turbulence-driven secondary flow on the mean flow. This latter observation underlines the importance of including the effects of these secondary motions in the calculation of this class of flows. A weakness in the present method was detected however in the bulk flow since friction factors were generally under-predicted by some 10%. This appears to be a characteristic of the

ASTM used since a similar under-prediction was obtained in the square duct calculations of Launder and Ying (1973).

The calculated turbulence structure was found generally to be in less satisfactory agreement with the measurements, although in some cases the differences were little more than those found between the various measurements for a particular passage shape. The most obvious and consistent shortcoming was the lack of anisotropy displayed in the calculated near-wall cross-plane normal stresses. This was attributed to the values of the empirical constants used in the ASTM since these were selected for prediction of mean and secondary flow, rather than for calculation of near-wall stresses. This conflict between predictions of stresses and flow with the Launder and Ying ASTM has been referred to before by one of its originators (Launder, 1976). It is likely that some form of modification simulating the damping effect of the wall on the normal stresses will be required in the ASTM before the stresses and flow can both be predicted satisfactorily with the same empirical constants. Another fairly consistent shortcoming was the under-prediction of near-wall turbulence kinetic energy levels, which in the present work were near those for local equilibrium. If the higher experimental levels are correct, this deficiency may be a further consequence of the constants used in the ASTM or of inadequate wall functions.

The present method failed to predict the asymmetric flow measured by Ali (1978) in a square duct with one wall rib-roughened. It is believed that this was due, as least in part, to the simplifications made in the ASTM used for turbulent stress calculation (particularly shear stress) and to inadequate representation of the

near-rough-wall region by the wall function used. From evidence in the measured secondary flow however, this region may have been disturbed at the measurement plane by the upstream rib, producing in any case a situation not able to be calculated by the present method which assumes uniform roughness and fully developed flow.

A constant turbulent Prandtl number isotropic eddy diffusivity heat flux model was used to calculate heat transfer in 6 different passage shapes with a range of 15 different geometries and various boundary conditions. The under-prediction of friction factor noted in the flow, was reflected to some extent in the calculated mean Nusselt numbers which were found in most cases to be 10% or more below the measurements. The predicted local Nusselt numbers were however found to be in fair agreement with the limited measurements available and showed, once again, the significant effect of secondary flow on the calculated profiles. These calculations appear to be the first 'fourth generation' type theoretical heat transfer studies to be made in non-circular ducts since the limited square duct calculations of Launder and Ying (1973) with a similar heat flux model.

The present method was also successfully used to calculate some second-order effects in the flow, such as that of the end wall on the flow characteristics in the measurement sub-channel of a rod-bundle test rig. Additionally, calculations made with the present procedure were used to help resolve apparently confused and scattered friction factor measurements in rod-bundles and also to indicate a possible inconsistency between the measured wall temperature and heat flux profiles in a narrow isosceles triangular duct.

The present work has therefore achieved the general objectives of the development of a finite-difference procedure for the calculation of fully developed turbulent flow and heat transfer in straight non-circular passages, that should be compact and flexible enough to be of use to a designer concerned with such problems. The examination made of the Launder and Ying algebraic stress model showed that reasonable mean and secondary flow and heat transfer characteristics can be obtained if incomplete prediction of normal stress levels is accepted, together with a little under-prediction of friction factor and mean Nusselt number.

9.3 Overall comparison of predictions

The present work has enabled, apparently for the first time, the characteristics of fully developed flows in a wide range of passage geometries to be predicted from the same calculation procedure, and compared. In this section the opportunity is taken to make a comparison between these predicted characteristics, focusing in particular on the similarities and differences found in the various passage flows studied.

The laminar heat transfer calculations showed, as expected, the mean Nusselt number to be mainly dependent on the passage geometry and heat transfer boundary conditions. Of the three types of the latter investigated, the largest peripheral variations of local Nusselt number and the lowest mean Nusselt number, for a given passage geometry, were obtained with the constant peripheral and axial heat flux (H3) boundary condition. This was attributed to the

variations in wall temperature present in the H3, but not in the H1 case, and was seen in the predictions for all the cases calculated. It follows that when the peripheral variations in temperature become small, the values of N_u for the two cases become similar (e.g. as in Table 8.2.3 as P/D increases).

The predicted axial velocity and wall shear stress distributions obtained for the 28 cases of turbulent flow in non-circular passages studied were generally found to be flatter than might be expected from the equivalent laminar flow calculations, taking into account the increased shear due to turbulence. The reason for this was clearly revealed by taking advantage of the facility in the present method of being able to make calculations for the hypothetical situation in which the turbulence driven secondary flow is suppressed. This showed for example that, although only $\frac{1}{2}\%$ to $1\frac{1}{2}\%$ of the mean flow, these secondary velocities were responsible for making the variation of wall shear almost negligible along much of the passage wall in many of the cases studied. A characteristic secondary flow circulation pattern emerged that was applicable to all the non-circular passages calculated. This was a circulation from the core into the corners or regions of lower axial velocity caused by converging passage walls, thence returning to the core via the walls and planes normal to the walls. The effect of these flows on axial velocity was evident in the contour and profile plots which showed, in the former, the constant velocity contours to bulge into duct corners or, more generally, into regions of lower axial velocity bounded by converging passage walls. These effects were even more marked with turbulence kinetic energy contours.

The calculated turbulence kinetic energy levels in most of the passage flows were in reasonable agreement with experiment in the passage core, but were well under-predicted near the walls. This under-prediction revealed an apparent conflict between the measured near-wall levels of turbulence kinetic energy (k) and the expected levels for local equilibrium. This latter condition is expected to dominate the near-wall region, according to the various measured turbulence kinetic energy balances that have been made, all of which show the only significant transport mechanisms to be production and dissipation in this region. However, many of the measured near-wall levels of k are significantly higher than this and are thus, also higher than the present predictions. The implication of this is that if the k and ϵ equations are modelled satisfactorily then either there are near-wall effects not properly corrected for in some of the measurements of k , or the generation and dissipation of k near the wall are not as dominating as the previous measurements and present predictions imply.

The turbulence length scale profiles calculated from the Buleev formula showed a remarkable similarity to those obtained from the present method in all the cases studied. This uniform agreement suggests that, for fully developed turbulent passage flows, transport effects on length scale may not be significant and further, that the Buleev formula may represent a limiting or simplified form of the transport equations involved in its calculation. Such a form (the Buleev or similar type of formula) could effect a useful saving in the replacement of a partial differential equation by an algebraic one in the calculation of this class of flows (thus giving the one-equation model used by Launder and Ying (1973) in their square duct calculations).

The failure of the present method to reproduce the near-wall anisotropy of the cross-plane normal stresses could, in fact, result in poor prediction of the secondary flows according to the views of Brundrett and Baines (1964) on the origin of these flows. There is, however, no such conflict with the view of Gessner (1973), who linked the origin and maintenance of secondary flow with the gradients of turbulent shear, rather than with the anisotropy of the cross-plane normal stresses. This link between turbulent shear stress gradients and secondary flow is also evident in the present method, since the controlling source terms in the cross-plane momentum equations contain normal stress gradients which are linked in the ASTM to the shear stress gradients (equations (4.2.10) and (4.2.11)) through axial velocity gradients (see however, comments in section 3.2, page 30)

The Launder and Ying based ASTM used in the present calculations thus appear to simulate the mechanism for the origin and maintenance of secondary flow in straight, non-circular passages. Indeed, from Launder and Ying and the present work, it is possible to make the following simple deductions about the secondary flow patterns that are likely to appear in a particular smooth passage, and the resulting effect of these flows on the mean flow characteristics:

A pair of converging walls will produce gradients of normal stress anisotropy, concentrated near the focus of the wall convergence. The work done by the mean flow on these stress gradients will give rise to a balancing convection of mean flow energy, namely the secondary flow, from the core in a direction along the bisecting plane into the wall

convergence. This secondary flow will have maximum velocities of between $\frac{1}{2}\%$ and 2% of the mean axial velocity and will recirculate to the core, via the walls, such that symmetry and continuity are satisfied. The secondary motions so generated, will distort the mean flow since axial velocity gradients, turbulence kinetic energy and wall shear stress will tend to increase in regions where secondary flow is directed towards the wall, and decrease in regions where it is directed away from the wall. This effect will be seen in axial velocity and turbulence kinetic energy contours which will bulge into a wall convergence, and in wall shear stresses which will be made more evenly distributed.

It is of interest to compare the friction factors in the various passages, calculated from the present method, notwithstanding the slight (but consistent) under-prediction when compared with experiment. With one exception the equivalent diameter concept correlates the non-circular passage values to the circular pipe prediction within 5%. The exception is in the narrow isosceles triangular duct where the values were 15% or more below this for an apex angle of 11.7%. This trend is in fact similar to that noted within the scatter of the measurements (in Section 3.2) and thus lends support to the suggestion that the equivalent diameter concept can be used to correlate friction factors in fully developed turbulent flow in non-circular ducts, provided there are no acute angled internal corners in the cross-section. In the latter case the values of f would be expected to be less than in the equivalent circular pipe case.

The calculated mean Nusselt numbers for air flow were found to be consistently 10% or more lower than the measurements, a situation

apparently improved with a slightly lower value of σ_c in the heat flux model. Although this and lower values of σ_c may be more in agreement with that implied by the constants used in the ASTM (equation (8.3.5)), it is more likely to be compensating for limitations in the calculations due to, for example, (i) the flow field in which the friction factor is also underpredicted, (ii) the wall function for enthalpy which was formulated from experimental data over a wide range of P_r mainly well above that for air and (iii) the simple isotropic eddy diffusivity heat flux model. On this latter point, if an improvement can be made in the prediction of cross-plane normal stresses, the use of the algebraic heat flux transport model (see Sections 4.4. and 8.3.1) may effect an improvement in heat transfer prediction, as evidenced by the recent calculations made by Chieng and Launder (1979) with this anisotropic eddy viscosity model in asymmetrically heated circular pipe flow.

Finally, it is of interest to check on how the equivalent diameter concept correlates the calculated N_u-R_e characteristics for the various passages. Comparing only the air flow calculations (to eliminate the uncertain effect of P_r), the elliptical duct and rod-bundle passage characteristics are within 10% of the circular pipe, but the triangular duct characteristics are lower and increasingly so with smaller apex angle (- 15% with $\theta = 60^\circ$ to - 50% with $\theta = 11.7^\circ$). Although far from conclusive with this limited evidence, the heat transfer calculations are consistent with the conclusions concerning equivalent diameter drawn from the predicted friction factors.

9.4 Recommendations for further work

In addition to the further studies that can usefully be made with the present method, many improvements are required in the turbulent stress modelling and computational procedures currently employed. In conjunction with these developments further experiments will be required. The suggested further work in each of these areas is summarised below:

(i) Further predictions

An extension can be made to enable multi-region analysis of finite rod bundles, following the lead of Benodeker and Date (1978) and using the data of, for example, Rowe (1973) to study the effects of interchannel flow and turbulent mixing. Some further studies can also usefully be made by developing the grid generation procedure for application to passages of more severe curvature such as the triangular or square array rod bundles with rods touching ($P/D = 1.0$). Comparisons can be made with the measurements of Levchenko et al (1968) and Gerrard and Baines (1977).

The square duct work of Tatchell (1975) and Reece (1977) can be followed-up by extending the present method to the calculation of developing flows in various non-circular passages.

A detailed study of turbulent length scale prediction and comparison with that from the Buleev and other formulae can be made, to discover any possible links and whether an algebraic formula for length scale can reasonably be deduced from, and used in place of, the partial differential equation for ϵ for non-circular passage flow calculations.

The present method can also be usefully adapted for the calculation of flow and heat transfer with temperature dependent fluid properties and non-Newtonian fluids in non-circular passages. Such problems are of considerable interest in the process industry. The development of wall functions for enthalpy suitable for very low Prandtl number fluids will also enable the present procedure to be used for the calculation of liquid metal flow and heat transfer in non-circular passages - particularly rod bundles for Nuclear power applications (Tables 3.2.1 and 3.3.1 show some sources of available experimental data).

(ii) Turbulent stress and heat flux model improvements

Normal stress prediction with the ASTM needs to be improved by the development of a wall damping modification that, if possible, still allows algebraic formulation of the stress transport equations. It may be that the empirical constants in the model became coefficients that vary across the flow. The note by Rodi (1975) and the work of Launder, Reece and Rodi (1975) could provide a useful starting point. An improvement in the normal stress prediction would also enable the AHFTM to be used in place of the isotropic eddy viscosity for a probable improvement in heat transfer calculations. An investigation could also usefully be made into the reasons for the apparent under-prediction in near-wall levels of turbulence kinetic energy with the present method.

As an alternative to the above (or in any case) an orthogonal curvilinear co-ordinate multi-equation stress and heat flux model approach can be made by extending the work of Reece (1977) and

Samaraweera (1978) to the calculation of flow and heat transfer in various non-circular passages. This would also require the development of the wall damping functions into a form suitable for arbitrary multiple walls.

(iii) Computational improvements

The flexibility of the finite-difference mesh can be improved by relaxing the orthogonality constraint although the increased complexities of a non-orthogonal mesh may ultimately be counter productive.

The stability and convergence of the numerical method can be improved by development of a more efficient solution algorithm for the finite-difference equations. Some form of simultaneous solution method should be aimed at, in place of the sequential method in the present procedure.

(iv) Experimental investigations

Detailed flow and heat transfer measurements are always required for the development and validation of turbulent stress and heat flux models. These measurements should include axial and secondary velocity, wall shear stress, turbulence intensity and turbulent shear stress. Such measurements for fully developed flow in elliptical ducts and some unsymmetrical ducts such as a $60^{\circ}/30^{\circ}$ right-angled triangular duct would be particularly useful. Developing flow measurements are also required in a good range of non-circular ducts. Secondary velocity measurements in rod bundle geometries are also needed to resolve the present uncertainty over secondary flow circulations.

Heat transfer measurements, both local and overall are required for a range of passage cross-sections, flows and fluids. Some detailed measurements in a few passages will be vital to the development of heat flux models. These measurements should include wall and fluid temperatures, wall heat flux and if possible fluid temperature fluctuations, as well as overall Nusselt numbers.

REFERENCES

- Acrivlellis, M. (1977) Hot Wire Measurements in Flows of Low and High Turbulence Intensity. Disa Info. No. 22: 1.
- Ali, T. (1978) Unpublished Measurements in a Square Duct with One Rough Wall. Imperial College, Uni. of London.
- Aly, A. M. M., Trupp, A. C. and Gerrard, A. D. (1978) Measurement and Prediction of Fully Developed Flow in an Equilateral Triangular Duct. J. Fluid Mech., 85: 57.
- Amsden, A. A. and Harlow, F. H. (1970) The SMAC Method: A Numerical Technique for Calculating Incompressible Fluid Flows. Report LA4370 Los Alamos Sc. Lab.
- Antonopoulos, K., Gosman, A. D. and Issa, R. (1978) A Simple Method for Generating Curvilinear Orthogonal Grids. Imperial College, Mech. Eng. Fluids Section Report.
- Axford, R. A. (1967) Two Dimensional, Multi-region Analysis of Temperature Fields in Reactor Tube Bundles, Nuc. Eng. & Design, 6: 25.
- Bandopadhyay, P. C. and Hinwood, J. B. (1973) On the Co-existence of Laminar and Turbulent Flow in a Narrow Triangular Duct. J. Fluid Mech., 59: 775.
- Barfield, W. D. (1970) Numerical Method for Generating Orthogonal Curvilinear Meshes. J. Comp. Phys., 5: 23.
- Barrow, H. and Roberts, A. (1970) Flow and Heat Transfer in Elliptical Ducts. Paper No. FC4.1, 4th Int. Heat Transfer Conf., Paris.
- Bayley, F. J. and Rapley, C. W. (1965) Heat Transfer and Pressure Loss Characteristics of Matrices for Regenerative Heat Exchangers. Trans. ASME 65-HT-35.
- Bender, D. J. and Magee, P. M. (1969) Turbulent Heat Transfer in a Rod Bundle with Liquid Metal Coolant. Report GEAP 10052.
- Bender, D. J., Switick, D. M. and Field, J. H. (1967) Turbulent Velocity Distribution in a Rod-Bundle. Report GEAP 5411.
- Benodeker, R. W. and Date, A. W. (1978) Prediction of Fluid Flow and Heat Transfer in Nuclear Rod Clusters. Indian Inst. of Tech. Report.
- Bobkov, V. P., Ibragimov, M. C. and Sabelev, G. I. (1968) Generalisation of Experimental Data on the Intensity of Velocity Pulsations in Turbulent Flow of Liquid in Channels of Various Cross-sections. Izv. Akad., Mechanics of Liquids and Gases No. 3: 162.

Bobkov, V. P., Ibragimov, M. C. and Subbotin, V. I. (1970) A Method of Calculation of Turbulent Heat Transfer Coefficients in Channels of a Complex Form. Reactor Heat Trans. Conf., Babylon.

Bobkov, V. P., Ibragimov, K. Kh., Sinyavskii, V. F. and Tychinskii, N. A. (1974) Heat Exchange for Flow of Water in a Densely Packed Triangular Bundle of Rods. Soviet J. Atomic Energy, 37: 823.

Borishanskiy, V. M., Gotovskiy, M. A. and Firsova, E. V. (1971) The Effect of Pitch on Heat Transfer from Rod Clusters in Longitudinal Coolant Flow ($Pr \geq 1$). Heat Trans. Soviet Res., 3: 91.

Bradshaw, P. (Editor) (1978) Turbulence. Topics in Applied Physics 12, Springer-Verlag.

Brighton, J. A. and Jones, J. B. (1964) Fully Developed Turbulent Flow in Annuli. Trans ASME 64-FE-2.

Brundrett, E. and Baines, W. D. (1964) The Production and Diffusion of Vorticity in Duct Flow. J. Fluid Mech., 19: 375.

Brundrett, E. and Burroughs, P. R. (1967) The Temperature Inner-law and Heat Transfer for Turbulent Air Flow in a Vertical Square Duct. Int. J. Heat Mass Trans., 10: 113.

Buleev, N. I. (1963) Theoretical Model of the Mechanism of Turbulent Exchange in Fluid Flows. AERE Trans. 957.

Buleev, N. I. (1964) Theoretical Model for Turbulent Heat Transfer in Three-dimensional Flow. Paper No. A/CONF/28/P/329, 3rd U.N. Conf. Peaceful Uses of Atomic Energy, Geneva.

Cain, D. and Duffy, J. (1971) An Experimental Investigation of Turbulent Flow in Elliptical Ducts. Int. J. Mech. Science 13: 451.

Cain, D., Roberts, A. and Barrow, H. (1972) A Theoretical Study of Fully Developed Flow and Heat Transfer in Elliptical Ducts. Paper No. C120/72, Proc. I. Mech. E. Conf. on Compact High Duty Heat Exchangers.

Cain, D., Roberts, A. and Barrow, H. (1973) An Experimental Investigation of Turbulent Flow and Heat Transfer in Elliptical Ducts. Wärme-und-Stoffübertragung, 2: 101.

Carajilescov, P. (1975) Experimental and Analytical Study of Axial Turbulent Flows in an Interior Sub-channel of a Bare-rod Bundle. Ph.D. Thesis, M.I.T.

Carajilescov, P. and Todreas, N. E. (1976) Experimental and Analytical Study of Axial Turbulent Flows in an Interior Sub-channel of a Bare-rod bundle. J. Heat Trans., Trans. ASME, 98: 262.

Caretto, L. S., Gosman, A. D., Patankar, S. V. and Spalding, D. B. (1972) Two Calculation Procedures for Steady Three-dimensional Flows with Recirculation. Proc. 3rd Int. Conf. on Numerical Methods in Fluid Mech., Paris, :60.

Carlson, L. W. and Irvine, T. F. (1961) Fully Developed Pressure-drop in Triangular Shaped Ducts. J. Heat Trans. Trans. ASME 60-WA-100: 441.

Cebeci, T., Smith, A. M. O. and Mosinskis, G. (1970) Solution of the Incompressible Turbulent Boundary Layer Equation with Heat Transfer. J. Heat Trans., Trans. ASME, 92: 133.

Champagne, F. H., Harris, V. G. and Corrsin, S. (1970) Experiments in Nearly Homogeneous Turbulent Shear Flow. J. Fluid Mech., 41: 81.

Cheng, K. C. (1969) Laminar Forced Convection in Regular Polygonal Ducts with Uniform Peripheral Heat Flux. J. Heat Trans., Trans. ASME 91: 156.

Chieng, C. C. and Launder, B. E. (1979) On the Calculation of Turbulent Transport in Flow Through an Asymmetrically Heated Pipe. Num. Heat Trans., 2: 359.

Chiranjivi, C. and Sankara Rao, P. S. (1971) Laminar and Turbulent Forced Convection Heat Transfer in a Symmetric Trapezoidal Channel. Indian J. Tech., 9: 416.

Claiborne, H. C. (1952) A Critical Review of the Literature on Pressure-drop in Non-circular Ducts and Annuli. Report ORNL 1248, Oakridge Nat. Lab.

Cook, K. W. (1969) Velocity Distributions in Sodium Cooled Fast Reactor Fuel Channels. Trans. ASME 69WA-NE-9.

Cope, R. C. and Hanks, R. W. (1972) Transitional Flow in Isosceles Triangles. Ind. Eng. Chem. Fund., 11: 106.

Cremers, C. J. and Eckert, E. R. G. (1962) Hot Wire Measurements of Turbulence Correlations in a Triangular Duct. J. App. Mech., Trans. ASME 29: 609.

Daly, B. J. and Harlow, F. H. (1970) Transport Equations in Turbulence. Phys. Fluids, 13: 2634.

Deissler, R. G. and Taylor, M. F. (1956) Analysis of Axial Turbulent Flow and Heat Transfer Through Banks of Rods or Tubes. Paper No. TID 7529, Reactor Heat Trans. Conf., New York.

Deissler, R. G. and Taylor, M. F. (1958) Analysis of Turbulent Flow and Heat Transfer in Non-circular Ducts. NACA Tech. Note 4384.

Dingee, D. A., Bell, W. B., Chastain, J. W. and Fawcett, S. L. (1955) Heat Transfer from Parallel Rods in Axial Flow. Report BMI 1026, Battelle Mem. Inst.

Dingee, D. A. and Chastain, J. W. (1956) Heat Transfer from Parallel Rods in Axial Flow. Paper No. TID 7529. Reactor Heat Trans. Conf., New York.

- Dittus, F. W. and Boelter, L. M. K. (1930) University of California Publications in Engineering, 2: 443.
- Draycott, A. and Lawther, K. R. (1961) Improvement of Fuel Element Heat Transfer by Use of Roughened Surfaces and Application to a 7 Rod Cluster. Paper No. 64, Int. Heat Transfer Conf., Colorado.
- Duffy, J. and Cain, D. (1972) On the Use of the Preston Tube in Elliptical Ducts. Aero. J., 76: 371.
- Dunwoody, N. T. (1962) Thermal Results for Forced Heat Convection Through Elliptical Ducts. J. App. Mech., Trans. ASME 29: 165.
- Dwyer, O. E. (1963) Eddy Transport in Liquid-Metal Heat Transfer. A.I.Ch.E.J., 9: 261.
- Dwyer, O. E. (1966) Analytical Study of Heat Transfer to Liquid Metals Flowing In-line Through Closely Packed Rod-bundles. Nuc. Sc. & Eng., 25: 343.
- Dwyer, O. E. and Berry, H. C. (1970) Laminar Flow Heat Transfer for In-line Flow Through Unbaffled Rod Bundles. Nuc. Sc. & Eng., 42: 81.
- Dwyer, O. E. and Berry, H. C. (1971) Turbulent Flow Heat Transfer for In-line Flow Through Unbaffled Rod Bundles: Molecular Conduction Only. Nuc. Sc. & Eng., 46: 284.
- Dwyer, O. E. and Berry, H. C. (1972) Heat Transfer to Liquid Metals Flowing Turbulently and Longitudinally Through Closely-spaced Rod-bundles, Part 1. Nuc. Eng. & Des., 23: 273.
- Dwyer, O. E. and Tu, P. S. (1959) Analytical Study of Heat Transfer Rates for Parallel Flow of Liquid Metals Through Rod-bundles, Part 1. Paper No. 119, A.I.Ch.E., 3rd Heat Trans. Conf.
- Eckert, E. R. G. and Irvine, T. F. (1956) Flow in Corners of Passages with Non-circular Cross-sections. Trans. ASME, 78: 709.
- Eckert, E. R. G. and Irvine, T. F. (1957) Incompressible Friction Factor, Transition and Hydrodynamic Entrance-length Studies of Ducts with Triangular and Rectangular Cross-sections. 5th Mid-West Conf. in Fluid Mech.: 122.
- Eckert, E. R. G. and Irvine, T. F. (1960) Pressure-drop and Heat Transfer in a Duct with Triangular Cross-section. J. Heat Trans., Trans. ASME, 59-HT-10.
- Eckert, E. R. G., Irvine, T. F. and Eichhorn, R. (1954) Laminar Transitional and Turbulent Flow in Triangular Passages. Report 54-443, W.A.D.C.
- Eichelbrenner, E. A. and Preston, J. H. (1971) On the Role of Secondary Flow in Turbulent Boundary Layers in Corners. J. Mechanique, 10: 91.

- Eifler, W. and Nijssing, R. (1965) Fundamental Studies of Fluid Flow and Heat Transfer in Fuel Element Geometries. Report EUR 2193.e, Euratom.
- Eifler, W. and Nijssing, R. (1967) Experimental Investigation of Velocity Distribution and Flow Resistance in a Triangular Array of Parallel Rods. Nuc. Eng. & Des., 5: 22.
- Forsythe, G. E. and Wasow, R. W. (1960) Finite-difference Methods for Partial Differential Equations. J. Wiley.
- Friedland, A. J. and Bonilla, C. F. (1961) Analytical Study of Heat Transfer Rates for Parallel Flow of Liquid Metals Through Tube-bundles II. A.I.Ch.E.J., 7: 107.
- Friedland, A. J., Dwyer, O. E., Maresca, M. W. and Bonilla, C. F. (1961) Heat Transfer to Mercury in Parallel Flow Through Bundles of Circular Rods. Paper No. 62, Int. Heat Transfer Conf., Colorado.
- Gerard, R. (1974) Finite Element Solution for Flow in Non-circular Conduits. Proc. ASCE 100 (3): 425.
- Gerard, R. and Baines, W. D. (1977) Turbulent Flow in Very Non-circular Conduit. Proc. ASCE (HY8), 103: 829.
- Gessner, F. B. (1973) The Origin of Secondary Flow in Turbulent Flow Along a Corner. J. Fluid Mech., 58: 1.
- Gessner, F. B. and Emery, A. F. (1976) A Reynolds Stress Model for Turbulent Corner Flows Part I, J. Fluid Eng. Trans. ASME 76-FE-C.
- Gessner, F. B. and Jones, J. B. (1961) A Preliminary Study of Turbulence Characteristics of Flow Along a Corner. J. Basic Eng., Trans. ASME 83: 657.
- Gessner, F. B. and Jones, J. B. (1975) On Some Aspects of Fully Developed Turbulent Flow in Rectangular Channels. J. Fluid Mech., 23: 689.
- Gessner, F. B. and Po, J. K. (1976) A Reynolds Stress Model for Turbulent Corner Flows Part II. J. Fluid Eng. Trans. ASME 76-FE-D.
- Gosman, A. D., Pun, W. M., Runchal, W. K., Spalding, D. B. and Wolfshtein, M. (1969) Heat and Mass Transfer in Recirculating Flows. Academic Press.
- Gosman, A. D., Launder, B. E., Newton, P. A. and Reece, G. J. (1977) A User's Guide to the TEACH-C Computer Program. Imperial College Mech. Eng. Report CAL.
- Gosman, A. D. and Rapley, C. W. (1978) A Prediction Method for Fully Developed Flow Through Non-circular Passages. Paper No. IC/FS/78, Int. Conf. Numerical Methods Lam. Turb. Flow, Swansea.

Gosman, A. D. and Rapley, C. W. (1980) Fully-developed Flow in Passages of Arbitrary Cross-section. Recent Advances in Numerical Methods in Fluid Flow (Chapter 11), Pineridge Press, Swansea: 335

Hall, C. and Svenningsson, P. J. (1971) Secondary Flow Velocities in a Rod Bundle of Triangular Array. Report AE-RL-1326, AB Atomenergi, Sweden.

Hanjalic, K. and Launder, B. E. (1972) A Reynolds Stress Model of Turbulence and its Application to Asymmetric Boundary Layers. J. Fluid Mech. 52: 609.

Harlow, F. H. and Welch, J. E. (1965) Numerical Calculation of Time Dependent Viscous Incompressible Flow of Fluids with Free Surface. Phys. of Fluids, 8: 2182.

Hartnett, J. P., Koh, J. C. Y. and McComas, S. T. (1962) A Comparison of Predicted and Measured Friction Factors for Turbulent Flow Through Rectangular Ducts. Trans. ASME 84: 82.

Hinze, O. (1967) Secondary Currents in Wall Turbulence. Phys. of Fluids (Supp.), 10: 122.

Hinze, O. (1975) Turbulence. McGraw-Hill.

Hoagland, L. C. (1960) Fully Developed Turbulent Flow in Straight Rectangular Ducts - Secondary Flow its Cause and Effect on the Primary Flow. Ph.D. Thesis, M.I.T.

Hoffman, H. W., Wantland, J. L. and Stelzman, W. J. (1961) Heat Transfer with Axial Flow in Rod Clusters. Paper No. 65, Int. Heat Trans. Conf., Colorado.

Ibragimov, M. H., Isupov, I. A., Kobzar, L. L. and Subbotin, V. I. (1966) Calculation of the Tangential Stresses at the Wall of a Channel and the Velocity Distribution in the Turbulent Flow of a Fluid. Soviet Atomic Energy, 21: 731.

Ibragimov, M. H., Isupov, I. A., Kobzar, L. L. and Subbotin, V. I. (1967) Calculation of Hydraulic Resistivity Coefficients for Turbulent Fluid Flow in Channels of Non-circular Cross-section. Soviet Atomic Energy, 23: 1042.

Ibragimov, M. H., Petrishchev, V. S., and Sabelev, G. I. (1971) Calculation of Heat Transfer in Turbulent Flow with Allowance for Secondary Flow. Int. J. Heat Mass Trans., 14: 1033.

Iqbal, M., Khattry, A. K. and Aggarawala, B. D. (1972). On the Second Fundamental Problem of Combined Free and Forced Convection Through Vertical Non-circular Ducts. Appl. Sci. Res., 26: 183.

Irwin, H. P. A. H. (1973) Measurements in a Self Preserving Plane Wall Jet in a Positive Pressure Gradient. J. Fluid Mech., 61: 33.

- James, D. D., Martin, B. W. and Martin, D. G. (1966) Forced Convection Heat Transfer in Asymmetrically Heated Ducts of Rectangular Cross-section. Chem. Eng. Prog., 62: 73.
- Jayatilleke, C. L. V. (1969) The Influence of Prandtl Number and Surface Roughness on the Resistance of the Laminar Sub-layer to Momentum and Heat Transfer. Prog. in Heat Mass Trans. (Pergamon): 193.
- Johnk, R. E. and Hanratty, T. J. (1962) Temperature Profiles for Turbulent Flow of Air in a Pipe I. Chem. Eng. Sc., 17: 867.
- Jones, W. P. and Launder, B. E. (1969) On the Prediction of Laminar Boundary Layers. Trans. ASME 69-HT-13.
- Kacker, S. C. (1973) Some Aspects of Fully Developed Turbulent Flow in Non-circular Ducts. J. Fluid Mech., 57: 583.
- Kader, B. A. and Yaglom, A. M. (1972) Heat and Mass Transfer Laws for Fully Developed Turbulent Wall Flows. Int. J. Heat Mass Trans., 15: 2329.
- Kays, W. M. (1966) Convective Heat and Mass Transfer. McGraw-Hill.
- Kays, W. M. and London, A. L. (1958) Compact Heat Exchangers. McGraw-Hill.
- Kidd, G. J. and Stelzman, W. J. (1968) The Temperature Structure and Heat Transfer Characteristics of an Electrically Heated Model of a 7 Rod Cluster. Trans. ASME 68-WA-HT33.
- Kjellstrom, B. (1971) Studies of Flow Parallel to a Rod Bundle of Triangular Array. Report AE/RV/196, AB Atomenergi, Sweden.
- Kline, S. J., Reynolds, W. C., Schraub, F. A. and Runstadler, P. W. (1967) The Structure of Turbulent Boundary Layers. J. Fluid Mech., 30: 741.
- Knudsen, J. G. and Katz, D. L. (1958) Fluid Dynamics and Heat Transfer. McGraw-Hill.
- Kokorev, L. S., Korsun, A. S., Kostyunin, B. N. and Petrovichev, V. I. (1971a) Hydraulic Drag and Heat Transfer in Turbulent Flow of Liquids in Triangular Channels. Heat Trans. Soviet Res., 3: 56.
- Kokorev, L. S., Korsun, A. S., Kostyunin, B. N., Petrovichev, V. I. and Struenze, R. L. (1971b) Effects of Secondary Flows on the Velocity Distribution and Hydraulic Drag in Turbulent Liquid Flow in Non-circular Channels. Heat Trans. Soviet Res. 3: 66.
- Kolmogorov, A. N. (1942) Equations of Turbulent Motion of an Incompressible Fluid. Izv. Akad, 6: 56.
- Laufer, J. (1954) The Structure of Turbulence in Fully Developed Pipe Flow. NACA 1174.

Launder, B. E. (1976) Written Discussion of Paper, J. Fluid Eng. Trans. ASME 76-FE-D (Gessner and Po).

Launder, B. E. and Priddin, C. H. (1973) A Comparison of Some Proposals for Mixing Length Near a Wall. Int. J. Heat Mass Trans., 16: 700.

Launder, B. E., Reece, G. J. and Rodi, W. (1975) Progress in the Development of a Reynolds Stress Turbulence Closure. J. Fluid Mech. 68: 537.

Launder, B. E. and Spalding, D. B. (1972) Mathematical Models of Turbulence. Academic Press.

Launder, B. E. and Spalding, D. B. (1974) The Numerical Computation of Turbulent Flows. Comp. Meth. App. Mech. and Eng., 3: 269.

Launder, B. E. and Ying, W. M. (1972) Secondary Flows in Ducts of Square Cross-section. J. Fluid Mech., 54: 289.

Launder, B. E. and Ying, W. M. (1973) Prediction of Flow and Heat Transfer in Ducts of Square-Section. Proc. I.Mech.E., 187: 455.

Lawn, C. J. (1971) The Determination of the Rate of Dissipation in Turbulent Pipe Flow. J. Fluid Mech., 48: 477.

LeI'Chuk, V. L., Shuyskaya, K. F., Sorokin, A. G. and Bragina, O. N. (1977) Heat Transfer in the Inlet Length of Fuel Elements Modelling Rod Bundles in Longitudinal Air Flow. Heat Trans. Soviet Res., 9: 100.

Le Tourneau, B. W., Grimble, R. E. and Zerbe, E. (1955) Pressure-drop Through Parallel Rod Assemblies Having a 1.12 Equilateral Triangular Pitch. Report WAPD-TH-118, Westinghouse Elec. Corp.

Leutheusser, H. J. (1963) Turbulent Flow in Rectangular Ducts. Proc. ASCE 89: 1.

Levchenko, Y. D., Subbotin, V. I. and Ushakov, P. A. (1968) The Distribution of Coolant Velocity and Wall Stress in Closely Packed Rods. Soviet Atomic Energy, 22: 262.

Ligget, J. A., Chin, C.-L. and Miao, L. S. (1965) Secondary Currents in Corners. Proc. ASCE (HY6), 91: 99.

Lowdermilk, W. H., Weiland, W. F. and Livingood, J. N. B. (1954) Measurements of Heat Transfer and Friction Coefficients for Flow of Air in Non-circular Ducts at High Surface Temperatures. NACA Res. Mem. E53J07.

Malak, J., Hejna, J. and Schmidt, J. (1975) Pressure Losses and Heat Transfer in Non-circular Channels with Hydraulically Smooth Walls. Int. J. Heat Mass Trans., 18: 139.

Mantle, R. L. (1966) A New Type of Roughened Heat Transfer Surface Selected by Flow Visualisation Techniques. Proc. 3rd Int. Heat Trans. Conf., Chicago, 1: 45.

- Marco, S. M. and Han, L. S. (1955) A Note on Limiting Laminar Nusselt Number in Ducts with Constant Temperature Gradient by Analogy to Thin Plate Theory. *Trans. ASME*, 77: 625.
- Marek, J., Maubach, K. and Rehme, K. (1973) Heat Transfer and Pressure Drop Performance of Rod Bundles Arranged in Square Arrays. *Int. J. Heat Mass Trans.*, 16: 2215.
- Maresca, M. W. and Dwyer, O. E. (1964) Heat Transfer to Mercury Flowing In-line Through a Bundle of Circular Rods. *J. Heat Trans. Trans. ASME*, 86: 180.
- Markończy, G. (1972) Convective Heat Transfer in Rod Clusters with Turbulent Axial Coolant Flow. *Wärme-und-Stoffübertragung*, 5: 204.
- Melling, A. and Whitelaw, J. H. (1976) Turbulent Flow in Rectangular Ducts. *J. Fluid Mech.*, 78: 289.
- Meyder, R. (1975) Turbulent Velocity and Temperature Distribution in the Central Sub-channel of Rod Bundles. *Nuclear Eng. & Design*, 35: 181.
- Miller, P., Byrnes, J. J. and Benforado, D. M. (1956) Heat Transfer to Water Flowing Parallel to a Rod Bundle. *A.I.Ch.E.J.*, 2: 226.
- Nakamura, H., Hiraoka, S. and Yamada, I. (1972) Laminar Forced Convection Flow and Heat Transfer in Arbitrary Triangular Ducts. *Heat Trans. Jap. Res.*, 1: 120.
- Naot, D., Shavit, A. and Wolfshtein, M. (1974) Numerical Calculation of Reynolds Stresses in a Square Duct with Secondary Flow. *Wärme-und-Stoffübertragung*, 7: 151.
- Nijsing, R. (1972) Heat Exchange and Heat Exchangers with Liquid Metals. Report AGARD-LS-57-72.
- Nijsing, R. and Eifler, W. (1972) Axially Varying Heat Flux Effects in Tubes, Flat Ducts and Widely Spaced Rod Bundles Cooled by a Turbulently Flowing Liquid Metal. *Nuc. Eng. & Design*, 23: 331.
- Nijsing, R., Gargantini, I. and Eifler, W. (1966) Analysis of Fluid Flow and Heat Transfer in a Triangular Array of Parallel Heat Generating Rods. *Nuc. Eng. & Design*, 4: 375.
- Nikuradse, J. (1926) Investigations on the Distribution of Velocity in Turbulent Flow. *VDI-Forschungsheft*: 281.
- Nikuradse, J. (1930) Turbulent Flow in Non-circular Shaped Pipes. *Ing.-Arch.*, 1: 306.
- Novotny, J. L., McComas, S. T., Sparrow, E. M. and Eckert, E. R. G. (1964) Heat Transfer for Turbulent Flow in Rectangular Ducts with Two Heated and Two Unheated Walls. *A.I.Ch.E.J.*, 10: 466.

- Palmer, L. D. and Swanson, L. L. (1961) Measurements of Heat Transfer Coefficients, Friction Factor and Velocity Profiles for Air Flowing Parallel to Closely Spaced Rod Bundles. Paper No. 63, Int. Heat Trans. Conf., Colorado.
- Pankin, W., Jahn, M. and Reineke, H. H. (1974) Forced Convection Heat Transfer in the Transition from Laminar to Turbulent Flow in Closely Spaced Circular Tube Bundles. Paper No. FC8.7, 5th Int. Heat Transfer Conf., Tokyo.
- Parrette, J. R. and Grimble, R. E. (1956) Average and Local Heat Transfer Coefficients for Parallel Flow Through a Rod Bundle. Report WAPD-TH180, Westinghouse Elec. Corp.
- Patankar, S. V. and Spalding, D. B. (1970) Heat and Mass Transfer in Boundary Layers, Intertext.
- Patankar, S. V. and Spalding, D. B. (1972) A Calculation Procedure for Heat, Mass and Momentum Transfer in 3-D Parabolic Flows. Int. J. Heat Mass Trans., 15: 1787.
- Patankar, S. V., Pratap, V. S. and Spalding, D. B. (1975) Prediction of Turbulent Flow in Curved Pipes. J. Fluid Mech., 67: 583.
- Patel, V. C. (1965) Calibration of the Preston Tube and Limitations on its Use in Pressure Gradients. J. Fluid Mech., 23: 185.
- Perkins, H. J. (1970) The Formation of Streamwise Vorticity in Turbulent Flow. J. Fluid Mech., 44: 721.
- Pfann, J. (1973) Heat Transfer in Turbulent Longitudinal Flow Through Unbaffled Assemblies of Fuel Rods. Nuc. Eng. & Design, 25: 217.
- Pfann, J. (1975) Turbulent Heat Transfer to Longitudinal Flow Through a Triangular Array of Circular Rods. Nuc. Eng. & Design, 34: 203.
- Pope, S. B. (1978) The Calculation of Turbulent Recirculating Flows in General Orthogonal Co-ordinates. J. Comp. Phys., 26: 197.
- Preston, J. H. (1954) The Determination of Turbulent Skin Friction by Means of Pitot Tubes. J. Royal Aero. Soc., 58: 109.
- Ramm, H. and Johannsen, K. (1975a) A Phenomenological Turbulence Model and its Application to Heat Transport in Infinite Rod Arrays with Axial Turbulent Flow. J. Heat Trans. Trans. ASME 97, 75-HT-MM: 231.
- Ramm, H. and Johannsen, K. (1975b) Prediction of Local and Integral Turbulent Transport Properties for Liquid Metal Heat Transfer in Triangular Rod Arrays. J. Heat Trans., Trans. ASME 97, 75-HT-NN: 238.
- Rapier, A. C. and Redman, J. D. (1964) The Calculation of Velocity Distributions in Rod Clusters. Report TRG 838, UKAEA.
- Rapley, C. W. (1978) Regenerator Matrices for Automotive Gas Turbines, Paper No. HX-3, 6th Int. Heat Trans. Conf., Toronto.

- Rapley, C. W., Evans, A., Tuck, P. R. and Webb, A. I. C. (1974) The Heat Transfer Performance of Sine-duct Type Passages. Paper No. HE1.5, 5th Int. Heat Trans. Conf., Tokyo.
- Redman, J. D., McKee, G. and Rule, I. C. (1966) An Experimental Study of Turbulent Forced Convection Heat Transfer to Gases in Axial Flow Rod Cluster Passages. Report TRG931, UKAEA.
- Reece, G. J. (1977) A Generalized Reynolds Stress Model of Turbulence. Ph.D. Thesis, University of London.
- Rehme, K. (1972) Pressure-drop Performance of Rod Bundles in Hexagonal Arrangements. Int. J. Heat Mass Trans. 15: 2499.
- Rehme, K. (1974) Turbulent Flow in Smooth Concentric Annuli with Small Radius Ratios. J. Fluid Mech., 64: 263.
- Rehme, K. (1975) Turbulence Measurements in Smooth Concentric Annuli with Small Radius Ratios. J. Fluid Mech., 72: 189.
- Rodi, W. (1975) A Note on the Empirical Constants in the Kolmogorov Eddy Viscosity Expression. J. Fluid Eng., Trans. ASME: 386.
- Rotta, J. (1951) Statistical Theory of Non-homogeneous Turbulence. Z. Phys., 129: 547.
- Rowe, D. S. (1973) Measurement of Turbulent Velocity, Intensity and Scale in Rod Bundle Flow Channels. Report BNWL-1736, Battelle Mem. Inst.
- Rowe, D. S., Johnson, B. M. and Knudsen, J. G. (1974) Implications Concerning Rod Bundle Cross-flow Mixing Based on Measurements of Turbulent Structure. Int. J. Heat Mass Trans., 17: 407.
- Samaraweera, D. S. A. (1978) Turbulent Heat Transport in Two and Three Dimensional Temperature Fields. Ph.D. Thesis, University of London.
- Schiller, L. (1923) The Flow Resistance of Pipes of Various Cross-sections and Roughness. ZAMM, 3: 2.
- Schlichting, H. (1968) Boundary Layer Theory. McGraw-Hill.
- Schmidt, F. W. and Newell, M. E. (1967) Heat Transfer in Fully Developed Laminar Flow Through Rectangular and Isosceles Triangular Ducts. Int. J. Heat Mass Trans., 10: 1121.
- Science Research Council (1975) Report AM6 on the Round Table Meeting 'Convective Heat and Mass Transfer in Gases at High Temperatures'.
- Shah, R. K. (1975) Laminar Flow Friction and Forced Convection Heat Transfer in Ducts of Arbitrary Cross-section. Int. J. Heat Mass Trans., 18: 849.

- Shah, R. K. and London, A. L. (1978) Laminar Forced Convection in Ducts. Academic Press.
- Smith, J. W., Gowen, R. A. and Wasmund, B. O. (1967) Eddy Diffusivities and Temperature Profiles for Turbulent Heat Transfer to Water in Pipes. Chem. Eng. Prog., 63: 92.
- Sparrow, E. M. (1962) Laminar Flow in Isosceles-triangular Ducts. A.I.Ch.E.J., 8: 599.
- Sparrow, E. M. and Haji-Sheikh, A. (1965) Laminar Heat Transfer and Pressure Drop in Isosceles-triangular, Right-triangular and Circular Sector Ducts. J. Heat Trans., Trans ASME, 87C: 426.
- Sparrow, E. M., Lloyd, J. R. and Hixon, C. W. (1966) Experiments on Turbulent Heat Transfer in an Asymmetrically Heated Rectangular Duct. J. Heat Trans., Trans. ASME 88C: 170.
- Sparrow, E. M. and Loeffler, A. L. (1959) Longitudinal Laminar Flow Between Cylinders Arranged in Regular Array. A.I.Ch.E.J., 5: 325.
- Sparrow, E. M., Loeffler, A. L. and Hubbard, H. A. (1961) Heat Transfer to Longitudinal Laminar Flow Between Cylinders. J. Heat Trans., Trans. ASME 83: 415.
- Sparrow, E. M. and Siegel, R. (1959) A Variational Method for Fully Developed Laminar Heat Transfer in Ducts. J. Heat Trans., Trans. ASME 81: 157.
- Subbotin, V. I., Ushakov, P. A., Gabrianovich, B. N. and Zhukov, A. B. (1960) Heat Exchange During the Flow of Mercury and Water in Tightly Packed Rod Bundles. Soviet J. Atomic Energy, 9: 1001.
- Subbotin, V. I., Ushakov, P. A., Kirillov, P. L., Ibragimov, M. K., Ivanovsky, M. N., Nomophilov, E. V., Ovechkin, D. M., Sorokin, D. N. and Sorokin, V. P. (1964) Heat Removal from the Reactor Fuel Elements Cooled by Liquid Metals. Paper No. A/CONF.28/P/328 Proc. 3rd U.N. Int. Conf. Peaceful Uses of Atomic Energy, Geneva.
- Subbotin, V. I., Ushakov, P. A., Levchenko, Y. D. and Alexandrov, A. M. (1971) Velocity Field of Turbulent Fluid Flow in a Longitudinal Streamline of Clusters of Rods. AEC-tr-7189.
- Sukomel, A. S., Velichko, V. I., Abrosimov, Y. G. and Gutsev, D. F. (1975) An Investigation of Heat Transfer in the Entry Section of a Rectangular Duct. Thermal Eng., 22: 99.
- Sutherland, W. A. and Kays, W. M. (1966) Heat Transfer in Parallel Rod Arrays. J. Heat Trans., Trans. ASME 88: 117.
- Tao, L. N. (1961) On Some Laminar Forced Convection Problems. J. Heat Trans., ASME 83: 466.
- Tatchell, D. G. (1975) Convection Processes in Confined Three-dimensional Boundary Layers. Ph.D. Thesis, University of London.

- Tennekes, H. and Lumley, J. L. (1972) A First Course in Turbulence. The MIT Press.
- Thomas, D. L. and Easter, P. G. (1972) Measurements of Wall Shear Stress in a Duct of Square Cross-section. Report RD/B/N2477, CEGB.
- Thompson, J. F., Thames, F. C. and Mastin, C. W. (1974) Automatic Numerical Generation of Body Fitted Curvilinear Co-ordinate System for Fields Containing Any Number of Arbitrary Two-dimensional Bodies. J. Comp. Phys., 15: 299.
- Townsend, A. A. (1961) Equilibrium Layers and Wall Turbulence. J. Fluid Mech., 11: 97.
- Tracy, H. J. (1965) Turbulent Flow in a Three-dimensional Channel. Proc. ASCE (HY6), 91: 9.
- Trupp, A. C. and Aly, A. M. M. (1978) Predicted Turbulent Flow Characteristics in Triangular Rod Bundles. Mech. Eng. Report ER25.26, University of Manitoba.
- Trupp, A. C. and Azad, R. S. (1975) The Structure of Turbulent Flow in Triangular Array Rod Bundles. Nuc. Eng. & Design, 32: 47.
- Ushakov, P. A., Subbotin, V. I., Gabrianovich, B. N., Talanov, V. D. and Sviridenko, I. P. (1962) Heat Transfer and Hydraulic Resistance in Tightly Packed Corridor Bundle of Rods. Soviet Atomic Energy, 13: 761.
- Walker, V., White, L. and Burnett, P. (1972) Forced Convection Heat Transfer for Parallel Flow Through a Roughened Rod Cluster. Int. J. Heat Mass Trans., 15: 403.
- Wantland, J. L. (1956) Compact Tubular Heat Exchangers. Paper No. TID 7529, Reactor Heat Trans. Conf., New York.
- Weisman, J. (1959) Heat Transfer to Water Flowing Parallel to Tube Bundles. Nuc. Sc. & Eng., 6: 78.
- Wibulswas, P. (1966) Laminar Flow Heat Transfer in Non-circular Ducts. Ph.D. Thesis, University of London.
- Wilkie, D. (1966) Forced Convection Heat Transfer from Surfaces Roughened by Transverse Ribs. Paper No. 1, 3rd Int. Heat Trans. Conf., Chicago.
- Winslow, A. M. (1967) Numerical Solution of the Quasilinear Poisson Equation in a Non-uniform Triangular Mesh. J. Comp. Phys., 2: 149.
- Ying, W. M. (1971) Fully-developed Flow with Swirl in Non-circular Ducts. Ph.D. Thesis, University of London.

NOMENCLATURE

<u>Symbol</u>	<u>Meaning</u>
a	Half major axis length of an ellipse
$a_{j\ell}^{mi}$	Fourth order tensor defined in equations (A2.5)
AR	Aspect ratio
$A_N, A_S,$ A_E, A_W	Coefficients in the finite-difference equations defined in equations (5.3.15)
b	Half minor axis length of an ellipse
$B_e, B_w,$ B_n, B_s	Diffusion coefficients in the finite-difference equations, defined in equation (5.3.9)
c	Enthalpy fluctuation
C	Time-averaged enthalpy
$C_e, C_w,$ C_n, C_s	Convection coefficients in the finite-difference equations, defined in equation (5.3.9)
C_D	Constant in turbulence energy dissipation rate formula, equation (3.4.6)
C_p	Specific heat
$C_1, C_2,$ C_3, C_4	Constants in ASTM, defined by equations (4.2.29) to (4.2.32)
C_μ	Constant in turbulent viscosity formula, equation (3.4.7)
C_ν	Constant in turbulent viscosity formula, equation (3.4.5)
C_ϕ	Source in the ϕ equation (5.3.1)
C_{1c}	Constant in AHFTM (equations (4.4.6) and (4.4.7))
$C_{\epsilon 1}, C_{\epsilon 2}$	Constants in the ϵ transport equation (4.3.5) and table 4.7.1
$C_{\phi 1}, C_{\phi 2}$	Constants in the ASTM, equations (4.2.29) to (4.2.32) and table 4.7.1
D	Rod or tube diameter
D_c	Molecular diffusivity of enthalpy
D_e	Equivalent diameter

D_ϕ	Diffusion (exchange) coefficient of ϕ
e	Component of linearised source in the finite-difference equation (5.3.14)
e_r	Convergence residual equation (5.9.2)
E	Constant in velocity log-law of the wall, equation (4.6.2) and table (4.7.1)
E_r	Residuals, equation (5.9.2)
f	Friction factor
F_E etc.	Coefficients, defined in equations (5.4.8)
g	Component of linearised source in the finite difference equation (5.3.10)
G_i	Mass velocity in direction i
h_i	Metric coefficient in co-ordinate direction i
h_L	Local heat transfer coefficient, equation (8.1.1)
\bar{h}	Peripherally averaged heat transfer coefficient, equation (8.1.6)
\bar{H}	Product of metric coefficients
$H_i(j)$	Inverse of local radius of curvature of j line
i	Co-ordinate direction
j	Co-ordinate direction
k	Turbulence kinetic energy
k_f	Fluid thermal conductivity
ℓ	Turbulence length scale
ℓ_m	Mixing length
N_u	Mean Nusselt number, equation(8.1.6)
N_{uL}	Local Nusselt number, equation (8.1.8)
\bar{N}_u	Peripherally averaged Nusselt number
N_R	Reference quantity for normalising the residuals, equation (5.9.2)
p	Time averaged pressure

p'	Pressure fluctuation
p^*	Guessed time-averaged pressure
P	Rod or tube pitch, also production rate of turbulence kinetic energy
P_e	Grid cell Peclet number ($= G\delta S/D_\phi$)
P_r	Laminar Prandtl number
P^*	Jayatilke (1959) sub-layer function, equation (4.6.7)
\dot{q}''	Heat flux
$\overline{\dot{q}''}$	Average heat flux, equation (8.1.5)
r	Rod or tube radius
r_i	Local radius of curvature for co-ordinate direction i
Re	Reynolds number (based on $\overline{U_3}$)
R_s	Residual source, equation (5.9.1)
s, S	Curvilinear arc length
s^+, S^+	Dimensionless curvilinear arc length, equation (4.6.3)
t_{ij}	Turbulent stress tensor
T	Time-averaged temperature
T_b	Bulk time-averaged fluid temperature, equation (8.1.2)
T_w	Local wall temperature
$\overline{T_w}$	Average wall temperature, equation (8.1.4)
T_{CL}	Passage time-averaged centre-line temperature
u_i	Velocity fluctuation in direction i
$\overline{u_i u_j}$	Reynolds stress tensor
\tilde{u}_i	Turbulence intensity in direction i
U	Resultant time averaged velocity
U_i	Time-averaged velocity component in direction i
$\overline{U_i}$	Mean time-averaged velocity in direction i
U^*	Mean friction velocity (equation 4.6.1)

U_{iA}^* etc.	Guessed time-averaged velocity in direction i
U_{iL}^*	Local friction velocity in direction i
U_{iCL}	Time-averaged centre-line velocity in direction i
U_{imax}	Maximum time-averaged velocity in direction i if it is not U_{iCL}
U^+	Dimensionless velocity ($= U_i/U^*$)
V_p	Volume of a control volume
x_i	Cartesian co-ordinate direction i
y_i	Orthogonal curvilinear co-ordinate direction i
y^+	Dimensionless distance from a surface (see s^+)
Δz	Incremental length in the axial direction

GREEK SYMBOLS

α	Constant in Reynolds stress transport equations (A2.5) and (A2.6)
$\alpha_1, \alpha_2, \alpha_3$	Constants in Gessner and Emery (1976) ASTM, equations (3.4.17) to (3.4.20)
β	Constant in Reynolds stress transport equations, (A2.5) and (A2.6)
γ	Constant in Reynolds stress transport equations, (A2.5) and (A2.6)
γ_c	Turbulent (eddy) diffusivity of enthalpy
δ_{ij}	Kronecker delta
κ	Constant in velocity log-law of the wall, equation (4.6.2) and table 4.7.1
λ	Constant in Reynolds stress transport equations, equation (4.2.8)
μ	Laminar viscosity
μ_t	Turbulent (eddy) viscosity ($= \rho \nu_t$)
μ_{eff}	Effective turbulent viscosity ($= \mu + \mu_t$)
ν	Laminar kinematic viscosity
ν_t	Turbulent (eddy) kinematic viscosity

ϵ	Turbulence kinetic energy dissipation rate
η	Constant in Reynolds stress transport equations, (A2.5) and (A2.6)
ρ	Fluid density
σ_c	Turbulent Prandtl number for enthalpy, table 4.7.1
σ_k	Turbulent Prandtl number for turbulence kinetic energy, table 4.7.1
σ_ϵ	Turbulent Prandtl number for dissipation rate of turbulence energy, table 4.7.1
θ	Angular co-ordinate
τ_{ij}	Viscous stress tensor
τ_0	Resultant local wall shear stress
$\overline{\tau_0}$	Average wall shear stress
τ_{0i}	Local component wall shear stress in direction i
τ_{0max}	Maximum local wall shear stress
τ_{ij}	Total stress tensor
ϕ	Scalar quantity, also angular co-ordinate direction

ABBREVIATIONS

AHFTM	Algebraic heat flux transport model, equations (4.4.6) and (4.4.7)
ASTM	Algebraic stress transport model, equations (4.2.23) to (4.2.28)
H1, H2, H3	Heat transfer boundary conditions, defined in section 5.5
SIMPLE	Semi-implicit method for pressure-linked equations, section 5.4
TDMA	Tri-diagonal matrix algorithm, Appendix 7

AI.1 Proc. International Conference on Numerical Methods in Laminar and Turbulent Flow, Swansea, pp 271-285. July, 1978.

square or rectangular.

A feature of turbulent flow in non-circular passages which is absent from laminar flow is the 'secondary flows' that are generated in the cross-sectional plane in order to maintain equilibrium between the Reynolds stresses and pressure gradients. These flows have the effect of transporting some of the core fluid into the corners of the duct, causing the flow to spiral in the axial direction in separate cells located across the cross-section. Although the secondary velocities are usually not more than 1% or 2% of the mean axial velocity, evidence from comparison of prediction and experiment in rectangular ducts (e.g. Launder and Ying, 1972) indicates that they can influence local values of axial velocity and wall shear stress by as much as 30% and certain turbulence properties by more than 50%. Any prediction procedure must therefore include secondary flow effects if it is to produce realistic results.

Detailed measurement of turbulent flows has been possible since about 1960 due to the refinement of anemometry techniques. Investigations of turbulent flow in non-circular passages seem to have been concentrated on square and rectangular ducts (see e.g. references in Melling and Whitelaw, 1976) and the axial flow passages in rod bundles (see e.g. references in Carajilescov and Todreas, 1975). Apparently the only other geometries to receive any detailed attention are the 11.7° vertex-angled isosceles triangular duct of Cremers and Eckert (1965) and the equilateral triangular duct of Aly et al (1978).

Prediction techniques capable of simulating the important details of turbulent flow in non-circular passages appear to have been mainly developed for square and rectangular passages (e.g. Hanjalic and Launder, 1972, Launder and Ying, 1973, Naot et al, 1974, Tatchell, 1975, Gessner and Emery, 1976). The prediction method of Launder and Ying (1973) has recently been applied to two other geometries, an equilateral triangular duct (Aly et al, 1978) and the axial flow channel in triangular rod bundles (Carajilescov and Todreas, 1975). The predictions all show effects of secondary flow which are in general agreement with the expected behaviour. There are however some discrepancies between the predicted and experimental distributions of turbulence quantities and secondary velocities. Nevertheless there is sufficient encouragement in these predictions to seek a prediction procedure that is capable of application to a variety of passage shapes.

In the present paper, a general procedure is described for the calculation of flow and heat transfer in straight passages of arbitrary cross-section. The procedure contains some elements of the earlier work of Launder and Ying (1973), Tatchell (1975)

A PREDICTION METHOD FOR FULLY-DEVELOPED FLOW THROUGH NON-CIRCULAR PASSAGES.

A.D. Gosman and C.W. Rapley

Mech. Eng. Dept., Imperial College, University of London, U.K.
Mech. Eng. Dept., Sunderland Polytechnic, U.K.

INTRODUCTION

There is an urgent need for detailed predictions of fluid flow and heat transfer in straight passages of non-circular cross-section. Such predictions would enable designs of compact heat exchangers and the many other non-circular passages in cooling and other engineering component systems to be made directly on the basis of the fluid flow and thermal performance required, so enabling optimum use of the available space.

For certain shapes of passage cross-section the overall heat transfer and pressure drop performance for turbulent flow can be adequately predicted by using the equivalent diameter of the passage in conjunction with the well established circular duct correlations. For example, the square duct friction measurements of Hartnett et al (1962) are well predicted by the Blasius equation, as are the friction measurements of Barrow and Roberts (1970) for elliptical ducts. The friction factor for triangular ducts however is over-predicted by the Blasius equation by some 20% for acute-angled isosceles triangles (Carlson and Irvine, 1961) and by about 10% for the equilateral triangular duct of Aly et al (1976). It seems that when the passage shape involves an acute-angled internal corner, not even the overall performance can be obtained from circular duct data. Furthermore, even if overall prediction can be obtained in this way for a particular duct, little or no information is available on local values of quantities such as wall shear stress and heat transfer coefficient.

Considerable work has been done on the analysis of fully developed laminar flow through a wide range of non-circular passages. A useful summary can be found in Shah and London (1974). When it comes to turbulent flow, however, there is little either experimental or predicted fluid flow and heat transfer information available for non-circular passage shapes other than

and Gessner and Emery (1976).

THE PRESENT PROCEDURE

In essence, the present method solves the mean flow momentum equations by finite differences on an orthogonal curvilinear grid generated to fit the passage shape. The Reynolds stresses are calculated with an algebraic model which links the stresses to mean velocity gradients through the turbulence kinetic energy and its dissipation rate, whose values are obtained by solving their modelled transport equations by finite differences on the orthogonal curvilinear grid. Sample predictions are here presented for laminar and turbulent flow in ducts of equilateral triangular cross-section and comparisons are made with existing analytical and experimental data.

Differential Equations and turbulence model

For steady flow of an incompressible fluid, the Reynolds equation with negligible body forces can be written in vector notation as

$$\nabla \cdot G\mathbf{U} + \nabla \cdot \boldsymbol{\tau} + \nabla p = -\nabla \cdot \rho\overline{\mathbf{u}\mathbf{u}}$$

and the mass conservation equation as

$$\nabla G = 0$$

where ρ , \mathbf{U} , G and p are the time averaged density, velocity, mass velocity and pressure respectively, $\boldsymbol{\tau}$ the molecular stress tensor and $\rho\overline{\mathbf{u}\mathbf{u}}$ the Reynolds stress tensor.

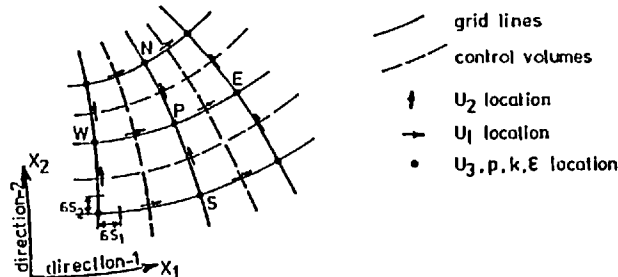


Figure 1. Part of orthogonal grid showing the co-ordinate system and grid notation

These equations are expanded in general orthogonal co-ordinates X_1 , X_2 and X_3 for fully-developed flow in straight passages and re-cast in terms of arc lengths dS_1 , dS_2 and dS_3 where $dS_1 = l_1 dx_1$, $dS_2 = l_2 dx_2$ and $dS_3 = l_3 dx_3$ (l_1, l_2 and l_3 being the metric coefficients in co-ordinate directions X_1 , X_2 and X_3

respectively). Co-ordinates X_1 and X_2 are in direction-1 and 2 respectively in the cross-flow plane as shown in figure 1 and X_3 in the (straight) axial direction-3. In the following equations, suffices 1, 2 and 3 are used to indicate directions 1, 2 and 3 respectively with the second suffix of molecular stress $\boldsymbol{\tau}$ indicating the direction of the normal to the plane on which the stress acts. The expanded Reynolds equations for directions 1, 2 and 3 respectively are:

$$\frac{\partial(G_1 U_1)}{\partial S_1} + \frac{\partial(G_2 U_1)}{\partial S_2} + \frac{\partial \tau_{11}}{\partial S_1} + \frac{\partial \tau_{12}}{\partial S_2} + \frac{\partial(\rho \overline{u_1^2})}{\partial S_1} + \frac{\partial(\rho \overline{u_1 u_2})}{\partial S_2} + \frac{\partial p}{\partial S_1} + \frac{1}{r_2}(G_1 U_1 - G_2 U_2 + \tau_{11} - \tau_{22} + \rho \overline{u_1^2} - \rho \overline{u_2^2}) + \frac{2}{r_1}(G_2 U_1 + \tau_{12} + \rho \overline{u_1 u_2}) = 0 \quad (1)$$

$$\frac{\partial(G_1 U_2)}{\partial S_1} + \frac{\partial(G_2 U_2)}{\partial S_2} + \frac{\partial \tau_{21}}{\partial S_1} + \frac{\partial \tau_{22}}{\partial S_2} + \frac{\partial(\rho \overline{u_1 u_2})}{\partial S_1} + \frac{\partial(\rho \overline{u_2^2})}{\partial S_2} + \frac{\partial p}{\partial S_2} + \frac{1}{r_1}(G_2 U_2 - G_1 U_1 + \tau_{22} - \tau_{11} + \rho \overline{u_2^2} - \rho \overline{u_1^2}) + \frac{2}{r_2}(G_1 U_2 + \tau_{12} + \rho \overline{u_1 u_2}) = 0 \quad (2)$$

$$\frac{\partial(G_1 U_3)}{\partial S_1} + \frac{\partial(G_2 U_3)}{\partial S_2} + \frac{\partial \tau_{13}}{\partial S_1} + \frac{\partial \tau_{23}}{\partial S_2} + \frac{\partial(\rho \overline{u_1 u_3})}{\partial S_1} + \frac{\partial(\rho \overline{u_2 u_3})}{\partial S_2} + \frac{\partial p}{\partial S_3} + \frac{1}{r_1}(G_2 U_3 + \tau_{23} + \rho \overline{u_2 u_3}) + \frac{1}{r_2}(G_1 U_3 + \tau_{13} + \rho \overline{u_1 u_3}) = 0 \quad (3)$$

The mass conservation equation becomes

$$\frac{\partial G_1}{\partial S_1} + \frac{\partial G_2}{\partial S_2} + \frac{G_1}{r_2} + \frac{G_2}{r_1} = 0 \quad (4)$$

For laminar flow the terms containing the Reynolds stresses $\rho \overline{u_1^2}$, $\rho \overline{u_1 u_2}$ etc. disappear from equations (1) to (3) and since the molecular stresses are related only to gradients of U_1 and U_2 with respect to S_1 and S_2 , equations (1) and (2) disappear and there are no secondary flows. This also implies that for turbulent flow it will be insufficient to model the cross-flow plane Reynolds stresses on the molecular stresses using an isotropic turbulent viscosity μ_t (e.g. $\rho \overline{u_1^2} = \mu_t \partial U_1 / \partial S_1$) since no secondary flows will be generated.

In order to produce secondary flows in turbulent flow the prediction procedure of Launder and Ying (1973) used an algebraic stress model developed from a degenerate form of the cross-flow plane Reynolds stress transport equation in which transport by convection and diffusion are neglected. By taking dissipation of Reynolds stress to be locally isotropic (fine scale motions) and using the Hanjalić and Launder (1972) pressure-strain relationship, Launder and Ying reduced the differential transport equation to algebraic equations from which the cross-flow plane Reynolds stresses could be extracted.

Gessner and Emery (1976) showed that the axial flow plane Reynolds stresses could also be extracted to give the following set of equations for the five (kinematic) Reynolds stresses appearing in equations (1) to (3):

$$\overline{u_1 u_3} = -C_4 \frac{k^2}{\epsilon} \frac{\partial U_3}{\partial S_1}, \quad \overline{u_2 u_3} = -C_4 \frac{k^2}{\epsilon} \frac{\partial U_3}{\partial S_2} \quad (5), (6)$$

$$\overline{u_1^2} = C_3 k - C_2 C_4 \frac{k^2}{\epsilon^2} \left(\frac{\partial U_3}{\partial S_1} \right)^2 \quad (7)$$

$$\overline{u_2^2} = C_3 k - C_2 C_4 \frac{k^2}{\epsilon^2} \left(\frac{\partial U_3}{\partial S_2} \right)^2 \quad (8)$$

$$\overline{u_1 u_2} = -2C_2 C_4 \frac{k^2}{\epsilon^2} \left(\frac{\partial U_3}{\partial S_1} \right) \left(\frac{\partial U_3}{\partial S_2} \right) \quad (9)$$

where k is the turbulence energy and ϵ its dissipation rate, and C_2 , C_3 and C_4 are empirical constants. The Reynolds stress model represented by equations (5) to (9) has been adopted in the present procedure.

The quantity $\rho C_4 k^2 / \epsilon$ can be identified as a turbulent viscosity μ_t (Lauder and Spalding, 1972) i.e.

$$\mu_t = C_4 \rho k^2 / \epsilon$$

which means that equations (5) and (6) reduce to a simple isotropic viscosity model for the Reynolds stresses $\rho \overline{u_1 u_3}$ and $\rho \overline{u_2 u_3}$ in the axial planes. This is not so however for the cross-flow plane Reynolds stresses $\rho \overline{u_1^2}$, $\rho \overline{u_2^2}$ and $\rho \overline{u_1 u_2}$ which are seen to depend on mean strain rates in planes normal to the cross-flow plane. It is this cross-planar effect that produces secondary flows in the cross-flow plane.

In the application of the Reynolds stress model to particular geometries by Launder and Ying (1973), Aly et al (1978) and Carajilescov and Todreas (1975), the dissipation rate of turbulence energy ϵ was calculated from the algebraic relation $\epsilon = C_D k^{3/2} / L$ where C_D is an empirical constant and L a turbulence length scale, the spatial distribution of which must be specified. Although Launder and Ying (1973) and Aly et al (1978) obtained some success by calculating L from a formula proposed by Duleev (1963), Carajilescov and Todreas (1975) found it necessary to resort to experimental measurements in order to produce a satisfactory length scale prescription. This need for a complex empirical input was considered undesirable in a prediction procedure for general non-circular passage shapes and so, following the practice of Tatchell (1975), it is removed in the present procedure by calculating ϵ from its modelled transport equation (Hanjalic and Launder, 1972). The turbulence energy k is also calculated from its modelled

transport equation, in a form used by many previous workers (e.g. Hanjalic and Launder, 1972). Both modelled transport equations have the following general form:

$$\frac{\partial(G_1 B)}{\partial S_1} + \frac{\partial(G_2 B)}{\partial S_2} - \frac{\partial(D_B \frac{\partial B}{\partial S_1})}{\partial S_1} - \frac{\partial(D_B \frac{\partial B}{\partial S_2})}{\partial S_2} + F = 0 \quad (10)$$

where for turbulence energy, $B = k$ and $F = \rho \epsilon - P$ and for dissipation rate of turbulence energy, $B = \epsilon$ and $F = C_{\epsilon 1} \rho \epsilon^2 / k - C_{\epsilon 2} \rho P / k$. $C_{\epsilon 1}$ and $C_{\epsilon 2}$ are empirical constants, P is the generation rate of turbulence energy and D_B the turbulent diffusivity given by:

$$D_B = \mu + \mu_t / \sigma_B$$

where σ_B is the effective turbulent Prandtl number.

Equations (1) to (10), together with the boundary conditions (discussed below) form a closed set representing steady fully developed turbulent flow through non-circular passages.

In order to be consistent with the aim of obtaining a prediction procedure for general geometries, no attempt has been made to optimise the empirical constants, whose values have simply been taken from previous studies. (Lauder and Spalding, 1972; Launder and Ying, 1973) and we summarise below:

$$C_2 = 0.0185, C_3 = 0.57, C_4 = 0.09$$

$$C_{\epsilon 1} = 1.55, C_{\epsilon 2} = 2.0, \sigma_k = 1.0, \sigma_\epsilon = 1.185$$

It is recognised that more appropriate values of these constants may well emerge from future comparisons of predictions and experimental data as it becomes available for different passage geometries.

Treatment of boundary conditions at walls

Wall functions are used to match the interior flow with the wall conditions and thus avoid the large number of grid nodes that would otherwise be necessary in this region of high gradients. These wall functions are applied to the grid cells next to the wall, which is assumed to be a region of constant shear so that the wall shear stress τ_0 and velocity variation with normal distance from the wall y are related by the well known log-law:

$$U/U_\tau = (\ln(Ey^+)) / \kappa$$

where U_τ is the local friction velocity ($= \tau_0 / \rho C_\mu^{1/2} k^{1/2}$), $y^+ = y \tau_0 / \nu$ and constants E and κ are chosen according to the texture of the wall surface. For a smooth plane wall the

values assigned (Schlichting, 1968) are:

$$E = 9.025, \quad \kappa = 0.4$$

The turbulence energy k near the wall is obtained as for the interior nodes with generation and dissipation calculated using the local value of wall shear stress.

The value of ϵ near the wall is obtained by neglecting transport of ϵ by convection and diffusion and assuming a length scale that varies linearly with y (Launder and Spalding, 1972) so that

$$\epsilon = C_\epsilon^{3/4} k / \kappa y$$

Finite-difference equations

When the velocity gradient relationships are substituted for the molecular stresses in the differential equations (1) to (3), these together with equations (10) may be compactly represented in terms of the single transport equation:

$$\frac{\partial(G_1\phi)}{\partial S_1} + \frac{\partial(G_2\phi)}{\partial S_2} - \frac{\partial(D_\phi \frac{\partial\phi}{\partial S_1})}{\partial S_1} - \frac{\partial(D_\phi \frac{\partial\phi}{\partial S_2})}{\partial S_2} = C_\phi \quad (11)$$

where ϕ stands for any of the main dependant variables U_1 , U_2 , U_3 , k and ϵ ; D_ϕ and C_ϕ are respectively the corresponding diffusivity and source, although the latter is really a catch-all for all the terms not already contained in the general equation.

An element of the curvilinear grid system employed in the calculations is shown in figure 1 (an example of a complete grid numerically computed by a simple method similar to that described by Antonopoulos et al (1978) is shown in figure 2b). The variables p , U_3 , k and ϵ are calculated at the grid nodes but following what is now conventional practice, the cross-flow velocities U_1 and U_2 are computed at intervening locations, mid-way between the pressures which drive them.

The finite difference equivalent of equation (11) is derived, for each grid location, by approximate integration over imaginary, contiguous control volumes surrounding each location, examples of which are shown in figure 1. The main approximation involved concerns the variation of the dependant variable ϕ between the nodes: generally a linear variation is assumed, this 'central difference' representation being adequate when, as in the present case, the cross-flow velocities are small (strictly the relevant quantity is the cross-flow Peclet number $Pe = U\delta S/D$, where U , δS and D are the local velocity, grid spacing and eddy diffusivity respectively). However, provision is made to switch over to upwind differencing if Pe becomes large, in

the manner described by Caretto et al (1972), in order to preserve accuracy and computational stability.

The resulting sets of finite difference equations for each variable are conservative and give rise to, not additionally diagonally-dominant coefficient matrices, these being desirable, if not essential, requirements for a general numerical procedure. The equations are, in the notation of figure 1, of the form:

$$a_p \phi_p = a_E \phi_E + a_W \phi_W + a_N \phi_N + a_S \phi_S + C_\phi$$

where $a_p = a_E + a_W + a_N + a_S - C_p$. The a 's are coefficients expressing the combined effects of convection and diffusion and the C 's are coefficients of a linearised approximation to the C_ϕ integral.

Departures from the above practices are made in the case of the continuity equation (4) which, after integration, is combined with the cross-flow momentum equations to yield a finite difference equation for pressure (strictly a pressure correction) of the form of (11) above. Details of the derivation are given in Caretto et al (1972).

Solution Procedure

For a given computational grid (which, as mentioned earlier, is itself computed numerically), the finite difference equations are assembled and solved by two nested iteration sequences. The outer sequence causes the variables to be updated sequentially and repeated until convergence is achieved, the order being to solve the momentum equations for the cross-flow velocities, the 'continuity' equation for the pressures (which are then used to bring the velocities into continuity balance), the axial momentum equation for the axial velocity and the turbulence equations for the turbulence parameters. The inner sequence effects the solution of the (linearised) equations for each variable by a line-iteration of 'ADI' procedure based on the tri-diagonal matrix algorithm.

Convergence of the overall procedure is by no means assured, due to the coupling and non-linearity of the equations, the former feature being particularly prominent in the Reynolds stress modelling here employed. However, experience has shown that a combination of under-relaxation and a special starting procedure wherein a nearly converged solution is obtained before the cross-flow equations are brought into the calculation, is invariably successful. When, as in the test cases presented later, the grid is such as to cause large variations in the finite difference coefficients over the field, it has also proven beneficial to apply extra 'sweeps' of the line-iteration procedure in regions of small coefficients.

The calculations are taken as converged when the sums over the

field of the absolute mass and momentum residuals are less than a small prescribed fraction (usually of order 10^{-1}) of the axial mass and momentum fluxes. Further, tests with various sizes of grids revealed that the solutions obtained are substantially grid independent for mesh numbers of about 250 and greater.

APPLICATION OF THE PROCEDURE TO PREDICTION OF FLOW IN AN EQUILATERAL TRIANGULAR DUCT

Flow in an equilateral triangular duct was selected as a useful test of the prediction procedure since recent turbulent flow experimental data was available (Aly et al, 1978) and the many symmetry flow elements in the duct could be used to check the consistency of the finite difference procedure across the orthogonal mesh. With regard to the latter point, in this particular geometry there are six symmetry elements of flow,

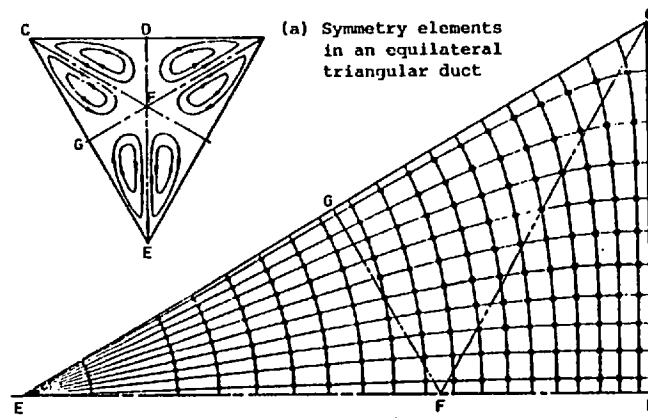


Figure 2. (b) Orthogonal grid for half-duct domain

each bounded by corner bisectors as shown in figure 2a. This figure also shows the secondary cells expected with turbulent flow (Schlichting, 1968) where each symmetry element contains a cell. A solution to the flow through the duct is represented by a solution for just one of these symmetry elements. The predictions of turbulent flow made with the present procedure and shown in figures 5 to 8 (and also the predictions of Aly et al, 1978) were obtained from solution of a symmetry flow element such as CFD in figure 2a. However initial tests of the present procedure were made by solving the flow in a one-half duct domain, and then examining for the required symmetry, as described below.

Tests for symmetry of the numerical solution

Checks were made to ensure that the asymmetry of the curvilinear grid did not prevent the expected flow symmetries from being obtained. This was done by solving the flow in one half of an equilateral triangular duct where a triple flow symmetry should prevail. A typical orthogonal grid generated to fit the half-duct domain is shown in figure 2b with lines CF and GF superimposed to divide the domain into the expected three flow symmetry elements CFD, CFG and EFG. The size, shape and orientation of the control volumes will clearly be different in each of the symmetry elements.

The computed fully developed laminar flow wall shear stress distribution (along EC) is shown in figure 3 where the expected symmetry about the mid-wall point $Z/2B=0.5$ has been obtained. A more sensitive test however is the prediction of the three similar counter-rotating cells of secondary flow in fully developed turbulent flow. The result of this calculation is shown in figure 4 where the secondary flow velocity vectors are drawn to scale at each grid node. Evidently the symmetries have been successfully obtained.

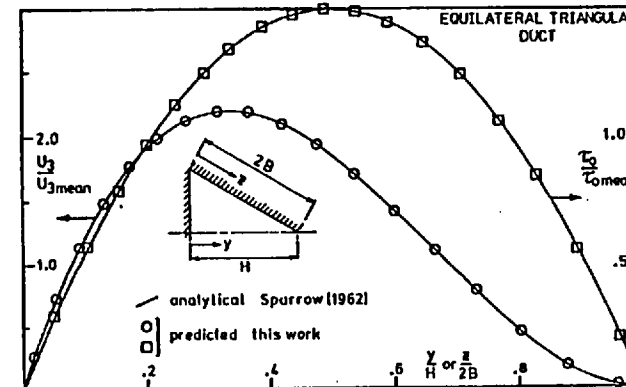


Figure 3. Laminar flow

To complete the symmetry assessment the fully developed turbulent flow distributions of axial velocity, turbulence energy and wall shear stress calculated for the half-duct domain are compared in figures 5 and 6 with distributions calculated for a single flow symmetry element. Satisfactory agreement has been obtained.

Comparison of predictions with published data

The predicted wall shear stress and the axial velocity across a symmetry plane for fully developed laminar flow are shown in

Figure 3 to be in excellent agreement with the analytically-derived distributions of Sparrow (1962). The computed axial

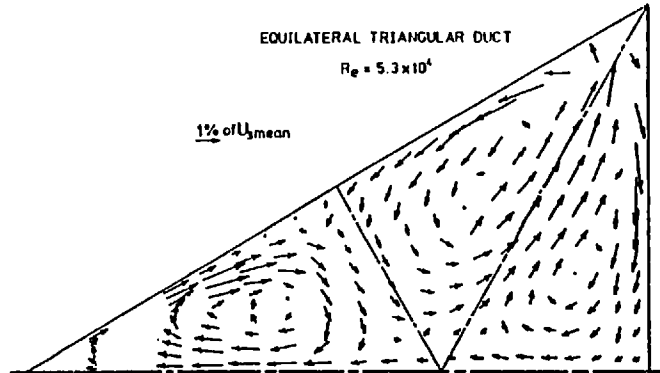


Figure 4. Secondary Flow Vectors

velocity and turbulence energy distributions along a symmetry plane and the wall shear stress distribution for fully developed turbulent flow are shown in figures 5 and 6 respectively (U_3 is the mean friction velocity) together with experimental data and predictions from Aly et al (1978). To assess the effect of secondary flows, predictions in which secondary calculation has been suppressed are also indicated.

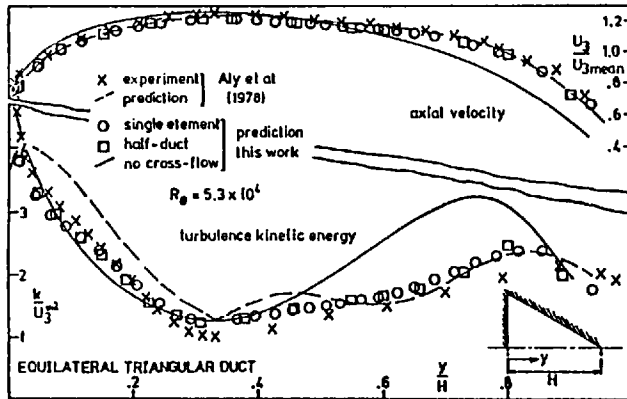


Figure 5. Axial velocity and turbulence energy

The effect of secondary flows in transporting some of the core fluid along corner bisectors into the corners is clearly shown in the axial velocity distribution of figure 5 as is the

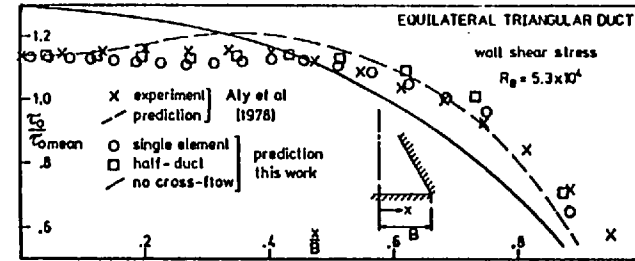


Figure 6. Wall shear stress

equalising effect on the wall shear stress distribution in figure 6. The effect of neglecting secondary flows is typically shown in figure 6 where local wall shear stress into the corner is under-estimated by more than 25%. The prediction of Aly et al (1978) using prescribed length scale reduces this to about 18% and the present procedure gives a further reduction to a more acceptable 10%. In accord with the findings for square ducts (Launder and Ying, 1972), the turbulence energy distribution is seen to be more sensitive than axial velocity and wall shear to secondary flows with reduction in local turbulence energy of more than 75% along the centre-plane at Y/H between 0.6 and 0.8. This reduction can be mainly attributed to the reduced generation of turbulence energy due to lower axial velocity gradients in this region. The comparison of the present prediction with experiment is quite satisfactory when it is considered that the experimental data is obtained as the sum of the squares of separate measurements of turbulence intensity, each with its own uncertainties.

The calculated turbulence intensities along a symmetry plane are compared in figure 7 with the experimental data of Aly et al (1978) (who do not themselves show predictions). Reasonable agreement is obtained between prediction and experiment, both of which show the expected departure from isotropy of the turbulence as the wall is approached.

The computed friction factor/Reynolds number characteristic is compared in figure 8 with the limited experimental data and the predictions of Aly et al (1978) and the Blasius equation (using the equivalent diameter). The friction factors produced by the present method lie below the measurements by some 8% at the lower Reynolds numbers, with the discrepancy decreasing as Reynolds number increases. This trend is consistent with the

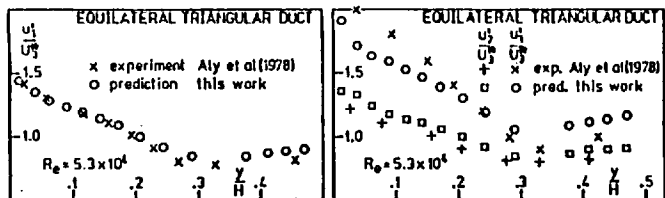


Figure 7. Turbulence Intensities

high turbulence Reynolds number assumption inherent in the Reynolds stress model used. Undoubtedly better agreement could be obtained, as in the study of Aly et al (1978), by

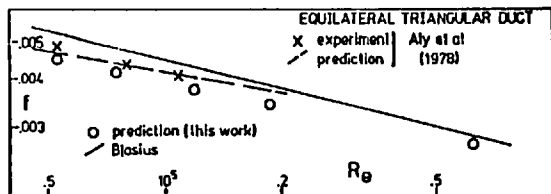


Figure 8. Friction Factor Characteristic

adjusting the empirical constants in the turbulence model. However, we prefer not to make such adjustments until a wider range of passage geometries have been investigated.

SUMMARY AND CONCLUSIONS

A procedure has been developed for computer prediction of fully developed laminar and turbulent flow in non-circular passages. Tests show that the procedure produces the expected symmetries in the flow and yields excellent agreement with exact solutions for laminar flow. The algebraic stress model used has produced the expected secondary flow effects in the turbulent flow predictions which are generally in accord with experiment.

The paucity of detailed experimental data available for turbulent flow in non-circular passages other than square or rectangular is an indication of the difficulty and expense of building accurate test rigs and obtaining reliable experimental data. The alternative of simulating the performance on the computer must be considered very desirable in view of the vast number of possible non-circular passage shapes and arrangements. The authors believe that the present method has many of the features required for such a prediction procedure. Currently, the method is being applied to other passage geometries,

including the axial flow passage in rod bundles and is also being extended to include heat transfer. A study is also being made of more recently proposed Reynolds stress models (e.g. Reece, 1976) to see if they have any advantage over the model used in the present method.

ACKNOWLEDGEMENTS

The authors acknowledge the support of the Department of Mechanical Engineering at Imperial college and at Sunderland Polytechnic.

REFERENCES

1. Aly, A.M.M., A.C. Trupp and A.D. Gerrard (1978) Measurement and Prediction of Fully Developed Turbulent Flow in an Equilateral Triangular Duct. *J. Fluid Mech.*, **85**, 57-83.
2. Antonopoulos, K., A.D. Gosman and R. Issa (1978) A Simple Method of Calculating Curvilinear-orthogonal Co-ordinate Meshes for Complex Geometries. Imperial College Mech. Eng. Report in preparation.
3. Barrow, H. and A. Roberts (1970) Flow and Heat Transfer in Elliptic Ducts. 4th Int. Heat Trans. Conf., Paper No FC4.1.
4. Buleev, N.I. (1963) Theoretical Model of the Mechanism of Turbulent Exchange in Fluid Flow. *AERE Trans.* 957.
5. Carajlescov, P. and N.E. Todreas (1975) Experimental and Analytical Study of Axial Turbulent Flows in an Interior sub-channel of a Bare Rod Bundle. *ASME Paper No. 75-WA/HT-51*.
6. Carlson, L.W. and T.F. Irvine, Jr. (1964) Fully Developed Pressure Drop in Triangular Shaped Ducts. *J. Heat Trans.*, *Trans. ASME*, **83**, 441-44.
7. Carretto, L.S., A.D. Gosman, S.V. Patankar and D.B. Spalding (1972) Two Numerical Procedures for Three Dimensional Recirculating Flows. *Proc. Second Int. Conf. on Numerical methods in Fluid Dynamics*, Springer Verlag, New York.
8. Cremers, C.J. and E.R.G. Eckert (1962) Hot Wire Measurements of Turbulence Correlations in a Triangular Duct. *J. App. Mech.*, *Trans. ASME*, **4**, 609-614.
9. Eckert, E.R.G. and T.F. Irvine (1956) Flow in Corners of Passages with Non-circular Cross Sections. *Trans. ASME*, **78**, 709-718.
10. Gessner, F.B. and A.F. Emery (1976) A Reynolds Stress Model for Turbulent Corner Flows - Part 1. *ASME J. Fluids Eng. Paper No. 76-FE-C*.
11. Hanajlic, K. and B.E. Launder (1972) A Reynolds Stress Model of Turbulence and its Application to Thin Shear Flows. *J. Fluid Mech.*, **52**, 609-638.
12. Hartnett, J.P., J.C. Koh and S.T. McComas (1962) A Comparison of Predicted and Measured Friction Factors for Turbulent Flow Through Rectangular Ducts. *Trans. A.S.M.E. J. Heat Transfer*, **84**, 82-88.

- A1.2 'Recent Advances in Numerical Methods in Fluid Flow'.
Pineridge Press, Swansea; pp 335 - 399.
In press, publication date: June, 1980.
(first page proof shown below)

335

CHAPTER 11

FULLY-DEVELOPED FLOW IN PASSAGES OF ARBITRARY CROSS-SECTION

A.D. GOSMAN, Mechanical Engineering Department, Imperial College

C.W. RAPLEY, Mechanical Engineering Department, Sunderland Polytechnic.

1. INTRODUCTION

The general field of 'duct' or 'passage' or 'confined' flows as they are variously called is a very large one, embracing as it does an infinite variety of geometrical configurations, fluids and flow rates, whose various combinations give rise to virtually every kind of flow structure imaginable. Thus, at the lower end of the scale of complexity there are the familiar steady, laminar, fully-developed single-phase flows in straight circular tubes, whose accessibility to straightforward analysis has made them a standard feature of introductory textbooks and courses on fluid mechanics. Towards the other end of the scale, where lies many of the duct flows encountered in practical circumstances, the fluid motion is almost invariably unsteady, due to the onset of turbulence and other phenomena and sometimes consists of more than one phase, while the enclosing duct is often curved and exhibits changes of shape and size of cross-section, which may be so abrupt as to provoke separation: by contrast with the earlier example, problems of this kind lie at the frontiers of current research and are only beginning to be accessible to predictive analysis.

The obstacles to prediction of all classes of duct flows are of two kinds: firstly, it is necessary to be able to translate them into a closed mathematical problem, consisting of the governing equations of motion and the associated boundary conditions. If the motion is laminar, this presents no especial difficulties, for the equations are well known: however it is equally known that the practical necessity to describe turbulent motion in terms of its time-averaged behaviour gives rise to formidable problems of closure (see, e.g. Bradshaw, 1978).

The second kind of obstacle relates to the solution of the equations, which must invariably be done numerically for

APPENDIX 2

THE MODELLED REYNOLDS STRESS
TRANSPORT EQUATIONS

The exact form of the Reynolds Stress Transport Equations can be derived from the Navier-Stokes equations (see Hinze, 1975 p. 324) and arranged in the following way:

$$\begin{aligned}
 U_k \frac{\partial (\overline{u_i u_j})}{\partial x_k} &= - (\overline{u_j u_k} \frac{\partial u_i}{\partial x_k} + \overline{u_i u_k} \frac{\partial u_j}{\partial x_k}) \\
 \text{(convection)} & \qquad \qquad \qquad \text{(generation)} \\
 & - 2\nu \overline{(\frac{\partial u_i}{\partial x_k}) (\frac{\partial u_j}{\partial x_k})} \\
 & \qquad \qquad \qquad \text{(dissipation)} \\
 & + \overline{(p'/\rho) (\frac{\partial u_i}{\partial x_j} + \frac{\partial u_j}{\partial x_i})} \\
 & \qquad \qquad \qquad \text{(re-distribution)} \\
 & - \frac{\partial}{\partial x_k} [\overline{u_i u_j u_k} - \nu \overline{u_i u_j}] \\
 & + \overline{(p'/\rho) (\delta_{jk} u_i + \delta_{ik} u_j)} \Big/ \partial x_k \\
 & \qquad \qquad \qquad \text{(diffusion)} \qquad \qquad \qquad \text{(A2.1)}
 \end{aligned}$$

The accepted physical significance of the various terms is indicated. The modelled equations are obtained by replacing the unknown quantities in the dissipation, diffusion and re-distribution terms by expressions containing calculable ones. In the present work, the modelling used follows closely that developed and used successfully by Hanjalic and Launder (1972), which is summarised below.

The small-scale motions responsible for dissipation of the stresses may be assumed reasonably isotropic, particularly at high Reynolds numbers. Consequently the dissipation term in equation A2.1 can be related directly to the isotropic dissipation rate ϵ of turbulence energy as:

$$2\nu \overline{(\partial u_i / \partial x_k)(\partial u_j / \partial x_k)} = 2\delta_{ij}\epsilon/3 \quad (\text{A2.2})$$

For high Reynolds number flows, the viscous diffusion term can be neglected and the implication of experimental measurement (Hanjalic and Launder, 1972) is that diffusion due to pressure fluctuations is also unlikely to be significant and so that term is also neglected. Hanjalic and Launder (1972) showed that the triple correlations could be approximated in terms of double correlations from a systematic simplification of the triple correlations transport equations. Subsequent experiments by Irwin (1973) have confirmed this approximation which is written as:

$$\begin{aligned} - \overline{u_i u_j u_k} &= C_S (k/\epsilon) (\overline{u_i u_\ell} \partial \overline{u_j u_j} / \partial x_\ell + \overline{u_j u_\ell} \partial \overline{u_k u_i} / \partial x_\ell \\ &+ \overline{u_k u_\ell} \partial \overline{u_i u_j} / \partial x_\ell) \end{aligned} \quad (\text{A2.3})$$

Finally, Hanjalic and Launder (1972) dealt with the 're-distribution' or 'pressure-strain' terms by developing some proposals made by Rotta (1951) in which pressure could be eliminated. This eventually led to the following expressions in terms of the kinematic stresses and mean strain rates:

$$\begin{aligned} \overline{(\rho'/\rho)(\partial u_i/\partial x_j + \partial u_j/\partial x_i)} &= - C_{\phi 1}(\epsilon/k) (\overline{u_i u_j} - 2\delta_{ij}l/3) \\ &+ \overset{mi}{a_{lj}} \partial U_\ell / \partial x_m + \overset{mj}{a_{li}} \partial U_\ell / \partial x_m \end{aligned} \quad (A2.4)$$

Here δ_{ij} is the Kronecker delta, $C_{\phi 1}$ is a coefficient taken to be constant and the fourth order tensors are given by the following approximation:

$$\begin{aligned} \overset{mi}{a_{lj}} &= \alpha \overline{u_m u_i} \delta_{lj} + \beta (\overline{u_m u_\ell} \delta_{ij} + \overline{u_m u_j} \delta_{i\ell} \\ &+ \overline{u_i u_j} \delta_{m\ell} + \overline{u_i u_\ell} \delta_{mj}) + (\gamma \delta_{mi} \delta_{lj} \\ &+ \eta (\delta_{m\ell} \delta_{ij} + \delta_{mj} \delta_{i\ell})) k + C_{\phi 2} (\overline{u_m u_i} \cdot \\ &\overline{u_\ell u_j} - \overline{u_m u_j} \cdot \overline{u_i u_\ell} - \overline{u_m u_\ell} \cdot \overline{u_i u_j}) / k \end{aligned} \quad (A2.5)$$

As shown by Hanjalic and Launder, constraints arising from symmetry and mass continuity requirements allows the further coefficients α , β , γ and η to be expressed in terms of $C_{\phi 2}$ as:

$$\begin{aligned} \alpha &= (10 - 8 C_{\phi 2})/11, & \beta &= - (2 - 6 C_{\phi 2})/11, \\ \gamma &= - (4 - 12 C_{\phi 2})/55, & \eta &= (6 - 18 C_{\phi 2})/55 \end{aligned} \quad (A2.6)$$

Substitution of equations A2.2 to A2.4 into equations A2.1 yields:

APPENDIX 3 GENERAL ORTHOGONAL CO-ORDINATE
TRANSFORMATIONS

In the transformation method of Pope (1978), vectors and tensors are represented in terms of their components in the direction of their orthogonal co-ordinate lines relative to the Cartesian system. Distances ds in the orthogonal co-ordinate system y_i are related to the Cartesian system x_i by

$$ds^2 = dx_i^2 = (h_i dy_i)^2 = (dy(i))^2 \quad (A3.1)$$

where the scale factors h_i are excluded from the summation convention.

The transformations used are:-

$$\text{scalar } \phi: \quad \partial\phi/\partial x_i \rightarrow \nabla(i) \phi \quad (A3.2)$$

$$\text{vector } A_i: \quad \partial A_i/\partial x_i \rightarrow \nabla(i) A(i) \quad (A3.3)$$

$$\begin{aligned} \text{tensor } T_{ij}: \quad \partial T_{ij}/\partial x_i &\rightarrow \nabla(i) T_{ij} - H_i(j) T(ii) \\ &+ H_j(i) T(ij) \end{aligned} \quad (A3.4)$$

where $\nabla(i) \equiv (h_i/\bar{H})\partial/\partial y(i)\bar{H}/h_i$ with \bar{H} as the product of the scale factors (thus \bar{H} represents the volume ratio between co-ordinate systems). $H_i(j)$ is the inverse of the local radius of curvature of the j co-ordinate line. The derivation and further details of these transformations are given in Pope (1978).

The above transformations enable equations written in Cartesian co-ordinates to be transformed directly into the general orthogonal system.

Applying these transformations to the Reynolds equations (2.2.1) and continuity equation (2.2.2) there results:-

$$\begin{aligned} \nabla(i) (\rho U(i)U(j)) &= - \partial p / \partial x(i) - \nabla(i) (\tau(ij)) \\ &+ H_i(j) [\rho U(i)U(i) + \tau(ii)] \\ &- H_j(i) [\rho U(i)U(j) + \tau(ij)] \end{aligned} \quad (A3.5)$$

$$\nabla(i) (\rho U(i)) = 0 \quad (A3.6)$$

In this compact general orthogonal form, the terms in the Reynolds equations (A3.5) retain their clear physical significance, as in the original Cartesian tensor version. In addition, the physical significance of the extra terms (with square brackets), gained as a consequence of co-ordinate curvature and momentum being conserved in a straight line only, is clearly evident.

The scalar transport equation 2.3.1 transforms into orthogonal co-ordinates as

$$\nabla(i)(\rho U(i)C) = \nabla(i)(D_c \partial C / \partial x(i) - \overline{u_i c}) + S_c \quad (A3.7)$$

APPENDIX 4 MODELLING THE TURBULENT HEAT FLUX
TRANSPORT EQUATIONS

An exact transport equation for $\overline{u_i c}$ can be obtained by multiplying the instantaneous thermal energy equation (with dependant variable $(C + c)$) by u_i and adding it to the x_i component of the Navier-Stokes equation multiplied by c . The time-averaged result, simplified by neglecting body forces and steady incompressible turbulent flow with negligible fluctuations in molecular viscosity and thermal conductivity is:

$$\begin{aligned}
 U_k \frac{\partial(\overline{u_i c})}{\partial x_k} &= - \overline{u_i u_k} \frac{\partial C}{\partial x_k} + \overline{u_k c} \frac{\partial U_i}{\partial x_k} \\
 \text{(convection)} & \qquad \qquad \qquad \text{(generation)} \\
 & - (D_C + \nu) \overline{\left(\frac{\partial c}{\partial x_k}\right) \left(\frac{\partial u_i}{\partial x_k}\right)} \\
 & \qquad \qquad \qquad \text{(dissipation)} \\
 & - \frac{\partial(\overline{u_k u_i c} + (\overline{p' c / \rho}) \delta_{ik})}{\partial x_k} \\
 & \qquad \qquad \qquad \text{(diffusion)} \\
 & + \overline{\left(\frac{p'}{\rho}\right) \frac{\partial c}{\partial x_i}} \\
 & \qquad \qquad \qquad \text{(redistribution)}
 \end{aligned} \tag{A4.1}$$

where p' is the fluctuating component of the instantaneous pressure, C is the enthalpy and c its fluctuating component. As in the derivation of the ASTM, local equilibrium is assumed so that convection and diffusion can be neglected and dissipation can be assumed negligible if the Reynolds number is high. The re-distribution

term can be modelling analogously to its pressure-strain counterpart in the Reynolds stress transport equation, as proposed by Launder (Chapter 6, Bradshaw, 1978)

$$\overline{(p'/\rho)\partial c/\partial x_i} = C_1 C(\epsilon/k)\overline{u_i c} + C_2 C\overline{u_k c}\partial u_i/\partial x_k \quad (A4.2)$$

This gives a modelled turbulent heat flux transport equation of:

$$\begin{aligned} - \overline{u_i u_k} \partial c/\partial x_k - \overline{u_k c} \partial u_i/\partial x_k + C_1 C(\epsilon/k)\overline{u_i c} \\ + C_2 C\overline{u_k c} \partial u_i/\partial x_k = 0 \end{aligned} \quad (A4.3)$$

The turbulent heat fluxes $\overline{u_k c}$ can be extracted from equation (A4.3) as algebraic equations involving k , ϵ and gradients of velocity and enthalpy.

APPENDIX 5 ORTHOGONAL CURVILINEAR GRID
CALCULATION METHOD

A simple numerical finite-difference method (Antonopoulos et al, 1978) was used to calculate the orthogonal curvilinear co-ordinate grids required to fit each passage cross-sectional shape. A rectangular mesh of straight lines y_1 and y_2 in transformed space is mapped into a set of orthogonal curvilinear lines with Cartesian co-ordinates x_1 and x_2 in the required non-rectangular physical field, as illustrated in figure A5.1. This basic concept has, of course, been used many times before (e.g. Winslow, 1967; Barfield, 1970, Thompson, Thames and Mastin, 1974, Pope, 1978). The condition of orthogonality leads to the following pair of Laplace equations linking the two co-ordinate frames:

$$\begin{aligned} \partial^2 x_1 / \partial y_1^2 + \partial^2 x_1 / \partial y_2^2 &= 0 \\ \partial^2 x_2 / \partial y_1^2 + \partial^2 x_2 / \partial y_2^2 &= 0 \end{aligned} \tag{A5.1}$$

In these equations, the metric coefficients have all been assumed unity to simplify the calculation method for the cases presented in this thesis (this has the effect of making the transformation conformal). It is noted that these would need to be included if the present method is applied to passage geometries of more extreme curvature.

At the boundaries of the domain, the mesh must satisfy the shape equation of the boundary and, for orthogonality, the Cauchy-Riemann equations. The latter are satisfied by applying the

conditions

$$(\partial x_2 / \partial x_1)_{y_1} (\partial x_2 / \partial x_1)_{y_2} = - 1 \quad (A5.2)$$

The Laplace equations (A5.1) are solved by finite-differences with equations obtained by integration over the appropriate cells. With reference to figure A5.2, the equation for x_{1p} is

$$\begin{aligned} & ((x_{1E} - x_{1P}) / (y_{1E} - y_{1P}) - (x_{1P} - x_{1W}) / (y_{1P} - y_{1W})) / (y_{1E} - y_{1W}) \\ & + ((x_{1N} - x_{1P}) / (y_{1N} - y_{1P}) - (x_{1P} - x_{1S}) / (y_{1P} - y_{1S})) / (y_{1N} - y_{1S}) \end{aligned}$$

yielding

$$\begin{aligned} x_{1P} = & ((x_{1E} \Delta EP + x_{1W} \Delta PW) \Delta EW + (x_{1N} \Delta NP + x_{1S} \Delta PS) \Delta NS) \\ & / ((\Delta EP + \Delta PW) \Delta EW + (\Delta NP + \Delta PS) \Delta NS) \end{aligned} \quad (A5.3)$$

$$\begin{aligned} \text{where } \Delta EP &= 1 / (y_{1E} - y_{1P}) \\ \Delta PW &= 1 / (y_{1P} - y_{1W}) \\ \Delta EW &= 1 / (y_{1E} - y_{1W}) \\ \Delta NP &= 1 / (y_{2N} - y_{2P}) \\ \Delta PS &= 1 / (y_{2P} - y_{2S}) \\ \Delta NS &= 1 / (y_{2N} - y_{2S}) \end{aligned} \quad (A5.4)$$

A similar equation can be derived for x_{2p} . These equations are solved by point iteration with the boundary nodes updated before each iteration by applying the conditions of orthogonality (equation A5.2) mid-way between the boundary and the nearest interior node and simultaneously with the shape equation for the boundary. An example boundary is shown in figure A5.3 with the boundary node 'b' required

along the y_2 line through interior node 'a'. Equation A5.2 is written

$$\left(\frac{dx_2}{dx_1}\right)_{y_{1m}} \left(\frac{dx_2}{dx_1}\right)_{y_{2a}} = -1 \quad (\text{A5.5})$$

Integrating between a and b yields

$$\left(\frac{dx_2}{dx_1}\right)_{y_{1m}} (x_{2b} - x_{2a}) / (x_{1b} - x_{1a}) = -1 \quad (\text{A5.6})$$

The boundary shape equation is in this case

$$x_{2b} = 0 \quad (\text{A5.7})$$

From A5.6
$$x_{1b} = x_{1a} + x_{2a} \tan(\alpha/2) \quad (\text{A5.8})$$

which are the Cartesian co-ordinates of the boundary node 'b'. The approximations involved with this method enabled the boundary nodes to be calculated directly, as shown in the above illustration, and did not appear to cause a noticeable error in the solution for the passage shapes calculated.

In order to procure good convergence it was found necessary to calculate initial locations for the grid nodes in the physical plane. This was usually achieved with a combination of cylindrical polar and rectangular meshes calculated to fit the domain.

APPENDIX 6 SOURCE TERMS IN THE FINITE-DIFFERENCE EQUATIONS

A6.1 Introduction

In the formulation of the finite-difference equation for ϕ , the source is assumed constant over the area of integration in each control volume (see section 5.3 and equation (5.3.6)). The methods used to obtain the required finite-difference equivalent of various source terms with the orthogonal curvilinear mesh used in the present procedure are described in detail in this Appendix.

A6.2 Generation of turbulence kinetic energy

This part of the turbulence kinetic energy source received special attention in the present work as described in section 7.6. Referring to figure 5.2.2a, the finite-difference equivalent of equation (4.3.6) was obtained as follows:

$$\text{let } \bar{P} = (1/V_p) \int_S^n \int_W^e P \Delta Z dy_1 dy_2$$

$$\text{then } \bar{P} = - (\rho \overline{u_1 u_3})_m (\partial U_3 / \partial S_1)_m - (\rho \overline{u_2 u_3})_m (\partial U_3 / \partial S_2)_m$$

$$\text{where } (-\rho \overline{u_1 u_3})_m = [\mu_{te} (\partial U_3 / \partial S_1)_e S_{1PW} + \mu_{tw} (\partial U_3 / \partial S_1)_w S_{1PE}] / (S_{1PE} + S_{1PW})$$

$$\text{and } (\partial U_3 / \partial S_1)_m = [(\partial U_3 / \partial S_1)_e S_{1PW} + (\partial U_3 / \partial S_1)_w S_{1PE}] / (S_{1PE} + S_{1PW})$$

$$\begin{aligned} \text{with} \quad \mu_{te} &= (\mu_{tE} + \mu_{tP})/2 \\ \mu_{tw} &= (\mu_{tP} + \mu_{tW})/2 \\ (\partial U_3 / \partial S_1)_e &= (U_{3E} - U_{3P}) / S_{1PE} \\ (\partial U_3 / \partial S_1)_w &= (U_{3P} - U_{3W}) / S_{1PW} \end{aligned}$$

$$\begin{aligned} \text{and where} \quad - (\rho \overline{u_2 u_3})_m &= [\mu_{tn} (\partial U_3 / \partial S_2)_n S_{2PS} + \mu_{ts} (\partial U_3 / \partial S_2)_s S_{2PN}] \\ &\quad / (S_{2PN} + S_{2PS}) \end{aligned}$$

$$\begin{aligned} \text{and} \quad (\partial U_3 / \partial S_2)_m &= [(\partial U_3 / \partial S_2)_n S_{2PS} + (\partial U_3 / \partial S_2)_s S_{2PN}] \\ &\quad / (S_{2PN} + S_{2PS}) \end{aligned}$$

$$\begin{aligned} \text{with} \quad \mu_{tn} &= (\mu_{tN} + \mu_{tP})/2 \\ \mu_{ts} &= (\mu_{tP} + \mu_{tS})/2 \\ (\partial U_3 / \partial S_2)_n &= (U_{3N} - U_{3P}) / S_{2PN} \\ (\partial U_3 / \partial S_2)_s &= (U_{3P} - U_{3S}) / S_{2PS} \end{aligned}$$

A6.3 Cross-plane momentum source

The U_1 momentum source as shown in Table 5.3.1 but excluding the pressure gradient and laminar viscosity terms was treated in the following manner:

$$\begin{aligned} \text{let } C_1 &= - \partial(h_2 \rho \overline{u_1 u_1}) / \partial y_1 - \partial(h_1 \rho \overline{u_1 u_2}) / \partial y_2 \\ &\quad - h_1 h_2 (-\rho U_2 U_2 - \rho \overline{u_2 u_2}) / r_2 \\ &\quad + h_1 h_2 (-\rho U_1 U_2 - \rho \overline{u_1 u_2}) / r_1 \end{aligned}$$

$$\text{if } \bar{C}_1 = (1/V_p) \int_S^n \int_W^e C_1 \Delta Z dy_1 dy_2$$

$$\begin{aligned} \text{then } \bar{C}_1 &= - [\partial(\rho \bar{u}_1 \bar{u}_1) / \partial S_1]_m - [\partial(\rho \bar{u}_1 \bar{u}_2) / \partial S_2]_m \\ &+ [(\rho U_2 U_2 + \rho \bar{u}_2 \bar{u}_2) / r_2]_m \\ &+ [(\rho U_1 U_2 - \rho \bar{u}_1 \bar{u}_2) / r_1]_m \end{aligned}$$

where (referring to the U_1 cell in figure 5.2.2b)

$$- [\partial(\rho \bar{u}_1 \bar{u}_1) / \partial S_1]_m = - ((\rho \bar{u}_1 \bar{u}_1)_e - (\rho \bar{u}_1 \bar{u}_1)_w)^2 / (S_{1s} + S_{1n})$$

$$- [\partial(\rho \bar{u}_1 \bar{u}_2) / \partial S_2]_m = - ((\rho \bar{u}_1 \bar{u}_2)_n - (\rho \bar{u}_1 \bar{u}_2)_s)^2 / (S_{2e} + S_{2w})$$

$$[(\rho U_2 U_2 + \rho \bar{u}_2 \bar{u}_2) / r_1]_m = (\rho U_{2p}^2 + (\rho \bar{u}_2 \bar{u}_2)_p) / r_{1p}$$

$$[(\rho U_1 U_2 + \rho \bar{u}_1 \bar{u}_2) / r_2]_m = (\rho U_{1p} U_{2p} + (\rho \bar{u}_1 \bar{u}_2)_p) / r_{2p}$$

$$\text{with } (\rho \bar{u}_1 \bar{u}_2)_n = ((\rho \bar{u}_1 \bar{u}_2)_e + (\rho \bar{u}_1 \bar{u}_2)_w + (\rho \bar{u}_1 \bar{u}_2)_f + (\rho \bar{u}_1 \bar{u}_2)_g) / 4$$

$$(\rho \bar{u}_1 \bar{u}_2)_s = ((\rho \bar{u}_1 \bar{u}_2)_e + (\rho \bar{u}_1 \bar{u}_2)_w + (\rho \bar{u}_1 \bar{u}_2)_h + (\rho \bar{u}_1 \bar{u}_2)_k) / 4$$

$$U_{2p} = (U_{2a} + U_{2b} + U_{2c} + U_{2d}) / 4$$

$$(\rho \bar{u}_2 \bar{u}_2)_p = ((\rho \bar{u}_2 \bar{u}_2)_e + (\rho \bar{u}_2 \bar{u}_2)_w) / 2$$

$$(\rho \bar{u}_1 \bar{u}_2)_p = ((\rho \bar{u}_1 \bar{u}_2)_e + (\rho \bar{u}_1 \bar{u}_2)_w) / 2$$

$$r_{1p} = (r_{1e} + r_{1w}) / 2$$

$$r_{2p} = (r_{2e} + r_{2w}) / 2$$

A6.4 Enthalpy source

From Table 5.3.1 let

$$C_h = - \partial(h_1 h_2 \rho U_3 C) / \partial y_3$$

$$\text{if } \bar{C}_h = (1/V_p) \int_S^n \int_W^e C_h \Delta Z dy_1 dy_2$$

$$\text{then } \bar{C}_h = - [\partial(\rho U_3 C) / \partial S_3]_m$$

$$\bar{C}_h = - \rho C_p U_3 (\partial T / \partial S_3)_m \quad (\text{A6.4.1})$$

Also let

$$\theta_T = (\bar{T}_w - T) / (\bar{T}_w - T_b) \quad (\text{A6.4.2})$$

For fully developed temperature profiles

$$\partial \theta_T / \partial S_3 = 0 \quad (\text{A6.4.3})$$

and $\partial T / \partial S_3$ depends on the boundary conditions as follows:

(i) H1 (constant peripheral temperature and axial heat flux)

An energy balance for incremental axial length dS_3 of passage with perimeter M and with constant axial heat flux \dot{q}'' yields:

$$\dot{q}'' M = d \left(\int_0^A \rho C_p U_3 T dA \right) / dS_3 = \dot{m} C_p dT_b / dS_3$$

$$\text{i.e. } dT_b / dS_3 = \dot{q}'' M / \dot{m} C_p = \text{constant} \quad (\text{A6.4.4})$$

From (A6.4.3) it follows that

$$\partial T / \partial S_3 = dT_b / dS_3 = \text{constant} = B \quad (\text{A6.4.5})$$

with $(\partial T/\partial S_3)_m = B$ (A6.4.6)

(ii) H2 (constant peripheral and axial wall temperature)

From equation (A6.4.2), with $\bar{T}_w = T_w = \text{constant}$, then

$$dT_w/dS_3 - \partial T/\partial S_3 = \theta_T dT_w/dS_3 - \theta_T dT_b/dS_3$$

since $dT_w/dS_3 = 0$

then $\partial T/\partial S_3 = \theta_T dT_b/dS_3 = \theta_T B$ (A6.4.7)

with $(\partial T/\partial S_3)_m = B(T_w - T_p)/(T_w - T_b)$ (A6.4.8)

(iii) H3 (constant peripheral and axial heat flux)

As with the H1 boundary condition

$$\partial T/\partial S_3 = dT_b/dS_3 = \text{constant} = B$$
(A6.4.5)

and $(\partial T/\partial S_3)_m = B$ (A6.4.6)

APPENDIX 7 TRI-DIAGONAL MATRIX ALGORITHM (TDMA)

The TDMA (see for example, Forsythe and Wasow, 1960) solves a set of simultaneous linear equations of the general form:

$$\phi_i = A_i \phi_{i+1} + B_i \phi_{i-1} + C_i \quad (\text{A7.1})$$

where A_i , B_i and C_i are constants and the subscript i runs from 1 to N with $A_N = B_1 = 0$. If the equation set is re-written as

$$\phi_i = A_i' \phi_{i+1} + B_i' \quad (\text{A7.2})$$

where

$$A_i' = A_i / (1 - B_i A_{i-1}') \quad (\text{A7.3})$$

$$B_i' = (B_i B_{i-1}' + C_i) / (1 - B_i A_{i-1}') \quad (\text{A7.4})$$

then equations (A7.3) and (A7.4) become recurrence relations and equation (A7.2) can be solved by successive substitution.

In this 'block adjustment' procedure (Gosman et al, 1977), the sum of the residual sources are reduced to zero (i.e. the relevant conservation equation is satisfied) along strips of cells which cover the solution domain. From equation (5.3.13), for any variable ϕ , an increment $\delta\phi_i$ added to the value of ϕ_p at each node along a strip 'i' of cells will reduce the sum of the residual sources in that strip to zero if

$$\begin{aligned} \sum(A_p - g)(\phi_p + \delta\phi_i) &= \sum[A'_W(\phi_W + \delta\phi_{i-1}) + A'_E(\phi_E + \delta\phi_{i+1}) \\ &+ A'_N(\phi_N + \delta\phi_i) + A'_S(\phi_S + \delta\phi_i) + e'] \end{aligned} \quad (A8.1)$$

where \sum indicates the sum along a strip of cells. Re-arranging in terms of ϕ_i yields:

$$\begin{aligned} \delta\phi_i \sum(A'_E + A'_W - g) &= \delta\phi_{i+1} \sum A'_E + \delta\phi_{i-1} \sum A'_W \\ &+ \sum[A'_N(\phi_N - \phi_p) + A'_S(\phi_S - \phi_p) + A'_E(\phi_E - \phi_p) \\ &+ A'_W(\phi_W - \phi_p) + g\phi_p - e] \end{aligned} \quad (A8.2)$$

which has the form

$$d_i \delta\phi_i = a_i \delta\phi_{i+1} + b_i \delta\phi_{i-1} + c_i \quad (A8.3)$$

where a_i , b_i , c_i and d_i are coefficients which can be deduced from equation (A8.2).

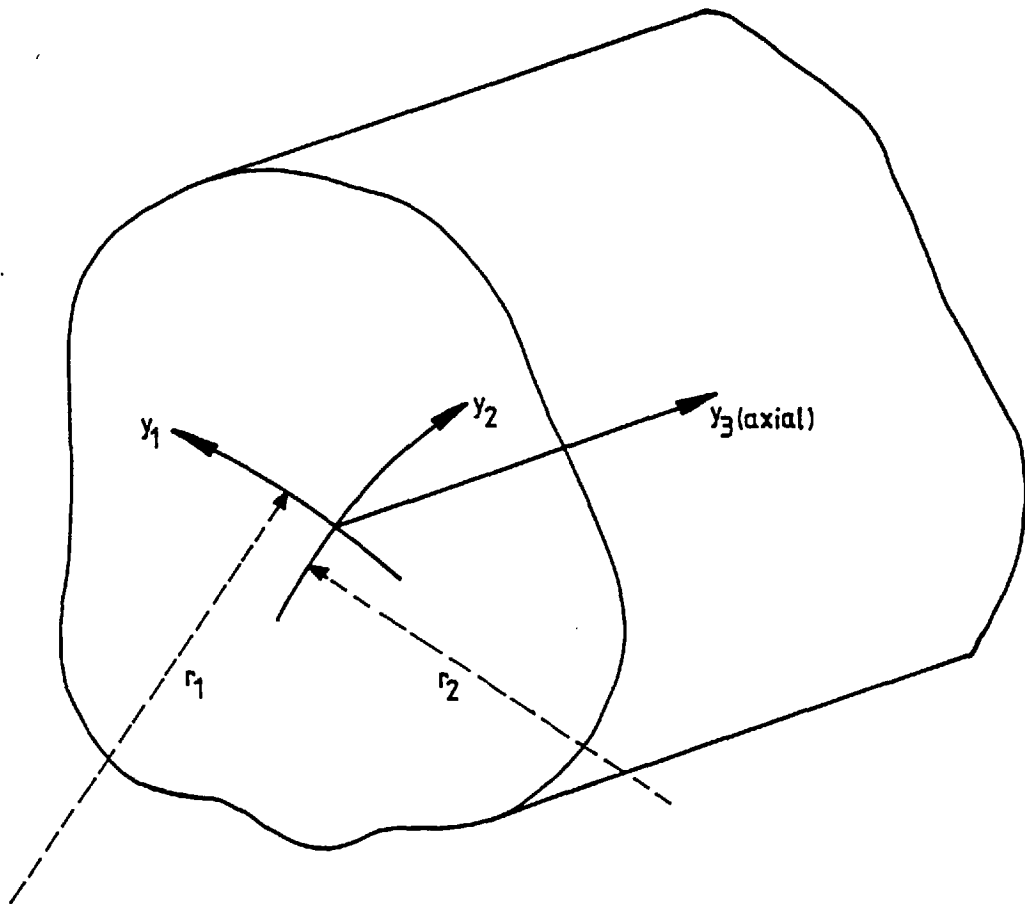


Figure 2.4.1 The orthogonal co-ordinate system.

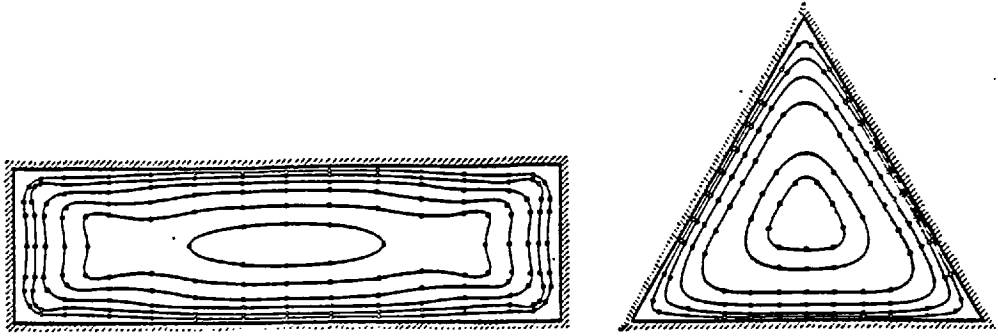
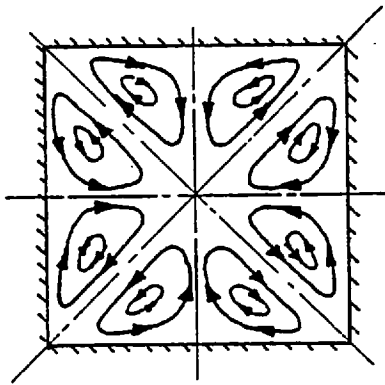
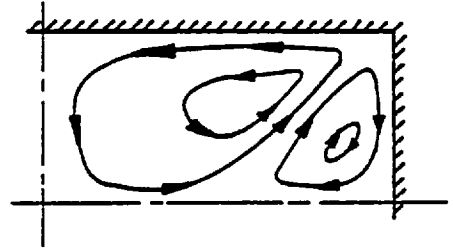


Figure 3.2.1 Experimental axial velocity contours (Nikuradse, 1926, 1930)



(a) square (e.g. Launder & Ying, 1972)



(b) rectangular (Gessner & Jones, AR = 2, 1975)

Figure 3.2.2 Secondary flow patterns in rectangular ducts from experiment.

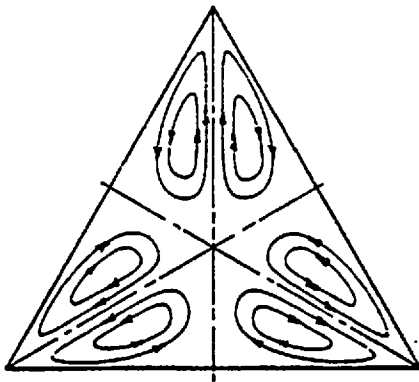


Figure 3.2.3 Secondary flow pattern in an equilateral triangular duct from experiment (Aly et al, 1978)

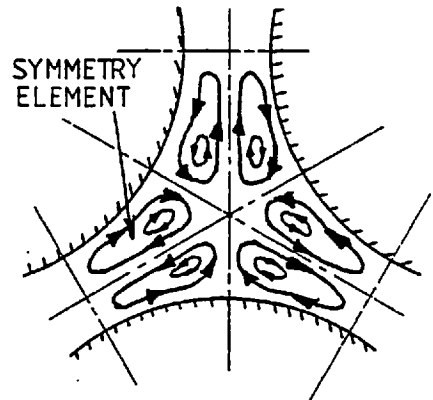


Figure 3.2.4 Secondary flow pattern in a triangular array rod bundle, postulated by Trupp & Azad (1975)

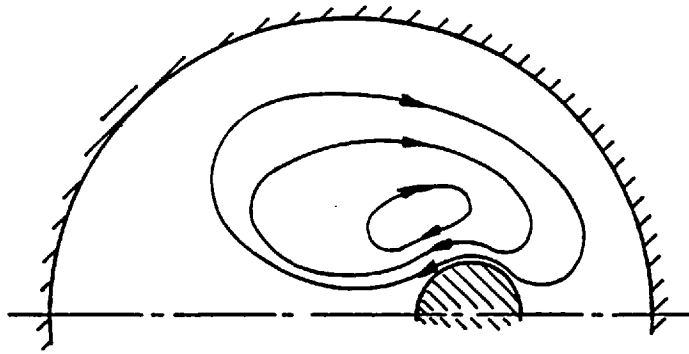
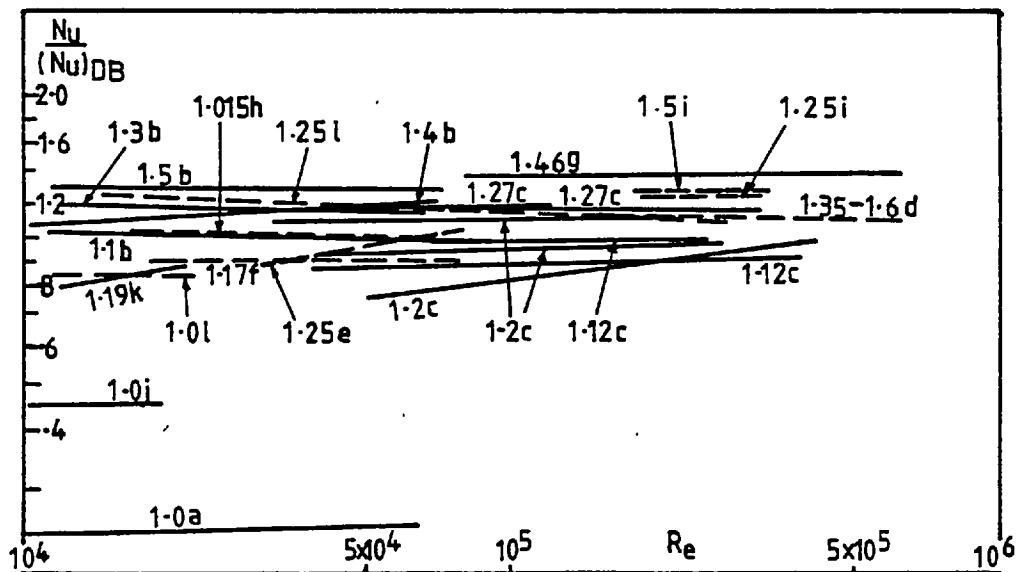


Figure 3.2.5 Secondary flow pattern from experiment in a circular tube containing an offset pin (Kacker, 1973)



Reference: a Bobkov et al(1974) g Miller et al(1956)
 b Borishansky et al(1971) h Palmer & Swanson(1961)
 c Dingee & Chastain(1956) i Redman et al(1966)
 d Draycott & Lawther(1961) j Subbotin et al(1960)
 e Kidd & Stelzman(1968) k Wantland(1956)
 f Lel'chuk et al(1977) l Sutherland & Kays(1966)

—— water - - - air

Figure 3.3.1 Experimental triangular-array rod bundle heat transfer

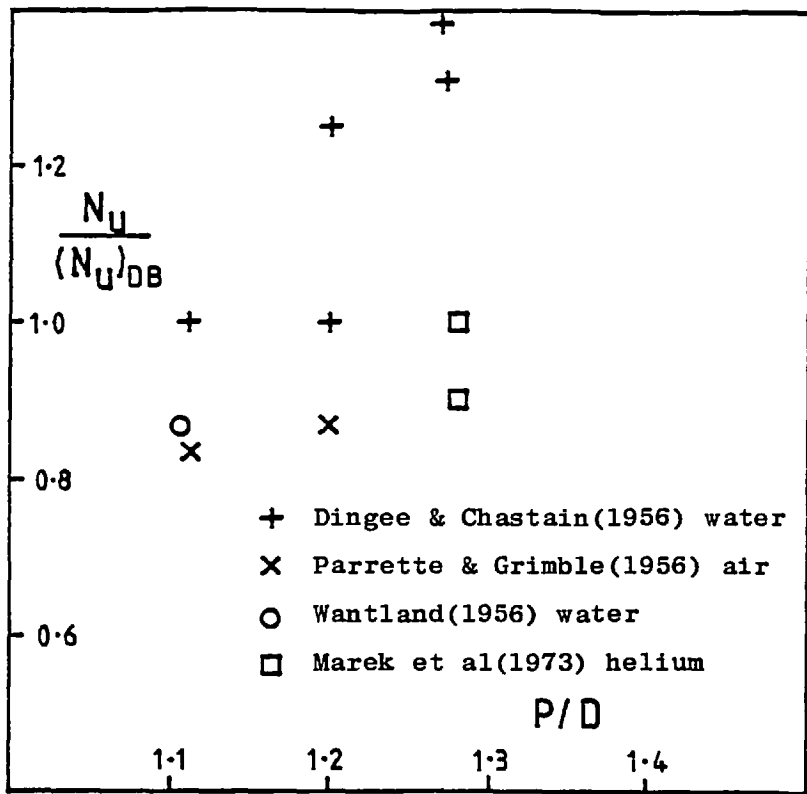


Figure 3.3.2 Experimental square-array rod bundle heat transfer with $Re = 5 \times 10^4$.

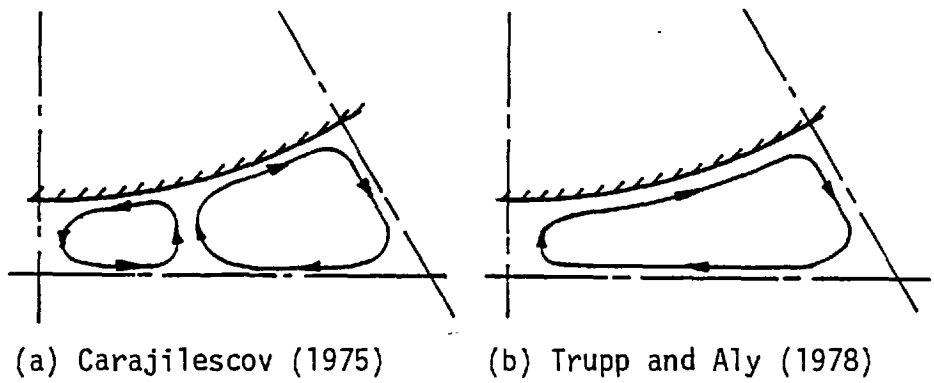
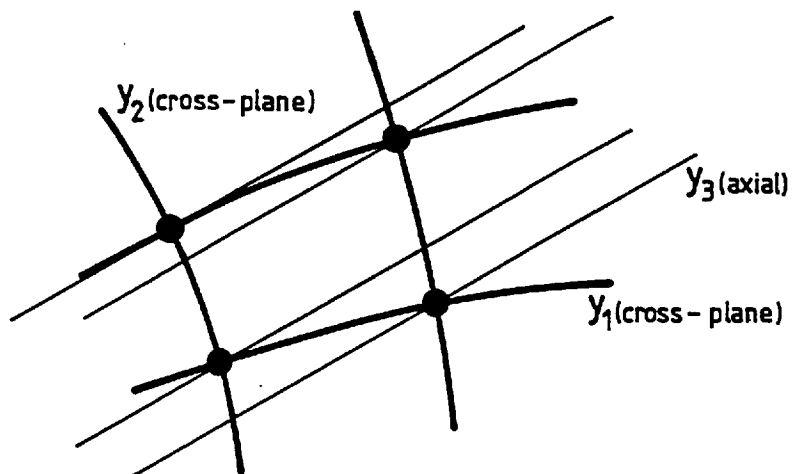
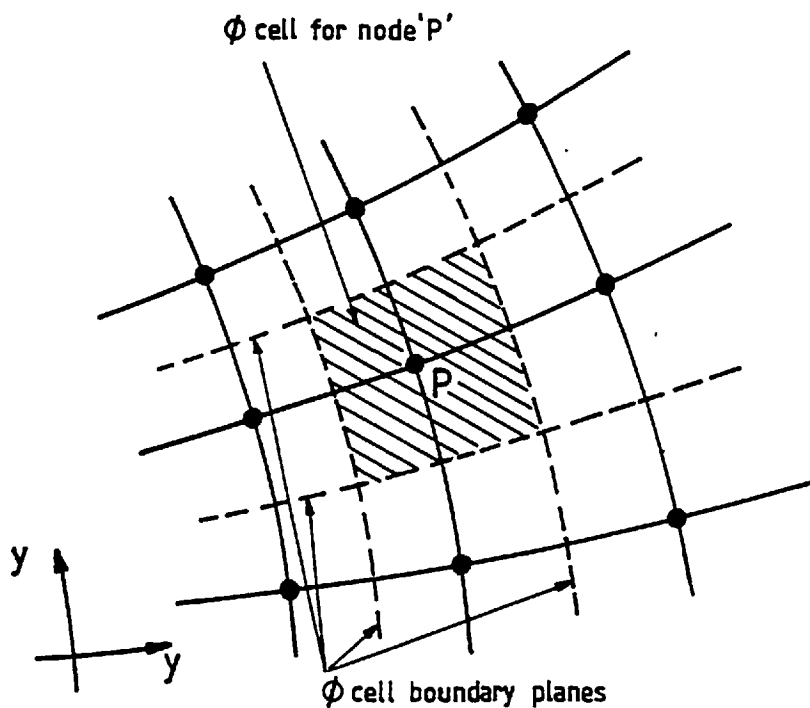


Figure 3.4.1 Calculated secondary flow patterns in a rod bundle with $P/D = 1.123$.

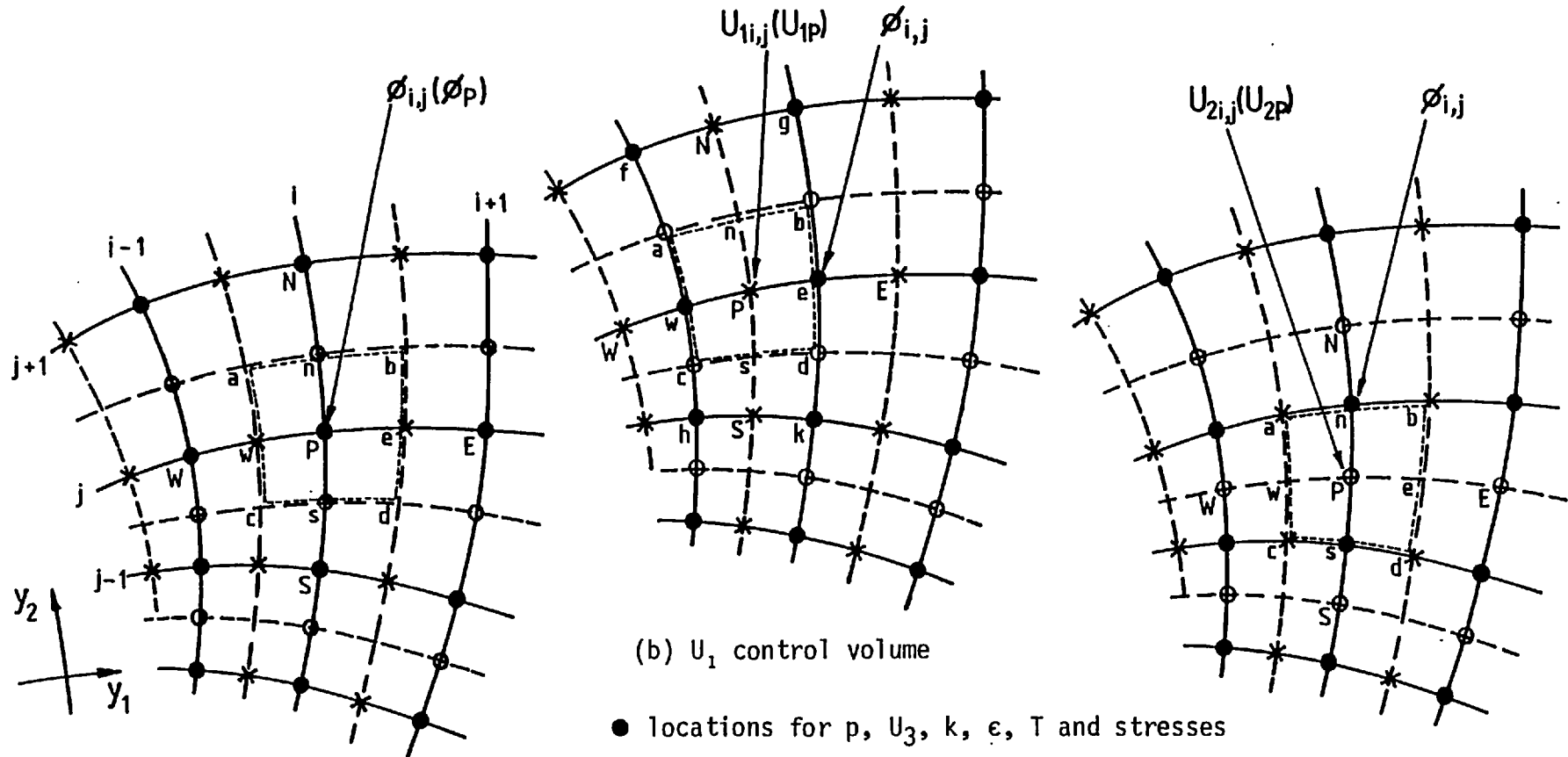


(a) a portion of the finite-difference grid



(b) a ϕ control-volume cell in the passage cross-plane

Figure 5.2.1 The main orthogonal curvilinear grid.



(a) ϕ control volume

(b) U_1 control volume

(c) U_2 control volume

● locations for p , U_3 , k , ϵ , T and stresses

× locations for U_1

○ locations for U_2

----- boundaries of control volume cells

Arc lengths:

between nodes		cell faces	
NP = S_{2PN}	EP = S_{1PE}	awc = S_{2w}	anb = S_{1n}
PS = S_{2PS}	PW = S_{1PW}	bed = S_{2e}	csd = S_{1s}

Figure 5.2.2 The staggered grid arrangement.

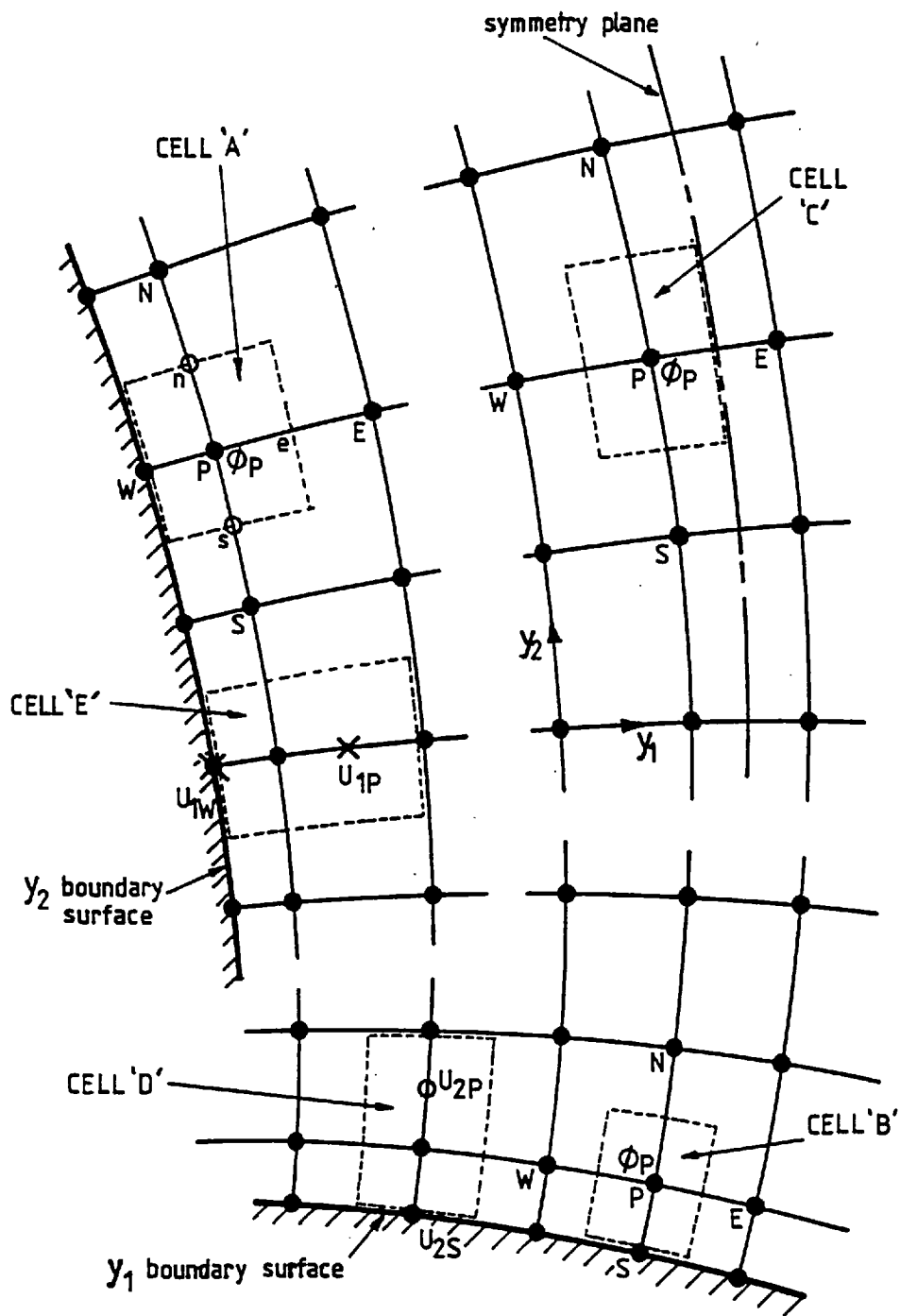


Figure 5.5.1 Near-boundary control volume cells

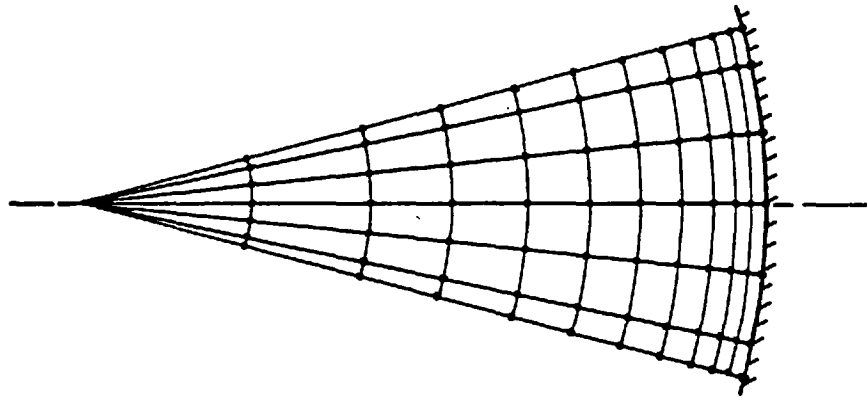


Figure 5.8.1 Polar-cylindrical grid for a circular tube

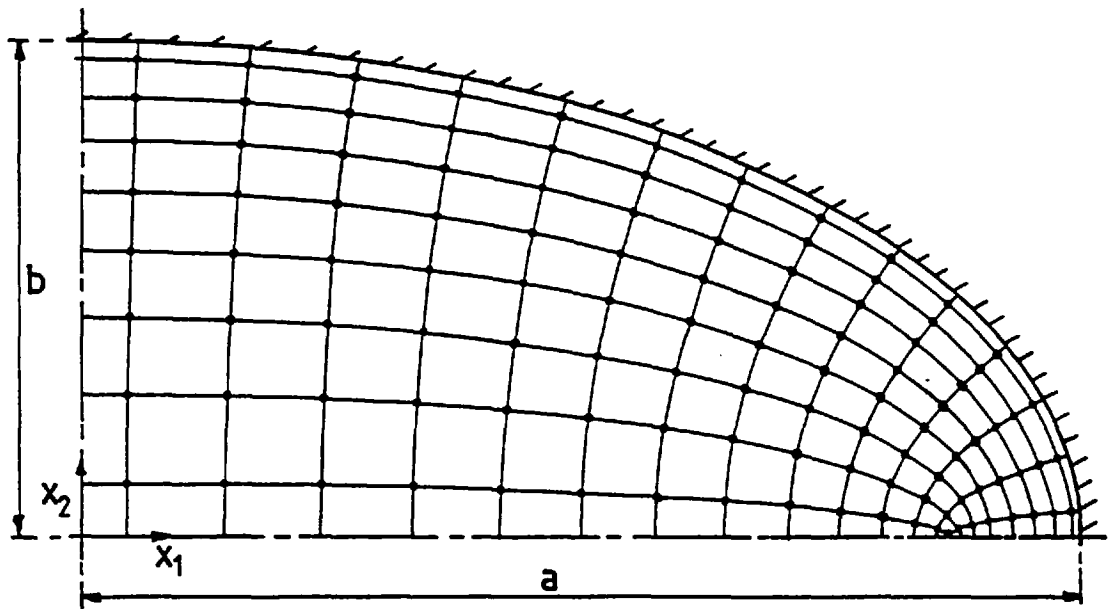


Figure 5.8.2 Curvilinear-orthogonal grid for a quadrant of an elliptical duct with $AR = 2.0$.

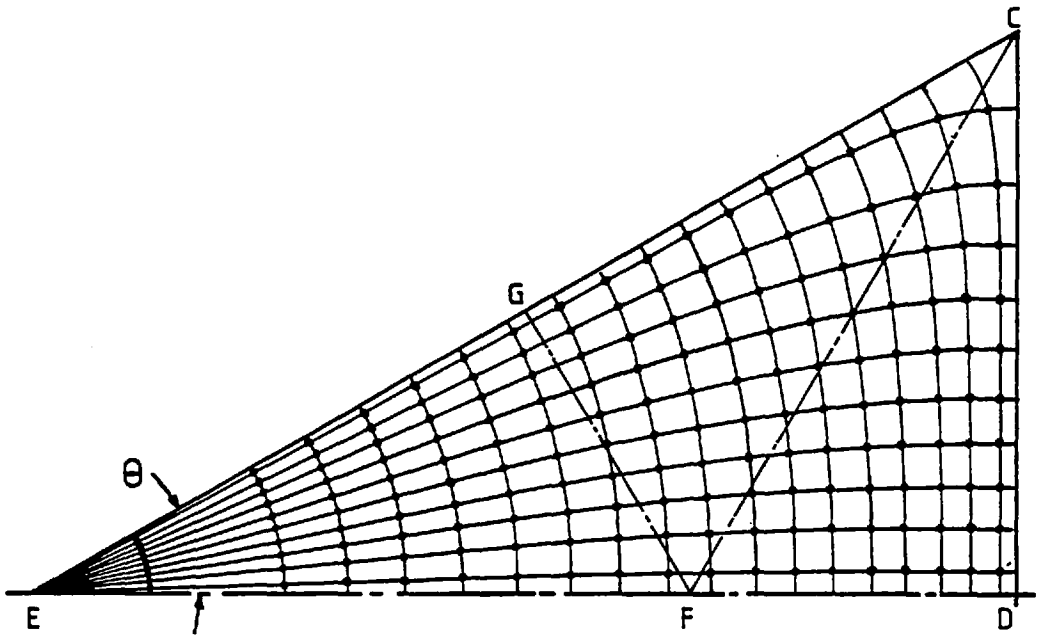


Figure 5.8.3 Curvilinear-orthogonal grid for an equilateral triangular half-duct.

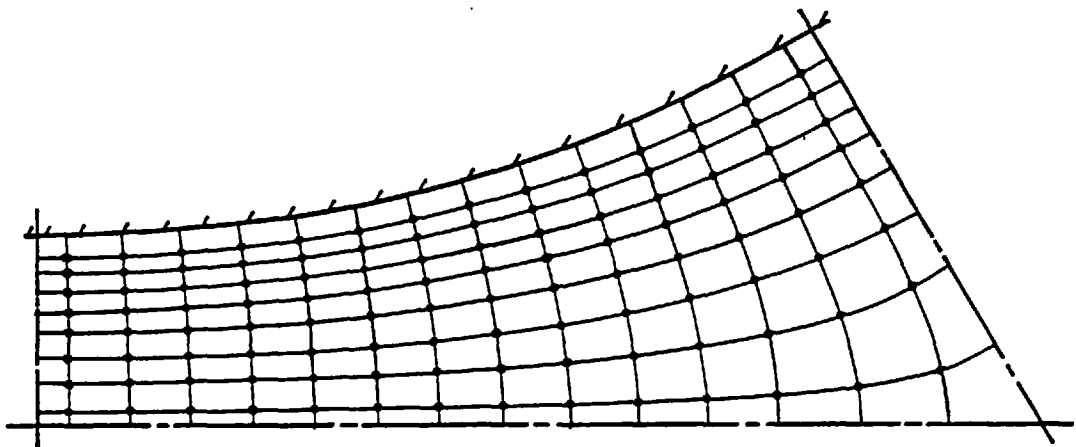


Figure 5.8.4 Curvilinear-orthogonal grid for a symmetry element of a triangular-array rod bundle with $P/D = 1.1$.

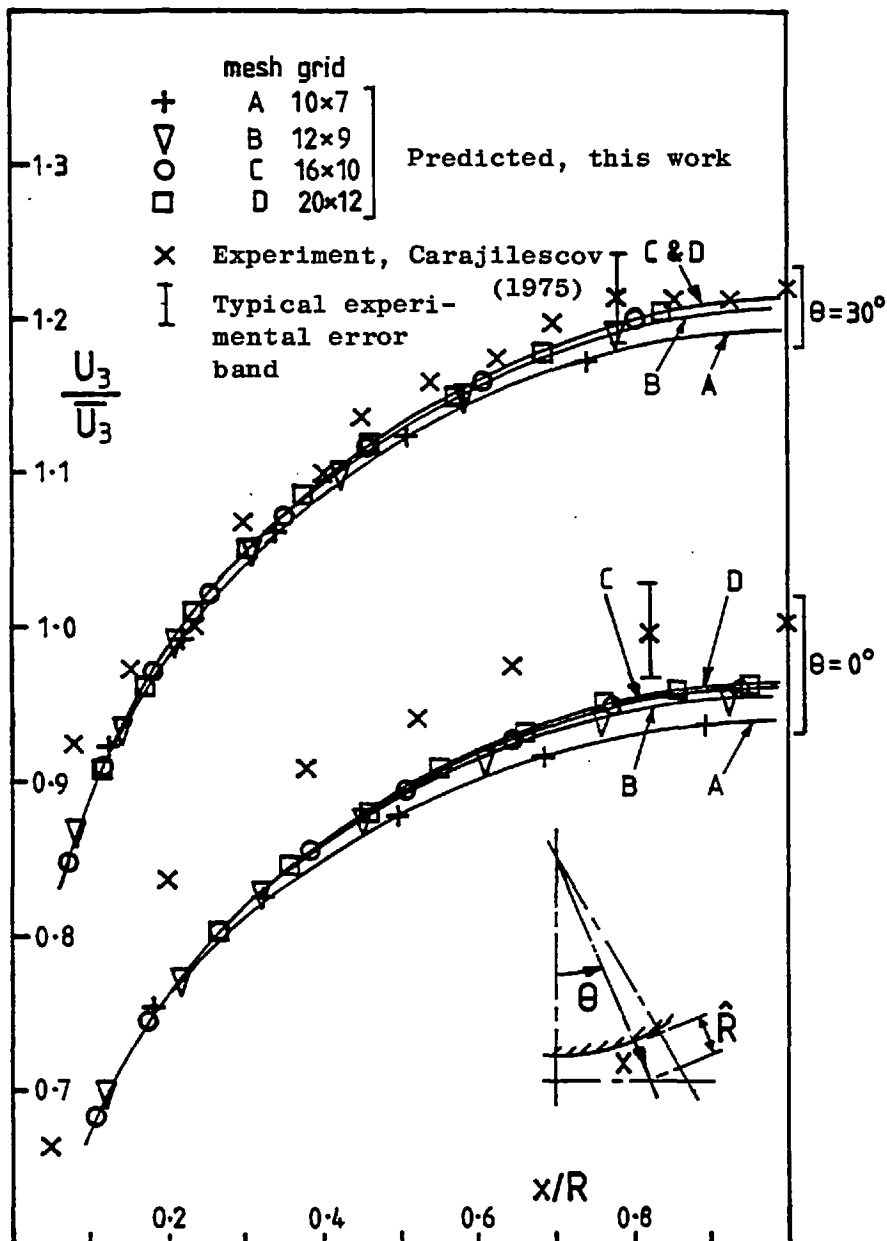


Figure 5.9.1 Grid refinement tests for axial velocity in a rod bundle with $P/D = 1.1$ and $Re = 2.7 \times 10^4$.

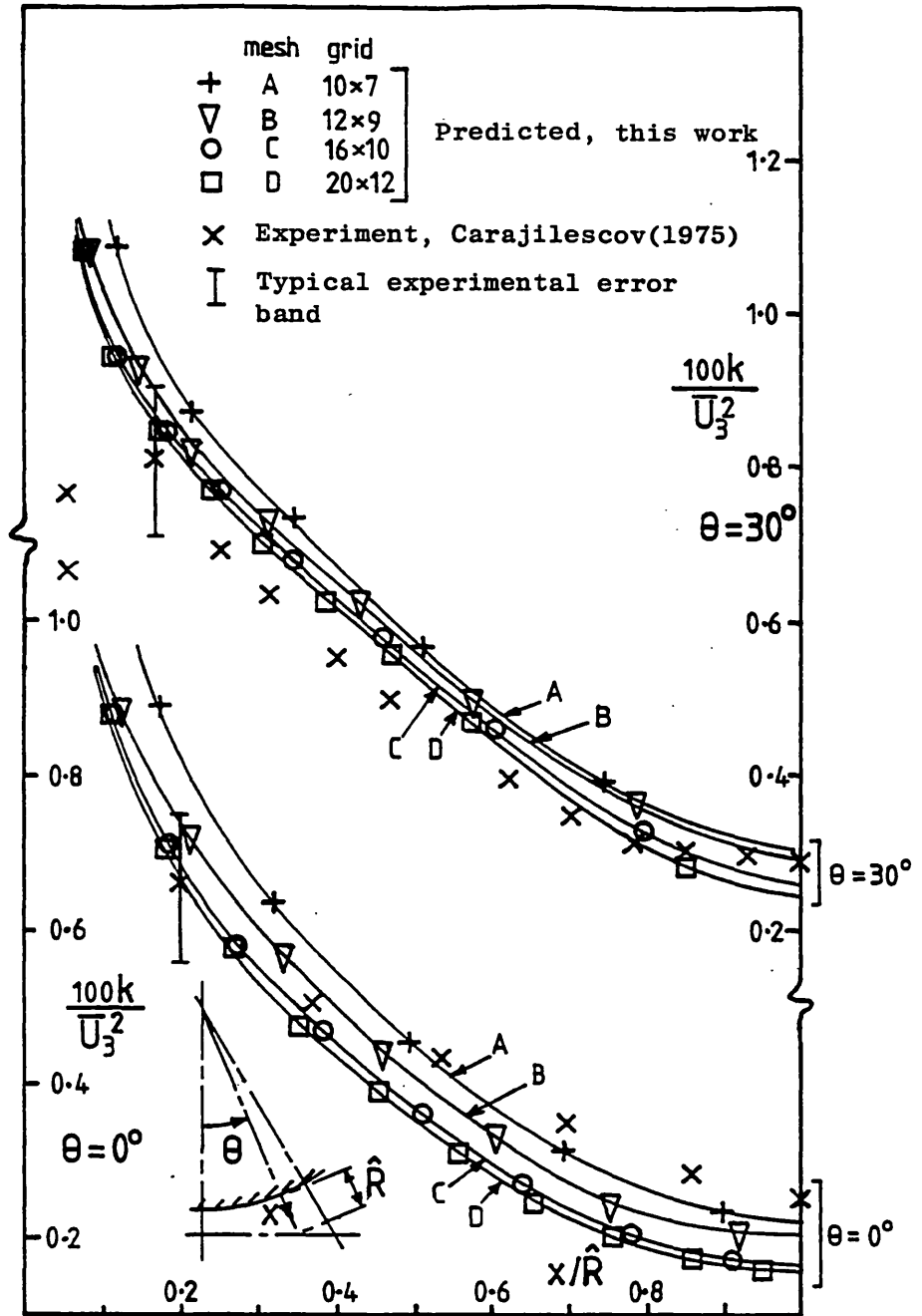


Figure 5.9.2 Grid refinement tests for turbulence kinetic energy in a rod bundle with $P/D = 1.1$ and $Re = 2.7 \times 10^4$.

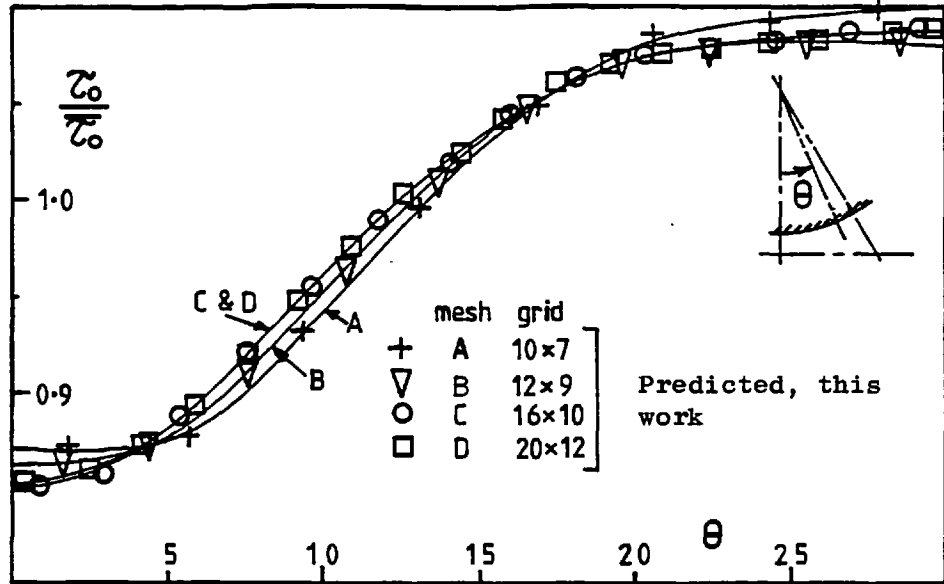


Figure 5.9.3 Grid refinement tests for wall shear stress in a rod bundle with $P/D = 1.1$ and $Re = 2.7 \times 10^4$.

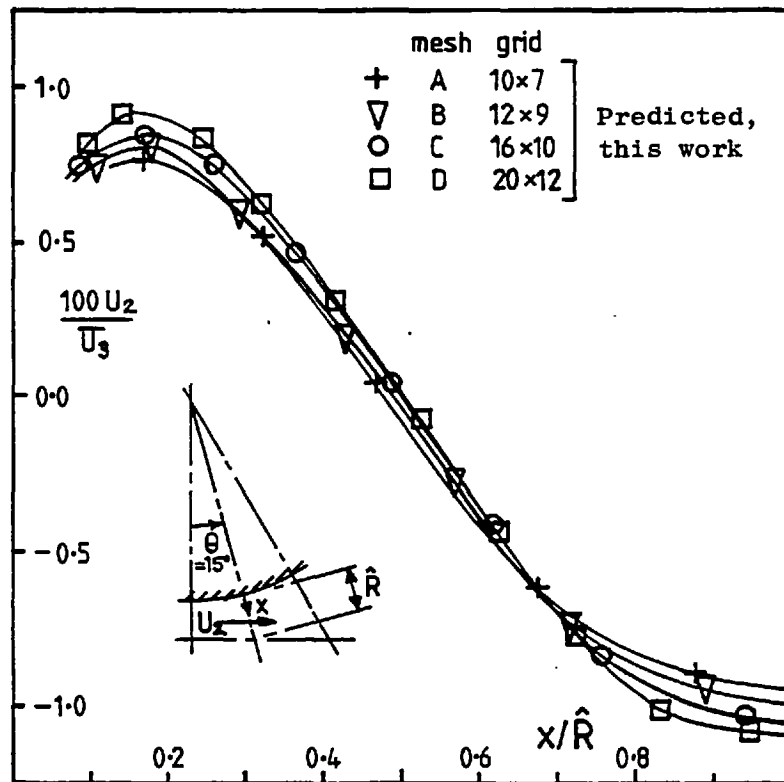


Figure 5.9.4 Grid refinement tests for secondary velocity (U_2) in a rod bundle with $P/D = 1.1$ and $Re = 2.7 \times 10^4$.

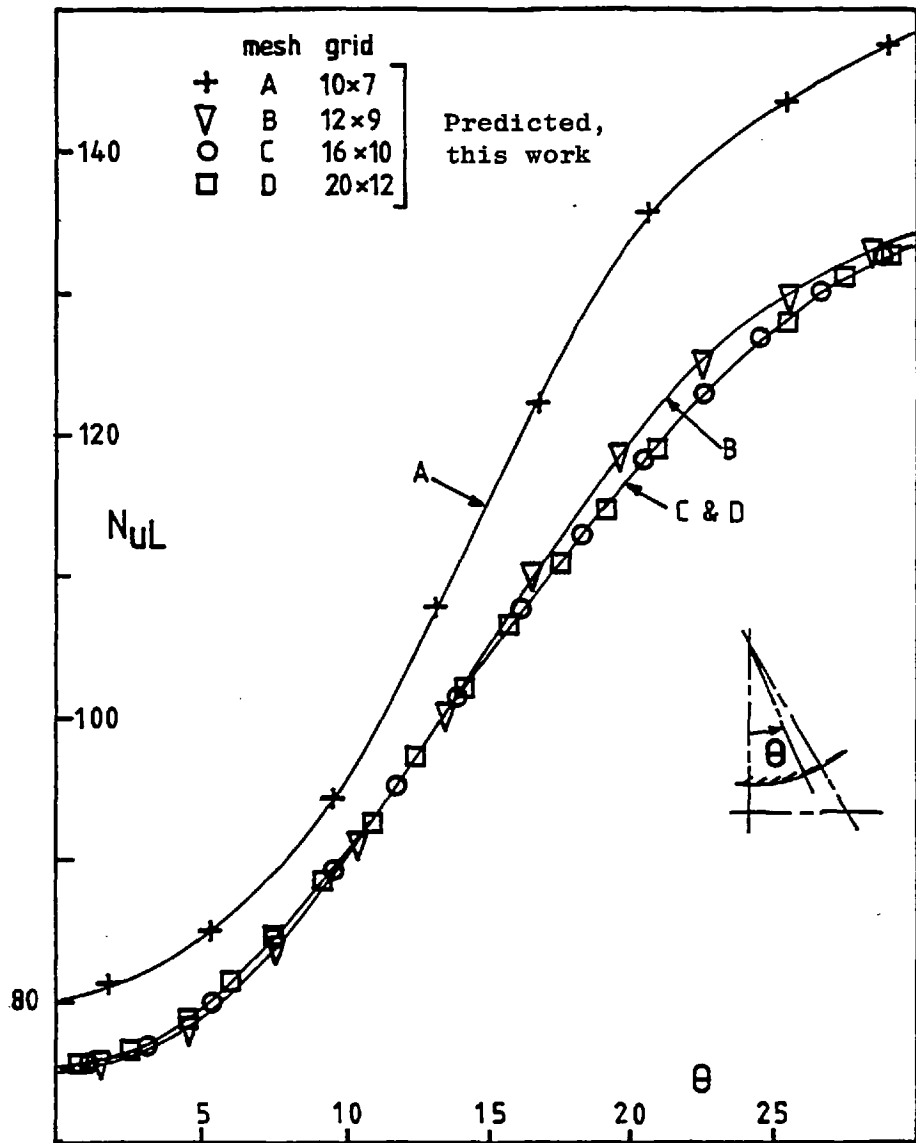
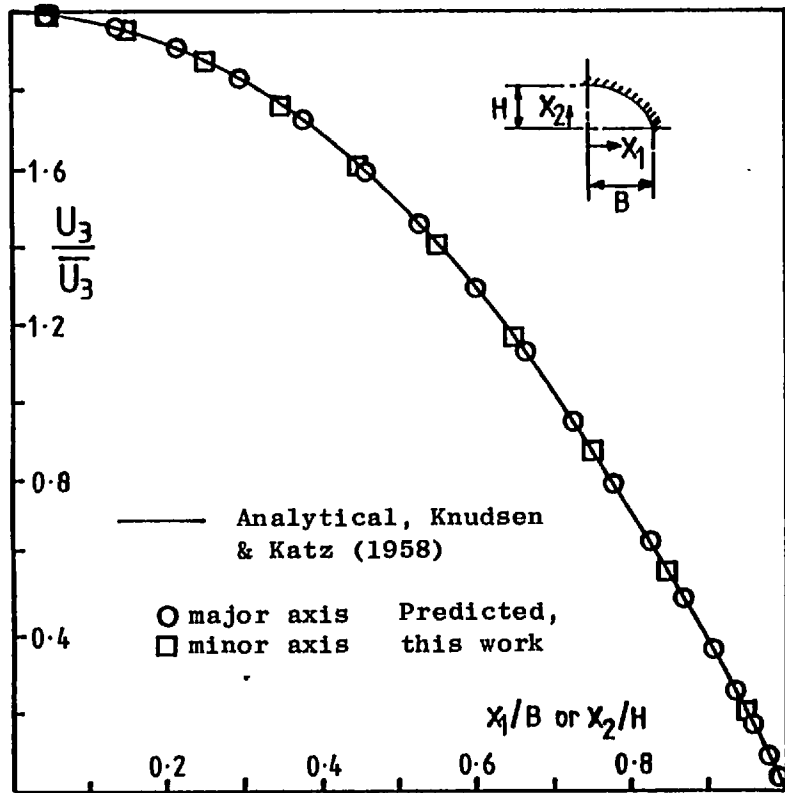
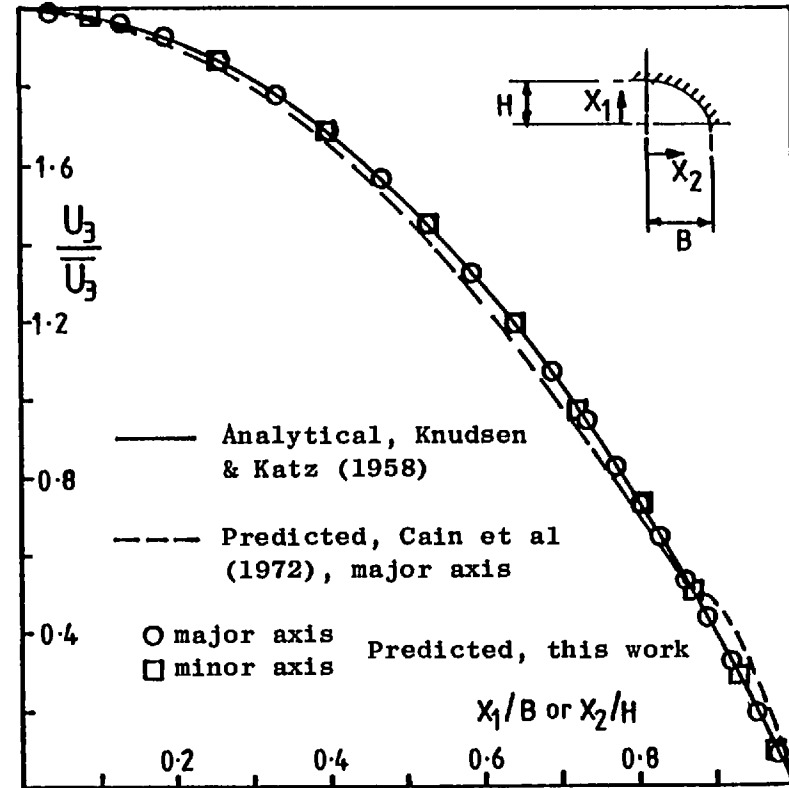


Figure 5.9.5 Grid refinement tests for local Nusselt number in a rod bundle with $P/D = 1.1$, $Re = 5 \times 10^4$ and $Pr = 0.7$.



(a) $AR = 5.0$



(b) $AR = 2.0$

Figure 6.2.1 Laminar centre-plane axial velocity profiles in elliptical ducts.

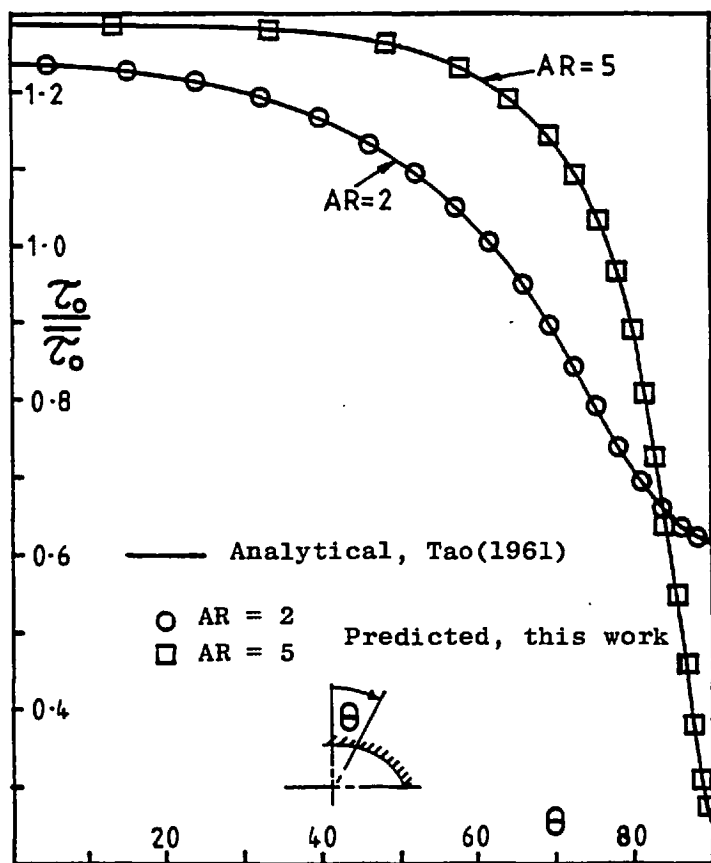


Figure 6.2.2 Laminar wall shear stress in elliptical ducts.

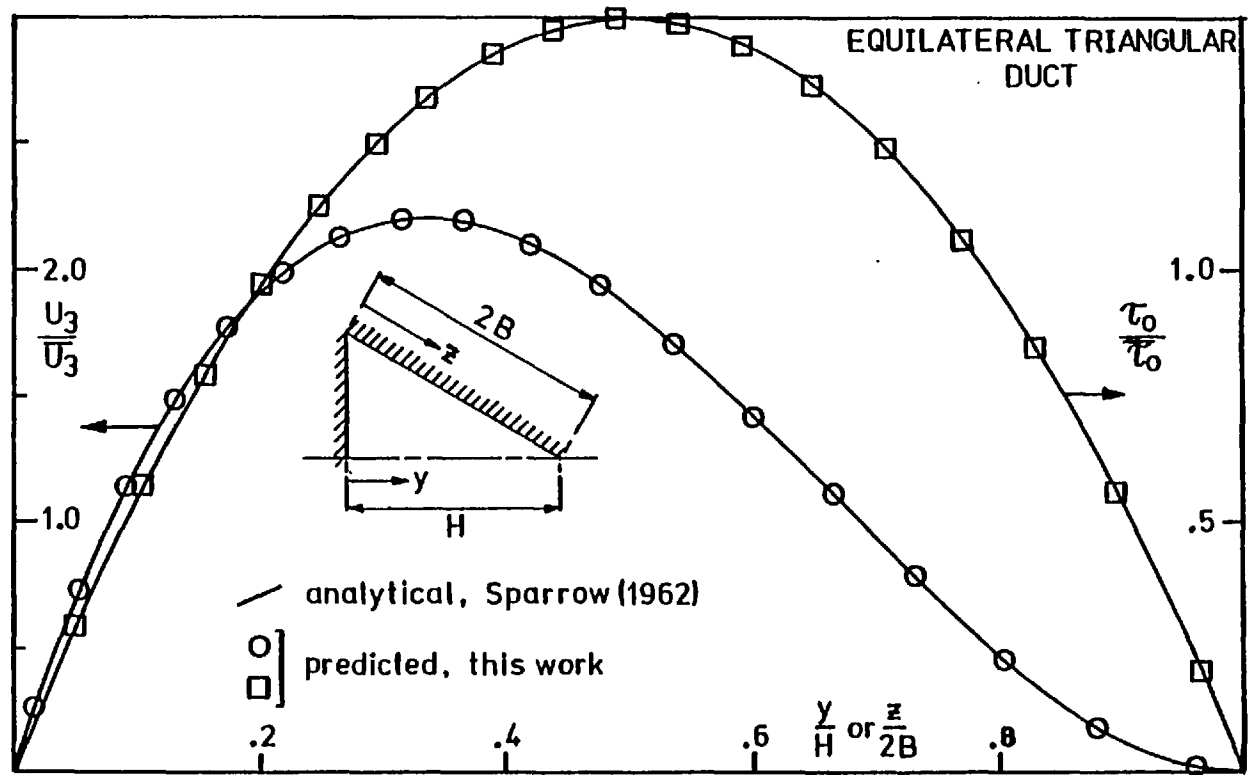


Figure 6.3.1 Laminar axial velocity and wall shear stress profiles in an equilateral triangular duct.

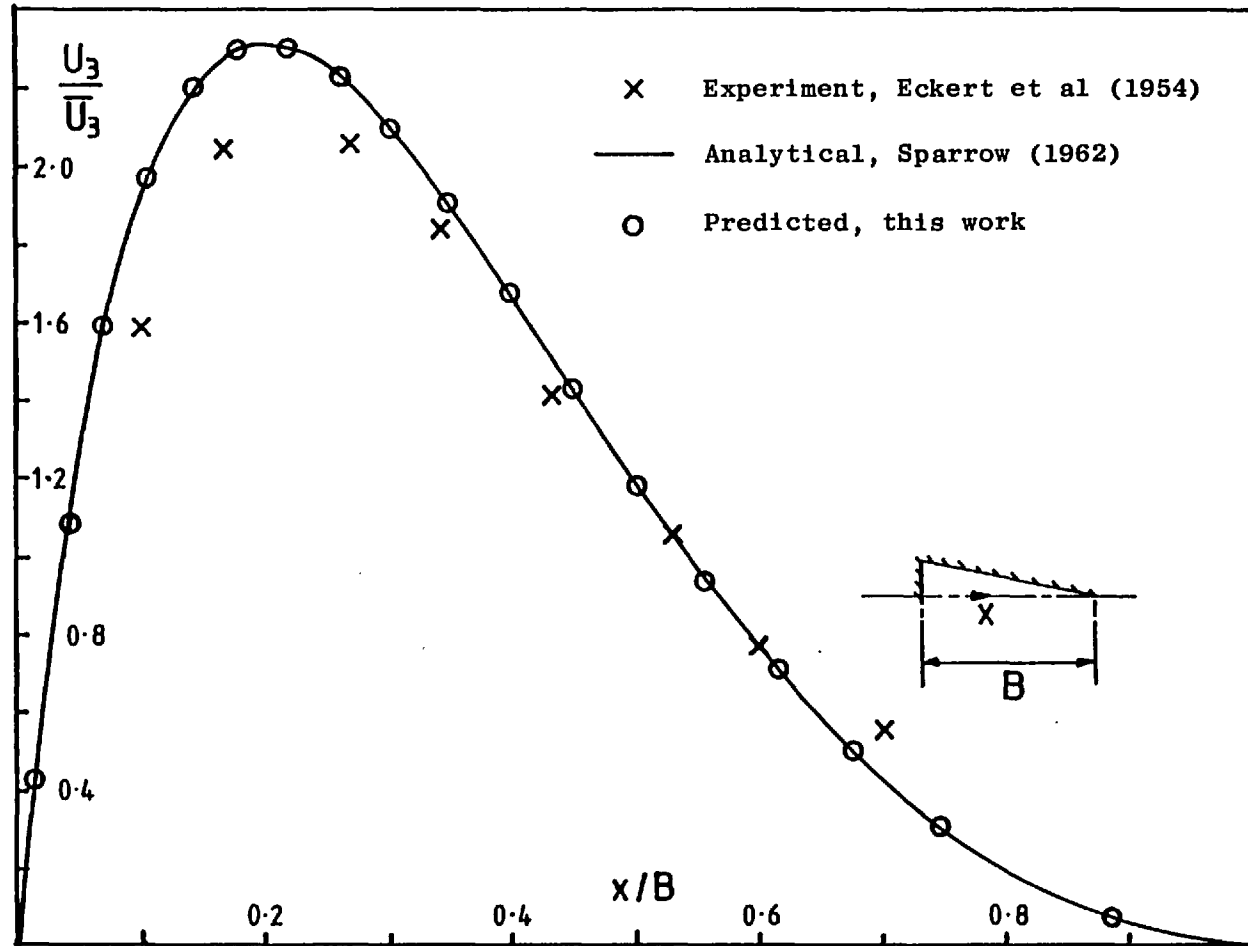


Figure 6.3.2 Laminar centre-plane axial velocity in an isosceles triangular duct of apex angle 22.1° .

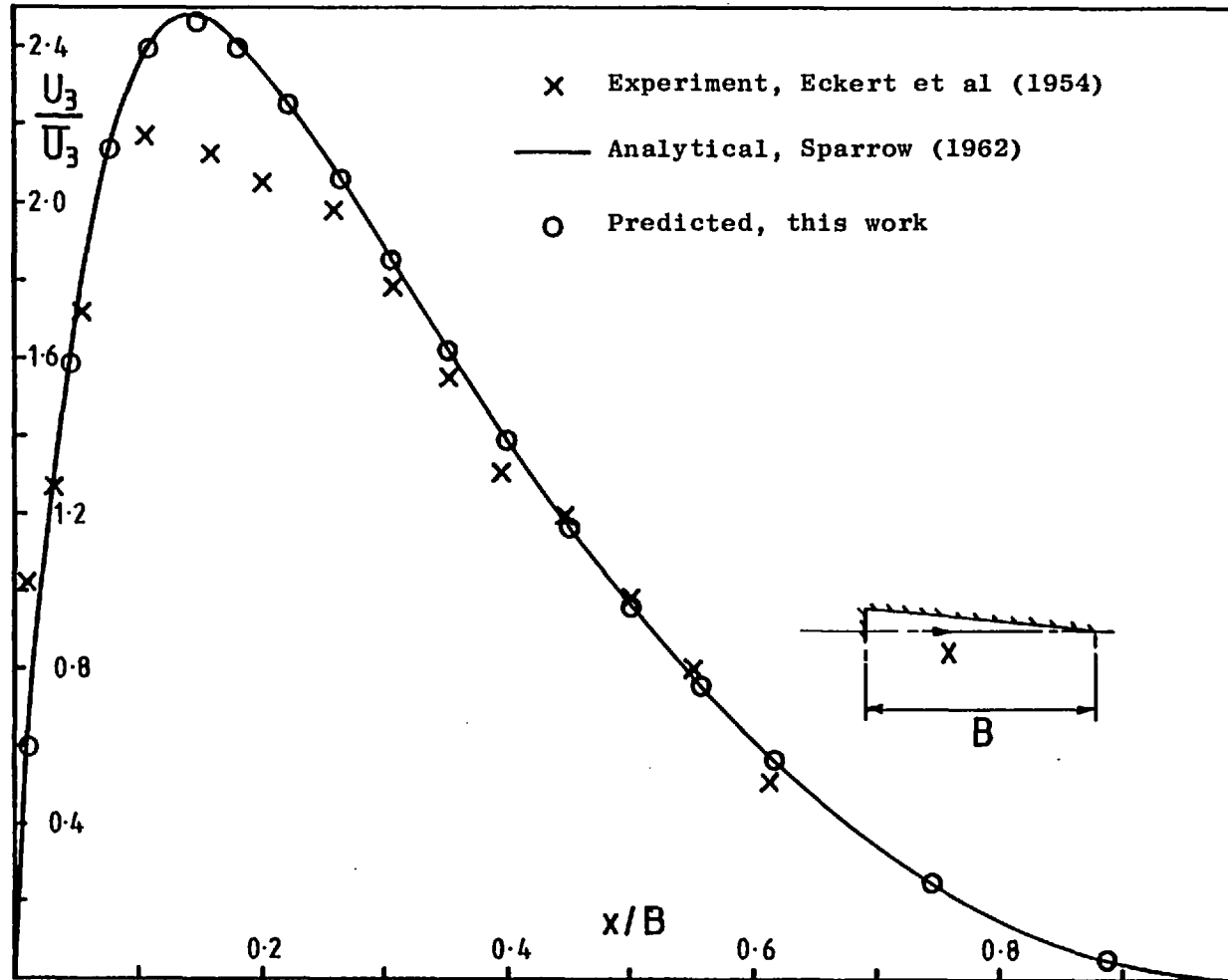


Figure 6.3.3 Laminar centre-plane axial velocity in an isosceles triangular duct of apex angle 11.7° .

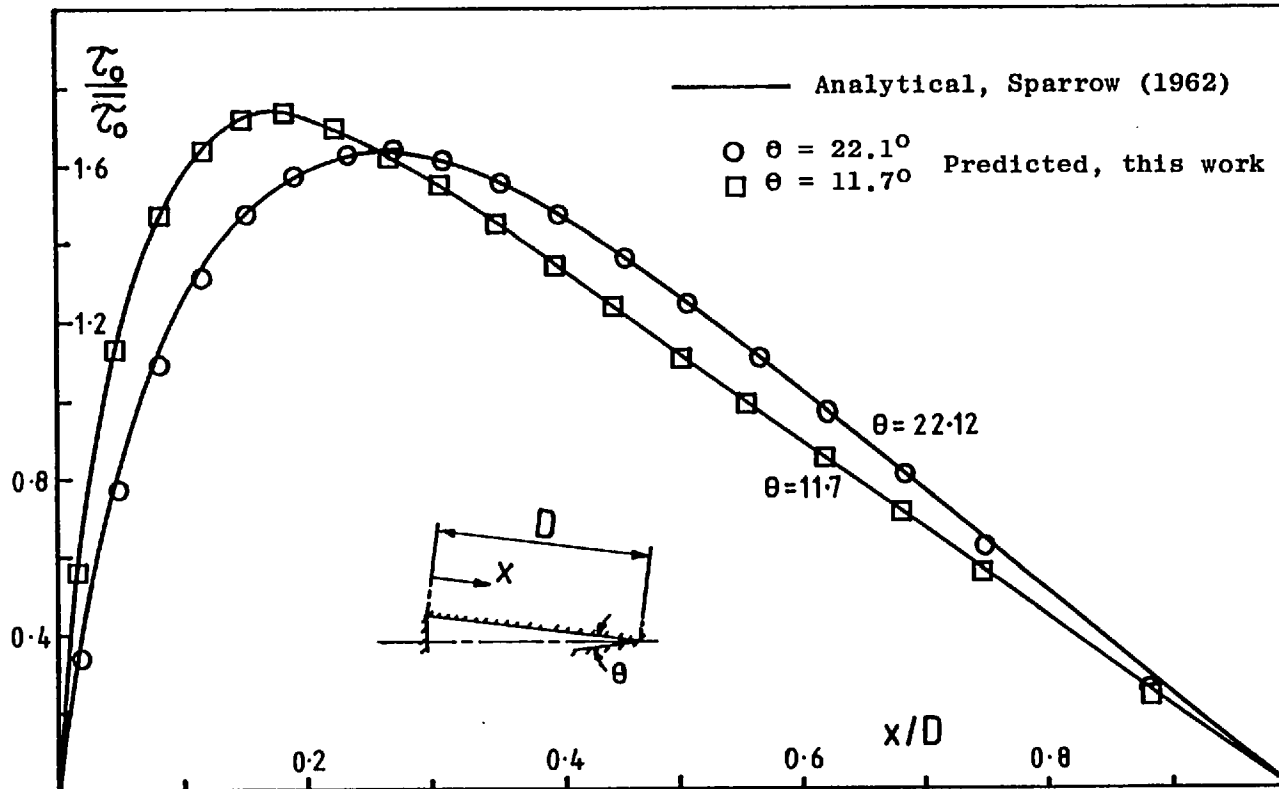
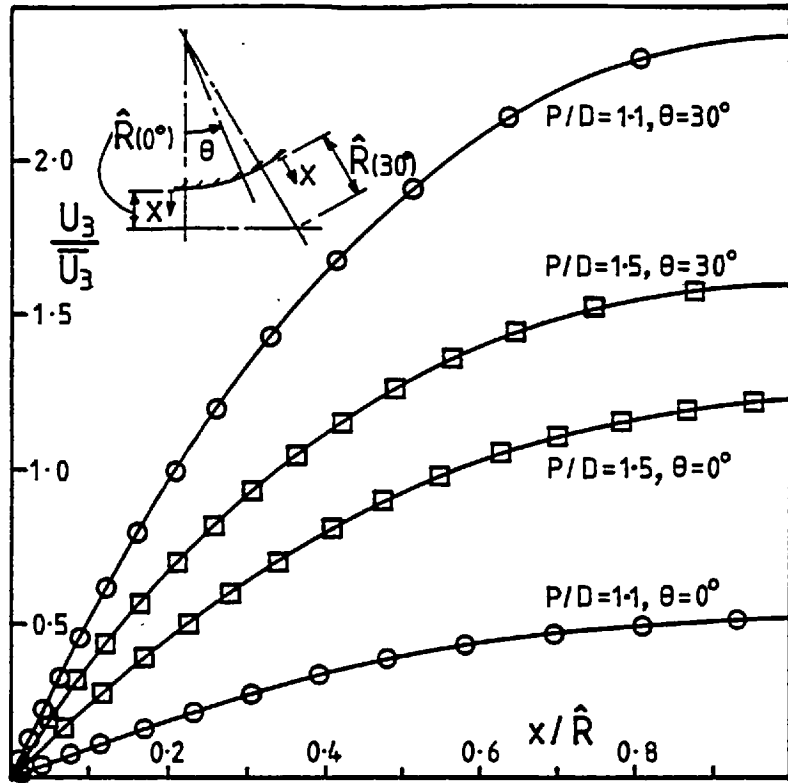


Figure 6.3.4 Laminar wall shear stress in isosceles triangular ducts



— Analytical, Sparrow & Loeffler (1959)

○ P/D = 1.1
 □ P/D = 1.5 } Predicted, this work

Figure 6.4.1 Laminar axial velocity in rod bundles.

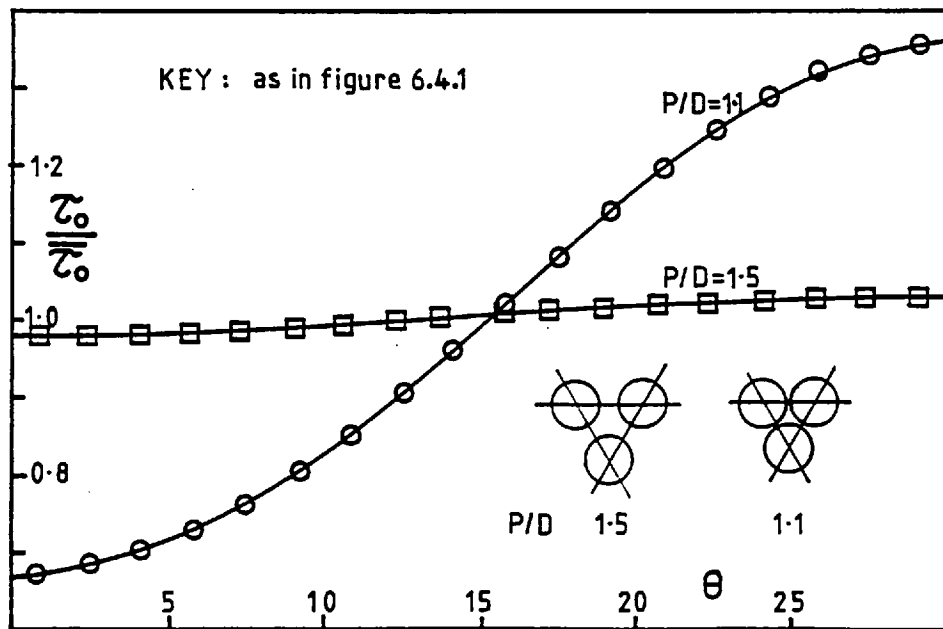


Figure 6.4.2 Laminar wall shear stress in rod bundles.

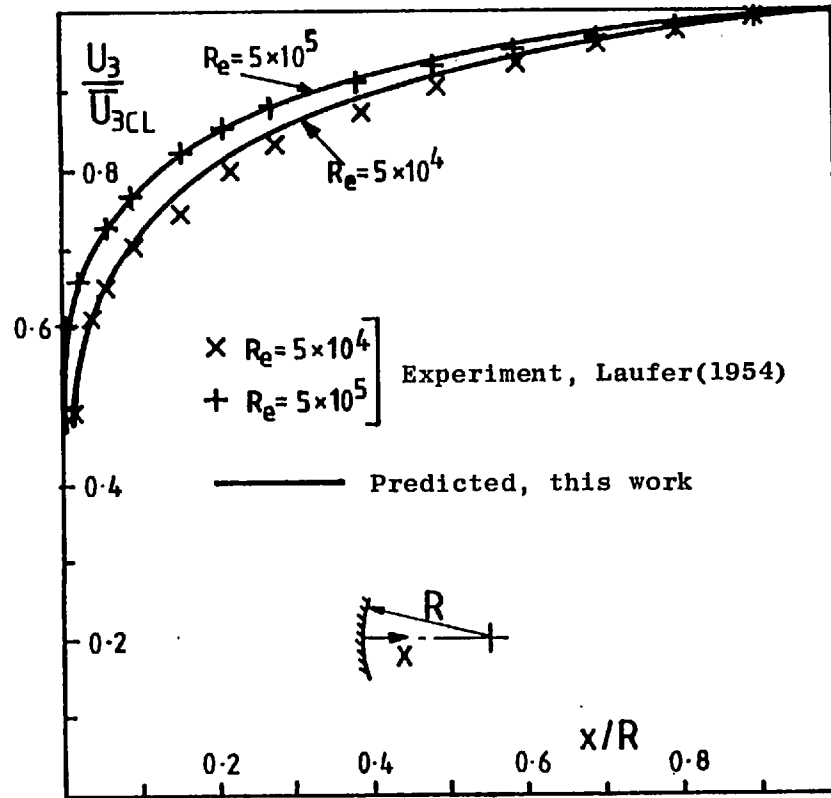


Figure 7.2.1 Axial velocity in a circular tube.

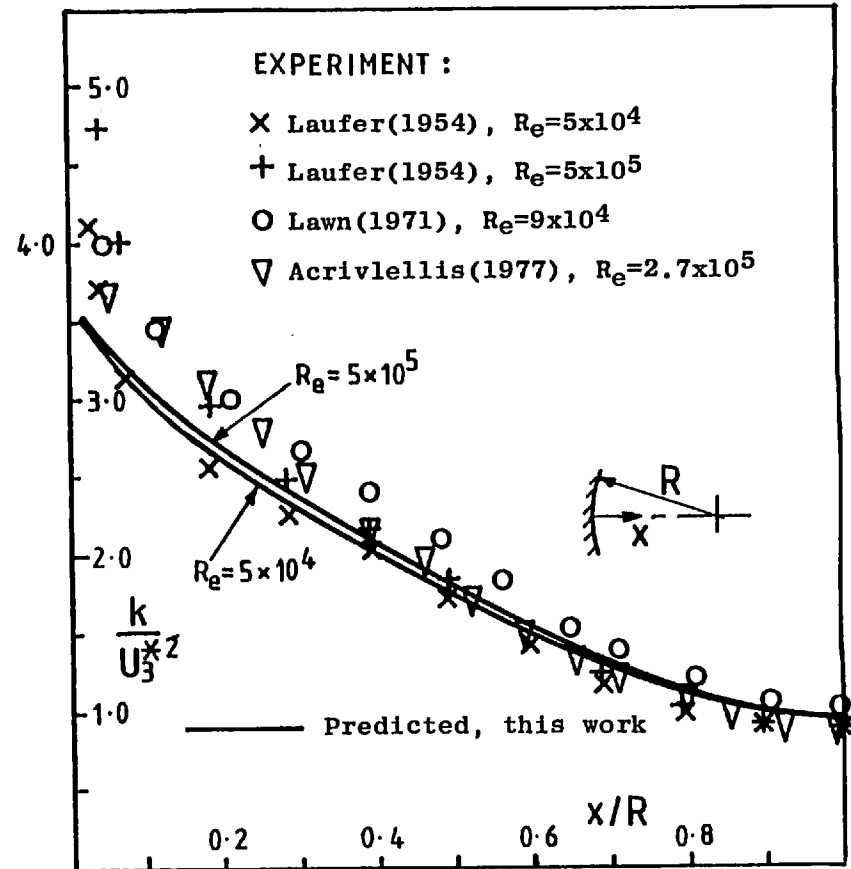
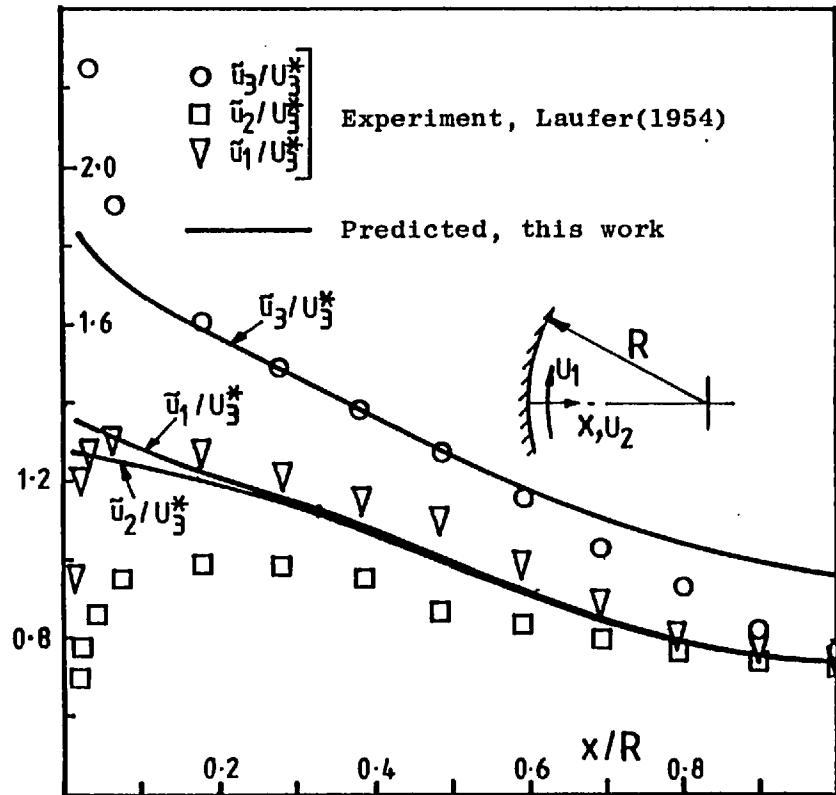
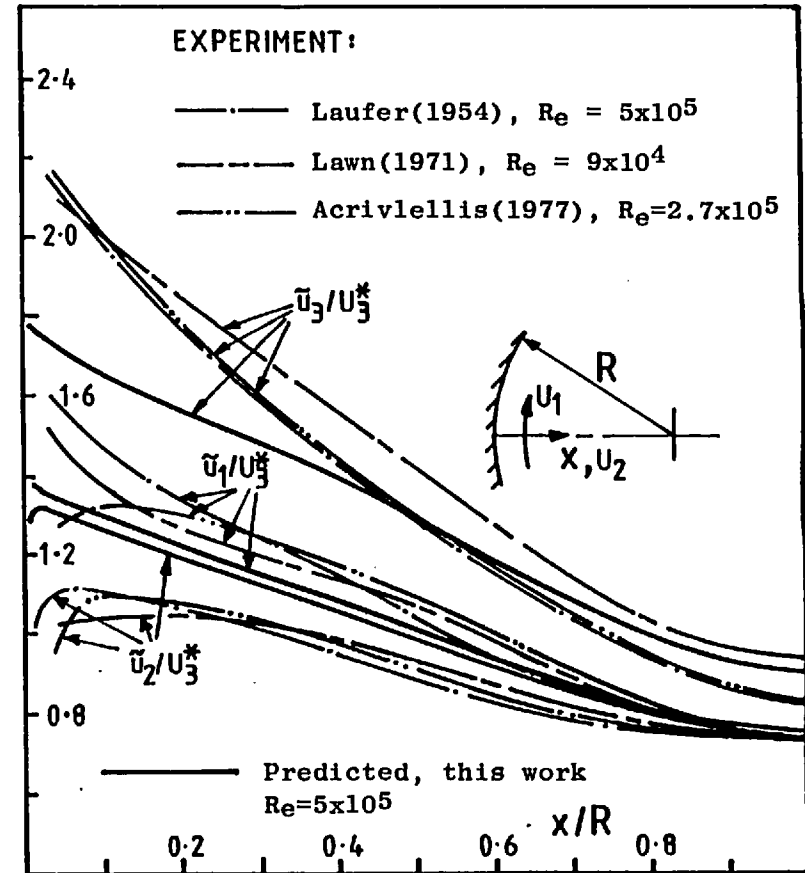


Figure 7.2.2 Turbulence kinetic energy in a circular tube.



(a) $Re = 5 \times 10^4$

Figure 7.2.3 Turbulence intensities in a circular tube.



(b) Various Re

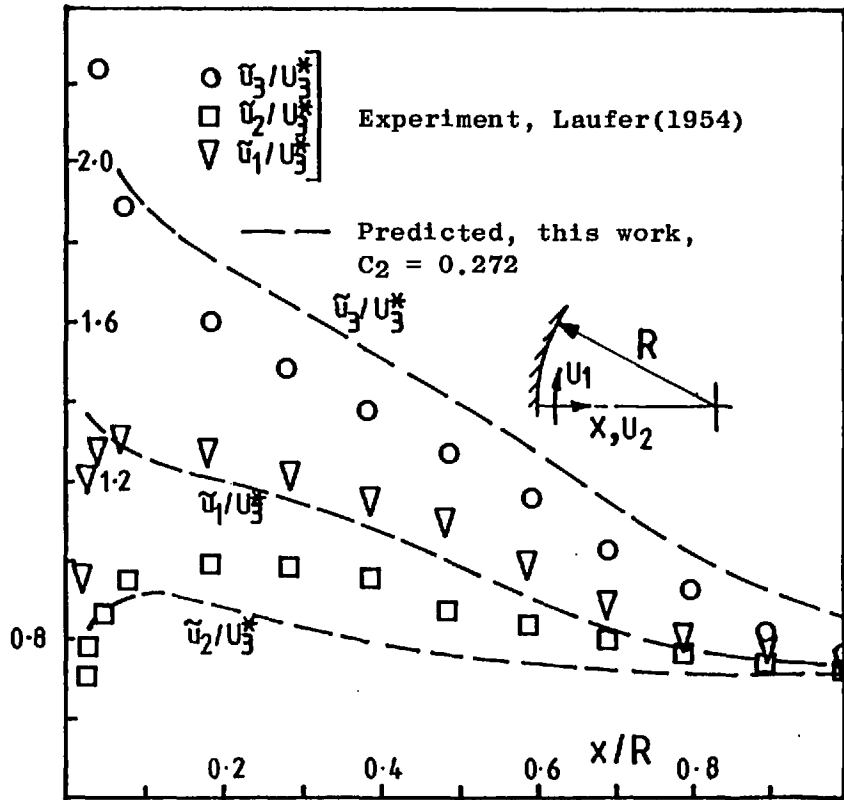


Figure 7.2.4 Calculated turbulence intensity profiles in a circular tube with $C_2 = 0.272$ and $Re = 5 \times 10^4$.

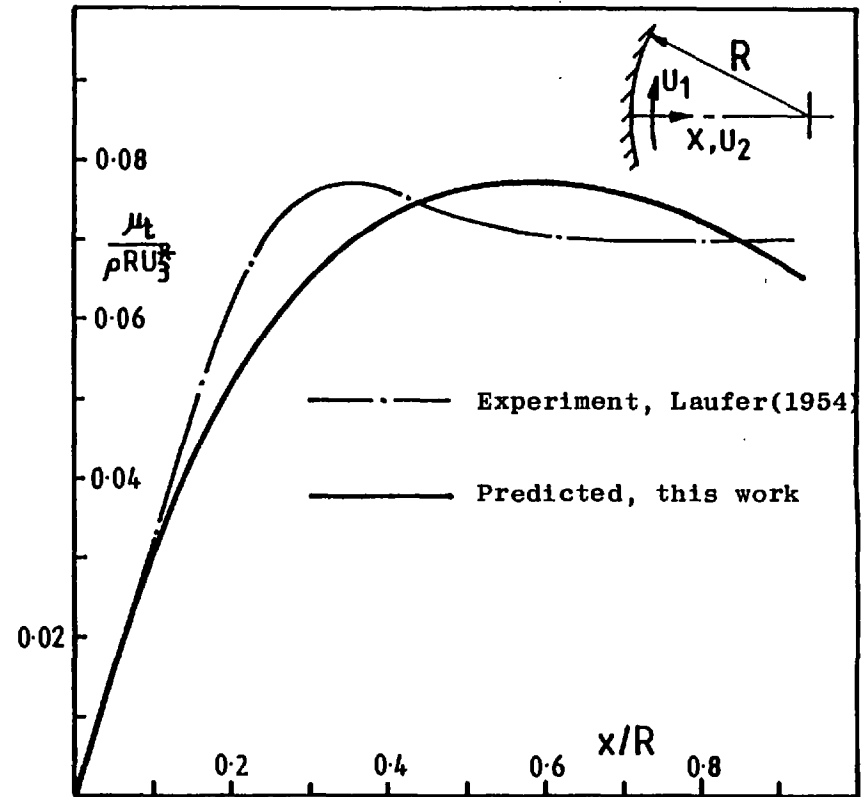


Figure 7.2.5 Eddy viscosity in a circular tube with $Re = 5 \times 10^4$.

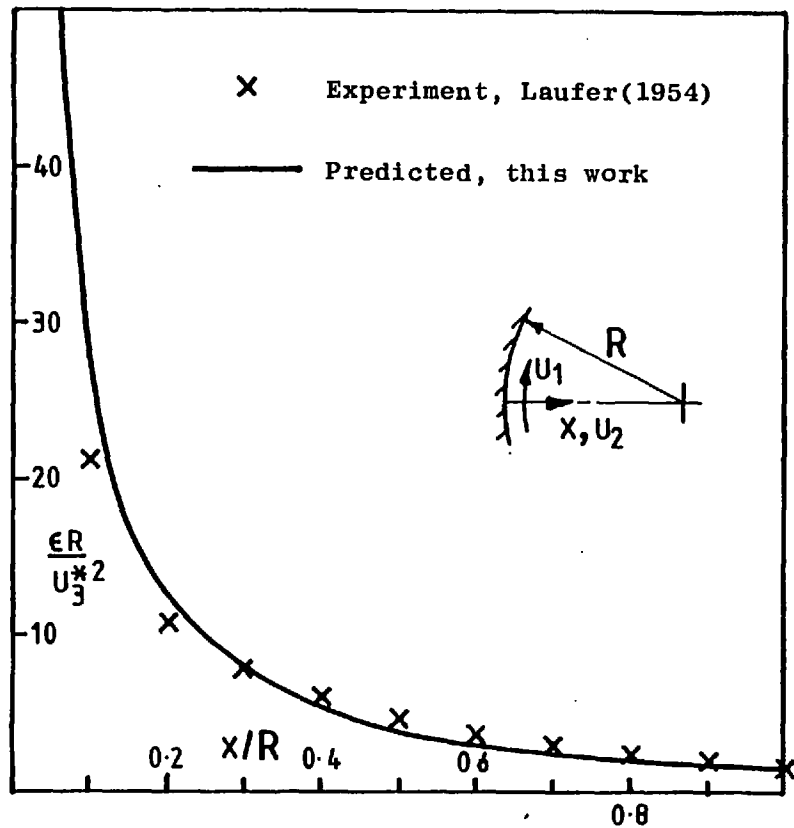


Figure 7.2.6 Dissipation rate of turbulence kinetic energy in a circular tube with $Re = 5 \times 10^4$

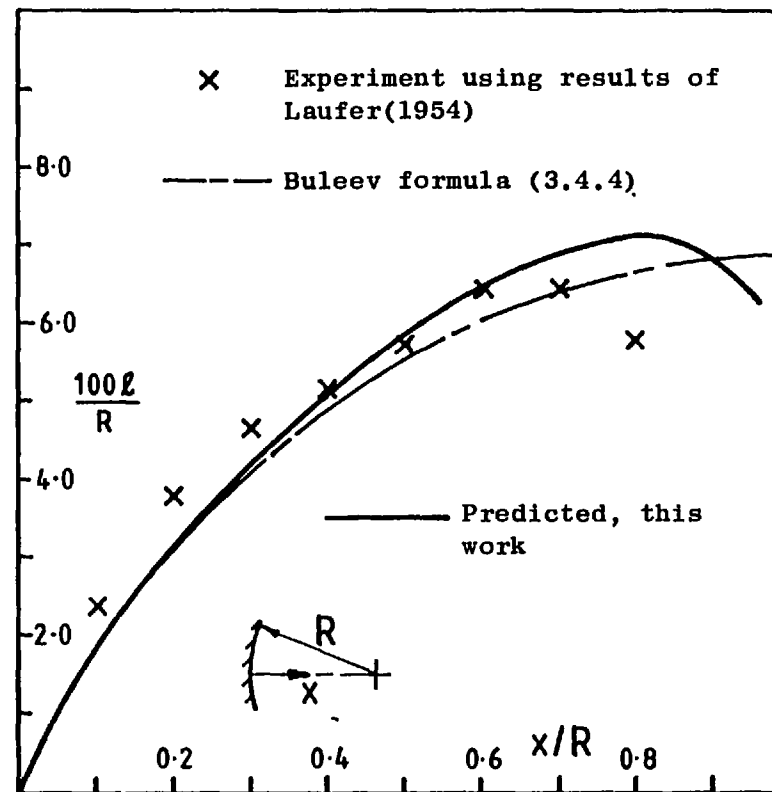


Figure 7.2.7 Length scale in a circular tube with $Re = 5 \times 10^4$

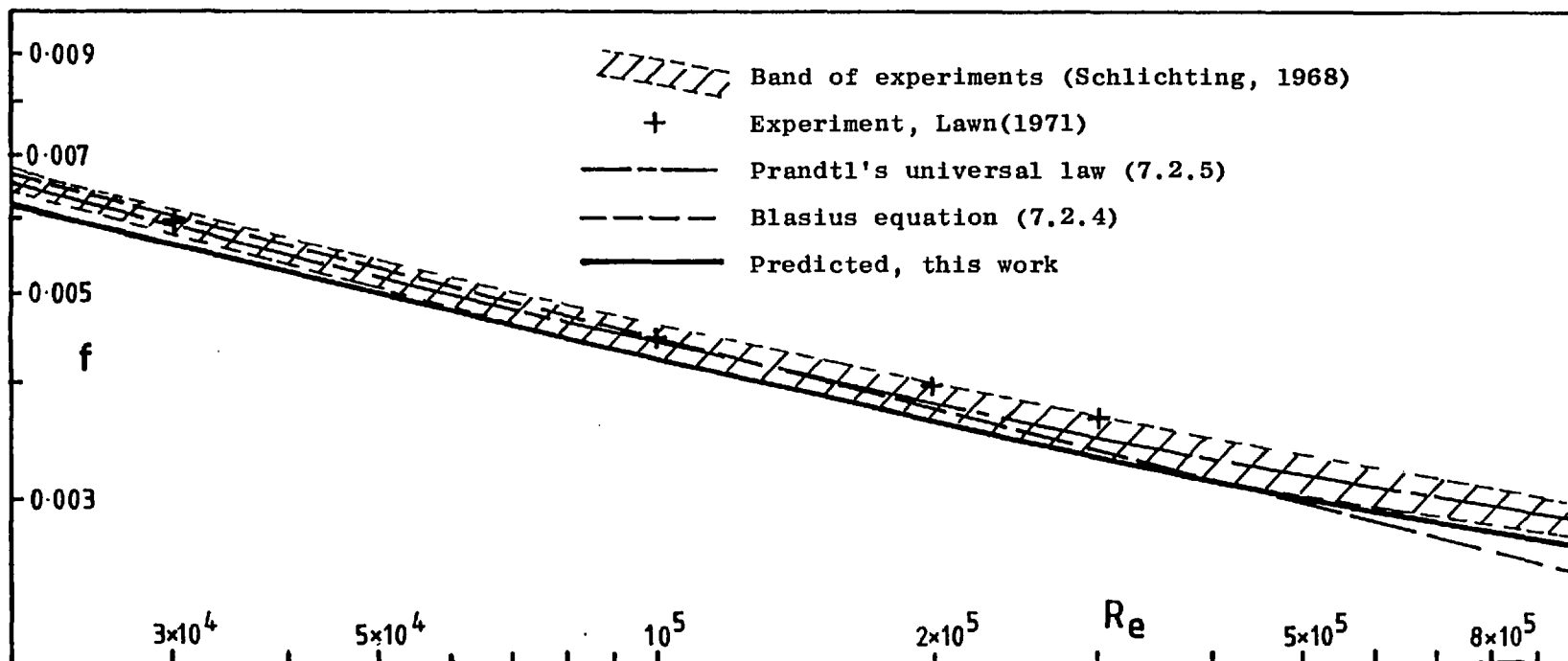


Figure 7.2.8 Friction factor characteristics for a circular tube

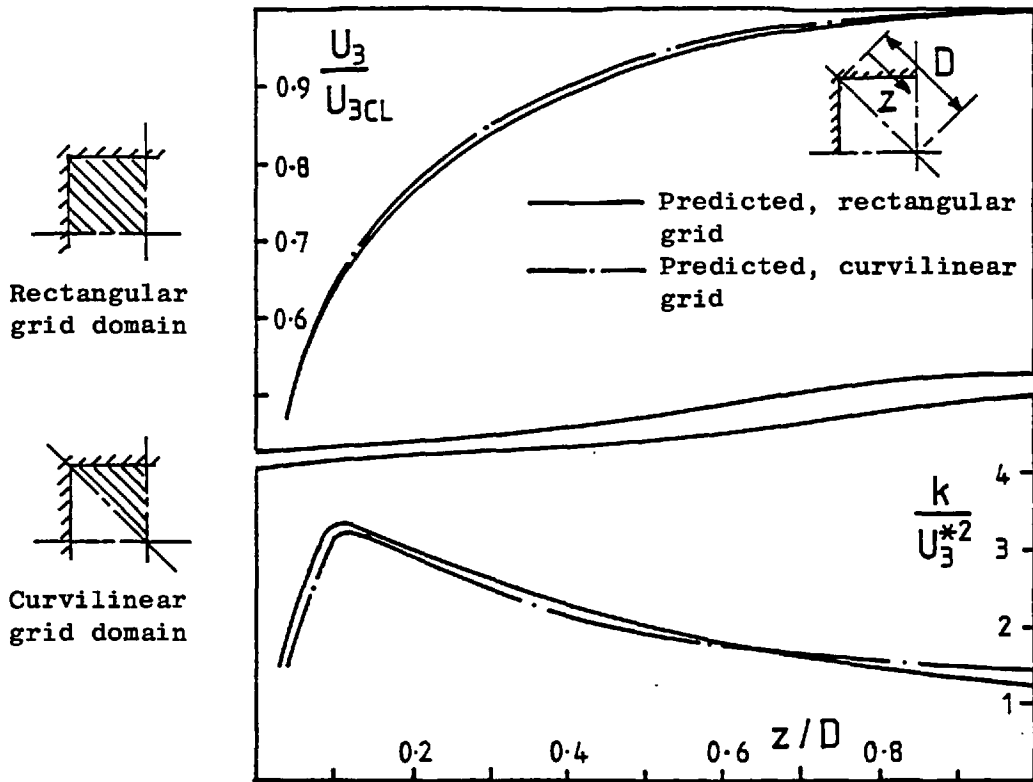


Figure 7.3.1 Predicted axial velocity and turbulence kinetic energy along a corner bisector in a square duct with $Re = 3.4 \times 10^4$.

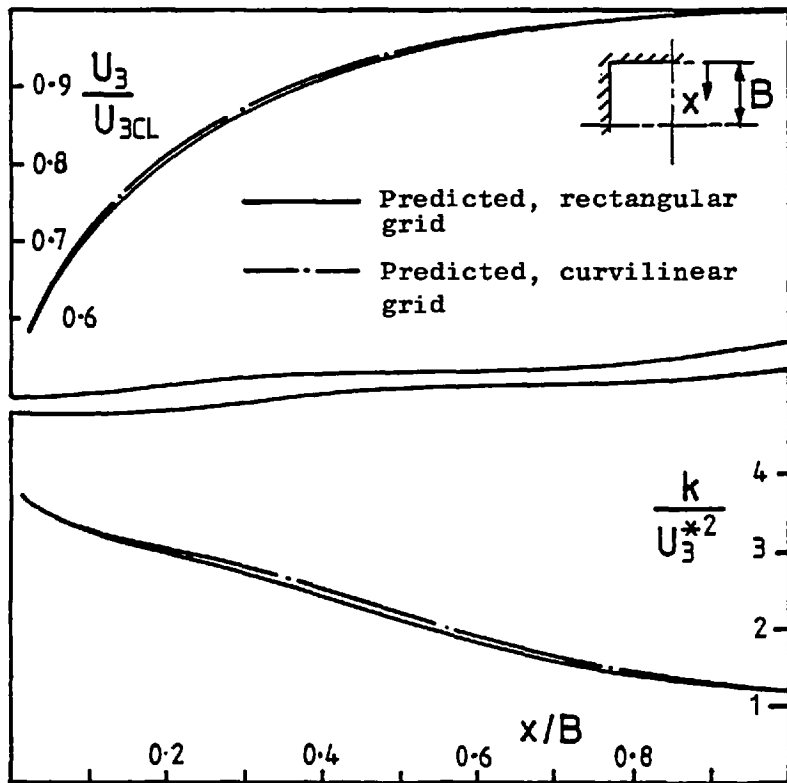


Figure 7.3.2 Predicted axial velocity and turbulence kinetic energy along a wall bisector in a square duct with $Re = 3.4 \times 10^4$.

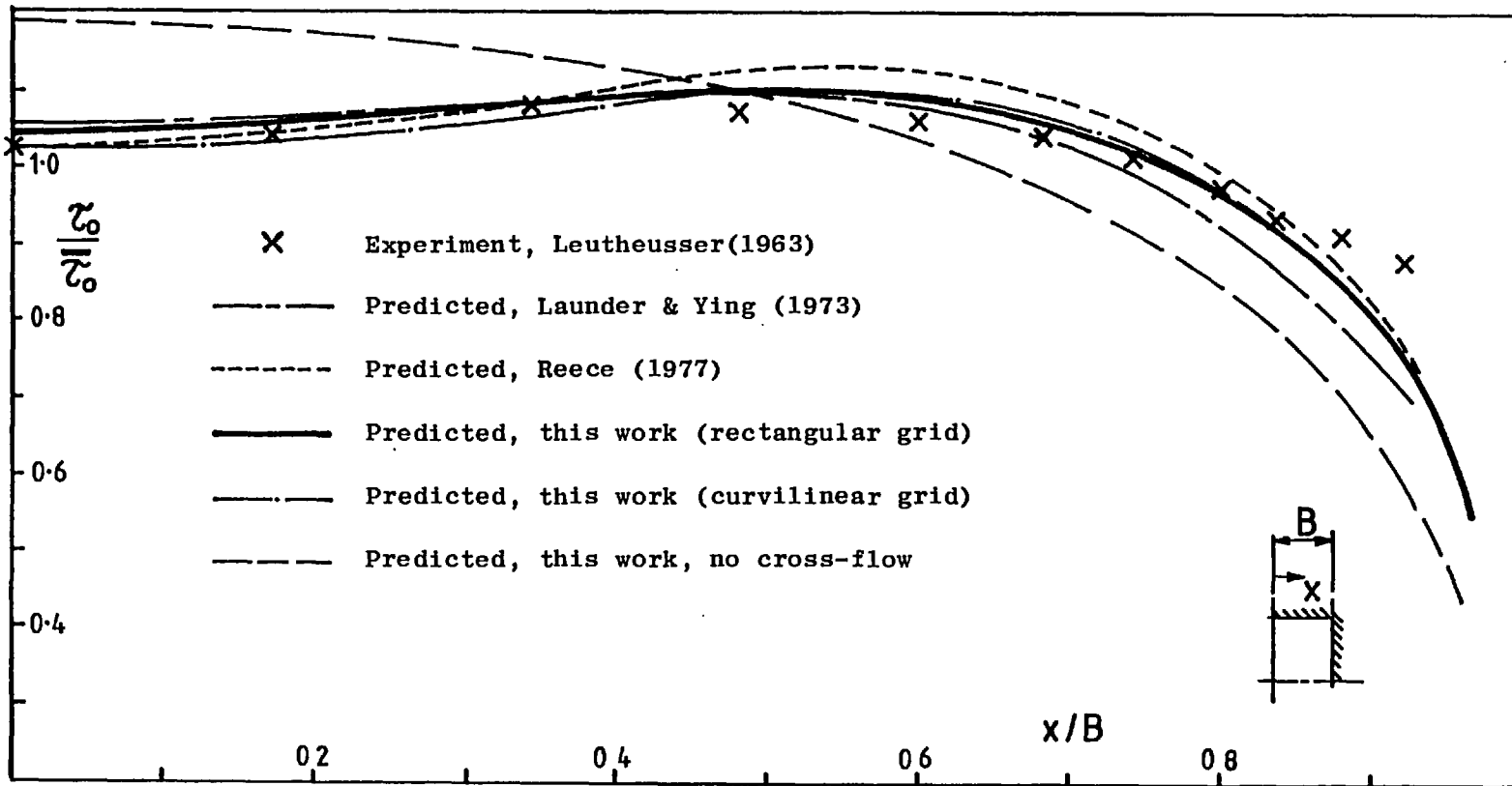


Figure 7.3.3 Wall shear stress in a square duct with $Re = 3.4 \times 10^4$

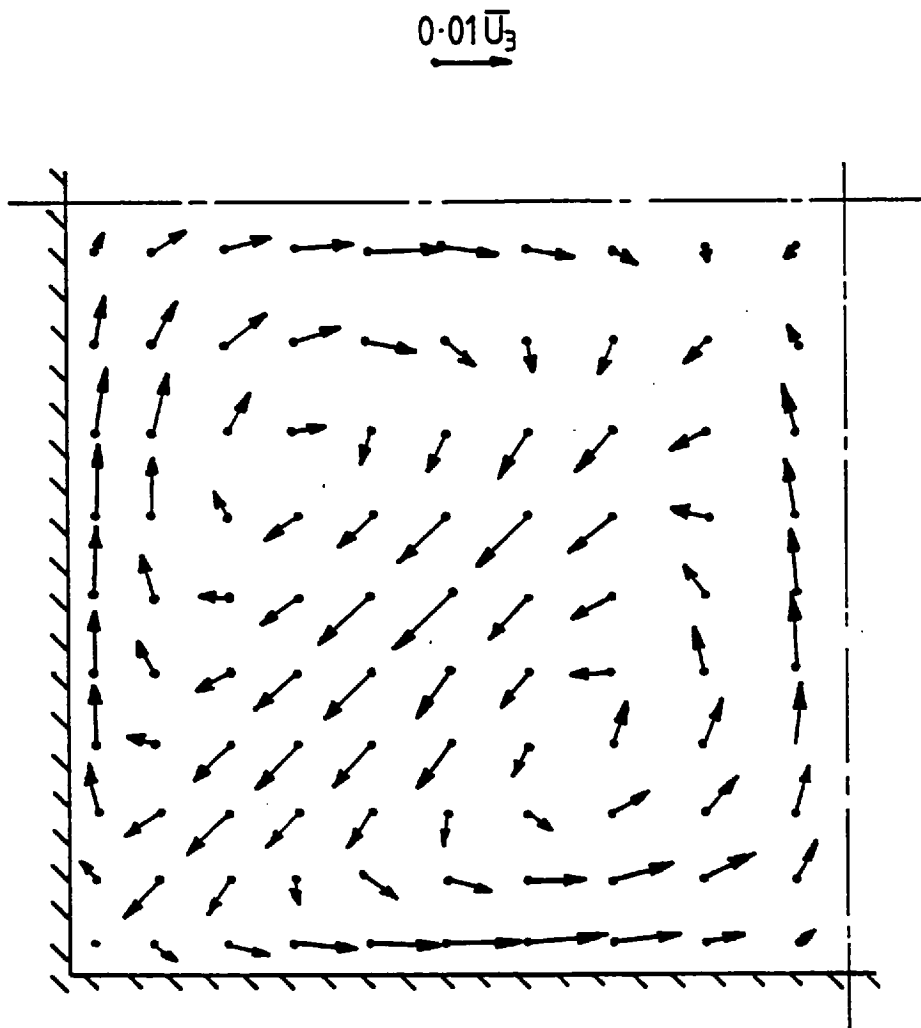


Figure 7.3.4 Predicted secondary velocity vectors in a square duct with $Re = 2.15 \times 10^5$

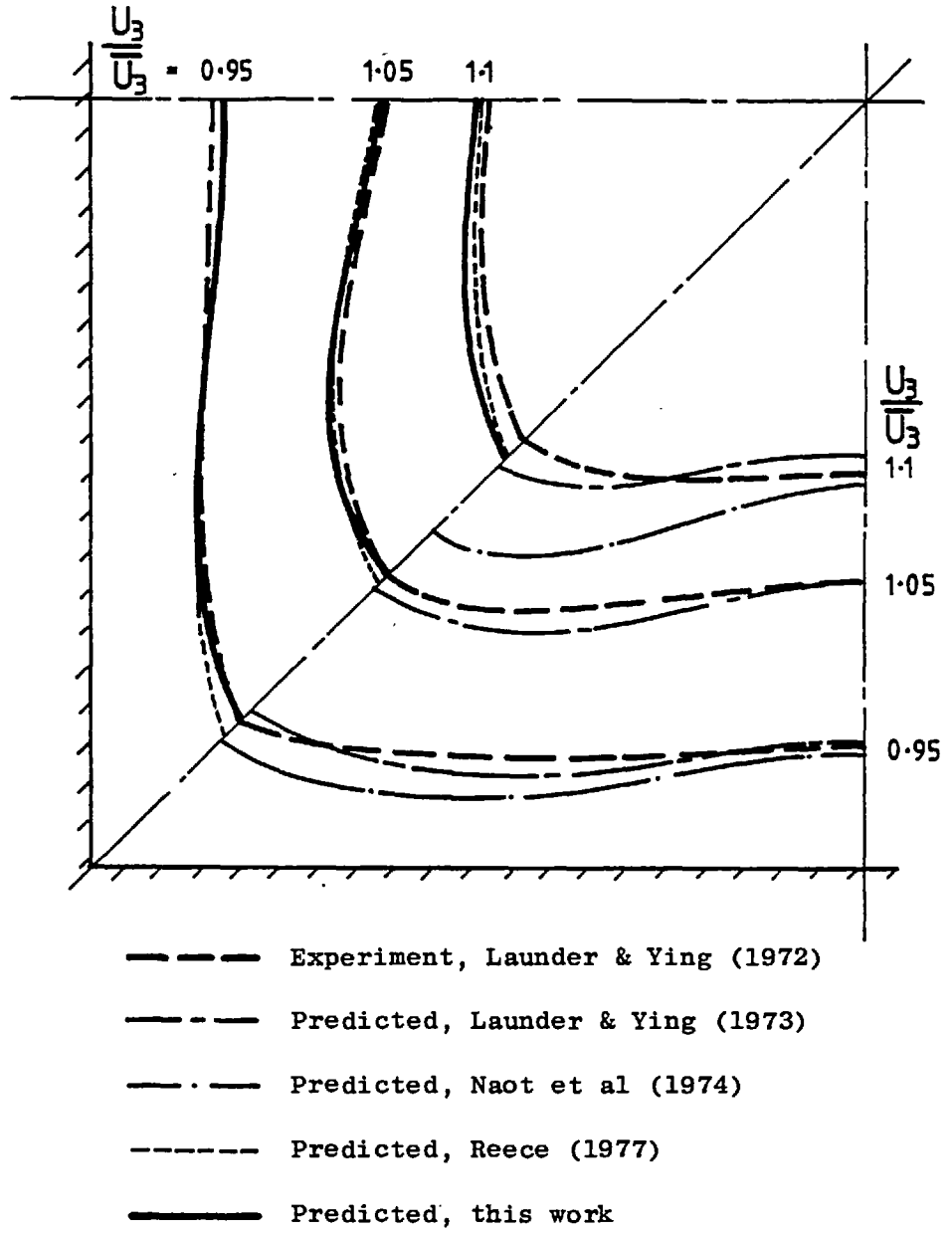


Figure 7.3.5 Axial velocity contours in a square duct with $Re = 2.15 \times 10^5$.

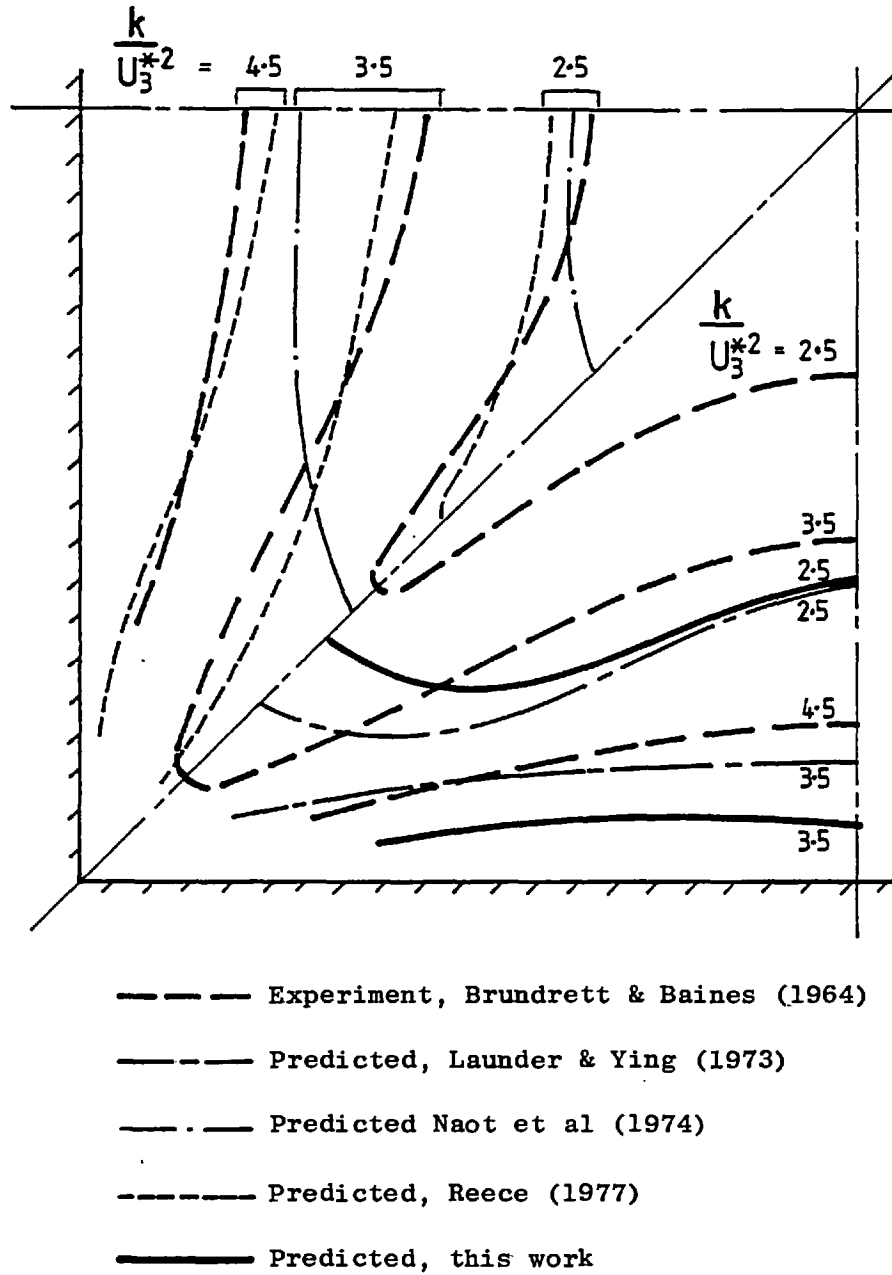


Figure 7.3.6 Turbulence kinetic energy contours in a square duct with $Re = 8.3 \times 10^4$.

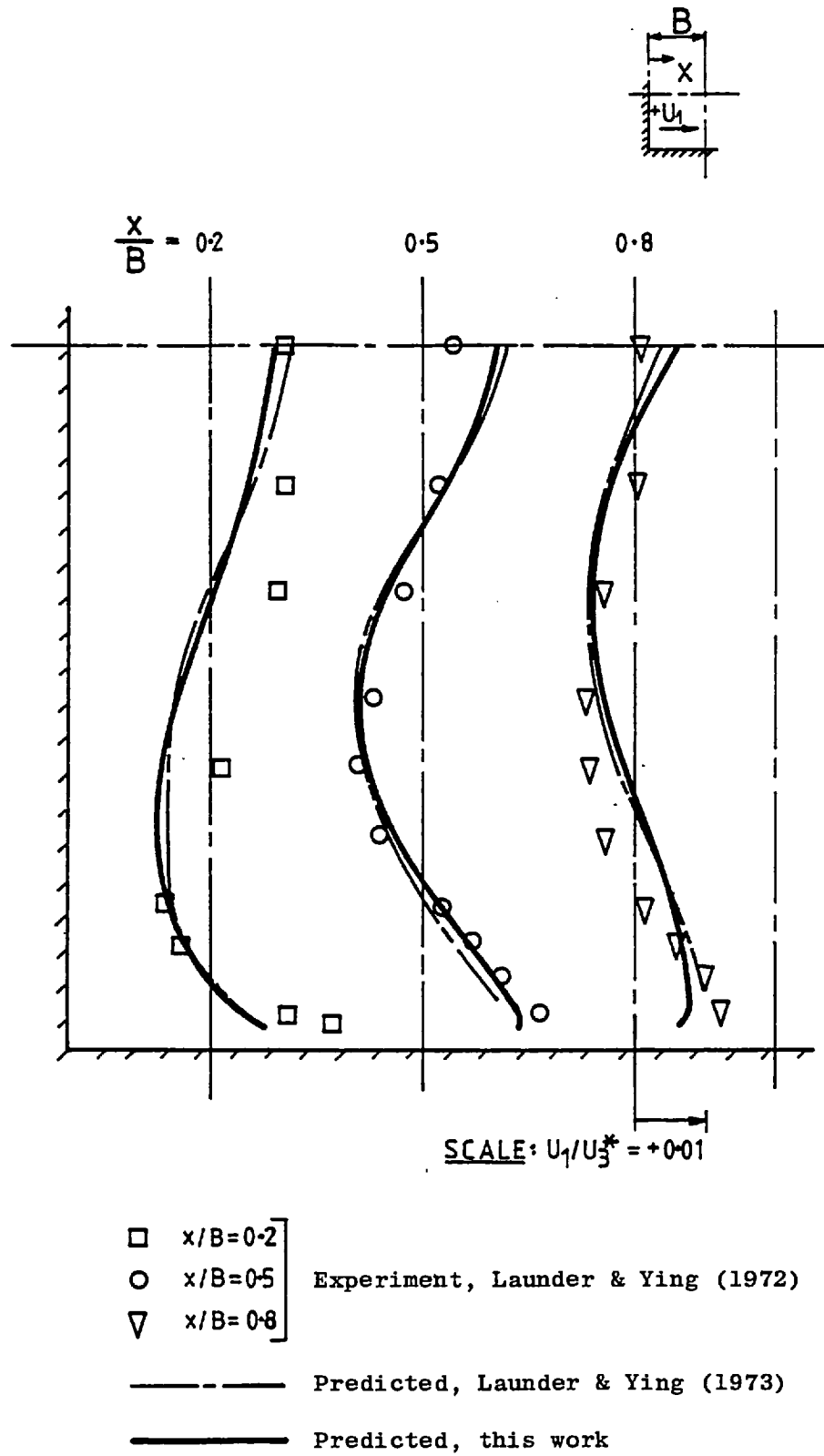


Figure 7.3.7 Secondary velocity profiles (U_1/U_3^*) in a square duct with $Re = 2.15 \times 10^5$.

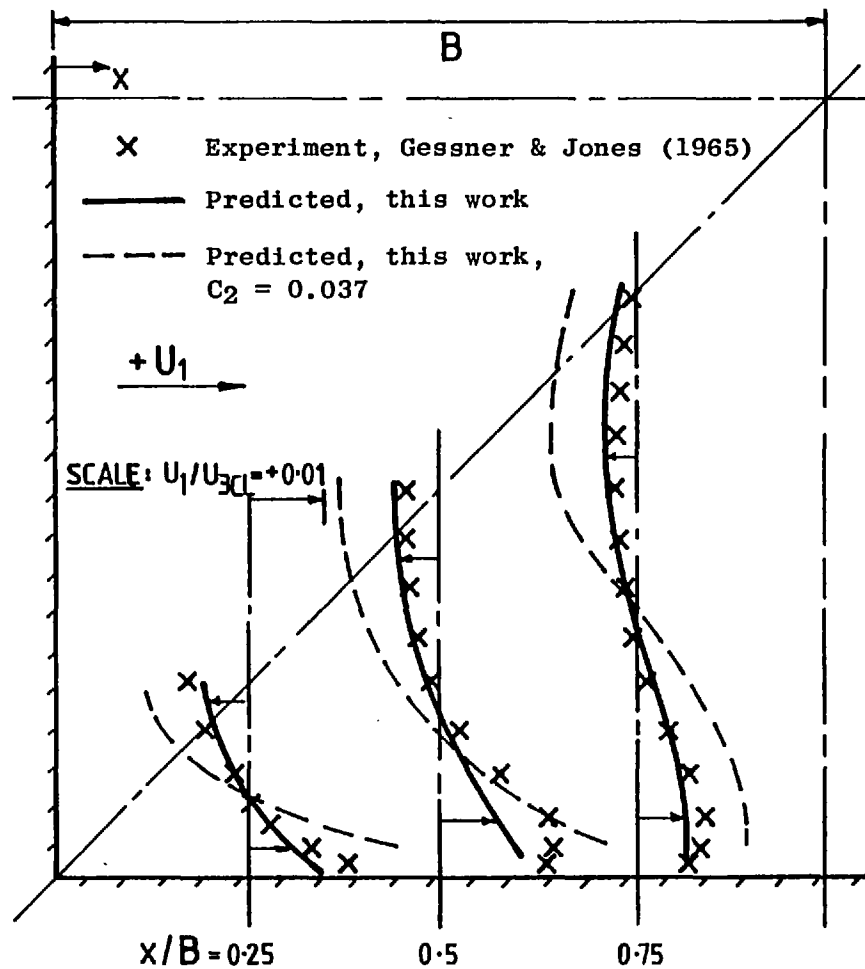


Figure 7.3.8 Secondary velocity profiles (U_1/U_{3CL}) in a square duct with $Re = 1.5 \times 10^5$

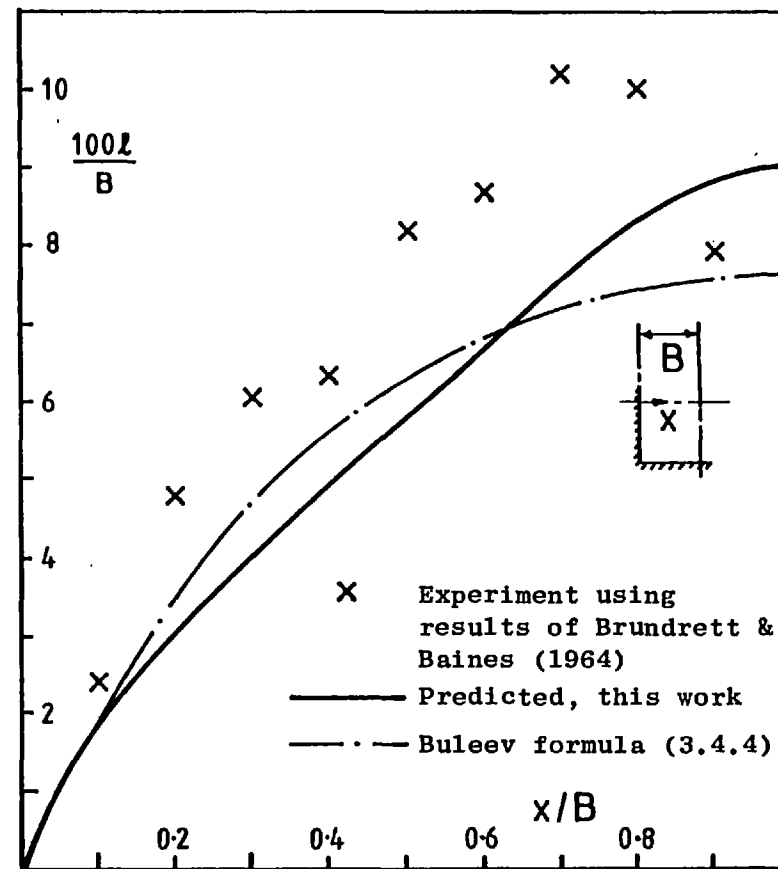


Figure 7.3.9 Length scale profiles along a centre-plane in a square duct with $Re = 8.3 \times 10^4$

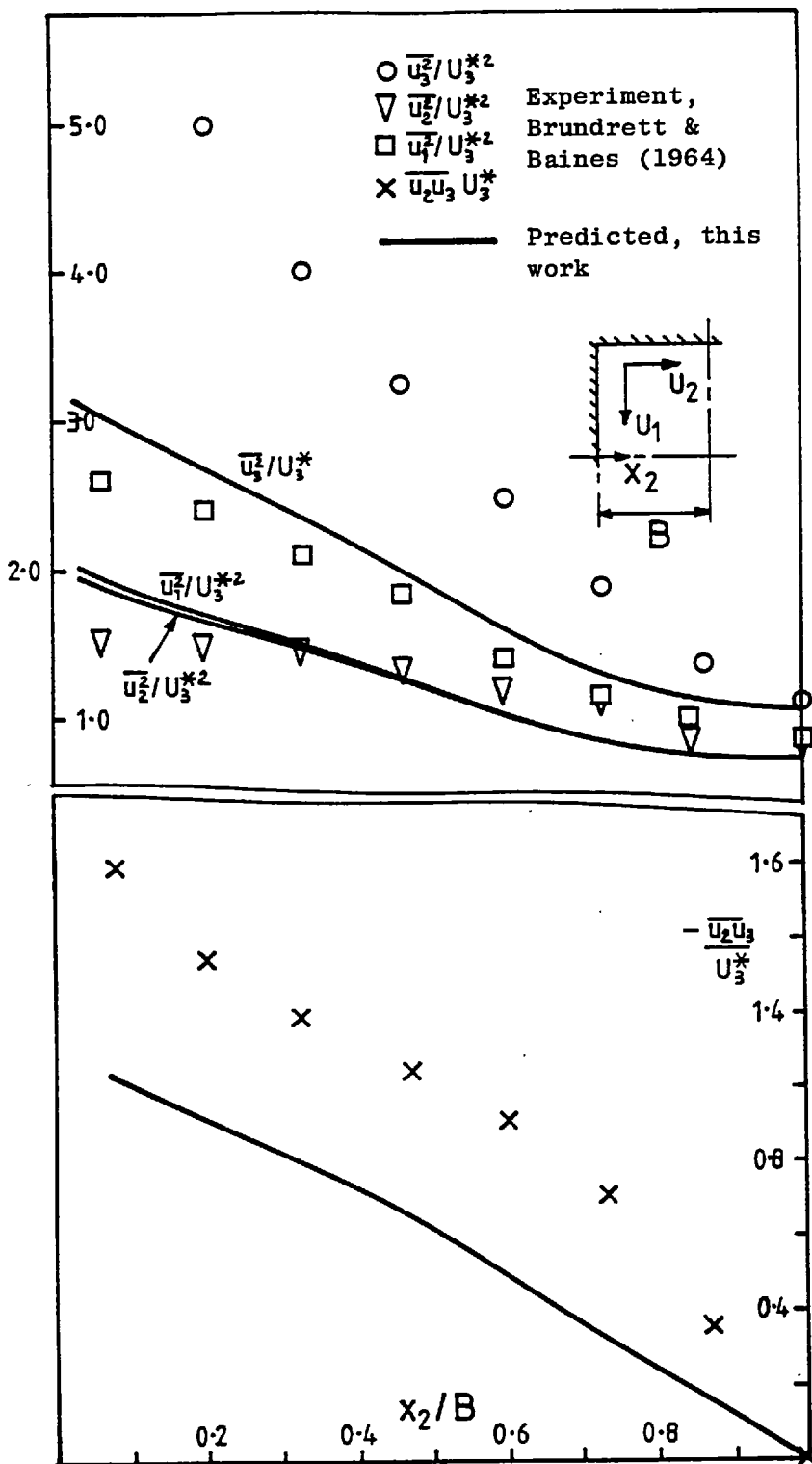


Figure 7.3.10 Reynolds stress profiles along a center-plane in a square duct with $Re = 8.3 \times 10^4$.

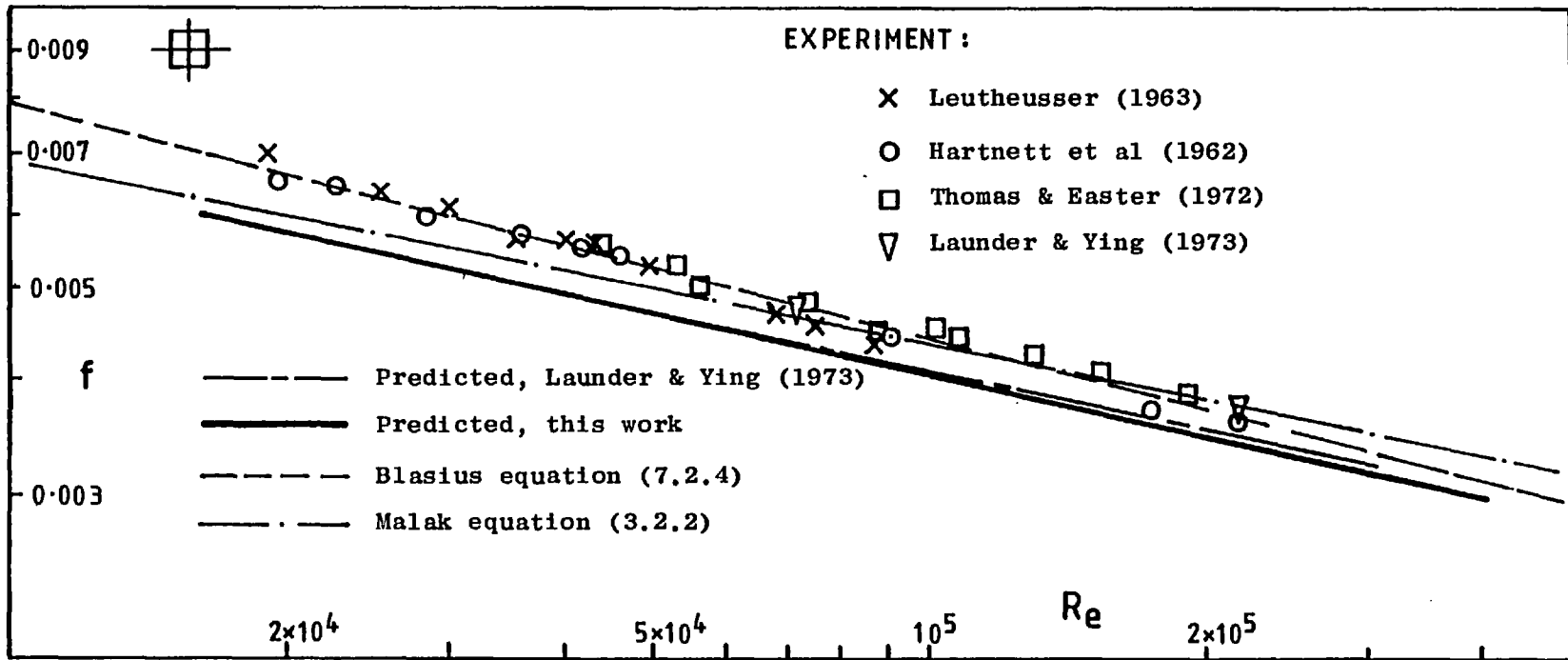
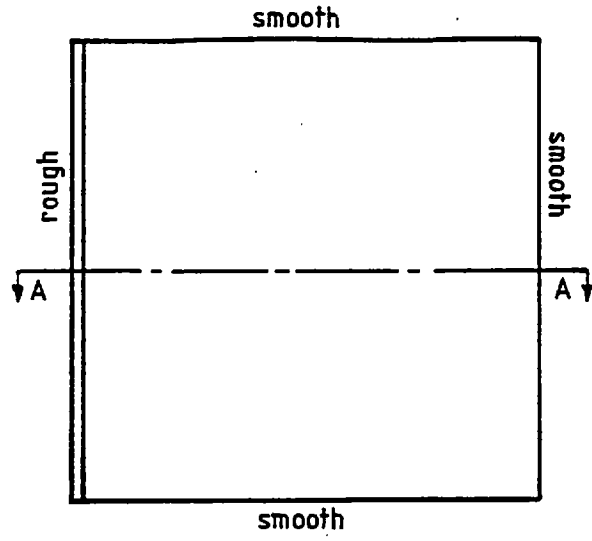
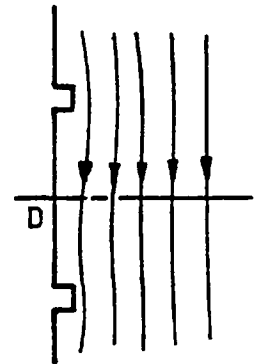


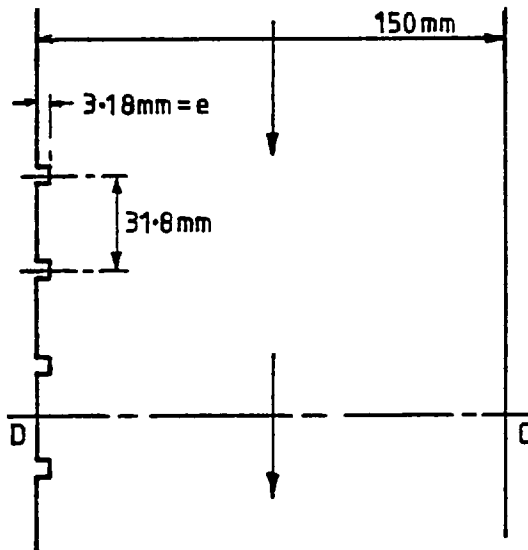
Figure 7.3.11 Friction factor characteristics for a square duct.



(a) Front elevation



(c) Possible flow past the ribs



(b) Plan view of section through AA

Figure 7.4.1 Details of the square duct with one rough wall

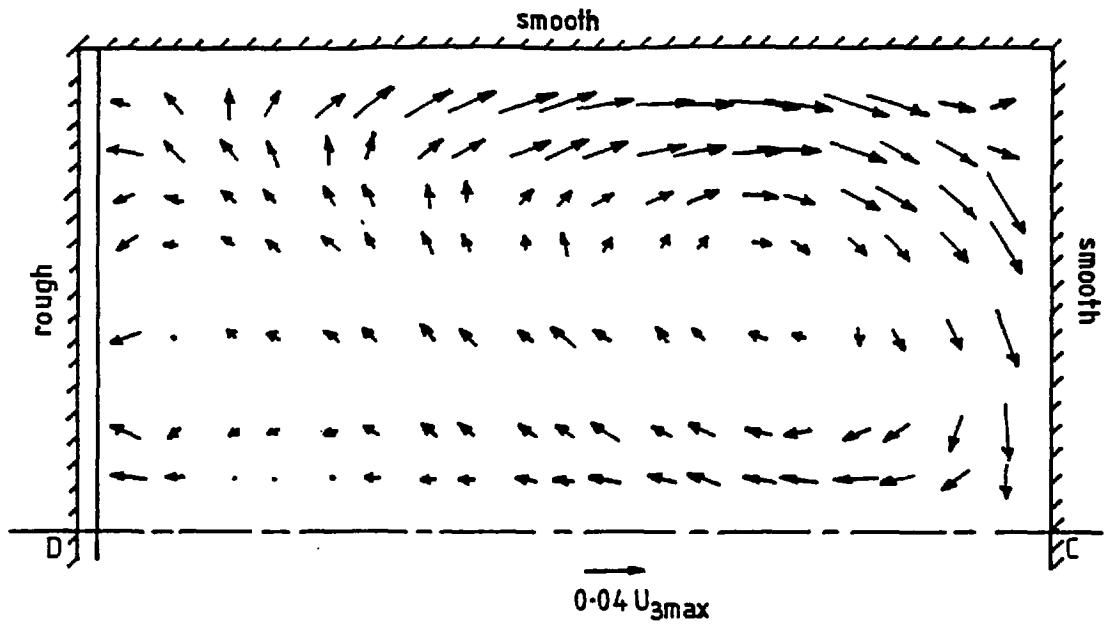


Figure 7.4.2 Experimental secondary velocity vectors in a square duct with one rough wall and $Re = 3.8 \times 10^5$ (Ali, 1978)

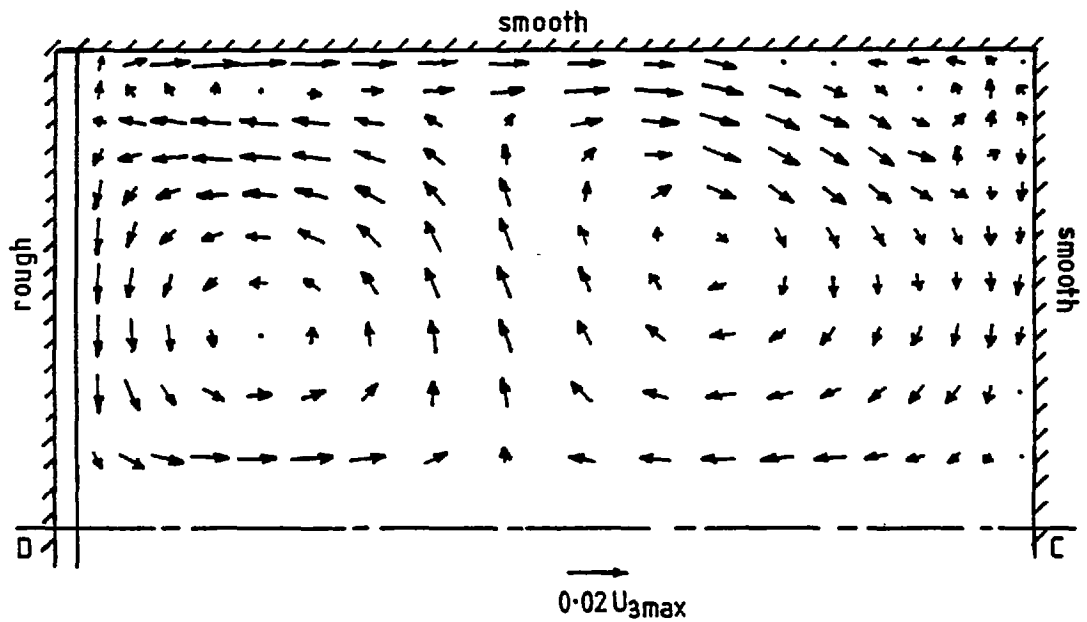


Figure 7.4.3 Predicted secondary velocity vectors in a square duct with one rough wall and $Re = 3.8 \times 10^5$ (this work)

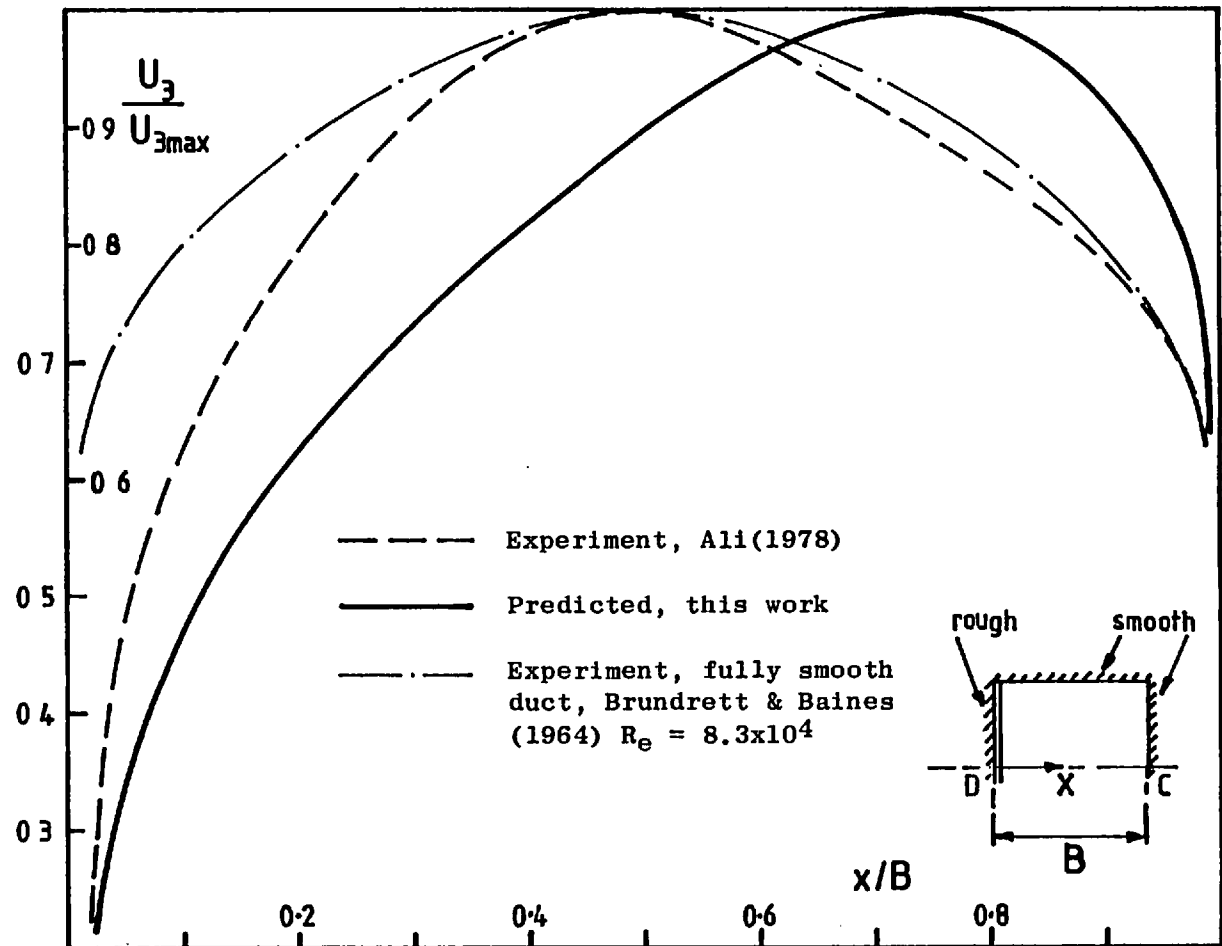


Figure 7.4.4 Centre-plane axial velocity profiles in a square duct with one rough wall and $Re = 3.8 \times 10^5$.

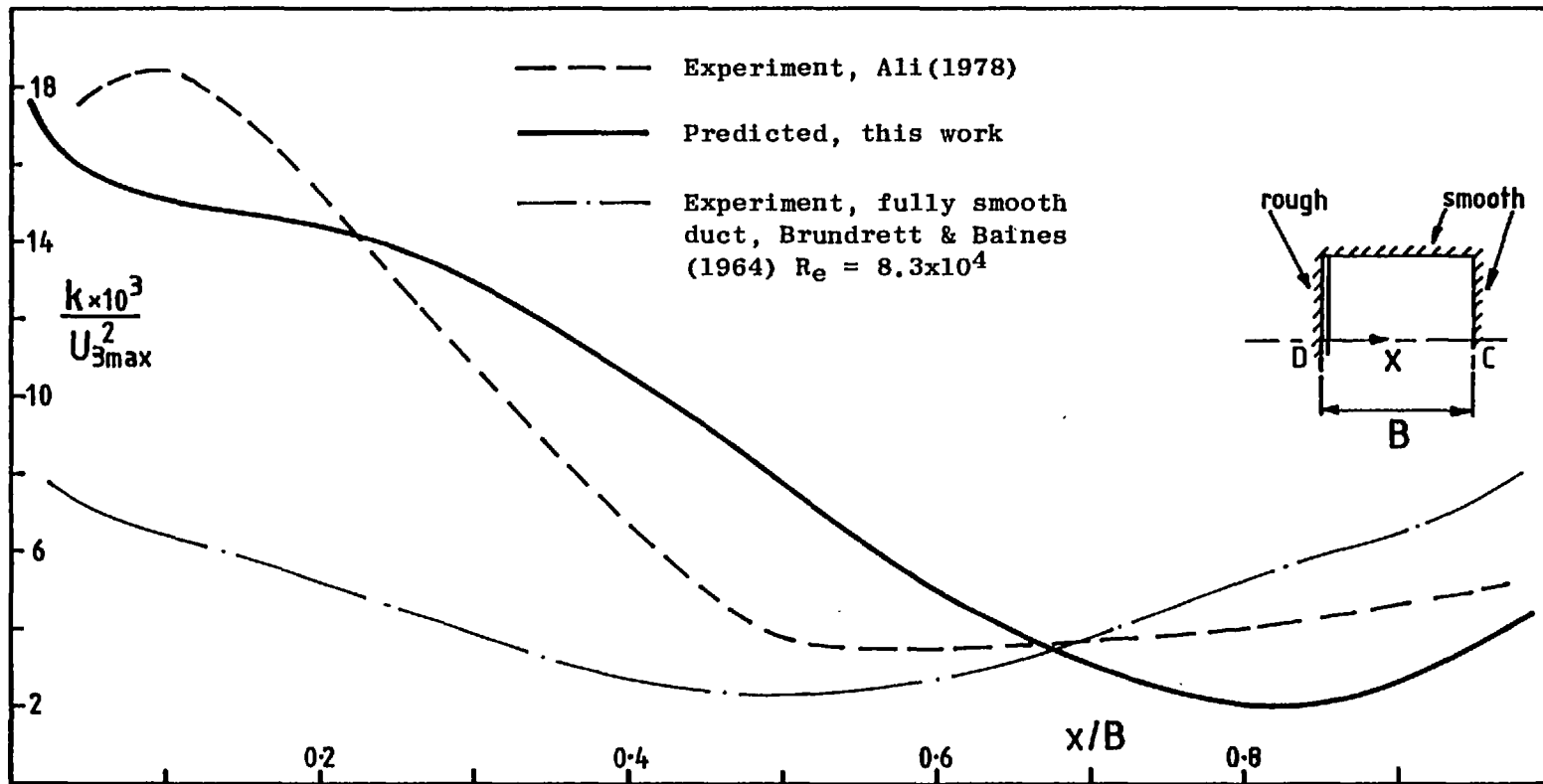


Figure 7.4.5 Centre-plane turbulence kinetic energy profiles in a square duct with one rough wall and $Re = 3.8 \times 10^5$

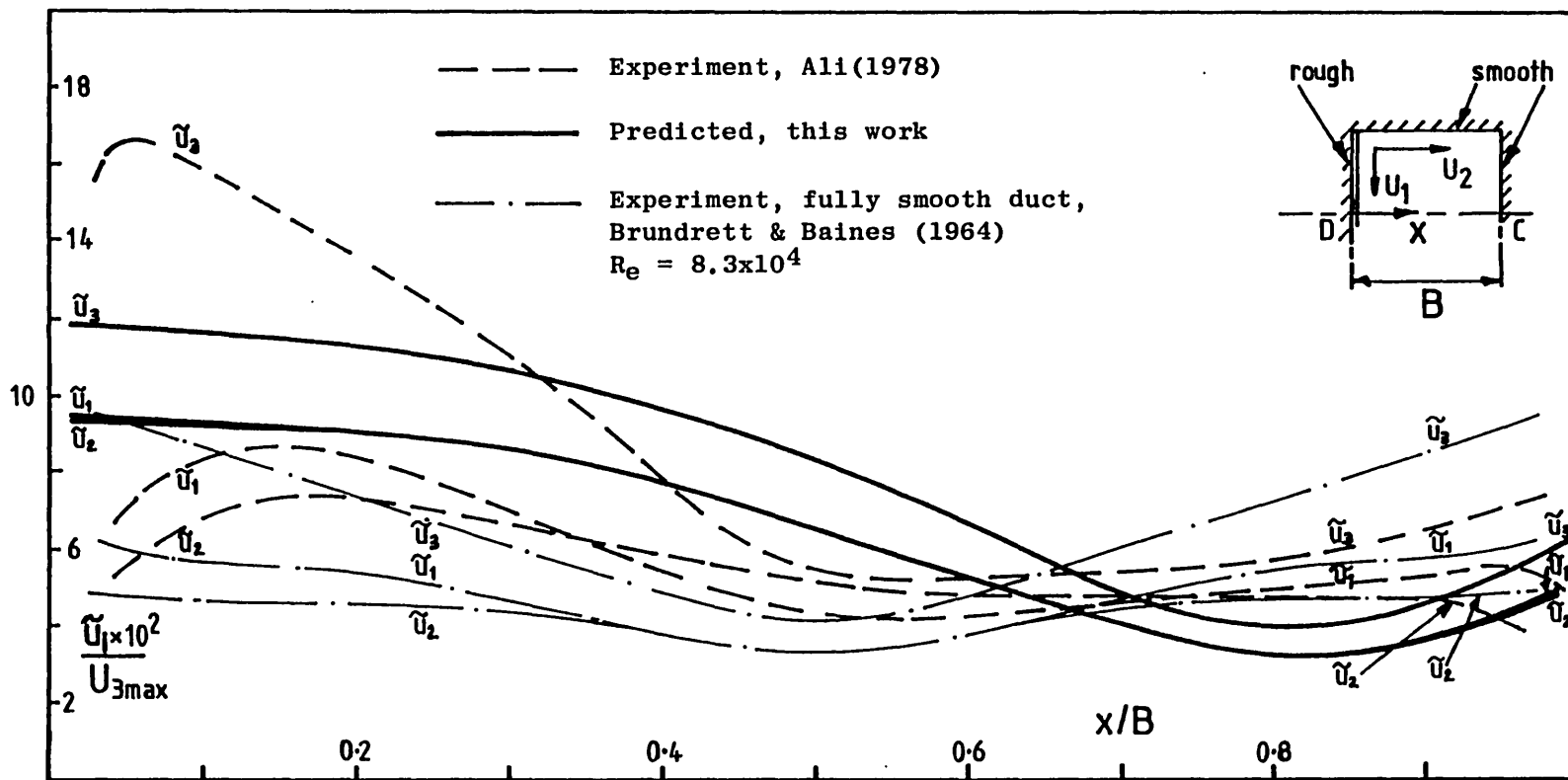


Figure 7.4.6 Centre-plane turbulence intensity profiles in a square duct with one rough wall and $Re = 3.8 \times 10^5$.

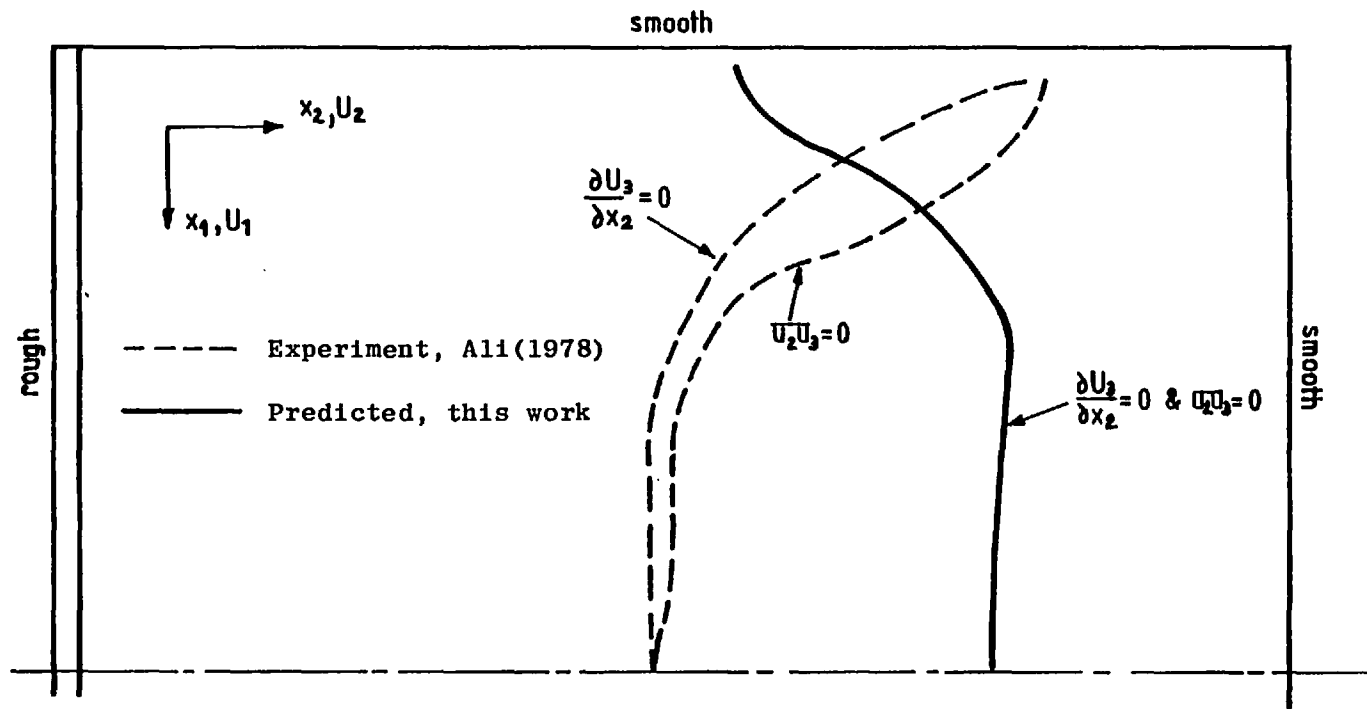


Figure 7.4.7 Loci of zero axial velocity gradient and shear stress in a square duct with one rough wall and $Re = 3.8 \times 10^5$.

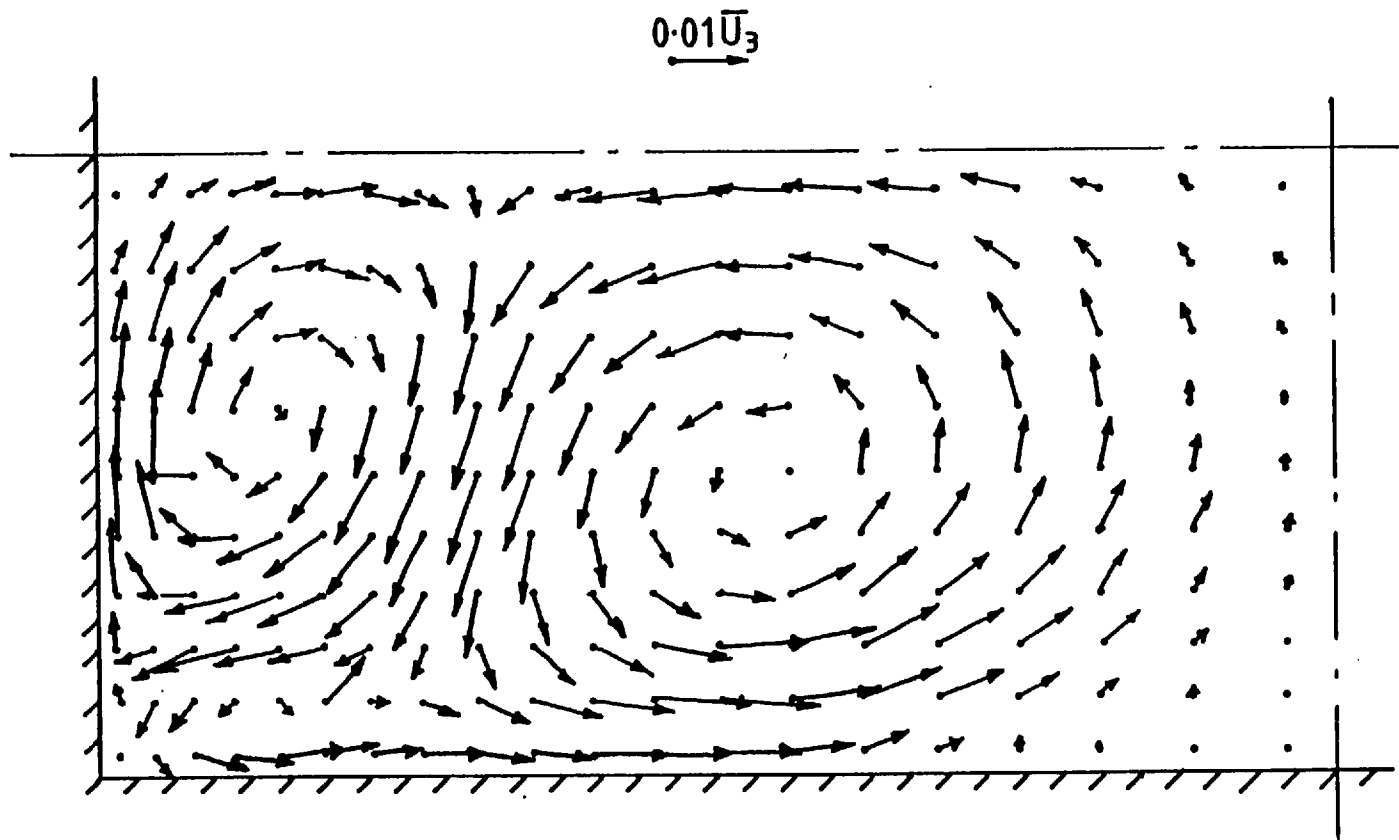
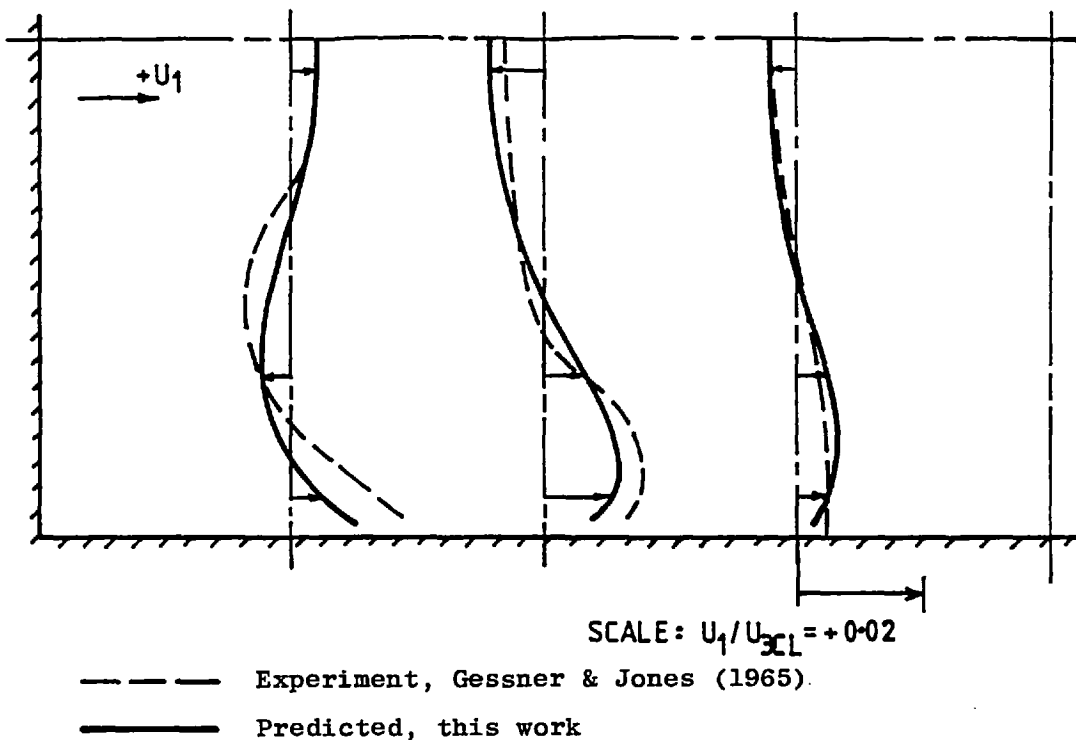
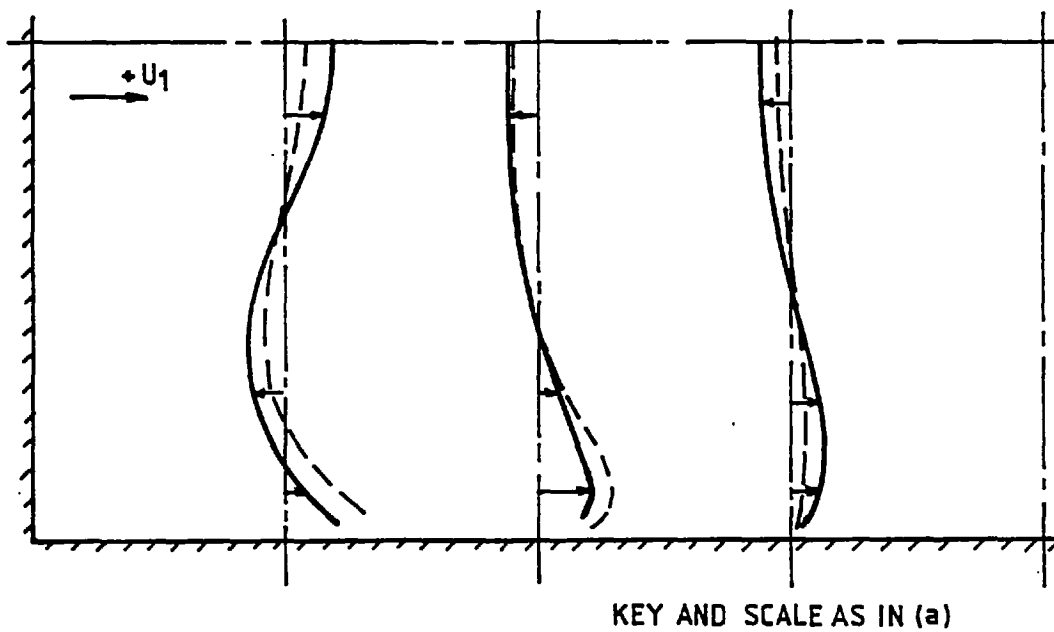


Figure 7.5.1 Predicted secondary velocity vectors in a rectangular duct with $AR = 2$ and $Re = 5 \times 10^4$.



(a) $Re = 5 \times 10^4$



(b) $Re = 3 \times 10^5$

Figure 7.5.2 Secondary velocity profiles (U_1/U_{3CL}) in a rectangular duct with $AR = 2$.

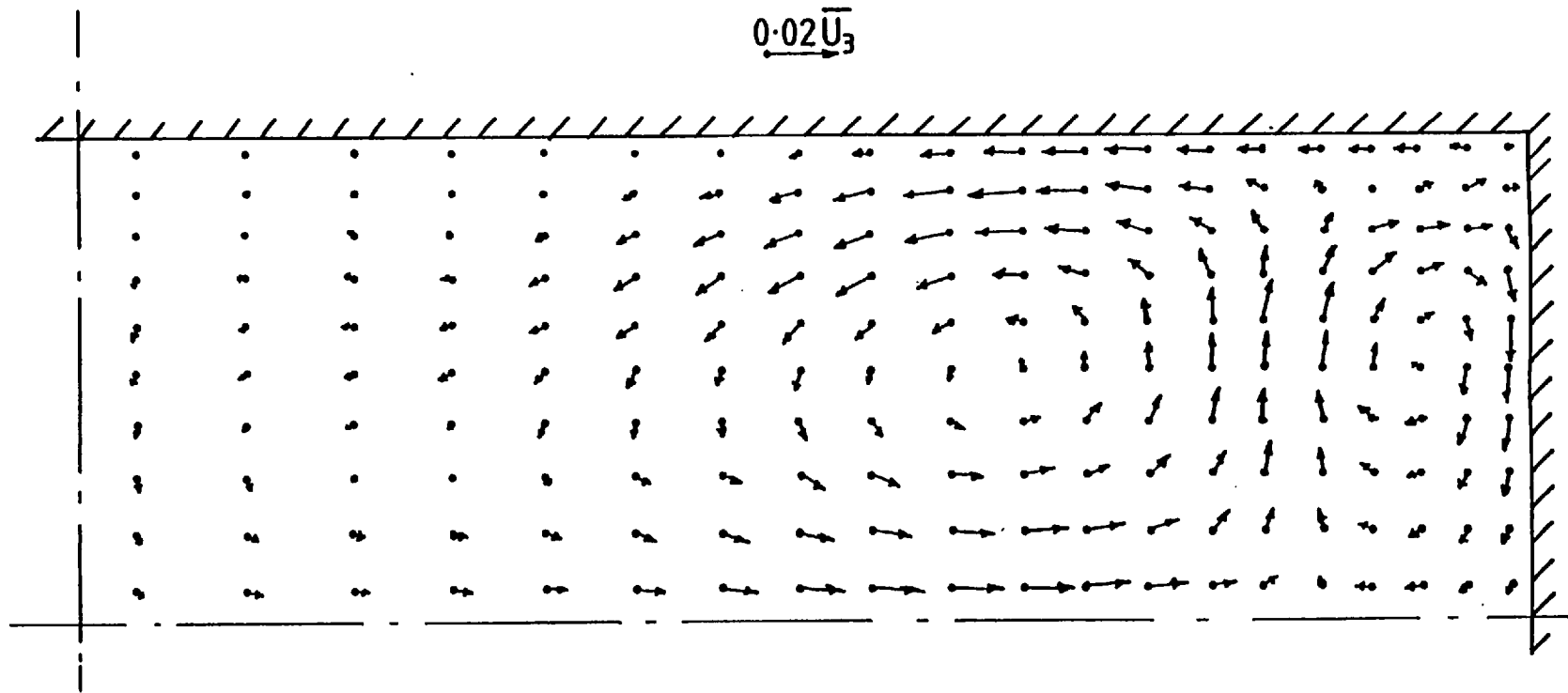


Figure 7.5.3 Predicted secondary velocity vectors in a rectangular duct with $AR = 3$ and $Re = 5.6 \times 10^4$.

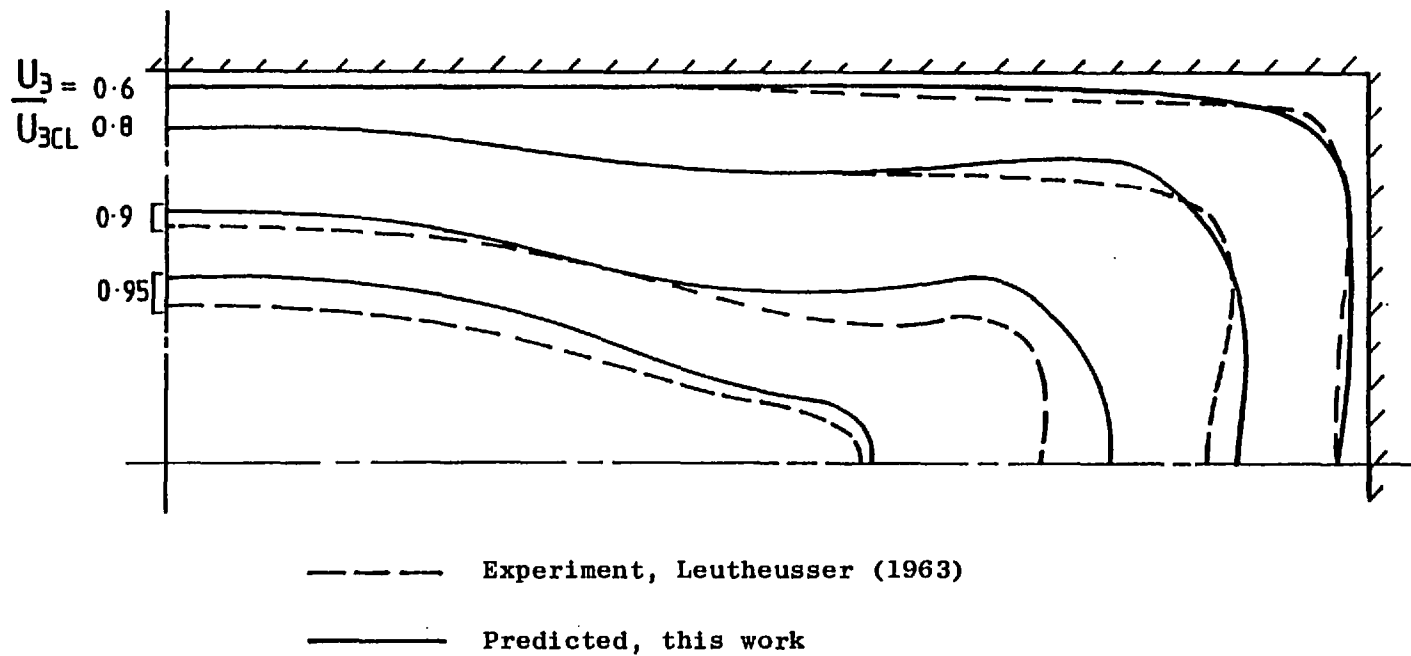


Figure 7.5.4 Axial velocity contours in a rectangular duct with $AR = 3$ and $Re = 5.6 \times 10^4$.

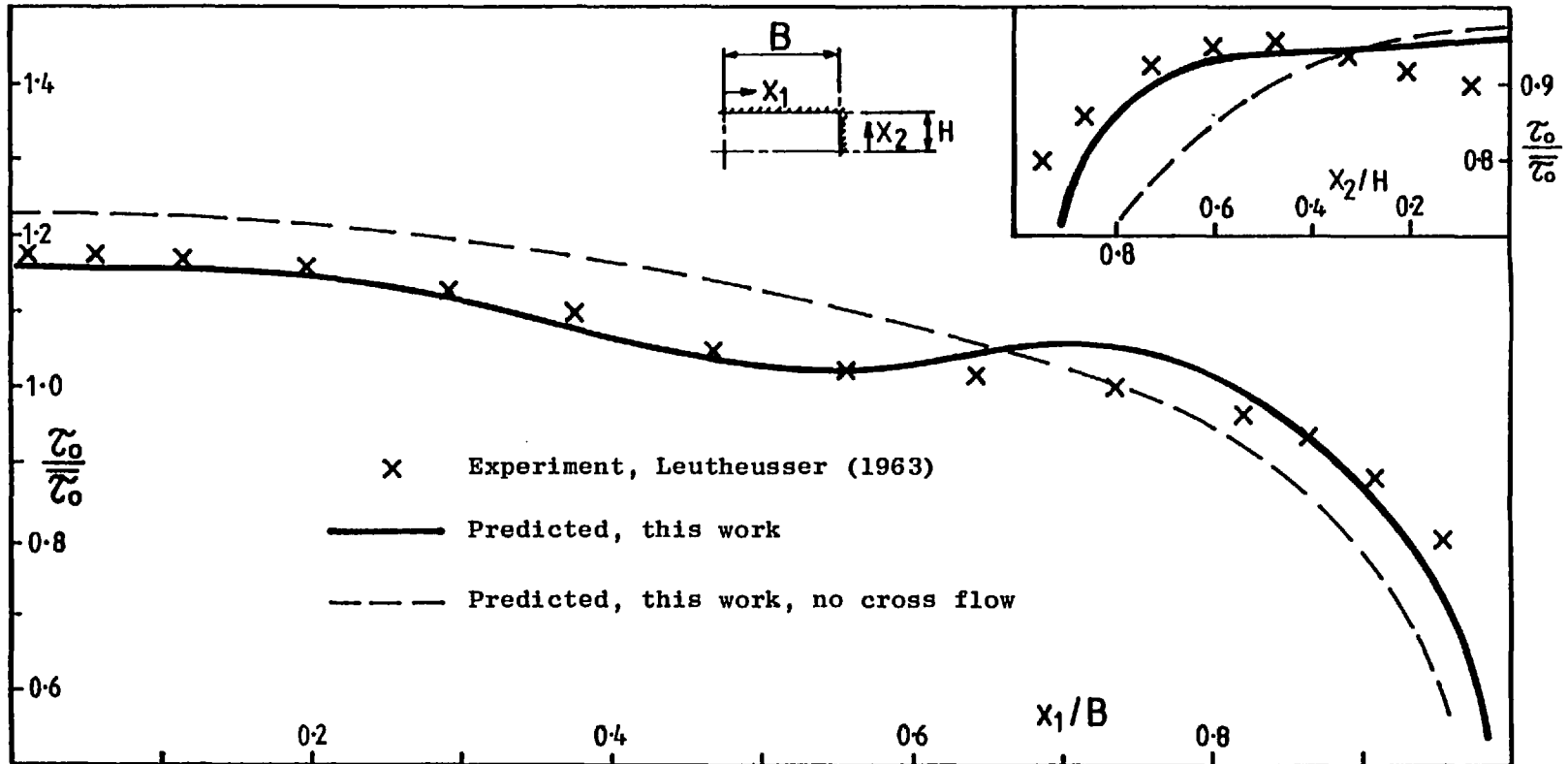


Figure 7.5.5 Wall shear stress in a rectangular duct with $AR = 3$ and $Re = 5.6 \times 10^4$.

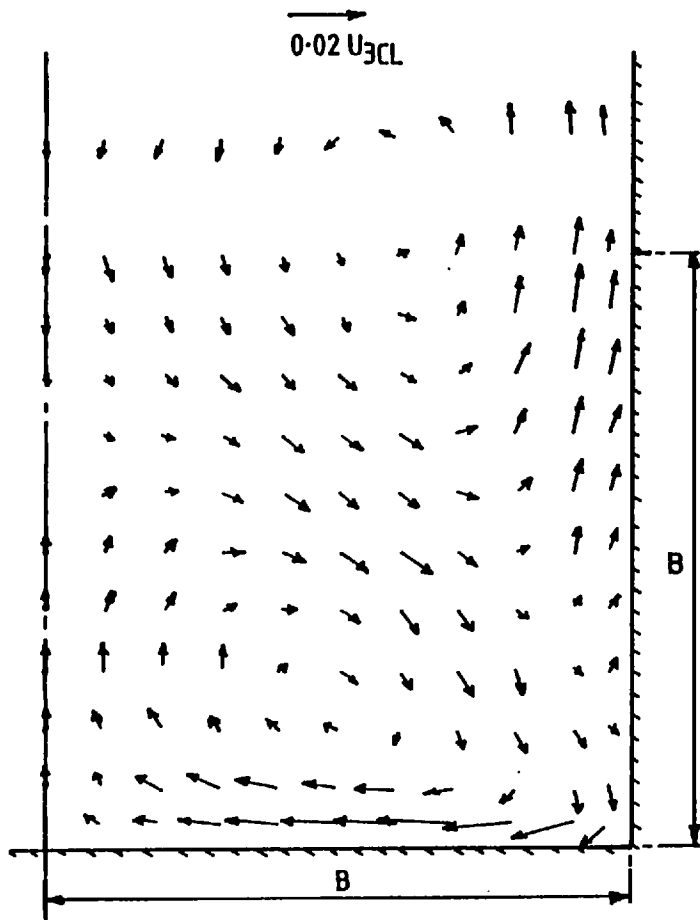


Figure 7.5.6 Measured secondary velocity vectors in the corner region of a rectangular duct with $AR = 6.4$ and $Re = 1.3 \times 10^5$ (Tracy, 1965)

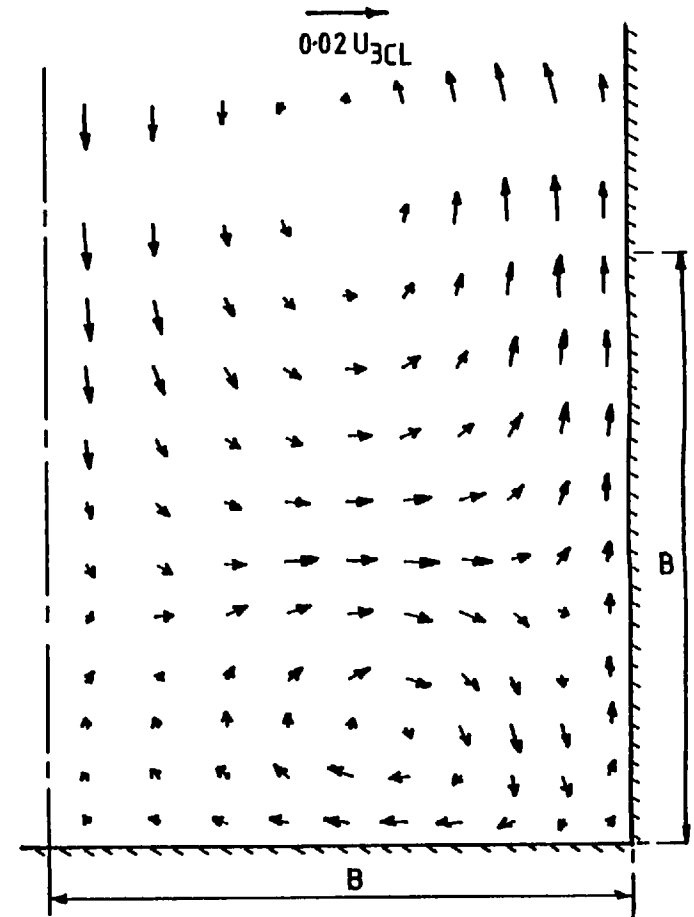
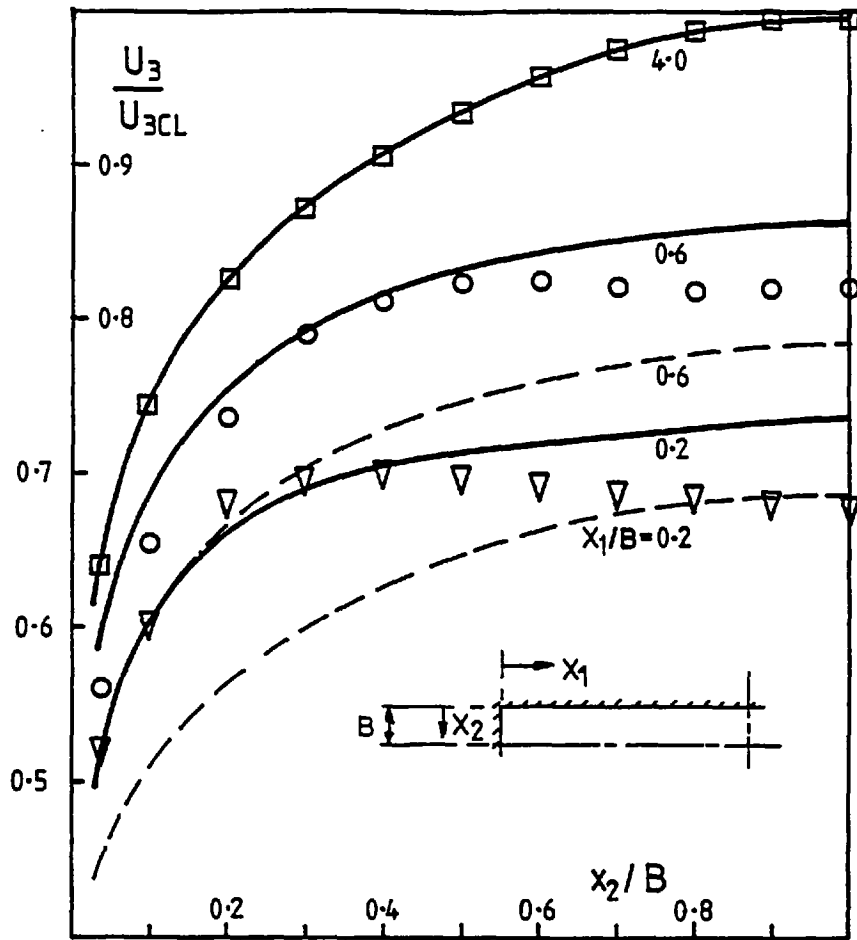


Figure 7.5.7 Predicted secondary velocity vectors in the corner region of a rectangular duct with $AR = 6.4$ and $Re = 1.3 \times 10^5$ (this work)



- ▽ $X_1/B=0.2$
- $X_1/B=0.6$
- $X_1/B=4.0$

Experiment, Tracy (1965)

————— Predicted, this work

- - - - - Predicted, this work, no cross flow

Figure 7.5.8 Axial velocity profiles in a rectangular duct with AR = 6.4 and $Re = 1.3 \times 10^5$.

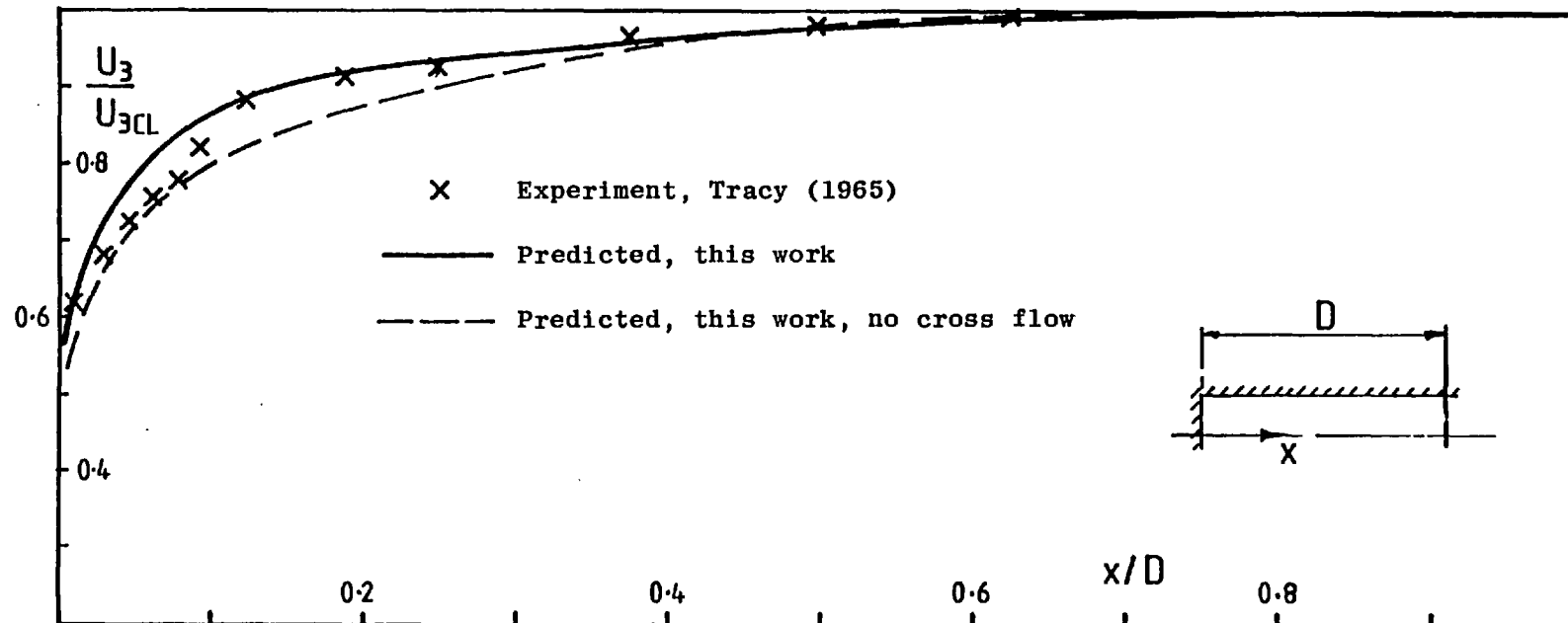
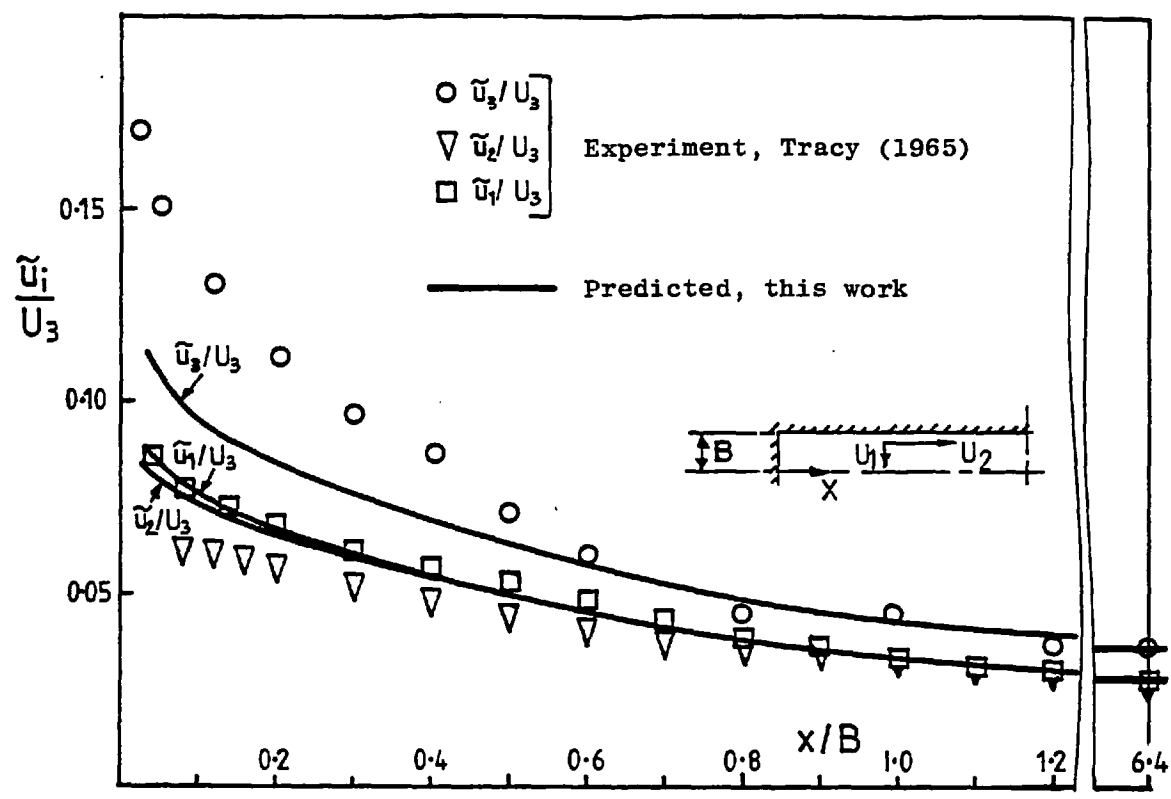
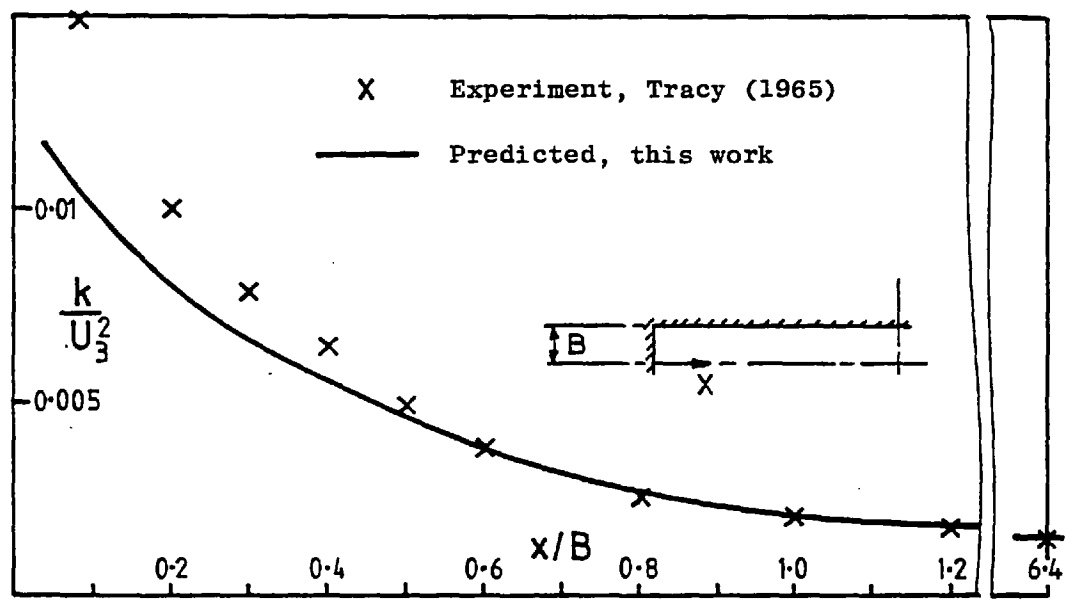


Figure 7.5.9 Centre-plane axial velocity profiles in a rectangular duct with $AR = 6.4$ and $Re = 1.3 \times 10^5$.

7.5.10
ast
→
3/4 cm



(a) turbulence intensities



(b) turbulence kinetic energy

Figure 7.5.10 Turbulence kinetic energy and intensities along the centre-plane in a rectangular duct with $AR = 6.4$ and $Re = 1.3 \times 10^5$.

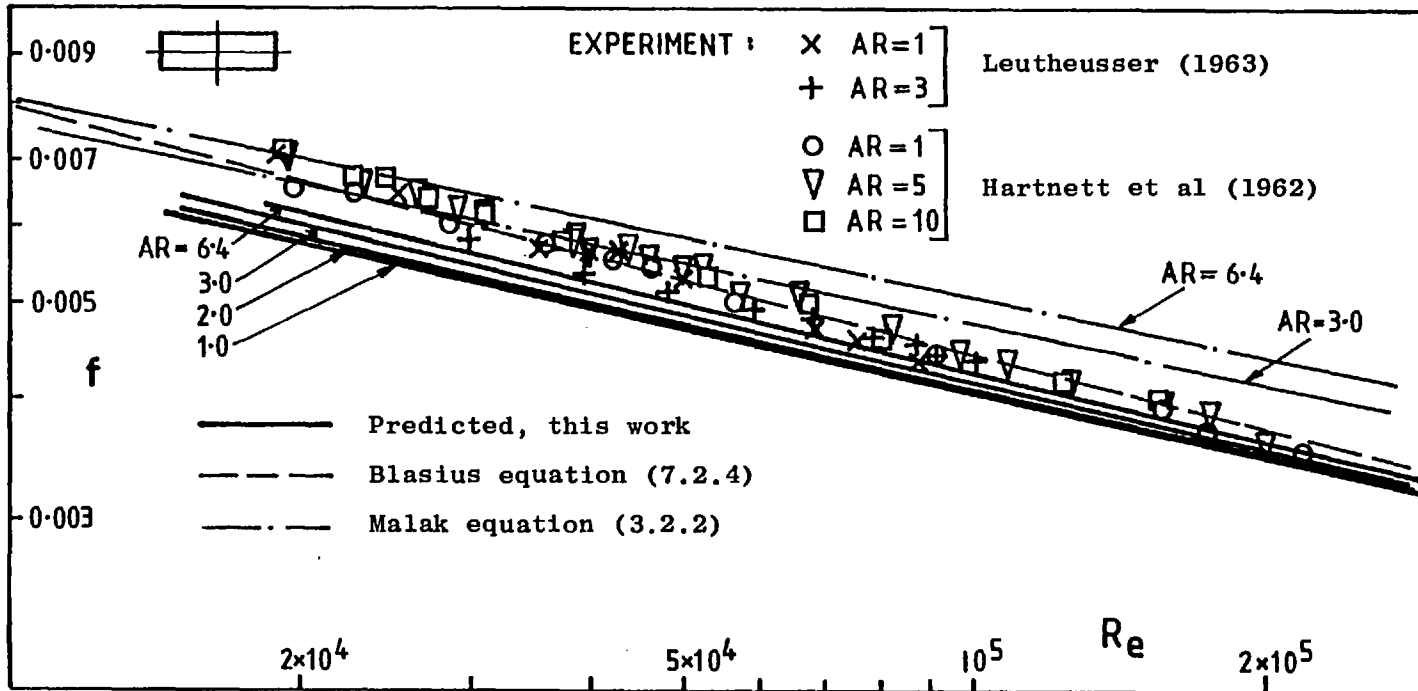


Figure 7.5.11 Friction factor characteristics for rectangular ducts.

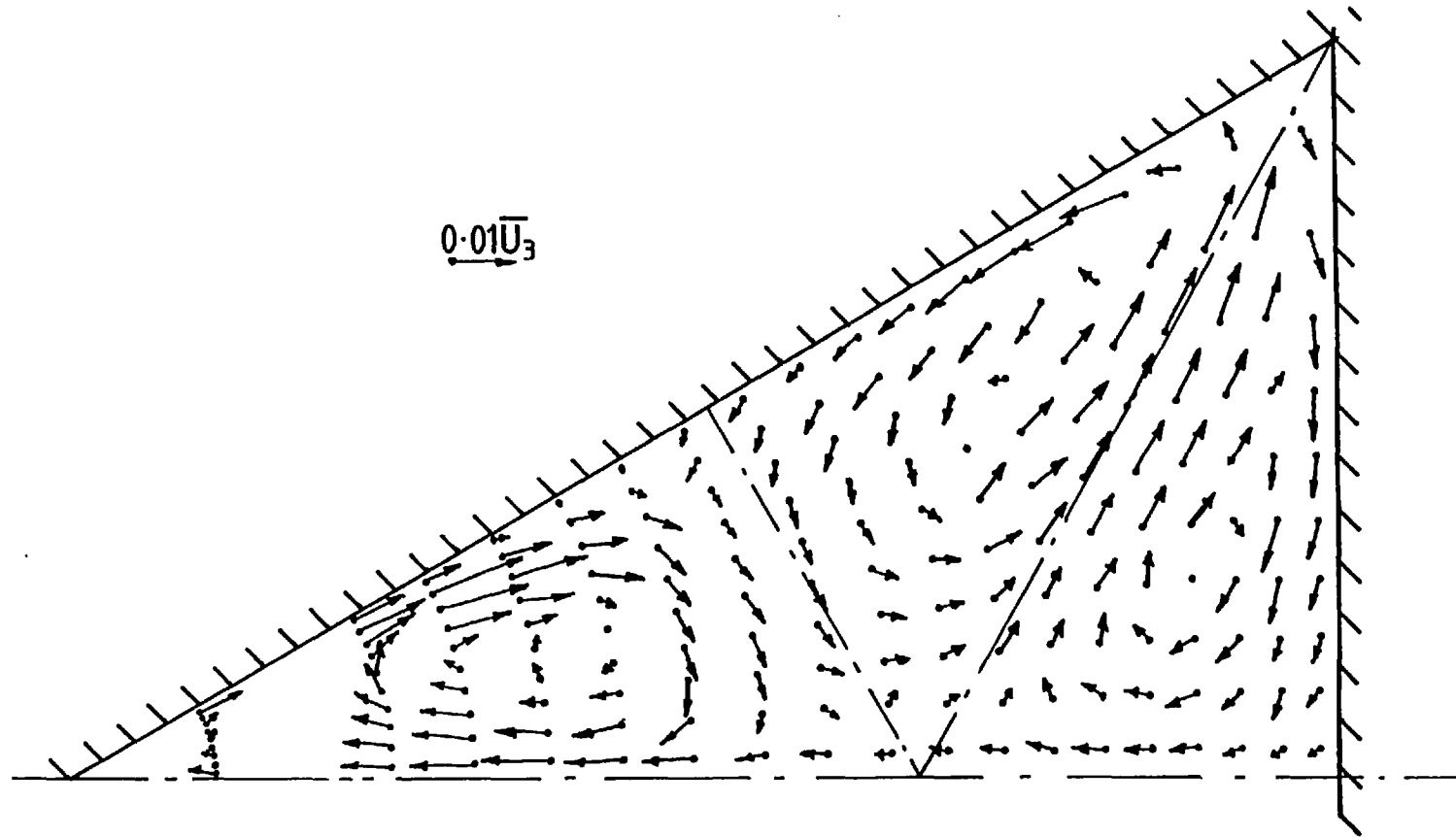


Figure 7.6.1 Predicted secondary velocity vectors in an equilateral triangular duct with $Re = 5.3 \times 10^4$.

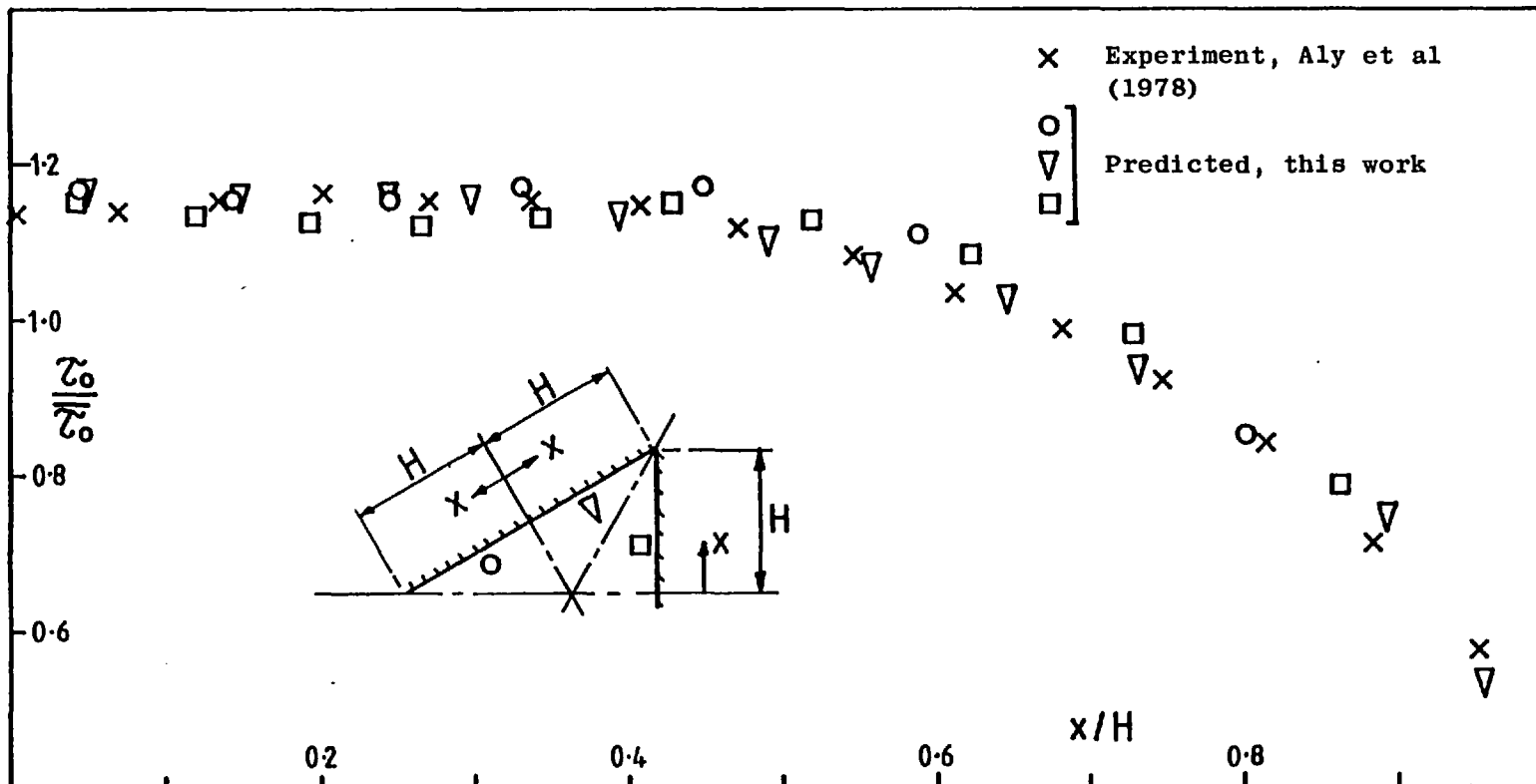


Figure 7.6.2 Predicted wall shear stress from symmetry tests in an equilateral triangular duct with $Re = 5.3 \times 10^4$.

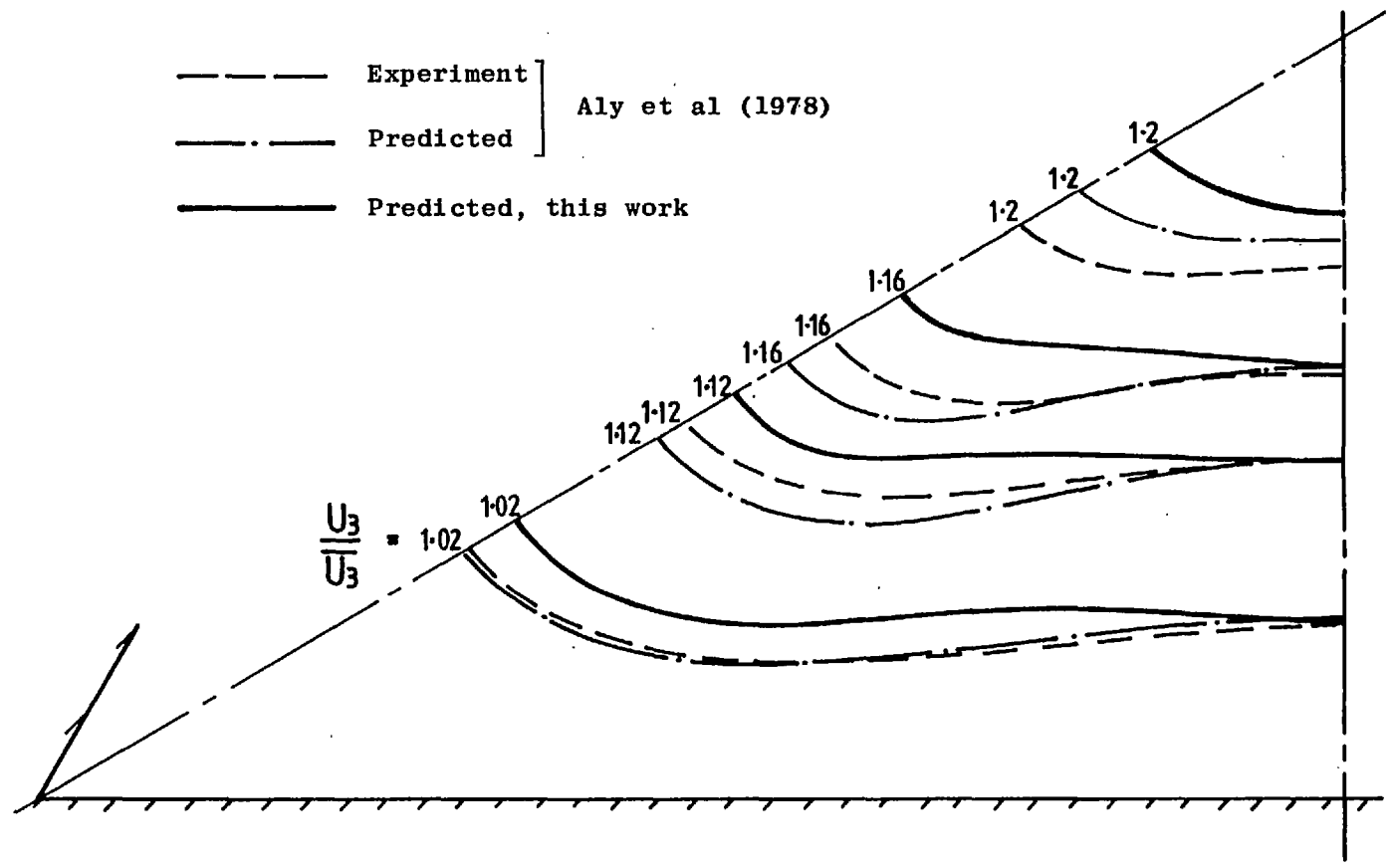


Figure 7.6.3 Axial velocity contours in an equilateral triangular duct with $Re = 5.3 \times 10^4$.

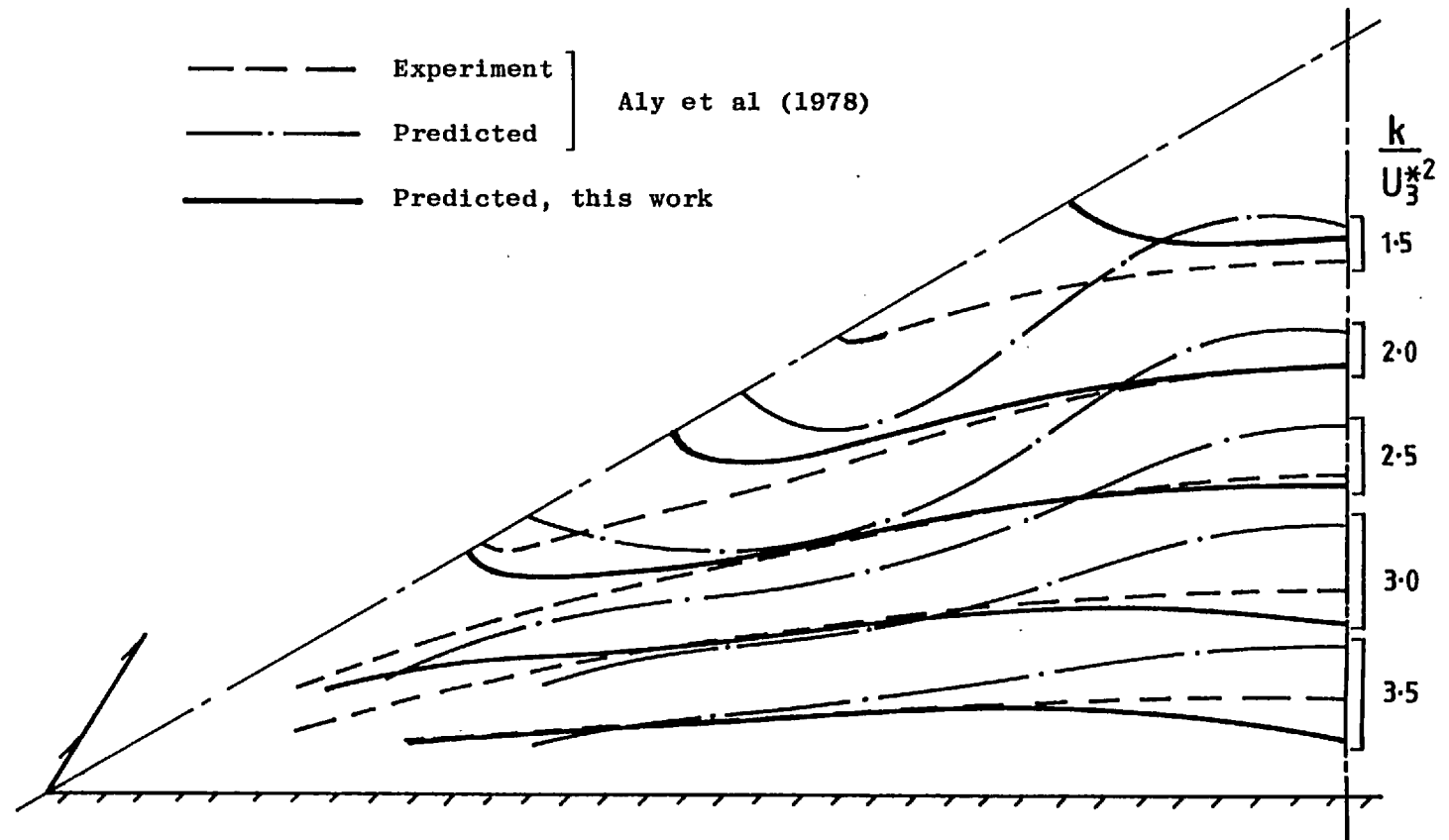


Figure 7.6.4 Turbulence kinetic energy contours in an equilateral triangular duct with $Re = 5.3 \times 10^4$.

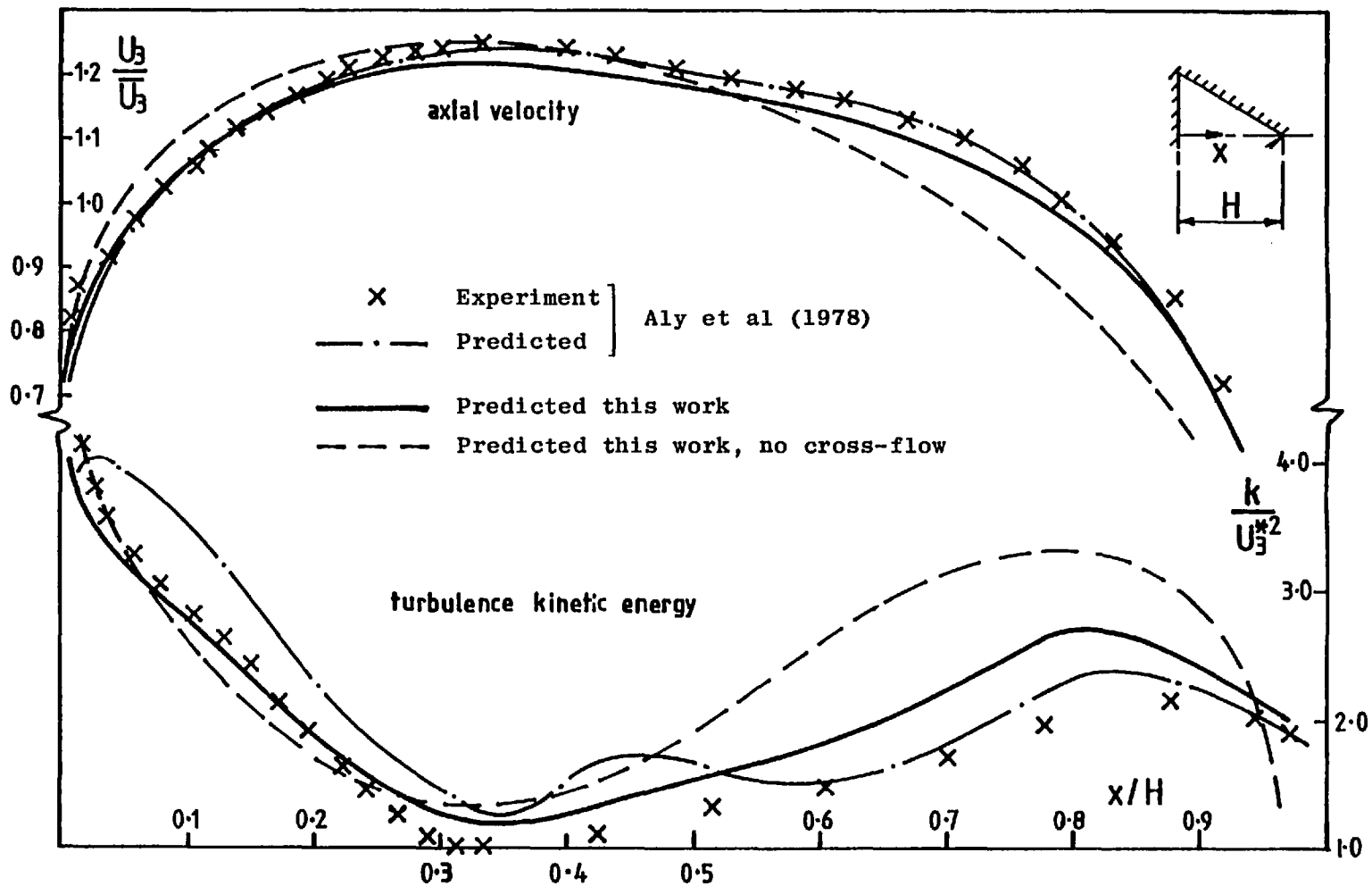


Figure 7.6.5 Centre-plane axial velocity and turbulence kinetic energy profiles in an equilateral triangular duct with $Re = 5.3 \times 10^4$.

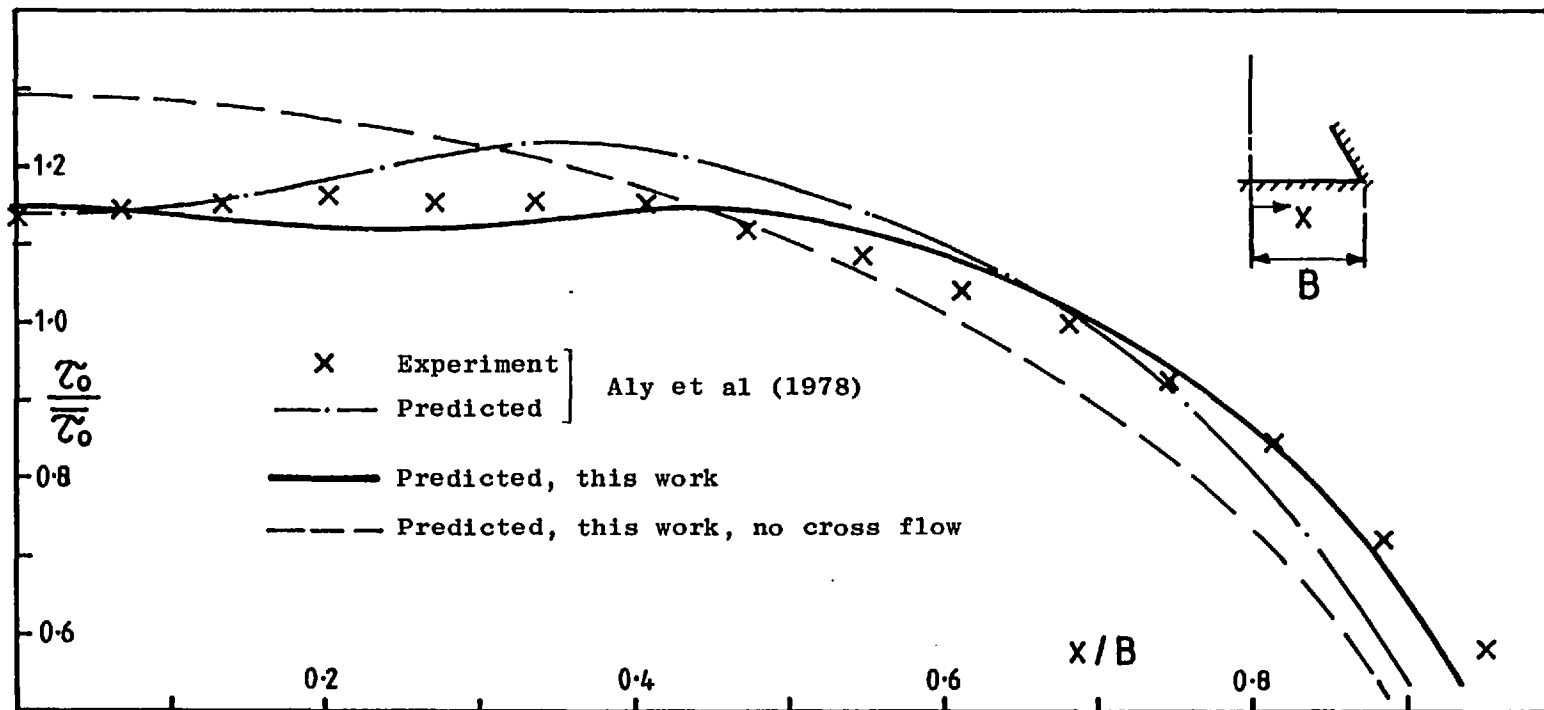


Figure 7.6.6 Wall shear stress in an equilateral triangular duct with $Re = 5.3 \times 10^4$.

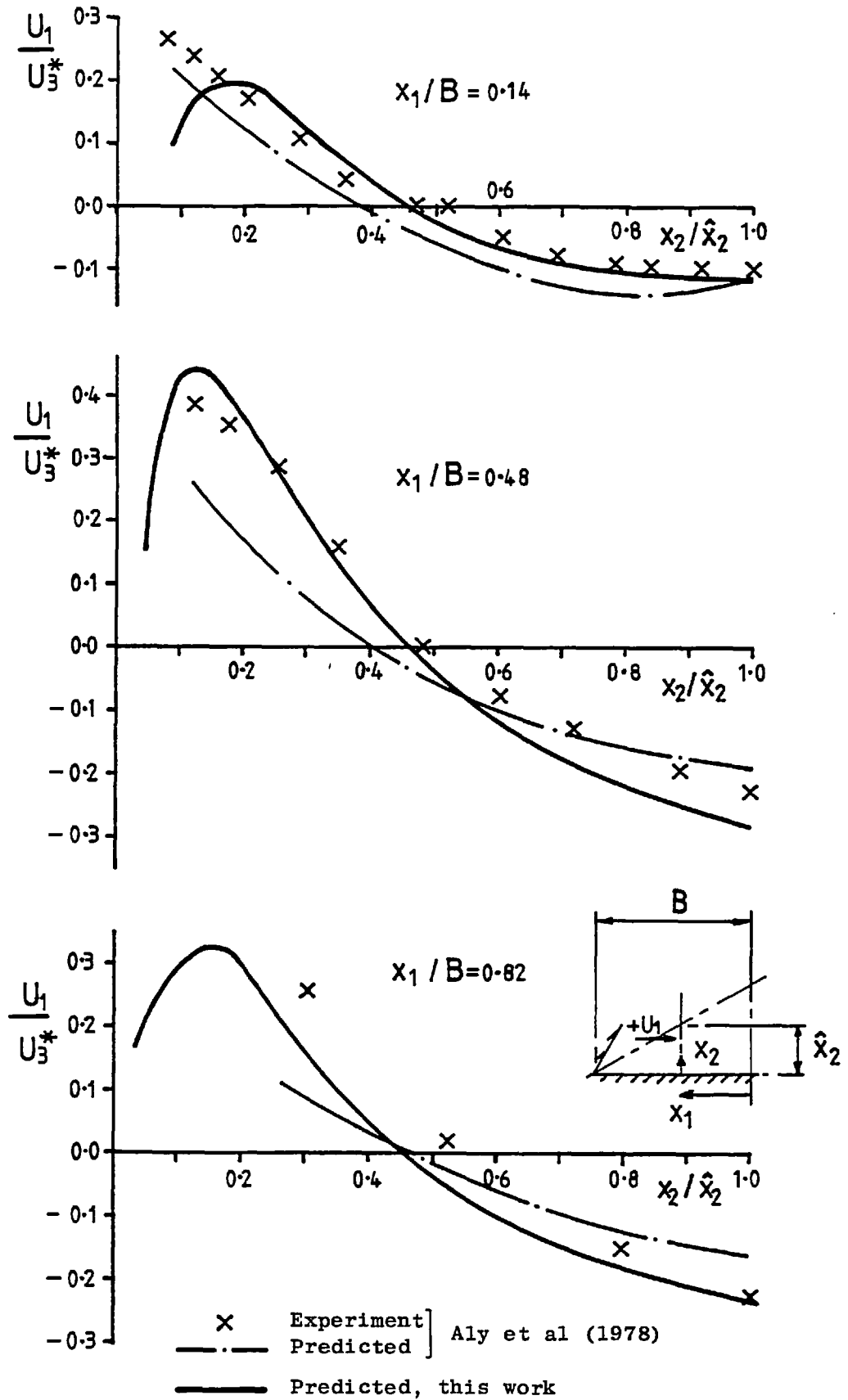


Figure 7.6.7 Secondary velocity profiles in an equilateral triangular duct with $Re = 5.3 \times 10^4$.

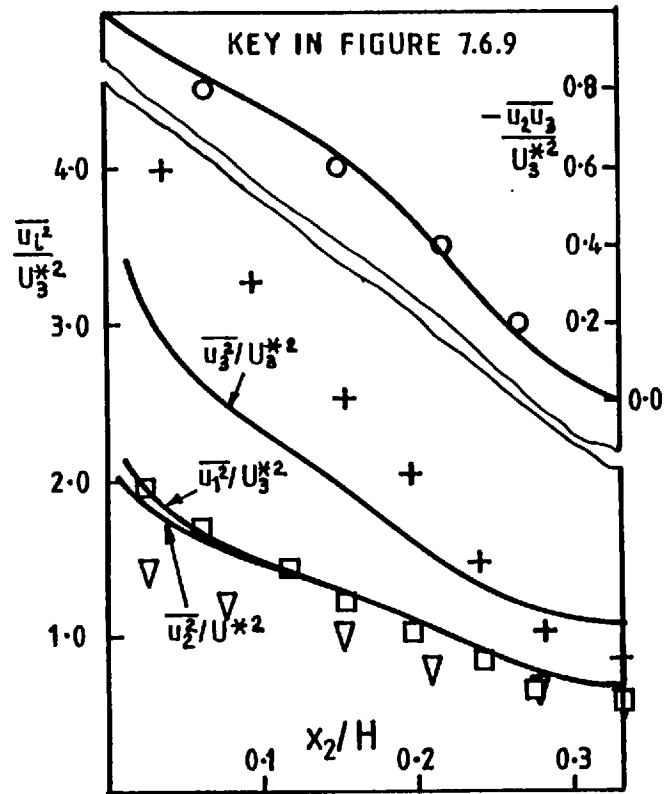


Figure 7.6.8 Centre-plane Reynolds stresses in an equilateral triangular duct with $Re = 5.3 \times 10^4$.

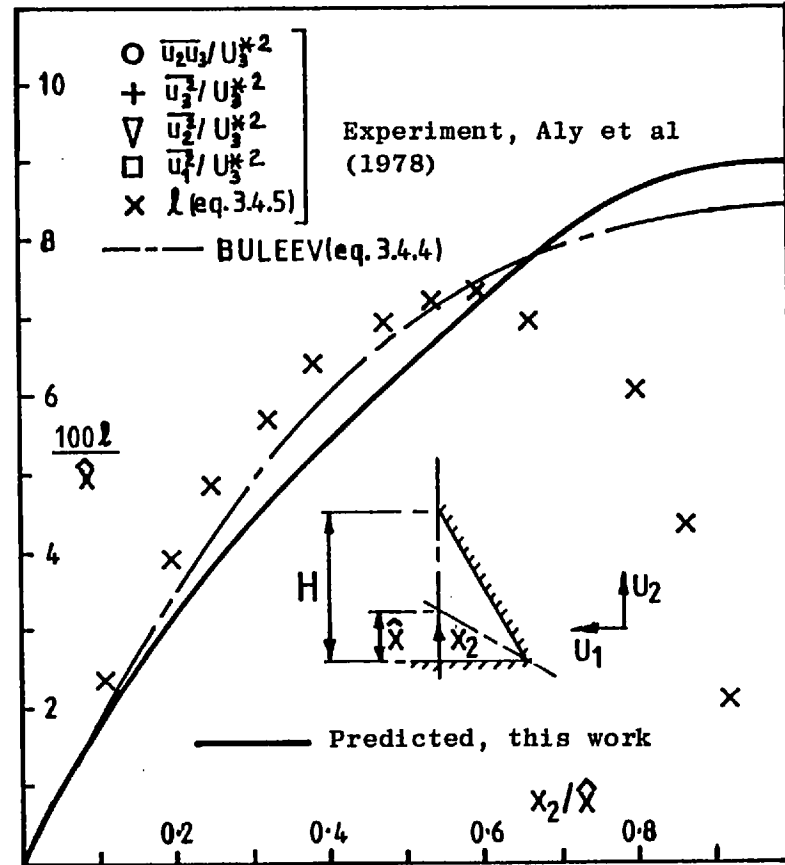


Figure 7.6.9 Centre-plane length scale profiles in an equilateral triangular duct with $Re = 5.3 \times 10^4$.

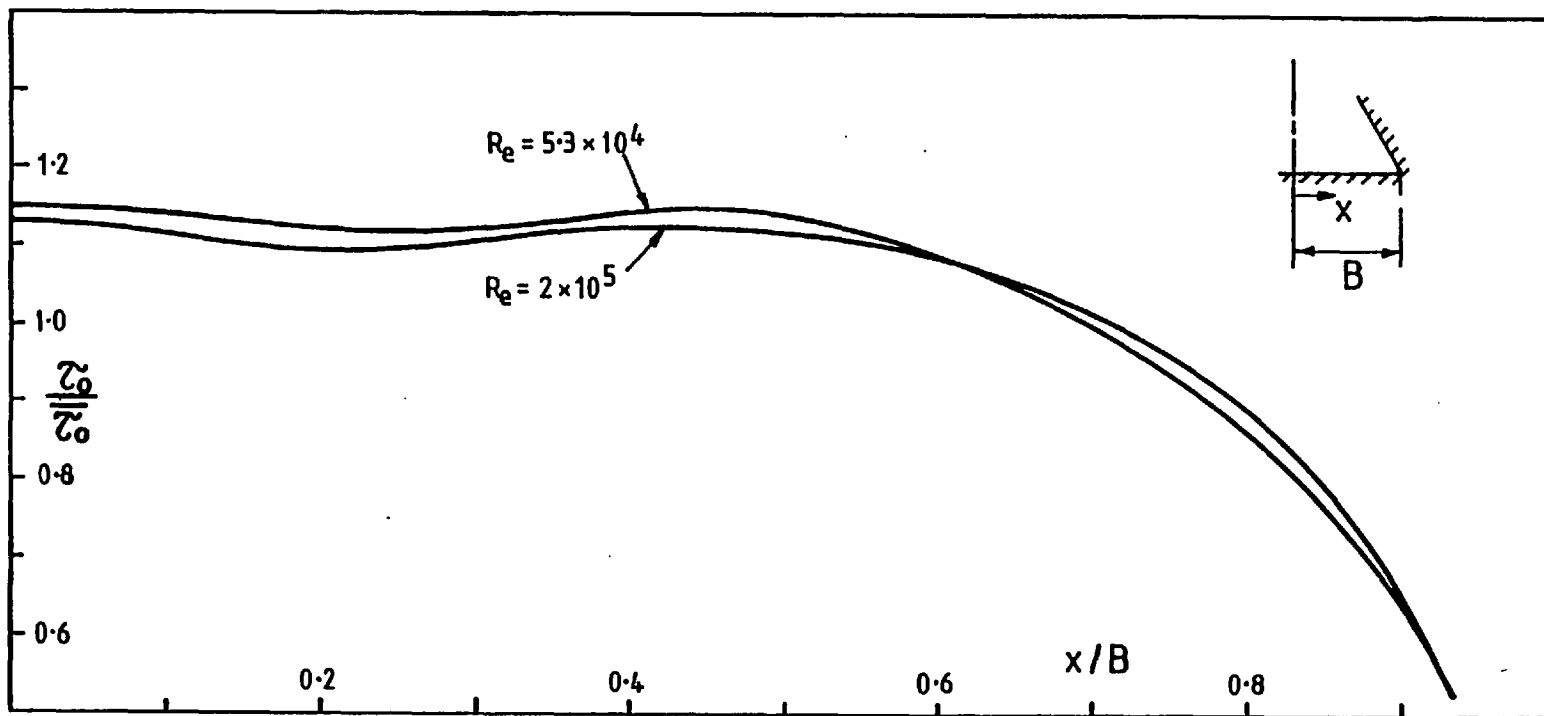


Figure 7.6.10 Predicted wall shear stress in an equilateral triangular duct.

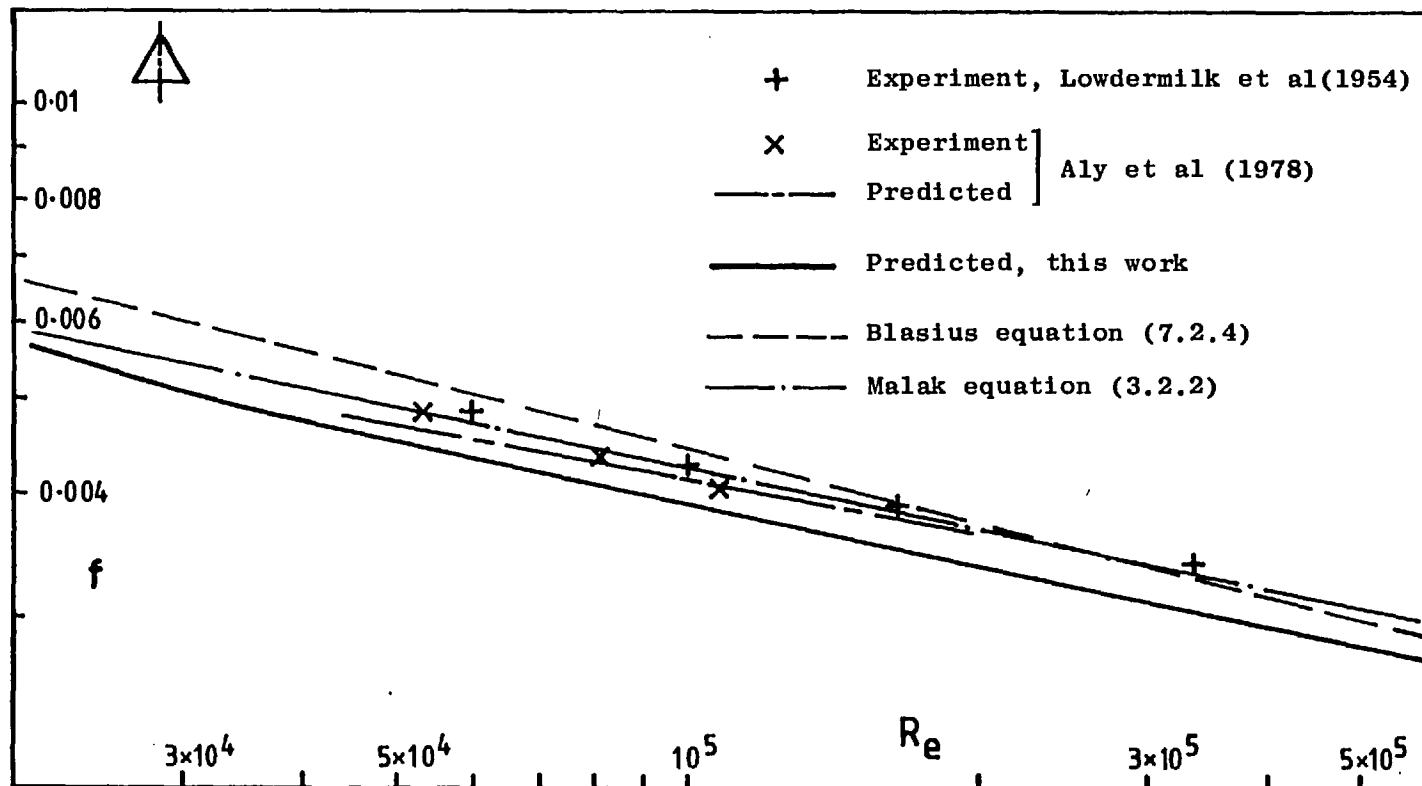


Figure 7.6.11 Friction factor characteristics for an equilateral triangular duct.

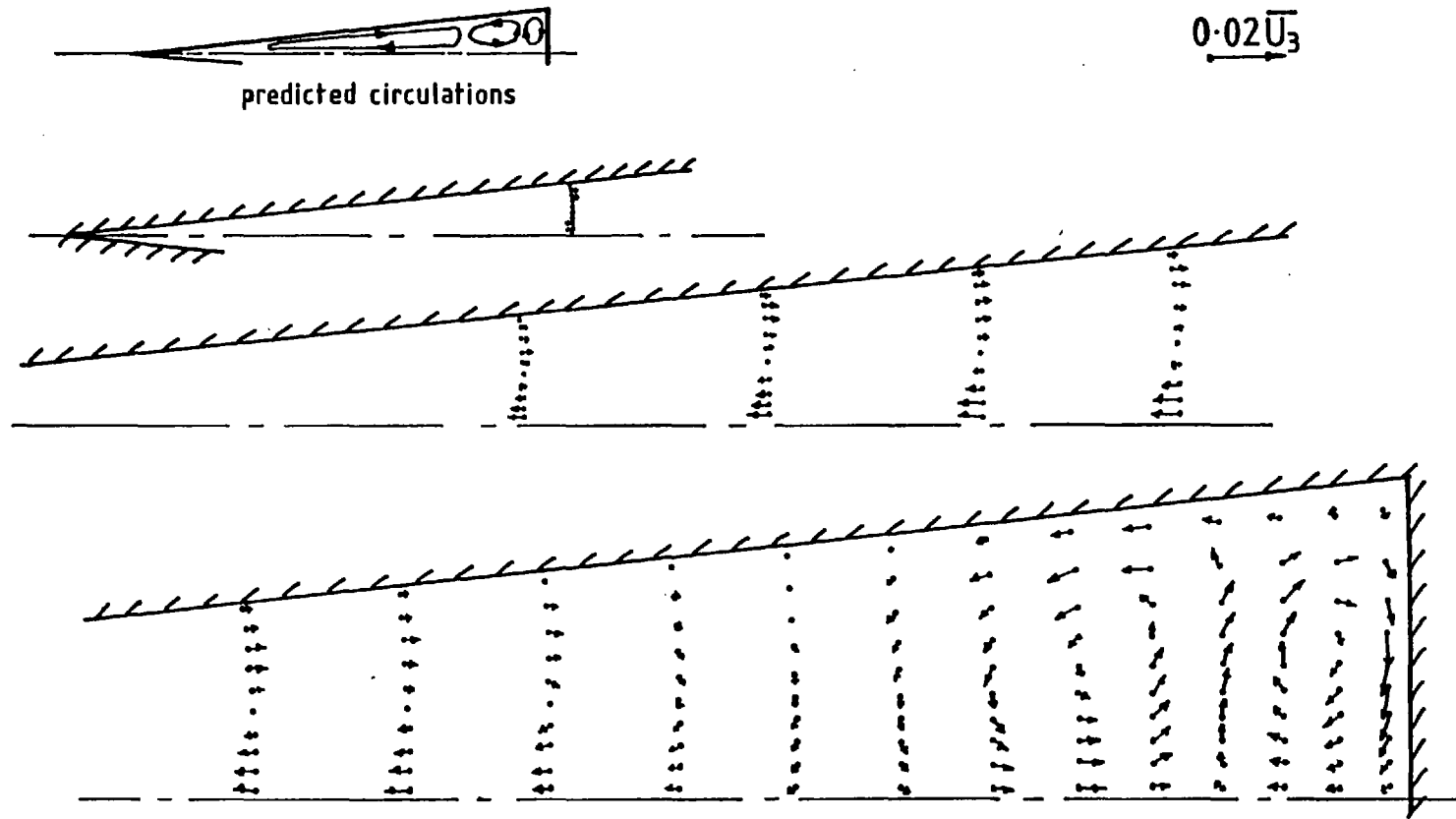


Figure 7.7.1 Predicted secondary velocity vectors in an isosceles triangular duct of apex angle 11.7° and with $Re = 1.09 \times 10^4$.

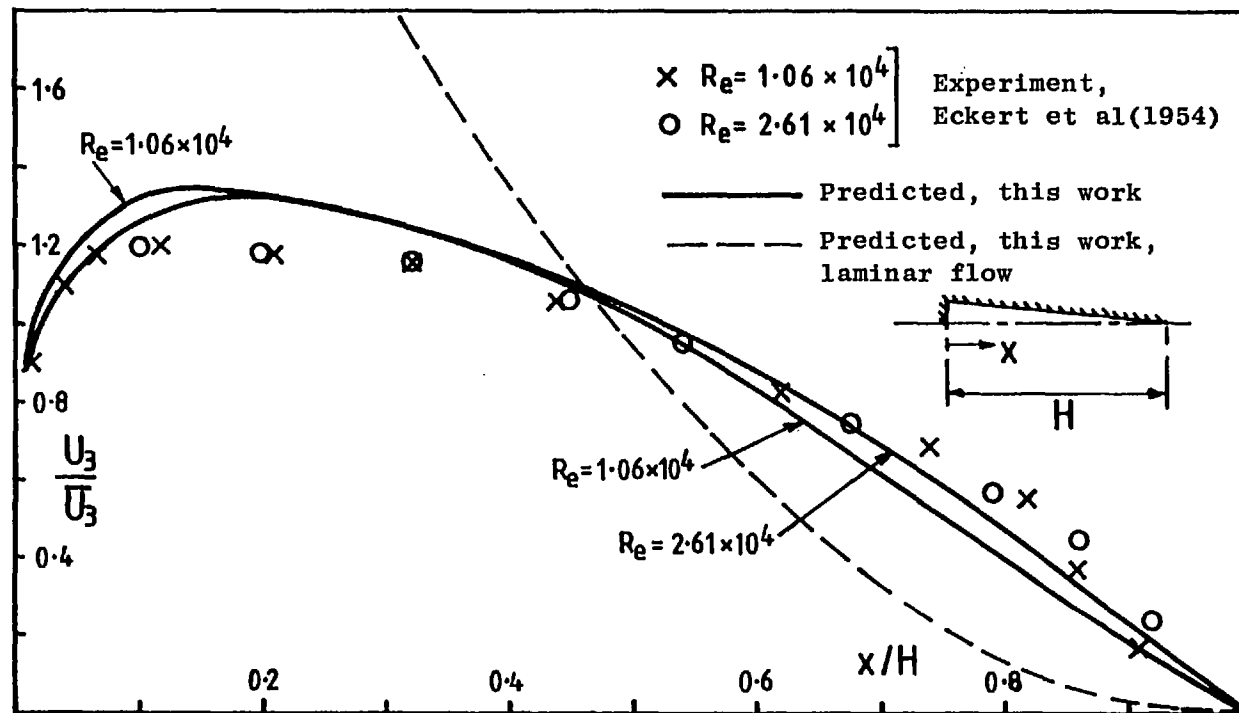


Figure 7.7.2 Centre-plane axial velocity profiles in an isosceles triangular duct of apex angle 11.7° .

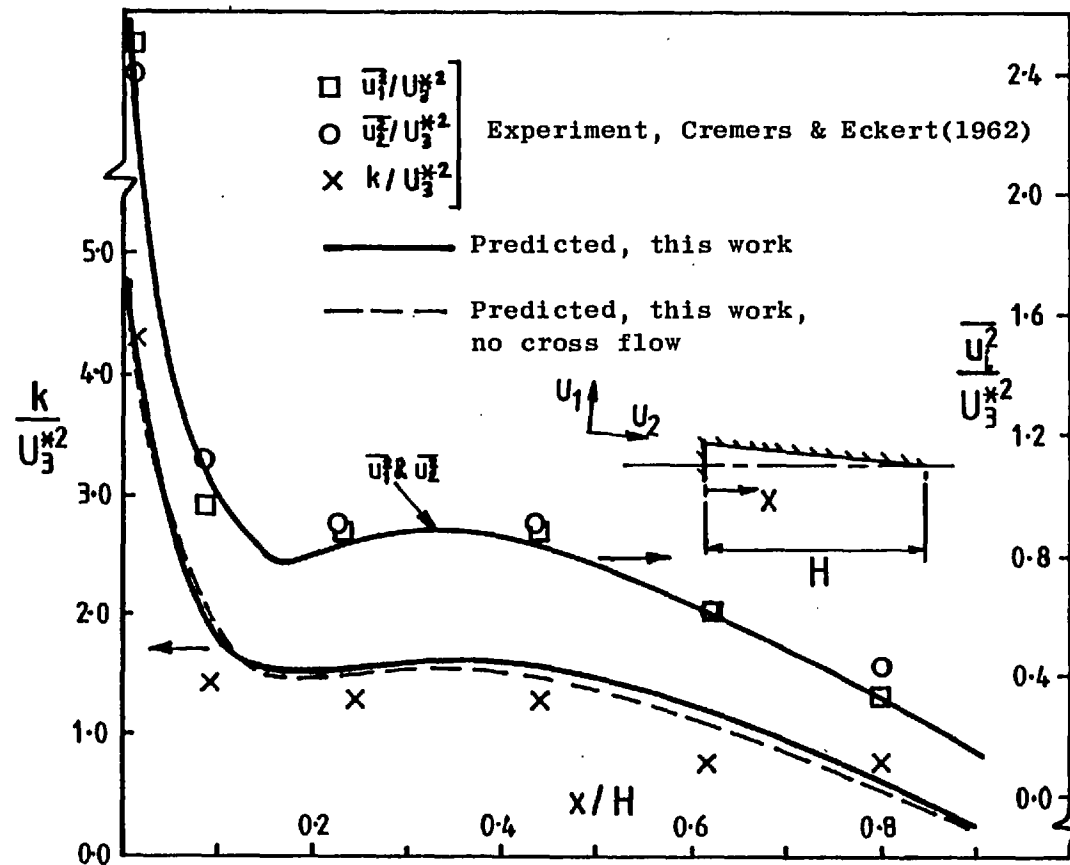


Figure 7.7.3 Centre-plane turbulence kinetic energy and normal stress profiles in an isosceles triangular duct of apex angle 11.7° and with $Re = 1.09 \times 10^4$.

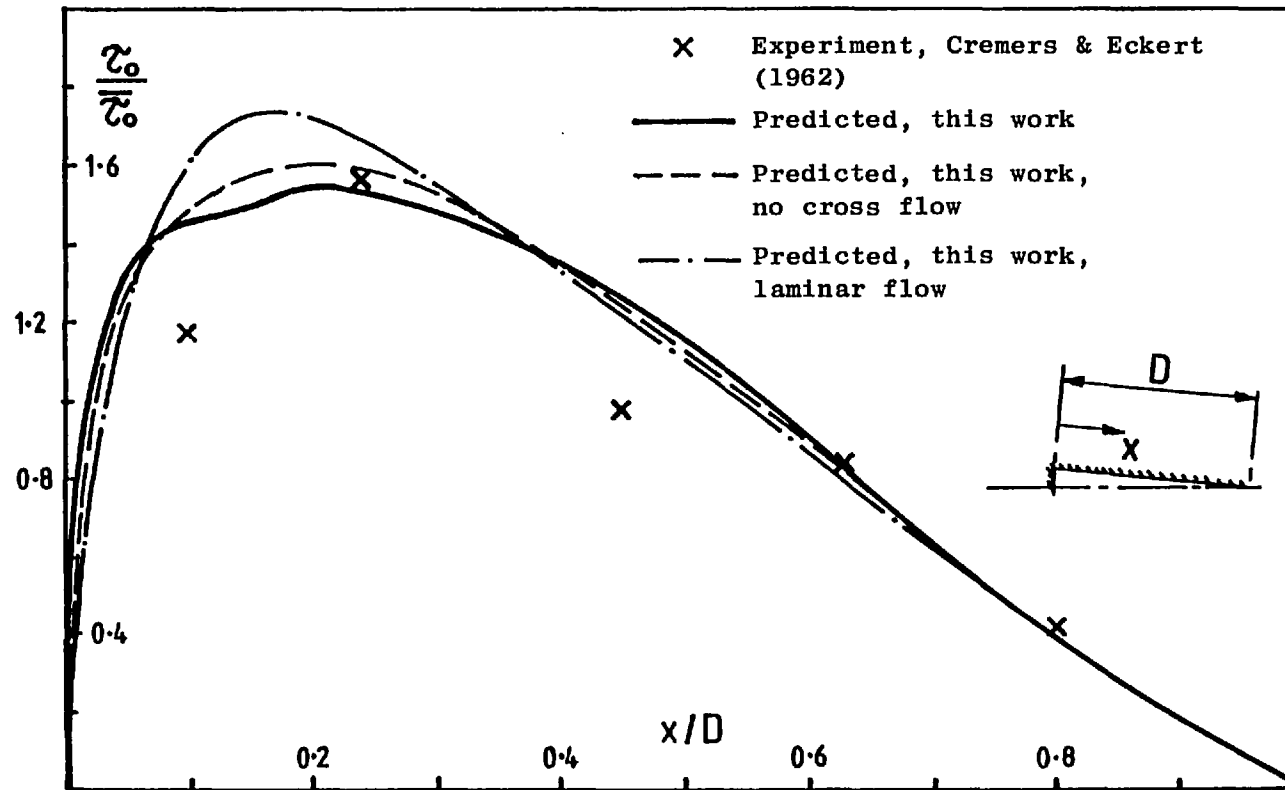


Figure 7.7.4 Centre-plane wall shear stress profiles in an isosceles triangular duct of apex angle 11.7° and with $Re = 1.09 \times 10^4$.

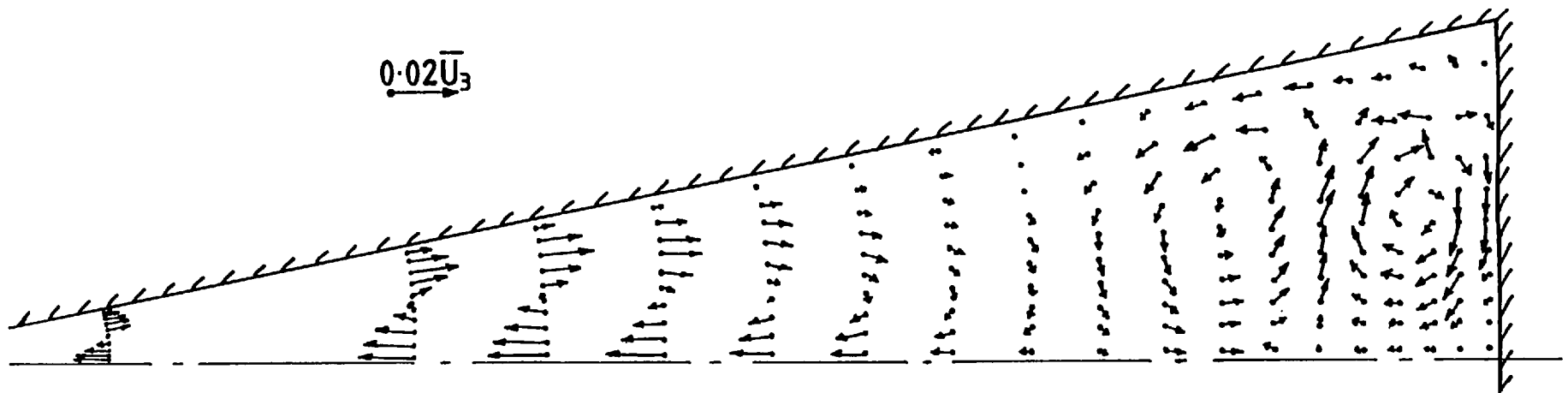


Figure 7.7.5 Predicted secondary velocity vectors in an isosceles triangular duct of apex angle 22.1° and with $Re = 3.0 \times 10^4$.

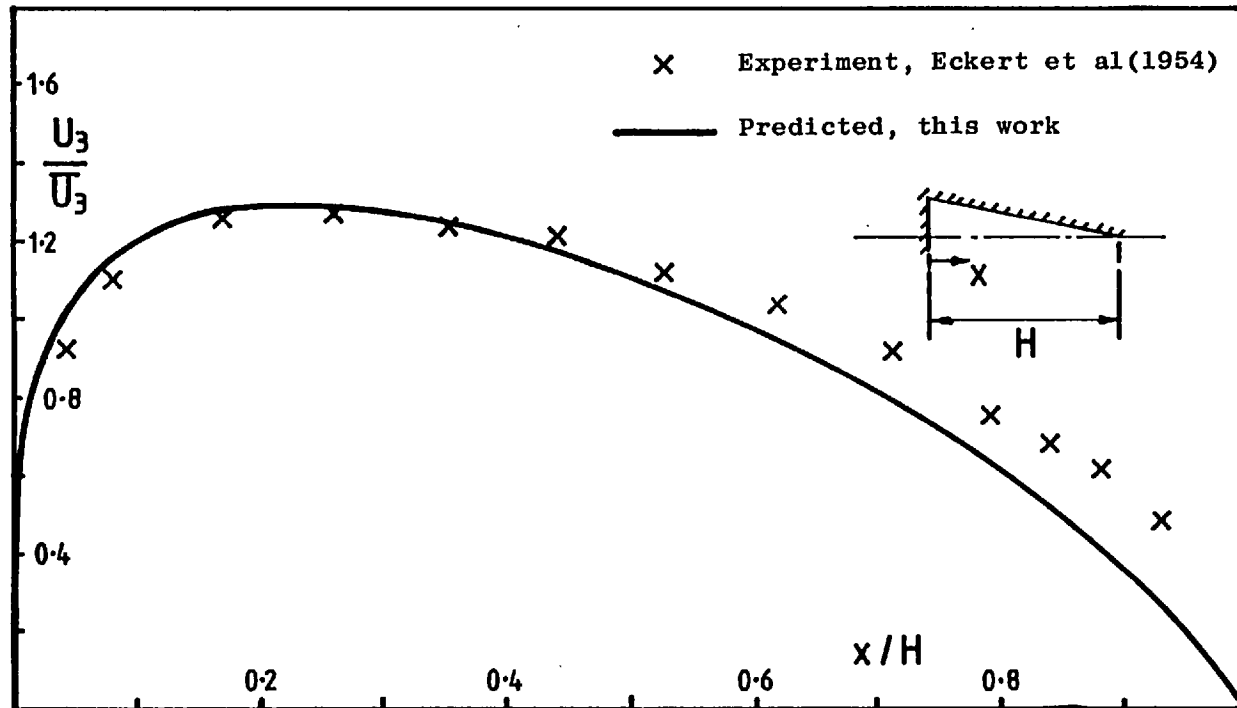


Figure 7.7.6 Centre-plane axial velocity profiles in an isosceles triangular duct of apex angle 22.1° and with $Re = 3.0 \times 10^4$.

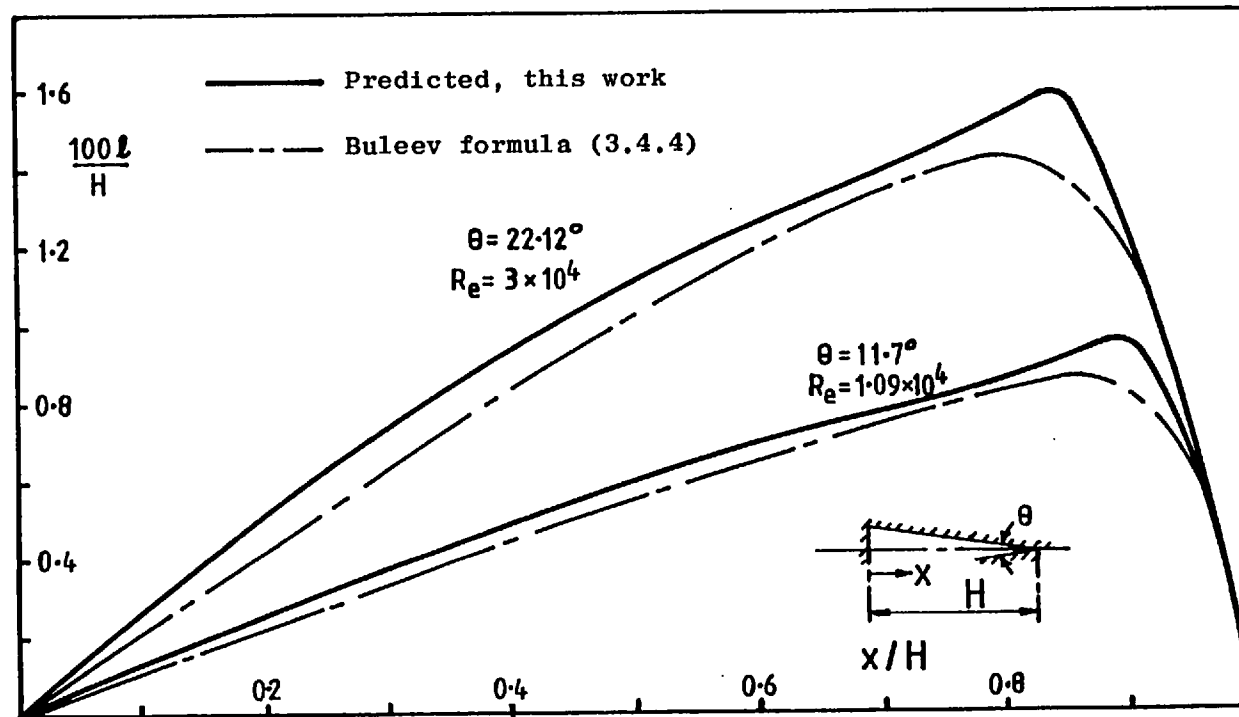


Figure 7.7.7 Predicted centre-plane length scale profiles in isosceles triangular ducts

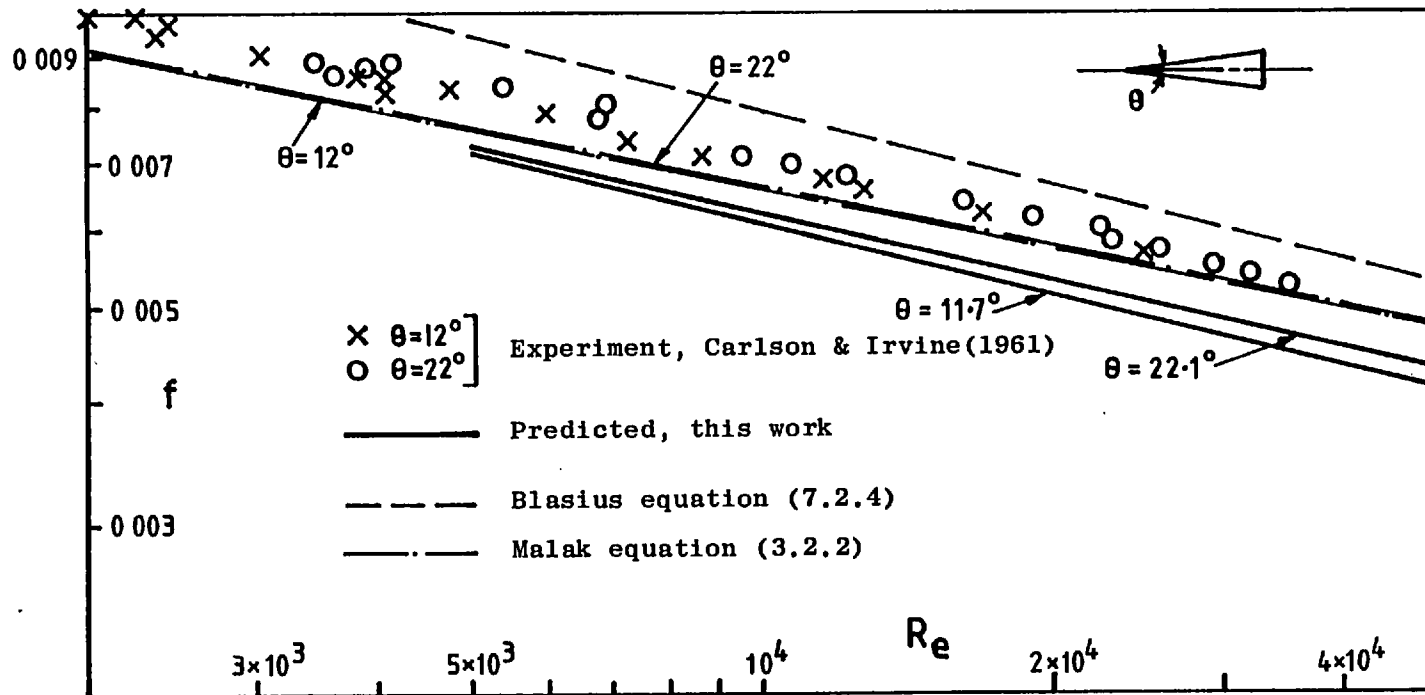


Figure 7.7.8 Friction factor characteristics for isosceles triangular ducts.

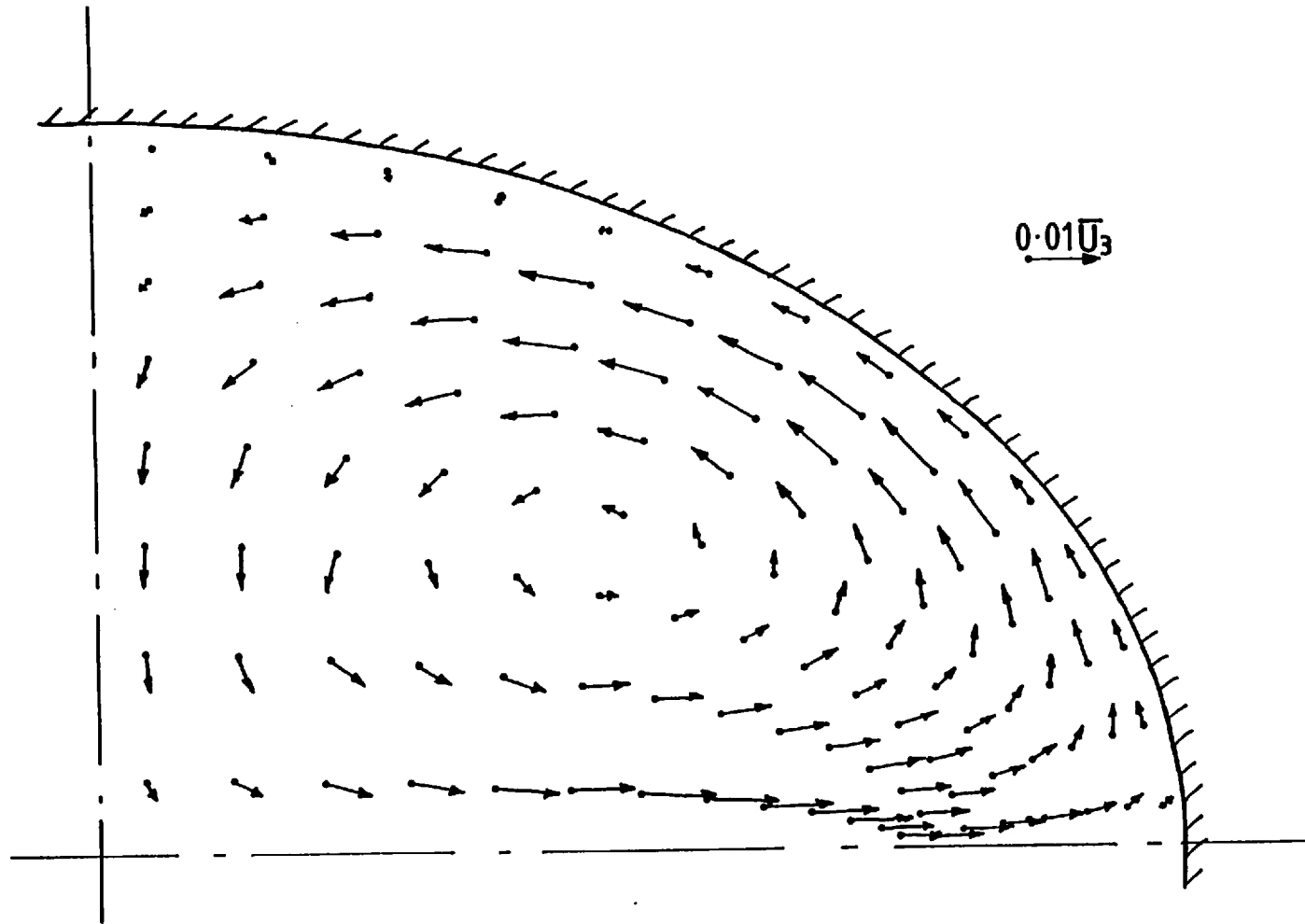


Figure 7.8.1 Predicted secondary velocity vectors in an elliptical duct with $AR = 1.5$ and $Re = 1.2 \times 10^5$.

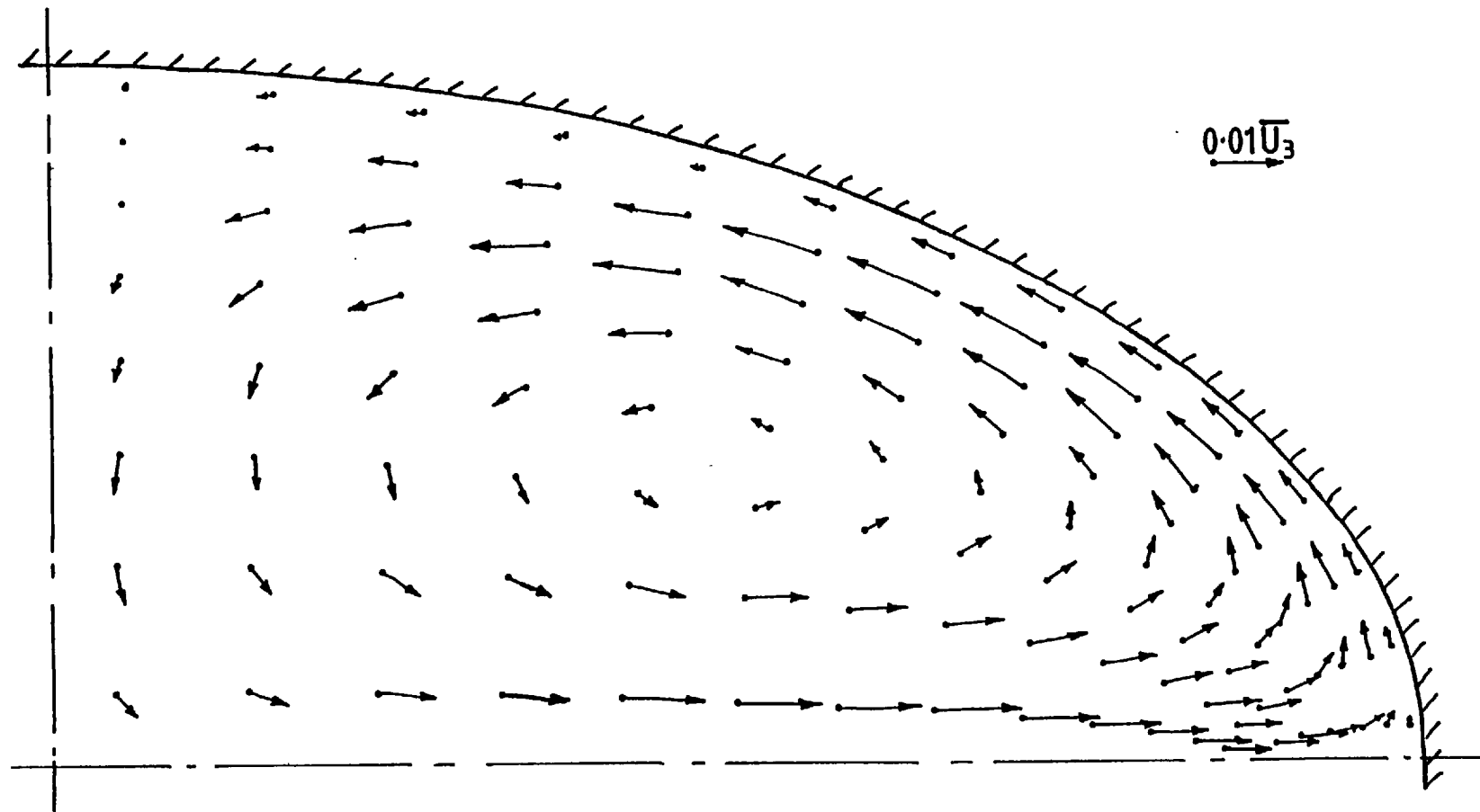


Figure 7.8.2 Predicted secondary velocity vectors in an elliptical duct with $AR = 2.0$ and $Re = 1.2 \times 10^5$.

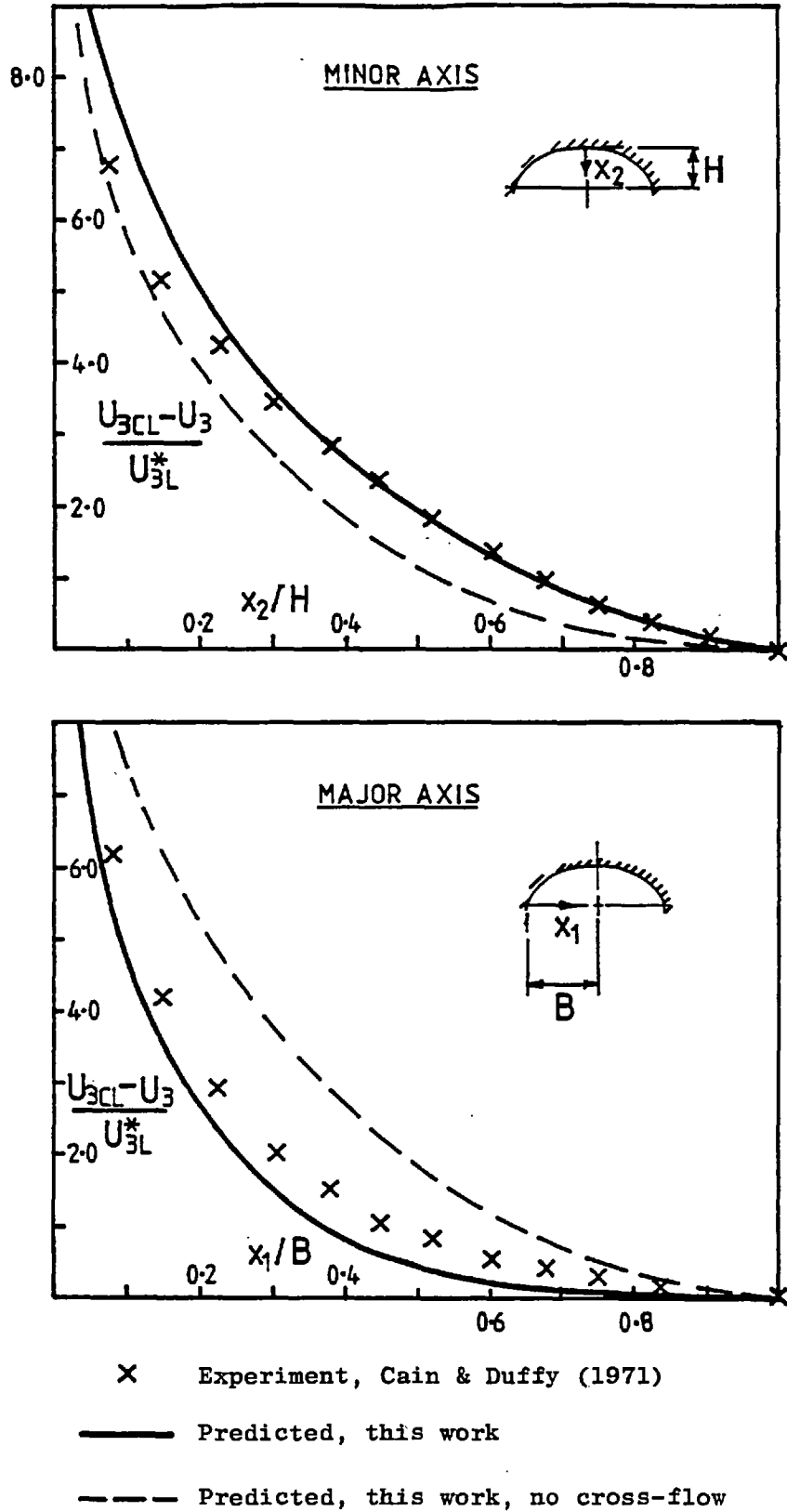


Figure 7.8.3 Axial velocity defect profiles along the centre planes of an elliptical duct with $AR = 1.5$ and $Re = 1.2 \times 10^5$.

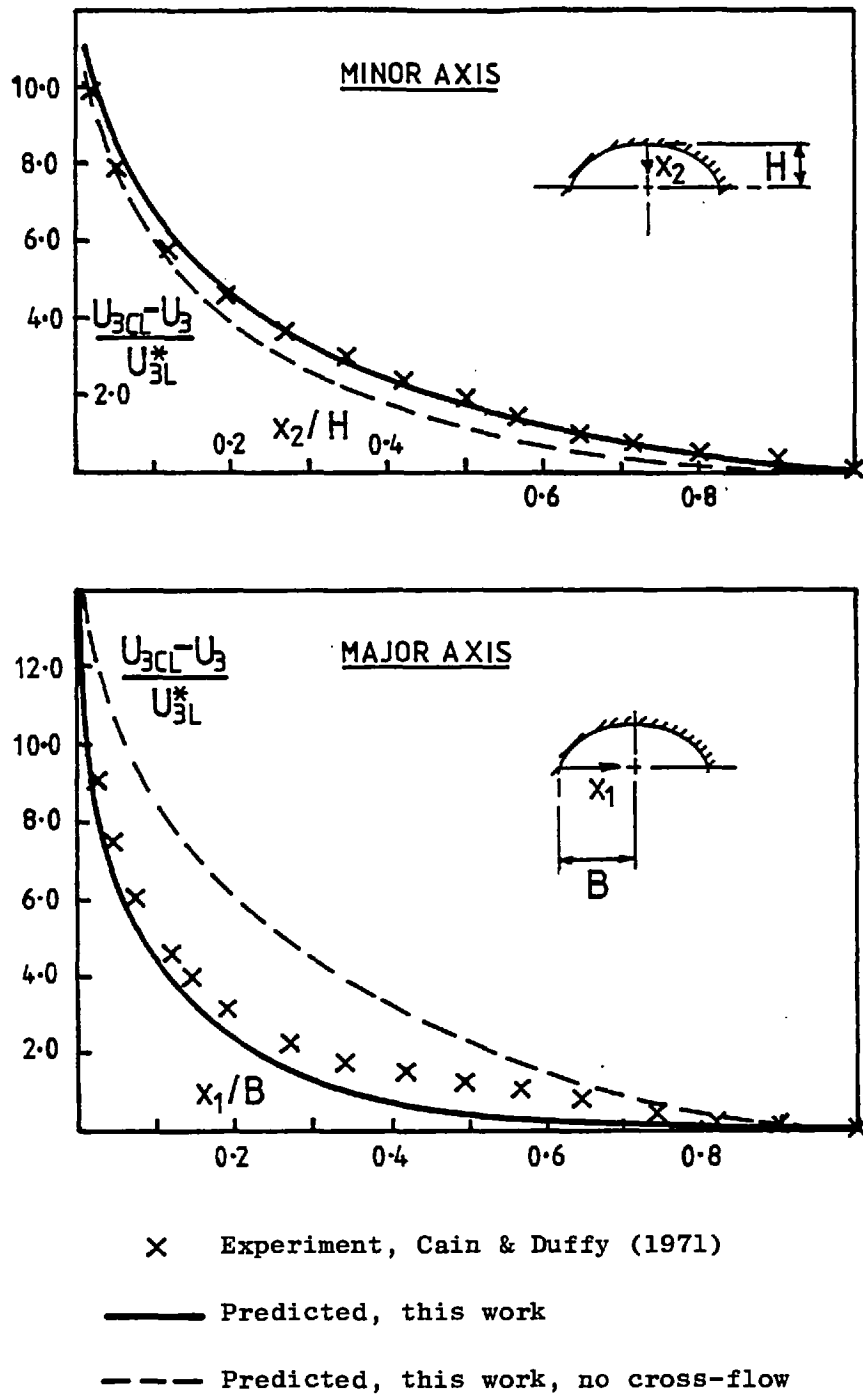
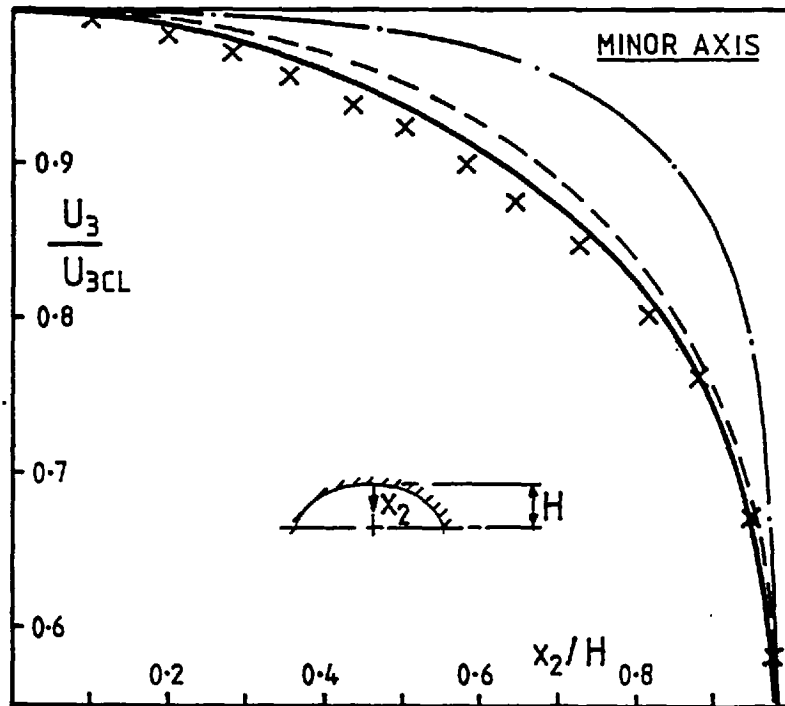
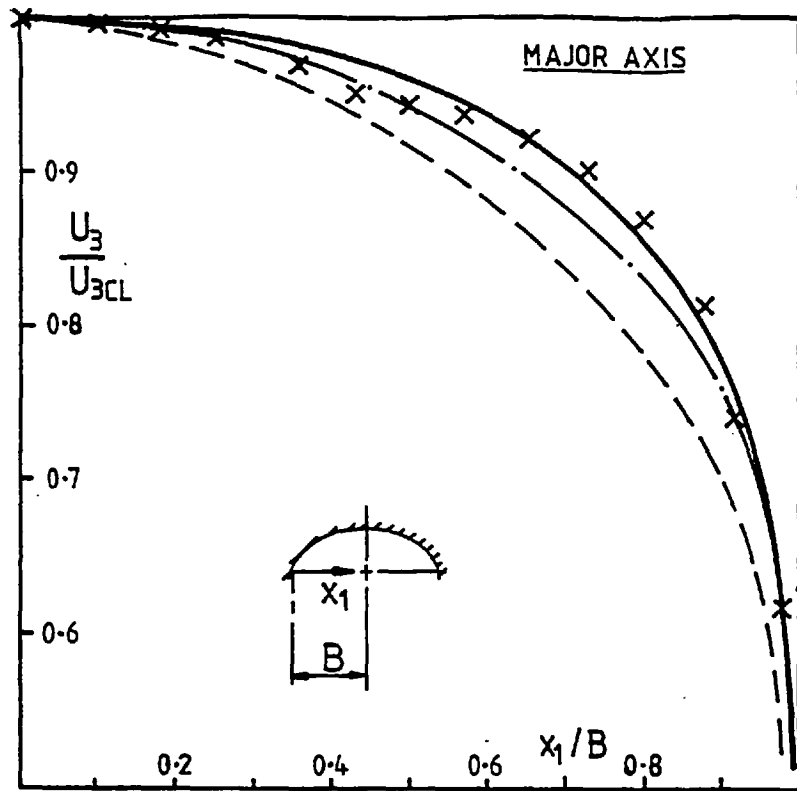
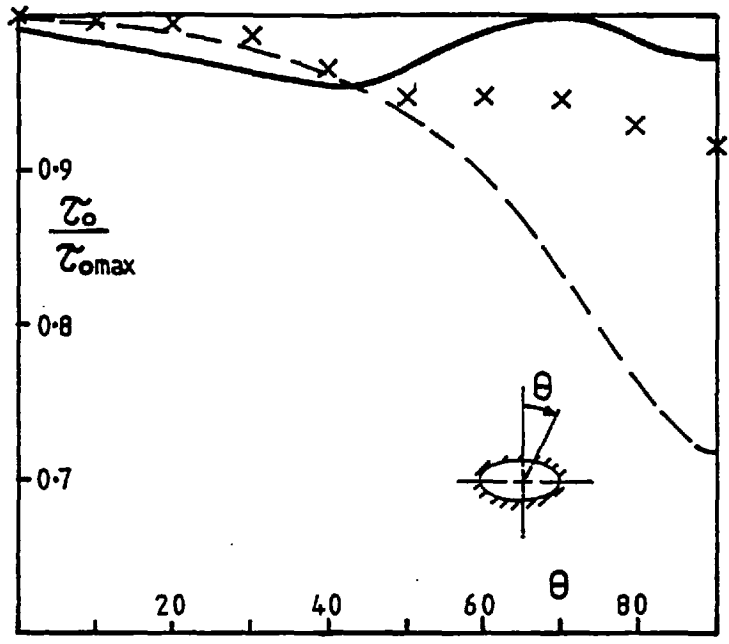


Figure 7.8.4 Axial velocity defect profiles along the centre-planes of an elliptical duct with AR = 2.0 and $Re = 1.2 \times 10^5$.

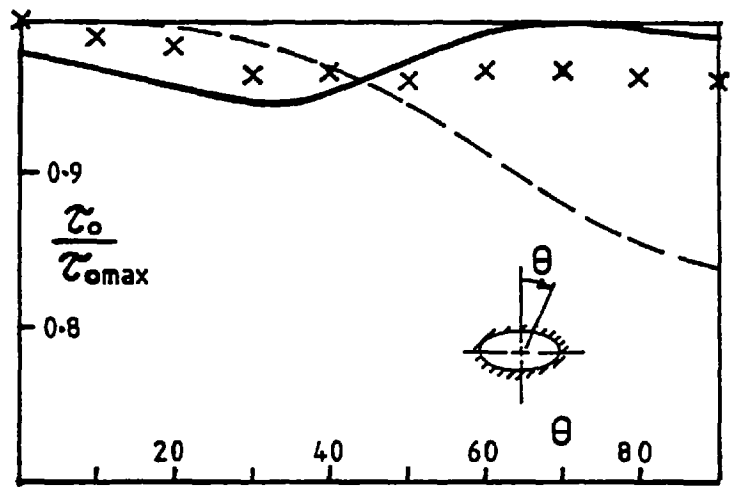


- x** Experiment, Cain & Duffy (1971)
- · — Predicted, Cain et al (1972)
- — — Predicted, this work
- — — Predicted, this work, no cross-flow

Figure 7.8.5 Axial velocity profiles along the centre-planes in an elliptical duct with $AR = 2.0$ and $Re = 1.2 \times 10^5$.



(a) $AR = 2.0$



(b) $AR = 1.5$

- × Experiment, Duffy & Cain (1972)
- Predicted, this work
- - - Predicted, this work, no cross-flow

Figure 7.8.6 Wall shear stress in elliptical ducts with $Re = 1.2 \times 10^5$.

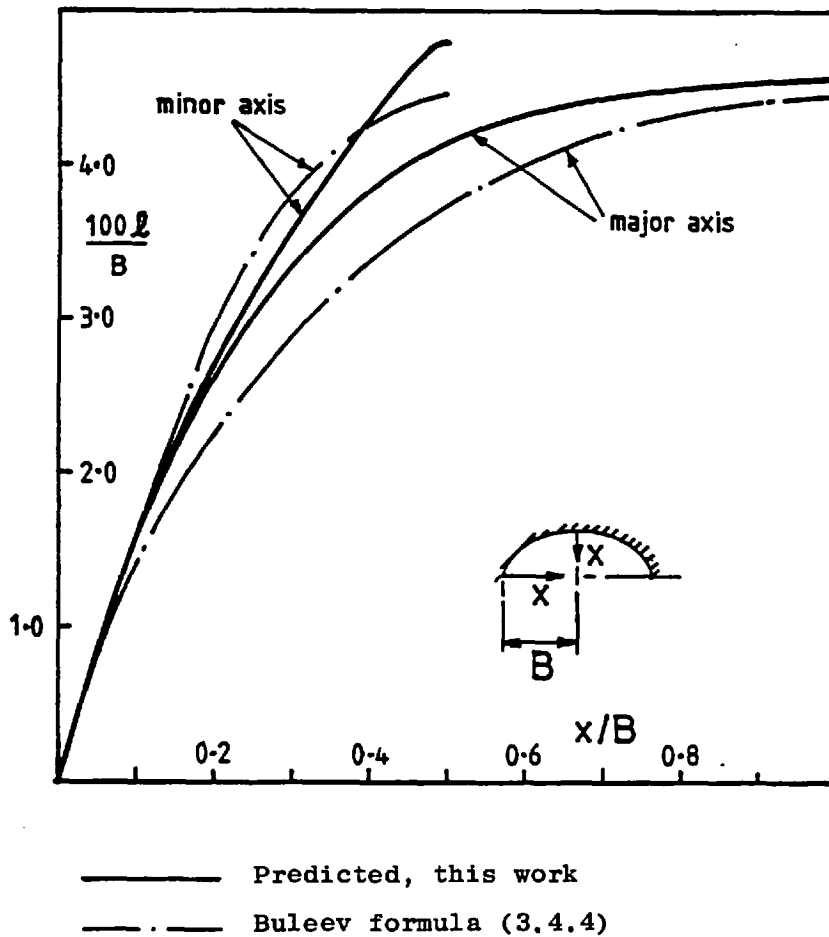


Figure 7.8.7 Predicted length scale profiles along the centre-planes in an elliptical duct with $AR = 2.0$ and $Re = 1.2 \times 10^5$.

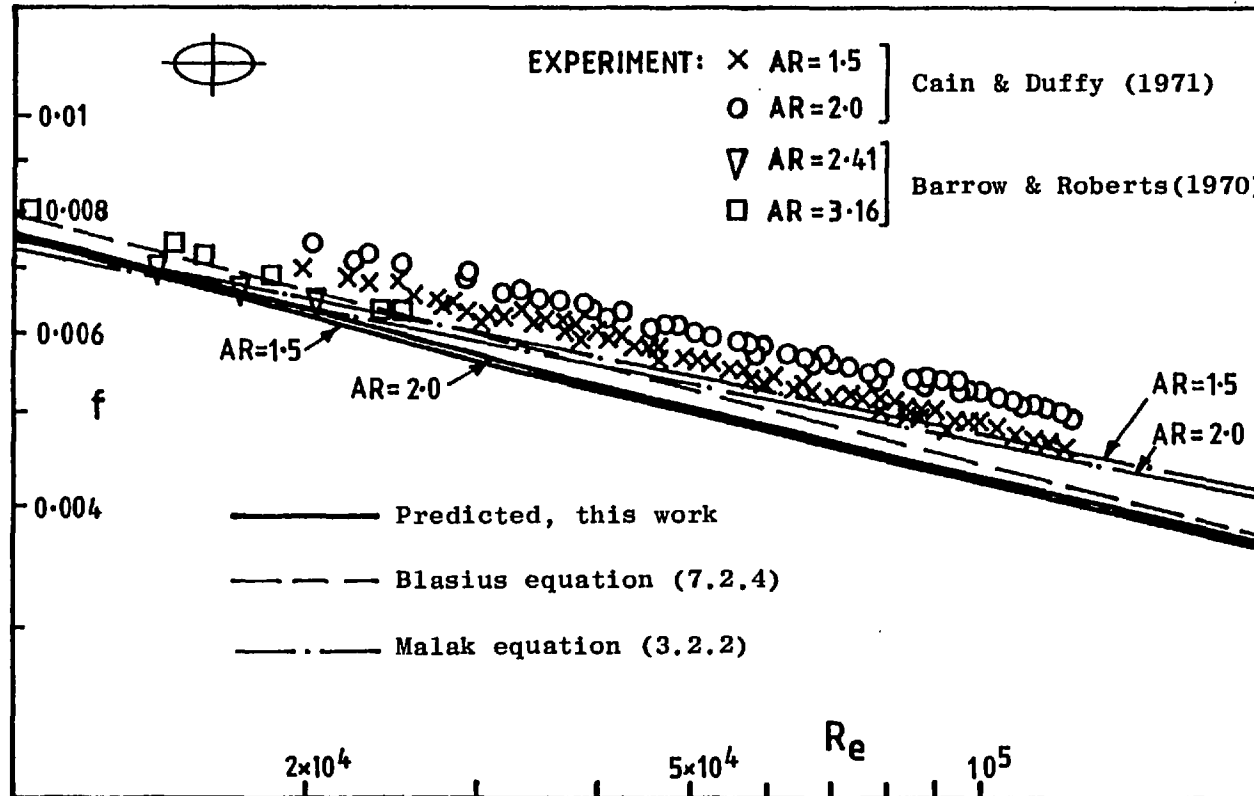
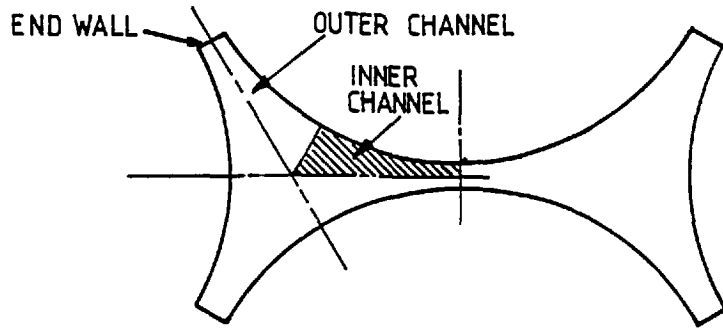
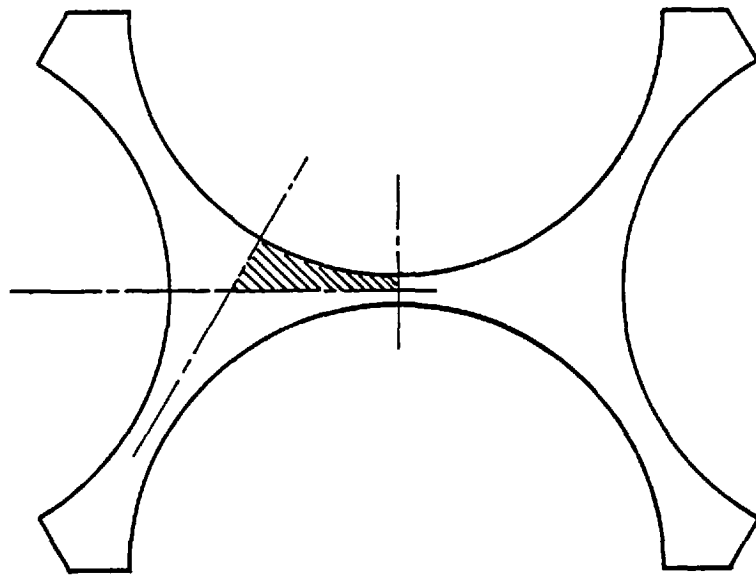


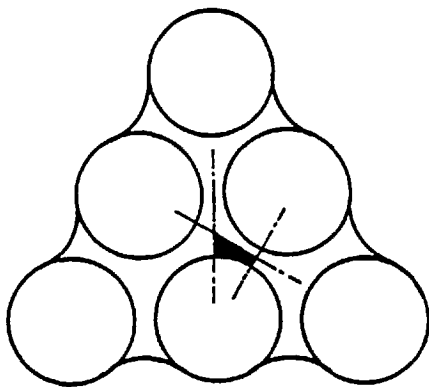
Figure 7.8.8 Friction factor characteristics for elliptical ducts.



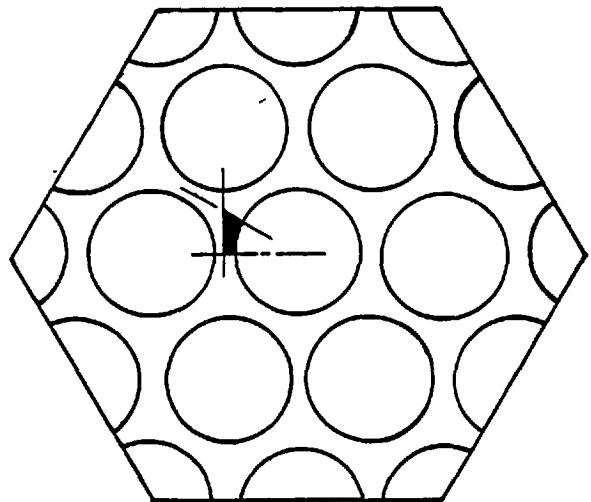
(a) Subbotin et al (1971)



(b) Carajilescov and Todreas (1976)



(c) Kjellstrom (1971)



(d) Trupp and Azad (1975)

Figure 7.9.1 Experimental rod bundle test sections of various authors.

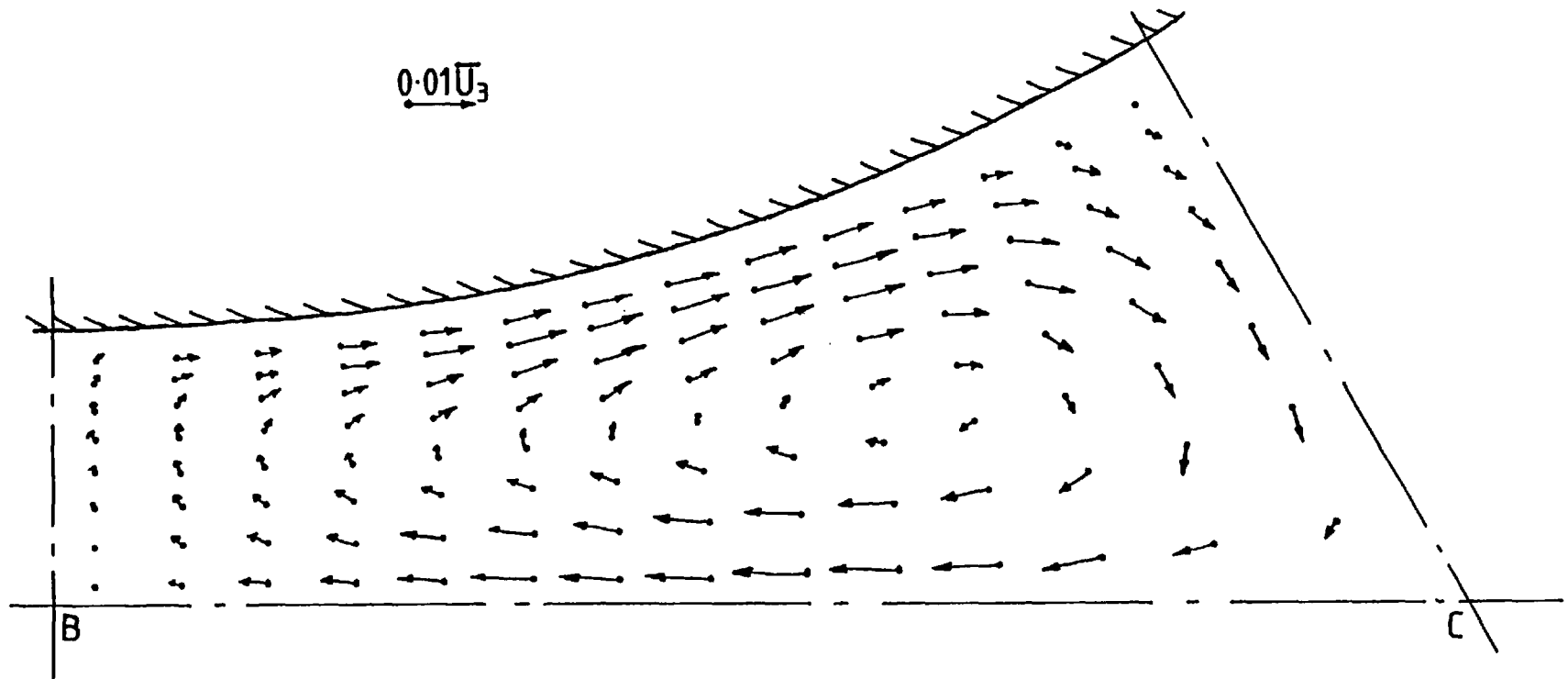


Figure 7.9.2 Predicted secondary velocity vectors in a rod bundle with $P/D = 1.123$ and $Re = 2.7 \times 10^4$.

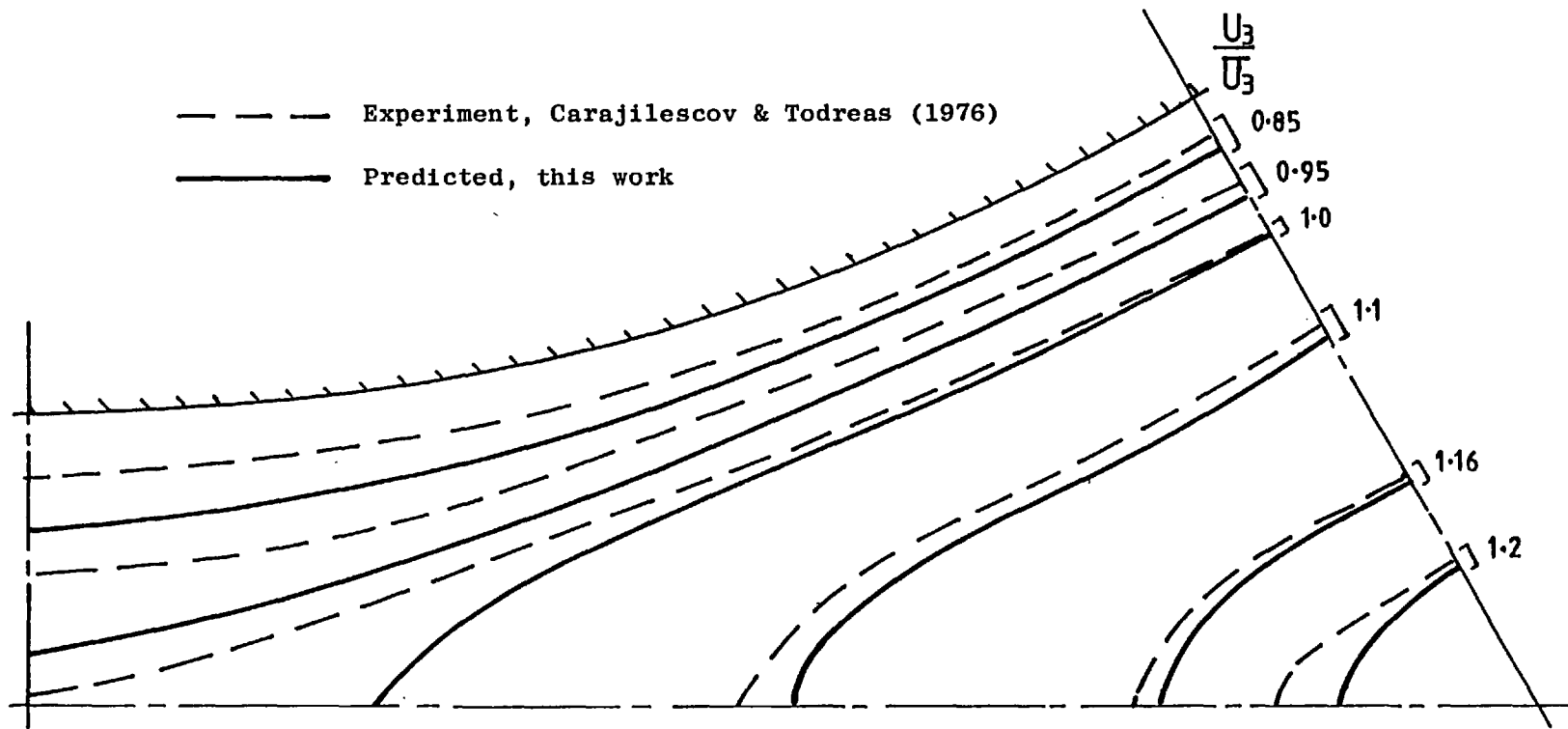


Figure 7.9.3 Axial velocity contours in a rod bundle with $P/D = 1.123$ and $Re = 2.7 \times 10^4$.

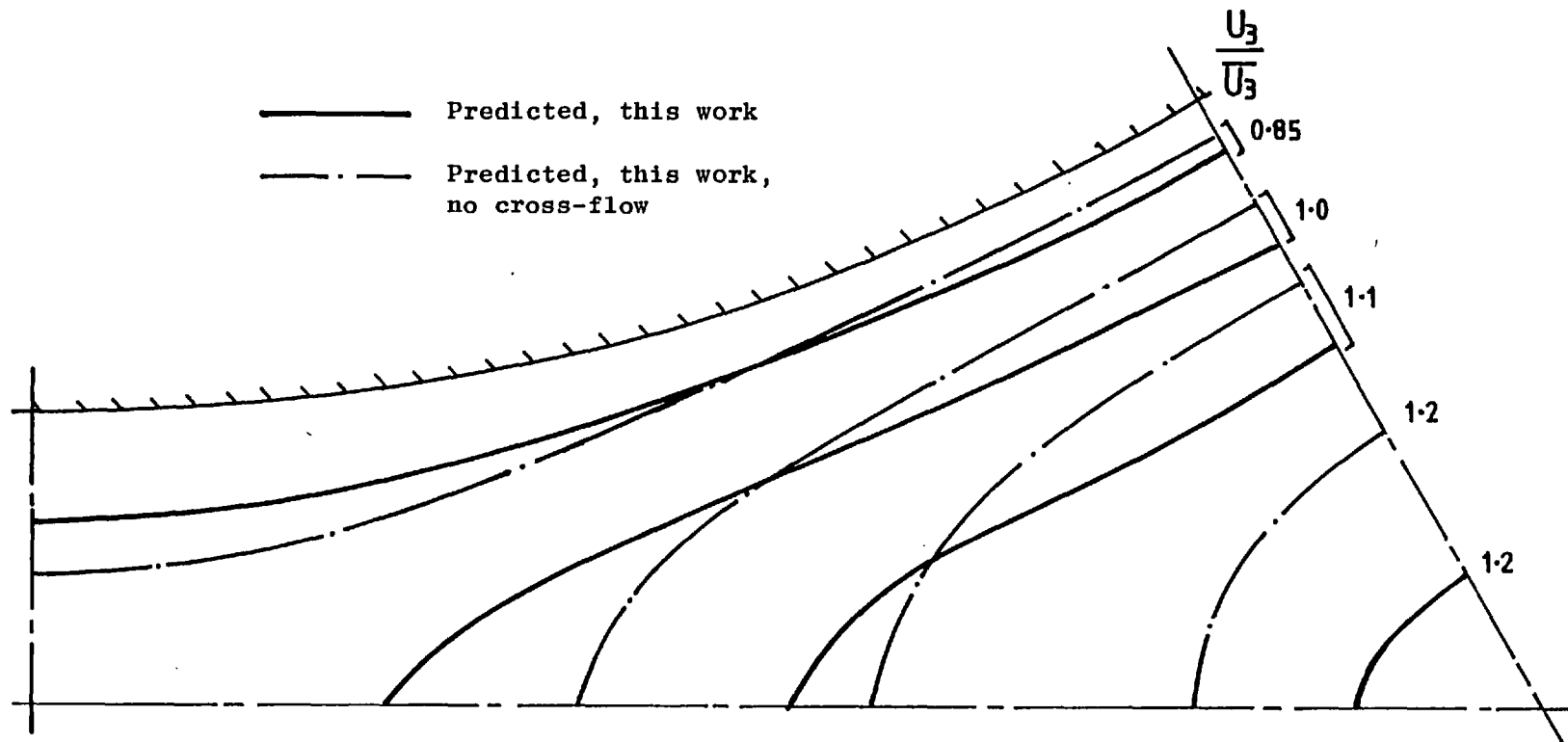


Figure 7.9.4 Predicted axial velocity contours in a rod bundle with $P/D = 1.123$ and $Re = 2.7 \times 10^4$.

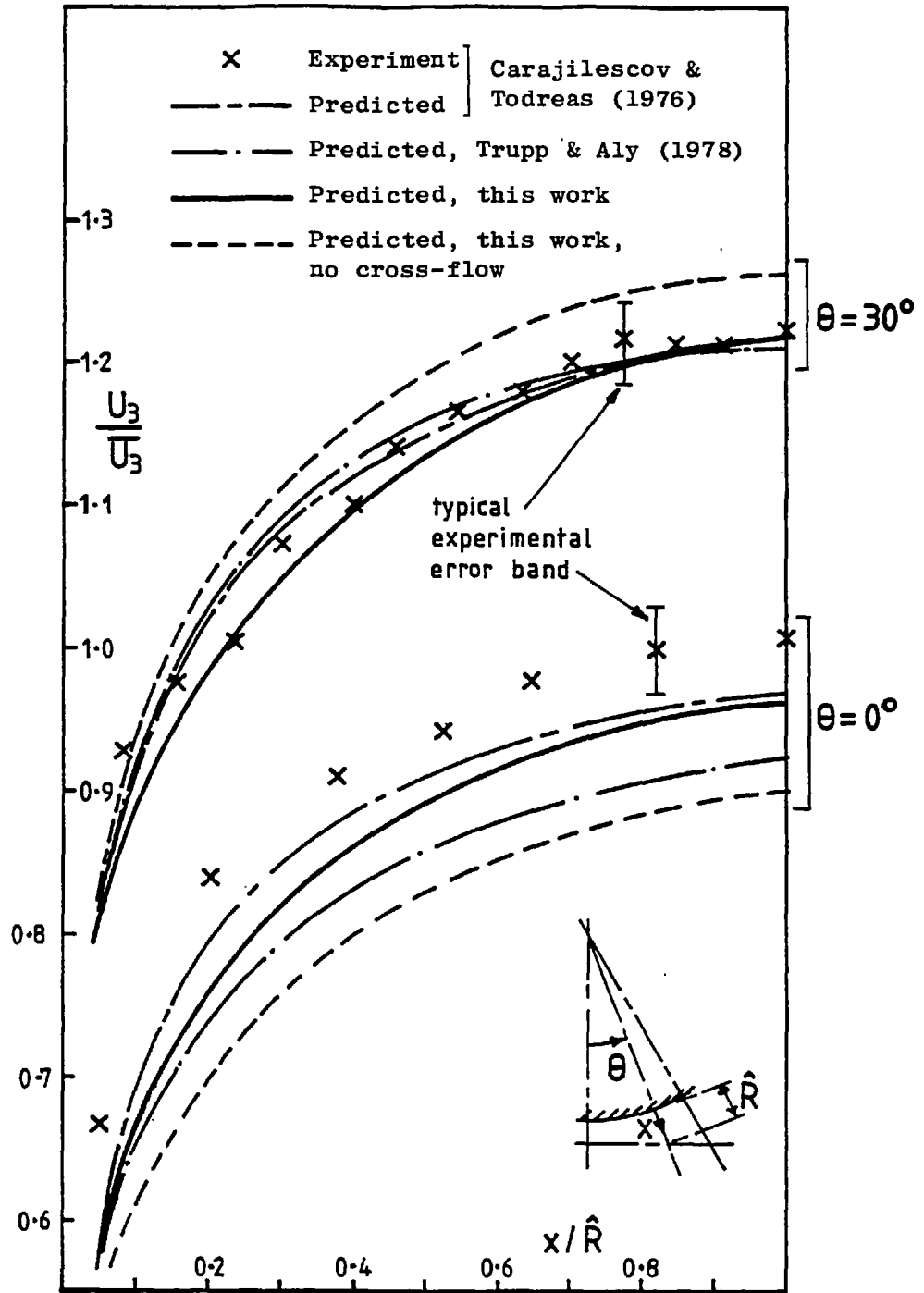


Figure 7.9.5 Axial velocity profiles in a rod bundle with $P/D = 1.123$ and $Re = 2.7 \times 10^5$.

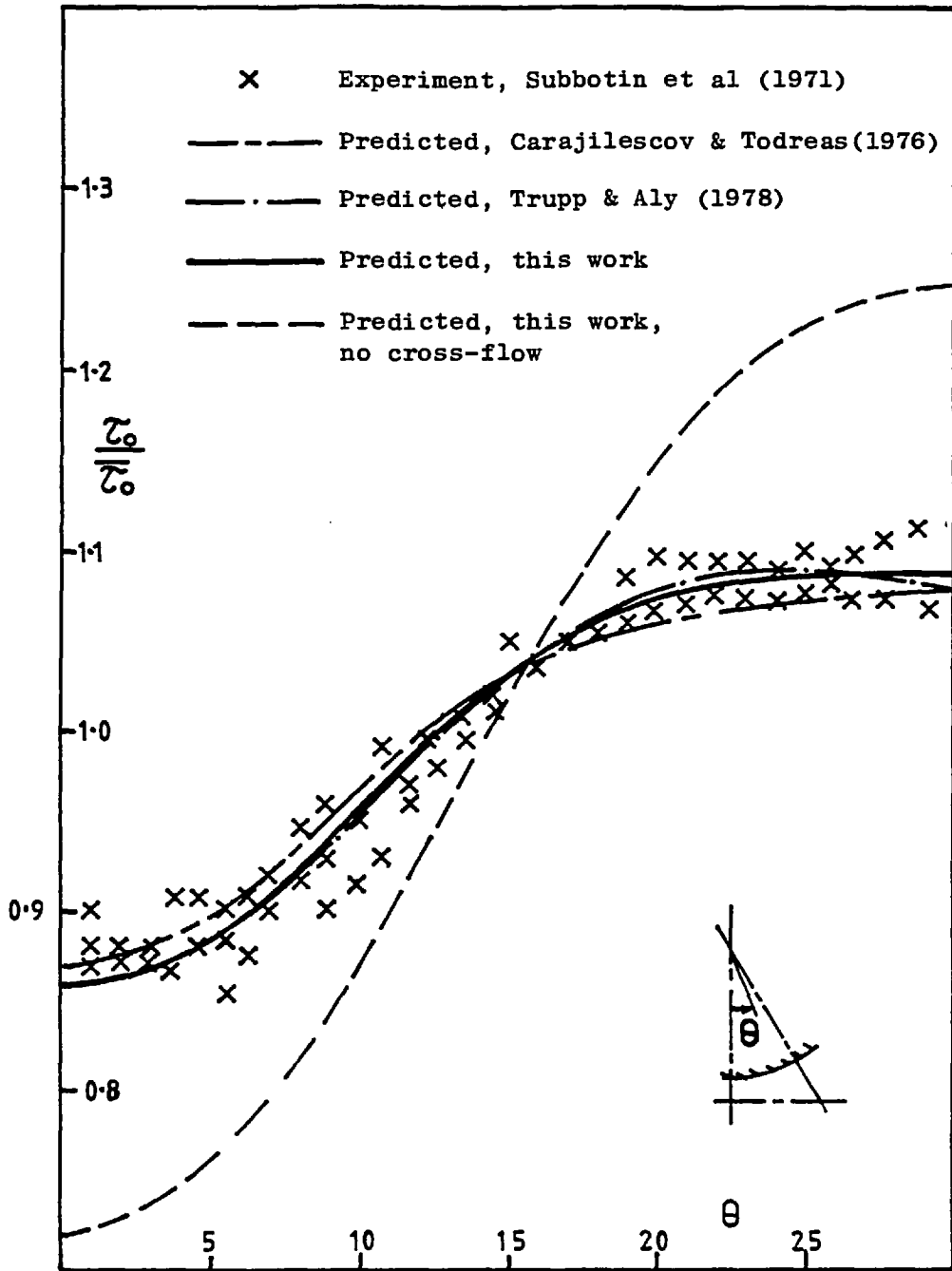


Figure 7.9.6 Wall shear stress in a rod bundle with $P/D = 1.123$ and $Re = 4.27 \times 10^4$.

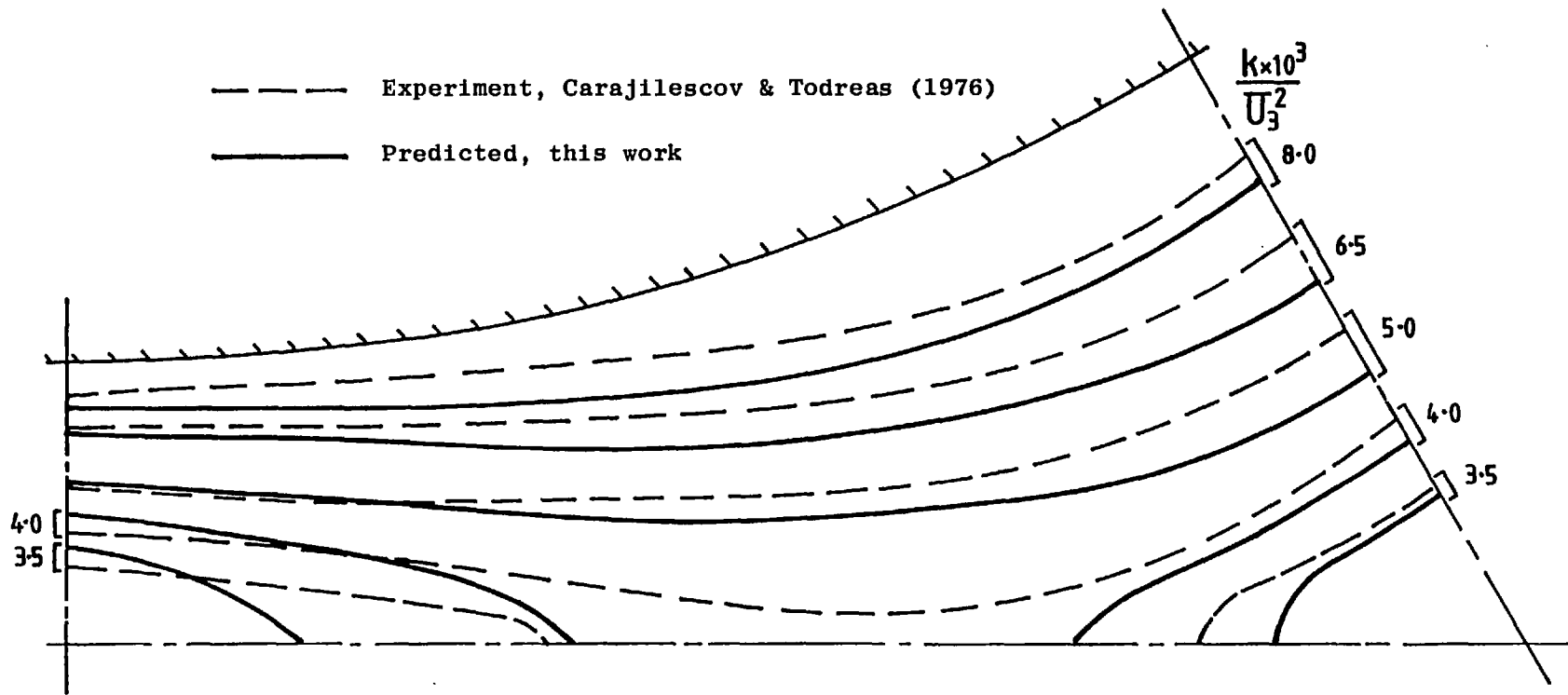


Figure 7.9.7. Turbulence kinetic energy contours in a rod bundle with $P/D = 1.123$ and $Re = 2.7 \times 10^4$.

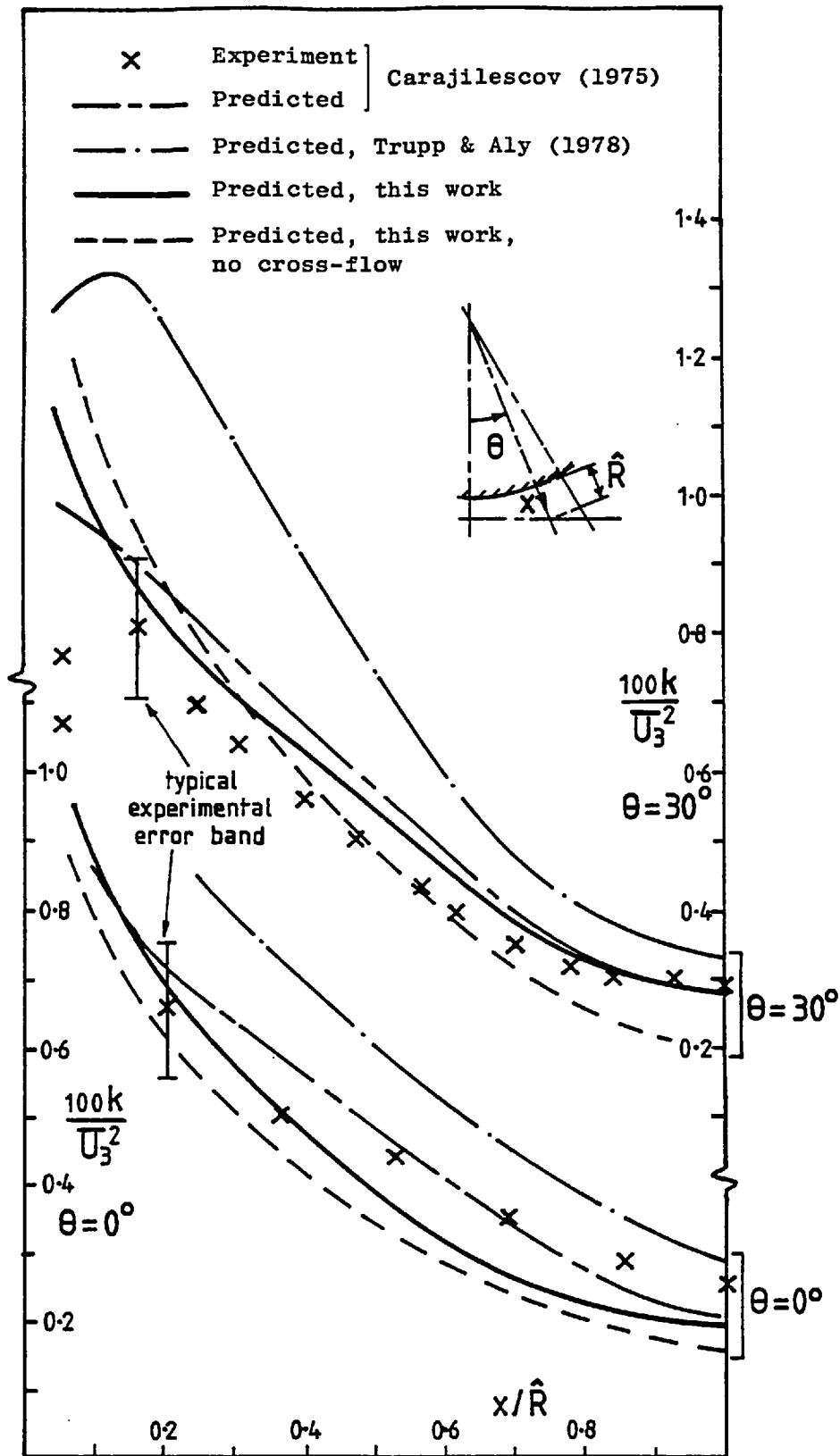


Figure 7.9.8 Turbulence kinetic energy profiles in a rod bundle with $P/D = 1.123$ and $Re = 2.7 \times 10^4$.

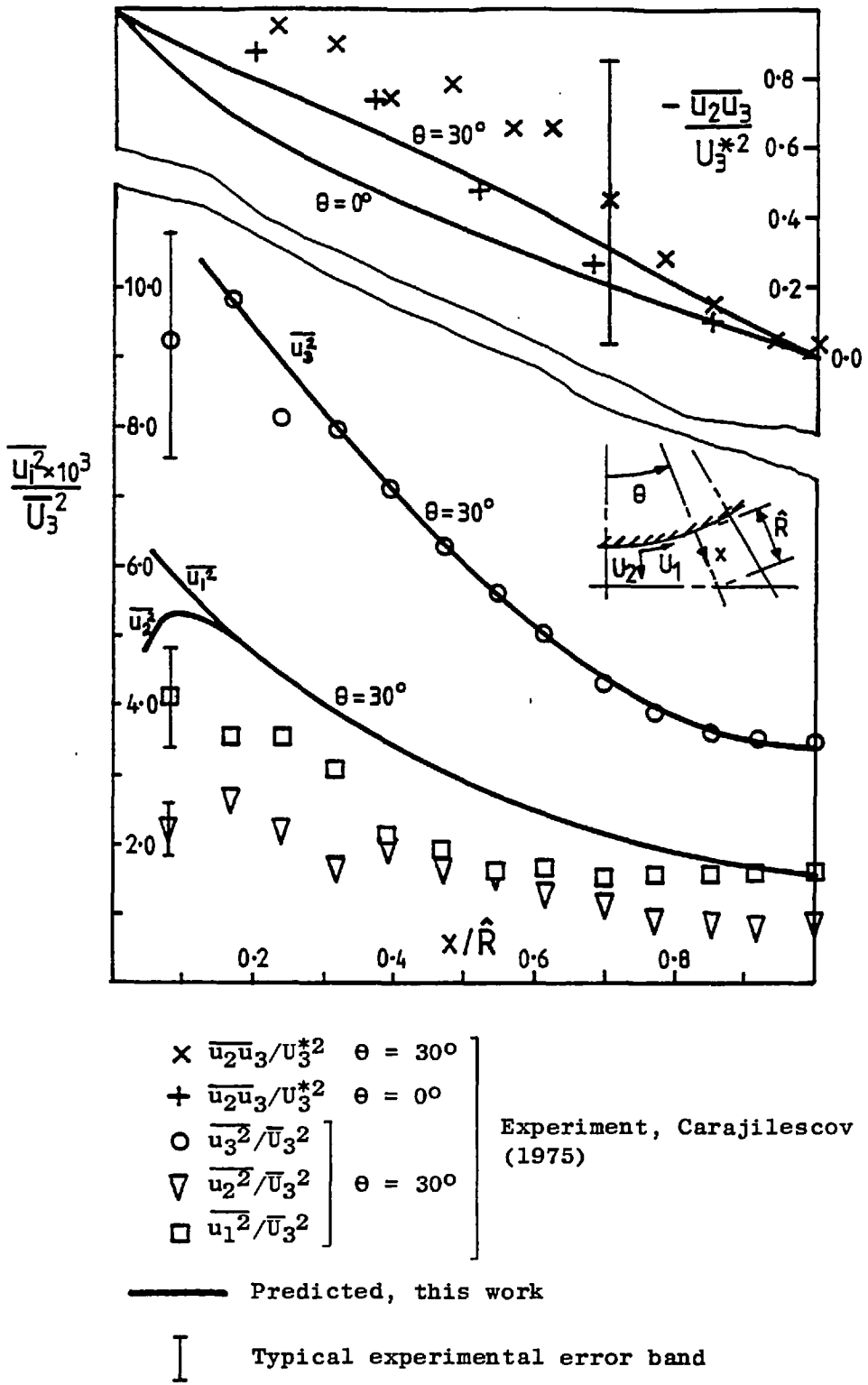


Figure 7.9.9 Reynolds stresses in a rod bundle with $P/D = 1.123$ and $Re = 2.7 \times 10^4$.

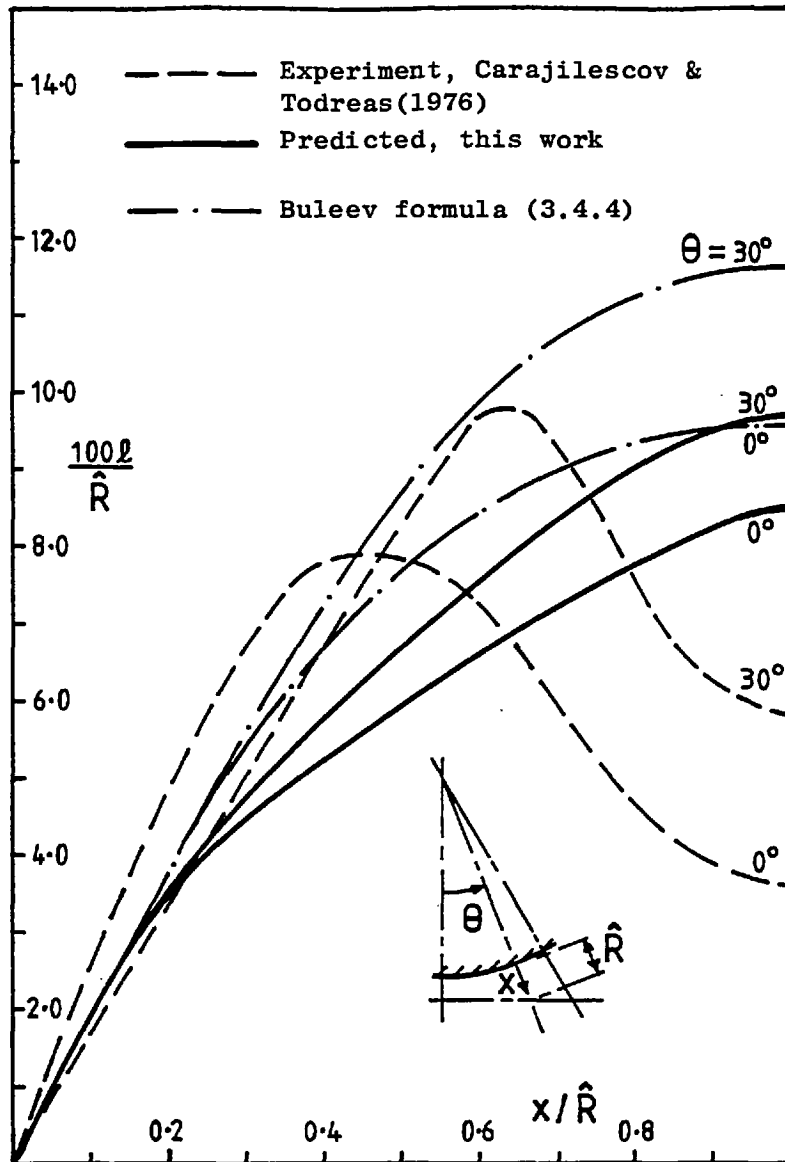


Figure 7.9.10 Length scale profiles in a rod bundle with $P/D = 1.123$ and $Re = 2.7 \times 10^4$.

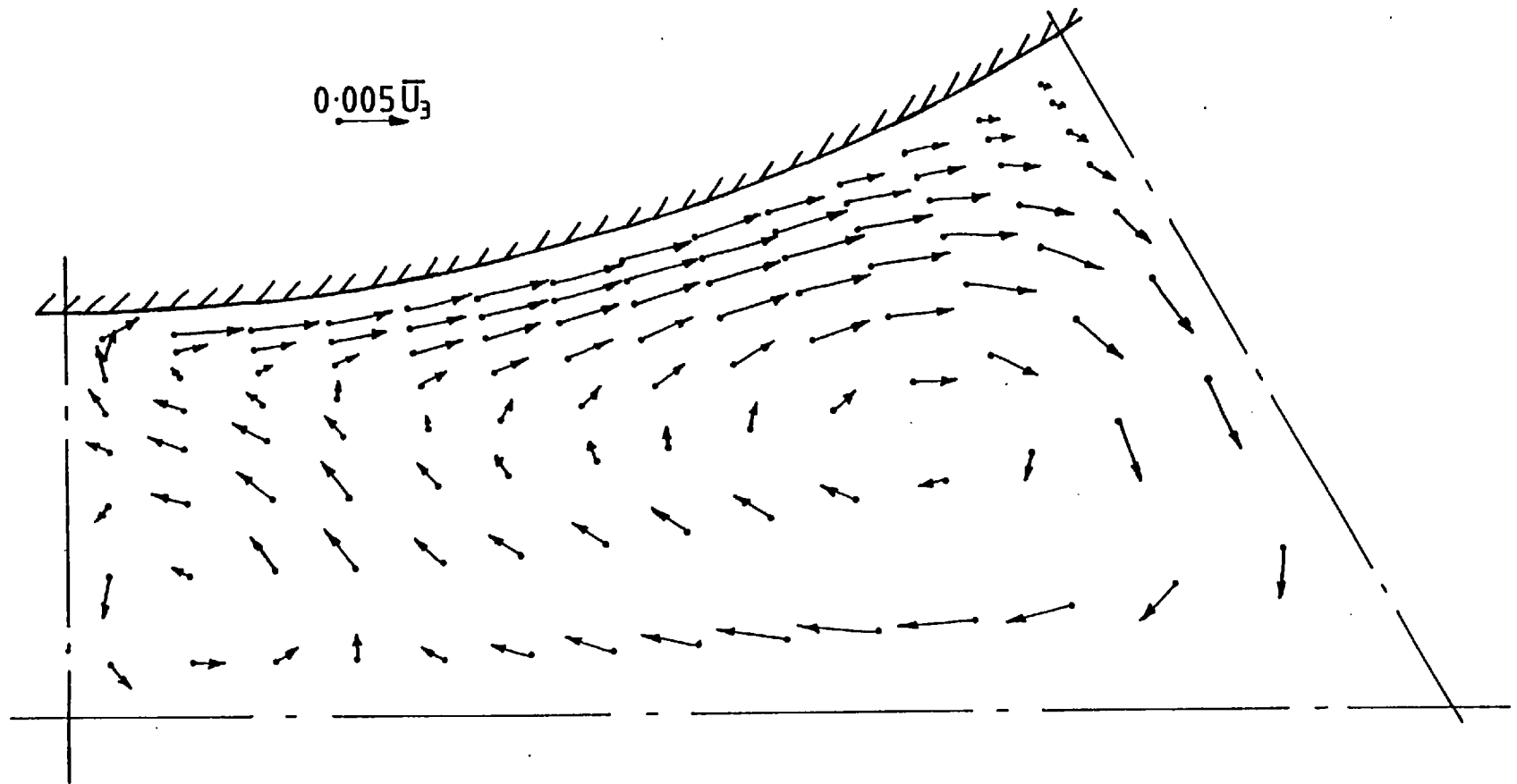


Figure 7.9.11 Predicted secondary velocity vectors in a rod bundle with $P/D = 1.2$ and $Re = 3.5 \times 10^4$.

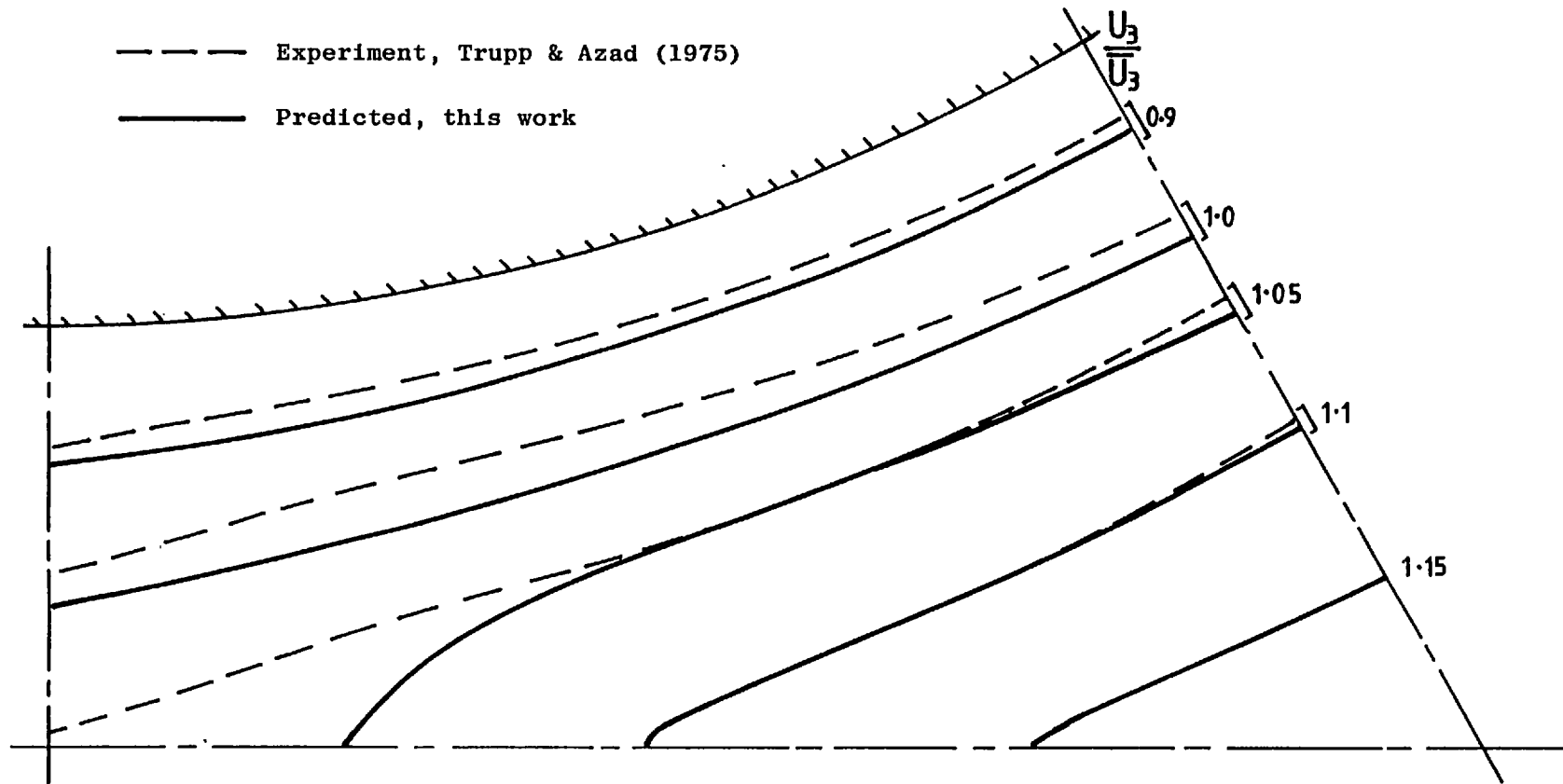


Figure 7.9.12 Axial velocity contours in a rod bundle with $P/D = 1.2$ and $Re = 3.5 \times 10^4$.

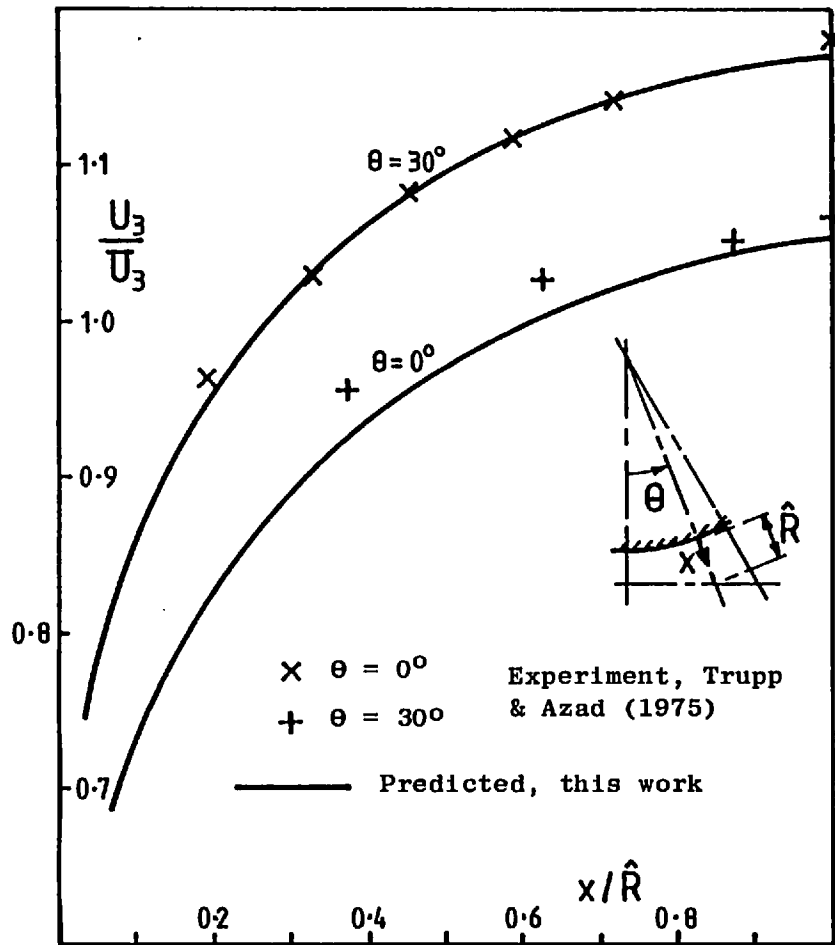


Figure 7.9.13 Axial velocity profiles in a rod bundle with $P/D = 1.2$ and $Re = 3.5 \times 10^4$.

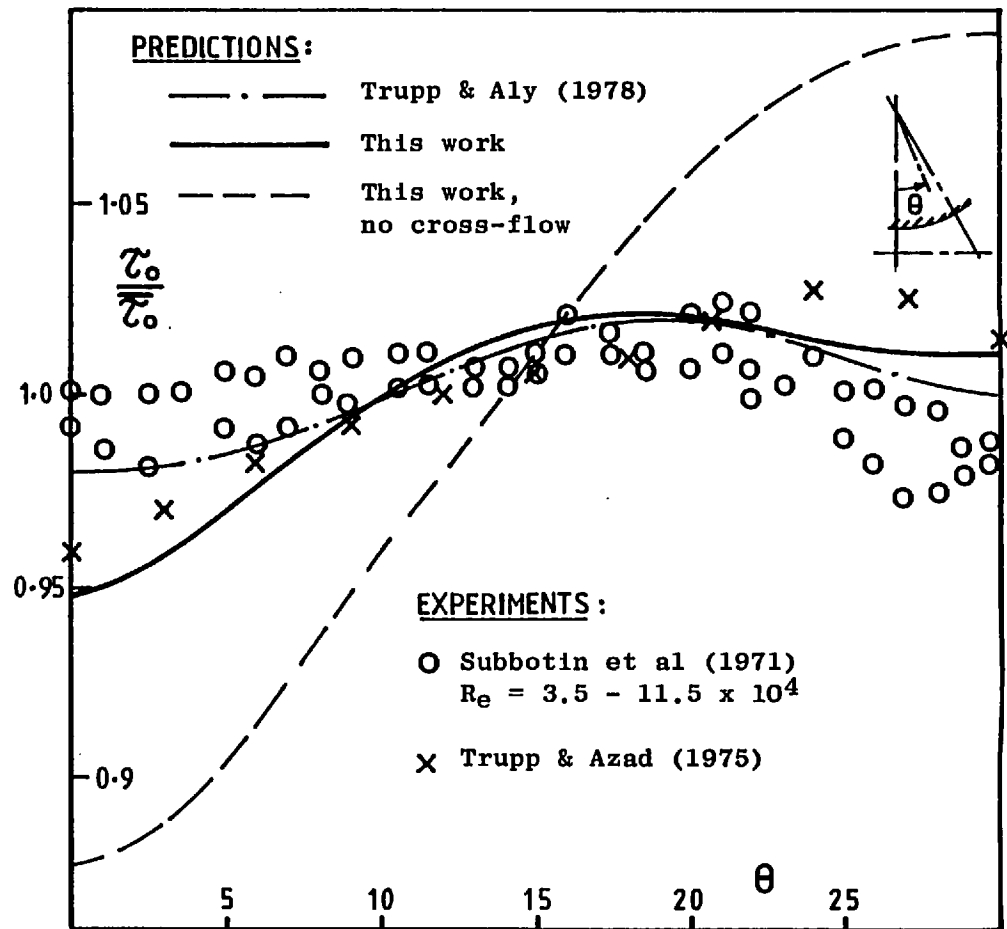


Figure 7.9.14 Wall shear stress in a rod bundle with $P/D = 1.2$ and $Re = 4.9 \times 10^4$.

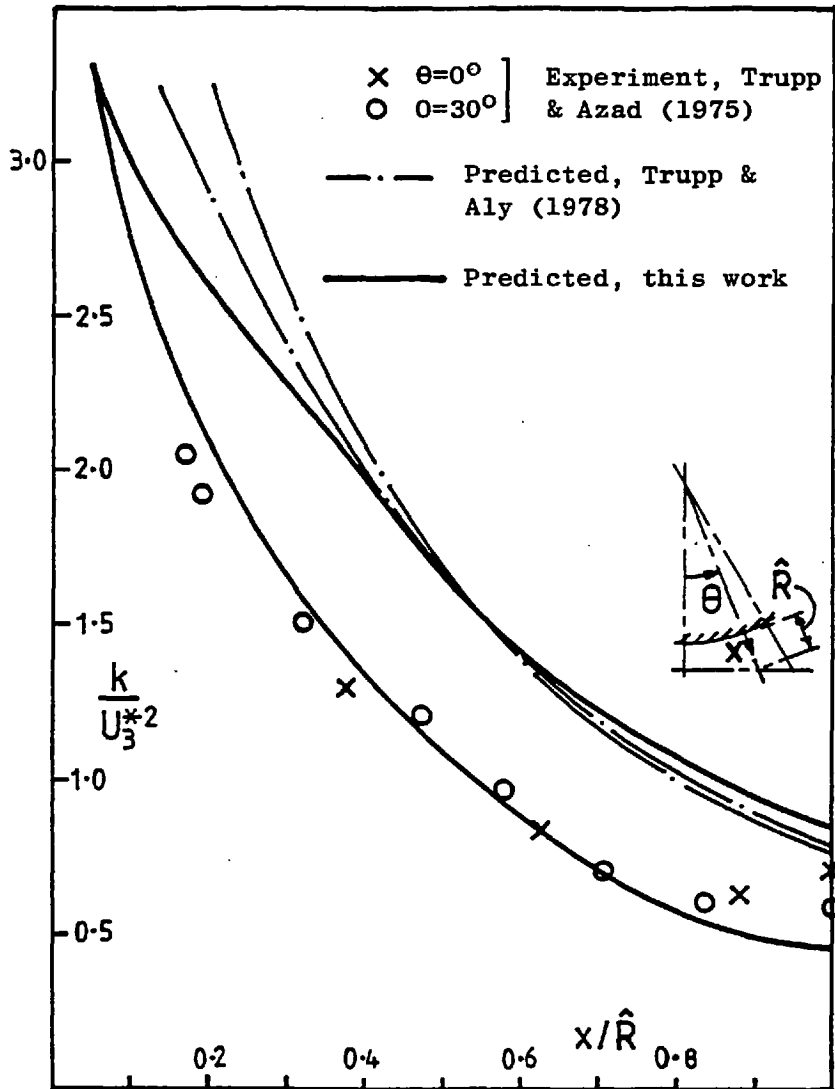


Figure 9.7.15 Turbulence kinetic energy profiles in a rod bundle with $P/D = 1.2$ and $Re = 4.9 \times 10^4$.

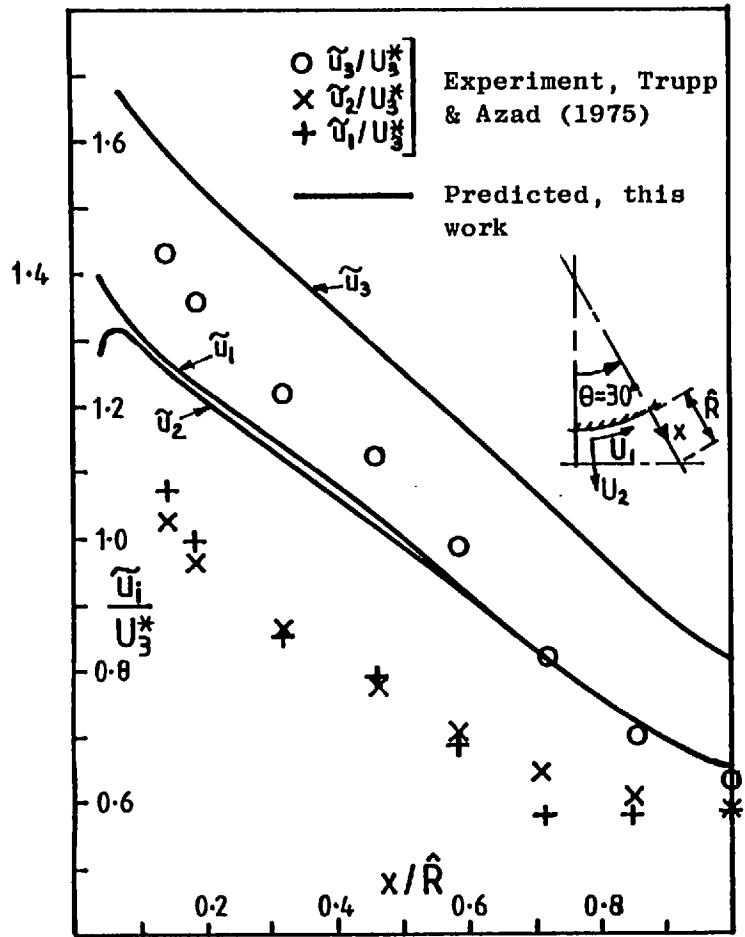


Figure 7.9.16 Turbulence intensities in a rod bundle with $P/D = 1.2$ and $Re = 4.9 \times 10^4$.

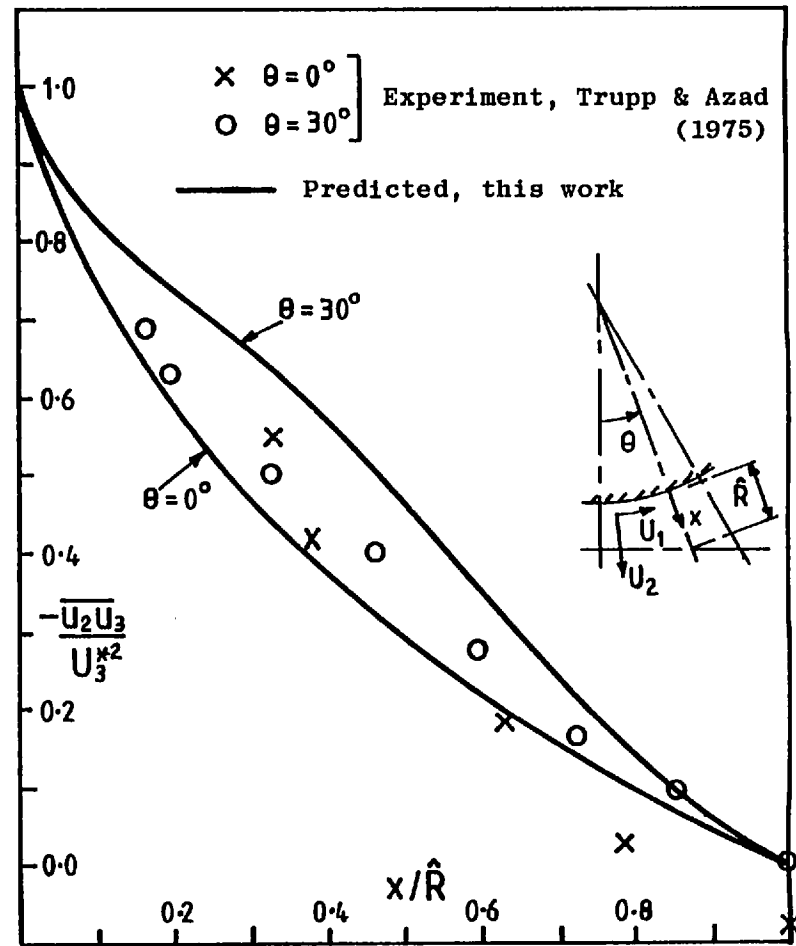


Figure 9.7.17 Turbulent shear stress in a rod bundle with $P/D = 1.2$ and $Re = 4.9 \times 10^4$.

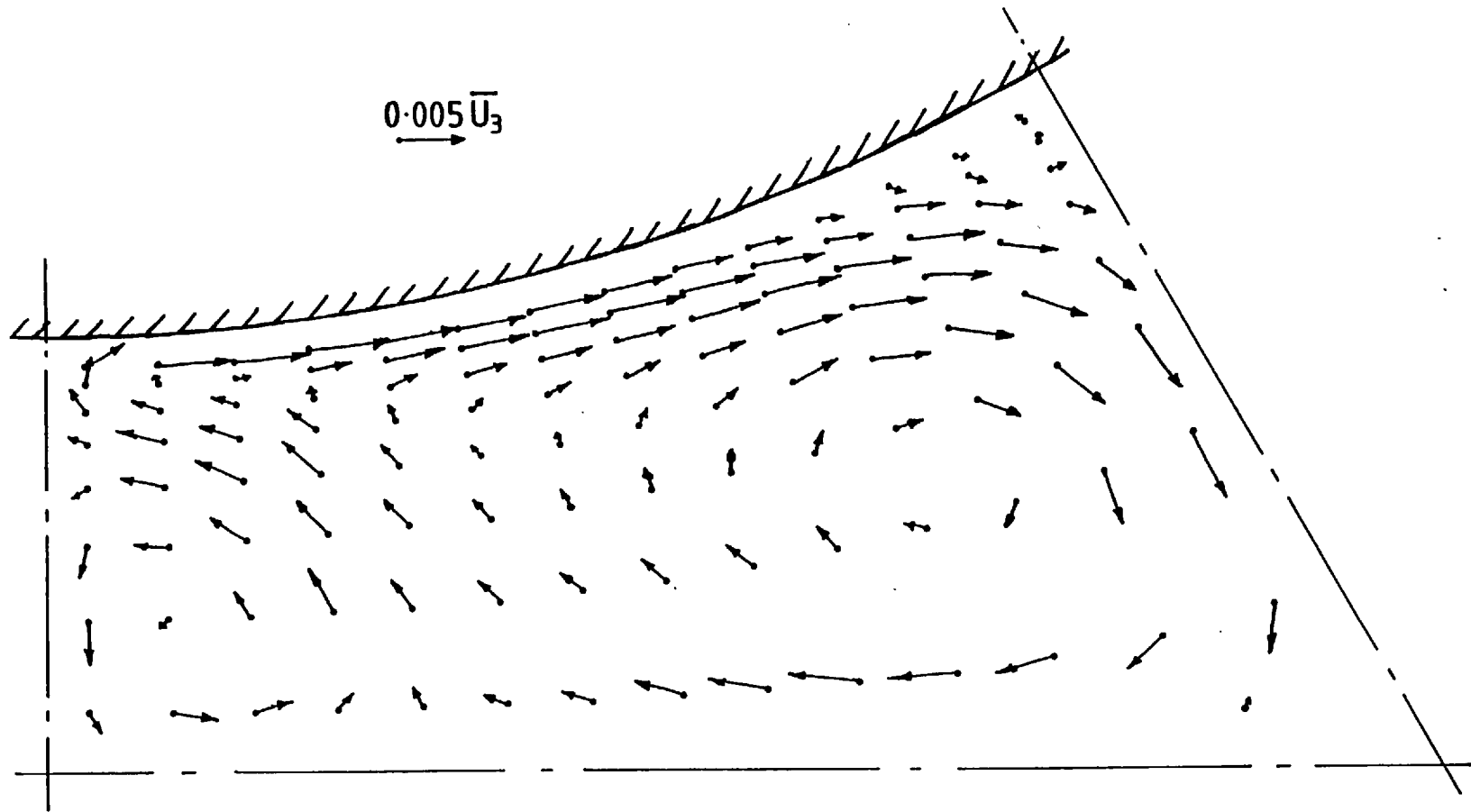


Figure 7.9.18 Predicted secondary velocity vectors in a rod bundle with $P/D = 1.217$ and $Re = 1.49 \times 10^5$.

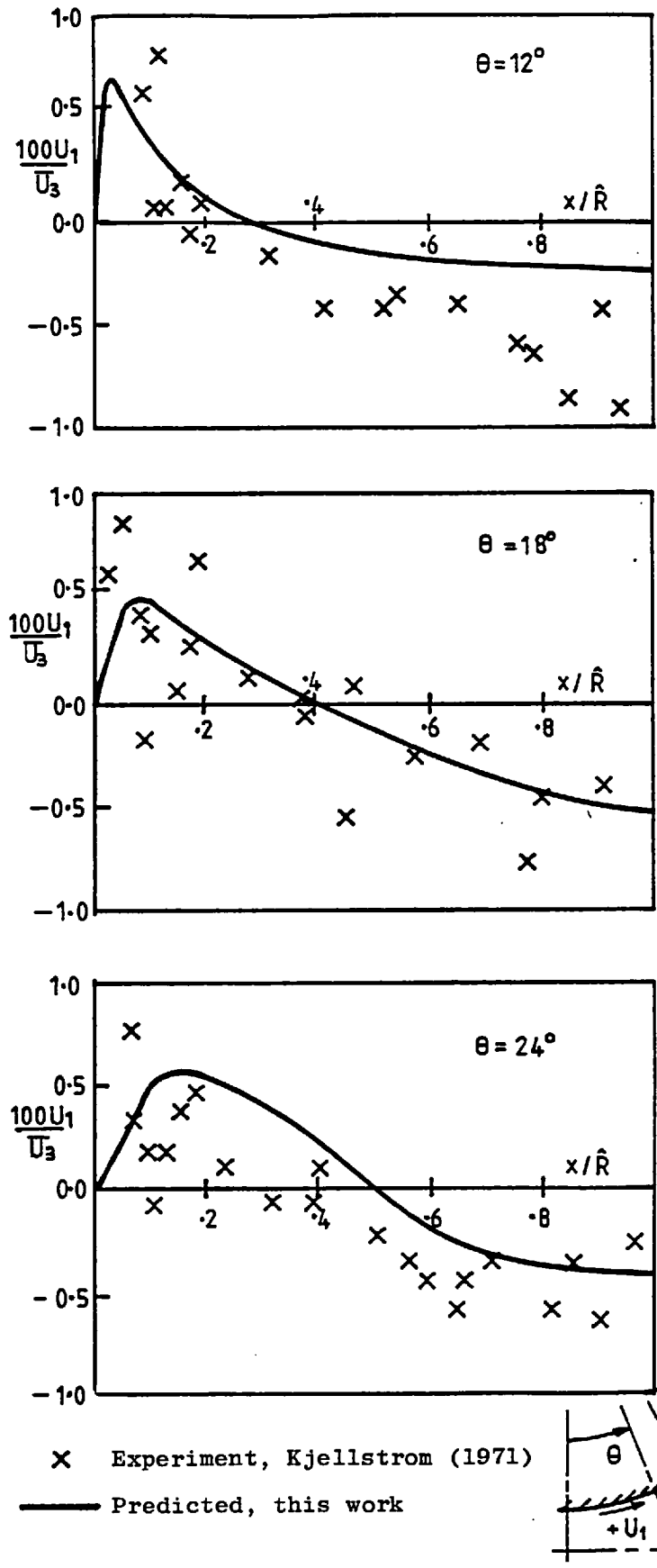


Figure 7.9.19 Circumferential secondary velocity in a rod bundle with $P/D = 1.217$ and $Re = 1.49 \times 10^5$.

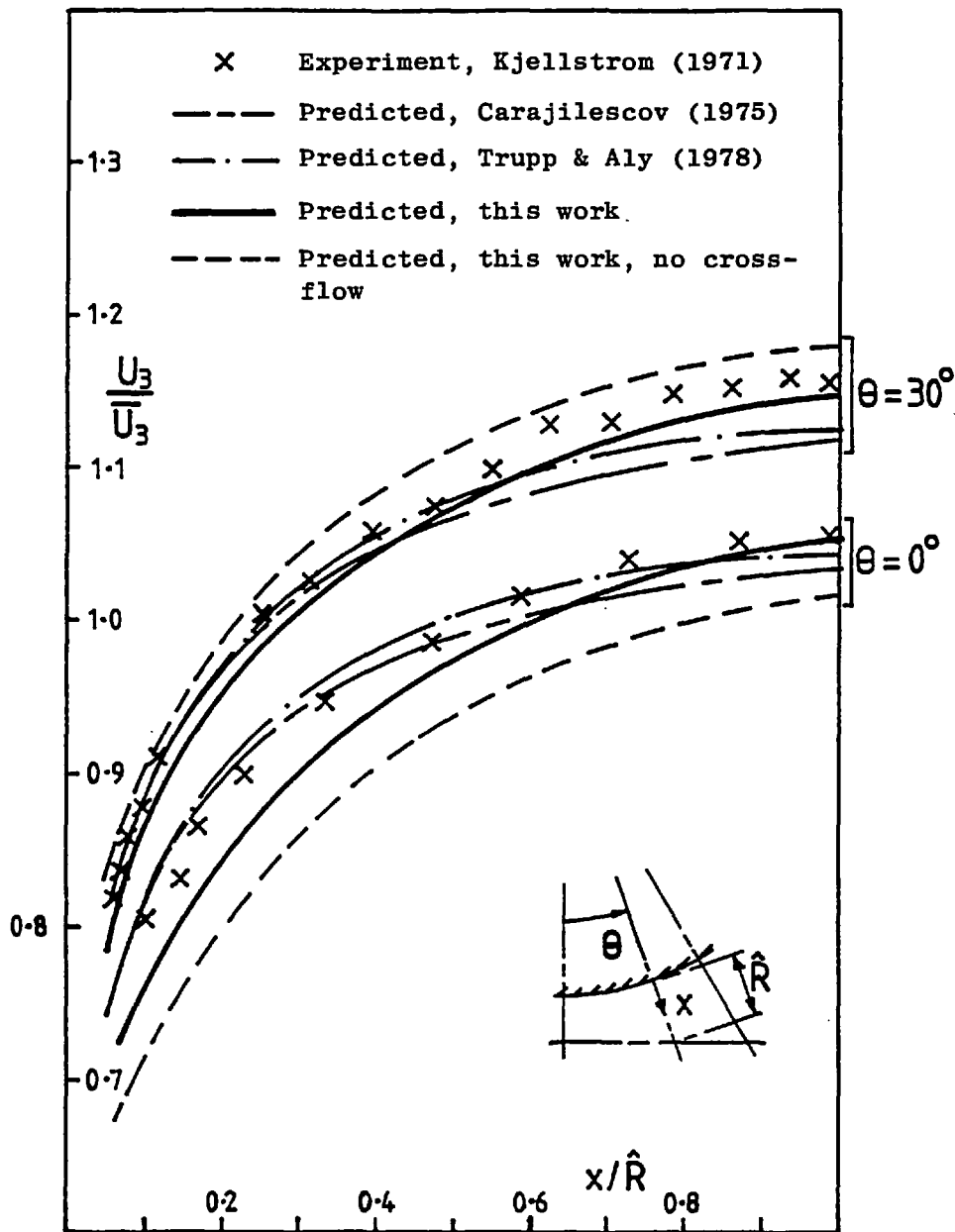


Figure 7.9.20 Axial velocity profiles in a rod bundle with $P/D = 1.217$ and $Re = 1.49 \times 10^5$.

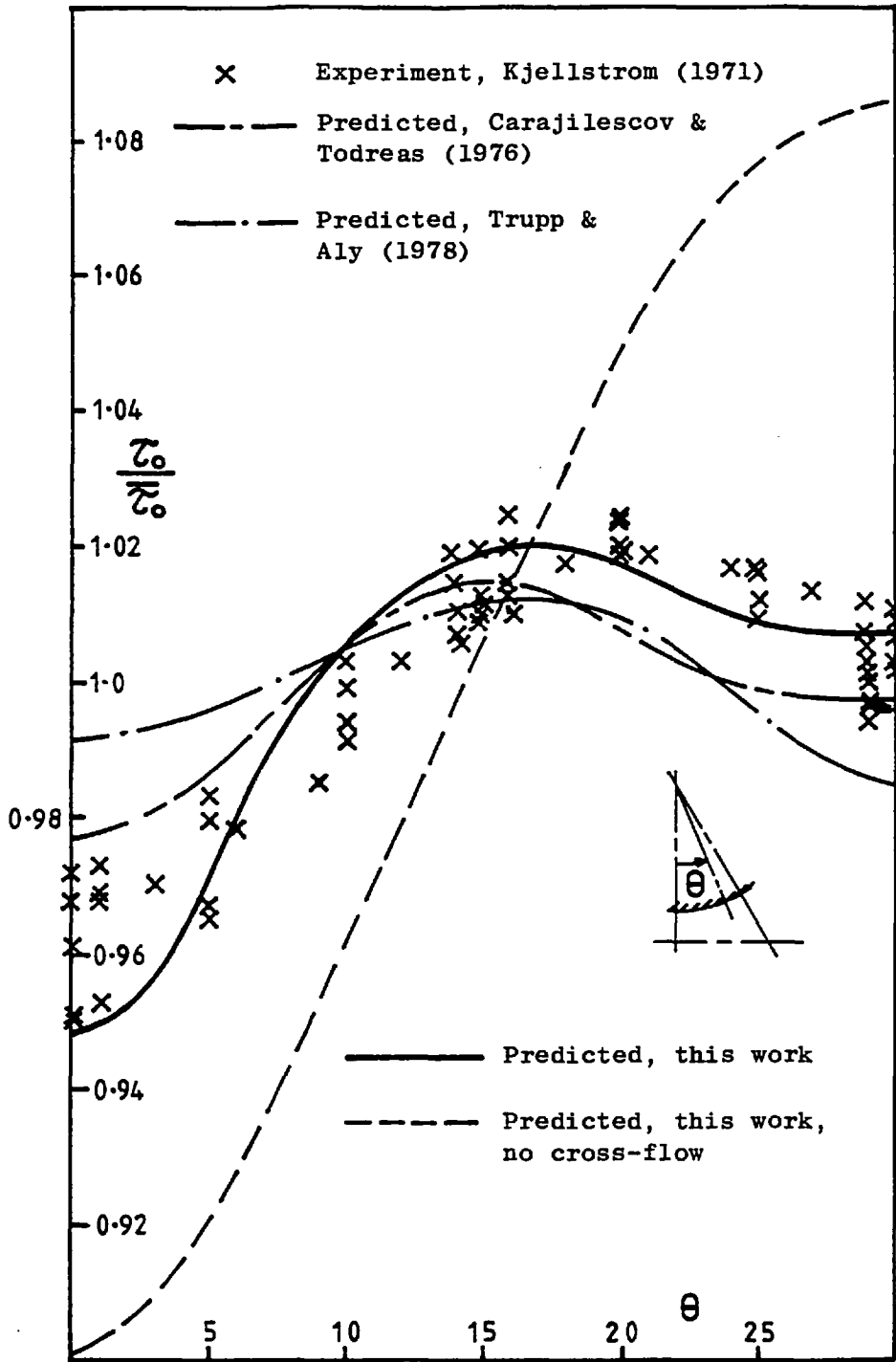


Figure 7.9.21 Wall shear stress in a rod bundle with $P/D = 1.217$ and $Re = 1.49 \times 10^5$.

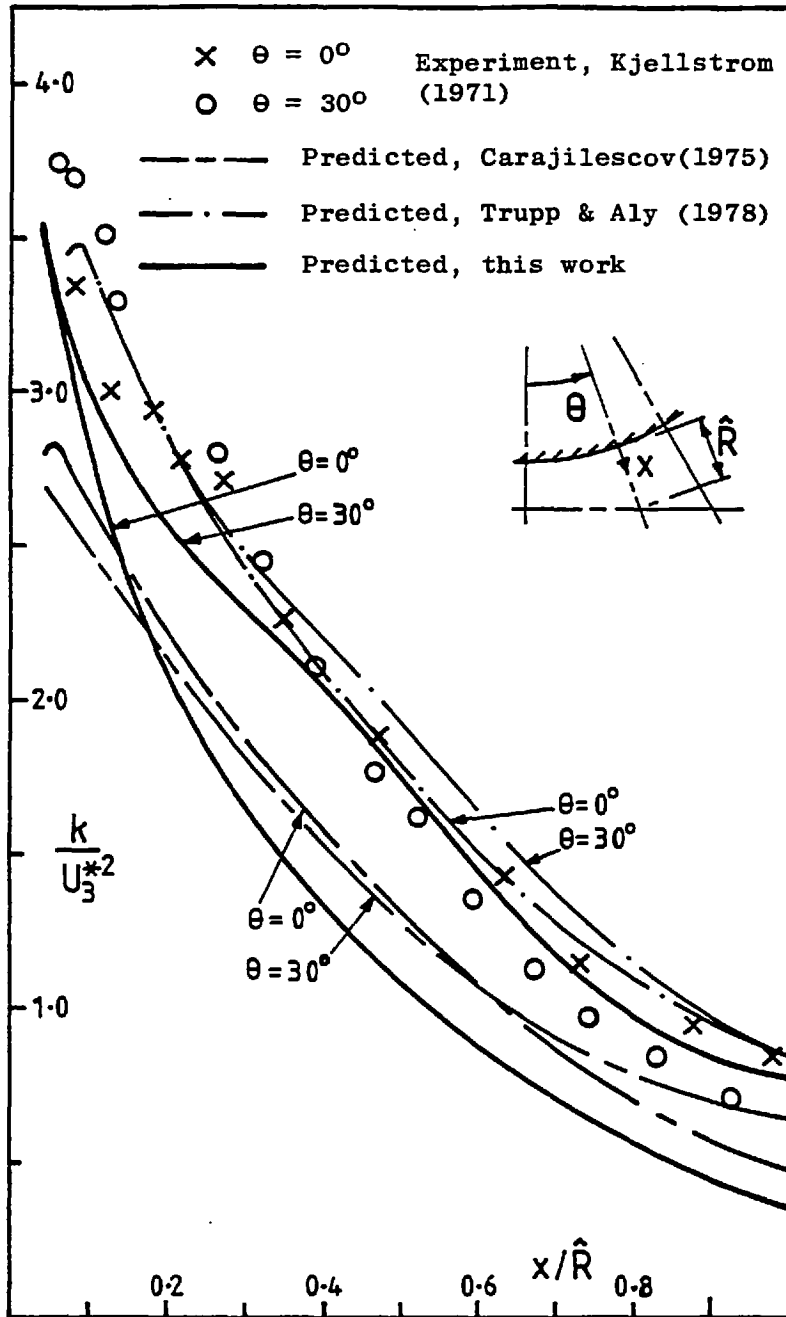


Figure 7.9.22 Turbulence kinetic energy profiles in a rod bundle with $P/D = 1.217$ and $Re = 1.49 \times 10^5$.

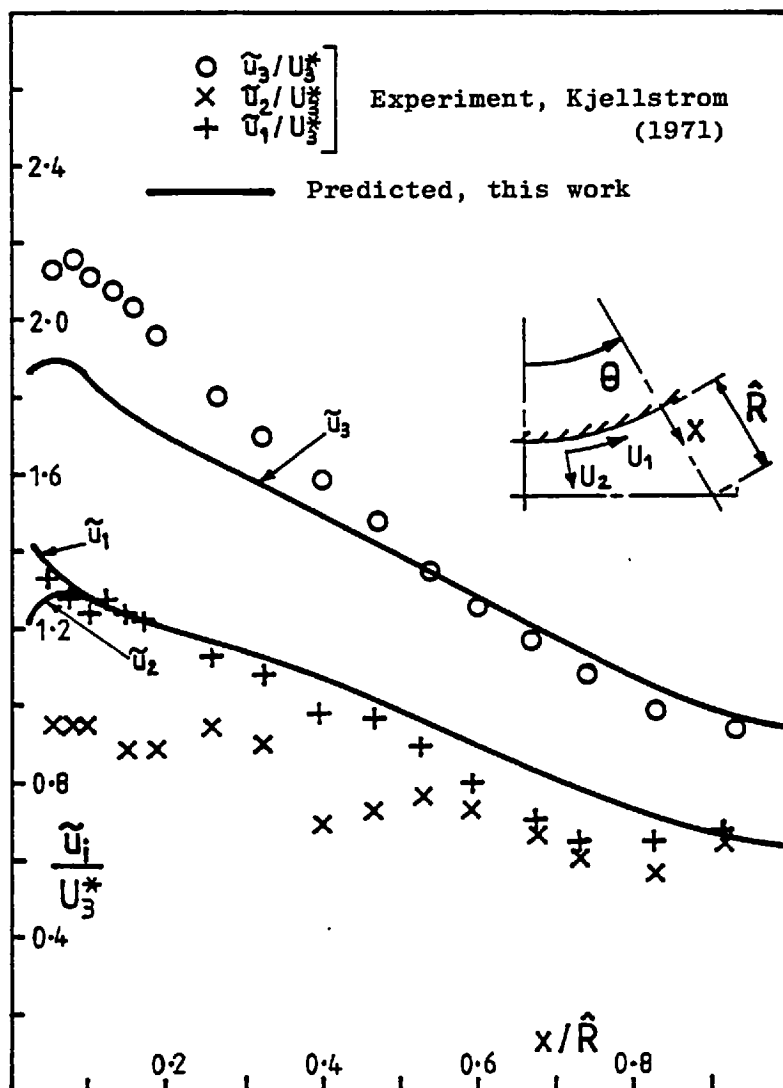


Figure 7.9.23 Turbulence intensity profiles along the $\theta = 30^\circ$ radial plane in a rod bundle with $P/D = 1.217$ and $Re = 1.49 \times 10^5$.

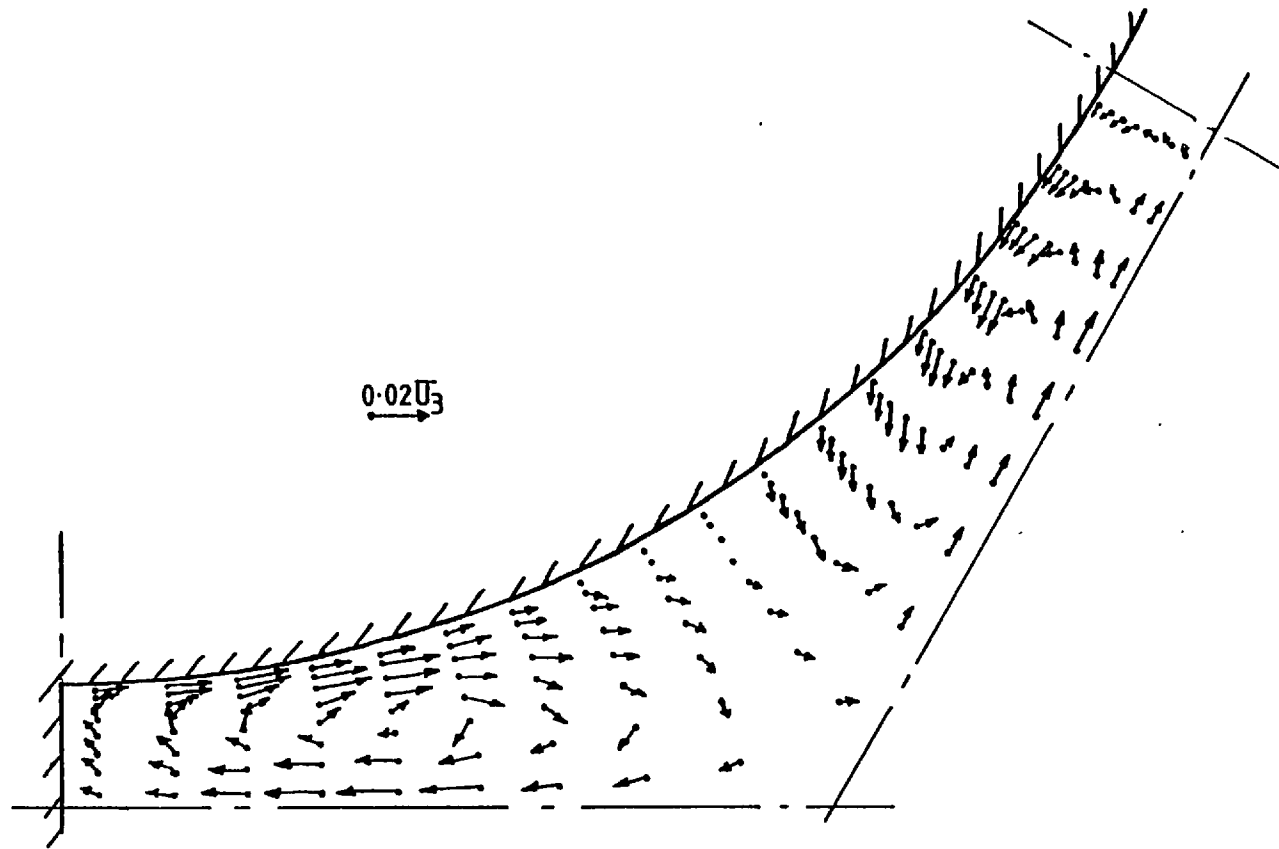


Figure 7.9.24 Predicted secondary velocity vectors in a symmetry quadrant of the Subbotin et al (1971) test channel with $P/D = 1.1$ and $Re = 4.27 \times 10^4$.

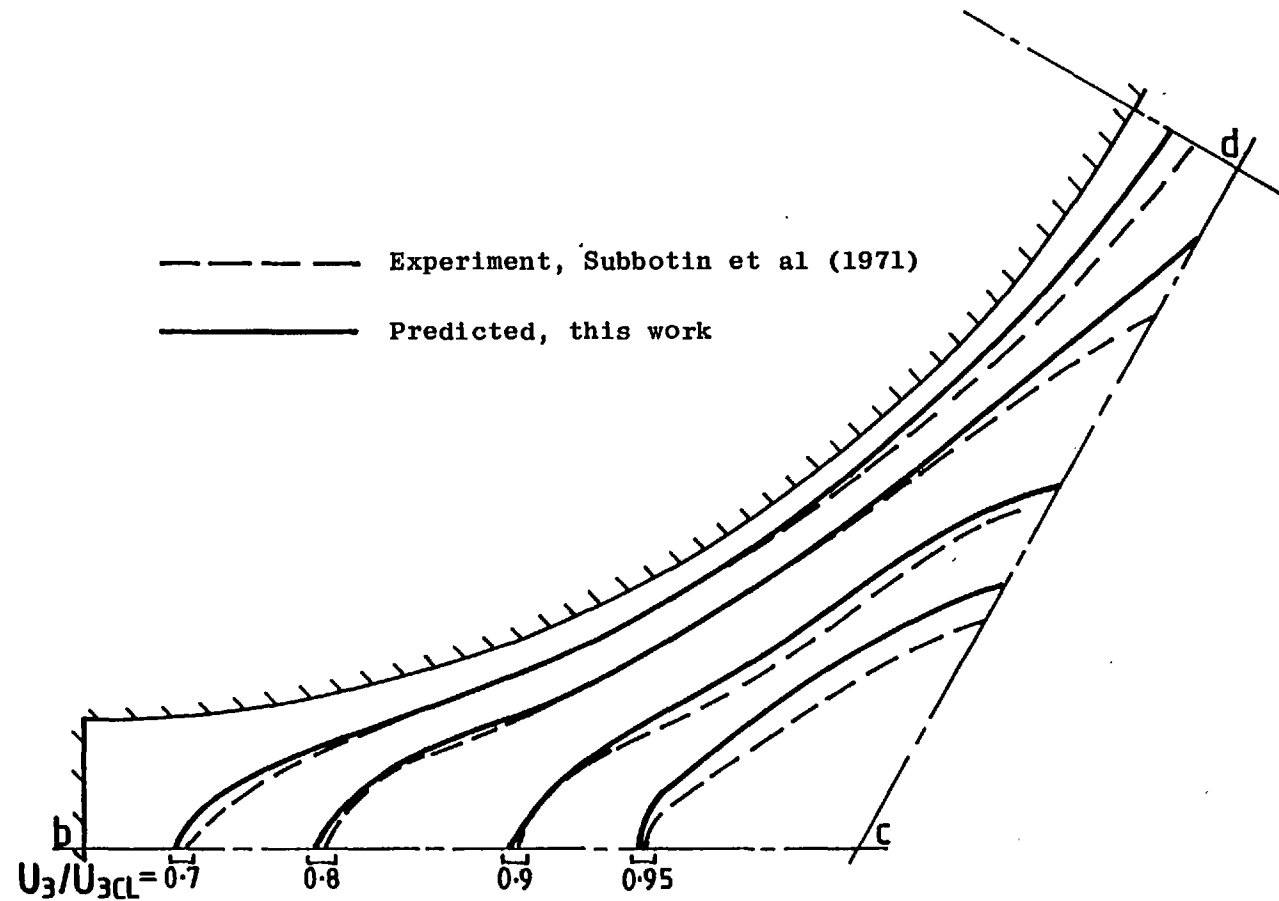


Figure 7.9.25 Axial velocity contours in a symmetry quadrant of the Subbotin et al (1971) test channel with $P/D = 1.1$ and $Re = 4.27 \times 10^4$.

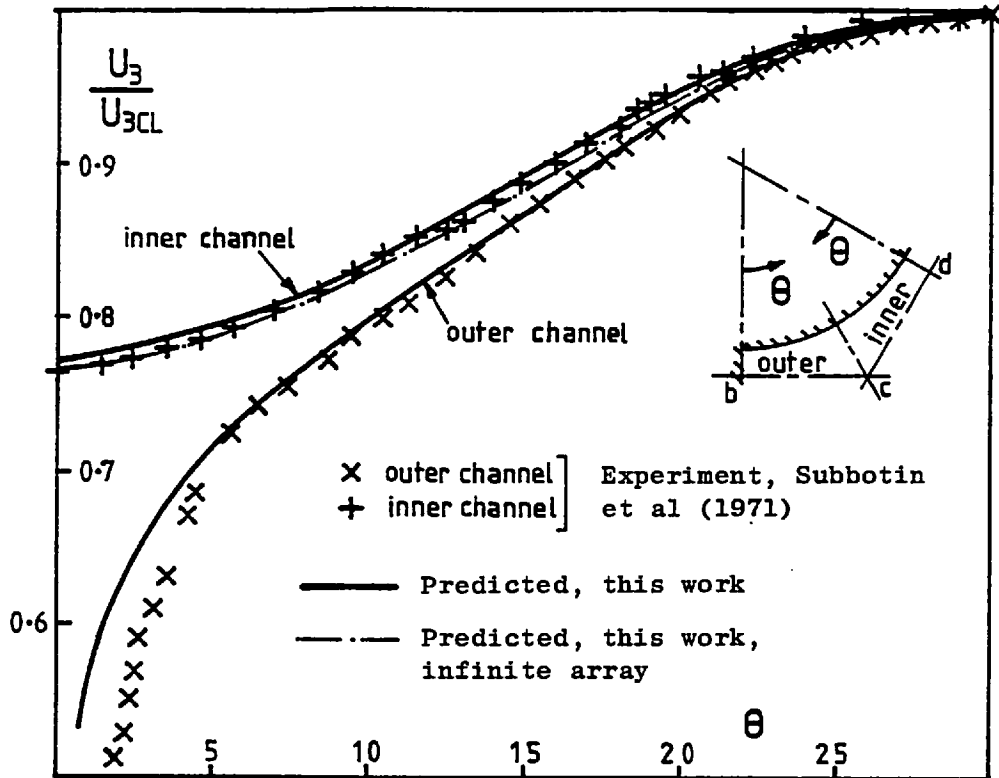


Figure 7.9.26 Axial velocity profiles along the centre-plane (bcd) of a symmetry quadrant of the Subbotin et al (1971) test channel with $P/D = 1.1$ and $Re = 4.27 \times 10^4$.

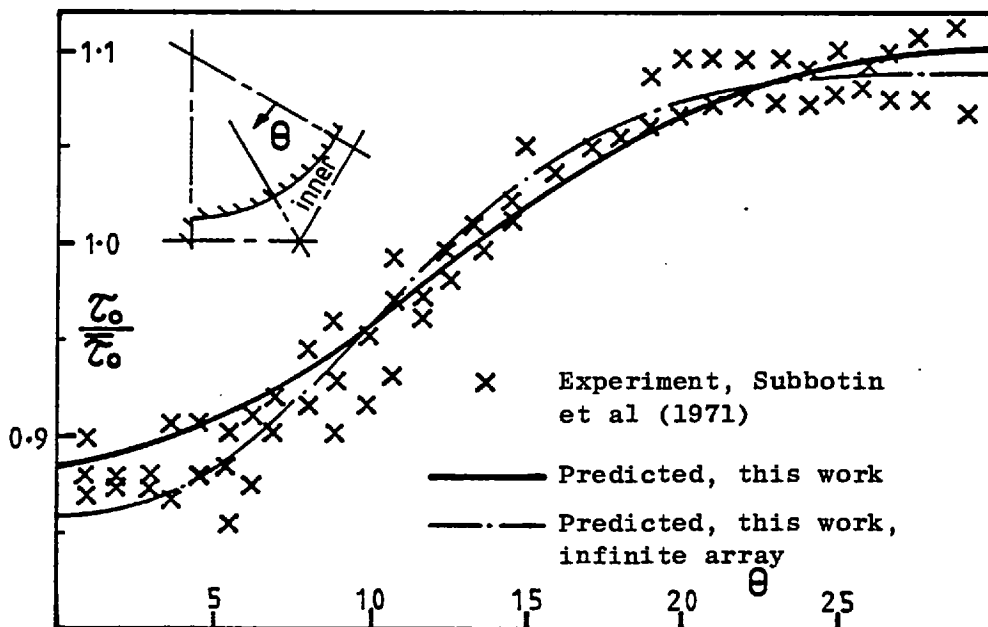


Figure 7.9.27 Wall shear stress in the inner channel of a symmetry quadrant of the Subbotin et al (1971) test channel with $P/D = 1.1$ and $Re = 4.27 \times 10^4$.

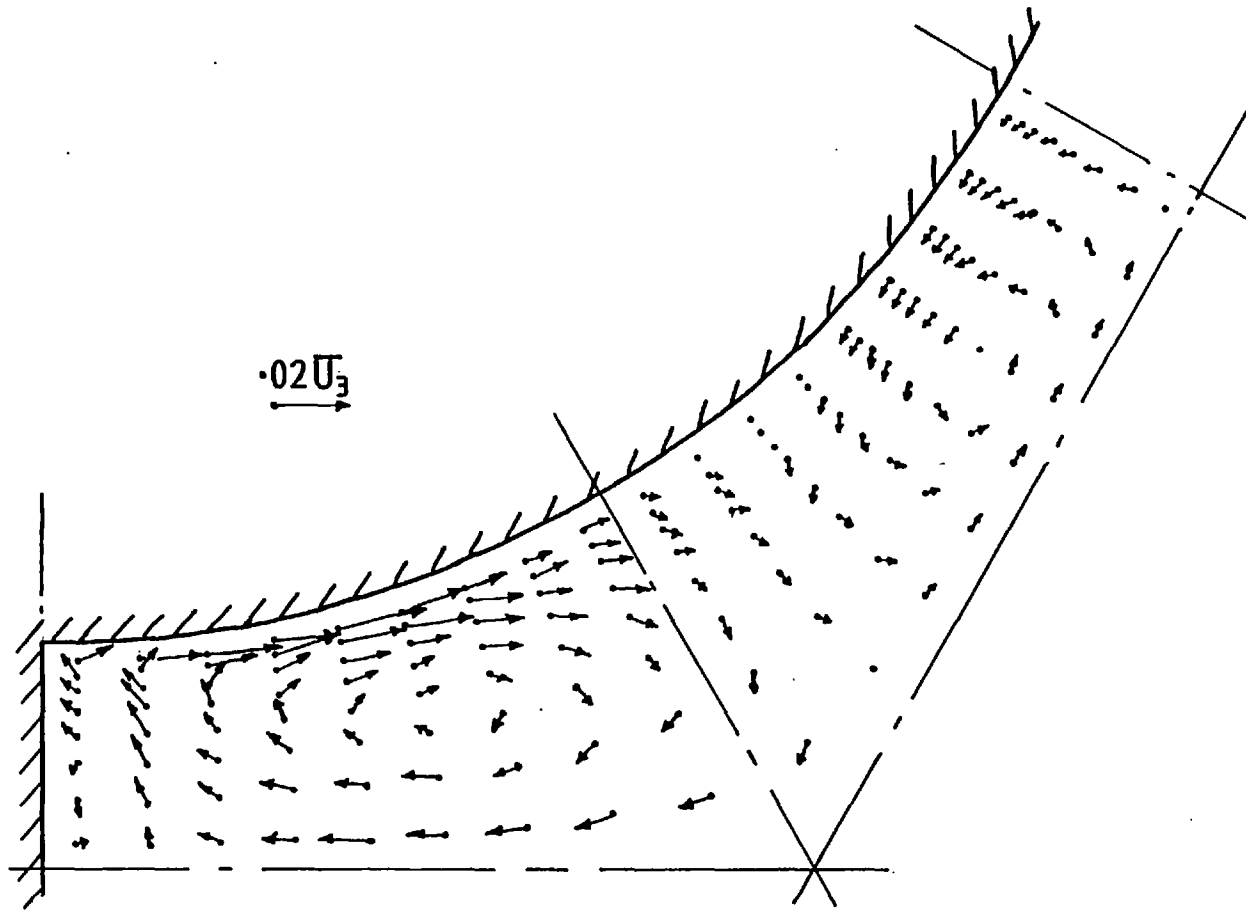


Figure 7.9.28 Predicted secondary velocity vectors in a symmetry quadrant of the Subbotin et al(1971) test channel with $P/D = 1.2$ and $Re = 3.48 \times 10^4$.

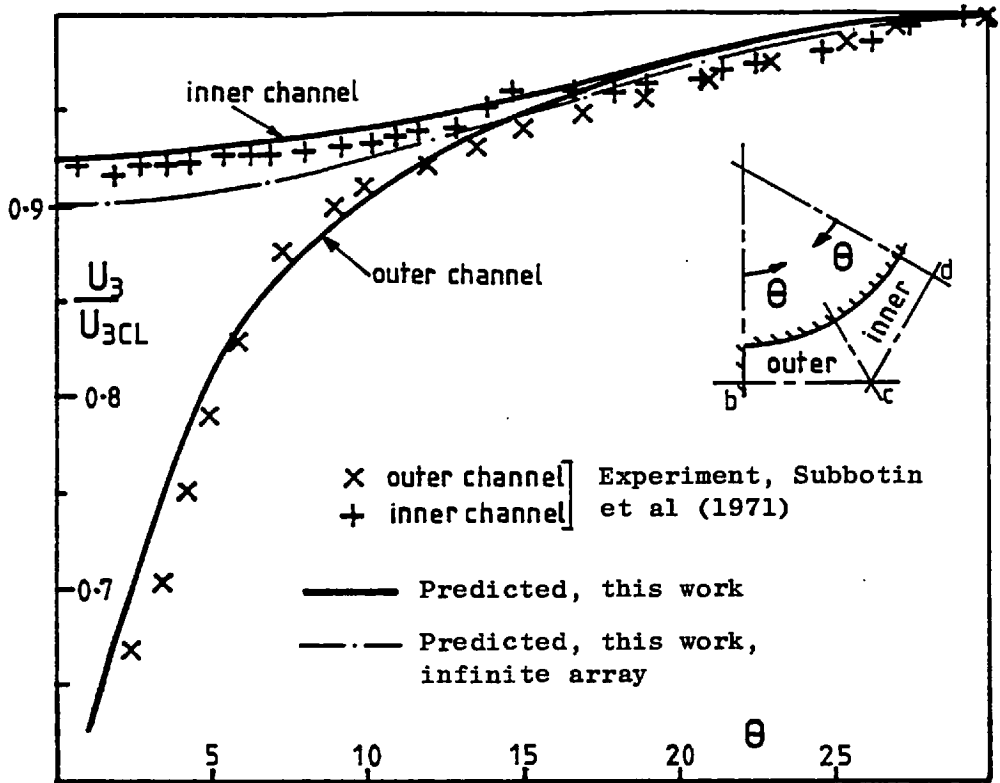


Figure 7.9.29 Axial velocity profiles along the centre-plane (bcd) of a symmetry quadrant of the Subbotin et al (1971) test channel with $P/D = 1.2$ and $Re = 3.48 \times 10^4$.

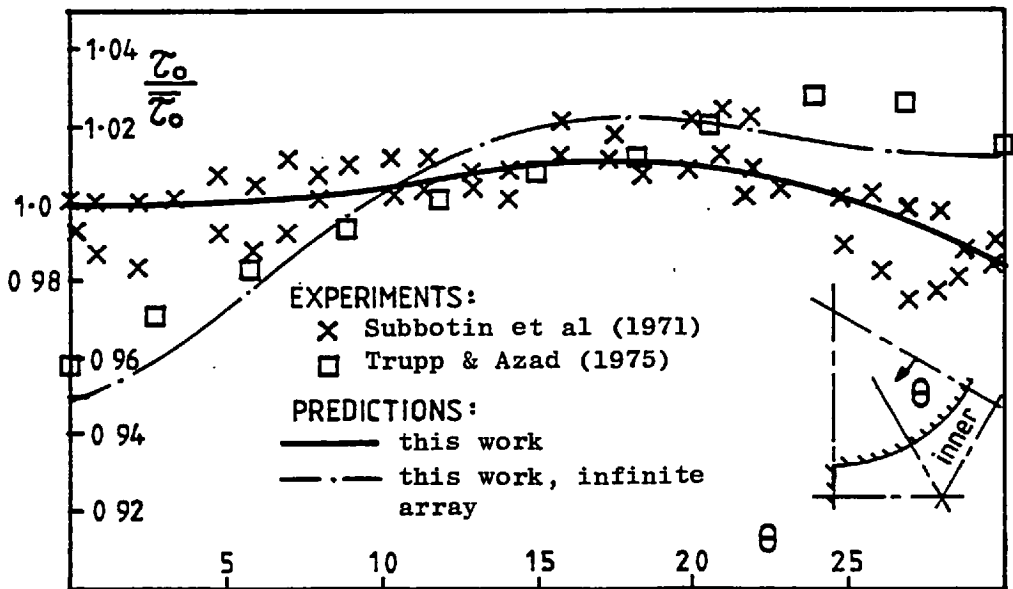
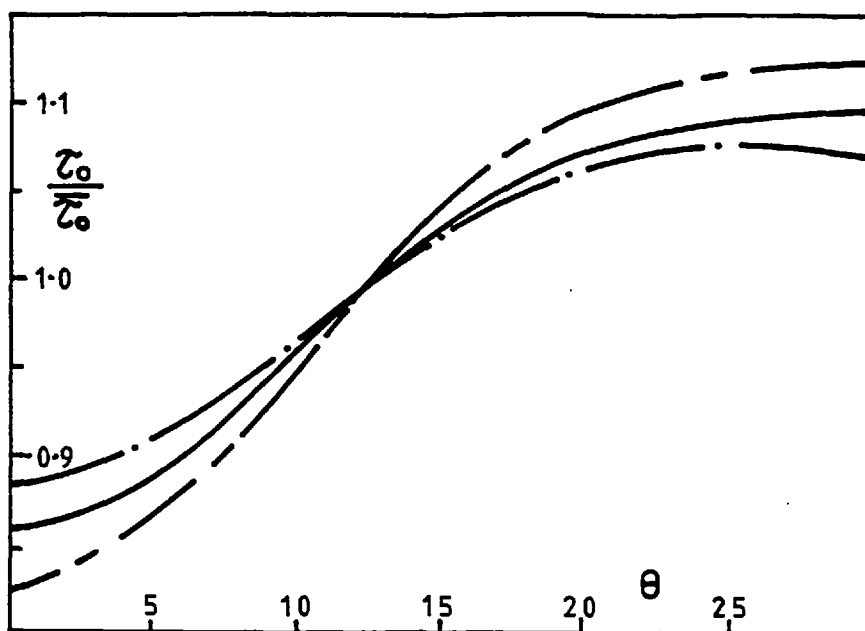
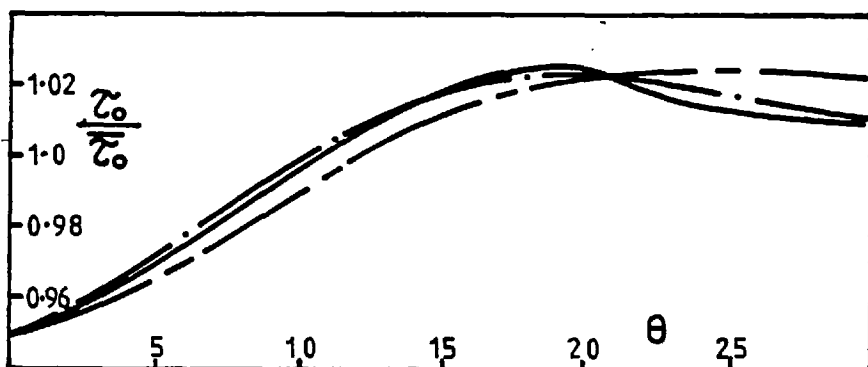


Figure 7.9.30 Wall shear stress in the inner channel of a symmetry quadrant of the Subbotin et al (1971) test channel with $P/D = 1.2$ and $Re = 3.48 \times 10^4$.



(a) $P/D = 1.1$



(b) $P/D = 1.2$

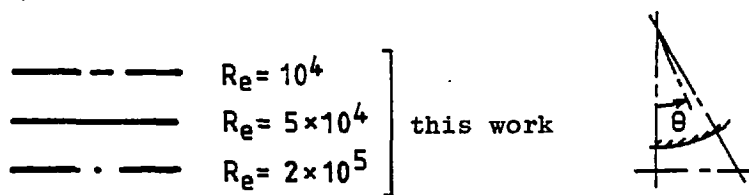


Figure 7.9.31 Predicted variation of local wall shear stress with Reynolds number in rod bundles.

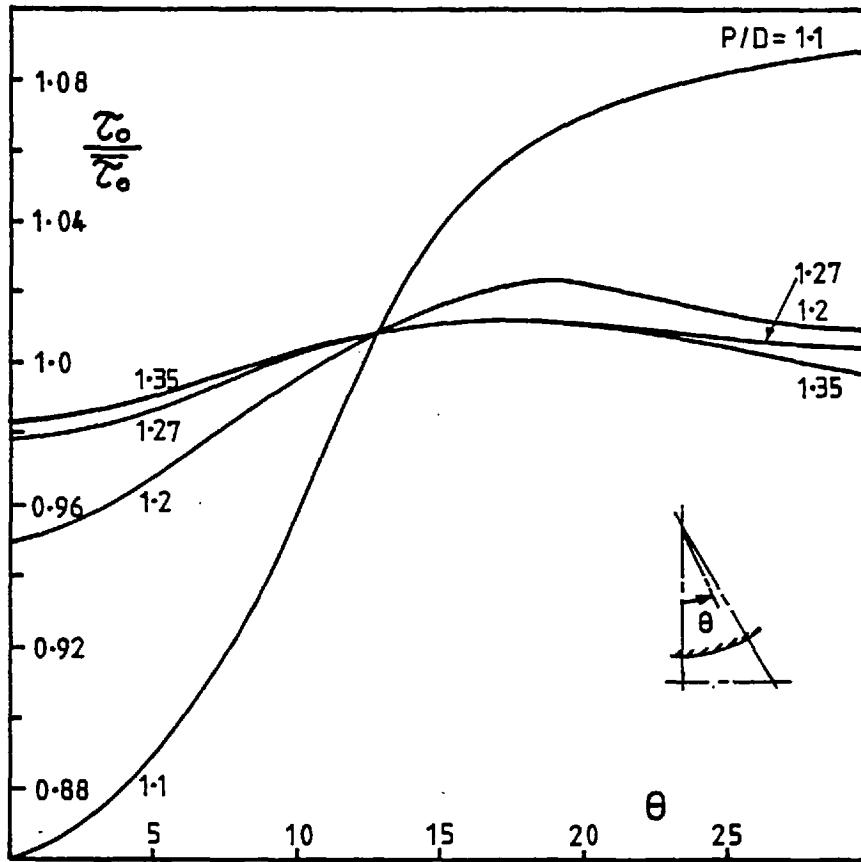
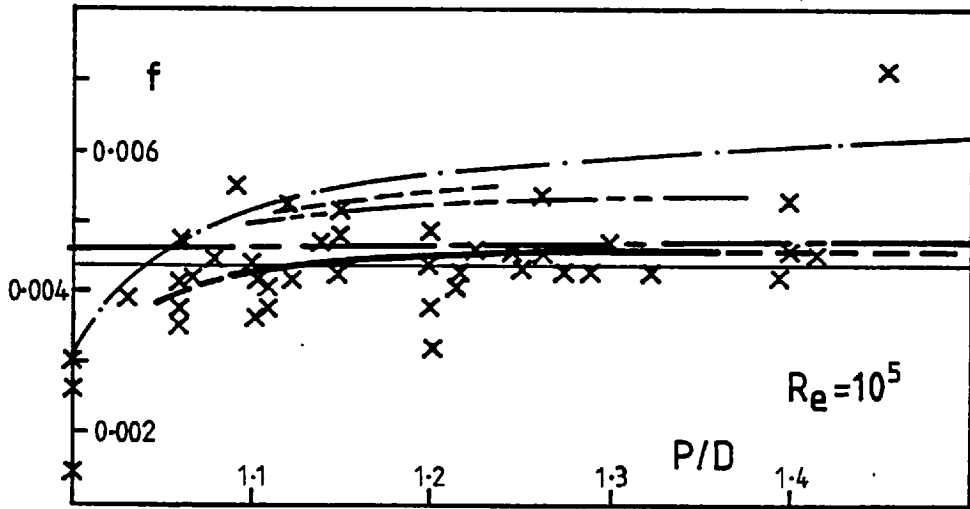
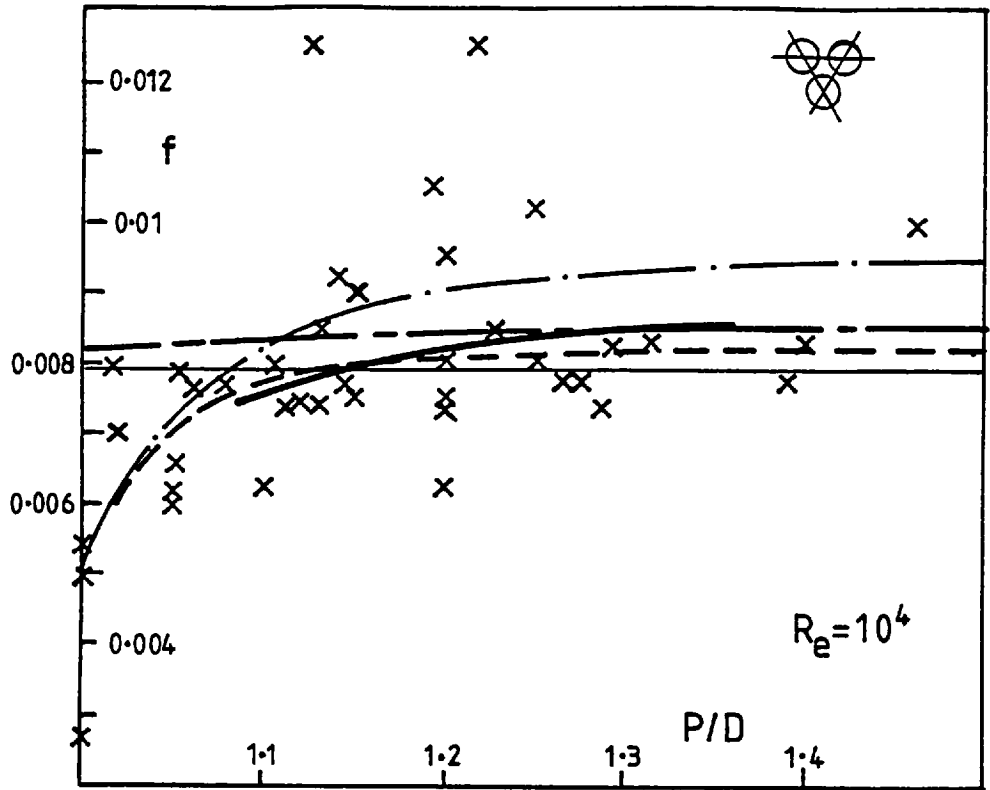


Figure 7.9.32 Predicted variation of local wall shear stress with P/D ratio in rod bundles with $Re = 5 \times 10^4$.



- x 29 different experimenters (before 1972)
- Experiment, Rehme (1972)
- Equivalent annulus prediction
- Predicted, this work
- Predicted, Carajilescov (1975)
- Predicted, Trupp and Aly (1978)
- . — Malak equation (3.2.2)
- Blasius equation (7.2.4)

Figure 7.9.33 Variation of friction factor with P/D ratio in rod bundles.

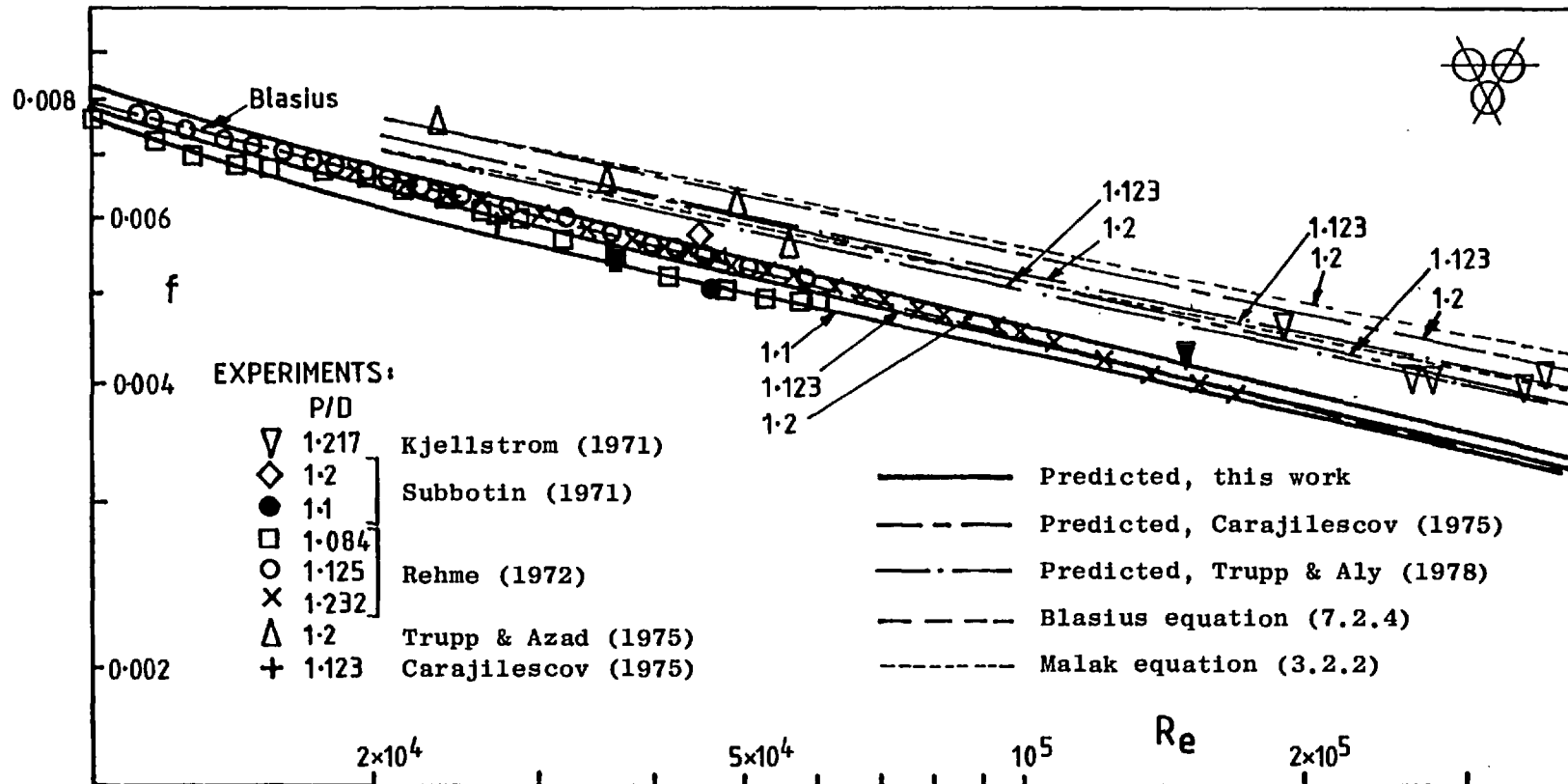
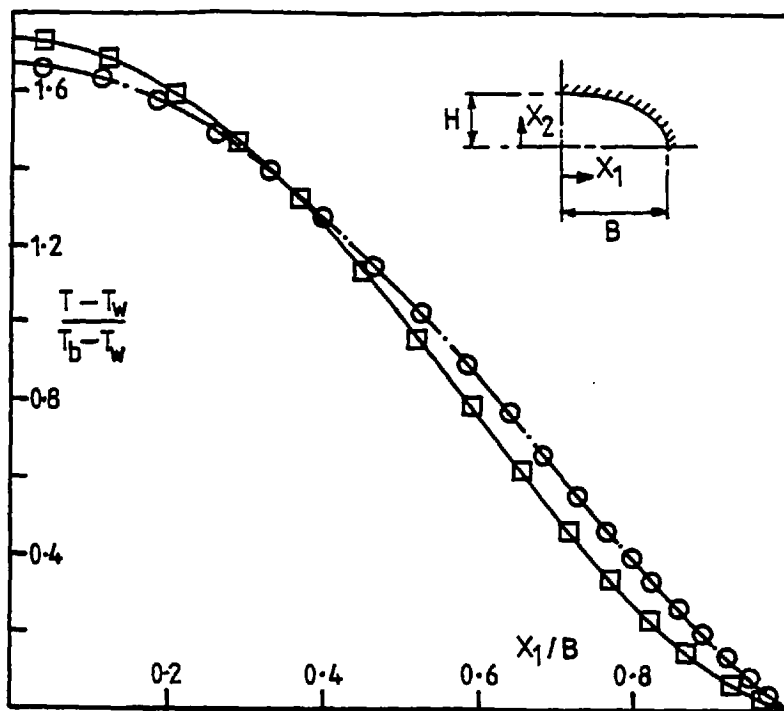
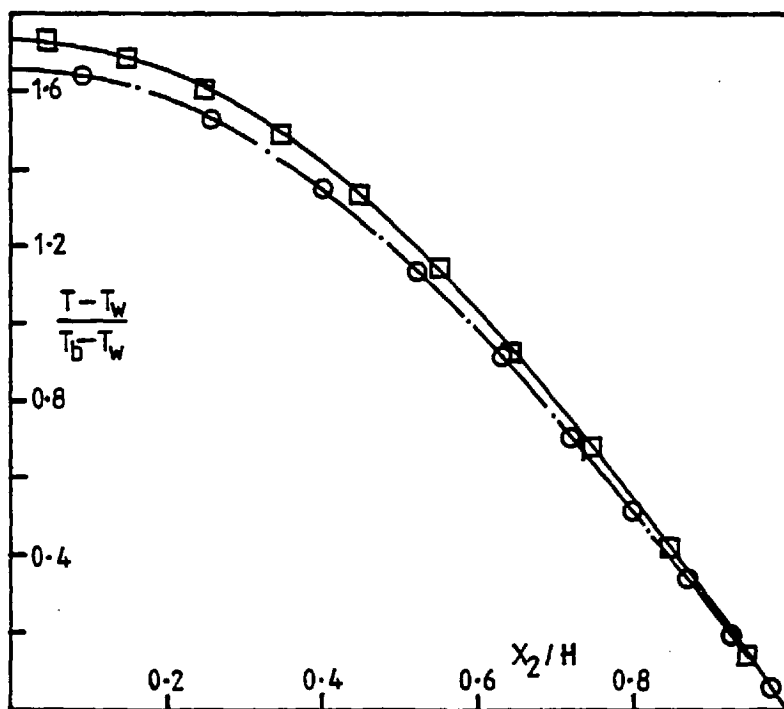


Figure 7.9.34 Friction factor characteristics for rod bundles.



(a) major axis



(b) minor axis

—	AR = 2	Analytical,	○	AR = 2	Predicted,
- · -	AR = 5	Tao (1961)	□	AR = 5	this work

Figure 8.2.1 Laminar temperature profiles in elliptical ducts for the H1 boundary condition.

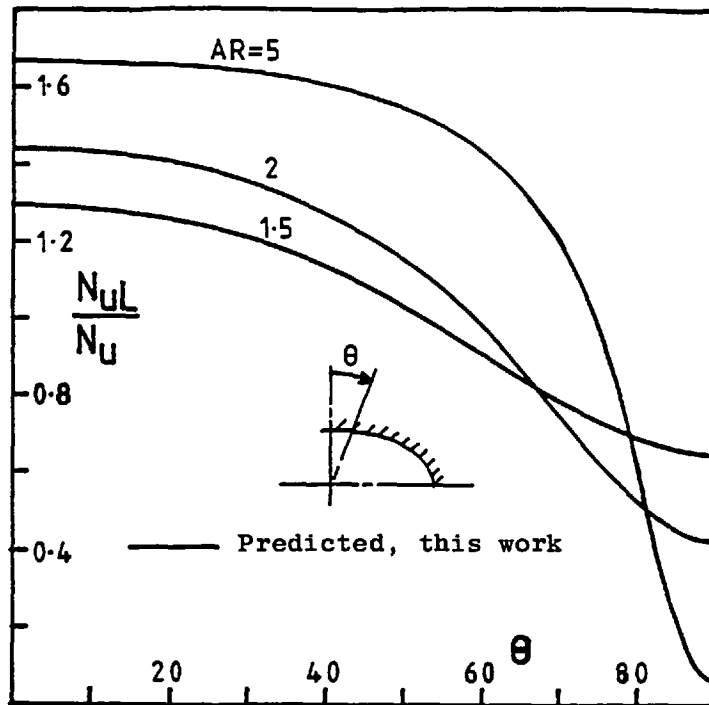


Figure 8.2.2 Local laminar Nusselt numbers in elliptical ducts with the H1 boundary condition.

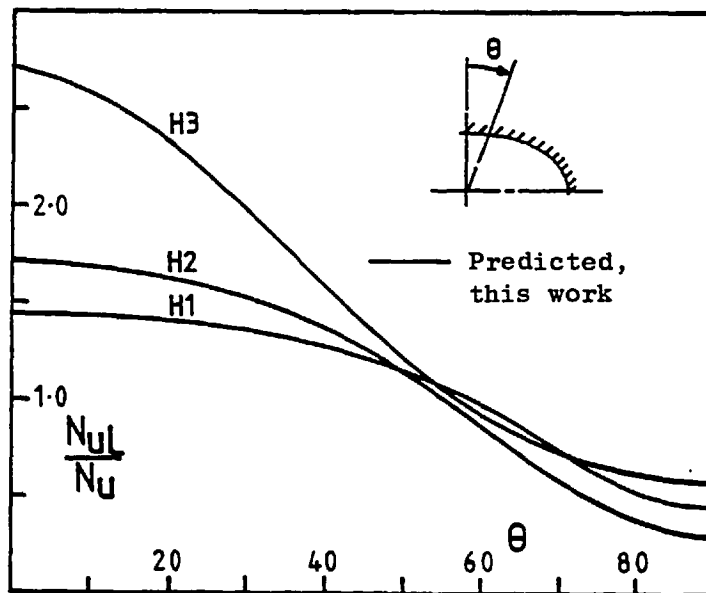


Figure 8.2.3 Local laminar Nusselt numbers in an elliptical duct with AR = 2.

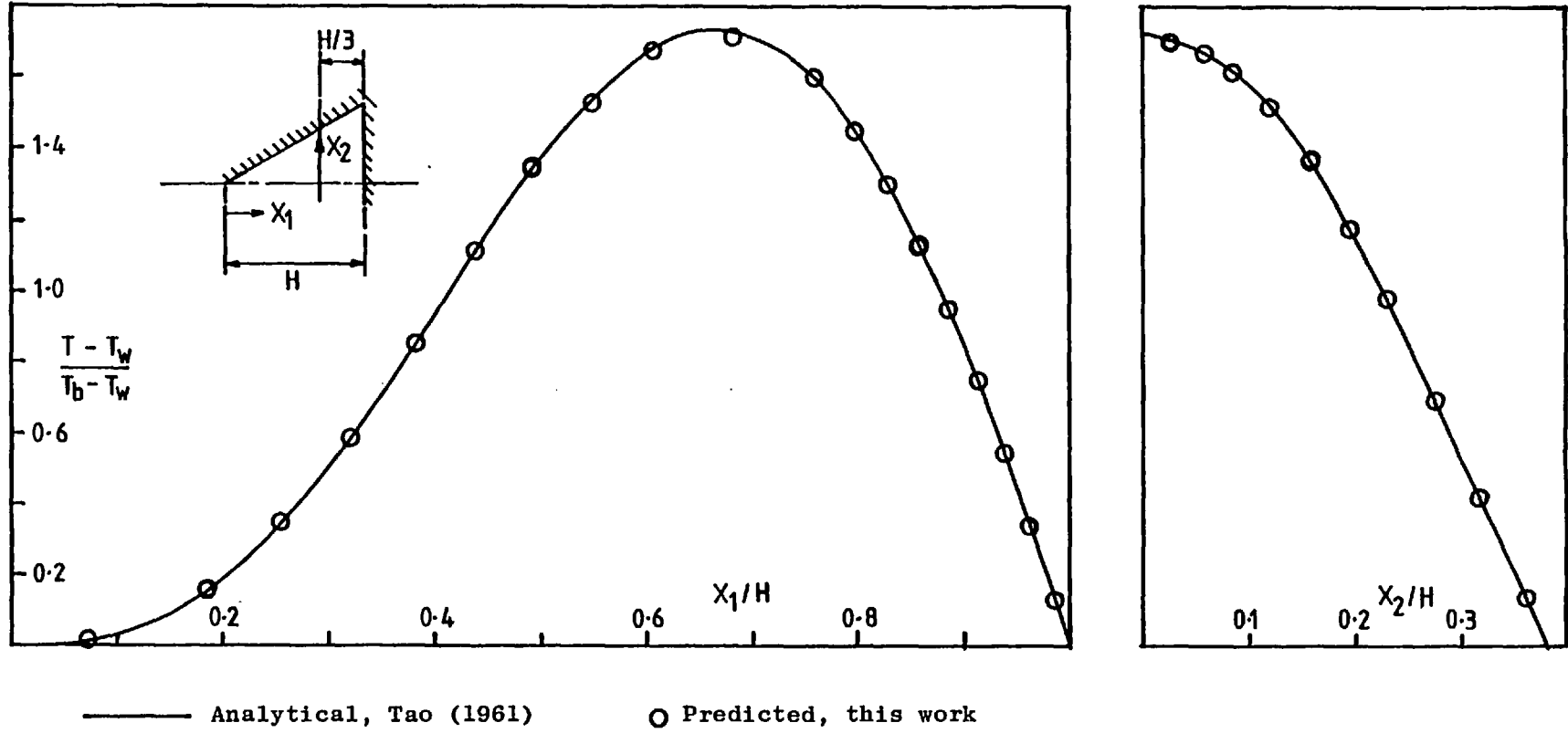


Figure 8.2.4 Laminar temperature profiles in an equilateral triangular duct with the H1 boundary condition

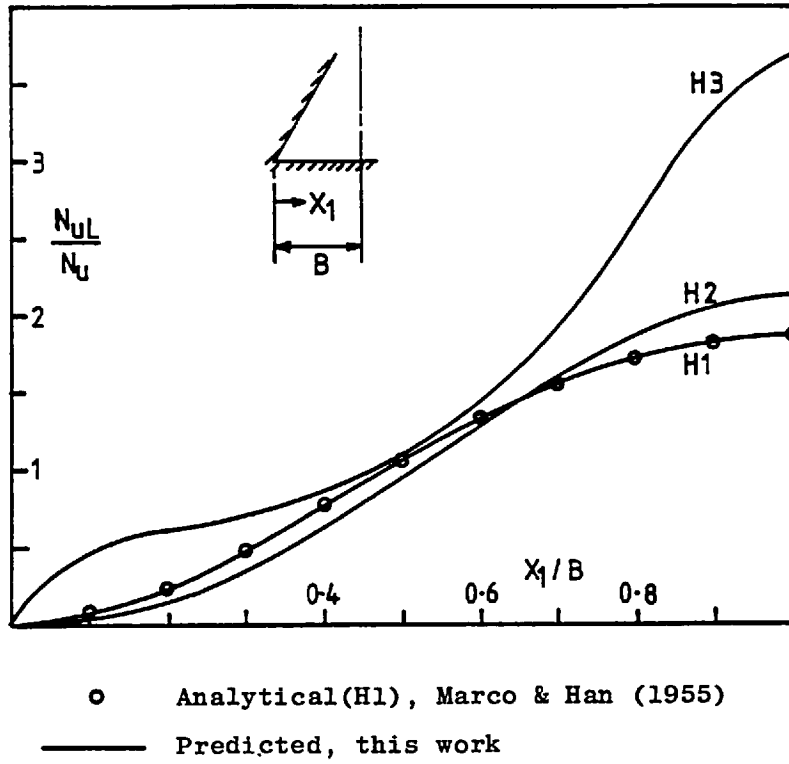


Figure 8.2.5 Local laminar Nusselt numbers in an equilateral triangular duct.

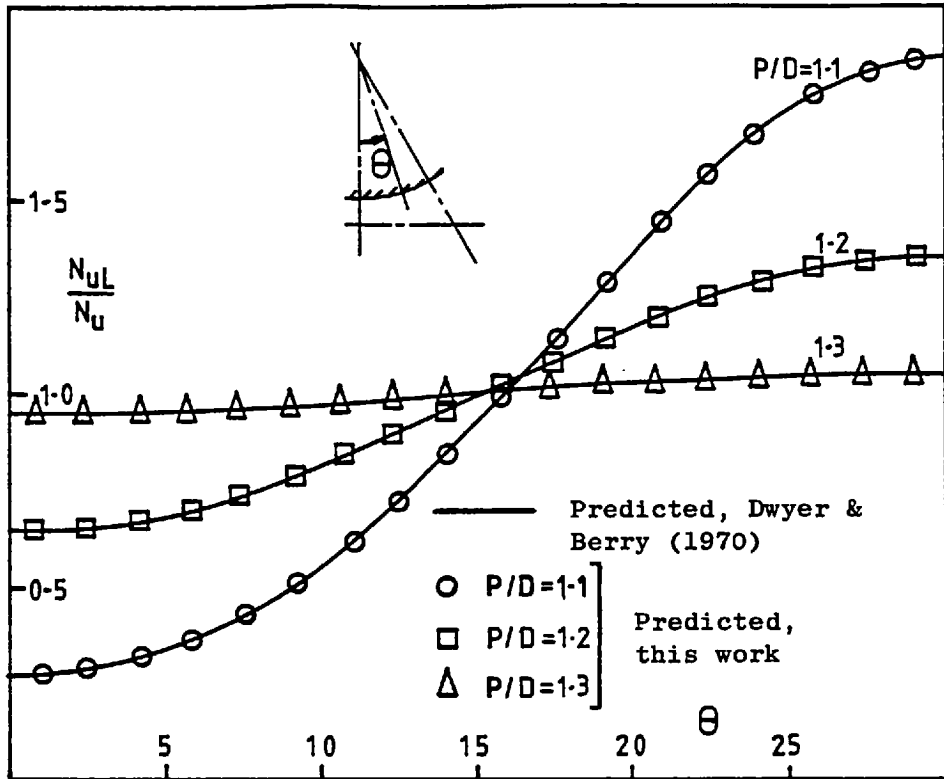


Figure 8.2.6 Local laminar Nusselt numbers in rod bundles with the H1 boundary condition.

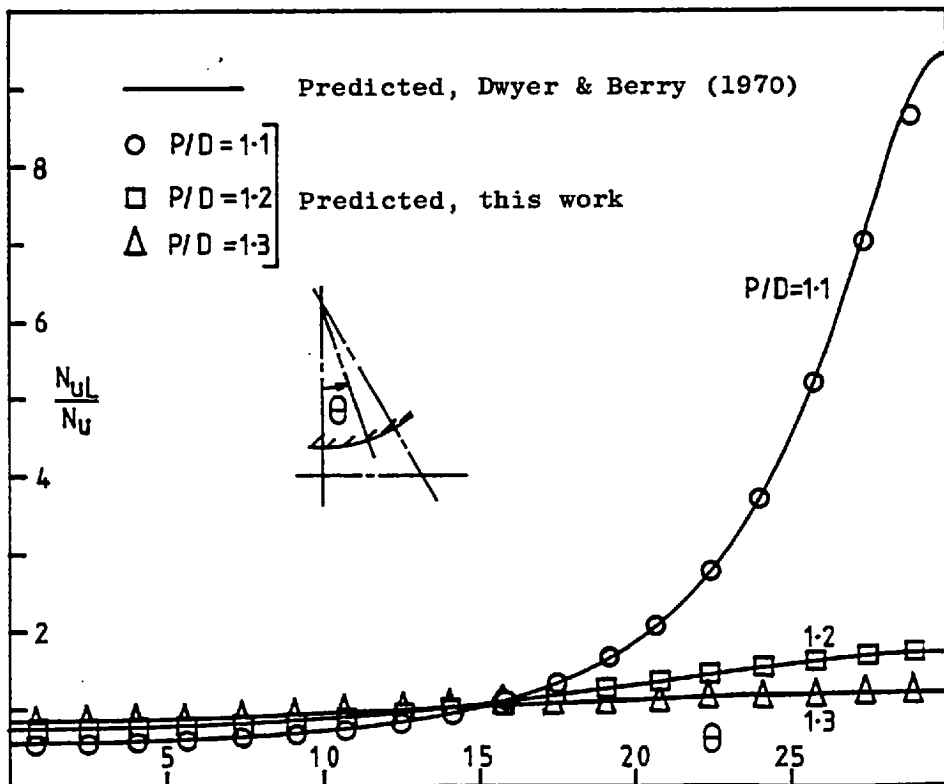


Figure 8.2.7 Local laminar Nusselt number in rod bundles with the H3 boundary condition.

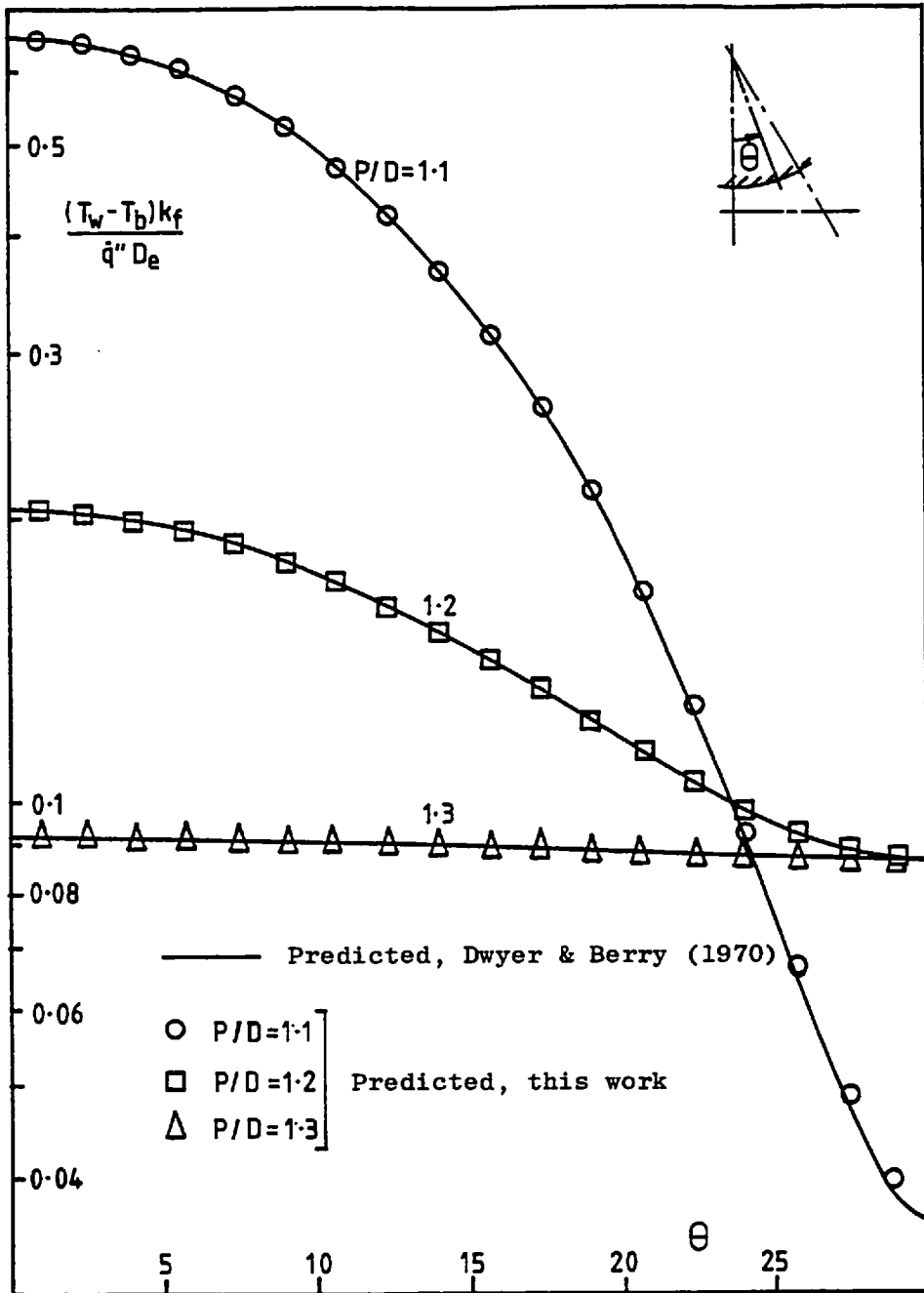


Figure 8.2.8 Local laminar wall temperatures in rod bundles with the H3 boundary condition

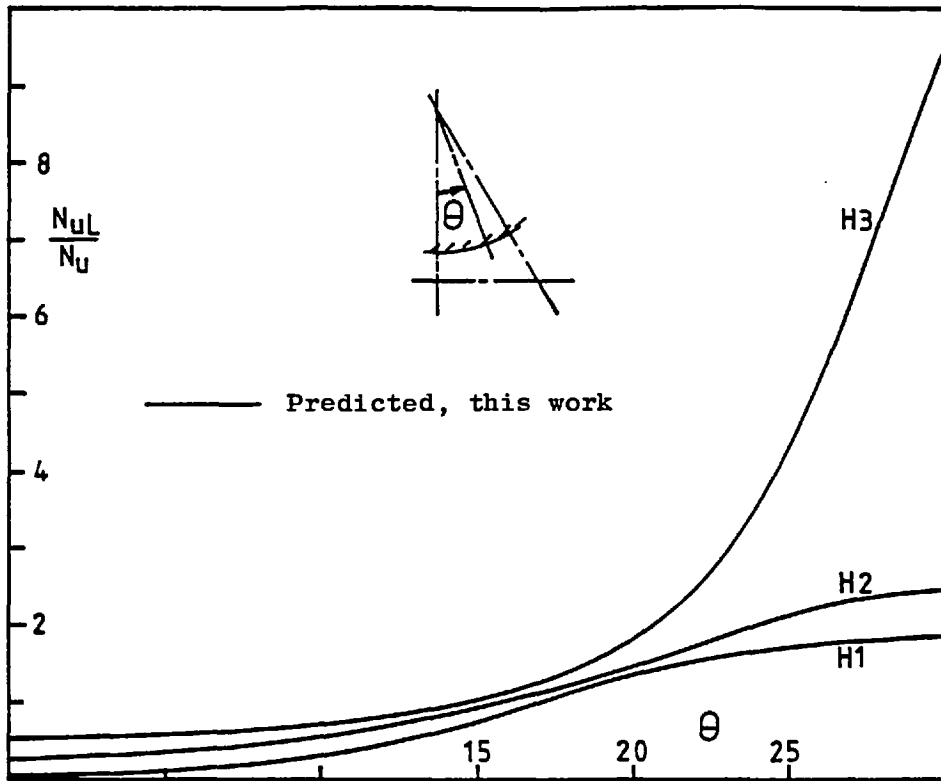


Figure 8.2.9 Local laminar Nusselt numbers in a rod bundle with $P/D = 1.1$.

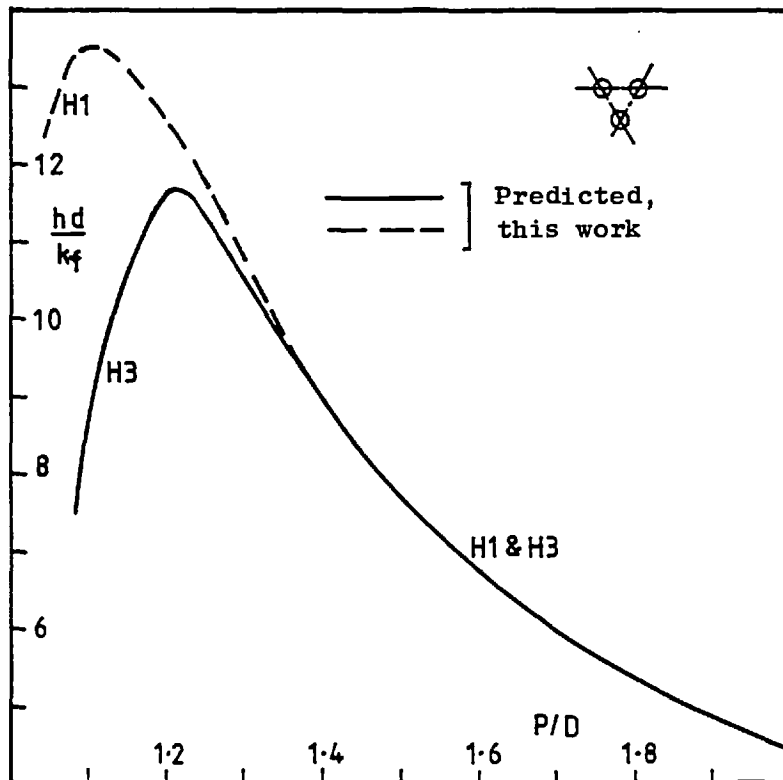


Figure 8.2.10 Rod-based mean Nusselt numbers in rod bundles with the H3 boundary condition.

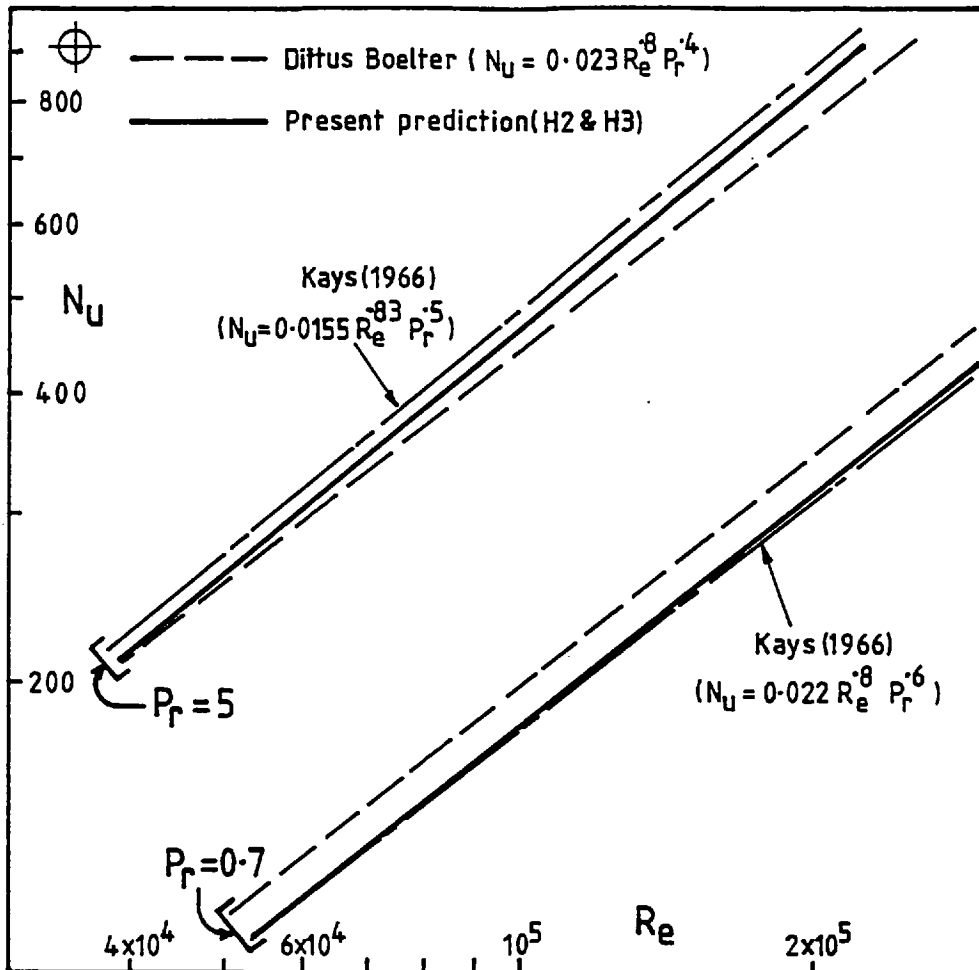


Figure 8.3.1 Mean Nusselt numbers in a circular tube.

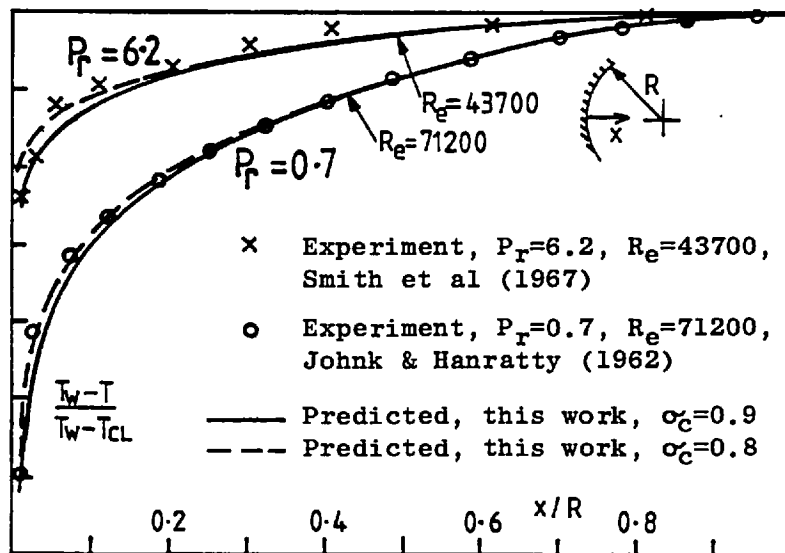


Figure 8.3.2 Temperature profiles in a circular tube.

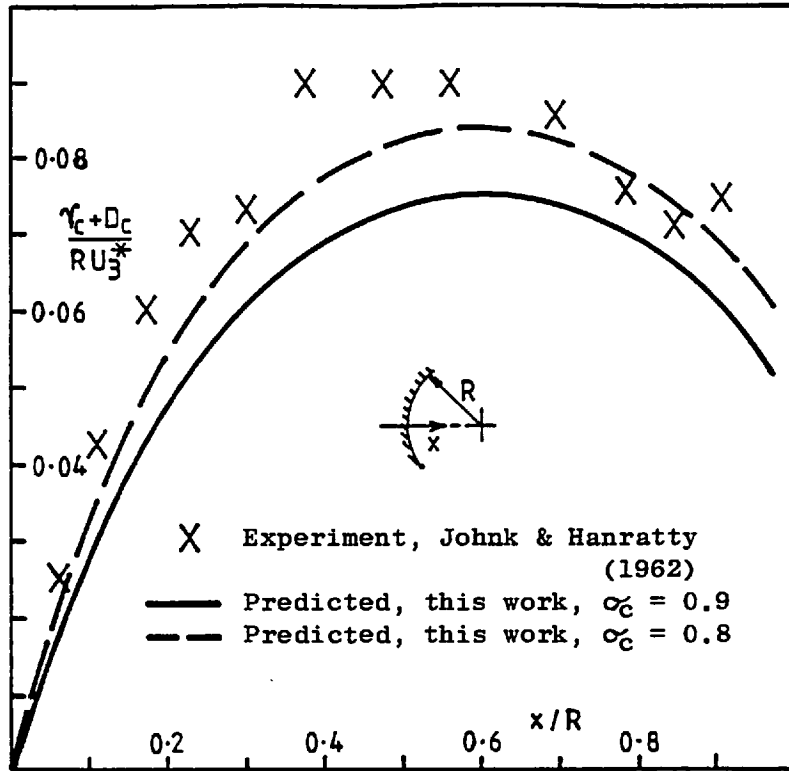
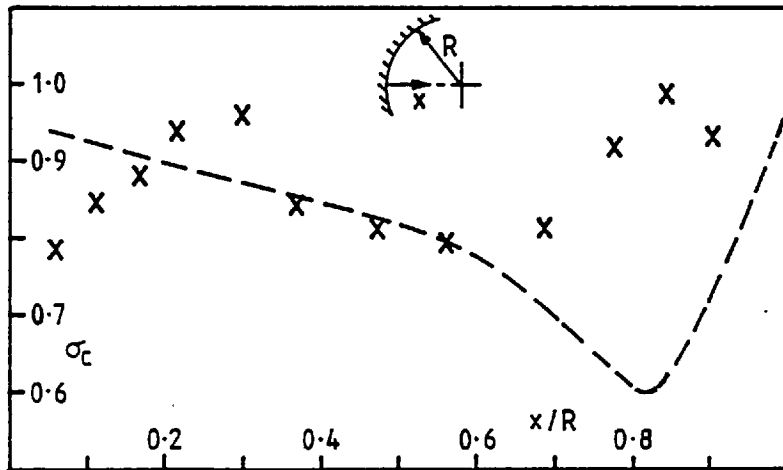


Figure 8.3.3 Eddy diffusivity in a circular tube with $P_r = 0.7$ and $Re = 71200$.



- X Experiment, water ($P_r = 6.2$), $Re = 43700$, Smith et al (1967)
 - - - Experiment, from the measurements of Laufer (1954) with $Re = 50000$ and Johnk and Hanratty (1962) with $Re = 71200$, air ($P_r = 0.7$)

Figure 8.3.4 Turbulent Prandtl number in a circular tube

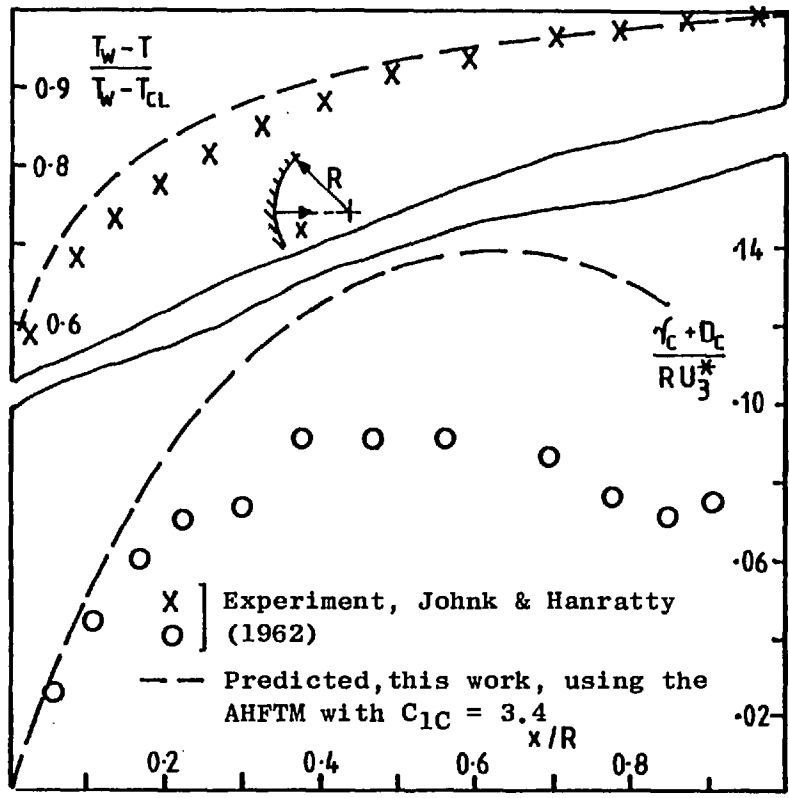


Figure 8.3.5 Temperature and eddy diffusivity profiles in a circular tube, predicted with the AHFTM with $C_{1C} = 3.4$ and $Pr = 0.7$. ($Re = 7.12 \times 10^4$)

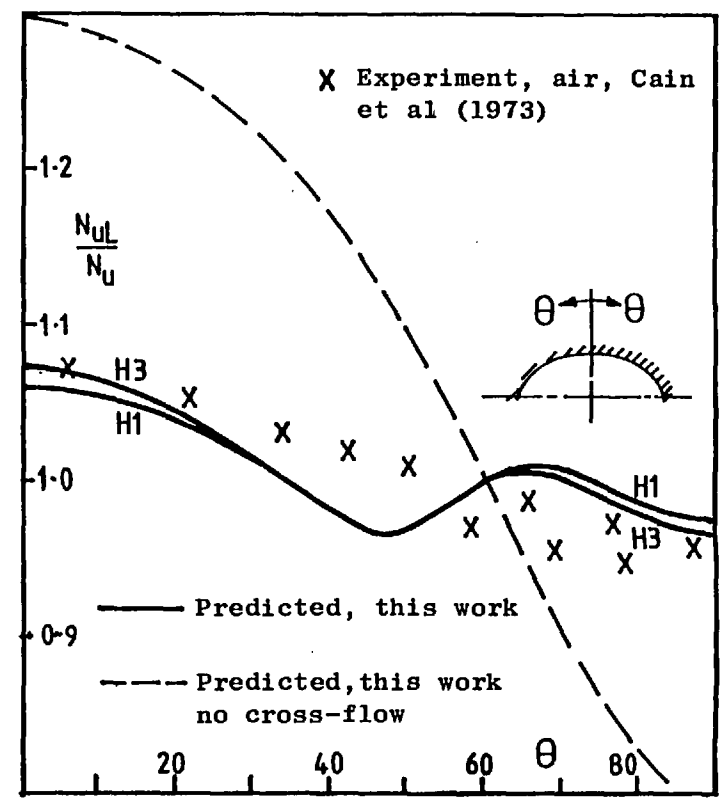
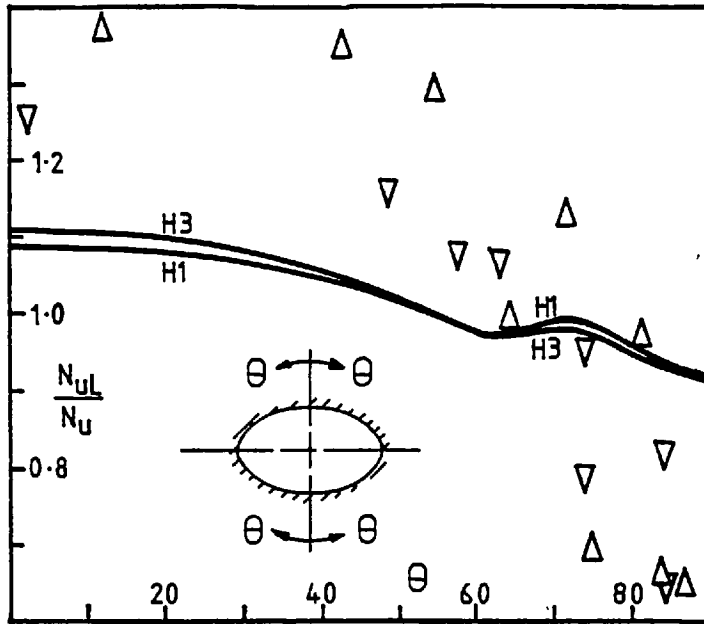
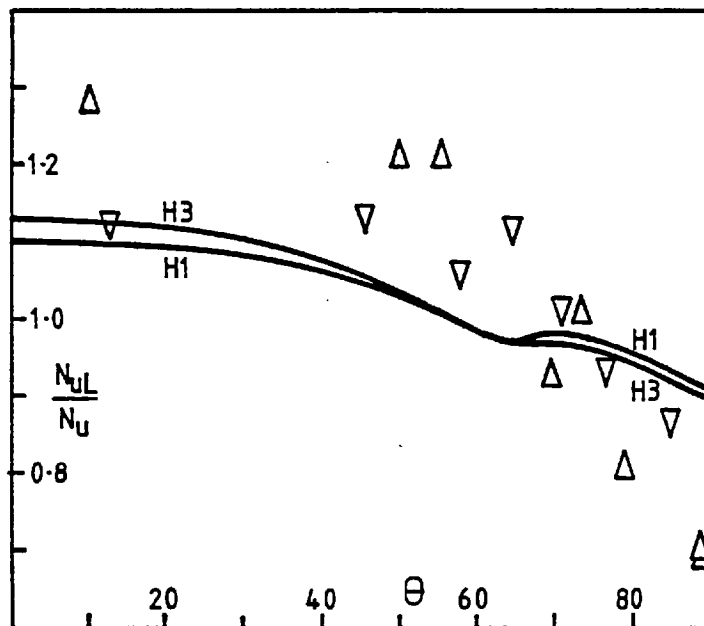


Figure 8.3.6 Local Nusselt numbers in an elliptical duct with $AR = 2$, $Pr = 0.7$ and $Re = 6.7 \times 10^4$.



(a) $AR = 8/3$ and $Re = 8 \times 10^4$



(b) $AR = 2.93$ and $Re = 6.47 \times 10^4$

Δ upper surface] Experiment, water, Cain et al(1973)
 ∇ lower surface]

— Predicted, this work, $Pr = 5$

Figure 8.3.7 Local Nusselt numbers in elliptical ducts with $AR = 8/3$ and 2.93 .

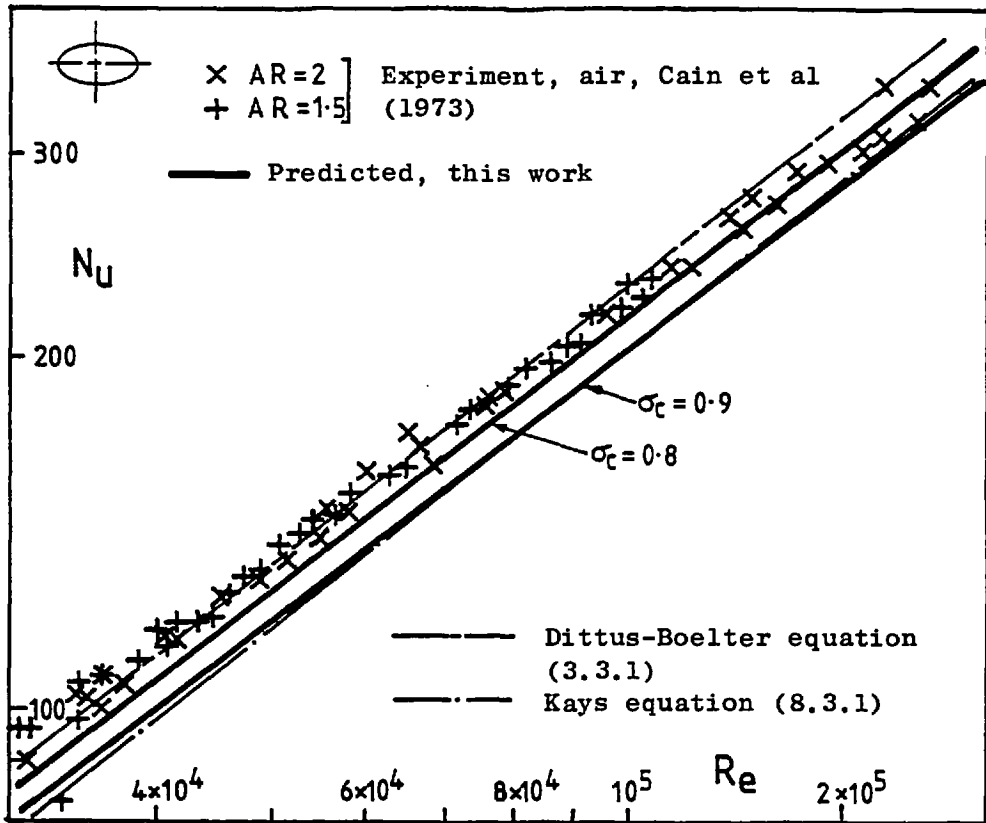


Figure 8.3.8 Mean Nusselt numbers in elliptical ducts with $P_r = 0.7$.

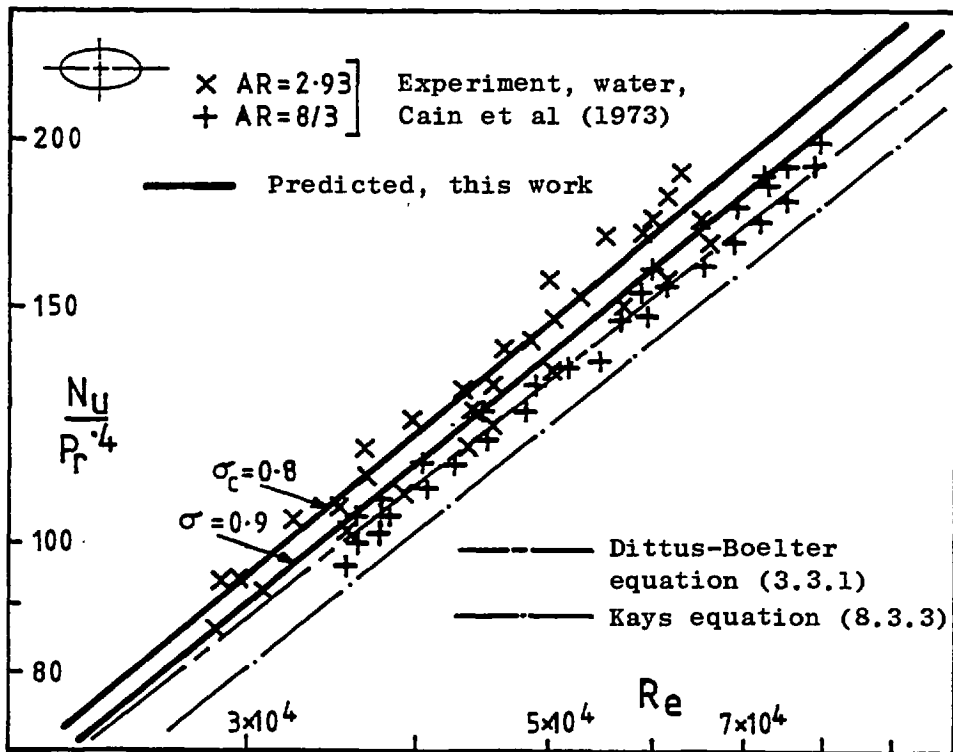


Figure 8.3.9 Mean Nusselt numbers in elliptical ducts with $P_r = 5.0$.

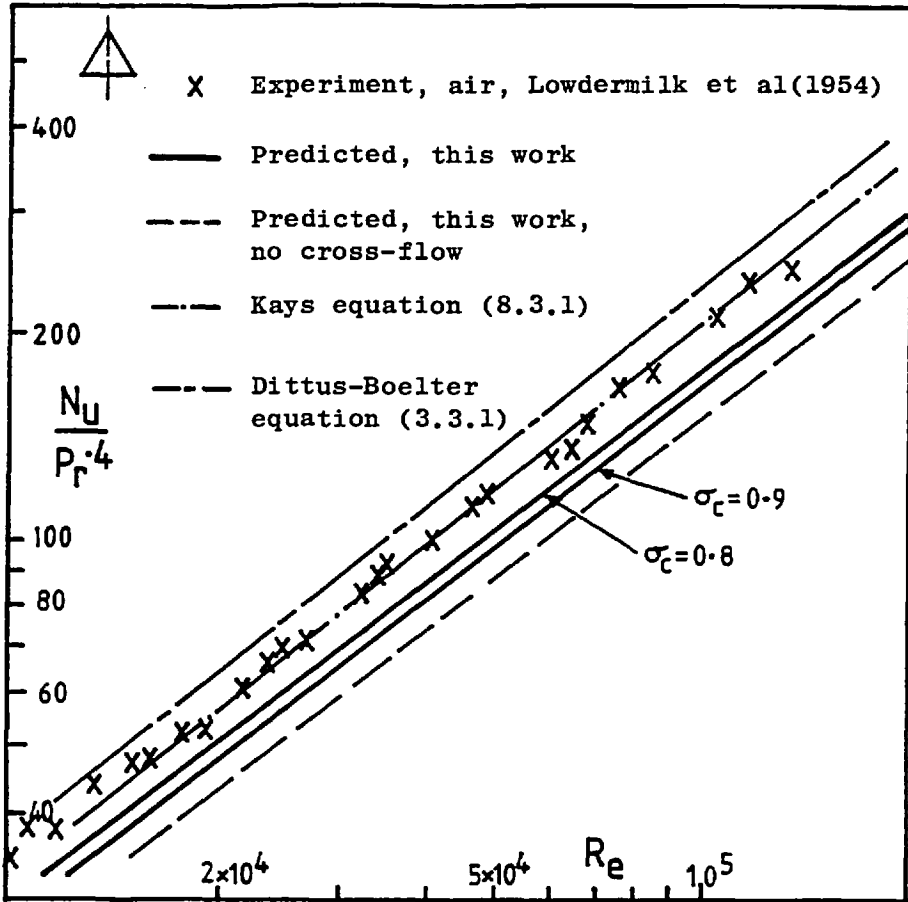


Figure 8.3.10 Mean Nusselt numbers in an equilateral triangular duct with $Pr = 0.7$.

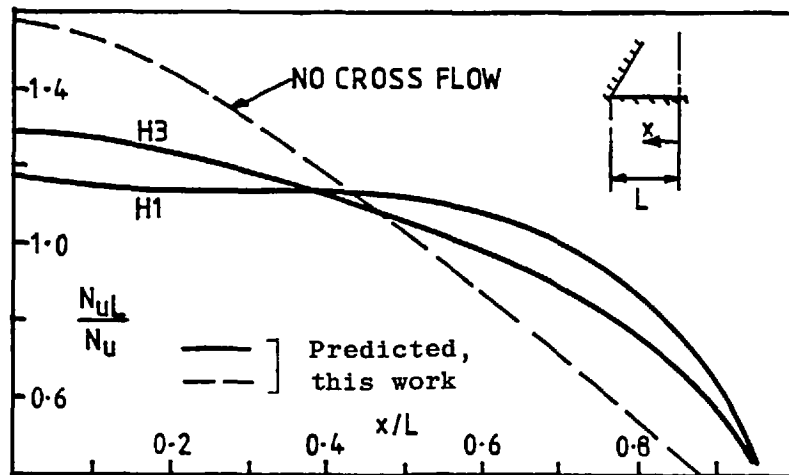


Figure 8.3.11 Predicted local Nusselt numbers in an equilateral triangular duct with $Pr = 0.7$.

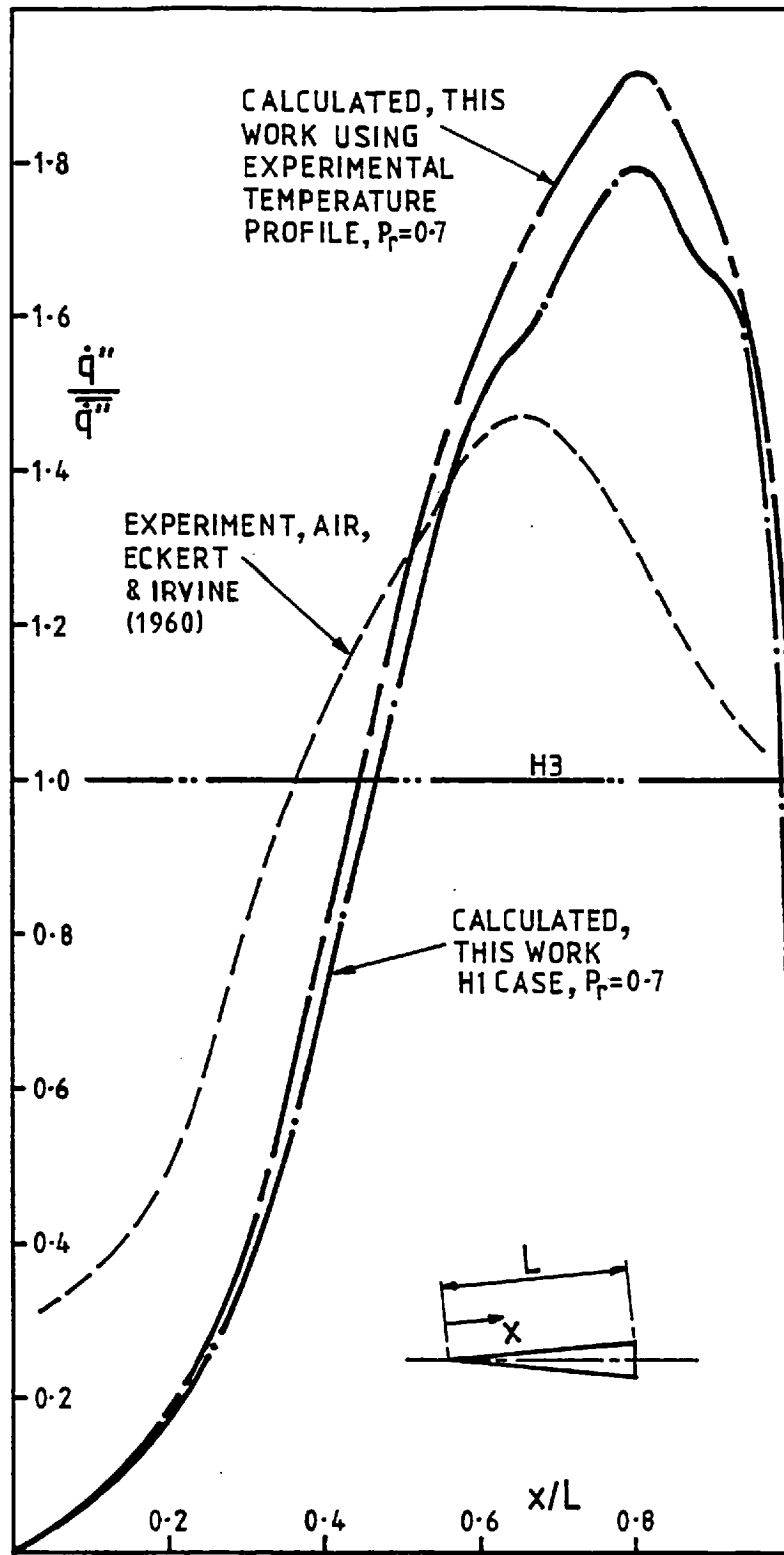


Figure 8.3.12 Peripheral heat flux in an isosceles triangular duct of apex angle 11.7° and with $Re = 1.5 \times 10^4$.

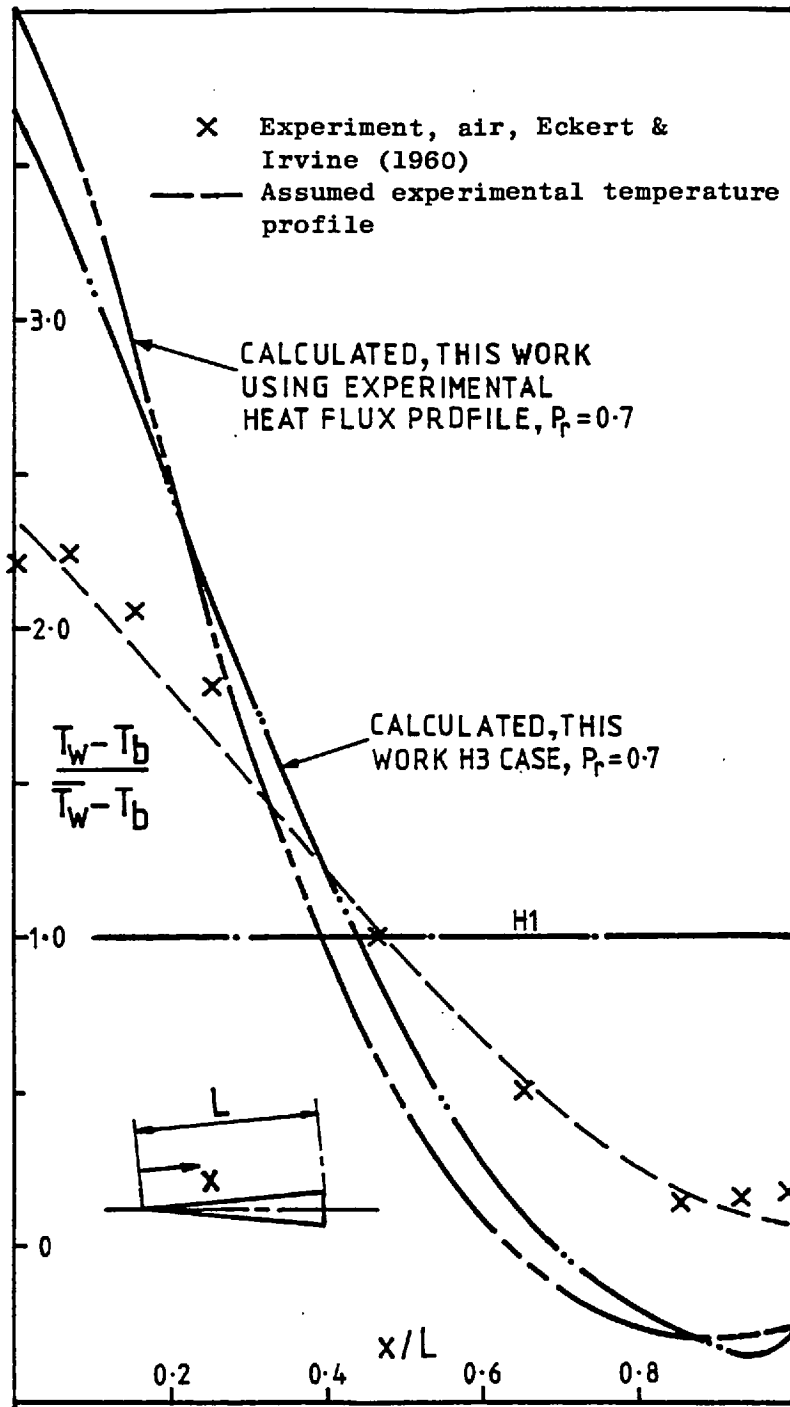


Figure 8.3.13 Peripheral wall temperature in an isosceles triangular duct of apex angle 11.7° .

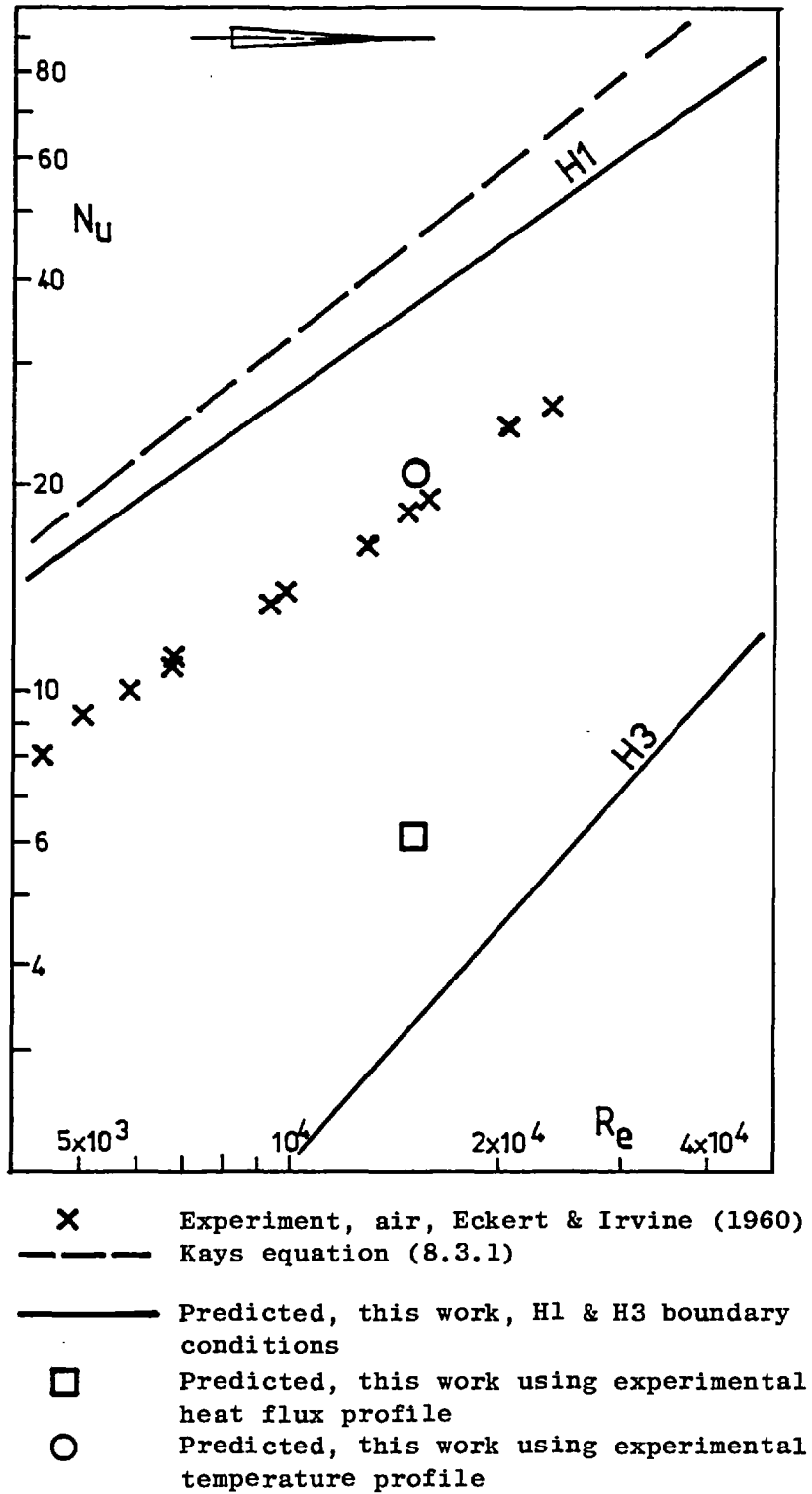


Figure 8.3.14 Mean Nusselt numbers in an isosceles triangular duct of apex angle 11.7° and with $Pr = 0.7$.

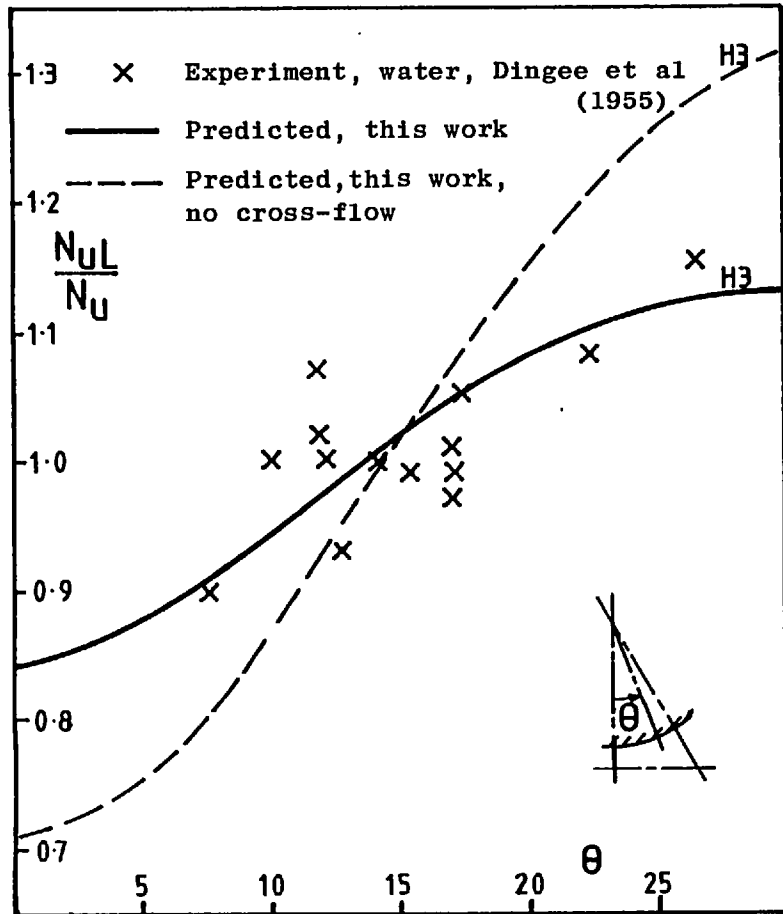


Figure 8.3.15 Local Nusselt numbers in a triangular array rod bundle with $P/D = 1.12$, $Pr = 1.75$ and $Re = 6 \times 10^4$.

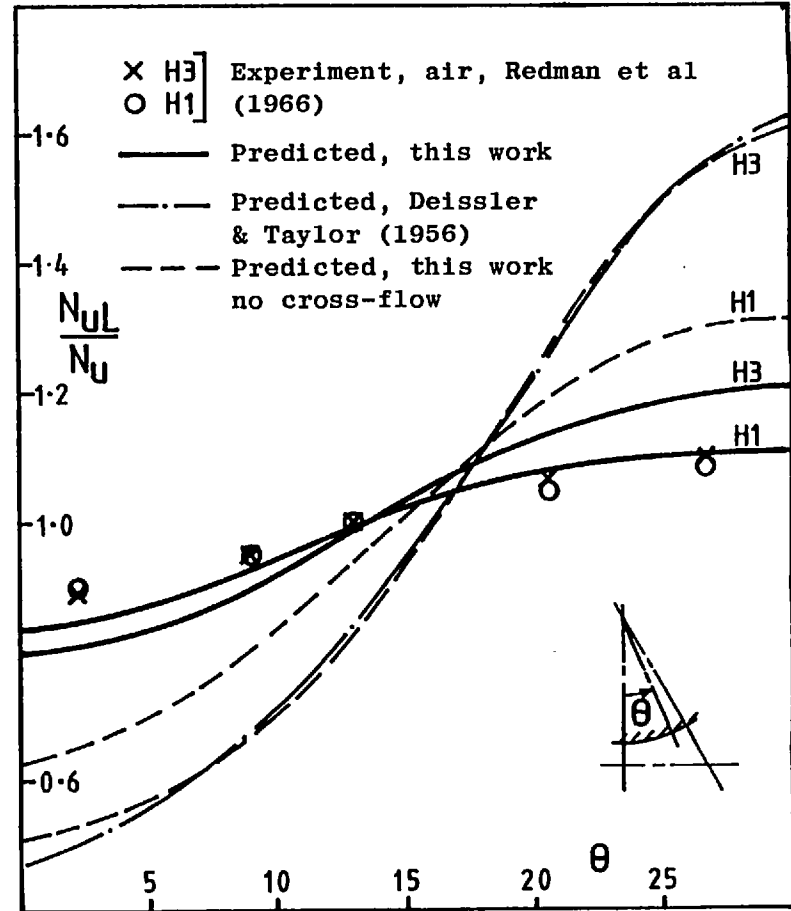


Figure 8.3.16 Local Nusselt numbers in a triangular array rod bundle with $P/D = 1.1$, $Pr = 0.7$ and $Re = 2.2 \times 10^5$.

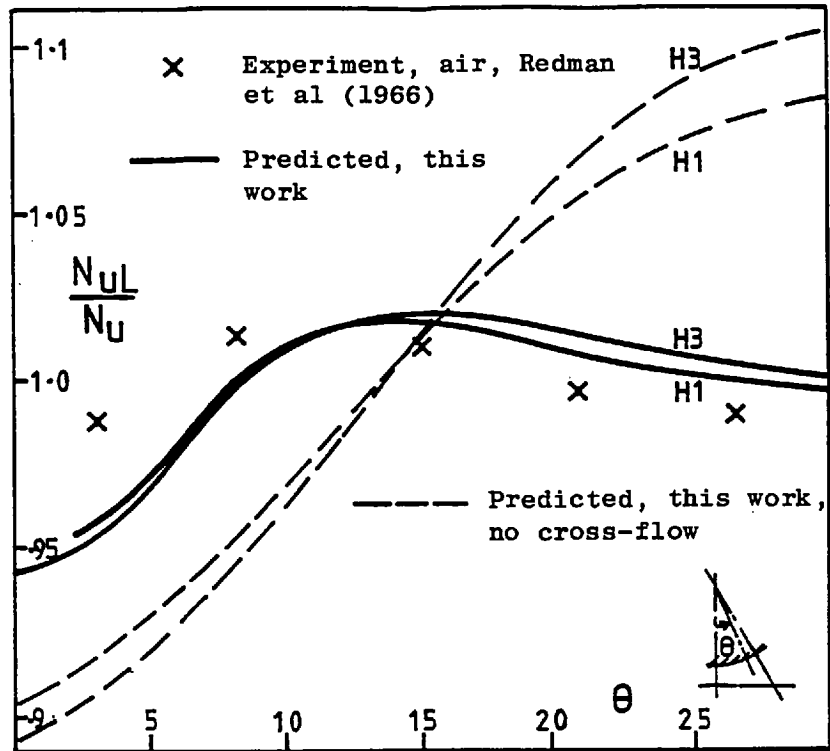
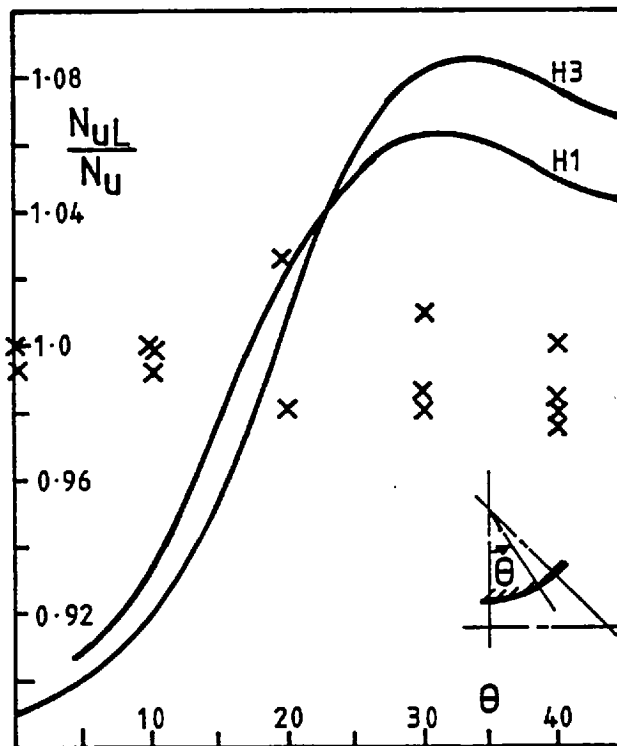


Figure 8.3.17 Local Nusselt numbers in a triangular array rod bundle with $P/D = 1.25$, $Pr = 0.7$ and $Re = 4.7 \times 10^5$.



x Experiment, air, Parrette & Grimble (1956)

— Predicted, this work

Figure 8.3.18 Local Nusselt numbers in a square array rod bundle with $P/D = 1.2$, $Pr = 0.7$ and $Re = 1.5 \times 10^5$.

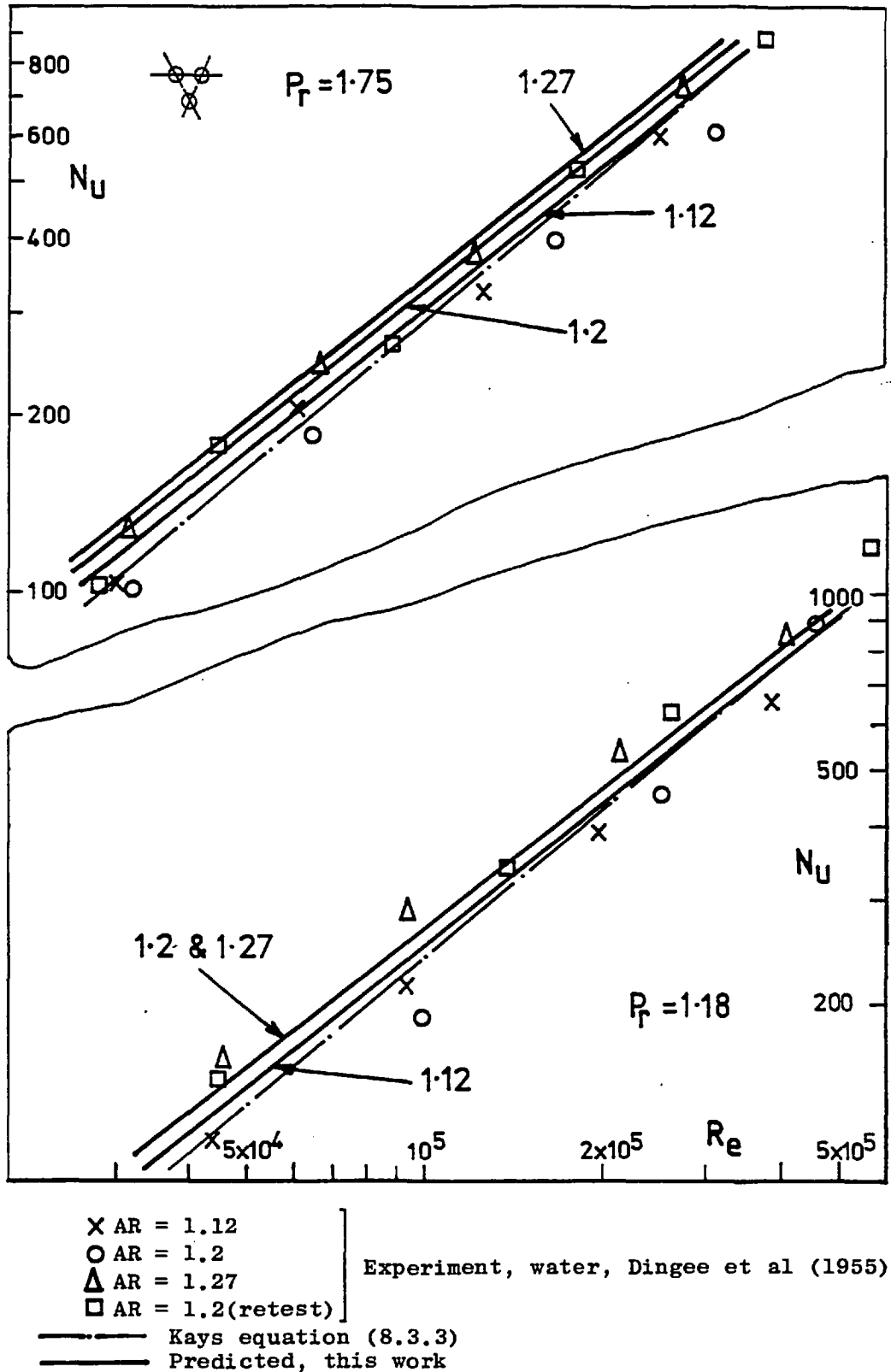


Figure 8.3.19 Mean Nusselt numbers in triangular array rod bundles with water flow.

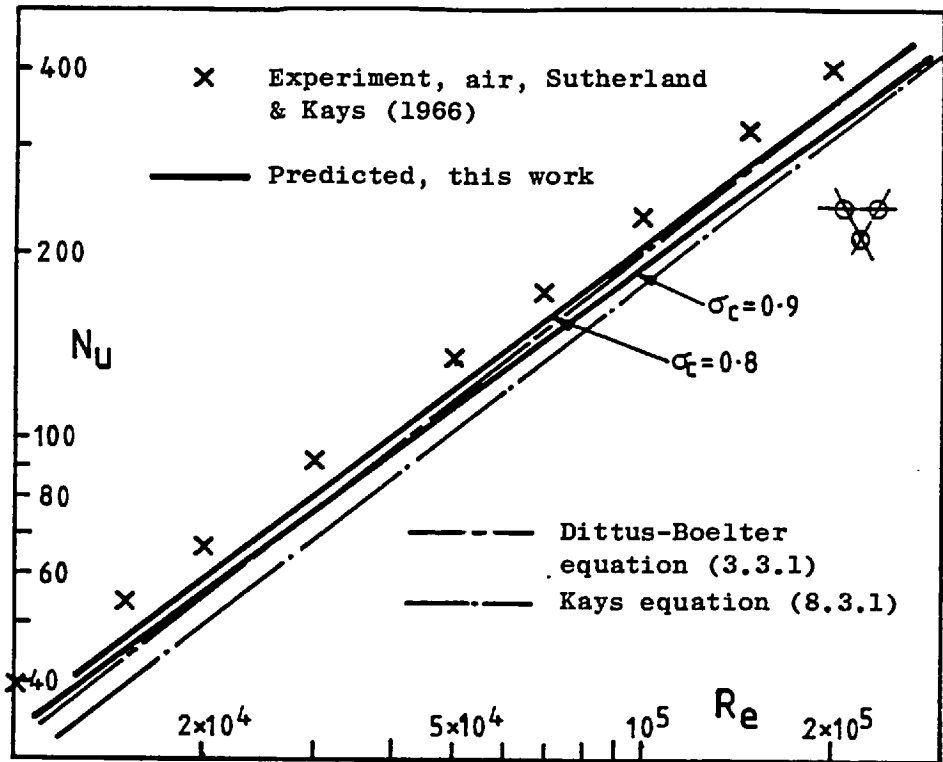


Figure 8.3.20 Mean Nusselt numbers for a triangular array rod bundle with $P/D = 1.15$ and $Pr = 0.7$.

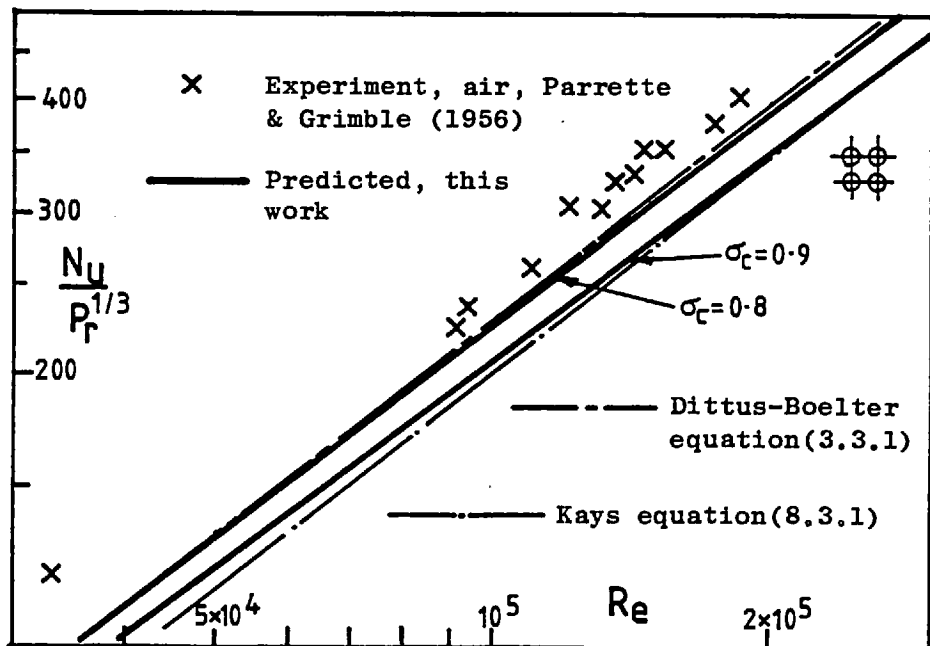


Figure 8.3.21 Mean Nusselt numbers in a square array rod bundle with $P/D = 1.2$ and $Pr = 0.7$.

- × Dingee et al (1955), water
- Miller et al (1956), water
- I Subbotin et al (1960), water
- Palmer & Swanson (1961), air
- + Subbotin et al (1964), water
- Redman et al (1966), air
- Sutherland & Kays (1966), air
- Kidd & Stelzmann (1968), air
- △ Borishanskiy et al (1971), water
- Markoczy (1972), air
- H Bobkov et al (1974), water
- ▽ Lel'chuk et al (1977), water

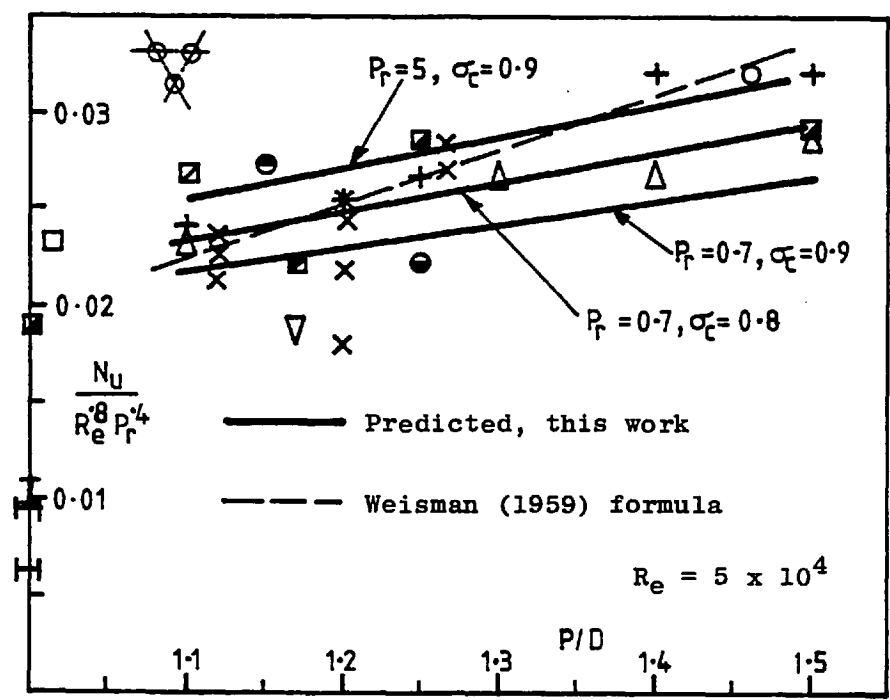
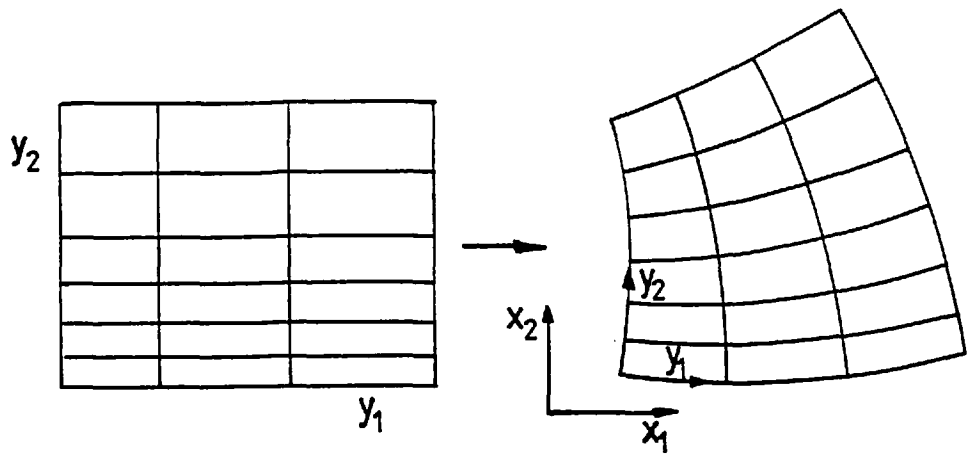
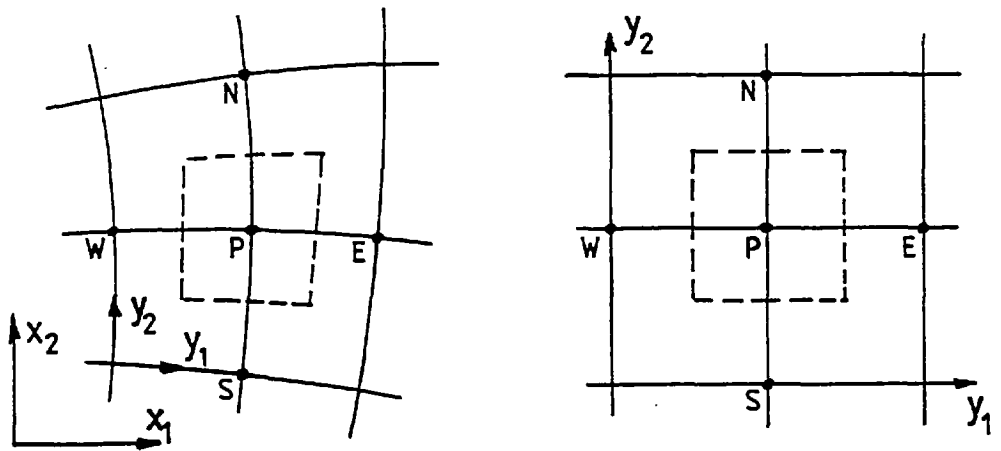


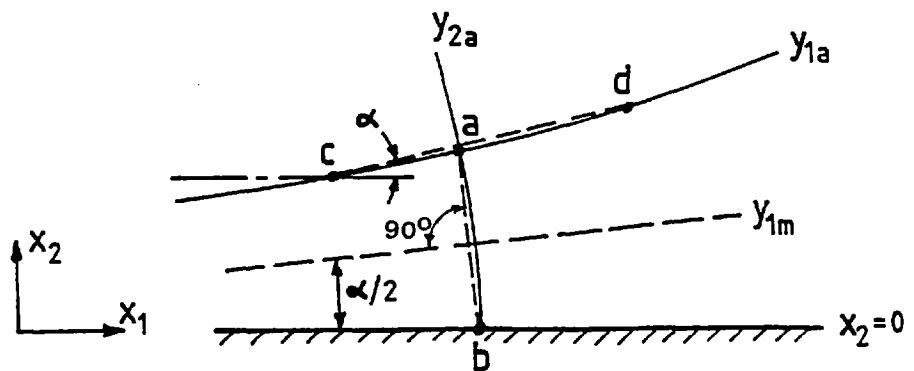
Figure 8.3.22 Mean heat transfer in triangular array rod bundles.



A5.1 The transformation



A5.2 Grid cells



A5.3 Boundary node

Figures A5 The grid generation procedure.